Analytical study of particle dark matter structuring on small scales and implications for dark matter searches

Gaétan Facchinetti

THÈSE POUR OBTENIR LE GRADE DE DOCTEUR
DE L'UNIVERSITE DE MONTPELLIER

En Physique

École doctorale : Information, Structures, Systèmes

Unité de recherche : Laboratoire Univers et Particules de Montpellier

Analytical study of particle dark matter structuring on small scales and implications for dark matter searches

Présentée par Gaétan Facchinetti
Le 5 juillet 2021

Sous la direction de Julien Lavalle

Devant le jury composé de

Pierre Salati, Professeur, LAPTh Annecy-le-Vieux & USMB	Président
Julien Lavalle, Chargé de recherche, LUPM Montpellier	Directeur
Shin'ichiro Ando, Associate professor, GRAPPA Amsterdam & IPMU Tokyo	Rapporteur
Pasquale Serpico, Directeur de recherche, LAPTh Annecy-le-Vieux	Rapporteur
Céline Boehm, Professor, University of Sydney	Examinatrice
Marco Cirelli, Directeur de recherche, LPTHE Paris	Examinateur
Jorge Peñarrubia, Professor, University of Edinburgh	Examinateur
Tracy Slatyer, Associate professor, MIT Boston	Examinatrice

UNIVERSITÉ DE MONTPELLIER

"Many things that seem threatening in the dark become welcoming when we shine a light on them."

Uncle Iroh character from Avatar: the last airbender and Legend of Korra

Remerciements

Je souhaite tout d'abord remercier Julien Lavalle pour avoir été mon directeur de thèse. Merci pout ton implication, pour ton suivi et ton aide dans le travail. Grâce à toi, j'ai pu m'imprégner de la richesse d'un domaine de recherche passionnant et y contribuer activement. Je suis aussi reconnaissant de l'opportunité que tu m'as donné de voyager à l'autre bout du monde (littéralement) pour présenter mes résultats. Merci de l'engagement dont tu as fait preuve pour que je m'intègre du mieux possible à la communauté. En outre, je n'oublierai jamais la dimension humaine, la bonne humeur et tous les bons moments passés en dehors du laboratoire. J'espère que nous pourrons encore longtemps collaborer ensemble. Je remercie aussi Martin Stref et Thomas Lacroix qui m'ont accompagnés dans les premiers mois de ce travail et avec qui j'ai toujours un immense plaisir de travailler, vous m'avez donné une incroyable impulsion pour débuter sur de bons rails.

I would like to thank now all the other members of the IFAC team at LUPM and L2C: Felix, Sacha, Cyril, Karsten, Vivian, Michele, Gilbert, Jean-Loïc, Loïc, Rupert, Mihael, Riccardo, Rodrigo, Marco. Not to forget Guillermo who managed to tolerate my ever-changing moods and my singing skills in the office during these last two years. All our meetings and (physics) discussions have always been very interesting and instructive. I would also like to address my thanks to Michel Rausch, David Conte, Robin Durocq and Vincent Vennin, for their warm welcome in Strasbourg and in the S.low.SUGRA group, and to the members of some recurrent work sessions not cited above, in particular Miguel A. Sánchez-Conde and David Maurin, for taking the time to discuss some of my preliminary results. I also thank all the GaDaMa members for the various discussions and lively meetings we had in the past three years. I will keep a fond memory of all the PhD students and post-docs I met during the conferences and schools I attended, may our path cross again in the future. I am very grateful to the members of my thesis committee, for accepting to judge this work. Special thanks to the rapporteurs for accepting to review the manuscript.

J'ai été extrêmement bien accueilli au LUPM et je remercie pour cela les membres de l'administration, de la logistique et des services informatiques, qui ont été d'une grande aide au quotidien, ainsi que les membres du conseil d'unité avec qui j'ai eu plaisir à interagir. Merci également aux membres de l'école doctorale pour leur accompagnement. Furthermore, I thank all the young researchers, PhD students and post-docs of the LUPM and L2C whom I have had the pleasure to meet. I enjoyed the very lively atmosphere you contributed to set inside and mostly outside the lab. Without you, these three years would have been substantially less fun. Let me mention those who have not been cited above: Michelle, Duncan, Loann, Justine, Ronan, Quentin, Stephan, Lorenzo, Lucien, Svetla, Atreyee, Gabriel and Maria. Merci à Guillaume et Eva pour avoir été des colocataires formidables.

Je me dois maintenant de remercier les soutiens de longue date, ceux qui m'ont donné la confiance, l'ambition de m'améliorer continuellement et qui m'ont surtout transmis leur bonne humeur et permis de garder une bonne santé mentale. Tout d'abord, tous mes amis de Ginette qui étaient là avant mes débuts en physique et qui sont encore activement présents dans mon quotidien: Nawel, Réda, Anton, Clément, Héloïse, Théo et Victor. Ensuite, mes amis de Cachan, les phytems: Romain, Julia, Mathilde, Pierre-Emmanuel, Xavier, et surtout ceux qui sont maintenant comme une deuxième famille: Alexandre, Lucie, Cyril, Matthieu, Maylis, Camille, Charles, Claire, Enzo, Flora, Guillaume (x2), Marie et Rémi. Nos escapades aux quatre coins de la France et de l'Europe, nos longues discussions, nos soirées et toutes les émotions que l'ont a vécu ensemble ont été d'immenses bouffées d'air frais et ce malgré les 586 km (au moins) qui nous ont séparés ces trois dernières années. Merci de m'avoir réconforté quand j'en avais besoin et de m'avoir fait rire (beaucoup) le reste du temps. J'espère vous avoir auprès de moi pour encore longtemps (et être le témoin de tous vos mariages). *I'll be there for you 'cause you're there for me too* comme ils disent. Enfin, je souhaiterais tout particulièrement remercier l'ensemble de ma vraie famille. Merci maman et papa de croire en moi et de m'avoir toujours soutenu dans mes choix, dans mes études et plus généralement dans ma vie. Merci à Amélie pour sa bonne humeur constante et à mon frère, Romain, pour avoir été une source d'émulation positive depuis notre tendre enfance.

Contents

I

Dark Matter, the missing mass problem and small scale issues

"From a drop of water," said the writer, "a logician could infer the possibility of an Atlantic or a Niagara without having seen or heard of one or the other. So all life is a great chain, the nature of which is known whenever we are shown a single link of it."

Arthur Conan Doyle, A Study in Scarlet

Contents

The issue of the origin and nature of the cosmological dark matter (DM) is one of the greatest puzzles of modern physics: it seems that most of the matter that makes up the Universe is something unknown and invisible, as if it only interacted gravitationally with everything else or as if our understanding of gravity itself was incomplete. After the first compelling observational hints for the presence of DM (whatever DM means), all relying on its gravitational effects, several interpretations and models have been proposed, some provide a sensible explanation of the observed phenomena and may also predict other signatures observable with multiple detection technique. Yet, no other direct proof outside from gravitational has been found so far. DM can actually mean different things, related to different interpretations of its gravitational imprints: modification of standard gravity, or a new form of matter. More specifically, in this thesis, we will be focusing on an aspect that mixes the subatomic and macroscopic properties of DM: the structuring of DM on small (subgalactic) scales. We shall review the conceptual aspects, develop an analytical model, and investigate the consequences of such a structuring for DM detection and constraints.

To place this work in context and elaborate on the motivations, in this introductory chapter we brush a broad picture of the DM issue, the proposed models and current associated constraints or problems. We first give some historical facts as well as more details on the original striking pieces of evidence for its existence. Then, we turn to the input of modern cosmology and we introduce the ΛCDM model and its successes. In a third part, we highlight the recent tensions arising in that paradigm. Afterwards, we review the different theoretical approaches developed in the last 50 years and we conclude by discussing the different detection techniques and the current status of DM searches.

Note that most of this chapter is addressed to a large audience. It has been written with the intention of making it accessible, as much as possible, to non specialists. Technical developments are then shown in the following four chapters.

1.1 The first proofs of the missing mass problem

In this section, we detail the different observations that first led to the idea of the existence of DM and its presence in the Universe, which took root between the 1920's and the 1980's. The bringing-in of the more recent development of precise observational cosmology will be treated in the following section. These introductory paragraphs aim to provide the reader with key chronological events. We also refer to BERTONE et al. (2016) and PEEBLES (2017) for extensive historical reviews.

1.1.1 Local dynamics

The search for dark celestial bodies with gravitational influence started around the middle of the 19$^{\text{th}}$ century. One of the most famous examples is the explanation of the anomalous motion of Uranus by Le Verrier in 1846 (LE VERRIER 1859; KOLLERSTROM 2006a,b) with another planet that had never been seen before and which is the now called Neptune. Subsequently, at the beginning of the 20$^{\text{th}}$ century Lord Kelvin introduced a new way to analyse astronomical observations by performing a thermodynamical study of stellar systems with the idea to evaluate the amount of possible dark bodies from the velocity dispersion of observable objects. Referring to this pioneering work of Lord Kelvin, in 1906 Henri Poincaré argued that the amount of dark matter around us was more probably smaller or similar to that of visible

matter (POINCARÉ 1906); incidentally coining the word under its French translation *matière obscure*.

About 20 years later, by improving on previous analysis, Oort evaluated the *local* (*i.e.* in the Solar neighbourhood) gravitational potential by studying the motion of nearby stars (OORT 1932). From his result he inferred the local density of matter, he compared it to the local density of stars and he concluded on the presence of dark bodies (referred to as nebulous or meteoric matter) saying that they should not make more than half of the total density with the limit $\rho_\odot \lesssim 0.05\ \mathrm{M}_\odot\,\mathrm{pc}^{-3}$. Today, evaluations of DM density in the local environment of the Sun have tremendously improved thanks to continuous upgrade of instrumental and observational techniques, as well as of data analysis techniques. The improved precision in the data also allowed the experts to use refined dynamical and kinematic descriptions of the relevant stellar ensembles, see READ (2014) for a review. Recent estimates give, $\rho \sim 0.4 \pm 0.1\ \mathrm{GeV\,cm}^{-3}$ (CATENA et al. 2010; PIFFL et al. 2014; MCMILLAN 2017) compatible and in agreement with Oort first upper bound. Besides, recent methods include constraints from global dynamical consistency (rotation curves, discussed in Sect. 1.1.3, and Galactic mass models) as well as local dynamical constraints (BOVY et al. 2012). Recent measurements come from the Gaia telescope (GAIA COLLABORATION 2018) that allowed for unprecedented precision in the stellar kinematics of stars located in a sphere of 10 kpc around the Sun – an example of evaluation of the local DM density using this new database is given in BUCH et al. (2019).

1.1.2 Galaxy clusters

The first convincing historical hint for the presence of DM (beside luminous matter) was made by Fritz Zwicky while observing the Coma cluster (ZWICKY 1933, 1937). To this end he used the virial theorem that we briefly detail. Let us consider a stably-bound system made of a collection of self-gravitating objects of masses m_i, at positions $\mathbf{x}_i$ and with velocities v_i. The total kinetic energy K and the total gravitational potential energy W are

$$K \equiv \frac{1}{2}\sum_i m_i v_i^2 \quad \text{and} \quad W \equiv \frac{G_\mathrm{N}}{2}\sum_{\substack{i,j \\ i\neq j}} \frac{m_i m_j}{|\mathbf{x}_i - \mathbf{x}_j|} \tag{1.1}$$

where G_N is Newton's constant. The virial theorem states that the averaged values of these two quantities are related via

$$2\,\langle K\rangle + \langle W\rangle = 0\,. \tag{1.2}$$

This equation can be used to relate the total mass M of the system to the velocity dispersion $\langle v^2\rangle^{1/2}$. Assuming that all objects have the same mass and that the system is isotropic, homogeneous and spherical with radial extension R one shows

$$\left\langle v^2\right\rangle^{1/2} \sim \sqrt{\frac{3}{5}\frac{G_\mathrm{N} M}{R}}\,. \tag{1.3}$$

In 1933, Zwicky observed 800 galaxies inside the Coma cluster. Using an estimate of their mass around 10^9 $\mathrm{M}_\odot$ he deduced the total mass as the sum of the galaxy masses. Then, adopting an estimate for the total size of the cluster (10^6 lyr) and using Eq. (1.3) he evaluated the velocity dispersion to be $\sim$ 80 $\mathrm{km\,s}^{-1}$. However,

the observed velocity dispersion was of the order 1000 $\mathrm{km\,s^{-1}}$. This discrepancy gave the first hint for the presence of an *invisible* source of mass in the cluster that he called *dunkle Materie* (dark matter) and that would enhance the dispersion. Subsequently, in 1937, he computed a *corrected* average mass $\overline{m}$ of the galaxies and found roughly $\overline{m} > 4.5 \times 10^{10}$ $\mathrm{M_\odot}$. While the estimation was incorrect because of systematic uncertainties on the expansion rate of the Universe, see Sect. 1.2 (more recent studies have shown that it is about a factor of 10 lower), the conclusion for the presence of DM still holds. Today, X-ray measurements are also used to precisely evaluate the quantity of intra-cluster ionised gas which emits via thermal bremsstrahlung. By measuring the gas temperature, around $T \sim 10^7$–10^8 K, and assuming hydrostatic equilibrium one can reconstruct its mass distribution and show that it only accounts for a fraction of the missing mass pointed out by Zwicky. See the reviews SARAZIN (1986), ROSATI et al. (2002), and ETTORI et al. (2013).

Let us finish by mentioning another method to estimate the masses of galaxy clusters, which has been more recently used and which relies on gravitational lensing, a general relativistic effect (MASSEY et al. 2010). Such a method was actually proposed by ZWICKY (1937), but the necessary observational data became available only in the 1980's. Here one uses the fact that, according to general relativity, masses curve space-time and deflect the trajectories of light, which are no longer seen as straight lines. To put it simply, dense objects in the Universe act as lenses for background photons. Two regimes can be distinguished. The first is *strong lensing*, where photons pass close to the lens and are sufficiently deflected to form several images of the background objects. A common realisation of this phenomenon is the creation of Einstein rings. When the foreground massive system is at least axi-symmetric all background sources in the same line of sight are seen forming a ring around it. For a system of mass M, the radius of this ring is called the Einstein radius and takes the following expression

$$r_\mathrm{E} = d_\mathrm{L} \left(\frac{4G_\mathrm{N}M}{c^2} \frac{d_\mathrm{LS}}{d_\mathrm{L} d_\mathrm{S}} \right)^{1/2} \tag{1.4}$$

where d_LS, d_L and d_S are the distances between the lens and the source, the observer and the lens and the observer and the source respectively. Therefore this expression provides a way to evaluate M from the measurement of all the other quantities. When axi-symmetry is only approximate one observes arcs instead of a full circle. The position and shape of these arcs can, nonetheless, be used to constrain the mass of the system. The first strong lensing event was reported in 1987 (SOUCAIL et al. 1987) but such events are now common with instruments like the Hubble Space Telescope *e.g.* in (JAUZAC et al. 2015). The second regime is *weak lensing* happening when the lens is offset from the source line of sight and emitted photons fly too far from the lens for their deflection to be directly detected. However the lens can still slightly distort the image of the background sources and considering multiple sources equidistant from the lens, their images are all distorted of the same amount. In that case, the idea is then to statistically analyse a sufficient amount of sources, seeking a coherent signal of distortion. In practice both regimes can be combined to reconstruct the mass distribution of clusters, strong lensing probing the central parts and weak lensing the outskirts (CACCIATO et al. 2006; HOEKSTRA et al. 2013).

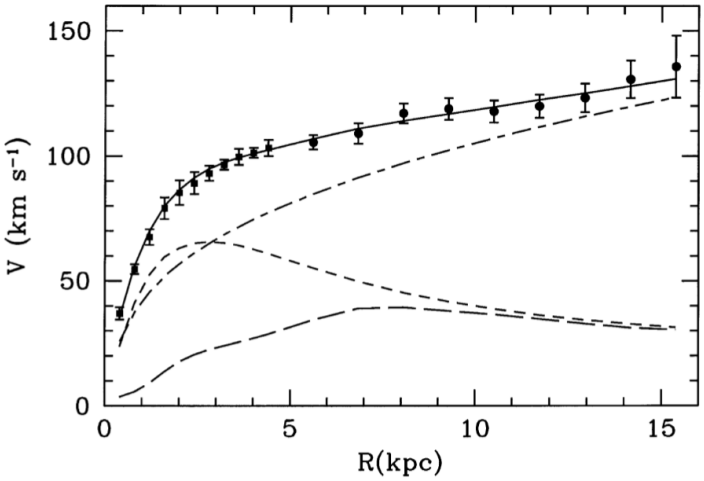

Figure 1.1 – Taken from (CORBELLI et al. 2000). Circular velocity with respect to the distance to the centre of the M33 galaxy. The points are the measured values with their error bars. The solid line is the total result from the model including DM. More precisely, the contribution of DM is shown in dash-dotted, the contribution of stars is shown in short dashes and the contribution of the gas in long dashes.

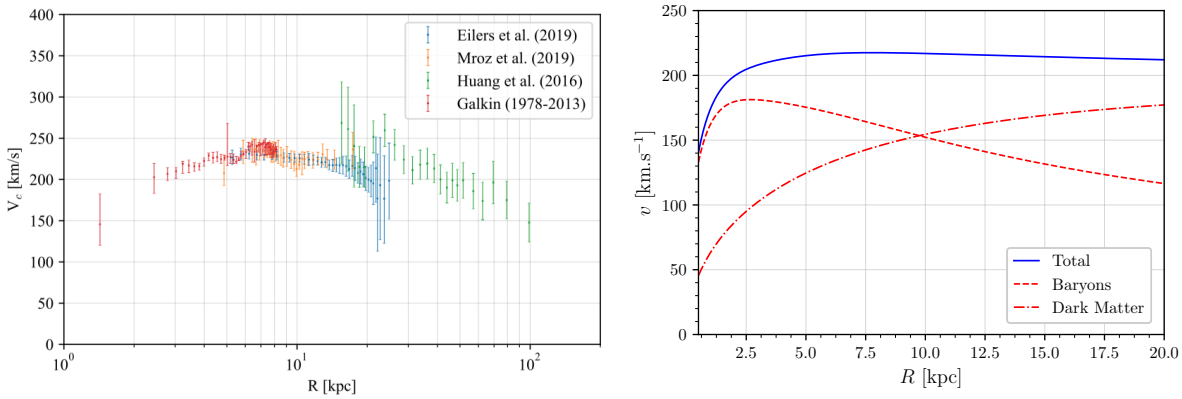

Figure 1.2 – Left panel: Rotation curve data points compiled in (PETAC 2020). The distance of the Sun to the galactic centre is taken as $R_\odot = 8.122 \pm 0.031$ kpc (except for the green point that are obtained considering $R_\odot = 8.34 \pm 0.16$ kpc). **Right panel:** Circular velocity for the Milky Way computed using a mass model picked from (MCMILLAN 2017) and *spherisizing* the stellar distribution.

1.1.3 Rotation curves

In spiral galaxies, in which the stars and gas concentrate in a disc whose stability is ensured by rotation, the measurement of the quasi-circular velocity of stars or gas as a function of their distance to the centre characterises a *rotation curve*. Astrophysicists noticed that theoretical predictions of rotation curves from Newton's law of gravitation[1] and observations mismatch, thus yielding compelling evidence of DM. In a very rough approach, if $\rho_b(\mathbf{r})$ represents the mass density of baryonic matter in a galaxy, by Newtonian dynamics one can approximately say that the circular velocity

[1] At these scales and for these objects the corrections of general relativity are negligible.

of an object at distance R from the centre is

$$v_c(R) \sim \sqrt{\frac{G_{\rm N}}{R}\int_{|\mathbf{r}|<R}\rho_{\rm b}(\mathbf{r})\mathrm{d}^3\mathbf{r}}\,. \tag{1.5}$$

Observations show that spiral galaxies are mainly composed of stars and neutral-hydrogen lying in a disc. Moreover one knows that both these two components have a mass density that decreases exponentially with the distance from the centre so that all the mass is approximately contained in the central region. For objects in the outskirts, it yields

$$v_c(R) \sim \sqrt{\frac{G_{\rm N}}{R}M} \propto R^{-1/2}\,, \tag{1.6}$$

with M the total inner mass. Therefore, the velocity should decrease with the radius R while direct measurements tend to show a flat asymptote. After the preliminary works of SLIPHER (1914), PEASE (1918), and BABCOCK (1939) this anomalous behaviour and its universality were highlighted in the 1970s. Firstly, Vera Rubin and Kent Ford refined the measurement of the rotation curve for the Andromeda galaxy in 1970, using the optical spectroscopy of ionized hydrogen (HII) emission regions (RUBIN et al. 1970). Secondly, in 1975, using the radio observations of the hyperfine 21 cm emission line of the hydrogen atoms (HI), the flat behaviour of the rotation curve was shown at larger distances (ROBERTS et al. 1975). This observation critically impacted on the discussion, giving a strong case for the potential presence of some unseen matter (FREEMAN 1970; ROGSTAD et al. 1972; WHITEHURST et al. 1972; ROBERTS et al. 1973) that should enhance v_c at large R. Subsequently, EINASTO et al. (1974) and OSTRIKER et al. (1974) also showed the similarities of the missing mass issue in galaxies and clusters; emphasizing its significance and linking it to a more generic cosmological anomaly. By the end of the 1980s little doubt was left about the existence of missing mass in galaxies, thanks to the work of Rubin's group and others who systematically analysed the rotation curves of several galaxies (BOSMA et al. 1979; RUBIN et al. 1980).

An example of the discrepancy between the observed and predicted rotation curves is illustrated in Fig. 1.1 for the M33 galaxy, it is so large that is barely alleviated by taking measurement uncertainties into account as shown by the error bars. Because of our position inside the MW it has always been more difficult to produce its rotation curve. However, the precision of the measurements has strongly increased since then and the implications for DM are getting clearer and clearer. In Fig. 1.2 taken from PETAC (2020) is a compilation of the latest observations for the MW used to constrain the DM distribution (see also IOCCO et al. (2015)). In the left panel of Fig. 1.2 the predicted rotation curve of the MW is shown with the contribution of baryons and dark matter, for a given mass model taken in (MCMILLAN 2017).

More broadly, similarly to what we have presented for galaxy clusters, it is also possible to directly study the velocity dispersion of stars and use the virial theorem in systems where the dynamical equilibrium is not set by rotation e.g. in (giant) elliptical galaxies or in (small) dwarf spheroidal galaxies. One then show that for any galaxy, whatever its morphology, an important amount of mass seems to be missing.

1.2 The input of cosmology

Cosmology is the study of the Universe as a whole and of its dynamics, which should be determined by its content and the general law of gravitation. The rigorous scientific and modern approach to this subject only begun in the 1920s when new powerful observational devices were put into service concomitantly to the appropriation of Einstein's General Relativity (GR) as a tool to understand the dynamics of the entire Universe. Using GR, Alexander Friedmann proposed in 1922 that the Universe necessarily was in an ongoing expansion. Two years later, in 1924, thanks to the new Hooker telescope of Mount Wilson, Edwin Hubble understood that many objects in space, which were taken to be nebulas, are in fact galaxies far beyond our own Milky-Way and he measured their velocities. Then, in 1927, Georges Lemaitre independently found the same result as Friedmann and with Hubble's observations, he was able to give an approximation of the expansion rate, which is commonly called the Hubble expansion rate H. In 1929 Hubble refined the evaluation of H. Cosmology was born and since then it has been in constant evolution thanks to new probes and more and more precise instruments and observations. Through times, observational data have improved both in quality and in quantity, and have progressively established the ΛCDM paradigm, which has been the standard cosmological model in vogue since the early 2000's. Let us give further details in the following.

1.2.1 A brief history of the Universe

Here we summarised the key concepts to understand the current cosmological observations and why they they are interpreted in terms of a large abundance of DM on large scales in the hot Big Bang model. A more formal introduction on cosmology is given in Chapter 2. As the Universe is in expansion one can look at its history back in time and inquire into the evolution of its size and content. If the expansion has never stopped until the current state, then the Universe must have been denser and denser at earlier and earlier times. As a matter of fact, at a critical point, it must have been so dense, that our current knowledge of the physical laws cannot even describe what happened before. Despite this limitation, it is common to imagine that the observed Universe was, at first, contracted to a singular point. In that fictitious framework, the moment back to this singular state is then called the Big Bang (BB), and conventionally defined as the 0 of our cosmic clock. One has motivated reasons today to think that, at early times, the Universe experienced a phase of *inflation* (accelerated expansion) sourced by one or several scalar fields, called inflaton. The inflaton then decayed into all the known species of elementary particles during a *reheating* phase. All the particles and radiation produced after inflation formed a hot dense plasma as the energy was such that they all interacted frequently. Note that the inflaton field also imprinted perturbations in the metric due to its quantum fluctuations and subsequently, inhomogeneities in the density fields. With the expansion of the Universe, interactions rarefied and the temperature decreased allowing for different changes in the particle content that were dictated by the particles nature/behaviour. Therefore let us now very briefly review the key events of the early Universe based on the current particle physics paradigm called the Standard Model (SM), which will be more precisely introduced in Sect. 1.4.2.

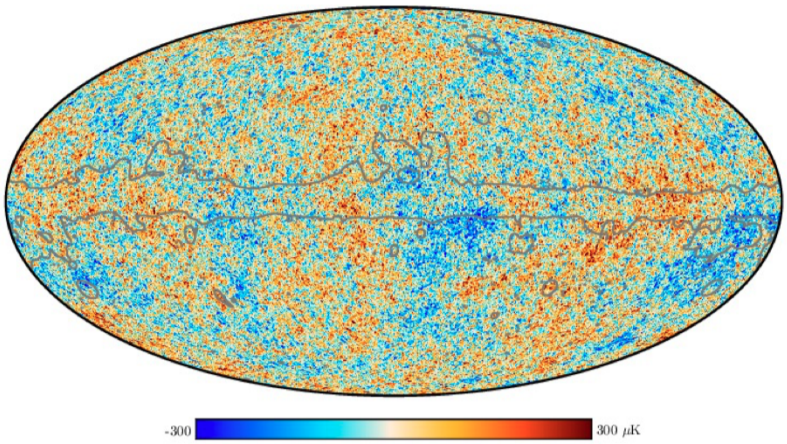

Figure 1.3 – Fluctuations of the CMB temperature around the average value – taken from (THE PLANCK COLLABORATION et al. 2020)

Approximately 20 ps after the BB, the electroweak phase transition gave a mass to the elementary particle when the Higgs field got trapped at the bottom of its potential well. Then, baryons (protons and neutrons) formed after the quantum chromodynamics phase transition when quarks got confined into hadrons, roughly 20 μs after the BB. Afterwards, at around 1 s, neutrinos, which only interacted weakly with the rest of the plasma, decoupled and slightly after, at around 6 s, electron and positron annihilated into photons according to $e^+ + e^- \leftrightarrow \gamma + \gamma$. After the annihilation, only the excess of matter over anti-matter remained[2]. Between roughly 10 s and 20 min the nuclei of light elements formed during the Big Band Nucleosynthesis (BBN). Afterwards, the amount of non-relativistic matter became dominant over the amount of radiation at a time called equivalence. From that point forward the small inhomogeneities in the matter density field started to grow. Eventually, electron and baryons assembled (essentially to form neutral hydrogen) at the *recombination* epoch through the process $e^- + p^+ \rightarrow \mathrm{H} + \gamma$, when the plasma temperature dropped below the binding energy $T \sim 0.3$ eV < 13.6 eV (at around 300 000 yr). Recombination freed previously interacting photons that were no longer energetic/hot enough to ionise the neutral gas. These photons have cooled down since then because of expansion, and form what is today observed as the cosmic microwave background (CMB). In the proper frame, CMB radiation is isotropic and follows a black-body distribution, a conclusive and compelling observational proof of the validity of the hot big bang model. Further statistical analyses of the fluctuations of the CMB temperature across the sky provide also decisive arguments as for the existence of a large amount of DM on cosmological scales. BBN and the measurement of the abundance of the light elements support the CMB observations. Subsequently began the dark ages where no more light was emitted in the Universe before the formation of the first stars and galaxies.

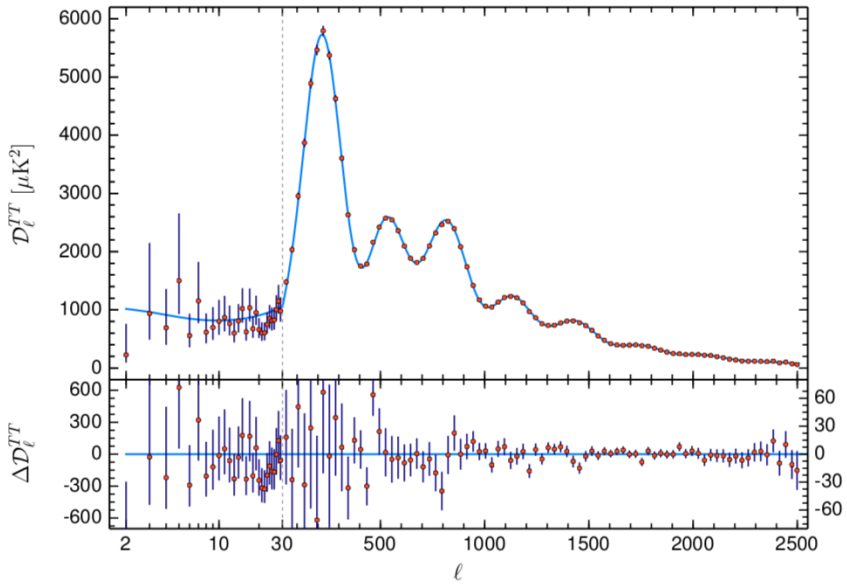

Figure 1.4 – Temperature anisotropy power spectrum of the CMB taken from (The Planck Collaboration et al. 2020) in the upper panel. The red points are the data while the blue curve is the best fit within the ΛCDM model. The agreement is remarkable as shown by the residuals in the lower panel.

1.2.2 The Cosmic Microwave Background

Henceforth, let us focus on the CMB and show how it confirms the existence of the missing mass problem on the cosmological scales. Thereafter we shall introduce in more details the ΛCDM model favoured by the CMB data. The CMB is a relic electromagnetic emission produced roughly 380 000 years after the BB. It had been theoretically predicted by (Alpher et al. 1948a,b; Gamow 1948a,b) and was observed for the first time, by accident, by Penzias and Wilson (Penzias et al. 1965) as a noise received by a 20-foot horn-reflector antenna at the Crawford Hill Laboratory in New Jersey. In the same issue of the Astrophysical Journal where the results were presented, Dicke et al. (1965) immediately identified this excess noise as the CMB. It originates from the recombination process that made the Universe electrically neutral. Indeed, before recombination, photons were in constant interaction with the baryons and electrons and the Universe was opaque. During recombination, they slightly decoupled and started to stream freely. Today one observes these photons emitted on a surface of the sky, the *last scattering surface*, as a nearly perfect black body with a temperature $\overline{T} = 2.72548 \pm 0.00057$ K (Fixsen 2009). However the distribution of temperature is not totally homogeneous and spatially fluctuates with an amplitude $\Theta(\mathbf{x}) = \delta T(\mathbf{x})/\overline{T} \sim 10^{-5}$ according to the position $\mathbf{x}$. The first experiment that measured the anisotropy was the COBE satellite (Bennett et al. 1996). The precision reached another level with the WMAP satellite launched in 2003 (Spergel et al. 2003) and today the most accurate map of the CMB temperature fluctuations is provided by the PLANCK satellite (The Planck Collaboration et al. 2020 – hereafter refereed to as Planck18). These anisotropies are the imprints, on the primordial photon bath, of the

[2]The matter excess over antimatter is an observational fact that is currently not explained in the context of the standard model of elementary particles. Current theoretical understanding relies on baryogenesis scenarios (including baryogenesis via leptogenesis), and demands particle physics beyond the standard model – see Cline (2006) and Davidson et al. (2008) for reviews.

primordial matter fluctuations that led to the formation of structures (Y. B. ZELDOVICH et al. 1969; PEEBLES 1982a,b) and they are a consequence of the baryon acoustic oscillations (BAO). Indeed, when baryons and photons were tightly coupled in a single fluid thanks to Thomson scattering between photons and electrons, light could produce an enormous pressure force on the baryons. In the meantime, there were density fluctuations (possibly stemmed from the inflaton, as seen above). Baryons were naturally prone to concentrating the fluid into the potential wells of the overdensities while photons were tending to expel it: there was a competition between pressure and gravity that gave rise to sound waves. The 0^{th} moment (monopole) of temperature fluctuations Θ_0 is proportional to the density contrast of baryons and photons and was governed, in the Fourier space, by the equation (DODELSON 2003)

$$\frac{\partial^2\Theta_0}{\partial t^2} + H(t)\left(1 - 3c_s^2(t)\right)\frac{\partial\Theta_0}{\partial t} + k^2c_s^2(t)\Theta_0 = F(k,t) \tag{1.7}$$

where F is a force term that is induced by the gravitational potential, c_s is the sound speed in the fluid and H is the expansion rate. This is an equation for wave propagation in real space with a force term and a friction term (*i.e.* a damped harmonic oscillator in Fourier space). It shows that the photons pushed the baryons out of the potential wells *i.e.* in a sound wave travelling at the velocity c_s so that the positive perturbations in the baryon-photon fluid density spread out of their original position. After a time t_{drag}, photons decouple and recombination occurs, freeing baryons from the radiative pressure. The shell of baryons had travelled a *comoving* distance $r_{\text{drag}} \sim 150$ Mpc defining a specific length scale. Other physical effects imprint on the CMB, like the Sachs-Wolf effect (SACHS et al. 1967) or the Sunyaev-Zeldovich effect (SUNYAEV et al. 1970), which we do not discuss here. We will rather focus now on the implications for DM. A detailed treatment of CMB is given in (DODELSON 2003; HU 2009; PETER et al. 2013; BAUMANN b) and a review on BAO can be found in (EISENSTEIN et al. 1998).

To extract the relevant statistical properties of the matter field at recombination, one actually recasts the skymap of CMB temperature fluctuations in terms of its the angular correlations. This is parametrised by expressing the temperature contrast as a function of a direction characterised by a unit vector $\hat{\mathrm{n}}$, and by expanding the underlying angular correlations over spherical harmonics. The associated two-point correlation function reads

$$\langle\Theta(\hat{\mathbf{n}})\Theta(\hat{\mathbf{n}}')\rangle = \sum_{\ell=0}^{\infty}\frac{2\ell+1}{4\pi}C_\ell P_\ell(\hat{\mathbf{n}}.\hat{\mathbf{n}}') \tag{1.8}$$

where the factor C_ℓ represents the power spectrum and P_ℓ is the Legendre polynomial of order ℓ. In the end, the commonly displayed value is $\mathcal{D}_\ell = \ell(\ell+1)C_\ell/(2\pi)$, as shown in Fig. 1.4. The data (red dots) exhibit 8 peaks with specific positions separated by $\Delta\ell \sim 300$ which is directly related to the *comoving* size $r_{\text{drag}} \sim 150$ Mpc. The shapes of these peaks is related to the matter content of the universe at recombination, and points to the need of a very large fraction of DM. Indeed the presence and amount of DM only impacts the value of the force term F in Eq. (1.7) since it only interacts gravitationally, while the amount of baryons impacts both c_s and F. The exact solution of this equation is not trivial, nevertheless it turns out that, because of this double dependence, it is impossible to properly recover the shape of the peaks simply by playing with the density of baryons, assuming that general relativity is reliable on these scales.

Figure 1.5 – Hubble eXtreme Deep Field observations. The figure is separated vertically in the middle: real observation on the left and mock observation from the Illustris collaboration (VOGELSBERGER et al. 2014) on the right.

Another convincing argument for DM is provided by the decreasing tail at large multipole ℓ. This behaviour is caused by diffusion damping (also called Silk-damping – SILK 1968) due to the imperfection of the photon-baryon fluid before recombination. Indeed, on typical distances $(n_e\sigma_{\rm T})^{-1}$, where n_e is the electron density and $\sigma_{\rm T}$ the Thomson scattering cross-section, photons stream freely. On typical times H^{-1} they encounter $n_e\sigma_{\rm T}cH^{-1}$ electrons and diffused in a random walk over a length $\lambda_{\rm D} \sim (n_e\sigma_{\rm T}cH)^{-1/2}$. Therefore on scales smaller than this typical distance photons do not follow the sound waves, thus smoothing out the temperature fluctuations. This translates into a drop in the correlation function at small scales. Without the presence of a component that interacts mostly gravitationally, the large-ℓ peaks would have vanished. The interaction of DM and photons is therefore constrained (BOEHM et al. 2002; BOEHM et al. 2005).

1.2.3 Structure formation

Beside the observational hints discussed above, all potentially interpreted in terms of its gravitational influence, the ubiquitous presence of DM, able to efficiently respond to the gravitational perturbations seeded by inflation, further provides the most fundamental ingredient to our current theoretical understanding of structure formation. It also provides us with a clear understanding as for why galaxies and galaxy clusters are embedded into extended DM halos. In the meantime, this gives a natural explanation to the previously discussed anomalies. In that picture, after recombination, DM, which dominates the energy budget of the Universe, drives the growth of the matter density fluctuations that survived the early epoch. After some time the over-dense regions become dense enough to collapse and virialise and they form bound objects called DM halos (MO et al. 2010). All the structures seen were then formed by the baryons falling in the middle of the halos, reaching a sufficient density to initiate star formation. To emphasize on this point, including CDM in cosmological numerical simulations of the Universe (SPRINGEL et al. 2005, 2008; DIEMAND et al. 2011; VOGELSBERGER et al. 2014) has provided replicas of galaxies or galaxy clusters with an exquisite resemblance. This is shown first in Fig. 1.5 by comparing a patch

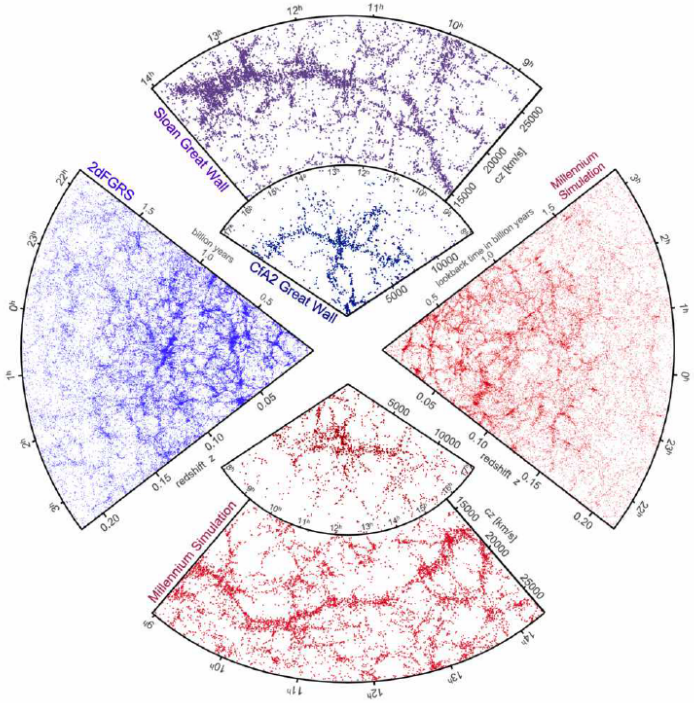

Figure 1.6 – Galaxy distribution in redshift from galaxy redshift surveys compared to the result of the Millenium simulation, taken from (SPRINGEL et al. 2006).

of the sky seen by the Hubble telescope with a mock version given by the Illustris collaboration. Secondly we also show in Fig. 1.6 the remarkable agreement between the galaxy distribution obtained in the Millenium simulation (SPRINGEL et al. 2006) and the one observed in galaxy surveys CfA2 (GELLER et al. 1989), 2dFGRS (COLLESS 1999) and SDSS (AHUMADA et al. 2020).

Furthermore, because of the different observations of the matter distribution in the Universe, one has to consider that the DM component is pressure-less and highly non-relativistic well before matter-radiation equivalence in order to understand the presence of clustering on the smallest scales observed. Indeed, DM particles with high velocity in the early Universe would have had time to free-stream out of the smallest over-dense region, smearing them out, before their growth. In other words, this effect induces a cut-off on the power spectrum (the two-point correlation function of the matter density) at small scales. The current constraints allow for models that are then called warm or cold DM (WDM or CDM). The latter option corresponding to the smallest velocity dispersion is the favoured one.

Eventually, let us mention that BAO does not only leave an imprint in the CMB ,but also in the galaxy distribution at low redshift observed by galactic surveys. The BOSS (SDSS-III) collaboration (ROSS et al. 2017) in particular has shown a correlation peak on comoving scales of the order ~ 150 Mpc in agreement with the CMB value, providing another argument in favour of DM.

1.2.4 The ΛCDM model

The CMB data is well fitted by a six-parameter model called ΛCDM that describes the Universe as expanding and flat and comprising baryonic matter, CDM and dark energy – parametrised as a cosmological constant Λ. The power spectrum of the

temperature fluctuations given by the best fit on this model is represented by the blue line in Fig. 1.4 and is in remarkable agreement with the data. The six parameters of ΛCDM are

- $\Omega_{\mathrm{b},0}$: the relative (to the critical density) abundance of baryons today
- $\Omega_{\mathrm{c},0}$: the relative abundance of CDM today
- h : the reduced Hubble expansion rate today
- $\mathcal{A}_s$: the amplitude of the initial power spectrum
- n_s : the spectral index of the initial power spectrum
- τ : the reionization optical depth

In the following chapters of this thesis we will make use of, and then further discuss, all parameters but the reionization optical depth. In this section we focus on the first thee only. The reduced Hubble expansion rate h is given by the ratio of the Hubble expansion rate today, denoted H_0, over a typical rate of 100 km.s^{-1}.Mpc^{-1}. From CMB data analyses, the Planck Collaboration has inferred a value of $h = 0.6736 \pm 0.0054$ (at a 68% confidence level – Planck18). Moreover according to the same Planck data analysis the abundances multiplied by the Hubble rate squared are $\Omega_{\mathrm{c},0}h^2 = 0.1200 \pm 0.0012$ and $\Omega_{\mathrm{b},0}h^2 = 0.02237 \pm 0.00015$. In a flat Universe the sum of the abundances of baryonic matter, radiation, CDM and dark energy $\Omega_{\Lambda,0}$ sum up to 1. Therefore giving the proportion of the three components

$$\Omega_{\mathrm{b},0} = 4.9\%\,, \quad \Omega_{\mathrm{c},0} = 26\%\,, \quad \text{and} \quad \Omega_{\Lambda,0} = 69\%\,. \tag{1.9}$$

This result tells us that on the scale of the Universe the ratio of DM over the total amount of matter is of order 84%. Consequently, not only do CMB data also points to the existence of DM but they also ascertains that it has to be the dominant form of matter.

1.2.5 Big Bang Nucleosynthesis

Approximately 10 s after the Big Bang the lightest elements, D = ^{2}H, T = ^{3}H, ^{3}He, ^{4}He, ^{7}Li, ^{7}Be, start to form thanks to the specific thermodynamical conditions (pressure, density, temperature, neutron lifetime) at that time. This period of light elements synthesis is called Big Bang nucleosynthesis, as opposed to stellar nucleosynthesis which will take place much later and will form heavier nuclei. See (Sarkar 1996) and (Olive et al. 2000) for reviews. Heavier elements having been produced much later in the centre of stars by nuclear fusion. The light element with the highest binding energy is the helium-4, however, it cannot be formed directly via 4 body interactions as the number density of photon n_γ is much higher than the number density of baryons n_{b} at that time. Therefore the chain of interactions was made of $2 \to 2$ processes

$$\begin{gathered} \mathrm{p + n} \to \mathrm{D} + \gamma \\ \mathrm{D + p} \to {}^3\mathrm{He} + \gamma, \quad \mathrm{D{+}D} \to \mathrm{p + T}, \quad \mathrm{D{+}D} \to {}^3\mathrm{He + n} \\ \mathrm{T{+}D} \to {}^4\mathrm{He + n}, \quad \mathrm{T{+}}{}^4\mathrm{He} \to {}^7\mathrm{Li} + \gamma \\ \dots \end{gathered}$$

The first one corresponds to the formation of deuterium, necessary to launch the chain. Interestingly, this process is very sensitive to the baryon-to-photon ratio $\eta = n_{\rm b}/n_\gamma \sim 10^{-10}$. Indeed, deuterium forms when the temperature of the plasma was around $T \sim 1$ MeV. However, the binding energy of deuterium being small ($E_{\rm b} \sim 2.2$ MeV), its production is prevented by the overwhelming abundance of photons, whose energy distribution tail destroys deuterium too efficiently before helium can be produced. As the photon temperature decreases to ~ 0.1 MeV, deuterium can remain longer in the plasma and its increasing fraction activates helium production. The final amount of deuterium present in the Universe can be seen as a leftover of the reaction that stopped when the temperature became too low; consequently, it is very sensitive to the initial conditions and η. That yields an interesting indirect probe of the baryon abundance even though measuring the primordial amount of deuterium in the Universe is challenging.COOKE et al. (2018) give $\eta = (5.931 \pm 0.051) \times 10^{-10}$ and $\Omega_{\rm b,0}h^2 = 0.02166 \pm 0.00015 \pm 0.00011$, independently confirming the value found with the CMB – at $2\,\sigma$ in this study. This value is too low to explain on its own the total matter content of the Universe it indirectly points towards the necessity of an additional exotic matter component.

1.3 The tensions in the ΛCDM paradigm

In the previous section, we have introduced the concept of DM and the ΛCDM model and mentioned its successes. However, for a few years, the ΛCDM model has been questioned by different observations. This thesis develops in the context of the small scale issues but for the sake of completeness, we start by discussing the large scale tensions that are also relevant for DM.

1.3.1 The large scale tensions

The Hubble tension. In Sect. 1.2.2 we gave the value of h inferred from CMB data analyses. However, this quantity can also be evaluated through late-time observations using the same method as that of Hubble first attempted. Using type 1A supernovae and cepheids as standard candles it is possible to determine our distance to remote galaxies. Plotting the galaxy population in a graph showing velocity against distance, the shape of the curve obtained is directly related to h. A combined analysis of datasets of supernovae finds an expansion rate of $h = 0.736 \pm 0.0039$ (RIESS et al. 1998; VERDE et al. 2019) with a discrepancy of $\sim 5\sigma$ with the Planck value. Such a difference indicates either systematics in the data or in the chain of analysis of one of the two experiments as suggested in (RIGAULT et al. 2015) or the signature of departure from the ΛCDM model and a hint for new physics. Therefore several models have been proposed to alleviate the tension (DI VALENTINO et al. 2016; KUMAR et al. 2016; RENK et al. 2017; POULIN et al. 2019; BANIHASHEMI et al. 2020) but their viability is challenged by the BAO and CMB observations. As of today, none of these models is significantly preferred, thus future observations will probe them further.

The S_8 tension. One defines by σ_8 the (square root of) the variance of the matter power spectrum on scales of the size $8h^{-1}$ Mpc^{-1}. The quantity S_8 is proportional to it, as defined by $S_8 = \sigma_8(\Omega_{\rm m,0}/0.3)^{0.5}$. Similarly to h this quantity can be derived both from the six ΛCDM parameter fitted on the CMB and from late time observations. The joint analysis KIDS1000+BOSS+2dfLenS has given $S_8 = 0.766^{+0.020}_{-0.014}$ (HEYMANS et al. 2020) while the value inferred from Planck is $S_8 = 0.832 \pm 0.013$ with a $\sim 3\sigma$ discrepancy between the two. This also is interesting for DM as it also suggests the potential

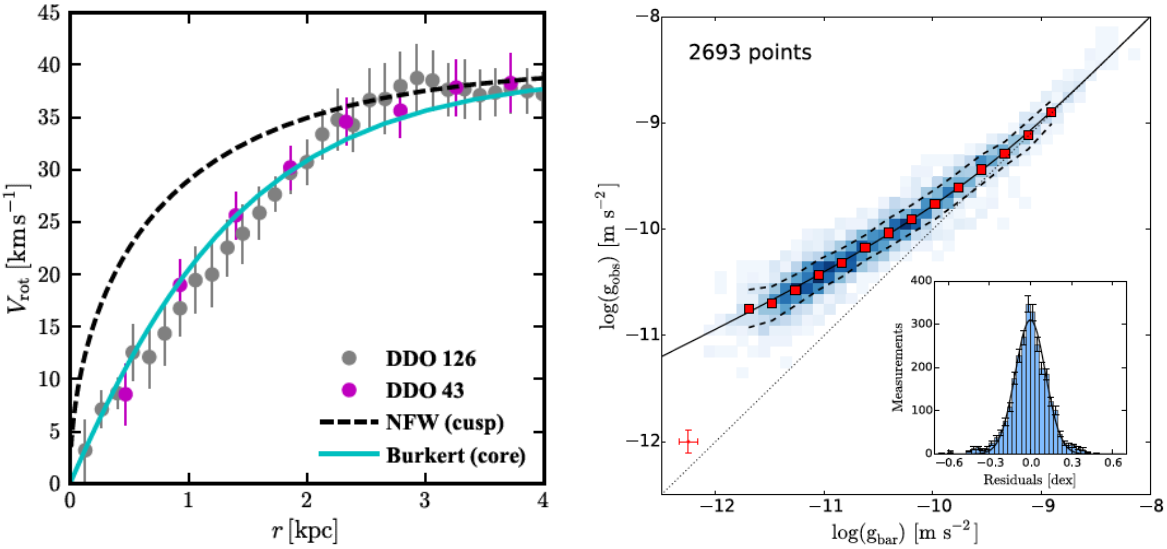

Figure 1.7 – Both panels are taken from (BULLOCK et al. 2017). **Left panel:** Rotation curve of a typical galaxy with asymptotic circular velocity of ~ 40 km s^{-1}. The dashed curve represents the expected NFW profile and the circles are data points taken from (OH et al. 2015). The solid blue line is an example of cored profile (BURKERT 1995) which better match the data. **Right panel:** The RAR relation for 2693 data points taken from a group of 153 galaxies and based on (MCGAUGH et al. 2016). Figure taken from (BULLOCK et al. 2017).

presence of new physics that could give hints on its nature (LESGOURGUES et al. 2016; MURGIA et al. 2016; ABELLAN et al. 2020; BOHR et al. 2020).

1.3.2 Issues for CDM on small scales

Small scales are the main topic of this thesis and related issues of ΛCDM are therefore of primordial interest. Here we need to clarify an important point that is, how small are the small scales? In practice, we will consider that everything under the size of a typical galaxy is within the small scale range. To be more precise for DM halos one can set a limit in mass at $M < 10^{11} M_{\odot}$ and in size at $R < 200$ kpc. A review on the small scales problem is available in D. H. WEINBERG et al. (2015) and BULLOCK et al. (2017). We summarise here the major conundrums and the possible solutions.

First and foremost, let us recap some of the main predictions of ΛCDM. As mentioned in Sect. 1.2.3 CDM is responsible for structure formation by growing the gravitational perturbations produced by inflation on all scales until turning unstable, and then collapsing and the forming bound objects. These halos are virialised objects with a self-similar structure. Small halos are contained into larger ones, themselves contained in even larger ones and so on. A limit to self-similarity is set by the minimal length scale of the matter density perturbations that survive the early epoch of the universe, which translates into a minimal halo mass of order $M_{\rm min} \sim 10^{-12}$ M$_{\odot}$, or even lower depending on the nature of DM (the values given are typical to particle CDM). Inside a galactic halo, one expects an abundant distribution of subhalos with self-similar properties. In particular, in CDM-only simulation, it is found that all subhalos of MW-like galaxies generally have a similar density profile (up to rescaling) that increases toward their centre. One talks about cuspy profiles in opposition to cored profiles in which the density would be homogeneously distributed around the centres.

The core-cusp problem. Observed rotation curves indicate that a substantial fraction of galactic halos are consistent with cored density profiles (NARAY et al. 2008; BLOK 2010; OH et al. 2015), which is in contradiction with CDM-only simulation results. An example is given in the right panel of Fig. 1.7. Moreover, the simulations also tend to over-predict the mass of DM in the central region of the halos (ALAM et al. 2002; OMAN et al. 2015).

The diversity issue. It appears that galaxies with a similar circular velocity asymptote in their outskirts can have inner circular velocities spanning a wide range of values, much wider than what is naively predicted by ΛCDM (OMAN et al. 2015). Even if the inclusion of the baryonic physics in the simulations could solve the core-cusp tension (see the next section) it would still fail solving the diversity issue. Consequently, together, they may be the most challenging problems for CDM.

The Tully-Fischer relation. Consider galaxies for which one knows the total baryonic mass $M_{\rm b}$ and the circular velocity v_c in the asymptotic part of the rotation curve. It is possible to place all these galaxies in a graph of $M_{\rm b}$ against v_c. The outcome gives the Tully-Fischer relation that shows $M_{\rm b} \propto v_c^4$ (MCGAUGH 2005). This can be stated more generally in terms of the Radial Acceleration Relation (RAR) that is equivalent but relies on different quantities: the gravitational acceleration due to baryons $g_{\rm bar}$ and the radial acceleration $g_{\rm obs} = v_c^2/r$ (LELLI et al. 2017). In the left panel of Fig. 1.7 one shows that in regions dominated by baryons, where $g_{\rm bar}$ is large, the observed acceleration follows $g_{\rm obs} \sim g_{\rm bar}$ as expected. For small values, it departs from this simple scaling due to the presence of DM. However, the smallness of the scatter around the mean value of $g_{\rm obs}$ at a given $g_{\rm bar}$ is difficult to explain from the DM contribution, especially in light of the diversity issue.

The plane of satellites problem. One observes that bright satellite galaxies (of the MW or other hosts) tend to lie in a specific plane and rotate coherently. At first, this seems to be in contradiction with cosmological simulations (PAWLOWSKI et al. 2014). However in-depth statistical analysis have proven that the presence of such planes – that may stem from the anisotropic accretion of satellites from cosmic filaments – is plausible (CAUTUN et al. 2015).

The missing satellite problem. In CDM-only simulations, thousands of subhalos are expected to be massive enough to contain stars and be observed in the inner 300 kpc of the MW (or any other MW-like galaxy) as dwarf, faint or ultra-faint satellite galaxies. However only ~ 50 are effectively observed (DES COLLABORATION 2015). This raised some concerns in the past even though we have know for several decades now that two concomitant explanations are at play. On the one hand, star/galaxy formation is very likely to become inefficient in small subhalos, as the gas is expelled by various processes quite early in the formation history of such small objects (BULLOCK et al. 2000; SOMERVILLE 2002; OKAMOTO et al. 2008; WADEPUHL et al. 2010). On the other hand, the census of Galactic satellites is not yet complete, as a large portion of the sky remains to be probed - there could therefore be a biased observational deficit. In the end, with more and more satellites being discovered over time (TORREALBA et al. 2018), the tension has now faded away.

The too-big-to-fail problem. Satellite galaxies are likely to form in the most massive subhalos, such as those observed in CDM-only simulations. However, it seems than the most massive substructures are then not observed while they are too big to have failed star formation (BOYLAN-KOLCHIN et al. 2011). However, similarly than for the missing satellites problem, inclusion of baryonic physics in the simulations has now reconciled their results with observations (SAWALA et al. 2016). Notice that

even if it is not necessary, solutions to the core-cusp problem could also resolve this tension by decreasing the expected central density of the subhalos.

1.3.3 Solutions to the small scale crisis

There are two classes of solutions, which may overlap, and that can give the correct explanation to the still unsolved aforementioned tensions on small scales. On the one hand, they may simply originate from the description of baryonic *feedback* in numerical simulation, which still relies on rather empirical prescriptions. However, even though very complex and challenging, the treatment of baryonic physics, star formation, etc., has considerably improved over the past years, and there is hope to reach more conclusive answers within the next decade (Vogelsberger et al. 2019). On the other hand, the previous tensions can also indicate a departure from the ΛCDM paradigm.

For several years now it has been shown in various simulations that cores in galaxies could be induced by baryonic feedback redistributing energy in the central parts (Pontzen et al. 2012; Madau et al. 2014; Chan et al. 2015; Oñorbe et al. 2015). The efficiency of baryon-induced core-formation (through supernova feedback, molecular cooling in the reionization epoch, etc.) may depend on the chosen *sub-grid* physics recipe but they all seem to show that it should occur in halos with mass $M \lesssim 10^{10}$ $M_\odot$. Complementarily, high resolution (non cosmological) simulations show formation of cores in all halos (Read et al. 2016). Recent studies have also shown that the RAR relation could also be obtained in simulations (Navarro et al. 2017; Paranjape et al. 2021). One may also need to invoke the effects of the halo environment such as tidal stripping and disk shocking. The Chapter 4 of this thesis will actually discuss such dynamical effects, but focusing on their impact on dark subhalos instead of on dwarf galaxies. In summary, baryonic physics is likely to play a major role in the understanding of these tensions between theory and observations, and it is important to investigate further its impact on the structuring of DM in the centres of halos. For now, the diversity problem, especially when put in front of the very small scatter characterising the Tully-Fisher or RAR diagrams, seems to be the most challenging. Therefore, one should remain open-minded to other classes of solutions.

If the tension is indeed caused by a departure from the ΛCDM paradigm that would provide an interesting probe for DM nature. Different classes of solutions are commonly considered.

First, instead of the usual CDM scenario with subhalos as light as 10^{-12} $M_\odot$ (or lower), one can also consider the WDM case. A priori both configurations are similar except for the DM particle velocity dispersion in the early Universe, nevertheless, that has serious consequences. Indeed, a small mass particle would have had a higher velocity in the early Universe and therefore would have suppressed the matter power spectrum on small scales because of the free-streaming damping effect – already brought up in Sect. 1.2.2 and detailed in Sect. 3.6. Consequently, this cut-off in the power spectrum prevents subhalos to form below some scale set by the free streaming mass but, more importantly, it also reduces the central density of subhalos alleviating the too-big-to-fail problem. Unfortunately, it has also been shown that this produces too small cores to suppress the core-cusp tension (Maccio′ et al. 2012).

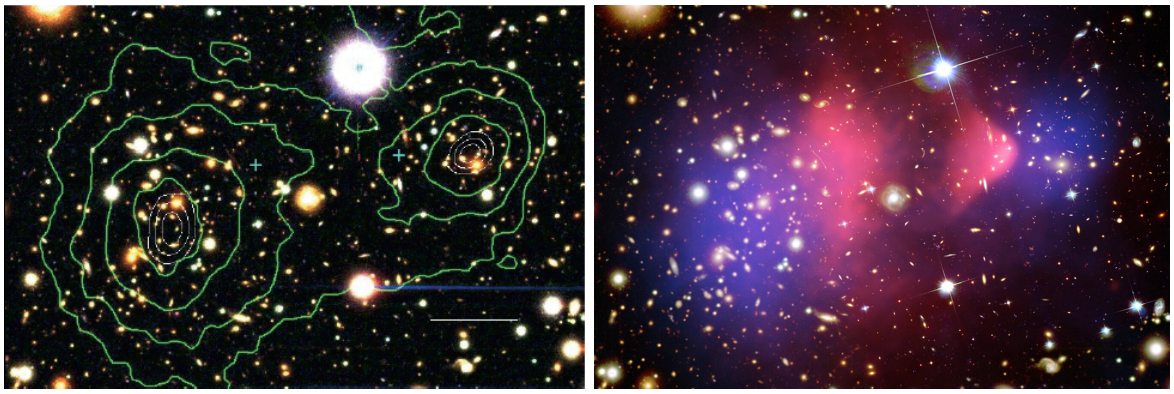

Figure 1.8 – Image of the Bullet Cluster. **Left panel:** Iso-contour of the gravitational potential reconstructed from lensing observations and taken from (CLOWE et al. 2006). **Right panel** Superposition of the X-ray image of the intra-cluster gas (pink) and reconstructed dark matter distribution from lensing. Credit: X-ray: NASA/CXC/CfA/(MARKEVITCH 2005), Optical and lensing map: NASA/STScI, Magellan/U.Arizona/(CLOWE et al. 2006), Lensing map: ESO WFI.

Another model that has recently gained a growing attention is self-interacting DM (SIDM) where DM is made of particles that can rather efficiently self-scatter (CARLSON et al. 1992; SPERGEL et al. 2000; SCHUTZ et al. 2014; TULIN et al. 2018). Interestingly, concrete realisations of SIDM can be easily constructed in particle physics from an effective point of view, although self-scattering is not by itself imposed by any theoretical prejudice. Let us denote the self-interaction transfer cross-section – an angular-weighted cross-section that characterises the averaged momentum transfer – by $\sigma_{\rm T}$. In a medium with a DM mass density ρ_χ particles scatter efficiently on a length scale $\lambda = (\rho_\chi \sigma_{\rm T}/m_\chi)^{-1}$, with m_χ the DM particle mass. Inside a halo, assuming it originally exhibits a cuspy profile, the central density is large and λ small. Then DM behaves like a fluid and momentum and energy can be redistributed inside the structure leading to the formation of a core, hence potentially solving the core-cusp problem (and, as a DM-only solution, also the too-big-to-fail problem) (NISHIKAWA et al. 2020). The required order of magnitude is $\lambda \sim 1$ - 10^3 kpc corresponding roughly to 0.5 cm^2 g^{-1} < $\sigma_{\rm T}/m_\chi$ < 10 cm^2 g^{-1} (ELBERT et al. 2015; FRY et al. 2015; ROBLES et al. 2019). Moreover for $\sigma/m_\chi > 5$ cm^2 g^{-1} the self interaction can lead to gravitational core collapse in the MW satellite galaxies that may produce a diversity of inner density profiles (KAHLHOEFER et al. 2019; SAMEIE et al. 2020). These are rather large cross-sections (equivalent to the neutron-neutron scattering cross-section) but they are actually not much constrained since not necessarily correlated with the scattering cross-section off baryons. Upper bounds can be set using galaxy cluster mergers. They provide constraints on the behaviour of the baryonic and the DM components of two clusters during a collision. In the SIDM context, they especially probe the strength of the DM self-scattering. The most famous of these mergers is called the Bullet cluster and yields $\sigma_{\rm T}/m_\chi \lesssim 1$ cm^2 g^{-1} (MARKEVITCH et al. 2004). This bound is lower than the cross-section needed to solve the core-cusp problem at the scale of galaxies. A way out is to have a velocity-dependent self-scattering cross-section, which would be suppressed at large dispersion velocities, like in galaxy clusters ($v \sim 1000$ km s^{-1} in galaxy clusters, while $v \sim$ 10-100 km s^{-1} in dwarf or regular galaxies). Therefore, the rate of DM self-scattering is constrained to be velocity-dependent, more precisely a decreasing function of the DM velocity.

Finally, let us briefly discuss the case of quantum pressure-induced cores in scenarios with ultra-light DM boson particles (then called fuzzy DM). The combination

of Poisson's and Schrodinger's equations for self-gravitating bosonic systems gives that the central mass distribution in structures made of light bosons are impacted when their de Broglie wavelength $\lambda = h/(mv)$ becomes of the order $\sim$ kpc. Thus making formation of cores possible for a particle mass of the order $m \sim 10^{-22}$ eV (Hui et al. 2017; Hui 2021).

To summarize, it is important to stress that although CDM is not fully in trouble while baryonic physics is not more plainly understood and fixed in cosmological simulations, these current issues on small scales represent an exciting challenge. There exist independent and purely DM potential solutions, like SIDM or fuzzy DM, and further theoretical inspection and observational tests of these scenarios will be decisive in the coming years. Conversely, testing the very features of CDM, like the presence of fully dark subhalos, also represents an important test to validate or exclude CDM. Anyway, these different classes of DM rely on specific realizations of the subatomic world, most assuming the existence of new particles and interactions. We briefly review a non-exhaustive list thereof below, as the intimate DM particle candidate properties should directly translate into dedicated search strategies.

1.4 Theoretical models of Dark Matter

In this section, we review the different classes of possible candidates for DM after discussing, in the first part, the possibility of a modified theory of gravity. The possibilities are numerous, from elementary particles to black holes, and our goal here is not to be exhaustive but rather to give a brief review of the most popular models that have not been completely ruled out so far and that remain appealing from a detection perspective.

1.4.1 Modified gravity

The theory of general relativity (GR) gives high precision predictions when tested on scales from a few centimetres to the solar system size. For instance, one can cite the historical observations of gravitational lensing around the sun (Dyson et al. 1920) and the explanation of the perihelion precession of Mercury – measured by Le Verrier (1859). Today it provides the correct corrections for GPS (Kouba 2002) and lensing observations are now common with the Hubble Space Telescope. The detection of gravitational waves by the LIGO/Virgo collaborations (LIGO and Virgo Collaborations 2016) and the first direct observation of a black hole in 2019 (EHT Collaboration 2019) have again provided new confirmations for the validity of the theory. However, on large scales, all the anomalous observations exposed in the previous sections could actually be related to limits of its applicability. On cosmological scales, on top of the DM issue, the presence of dark energy supports this possibility (Riess et al. 1998; Perlmutter et al. 1999). Several attempts have been made to provide a suitable extension of GR however it remains challenging to propose models that can be experimentally probed and that are theoretically consistent.

At the galactic level, rotation curves can be empirically explained using the MOdified Newtonian Dynamics (MOND formalism introduced by Milgrom (1983). See Famaey et al. (2012) for a review. There, the Newtonian gravitational acceleration is modified via a factor that depends on its strength. The typical acceleration of a star in a galaxy being $\sim$ 11 orders of magnitude below the gravitational acceleration at the surface of the Earth, the modification has to be important for low gravitational

accelerations while being negligible at high gravitational accelerations (in order not to spoil Newtonian dynamics on Earth). In more details, if one measures a gravitational acceleration $g_{\rm N}$ from the observed distribution of matter using Newtonian dynamics then, the true gravitational acceleration g must be related to $g_{\rm N}$ via the relation

$$\mu\left(\frac{g}{a_0}\right) g = g_{\rm N}\,. \tag{1.10}$$

The function μ is such that $\mu(x) \to 1$ for $x \gg 1$ and $\mu(x) \to x$ for $x \ll 1$ and gives a smooth transition between two regimes characterised by the scale acceleration a_0. In the weak acceleration regime $g \ll a_0$ the circular velocity of a system at distance R from a point mass M becomes

$$v_c(R) \sim (G_{\rm N} M a_0)^{1/4}\,. \tag{1.11}$$

Therefore the circular velocity no longer depends on the distance from the centre of the galaxy in the outskirts, consequently explaining the flatness of the rotation curves. Moreover, such a relation also explains the small scatter in the Tully-Fischer-RAR relations since without DM a tight correlation between the baryonic acceleration and the observed one is naturally expected. On the other hand, while successful of galactic scales, MOND fails to explain the dynamics of galaxy clusters, except at the price of an additional hot DM component (SANDERS 2003). Let us also mention that the Bullet Cluster (already broached it in the context of self-interacting DM) suggests the existence of a pressureless fluid supporting the two clusters involved. In Fig. 1.8 are represented the mass distribution of the gas that makes the main part of ordinary matter and the total mass distribution, mainly supported by a dark component. The baryonic matter and DM distributions are unambiguously offset, which is very challenging or nearly impossible to properly account for if the mass is only sourced by the baryons. On the other hand, while the gas particles are slowed down by their interactions, a (quasi)collisionless dark fluid is not (CLOWE et al. 2004, 2006), therefore naturally providing the offset[3].

Eventually, let us mention that the "covariantisation" of MOND remains a very challenging task; there is no unique and perfect way to construct a relativistic extension, based upon this empirical requirement, that passes all the observational constraints. Amongst the current relativistic extensions of MOND one can cite the Relativistic Aquadratic Lagrangian (RAQUAL) theory (J. BEKENSTEIN et al. 1984), the Tensor-Vector-Scalar (TeVeS) theories (J. D. BEKENSTEIN 2005; SKORDIS et al. 2006; SKORDIS 2008), the Bi-Scalar-Tensor-Vector (BSTV) theories (SANDERS 2005), the Generalized Einstein-Aether (GEA) theories (ZLOSNIK et al. 2007), the bimetric theories (BIMOND) (MILGROM 2010) and Dipolar Dark Matter (L. BLANCHET et al. 2017). It is thus difficult to make generic predictions for cosmology, large scale structures and the CMB in this context. For instance, SKORDIS et al. (2020) have proposed a theory in agreement with the CMB, however, the agreement to structure formation remains to be checked – it is, today, the biggest challenge to covariant versions of MOND. Besides, such theories introduce anyway an effective DM component through new degrees of freedom behaving as a pressureless fluid.

[3]Note that however this observation does not necessarily rule out MOND (ANGUS et al. 2006). Besides, the bullet cluster may be a too rare object emerging in ΛCDM (KRALJIC et al. 2015). If other similar ones where to be discovered in the future, this would challenge the cosmological paradigm.

1.4.2 Particle candidates

Our knowledge of the microscopic structure of known matter relies on nuclear physics, atomic physics, and at the smallest scales on quantum field theory. The standard model (SM) of elementary particles is a robust theoretical construction based upon powerful physical principles such as symmetries, gauge invariance, and the Higgs mechanism as a self-consistent mechanism to give masses to particles. Although DM could be made of macroscopic objects, let us first review the possibility that it be made of elementary particles. We shortly review the SM (see PARTICLE DATA GROUP et al. 2020 for an extensive review) before showing how DM candidates could emerge from exotic extensions.

The standard model

The SM is a non-abelian quantum field theory based on a (partially and spontaneously) broken $SU(3)_C \otimes SU(2)_L \otimes U(1)_Y$ gauge symmetry (SALAM et al. 1959; GLASHOW 1961; S. WEINBERG 1967). The $SU(3)_C$ group corresponds to quantum chromodynamics (QCD) and describes strong interactions, the corresponding charges are referred to as colours. The $SU(2)_L \otimes U(1)_Y$ part corresponds to the electroweak sector that unifies the electromagnetic and weak interactions. The L notation stands for *left* as this group only acts on particles according to their chirality, *i.e.* only on the left-handed particles. In this model, the matter is made of elementary fermions (with half-integer spins), six kinds of quarks (u, d, s, c, b, t) in the fundamental representation of $SU(3)_C$ and six leptons $(e, \mu, \tau, \nu_e, \nu_\mu, \nu_\tau)$ that can be packed into doublets of the fundamental representation of $SU(2)_L$ when left-handed and into singlet otherwise (neutrinos are only left-handed particles). Interactions are mediated via particles in the adjoint representation of the group: the gluons g for the strong interaction and the massless bosons W^1, W^2, W^3 and B for the electroweak interaction. At low energy ($E < \Lambda_{\rm EW} \sim 250$ GeV) a scalar field called the Higgs field H (ENGLERT et al. 1964; HIGGS 1964), coupled in a gauge-invariant way to fermions, falls at the bottom of its potential well, gets a vacuum expectation value (VEV) usually denoted $v \equiv \langle H \rangle$ and induces a spontaneous symmetry breaking, $SU(2)_L \otimes U(1)_Y \rightarrow U(1)_Q$. Here $U(1)_Q$ describes the electromagnetic interactions with Q the standard electromagnetic charge. The subsequent Goldstone bosons (GOLDSTONE et al. 1962) can be 'gauged-out', which transforms the W and B fields into three massive fields (with longitudinal polarisation) W^+, W^-, Z^0. The remaining massless field corresponds to the photon γ. Beside providing masses to gauge bosons, the Higgs field is also a fundamental piece of the theory because it provides gauge-invariant mass terms to the fermions. Finally, the gravitational interaction, fully described in GR by space-time curvature, is usually not considered as part of the SM but can be included at low energy by the introduction of a spin-2 particle called the graviton. However, the added terms in the Lagrangian are not renormalisable; non-physical divergences appear and cannot be removed with a final number of experimental inputs. The theory becomes non-predictive. Therefore to properly describe gravity in all regimes of energy one needs to extend the theory in the UV, which cannot be realised in a simple and generic way – for instance, string theory (POLCHINSKI 2007a,b) is a framework that provides a consistent theory albeit being hardly predictive and testable today.

Assuming DM is made of elementary particles, we can shortly review the properties the latter should have. As DM has not been yet seen via its interactions with

light, it must be electromagnetically neutral or have an extremely small charge. Moreover, it needs to be stable (or metastable with a cosmological lifetime) and massive to provide 80% of the total mass of the Universe. Therefore, all known particles are already ruled out except for neutrinos. However, denoting m_i the masses of the three neutrinos, one can evaluate their total abundance in the Universe today as being (LESGOURGUES et al. 2006):

$$\Omega_{\nu,0}h^2 = \sum_{i=1}^{3} \frac{m_i}{93.14\,\mathrm{eV}} \tag{1.12}$$

while the best constraints from ground experiments are of the order $m_i < 0.8$ eV – with a 90% confidence level (AKER et al. 2021) – that roughly gives $\Omega_{\nu,0}h^2 < 2.6 \times 10^{-2}$. The CMB puts a bound $\sum_i m_i < 0.24$ eV (with a 95% confidence level from Planck18) that yields $\Omega_{\nu,0}h^2 < 2.6 \times 10^{-3}$, far below the value for the total dark matter $\Omega_{\mathrm{c},0}h^2 = 0.12$. Moreover, if DM was made exclusively of neutrinos it would not fit in the WDM or CDM category neither, but would instead be hot DM (HDM) owing to their relativistic speed at the time of matter domination, a consequence of their small mass and their thermal production in the early universe. This is not supported by observations (*e.g.* Ly-alpha) which strongly favour hierarchical structure formation. Therefore it would be difficult to explain the presence of galaxies. Besides, the mass of fermionic DM particles is also constrained by their phase-space distribution in galaxies to $m \geq 1.7$ keV (TREMAINE et al. 1979; BOYARSKY et al. 2009a) .

Therefore, no SM particle can account for DM. One needs to rely on extensions of the SM to incorporate DM. It actually turns out that, while the SM allows for predictions of subatomic properties or processes which have been tested to unprecedented precision, it is not devoid of issues. For instance, it does not allow to fully understand the hierarchy of particle masses, the hierarchy between the Planck and electroweak scales, the specificity of neutrinos (initially described as massless and only left-handed particles), and it does not incorporate gravity even when it gets relevant in the very high-energy limit. Other issues are of observational nature: it does not provide an explanation to the asymmetry between matter and antimatter, nor to inflation, not the least to DM. Interesting theoretical solutions are given by extensions/modifications of the SM that can solve at least one problem inherent to particle physics and can at the same time provide a good DM candidate. In the following, we detail different DM models and explain how they have been introduced. See FENG (2010) for a review.

Sterile neutrinos

In the primary version of the SM, neutrinos are considered massless (GIGANTI et al. 2018). However, from neutrino oscillations, it is known that this is not strictly the case even if the upper bound from ground-based experiments gives $m_\nu < 1.1$ eV as seen above. Therefore one needs to correct the original version of the SM Lagrangian. As neutrinos are neutral it is possible to assume that they are Majorana particles. Even if Majorana masses cannot be generated by a usual Yukawa coupling, one can introduce the non-renormalisable Weinberg operator given, for electronic neutrinos for instance, by

$$\mathcal{L}_{\mathrm{W}} = \frac{1}{\Lambda}(L^T i\sigma^2 H)C(H^T i\sigma^2 L) + \mathrm{h.c.} \quad \text{with} \quad L = \begin{pmatrix} \nu_e \\ e \end{pmatrix}, \quad H = \begin{pmatrix} H^+ \\ H^0 \end{pmatrix} \tag{1.13}$$

where H is the Higgs doublet and C is the charge conjugation operator. When the Higgs acquires its VEV, $\langle H^0 \rangle = v$, this term becomes a Majorana mass term and one

obtains $m_\nu = v^2/\Lambda$ and then $\Lambda \sim \Lambda_{\rm GUT} \sim 10^{15}$ GeV – of the order the energy scale of the Grand Unified Theory (GUT) – to satisfy the upper bound on the neutrino mass. A simple physical realisation of a neutrino mass term comes when introducing a right-handed neutrino N_R that, in full generality, adds a Dirac mass term and but also a Majorana mass term so that

$$\begin{aligned}\mathcal{L} &= -m_{\rm D}\overline{\nu_L}N_R + \frac{1}{2}MN_R^T C^{-1}N_R \\ &= -\frac{1}{2}\begin{pmatrix}\overline{\nu_L} & \overline{N_L^c}\end{pmatrix}\begin{pmatrix}0 & m_{\rm D}\\ m_{\rm D} & M\end{pmatrix}\begin{pmatrix}\nu_R^c\\ N_R\end{pmatrix} + \text{h.c.}\end{aligned} \tag{1.14}$$

with $\overline{N_{\rm L}^c} = -N_R^T C^{-1}$ and $\nu_R^c = C\overline{\nu_L}^T$. The mass matrix has then two eigenvalues, one of which must be vanishingly small due to current constraints on neutrino masses. This can be realised by the so-called see-saw mechanism (Mohapatra et al. 1980). In the type-I seesaw limit (Adhikari et al. 2017) where $M \gg m_{\rm D} \sim v$ one has two mass eigenstates corresponding roughly to ν_L with mass $m_{\rm D}^2/M \ll v$ and to N_L^c with mass $M \gg v$. Therefore, the model provides here a natural explanation for he smallness of the neutrino mass (the light mass eigenstate being roughly the SM neutrino) and an explicit realisation of the Weinberg operator with $M \sim \Lambda_{\rm GUT}$. Moreover if it exists, N_R is then a singlet for all interactions, it is therefore called a sterile neutrino (in opposition to the other neutrinos said to be active) and could be a good DM candidate (Dodelson et al. 1994; Shi et al. 1999; Asaka et al. 2005). In addition, sterile neutrinos are also well motivated to explain the matter-antimatter asymmetry of the Universe.

In practice sterile neutrino mass can cover, a priori, a wide range of values as one can either have no Majorana mass and a Dirac mass or no Dirac mass and a pure Majorana mass or intermediate configurations. Moreover even in the seesaw case illustrated above if we do not require $m_{\rm D} \sim v$ then M can also be much smaller. In particular if $M \sim$ keV, the sterile neutrino becomes a good CDM or WDM candidate (depending on the production mechanism). These particles are unstable, as they can decay into an active neutrino and a photon, but their lifetime can be much longer than the age of the Universe. Nevertheless, this remains an interesting feature as the emitted photon in the decay is produced with an energy at half the mass of the sterile neutrino (in the rest frame) and provides a clean astrophysical signature. Therefore using X-ray observation and searching for an emission line puts constraints on the allowed mass range. See also Boyarsky et al. (2009b) and Boyarsky et al. (2018) for reviews.

Axion(-like) particles

Amongst the lightest possible DM candidates are the axions, introduced to solve the strong CP (charge-parity) problem of the SM. See Marsh (2016, 2017) for detailed reviews. Indeed, in full generality, one needs to introduce a CP-violating term in the SM Lagrangian,

$$\mathcal{L}_\theta = -\frac{\theta}{32\pi^2}\text{Tr}\left[\tilde{G}_{\mu\nu}G^{\mu\nu}\right] \tag{1.15}$$

where $G^{\mu\nu}$ is the gluon field strength tensor and $\tilde{G^{\mu\nu}} = \epsilon^{\mu\nu\rho\sigma}G_{\rho\sigma}/2$. The coupling constant θ is related to non trivial topological properties of $SU(3)_c$ and the associated instantons (Belavin et al. 1975). Therefore, even if this new term can be rewritten as a current derivative (and would therefore not produce any physical effect in the absence of instantons, like in QED), it actually contributes important non-perturbative

effects. In addition, it cannot be removed by chiral rotations[4] and it also contributes to the electric dipolar moment of the neutron $d_n \simeq 3.6 \times 10^{-16} \times \theta \; e$ cm. From experiments it has thus been shown that the value of θ is severely constrained, $\theta \lesssim 10^{-10}$, which could be considered a problem if one is sceptical about such a large degree of fine tuning. A possible solution is to introduce a new field, called the axion, coupling to $G\tilde{G}$ with a dynamics that naturally leads to the cancellation of θ. Several models have been introduced: the Peccei-Quinn-Weinberg-Wilczek (PQWW) axion (PECCEI et al. 1977; S. WEINBERG 1978; WILCZEK 1978) (completely ruled out today by beam dump experiements), the Kim-Shifman-Vainshtein-Zacharov (KSVZ) axion (KIM 1979; SHIFMAN et al. 1980) or the Dine-Fischler-Srednicki-Zhitnitsky (DFSZ) axion (ZHITNITSKY 1980; DINE et al. 1981). Note that the last two, however, also require the existence either of new heavy quarks, or a second Higgs doublet.

The idea is to introduce a new $U(1)_{\rm PQ}$ symmetry, which acts with chiral rotations, that is spontaneously broken at an energy much higher than the QCD confinement scale $f_a \gg \Lambda_{\rm QCD} \sim 150$ MeV to produce the axion field $a \in [0, 2\pi]$ as a pseudo-scalar Goldstone boson. Then the chiral anomaly provides a coupling of a with $G\tilde{G}$ (and $F\tilde{F}$, the field strength of QED) and the coefficient θ is replaced by $\theta + \mathcal{C}a/f_a$ in Eq. (1.15). Here we have introduced the integer colour anomaly $\mathcal{C}\delta_{ab} = 2{\rm Tr}\left[Q_{\rm PQ}T_aT_b\right]$, with T_a the generators of the $SU(3)_{\rm c}$ representation of the fermions and $Q_{\rm PQ}$ the PQ charge of the field responsible for the spontaneous breaking of the PQ symmetry. In the end, the vacuum energy is proportional to $\cos(\mathcal{C}a/f_a)$ (where θ has been absorbed by shifting a and $\mathcal{C}$ must be an integer to respect the shift symmetry $a \to a + 2\pi f_a$). Because now a is a dynamical field the energy can be minimised and a vacuum can be dynamically selected.

When the primordial plasma cools down below $T \sim \Lambda_{\rm QCD}$ the axion potential takes the form

$$V(a) = m_u \Lambda_{\rm QCD}^3 \left[1 - \cos\left(\frac{\mathcal{C}a}{f_a}\right)\right] \tag{1.16}$$

with m_u the up quark mass. Then, the axion becomes a pseudo Nambu Goldstone Boson (pNGB) with a mass $m_a^2 \simeq m_u\Lambda_{\rm QCD}^3/f_a$ that can be approximated by

$$m_a \simeq 10\,\mu{\rm eV}\left(\frac{10^{12}\,{\rm GeV}}{f_a}\right). \tag{1.17}$$

The field rolls down to a minimum of the potential, oscillating and forming a zero-momentum condensate which makes an excellent beyond the standard model CDM candidate. In this QCD axion DM scenario, in order to produce a consistent amount of DM, the typical bounds on the scale f_a are 10^9 GeV $< f_a < 10^{12}$ GeV corresponding to the mass range $10\ \mu$eV $< m_a < 0.1$ eV.

Eventually, QCD axions studies have paved the way to more generic ones in the context of axion-like particles (that generalise the QCD axion and are not necessarily related to the strong CP-problem) or ultralight axions (with a mass down to $m_a \sim 10^{-22}$ eV) making fuzzy DM – that can alleviate the core-cusp tension. However, the minimal mass is constrained from the Lyman-α forest (ARMENGAUD et al. 2017; IRŠIČ et al. 2017), from the tidal disruption of satellite galaxies (DU et al. 2018; MARSH et al. 2019), from the galactic rotation curves (BAR et al. 2018) and from several other observations. The experimental endeavour around axion searches, which have become priority after the waning of WIMP candidates, will be broached in Sect. 1.5.

[4] A similar term for $SU(2)_L$ can be removed by chiral rotations.

Weakly Interacting Massive Particles

Owing to their simple production mechanism in the early Universe and the fact that they are naturally cold DM candidates (Lee et al. 1977), Weakly Interacting Massive Particles (WIMPs) have been among the most popular models. They are neutral, stable, they have a mass in the GeV-TeV range and they interact weakly with the SM. Moreover, throughout the last 50 years, several BSM approaches initially designed to solve problems inherent to particle physics (e.g. the electroweak hierarchy problem) have predicted WIMP-like particles as by-products (often related to ensuring the stability of the proton). That was, at least before the null search of new physics around the TeV scale at the LHC, a very strong theoretical motivation to the searches of WIMPs. After the LHC campaign, WIMPs have lost their quasi-monopoly. Nonetheless, if it is true that the GeV-TeV mass range is indeed under experimental pressure, all the constraints rely on specific aspects of the WIMP-SM interactions. The vast parameter space is far from being entirely probed and WIMPs are still alive (Leane et al. 2018) and they remain a dominant class of models. They remain an interesting scenario especially in terms of simplicity and minimality, beside the possibility to detect them from a variety of observations or experiments. Let us reviews some of the model below.

Supersymmetry. Supersymmetry (SUSY) has been introduced in the 1970s as an extension of gauge theories by allowing the presence of anti-commuting spinors operators and thus symmetrising, in a way, fermions and bosons (Gervais et al. 1971; Neveu et al. 1971; Ramond 1971; Wess et al. 1974). See Martin (1998) for a review on the SUSY formalism. Therefore, in SUSY every particle has a super-partner with a spin that differs from its own by a half-integer: all fermions have bosonic super-partners and conversely. One of the most important features of SUSY is the solution given to the electroweak hierarchy problem (Gildener 1976). Indeed, even if the SM masses are correctly renormalised and there is no objection in having a Higgs boson with a mass of 125 GeV, if we introduce new physics and new degrees of freedom at the Planck scale, $M_{\rm Pl} \sim 10^{19}$ GeV (motivated by a UV completion of the SM including gravity) the Higgs mass should be contaminated by large radiative corrections. In SUSY the issue is avoided as the radiative corrections from loops of the bosonic super-partners exactly cancel those induced by the SM fermions (provided their masses are equal). Since the masses of superpartners are experimentally bound to be larger than those of the SM fermions, the cancellation is, however, not exact. Nevertheless, having them in the TeV mass range is in principle sufficient to explain why radiative corrections to the Higgs mass also remain in the TeV range, making it insensitive to UV physics. In addition, another appeal of SUSY comes from the fact that if extended to a gauge theory one obtains supergravity an effective realisation of superstrings theory (a special kind of string theory) at low energy – Nath et al. 1975 and Wess et al. 1992 for a review. More interesting for DM, it provides a set of particles called neutralinos that are natural WIMPs. In the minimal supersymmetric standard model (MSSM), the minimal extension of the SM, to provide a mass to *up* and *down* particles it is necessary to introduce two Higgs doublets H_u and H_d. Both their neutral components have then fermionic super-partners $\tilde{H}_u^0$ and $\tilde{H}_d^0$ called higgsinos that are neutral. Moreover, the B boson and one of the three W bosons are also partnered to neutral fermions, the bino $\tilde{B}^0$ and the wino $\tilde{W}^0$. The mass eigenstates of these four components are the neutralinos $\tilde{\chi}_i^0$ with $i \in [0, 4]$ and as their partner, they interact weakly with the SM particles. Therefore they have every properties to be WIMPs

except for stability. Nevertheless in SUSY, in order not to spoil the constraint on the proton decay rate, a supplemental discrete symmetry called R-parity is imposed in the model. A direct consequence of its definition is that one can introduce an invariant quantum number R that is $R = 1$ for SM particles and $R = -1$ for the superpartners and the lightest supersymmetric particle (LSP) becomes stable as it cannot decay into SM particle without violating R-parity. If the LSP is the lightest of the neutralinos it then becomes a perfect WIMP candidate. Other particles such as the gravitino (the superpartner of the graviton) are also good DM candidates, even though the latter is much more difficult to constrain as only interacting gravitationally with the SM, or the (right-handed) sneutrino (ASAKA et al. 2006; ARINA et al. 2007). See JUNGMAN et al. (1996) for a review of SUSY DM. Extensions of MSSM can also provide more viable candidates, such as the singlino of the NMSSM (ELLWANGER et al. 2010).

Extra dimensions. The possibility of spacetime having more than 4 dimensions has been under investigation since the first attempt by KALUZA (1921), trying to unify GR and electromagnetism by resorting to a compact fifth dimension. In particular, Klein studied the possibility of a fifth dimension that is compactified around a circle of small radius and therefore hidden to the observer (KLEIN 1926). While the first attempt resulted in theoretical issues, in the 1980's this idea became attractive again with the popularity of string theory (that cannot be formulated in 4 dimensions only). Furthermore, some scenarios are appealing as they allow to solve the hierarchy problem by lowering the Planck scale to the electroweak scale in the bulk the (space of the extra dimensions). Among the models that have been proposed are: a model with a new dimension at the millimeter scale (ARKANI–HAMED et al. 1998; ARKANI-HAMED et al. 1999), the Randall-Sundrum model (RANDALL et al. 1999) and the Universal Extra Dimensions (UED) model (APPELQUIST et al. 2001). From a phenomenological point of view, particles that are allowed to propagate through all dimensions of space exhibit, more massive, excited states – Kaluza-Klein (KK) states. In UED all SM particles are free to propagate in all dimensions and the lightest KK particle (LKP), if neutral and stable, can become a good WIMP (SERVANT et al. 2003; AGASHE et al. 2004). Stability is ensured via the conservation of a symmetry called the KK-parity (that is generally assumed but could be broken depending on the compactification scheme). A good candidate for WIMP is the KK-photon that can also approximately identified as the first excited state of the B-boson $B^{(1)}$ (as the mixing with the excited states of the W boson is small). See HOOPER et al. (2007) for a full review on UED DM.

Simplified effective models. With no experimental hints for SUSY or extra dimensions at the Large Hadron Collider (LHC), the focus on WIMPs is in part slightly shifting towards bottom-up approaches. Instead of looking for UV complete models that solve problems of the SM and bring DM candidates as a bonus (top-down approaches), we consider WIMPs as having generic properties (bottom-up approaches). More precisely, in this picture, they are a set of fermionic, scalar of vector particles that can interact through a set of mediators with the SM particles; the masses and coupling constants being treated as free parameters. This approach allows deriving generic constraints and prediction for classes of models (ABDALLAH et al. 2015; ARINA 2018; ATLAS COLLABORATION 2019). Moreover, it still represents a reliable and motivated way to probe physics beyond the SM because various UV-complete models can be mapped onto the same classes of Lagrangians at low energy. In Chapter 2 we study in details fermionic WIMPs in a simplified Lagrangian model with scalar, pseudo-scalar, vector and axial-vector interactions with the SM particles. Moreover, we show how a non-trivial configuration of the low-energy limit of the NMSSM can be analysed within that framework. Amongst the various possibilities of simplified

models one can cite the minimal DM models that aim at producing candidates with the most important DM features while only adding a minimal extension to the SM (Cirelli et al. 2006; E. Ma 2006; Honorez et al. 2007; Cirelli et al. 2015). Asymmetric DM (Nussinov 1985; D. B. Kaplan 1992; D. E. Kaplan et al. 2009a; Petraki et al. 2013; Zurek 2014; Garani et al. 2019), based on the idea that DM abundance originates from a mechanism similar to the abundance of ordinary matter over anti-matter, can be described from simplified models as well. In addition, they can also capture SIDM (Bernal et al. 2016; Chu et al. 2016; Hambye et al. 2020) as we also study in Chapter 2.

Other models

The aforementioned models have been amongst the most attractive ones and have drawn much attention. Let us mention here a few other possibilities. There is millicharged DM (mDM) that possesses a tiny electric charge and can therefore interact with the SM through the regular photon or via dark photons (Liu et al. 2019). This scenario is interesting as it can be probed by the sky-averaged 21-cm observations (Bowman et al. 2018). There are mirror DM models where DM is made of a hidden copy of the SM content (Foot 2014). In the atomic DM models, it is made of bound states (D. E. Kaplan et al. 2009b). Not to forget models where DM interacts only gravitationally (Fairbairn et al. 2018; Markkanen et al. 2018).

Besides, DM scenarios can usually be classified in terms of production mechanisms (*e.g.* thermal for WIMPs or sterile neutrinos, non-thermal for axions), giving new names to candidates with similar properties. An extremely massive ($m \sim 10^{12}$ to 10^{16} GeV) and non-thermally produced version of the WIMP is called the WIMPZILLA (Chung et al. 1998; Kolb et al. 1998). This makes a candidate produced through gravitational interactions only. Strongly Interacting Massive Particles (SIMPs) (Starkman et al. 1990) offer a realisation of SIDM. They are produced via a specific thermal process involving $3 \to 2$ interactions (Hochberg et al. 2014; Choi et al. 2016) instead of $2 \to 2$ interactions for the usual WIMP. Eventually, WIMP-like particles with very small couplings to the SM particles are referred to as Feebly Interacting Massive Particles (FIMPs) and their production mechanism, although thermal, is slightly different than that of the WIMP, see Sect. 2.3.3.

1.4.3 Macroscopic objects and primordial black holes

Historically the first mention of DM by Poincaré in 1906 was referring to dark bodies or dark stars. So far we have introduced DM particle models without discussing the possibility that DM might be made of such macroscopic objects of ordinary matter. We generically call MACHO (for Massive Astrophysical Compact Halo Object) any astrophysical body that does not emit light and is not associated with any planetary system. Examples include unassociated planets, low luminosity stars like white dwarfs and red dwarfs and also brown dwarfs. However, scenarios in which MACHOs that range between planetary to stellar masses are strongly disfavoured by microlensing surveys in the MW (Tisserand et al. 2007).

A non-baryonic class of MACHOs are primordial black holes (PBHs) (Zel'dovich et al. 1967; S. Hawking 1971; B. J. Carr et al. 1974) that provide a good DM candidate. PBHs are supposed to form in the primordial universe from rare and extremely high density fluctuations that collapse directly to BHs right after entering the horizon, after inflation. Since collapsing from gravitational instabilities, their formation are

boosted each time the radiation pressure in the universe drops. This happens for instance at the QCD phase transition (JEDAMZIK 1997; JEDAMZIK et al. 1999), or any other transition when relativistic degrees of freedom disappear (e^+e^- annihilation, etc.). The abundance of PBHs depends on the amplitude of the primordial power spectrum, and should be extremely small if the latter were at the level constrained by Planck. However, the amplitude is not constrained on small scales, and could actually be such that PBHs represent a significant fraction, if not all, of the DM in the universe. Present at the time of last-scattering and if numerous enough they provide the non-baryonic mass necessary to understand the anisotropies of the CMB, playing the role of DM. This scenario faces observational pressure too, with the microlensing studies constraining MACHOs, with BBN and CMB, with γ-ray and cosmic-ray instruments – due to Hawking's radiation (S. W. HAWKING 1974) – and with other probes (B. CARR et al. 2020b). Nonetheless, one window remains open for PBHs with mass $10^{17}\ \mathrm{g} < m_{\mathrm{PBH}} < 10^{22}\ \mathrm{g}$. Recent studies even suggested that PBHs could provide a solution to the asymmetry between matter and antimatter (B. CARR et al. 2020a) on top of being the main or only DM component. Finally, let us point out that PBHs have also regained interest thanks to the latest observations of black holes binary mergers with the gravitational waves detectors LIGO/Virgo (CLESSE et al. 2018; LIGO AND VIRGO COLLABORATIONS 2019). In the scenario inspired by LIGO/Virgo the fraction of DM in the form of PBHs is established at $\sim 10^{-3}$ (DE LUCA et al. 2020; A. HALL et al. 2020; FRANCIOLINI et al. 2021) even if a total fraction of 1 is still possible in some models (JEDAMZIK 2020a,b).

1.5 Searches for Dark Matter and constraints

So far, DM has been discussed in terms of its gravitational manifestations or signatures on different astrophysical scales. Dedicated searches for particle DM further follow three main strategies. The first one is to try to produce DM particles at colliders and spot missing energy in the reconstructed final states after a collision, signalling dark particles escaping the detectors. Direct detection methods focus on searching DM present in the Earth's surroundings via its its direct interactions with target SM particles/atoms in underground laboratories. Eventually, indirect methods search for the final products of DM annihilation or decay (indirect searches may also include searches for the impact of DM interactions with its environment - capture in stars or planets, stellar evolution, etc., somewhat connected to direct searches). For example one can search for an excess of gamma rays, cosmic rays or neutrinos over a controlled background that could be induced as by-products of the DM annihilation into SM particles (assuming that DM self-annihilates).

1.5.1 Particle collider searches

To find DM at colliders the generic method is to search in the detectors for an excess of events with a single final particle or jet and an important amount of missing transverse energy $\not{E}_{\mathrm{T}}$. Indeed at a proton-proton collider like the Large Hadron Collider (LHC), if DM interacts with the SM we expect to have events of the form $pp \to X + \mathrm{DM}$ where X is a single final state. Moreover, if these interactions are weak DM should not be seen by the detectors and therefore they should escape without depositing energy (leaving missing energy in the reconstruction of the event). The search is then dependant on the nature of the state $X = \gamma, W, \mathrm{jets}, Z, h, b, t$, and it requires a good reconstruction of the event and good control of the background. For instance in

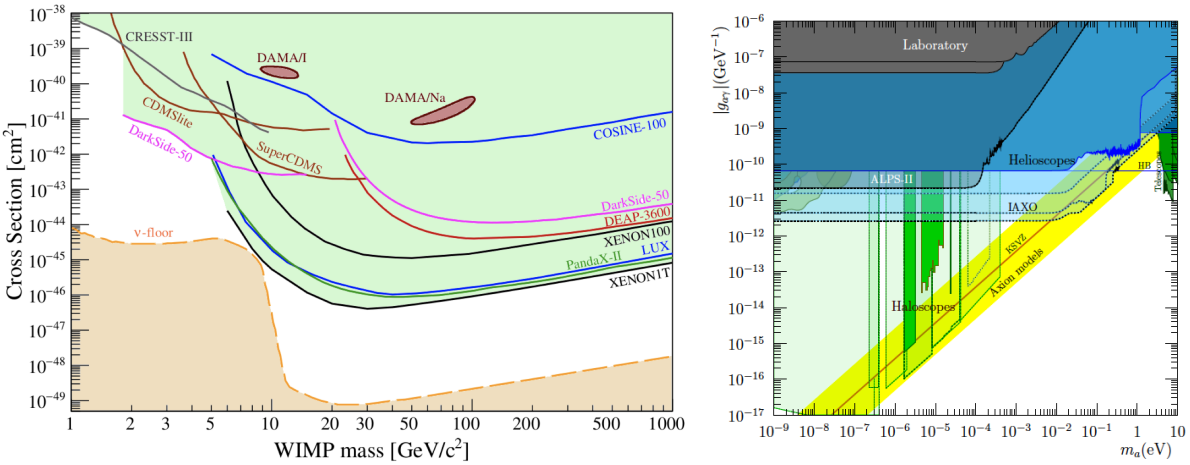

Figure 1.9 – Left panel: Compilation of exclusion limits at 90% of the spin-independent WIMP-nucleon cross-section with respect to the DM mass. The neutrino floor is also represented. Figure taken from SCHUMANN (2019). **Right panel:** Compilation of constraints on the axion-two-photons coupling with respect to the axion mass. The shaded areas show the reach of future experiments. Figure taken from IRASTORZA et al. (2018).

the detectors ATLAS (ATLAS COLLABORATION 2013) and CMS (CMS COLLABORATION 2008) at the LHC, if $X = \gamma$ one of the main background contamination comes from events $pp \to Z(\to \nu\bar{\nu}) + \gamma$ where the Z boson also escapes the detector. Selection cuts in the kinematics of the analysed events are necessary to optimise the background rejection. See a review in KAHLHOEFER (2017). As nothing has been detected so far, only constraints (dependent on the nature of the interactions) are set on the couplings between SM and DM particles. In the literature generic analysis are often performed using effective operators (FOX et al. 2011; J. GOODMAN et al. 2011) or simplified models (ABDALLAH et al. 2015; KRAML et al. 2017; ATLAS COLLABORATION 2019). Eventually, see MIMASU et al. (2015) for a review of ALPs searches at colliders.

1.5.2 Direct searches

Direct searches are one of the most efficient ways to search for certain classes of DM particles, especially WIMPs and axions. It has been shown however that building detectors for sterile neutrinos would be excessively challenging (ANDO et al. 2010). Let us divide the following discussion between the specific methods employed for WIMPs and then for axions.

WIMP direct searches

In the WIMP scenario, DM interacts weakly with the SM particles which offers a handle for detection using the scattering process $\chi + \mathrm{SM} \to \chi + \mathrm{SM}$. Such interactions can be classified in two categories, whether their cross-section depends on the velocity of the incoming particles or not. In the former case, direct detection prospects are suppressed due to the low velocity of DM particles. Therefore velocity-independent interactions are more efficiently probed with this technique. The goal of numerous experiments is to detect the recoil of a target SM particle induced by such scattering. Common methods relies on crystal targets such as DAMA/LIBRA (BERNABEI et al. 2018), EDELWEISS (ARNAUD et al. 2018), (Super)CDMS (AGNESE et al. 2018), CoGeNT

(AALSETH et al. 2013), CRESST (ANGLOHER et al. 2012) or noble liquid time projection chambers such as Xenon1T (APRILE et al. 2018), DarkSide-50 (AALSETH et al. 2018) or LUX (AKERIB et al. 2017). See SCHUMANN (2019) for a review. Due to the low expected event rate, background rejection is one of the hardest challenges for these experiments. To face it, experimental collaborations use several shielding tools: they usually place the detector underground and they only focus the search on a fiducial part of the total detector material. Except for the DAMA result (that we discuss later), no clear evidence of what could be a DM signal is found today with these methods. Thus, the results are shown as upper bounds on the scattering cross-section, as depicted in the left panel of Fig. 1.9. One still must be careful with these exclusion limits having in mind that they depend both on the nature of the interaction (spin-dependent or spin-independent), the nature of the recoiling particle (proton, neutron or electron) and on the DM phase-space distribution around Earth that is not perfectly constrained (M. W. GOODMAN et al. 1985; JUNGMAN et al. 1996; LEWIN et al. 1996; GREEN 2010; CATENA et al. 2012; LAVALLE et al. 2015; LACROIX et al. 2018) – not to mention the impact that subhalos in the vicinity of the Earth would have and that is not considered as studied in IBARRA et al. (2019).

To give more details we write the expected event rate as

$$\frac{\mathrm{d}R}{\mathrm{d}E_\mathrm{r}} = \frac{M}{m_\mathrm{N}}\frac{\rho_\chi}{m_\chi}\int \mathrm{d}^3\mathbf{v}\, f_\oplus(\mathbf{v}) v \frac{\mathrm{d}\sigma}{\mathrm{d}E_\mathrm{r}} \tag{1.18}$$

where M is the total target mass, m_N the mass of the target nuclei and m_χ the mass of the DM particle. The function ρ_χ is the local DM density and $f_\oplus$ is the velocity distribution of DM in the Earth-frame. It must be truncated from above since no particle in the Galactic frame has a velocity over the escape velocity v_esc[5]. The scattering cross-section is denoted σ, the velocity norm $v = |\mathbf{v}|$ and E_r represents the recoil energy. One can also trade the later variable for an angle as $E_\mathrm{r} = \mu_\mathrm{N}^2 v^2/m_\mathrm{N}(1-\cos\theta)$ with θ the scattering angle in the centre of mass frame. Here we also introduced the reduced mass $\mu_\mathrm{N} = m_\mathrm{N} m_\chi/(m_\mathrm{N}+m_\chi)$. Then if we denote by E_th the minimal energy threshold of the detector it imposes a minimal velocity $v_\mathrm{min} = \sqrt{m_\mathrm{N} E_\mathrm{th}/2}/\mu_\mathrm{N}$ of the incoming DM particle in order to have detection. Furthermore one can generally decompose the cross-section in a spin-independent and an spin-dependent part as follow

$$\frac{\mathrm{d}\sigma}{\mathrm{d}E_\mathrm{r}} = \frac{m_N}{2\mu_\mathrm{N}^2 v^2}\left[\sigma_\mathrm{SI} F_\mathrm{SI}^2(E_\mathrm{r}) + \sigma_\mathrm{SD} F_\mathrm{SD}^2(E_\mathrm{r})\right] \tag{1.19}$$

where σ_SI and σ_SD are the cross-sections at zero momentum transfer and F_SI and F_SD are the associated nuclear form factors that depend on the recoil energy (JUNGMAN et al. 1996). One can usually consider that it is possible to decompose the cross-section into several bits that go as

$$\frac{\mathrm{d}\sigma}{\mathrm{d}E_\mathrm{r}} \propto v^n \quad \text{with} \quad n = -2, 0\,, \tag{1.20}$$

so that the particle physics contribution to Eq. (1.18) is decoupled from the astrophysics part that can be written, according to the velocity dependence as,

$$g(v_\mathrm{min}) = \int_{v>v_\mathrm{min}} \mathrm{d}^3\mathbf{v}\, \frac{f_\oplus(\mathbf{v})}{v} \quad \text{and} \quad h(v_\mathrm{min}) = \int_{v>v_\mathrm{min}} \mathrm{d}^3\mathbf{v}\, f_\oplus(\mathbf{v}) v\,. \tag{1.21}$$

[5] In any case, a consistent phase-space distribution function should take that into account by being zero at large velocity. Therefore, formally, the integral can go to infinity. Moreover, one could also be sensitive to the tiny flux of high velocity unbound particle crossing the Galactic halo.

Let us now discuss the DAMA exception. Because of the Earth rotation around the Sun, and therefore in the local DM distribution, the total amount of detected events should be annually modulated (Drukier et al. 1986; Freese et al. 2013). The DAMA collaboration claims to have detected a DM annual modulation of at least $9.5\,\sigma$ (Bernabei et al. 2018). The corresponding parameter space is shown as contour plots in Fig. 1.9. However, this result is singular and in tension with the constraints set by the other instruments. Today it is investigated by the collaborations SABRE (Antonello et al. 2019) and COSINE-100 (Ko et al. 2019) – which has already excluded the discovery. Nonetheless, the origin of the DAMA excess, even if coming from systematic or environmental effects, is yet to be explained.

Finally, let us mention that the direct detection experiments for WIMPs will soon face the neutrino floor issue (Billard et al. 2014) shown in orange in Fig. 1.9. In other words, they will reach the sensitivity threshold for neutrinos to become a new part of the background, which is hard to reject. Proposals for distinguishing DM events from neutrino ones are considered and could come from the annual modulation and the preferred directionality of DM particle trajectories with respect to the detector, even though it will remain a challenging experimental task. On the other hand, probing the neutrino floor should also allow an alternative exploration of the neutrino sector of the SM (Boehm et al. 2019; Boehm et al. 2020).

Axion-like particle direct searches

In the case of ALPs, they can also be probed via direct detection techniques – see a review in Irastorza et al. (2018). Many of them are based on the Primakoff effect: the conversion of axions into detectable photons in a strong magnetic field. Some also use the axio-electric effect: the interaction of axions with electrons. This should be possible due to the allowed coupling of the axion field to the electromagnetic field tensor and to electrons,

$$\mathcal{L} = -\frac{1}{4} g_{a\gamma} a F_{\mu\nu} \tilde{F}^{\mu\nu} - g_{ae} \frac{\partial_\mu a}{2m_e} \bar{e} \gamma^\mu \gamma_5 e \tag{1.22}$$

where we introduce the couplings constants $g_{a\gamma}$ and g_{ae} that are the quantities probed by the experiments. Today the ADMX collaboration (Asztalos et al. 2010), because it has not detected axions in the Galactic halo, provides the best constraint on $g_{a\gamma}$ on a restricted range of mass. In order to cover the entire parameter space available to the QCD axion, other specific proposals for axion direct detection in the Galactic halo with such haloscopes are either under development or have obtained preliminary results. We can mention ABRACADABRA (Kahn et al. 2016; Ouellet et al. 2019), CASPEr (Budker et al. 2014) or MADMAX (MADMAX Working Group 2017). Furthermore, one can probe axions that could be produced in the Sun from the Primakoff effect (Primakoff 1951), which would lead to an axion flux originating from the Sun. Helioscopes are designed to convert these axions back to photons by means of intense magnetic fields, such as CAST (Arik et al. 2014) or IAXO (Armengaud et al. 2014) to put constraints on $g_{a\gamma}$ on a larger mass range. See the summary plot in the right panel of Fig. 1.9.

In addition, let us point out that the crystal-based detectors for WIMPs can also be used to search for ALPs again based on the Primakoff effect, examples are EDELWEISS (Armengaud et al. 2013) and the DAMA instrument (Bernabei et al. 2001). The liquid gas detectors are not sensitive to that effect but they can probe the equivalent of the photo-electric effect for axions (Derevianko et al. 2010). Interestingly,

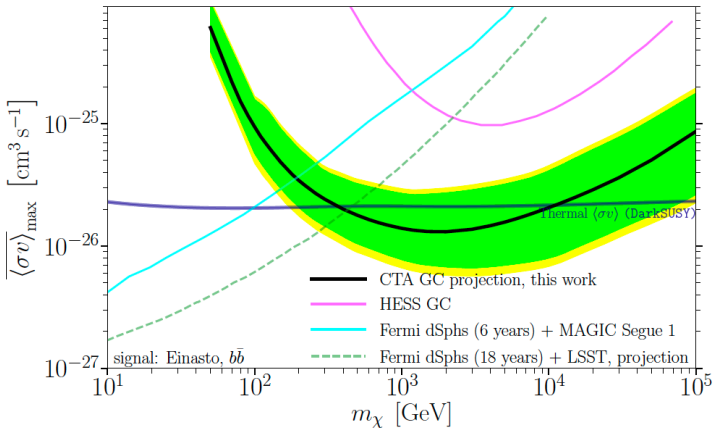

Figure 1.10 – Compilation of the upper bound on the annihilation cross-section from gamma-ray observations. Here the DM density distribution in the MW is assumed to follow an Einasto profile (EINASTO et al. 1974) and the gamma-ray signal is produced through the $b\bar{b}$ channel. This figure is taken from CTA CONSORTIUM (2020).

the Xenon1T collaboration has detected an electron recoil excess giving a 3.5σ significance to a solar-axion model (APRILE et al. 2020). However, this excess is sensitive to the background modelling and and its interpretation in terms of axions may be in tension with astrophysical observations as stated in DI LUZIO et al. (2020), so that it should be investigated further.

1.5.3 Indirect searches

The spectrum of indirect searches is vast and we present here the principal observations setting the strongest constraints on the aforementioned DM candidates. The method relies on the assumption that DM can self-annihilate or decay to produce SM particles, which may be detectable (PROFUMO et al. 2010; LAVALLE et al. 2012; CIRELLI 2013; GASKINS 2016; SLATYER 2017; PÉREZ DE LOS HEROS 2020). Therefore the idea mainly involves astrophysical observation in search of an excess of signal over a controlled background/foreground. Three different categories of SM targets are mainly probed: gamma rays, neutrinos and cosmic rays. Indirect searches can also rely on cosmological observables, such as the Sunyeav-Zeldovich effect (poorly constraining (COLAFRANCESCO 2004; LAVALLE et al. 2010)) or the CMB (energy deposition from annihilation or decay around recombination). In the following, we detail the current status of the searches in each case. In the end, we also mention the contribution of cosmology. As no DM signal has been unambiguously detected so far constraints are usually set on the decay rates and on the annihilation cross-section. In the most common scenarios, the latter appears in an average over the velocity distribution which can be decomposed as follows:

$$\langle\sigma_{\rm ann} v\rangle = \sigma_0 c + \sigma_1 c \left\langle \frac{v_{\rm rel}^2}{c^2} \right\rangle + \mathcal{O}\left(\frac{v_{\rm rel}^4}{c^4}\right) , \tag{1.23}$$

where the first and second terms are respectively called the s-wave and p-wave terms. The quantity c is the speed of light. Since in most astrophysical configurations DM is non-relativistic, indirect probes are essentially sensitive to the velocity-independent s-wave term. On the other hand, sensitivity to the p-wave term is usually much worse and strongly depends on the DM velocity dispersion in the targeted system (for instance, $v \sim 10^{-3}$ in the Milky Way today, while it was much smaller at recombination

time). Therefore constraints on σ_1 (for $\sigma_0 = 0$) are usually weaker than the constraints on σ_0. Note, however, that more intricate velocity dependencies can also be encountered *e.g.* with Sommerfeld enhancement effects become relevant (Hisano et al. 2004; Cirelli et al. 2006; Arkani-Hamed et al. 2009; Iengo 2009; Cassel 2010).

Gamma-ray observations

Gamma rays produced by astrophysical sources are observed today by different instruments. Direct observation is only possible in space as the atmosphere is opaque to photons in that energy range. The Fermi Large Area Telescope (Fermi-LAT) orbiting the Earth has been operating since 2010 and has provided among the most complete dataset in the energy range 0.1-100 GeV. It has a narrow point spread function (*i.e.* resolution angle) of $\theta_{\rm r} = 0.5^\circ$ and a wide field of view ~ 2.4 sr but its sensitivity decreases fast after 100 GeV. At higher energies, an improved sensitivity is obtained on Earth by resorting to imaging atmosphere Cherenkov telescopes (IACTs), which benefit from a much larger collection area (typical non-thermal gamma-ray fluxes fall off like power laws with energy). As IACTs are ground-based they do not directly detect individual photons but rather the particle shower produced by their interaction in the atmosphere via the Cherenkov effect. The current instruments are H.E.S.S., MAGIC, VERITAS and HAWC. In a few years, the Cherenkov Telescope Array (CTA) will become the leading observatory (CTA Consortium 2019) using this technology. The latter should have a good angular resolution $\theta_{\rm r} \sim 0.05^\circ$, however as all IACTs, it will have also a much narrower field of view (approximately a few tens of degrees squared).

In the past, special attention has been paid to the centre of the Galaxy. Indeed, the mass density profile of DM in the MW should be the highest towards its centre, enhancing there a possible emission from DM annihilation. To illustrate this, in the simplest scenario, the differential flux of photons coming from DM on a line of sight in direction $\hat{\mathbf{n}}$ satisfies

$$\frac{\mathrm{d}\phi_{\rm DM\to\gamma}}{\mathrm{d}E}(\hat{\mathbf{n}}) \propto \langle\sigma v\rangle \int_0^{+\infty} \rho^2_{\rm DM}(s,\hat{\mathbf{n}})\,\mathrm{d}s \tag{1.24}$$

with $\rho_{\rm DM}(s,\hat{\mathbf{n}})$ the mass density of DM along the line of sight. Therefore the higher the integral of $\rho_{\rm DM}(s,\hat{\mathbf{n}})$ the more annihilation products can be seen (assuming a local conversion to gamma rays). It turns out that an intense and diffuse gamma-ray emission has been discovered in the Fermi-LAT data that is currently difficult to fully interpret given the complex astrophysical environment close to the Galactic Centre. Indeed, our current knowledge of the gas content, of the (regular and turbulent) magnetic field configuration, of conventional cosmic-ray sources or other cosmic-ray acceleration mechanism, makes it extremely difficult to construct a reliable background model. Using simple background models leads to finding excess of gamma-rays in the GeV energy range (Fermi-LAT Collaboration 2017), but the relative amplitude of this excess is largely at the level of current theoretical errors. This is illustrated by the many explanations as for possible conventional contributions in this energy range – *e.g.* from the galactic bulge emission (Bartels et al. 2018; Macias et al. 2018) or millisecond pulsars (Bartels et al. 2016). Another interpretation relies on a DM annihilation signal (Daylan et al. 2016; Leane et al. 2019; Zhong et al. 2019), but in the absence of a more robust background modeling, it can hardly be considered as serious hint for DM. We can note in passing that conventional astrophysical emissions are much harder to calculate and to estimate as they often originate in non-linear and complex phenomena. On the other hand, a DM annihilation signal

prediction is simply the integral of a squared density along a line of sight. Recent studies have shown no significance for a DM signal and have even used this to place severe constraints on the DM annihilation cross-section (ABAZAJIAN et al. 2020). In the future, the amount of millisecond pulsars around the Galactic centre could be probed with gravitational wave detectors (CALORE et al. 2019b) to understand better whether or not they are responsible for the excess.

Instead of focusing on the very centre of the Galaxy where the data interpretation is complicated, it is also possible to look in surrounding patches of the sky, where the DM emission is still strong. As no DM emission has been detected there so far, these regions are used to set constraints on the DM annihilation cross-section (CIRELLI et al. 2010; FERMI-LAT COLLABORATION 2012a; CHANG et al. 2018). Furthermore, the constraints that CTA will be able to set, if no detection is made, have also been forecast (LEFRANC et al. 2015; SILVERWOOD et al. 2015; CTA CONSORTIUM 2020) – see Fig. 1.10. Other interesting targets are dwarf galaxies since they are background free. In addition, they should be embedded into a DM subhalo where the annihilation of DM particles should thus be enhanced. Constraints from dwarf spheroidal are amongst the best current constraints on the DM annihilation cross-section in the range 1-100 GeV (FERMI-LAT COLLABORATION 2015b). For similar reasons galaxy clusters are interesting extragalactic targets because the biggest reservoirs of DM at hand (ANDO et al. 2012). However, the intrinsic gamma-ray emission from these objects is however not well known and subject to large uncertainties - not background-free sources like dwarf galaxies. In complement to Fig. 1.10, constraints on decaying dark matter can be found in *e.g.* CIRELLI et al. (2012).

Another set of analysis relies on DM structuring. A DM signal would trace its distribution and therefore impact the angular power spectrum of the gamma-ray flux. MW subhalos can have an impact on the spatial distribution of the diffuse Galactic gamma-ray emission (ANDO 2009). On larger scales DM structuring can also leave an imprint on the extragalactic background (ANDO et al. 2006, 2007). In practice both effects need to be combined. The measurement of the angular power spectrum has been performed in ACKERMANN et al. (2012a) providing constraints on DM annihilation (ANDO et al. 2013). Furthermore, inside individual objects such as the MW or its satellites, the presence of substructures could also boost the DM annihilation signal, imposing more stringent constraints or improving the hope for a detection (STREF et al. 2017; ANDO et al. 2019). Eventually, in Chapter 5 a special focus will be given to the detectability of point-like subhalo in the MW with the Fermi-LAT and CTA instruments (BUCKLEY et al. 2010; PIERI et al. 2011; BERTONI et al. 2015; HÜTTEN et al. 2016; CALORE et al. 2017, 2019a).

Cosmic-ray observations

Unlike gamma rays, cosmic rays do not travel in straight lines as they diffuse on Galactic magnetic turbulences. Therefore, they do not trace the position of their source. Nevertheless, antimatter cosmic rays remain a good probe for DM searches. They have been observed by various instruments, the most important ones being PAMELA, the Alpha Magnetic Spectrometer (AMS-02) installed on the International Space Station (ISS) and ATIC, a balloon-borne instrument. The Fermi-LAT and IACTs are also sensitive to cosmic rays. Moreover, cosmic rays are also observed by the Voyager satellites that reached the outskirts of the solar system and left the heliopause. Two major observations for DM have been discussed in the past decades, the positron excess and the anti-proton excess.

The instruments PAMELA, Fermi-LAT, AMS-02 and others have put in evidence a rise in the positron fraction $\phi_{e^+}/(\phi_{e^+}+\phi_{e^-})$ at energies higher than ~ 10 GeV (ADRIANI et al. 2009; FERMI-LAT COLLABORATION 2012b; AMS COLLABORATION 2013), that cannot be interpreted in terms of a pure secondary contribution – produced from inelastic interactions of cosmic-ray nuclei with the interstellar gas (MOSKALENKO et al. 1998; DELAHAYE et al. 2009; LAVALLE 2011; BOUDAUD et al. 2017a). DM-induced interpretations of this excess have been proposed, backed with compatible particle models (TURNER et al. 1990; BALTZ et al. 2002; FOX et al. 2009; IBARRA et al. 2009; CUOCO et al. 2017). However, a positron production from annihilating thermally produced WIMP particles[6] would have to be strongly boosted by the presence of local subhalos in order to match the excess; to such an extent that is unlikely in the ΛCDM model (LAVALLE et al. 2007, 2008; PIERI et al. 2011) – although this constraint can be alleviated in specific scenarios with Sommerfeld enhancement for instance (CIRELLI et al. 2008). In addition, it also has to be consistent with the non-observation of a gamma-ray counterpart (BERTONE et al. 2009) and no overproduction of antiprotons (see the next paragraph). Moreover, standard astrophysical explanations exist, which significantly moderates the relevance of more exotic solutions. For instance, pulsars are well-known sources of positrons, which could contribute a significant part, if not all of the observed positron flux (HOOPER et al. 2009; PROFUMO 2009; SERPICO 2012; YUAN et al. 2014; BOUDAUD et al. 2018b). Predictions of the cosmic-ray lepton flux at high energy is also affected by a potentially large statistical variance since a small number of sources might dominate the yield in a rather restricted high-energy range (SHEN 1970; AHARONIAN et al. 1995; DELAHAYE et al. 2010).

Several studies have also performed statistical analysis of the antiproton flux data from AMS-02 and have found an excess that seems to be in agreement with a DM sourced production (CHOLIS et al. 2019; CUOCO et al. 2019). This is particularly intriguing because simply by knowing the cosmic ray flux in the Galaxy and the baryonic matter distribution one can compute the expected background of antiprotons. However, the discovery of an excess by performing fits on the data may be a biased result, especially because uncertainties in the models are large. Indeed, the production cross-section of antiproton is known to roughly 20% not forgetting to mention their propagation that is non-trivial to predict. As a matter of fact, a careful treatment of the data shows that they are fully consistent with a pure astrophysical origin (BOUDAUD et al. 2020). The presence of a DM-induced component could be tested more robustly in the future with the analysis of other antimatter cosmic-ray nuclei (KORSMEIER et al. 2018).

Eventually, the Voyager space probes, because they are no longer under the influence of the solar system magnetic field, can capture cosmic rays with sub-GeV energy and therefore set constraints on DM with a mass in the MeV range, providing a probe of s-wave annihilation complementary to the CMB. Besides, the p-wave constraints are even more stringent than the CMB bounds (BOUDAUD et al. 2017b, 2018a). Interestingly, the Voyager measurements can also constrain evaporating light PBHs (BOUDAUD et al. 2019).

Neutrino observations

Reviews on the implication of neutrino observation for DM can be found in JUNGMAN et al. (1996) and LAVALLE et al. (2012). Similarly to photons, neutrinos

[6] Assuming the s-wave cross-section $\langle\sigma_{\rm ann}v\rangle = \sigma_0 c \sim 3\times10^{-26}$ cm^3 s^{-1}, the typical value to obtain the correct abundance of DM in the Universe through the standard freeze-out mechanism – see Sect. 2.3.3.

travel in straight lines and trace the position of their source. However, they have a very low cross-sections therefore, assuming that the typical flux of high-energy neutrinos is similar to that of gamma rays, the expected event rate is comparatively very small. To get a sensitivity similar to that of gamma-ray telescope, one should scale the detection area by a factor $\sim \sigma_{\rm T}/G_{\rm F} \simeq 10^8$, where $\sigma_{\rm T}$ is the Thomson cross section, and $G_{\rm F}$ is the Fermi constant (the Fermi-LAT satellite has an effective detection area of ~ 1 m^2). This explains why neutrino telescopes need a huge detection volume to hope for detection of cosmic neutrinos. Neutrino telescopes are usually made of photomultipliers immersed under water or ice. The principle of cosmic neutrino detection mostly relies on the detection of their parent charged leptons, after electroweak conversion close to the detector, from the associated Cherenkov showers developing in water or ice. The current observatories are IceCube at the South Pole (ICECUBE COLLABORATION 2006), ANTARES in the Mediterranean sea (ANTARES COLLABORATION 2011), Super-Kamiokande (FUKUDA et al. 2003) and the Baikal-GVD (BAIKAL-GVD COLLABORATION 2019). KM3NET (KATZ 2006), successor of ANTARES is being built and since its starting up in 2010 IceCube has been (and will be further) upgraded to improve its sensitivity (ICECUBE COLLABORATION 2012; ROTT 2013). The minimal energy threshold goes from ~ 5 MeV in Super-Kamiokande to ~ 10 or 100 GeV in IceCube.

The first way to search for DM particles with neutrinos is via their possible production in the Galactic halo and, as for gamma rays, towards the Galactic centre (ICECUBE COLLABORATION 2011, 2013b). Another interesting method is to search for DM in the centre of the Sun or the Earth. Indeed owing to possible interactions with the elements making the Sun or the Earth, DM particles can be gravitationally captured and can accumulate in their centres. If DM self-annihilates in these dense regions neutrinos are the only SM products that escapes and can be detected. In the Sun, the capture rate of DM gets equilibrated by the annihilation rate in most of the relevant parameter space within a timescale shorter than the Sun's age (evaporation becomes sizable only for masses $\lesssim 5$ GeV), such that the DM particle population remains constant. The neutrino flux can therefore be predicted from the capture rate only, which is fixed by scattering interactions. This is why DM-induced solar neutrino searches are complementary with direct detection searches, and are expressed in the same parameter space (scattering cross section vs. mass). The capture rate depends on the spin-independent and spin-dependant terms of the cross-section with the elements it contains. As it is dominantly composed of hydrogen, solar observations are efficient to constrain the spin-dependent part (SUPER-KAMIOKANDE COLLABORATION 2011; ICECUBE COLLABORATION 2013a). In the case of the Earth, equilibrium cannot be assumed but its composition being mostly of spin-0 nuclei, it is a better target for spin-independent interactions (MIJAKOWSKI et al. 2020). Eventually, the IceCube collaboration has recorded very high-energy events (AARTSEN et al. 2014) that might be interpreted as DM particles with the mass in the PeV range (ESMAILI et al. 2015; MURASE et al. 2015) – even though other astrophysical explanations have been proposed. However, so far the statistics is too low to properly identify the origin of the events.

Cosmological probes

We have seen that cosmological observations have been decisive to confirm the missing mass problem from its gravitational effects on large scales. In practice, DM particle interactions with the SM particles (through decay, annihilation or scattering)

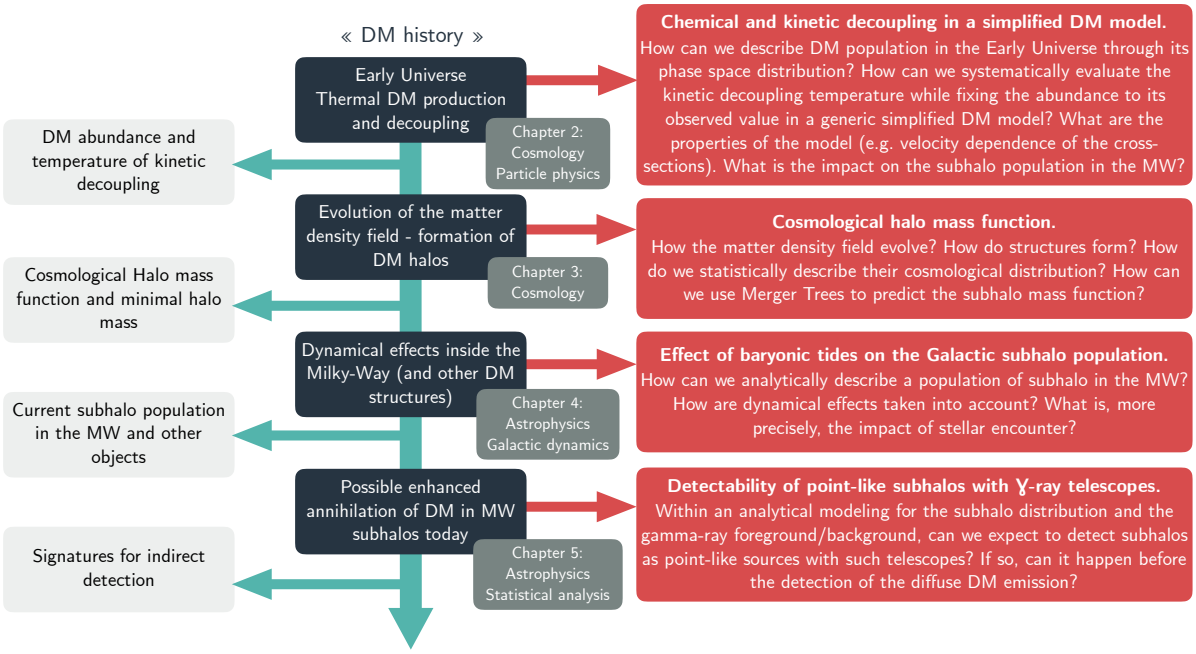

Figure 1.11 – Representation of the outline of this work.

would exchange energy with the photon bath and leave imprints on the temperature and polarisation power spectra or on the frequency spectrum of the CMB (Salati 1985; Slatyer et al. 2009; Ali-Haïmoud et al. 2015; Slatyer 2015; Slatyer et al. 2016). Moreover, they can also contribute extra-ionisation during the reionisation epoch (Liu et al. 2016) – when the hydrogen gas is ionised by the radiation emitted by the first stars and galaxies. The presence of the large ℓ peaks sets constraints on DM interactions with photons and neutrinos (Boehm et al. 2001; Boehm et al. 2002; Boehm et al. 2005; Wilkinson et al. 2016). In order to probe the Universe in the dark ages (before the formation of the first stars) down to the end of the reionisation epoch, a promising observation is that of the brightness temperature of the hydrogen atom 21 cm line (Furlanetto et al. 2006). As DM annihilation or decay could impact on this 21 cm signal, it will be of particular interest for DM searches (Lopez-Honorez et al. 2016; Liu et al. 2018; Schneider et al. 2020) with observations provided by various instruments (Bowman et al. 2010; Parsons et al. 2010; Paciga et al. 2011; Burns et al. 2012; Greenhill et al. 2012; Haarlem et al. 2013; Mellema et al. 2013; Tingay et al. 2013). BBN can also be another way to set complementary constraints and test the validity of scenarios (Serpico et al. 2004; Wilkinson et al. 2016). Eventually, the abundance of DM measured today provides by itself one of the most stringent cosmological constraints on particle models, both on their interactions with standard matter and their total annihilation cross section – for thermal production scenarios – (Lee et al. 1977; Vysotskii et al. 1977; Steigman 1979; Binétruy et al. 1984; Bernstein et al. 1985; Steigman et al. 2012).

1.6 Summary and outline

One often says that the problem of DM first appeared for the first time in 1933. The astrophysicist Fritz Zwicky was then interested in the Coma galaxy cluster and he discovered that the measured velocity dispersion of galaxies inside exceeded severely

the velocity dispersion inferred from Newtonian's dynamics with an estimation of the total mass made from all the visible matter. He then concluded on the possible presence of an *invisible* non-luminous matter, the DM, inside the cluster, enhancing by two orders of magnitudes its total mass to solve the issue (ZWICKY 1933, 1937). Although this was the first observational appearance of DM, this discovery did not receive much credit because most astrophysicists were concerned by the measurement errors. The issue drew even more attention in the 1970s in part due to Vera Rubin, Kent Ford and others who measured the velocity of stars in spiral galaxies and discovered that once again, one needed an additional dark and massive component to make physical sense of the kinematic observations of galactic scales: stars on the outer arms generically had higher velocities than expected (RUBIN et al. 1970). Today we know that introducing an effective exotic (non-standard) cold and collisionless DM component, whatever it really be (modification of gravity or new form of particles or matter), is necessary to explain many more cosmological and astrophysical observations such as the inhomogeneities in the CMB (Planck18, SPERGEL et al. 2003), BBN, the formation of structures such as galaxies and cluster of galaxies (HAWKINS et al. 2003), gravitational lensing effects (CLOWE et al. 2006) etc. No known form of matter could play the role of DM (e.g. the BBN and CMB constraints): it has to be an (or several) exotic species or a new degree of freedom of a more fundamental theory of gravity. The total rough evolution of the Universe is best described today by a simple model, called ΛCDM, whose main components are dark energy and a specific class of DM candidates identified as cold dark matter (CDM). In the end, there is now little doubt on its existence and understanding its nature is an important challenge, a key to better understand the dynamics, full content, and origin of our Universe

There are two possibilities to tackle the DM problem. The first one is to state that Einstein's law of gravitation is not valid on large length scales and should be modified or replaced. With this point of view, DM does not exist and our misunderstanding of gravity itself is the cause of all the *anomalous* observations. However, finding an accurate and physically acceptable modification is a real challenge. One could mention for instance the empirical proposal MOND (for MOdified Newtonian Dynamics) (MILGROM 1983) that relies on this eventuality but whose "covariantisation" remains a very challenging task or needs the introduction of DM as new degrees of freedom (FAMAEY et al. 2012). Several interesting attempts are still ongoing (SKORDIS et al. 2020). The second way to think of this problem is to introduce DM as new massive particles: "non-baryonic particles". They could be particles predicted by SM extensions: supersymmetry, Kaluza-Klein theories, string theory, etc, or particles introduced to solve more specific problems like axions or massive neutrinos. Not to forget that DM could also be made of other exotic, while macroscopic, objects, like primordial black holes (B. J. CARR et al. 1974; CHAPLINE 1975; B. CARR et al. 2016). Today DM particles are actively searched through different strategies, exemplified by a series of experiments or observational programs, e.g.: EDELWEISS (BENOIT et al. 2002; ARNAUD et al. 2018), CDMS (AALSETH et al. 2011)/SuperCDMS AGNESE et al. 2014, XENON1T (APRILE et al. 2018, 2020), AMS02, Gaia (THE GAIA COLLABORATION 2016; GAIA COLLABORATION 2018), Fermi-LAT (W. B. ATWOOD et al. 2009), etc. Direct detection experiments try to find DM through its direct interaction with classical SM matter, assuming that such an interaction exists. Indirect detection goal is to find by-products of DM-DM or DM-SM interactions anywhere in the Universe or their imprint on cosmological observables (such as photons or cosmic ray emissions that could only be sourced by the presence of DM). Eventually, the hope at colliders is to produce DM particles from the SM particle interactions and identify their presence

as the missing energy they carried out of the detectors with them.

While the CDM paradigm seems to be the best model to explain most current data, some tensions arose in the last decades, in particular at the galactic scale and below, then referred to as the small scale issues. Analysing the causes and possible solutions to these issues might be key in a deeper understanding of the nature of DM. On the other hand, since baryonic physics remains a potential clue, precisely determining the properties of CDM candidates on small scales and the related impact on DM searches, is an important step that must be studied in parallel. For instance, the (gravitational) detection of DM subhalos would not only confirm that a significant part of DM is cold, but it would also provide indications as for the interaction properties of DM particles. Therefore, having a precise understanding of features that single out CDM from other proposals, like the presence of abundant populations of subhalos in galaxies and clusters, is important to really test CDM through its intimate properties. This thesis develops in this context and addresses tightly related questions. The main goal is to understand, from first principles and without relying a priori on cosmological simulations, how dark matter (sub)halos are distributed in the Universe and what they can tell us about the DM particle nature. The different parts are centred around an analytical model for the description of the fine structure of DM that had been optimised to describe the DM distribution in the MW, with an unprecedented level of details (Stref 2018) – hereafter denoted SL17. It is based on a statistical description of the ensemble of all subhalos and it encompasses all the structures from the largest to the smallest down to $\sim 10^{-12}$ $M_\odot$ in some scenarios (a resolution orders of magnitude beyond the reach of cosmological simulations – Springel et al. 2008). It is constructed on an initial (also said cosmological) distribution assuming hard-sphere substructures following the total DM profile of the host. Based on consistent modelling of the different dynamical effects, subhalos are then pruned by tidal stripping and destroyed when becoming too weakly bounded. This model, fully described in Chapter 4, has been a motivation to explore various domains of theoretical high-energy physics at the crossroad between cosmology, particle physics, astrophysics and gravitational dynamics.

After this general introduction on DM, the rest of the document is divided into four other chapters following a chronological order in terms of the DM history and represented in Fig. 1.11. In Chapter 2, I study the physics of DM particles in the early Universe assuming DM is made of WIMPs equipped with a minimal set of interactions with SM particles, and I systematically link the particle physics properties to the kinetic decoupling temperature which is itself related to the minimal subhalo mass. In Chapter 3, I address the formation of DM structures and the derivation of the cosmological mass function for the subhalo population. In Chapter 4, I show how to implement a new dynamical effect in the semi-analytical subhalo model: the encounters with individual stars. Eventually, in Chapter 5, I discuss the possibility for subhalos in the MW to be detected as point-like sources of gamma rays with the Fermi-LAT and CTA instruments.

II

Halo minimal mass in a simplified particle physics model

"Chacun trouvait un terme pour désigner l'unité. Chacun affûta ses poignards pour zigouiller son contradicteur. Toutes ces positions signifiaient la même chose : dans l'espace-temps ondulait une singularité première. Une explosion la libéra. Alors, l'inétendu s'étendit, l'inéfafable connut le décompte, l'immuable s'articula, l'indifférencié prit des visages multiples, l'obscur s'illumina. Ce fut la rupture. Fin de l'Unicité !"

Sylvain Tesson, La panthère des neiges

Contents

The evolution of the Universe is known to be influenced by the microscopic behaviour of its particle content. In a scenario where DM particles are thermally produced in the early Universe through their interactions with the SM particles, the strength of the creation processes is particularly important as it fixes the total DM abundance measured today (I. B. ZELDOVICH et al. 1975; LEE et al. 1977; BINÉTRUY et al. 1984; SREDNICKI et al. 1988; GONDOLO et al. 1991; GRIEST et al. 1991). The relation between particle models and the quantity of DM measured is then determined by their chemical decoupling (BRINGMANN et al. 2007). Besides, the same interactions also fix a small scale cut-off for the mass of halos at formation, because of DM kinetic decoupling (BOEHM et al. 2005; GREEN et al. 2005; BERTSCHINGER 2006), as it will be explained in Chapter 3. In the CDM paradigm, the minimal mass can be as low as $\sim 10^{-12}$ $M_\odot$ (BRINGMANN 2009), in which case all large DM structures should be populated with a substantial number of subhalos (V. BEREZINSKY et al. 2003). The Galactic halo does not break the rule; a statistical description of the subhalo population in the MW is given in Chapter 4 by the SL17 model. There, the minimal halo mass is a free input parameter. In this chapter, we then address the question: What is a realistic value expected in a simplified WIMP model? The aim is twofold. Firstly, we want to classify a set of generic interactions by extracting the relevant behaviour that impacts the minimal mass of halos. We focus particularly on the velocity dependence of the cross-sections involved in the different interactions. Secondly, combined with the SL17 model, the long term goal of this study would be able to produce consistent forecasts for detection experiments, where the microscopic behaviour of DM impacts both the structuring in the MW and its signatures. Along this way, we pay specific attention to constraining this simplified particle model to correctly predict the observed DM abundance. In addition, we also look at the importance of a possible DM self-interaction.

Because no beyond the standard model theories have been confirmed experimentally yet, simplified models are currently flourishing (ABDALLAH et al. 2015; KRAML et al. 2017; ARINA 2018; ATLAS COLLABORATION 2019). If defining a UV complete theory and examining its phenomenological implications can be called a top-down approach, one then talks about bottom-up studies for simplified models. Nevertheless, we can exactly relate them to specific models without integrating out degrees of freedom (as necessary with high-dimensional effective field theory operators). An example is given in the conclusion of this chapter with the CP-odd sector of the NMSSM (DOMINGO 2017). In other words, simplified models can be seen as a tool to efficiently probe a large generic parameter space. Our contribution is thus, more specifically, to create a dictionary that relates a simplified particle model to the subhalo distribution in the MW (or other objects). Mapping a complex model to our simplified model, one can then infer some of the structuring properties of DM and the impact on detection experiments where the fine-grained structuring may play a role.

This chapter does not enter immediately into the details of the chemical and kinetic decoupling in a simplified particle model. It develops linearly. In Sect. 2.1 we introduce the mathematical aspects of the ΛCDM model. Then, in Sect. 2.2, we focus our attention on the description of the particle content of the Universe in terms of phase-space distributions: we review the definition of the phase-space function and its evolution rules by the Boltzmann equation. The next section, Sect. 2.3, dives into the thermodynamics of the early Universe and gives some first details on the WIMP history. It is followed by Sect. 2.4 that summarises the state of the art around the resolution of chemical and kinetic decouplings and shows how we implemented the master equations in our numerical codes. Eventually, the key

section Sect. 2.5, specifies the simplified model and, using all the aforementioned tools, shows specific examples of its link with the minimal halo mass. Eventually, we conclude and discuss our results, the possible improvements and the impact in terms of observations and constraints.

Unless mentioned otherwise, we use the natural units $\hbar = c = k_B = 1$ in the rest of the document. Moreover, Einstein's summation rules are implicit and Greek indices run from 0 to 3 while Latin indices run from 1 to 3. Metric signature is chosen to be mostly negative $(+,-,-,-)$. Note that some of the references cited in this chapter use the opposite signature and convention for indices. In addition, some also place the *time* component at the end making the Latin indices (or Greek in the opposite case) go from 0 to 3.

2.1 The mathematics of the expanding Universe

In this section the basics of Einstein's general relativity are introduced with the point of view of the action formalism, summarizing the extensive development done in the appendices of WALD (1984) – hereafter refereed to as W84. The main objective here is not to enter into high levels of technicality that differential geometry induces but rather to establish the notations and the main equations that are needed to properly introduce the description of a Universe where general relativity is the valid theory of gravity at all length scales. Eventually, we mention a few words about inflation, a period taking place before the standard picture of ΛCDM, which solves some of its caveats and sets its initial conditions.

2.1.1 A few words on general relativity

In the theory of general relativity, space-time (the fabric of the Universe) is described by a 4 dimensional pseudo-Riemannian manifold $(\mathcal{M}, g_{\mu\nu})$. On this manifold it is possible to define a natural volume element, that can be written, in a right handed coordinate basis (c.f. W84, Appendix B) as

$$\zeta = \frac{\sqrt{-g}}{4!}\varepsilon_{\mu\nu\rho\sigma}\,\mathrm{d}x^\mu \wedge \mathrm{d}x^\nu \wedge \mathrm{d}x^\rho \wedge \mathrm{d}x^\sigma = \sqrt{-g}\,\mathrm{d}x^0 \wedge \mathrm{d}x^1 \wedge \mathrm{d}x^2 \wedge \mathrm{d}x^3 \tag{2.1}$$

where $g = \det(g_{\mu\nu})$ and $\varepsilon_{\mu\nu\rho\sigma}$ is the permutation symbol such that $\varepsilon_{0123} = +1$. It is also common to define the volume form as the Hodge dual of the 0-form 1 i.e. $\zeta = \star(1)$. Because this expression is dependent on the metric, it is also convenient to use another 4-form ζ' defined by $\zeta = \sqrt{-g}\,\zeta'$. Then every component of the Universe and space-time itself is determined by the action

$$\mathcal{S}\left[g^{\mu\nu}, \{\psi_i\}_i\right] = \mathcal{S}_\mathrm{G}\left[g^{\mu\nu}\right] + \mathcal{S}_\mathrm{M}\left[g^{\mu\nu}, \{\psi_i\}_i\right] \tag{2.2}$$

where $\mathcal{S}_\mathrm{G}$ is the action for the metric and $\mathcal{S}_\mathrm{M}$ is the matter action dictating the behaviour of fields $\{\psi_i\}_i$ making the content of the Universe. More precisely, space-time is driven by the Einstein-Hilbert action defined as

$$\mathcal{S}_\mathrm{G}\left[g^{\mu\nu}\right] \equiv \frac{1}{16\pi G_\mathrm{N}} \int \sqrt{-g}\,(R - 2\Lambda)\,\zeta' \tag{2.3}$$

where Λ is a constant called the cosmological constant and R is the Ricci scalar built as the trace of the Ricci tensor $R = g^{\mu\nu}R_{\mu\nu}$. The latter quantity is directly linked to the

metric via the connection $\Gamma^{\rho}_{\mu\nu}$ given by the Christoffel symbol,

$$\begin{aligned} R_{\mu\nu} &\equiv \partial_\rho \Gamma^{\rho}_{\nu\mu} - \partial_\nu \Gamma^{\rho}_{\rho\mu} + \Gamma^{\rho}_{\rho\lambda}\Gamma^{\lambda}_{\nu\mu} - \Gamma^{\rho}_{\nu\lambda}\Gamma^{\lambda}_{\rho\mu} \\ \text{with} \quad \Gamma^{\rho}_{\mu\nu} &= \frac{1}{2} g^{\rho\lambda} \left\{ \partial_\mu g_{\lambda\nu} + \partial_\nu g_{\mu\lambda} - \partial_\lambda g_{\mu\nu} \right\} . \end{aligned} \tag{2.4}$$

In addition, the matter action $\mathcal{S}_{\rm M}$ is defined from the matter Lagrangian density $\mathcal{L}_{\rm M}\left[\{\psi_i\}_i\right]$ according to

$$\mathcal{S}_{\rm M}\left[g^{\mu\nu}, \{\psi_i\}_i\right] \equiv \frac{1}{16\pi G_{\rm N}} \int \sqrt{-g}\, \mathcal{L}_{\rm M}\left[\{\psi_i\}_i\right] \zeta' . \tag{2.5}$$

From the least action principle, $\mathcal{S}$ is to be minimised with respect to the metric field in order to obtain the gravitational equation of motion, *i.e.* $\delta S/\delta g^{\mu\nu} = 0$. Defining the stress-energy tensor $T_{\mu\nu}$ as the response of matter with respect to the modification of space-time (or more precisely to the change of the metric) as follows

$$T_{\mu\nu} \equiv -\frac{2}{\sqrt{-g}} \frac{\delta\left(\sqrt{-g}\mathcal{L}_{\rm M}\right)}{\delta g^{\mu\nu}} = -2\frac{\delta \mathcal{L}_{\rm M}}{\delta g^{\mu\nu}} + g_{\mu\nu}\mathcal{L}_{\rm M} \tag{2.6}$$

after computations (and up to minor troubles due to boundary conditions that can be overcome by a redefinition of $\mathcal{S}_{\rm G}$, c.f. W84) it yields the Einstein equation

$$\left\{ G_{\mu\nu} \equiv R_{\mu\nu} - \frac{1}{2} R g_{\mu\nu} \right\} + \Lambda g_{\mu\nu} = 8\pi G_{\rm N} T_{\mu\nu}, \tag{2.7}$$

where $G_{\mu\nu}$ is called the Einstein tensor. The space-time deformation is encoded in the left hand side while the content behaviour is described by the right hand side and this equation shows their interplay. Note that a common notation to describe the metric is to write down the invariant length element $\mathrm{d}s^2$ in $(\mathcal{M}, g_{\mu\nu})$,

$$\mathrm{d}s^2 \equiv g_{\mu\nu} \mathrm{d}x^\mu \mathrm{d}x^\nu . \tag{2.8}$$

Eventually, to complete this section let us mention the conservation of the stress-energy tensor. It is usually derived using the fact that the Riemann tensor satisfies the Bianchi identity. However, in order to keep on with the action framework let us summarise the proof done in (W84, appendix E) and show that it is a consequence of the diffeomorphism invariance of the matter action. Indeed, in order for the theory to be physical it must not depend on the choice of coordinate used and therefore $\mathcal{S}_{\rm G}$ and $\mathcal{S}_{\rm M}$ must be independent under the action of any diffeomorphism. In particular, consider a specific one-parameter family of diffeomorphism f_λ. Then the following identities must be satisfied

$$0 = \frac{\mathrm{d}\mathcal{S}_{\rm G}}{\mathrm{d}\lambda} = \int \frac{\delta \mathcal{S}_{\rm G}}{\delta g^{\mu\nu}} \delta g^{\mu\nu} \quad \text{and} \quad 0 = \frac{\mathrm{d}\mathcal{S}_{\rm M}}{\mathrm{d}\lambda} = \int \frac{\delta \mathcal{S}_{\rm M}}{\delta g^{\mu\nu}} \delta g^{\mu\nu} + \sum_i \int \frac{\delta \mathcal{S}_{\rm M}}{\delta \psi_i} \delta\psi_i . \tag{2.9}$$

where $\delta g^{\mu\nu} = \mathrm{d}g^{\mu\nu}/\mathrm{d}\lambda$ and $\delta\psi_i = \mathrm{d}\psi_i/\mathrm{d}\lambda$. Introducing $\mathfrak{L}_v$, the Lie derivative with respect to any given vector field v in the tangent bundle of $\mathcal{M}$ denoted $T\mathcal{M}$, it can be proven that $\delta g^{\mu\nu} = \mathfrak{L}_v(g^{\mu\nu}) = \nabla_\mu v_\nu + \nabla_\nu v_\mu$ with ∇ representing the covariant derivative. Moreover, if all ψ_i satisfy the equation of motion, then $\delta\mathcal{S}_{\rm M}/\delta\psi_i = 0$. Therefore, using the definitions of the Einstein tensor and of the stress-energy tensor in Eq. (2.6) it yields

$$\int (\nabla^\mu G_{\mu\nu}) v^\nu \, \zeta = 0 \quad \text{and} \quad \int (\nabla^\mu T_{\mu\nu}) v^\nu \, \zeta = 0 \quad \forall v \in T\mathcal{M} . \tag{2.10}$$

Because the equality is true for all vectors in the tangent bundle it implies the usual contracted Bianchi identity and the associated stress-energy conservation

$$\nabla_\mu G^{\mu\nu} = 0 \quad \text{and} \quad \nabla_\mu T^{\mu\nu} = 0 \tag{2.11}$$

where we used the fact that the connection used is specified by $\nabla_\mu g_{\alpha\beta} = 0$. Now, let us see in the next subsection, how all these notions are used to describe an homogeneous and isotropic universe with the Friedman-Lemaitre-Robertson-Walker metric.

2.1.2 The Friedman-Lemaitre-Robertson-Walker Universe

If we assume that the Universe is globally homogeneous and isotropic, a solution for the left hand side of the Einstein equation applied to the system *Universe* as a whole is of the form given by the Friedman-Lemaitre-Robertson-Walker (FLRW) metric

$$\mathrm{d}s^2 = \mathrm{d}t^2 - a^2 \left(\frac{\mathrm{d}r^2}{1 - Kr^2} + r^2 \mathrm{d}\Omega^2 \right), \tag{2.12}$$

with K the curvature with dimension length^{-2} whose sign determines the geometry: $K > 0$ (spherical), $K < 0$ (hyperbolic), $K = 0$ (flat). The dimensionless coefficient a is called the *scale factor*. Here we used the coordinate system (t, r, θ, ψ) where t is the called the cosmic time and (r, θ, ψ) are the usual spherical Euclidean spatial coordinates so that $\mathrm{d}\Omega^2 = \mathrm{d}\theta^2 + \sin^2\theta \mathrm{d}\psi^2$. A common notation is also to define $\mathrm{d}\chi = \mathrm{d}r/(1 - Kr^2)^{1/2}$ where χ is called the comoving distance. Using Cartesian spatial coordinates this metric can also be written $\mathrm{d}s^2 = \mathrm{d}t^2 - a^2 \gamma_{ij} \mathrm{d}x^i \mathrm{d}x^j$ where γ_{ij} reduces to the 3D Euclidean metric when $K = 0$. Another classic parametrisation introduces the conformal time η, related to the cosmic time through $a\mathrm{d}\eta = \mathrm{d}t$, such that

$$\mathrm{d}s^2 = a^2 \left(\mathrm{d}\eta^2 - \frac{\mathrm{d}r^2}{1 - Kr^2} + r^2 \mathrm{d}\Omega^2 \right). \tag{2.13}$$

Under these symmetry assumptions, the stress-energy tensor on the right-hand side of Eq. (2.7) is also constrained and takes the form of the perfect fluid tensor – see (S. WEINBERG 1972; W84) for more details – that is of a fluid with no heat conduction and no stress due to viscosity,

$$T_{\mu\nu} = (\rho + P) u_\mu u_\nu - P g_{\mu\nu}\,, \tag{2.14}$$

where ρ is the energy density of the fluid and P its pressure. Notice that both of these quantities depend only on t (or equivalently η). We also introduced the four-velocity of the fluid particles defined by $u^\mu \equiv \mathrm{d}x^\mu/\mathrm{d}\lambda$ on a geodesic described with the affine parameter λ. For an observer in the frame of the fluid, i.e. such that $u^i = 0$, it possible to write the stress-energy tensor in matrix notation,

$$T^\mu{}_\nu = \begin{pmatrix} \rho & 0 & 0 & 0 \\ 0 & -P & 0 & 0 \\ 0 & 0 & -P & 0 \\ 0 & 0 & 0 & -P \end{pmatrix}. \tag{2.15}$$

In the case of several perfect fluids making the Universe, the total energy tensor is the sum of the energy tensors $T_i^{\mu\nu}$ of the different species tagged by the letter i,

$$T^{\mu\nu} = \sum_i T_i^{\mu\nu} \quad \text{which implies} \quad \rho = \sum_i \rho_i \quad \text{and} \quad P = \sum_i P_i\,. \tag{2.16}$$

It is common to describe the evolution of the Universe using the Hubble parameter H and the conformal Hubble parameter $\mathcal{H}$ respectively defined as

$$H \equiv \frac{1}{a}\left\{\dot{a} \equiv \frac{\mathrm{d}a}{\mathrm{d}t}\right\} \quad \text{and} \quad \mathcal{H} \equiv \frac{1}{a}\left\{a' \equiv \frac{\mathrm{d}a}{\mathrm{d}\eta}\right\}. \tag{2.17}$$

Note that, in our notations, a dot (resp. a prime) over a quantity denotes its derivative with respect to the cosmic time t (resp. conformal time η). By definition of the conformal time, these two quantities are related by $\mathcal{H} = aH$. Consequently, Einstein's equation reduces to the Friedmann equations,

$$H^2 = \frac{8\pi G_{\mathrm{N}}}{3}\rho + \frac{\Lambda}{3} - \frac{K}{a^2} \quad \text{and} \quad \dot{H} + H^2 = -\frac{4\pi G_{\mathrm{N}}}{3}(\rho + 3P) + \frac{\Lambda}{3}. \tag{2.18}$$

From these expressions one can define an energy density for the cosmological constant $\rho_\Lambda = \Lambda/(8\pi G_{\mathrm{N}})$ and for the scalar curvature $\rho_K = -3K/(8\pi G_{\mathrm{N}} a^2)$ as well as a pressure term $p_\Lambda = -\rho_\Lambda$. In cosmology it is usual to work with abundances which represent the proportion of each species (including the cosmological constant and the curvature as species) in the Universe

$$\Omega_i \equiv \left\{\frac{1}{\rho_c} \equiv \frac{8\pi G_{\mathrm{N}}}{3H^2}\right\}\rho_i \quad \text{so that} \quad \Omega_K + \Omega_\Lambda + \sum_i \Omega_i = 1, \tag{2.19}$$

thanks to the first equation of Friedmann and with ρ_c the critical density. In addition, if the three components are assumed to be non interacting (except than gravitationally), the $\nu = 0$ equation of conservation for the stress-energy tensor in Eq. (2.11) can be applied individually to each species and it describes the evolution of the different energy densities with time according to

$$\dot{\rho}_i = -3H(\rho_i + P_i). \tag{2.20}$$

In what follows we assume no overall curvature, *i.e.* $K = 0$. As seen in Sect. 1.2.2, the CMB data point towards a Universe separable into three main general species: radiation (made of relativistic particles), matter (made of non-relativistic matter, i.e. CDM and baryons after recombination) and a cosmological constant Λ or a dark energy fluid. For each of these three components it is possible to define a constant equation of state as

$$w = P/\rho \tag{2.21}$$

that are $w_{\mathrm{r}} = 1/3$ (for radiation), $w_{\mathrm{m}} = 0$ (for matter) and $w_\Lambda = -1$ for the cosmological constant. While the value for w_Λ can directly been inferred from the definition of ρ_Λ and p_Λ, in the case of the radiation and matter a proof is given by Eq. (2.84) and Eq. (2.85). For a constant equation of state, Eq. (2.20) then yields a relation between ρ and the scale factor

$$\rho(t) = \rho(t_p)\left(\frac{a(t)}{a(t_p)}\right)^{-3(1+w)} \tag{2.22}$$

with t_p a reference point in time. A common notation is to tag by a 0 all quantities evaluated today and to set (without any loss of generality) $a(t_0) = 1$. Therefore, when applied to the three different components, it gives

$$\rho_{\mathrm{r}} = \rho_{\mathrm{r},0}a^{-4}, \quad \rho_{\mathrm{m}} = \rho_{\mathrm{m},0}a^{-3} \quad \text{and} \quad \rho_\Lambda = \mathrm{cst}. \tag{2.23}$$

Because the Universe has had a continuous expansion from $a = 0$ (what is commonly called the Big Bang) to $a = a_0 = 1$ today, at a very early time it was necessarily dominated by radiation. Then, with the increase of the scale factor, since data shows that $\rho_{\mathrm{m},0}^4 \rho_{\mathrm{r},0}^{-3} > \rho_\Lambda$, it was followed by a period of matter domination and since $\rho_\Lambda > \rho_{\mathrm{m},0}$ we are today in a period of cosmological constant domination. Let us insist on the fact that the instant $a = 0$ is fictitious and cannot be described without a theory of quantum gravity, therefore we only consider this point as a theoretical reference.

In cosmology it is also usual to parametrize time by the cosmological redshift $z(t) = a^{-1}(t) - 1$. The name *redshift* comes from the fact that it describes the factor by which the frequency of a geodesically propagating photon that was emitted at a time t and received today has shifted to a larger wavelengths because of expansion. The first Friedmann equation gives the evolution of H with the redshift

$$H(z) = H_0 \sqrt{\Omega_{\mathrm{r},0}(1+z)^4 + \Omega_{\mathrm{m},0}(1+z)^3 + \Omega_{\Lambda,0}}\,, \tag{2.24}$$

where $H_0 = H(z = 0)$, and the different abundances vary according to

$$\Omega_i(z) = \Omega_{i,0}(1+z)^{3(1+w_i)} \left(\frac{H_0}{H(z)}\right)^2 . \tag{2.25}$$

Eventually, the cosmic time and the redshift are related via $\mathrm{d}t = \mathrm{d}a/\dot{a}$. It yields

$$t_0 - t = \int_0^z \mathrm{d}z' \frac{1}{(1+z')H(z')} \tag{2.26}$$

where we recall that t_0 is the time today. In Fig. 2.1 we represent the evolution of H and of the different abundances with respect to the redshift z. The three different stages of the Universe evolution characterised by the domination of radiation, matter and then cosmological constant are visible in the left panel. The redshift of equivalence between matter and radiation is introduced as $z_{\mathrm{eq}} \equiv \Omega_{\mathrm{m},0}/\Omega_{\mathrm{r},0} - 1$. It defines the redshift at which the abundancies of matter and radiation are the same, at the transition between the radiation-dominated era and the matter-dominated era (where the blue and red lines cross).

2.1.3 A few words on inflation

Several observations point towards the presence of an inflationary stage (of accelerated expansion such that $\ddot{a} > 0$) at the beginning of the Universe, a stage which is implicitly assumed when introducing the standard cosmological ΛCDM model. Let us mention a few of the hints and describe briefly with a simple model its main features.

The first major issue is the apparent homogeneity of the temperature in the CMB. Indeed, at the time of last-scattering, when CMB was emitted, the size of a causally connected region then, corresponds to a patch of size $\sim 1^\circ$ in the sky today. Henceforth, there is no reason, a priori, for two points separated by an angle larger than $\sim 1^\circ$ to source the emission of a nearly-perfect black body with the same temperature T_{CMB} at a precision of $\delta T_{\mathrm{CMB}}/T_{\mathrm{CMB}} \sim 10^{-5}$. Introducing an early inflationary stage solves this problem by causally connecting the entire sky before the start of the standard cosmology regime. The second issue, that we are going to focus on, as an example, is the flatness problem. As detailed previously, the CMB data favour a

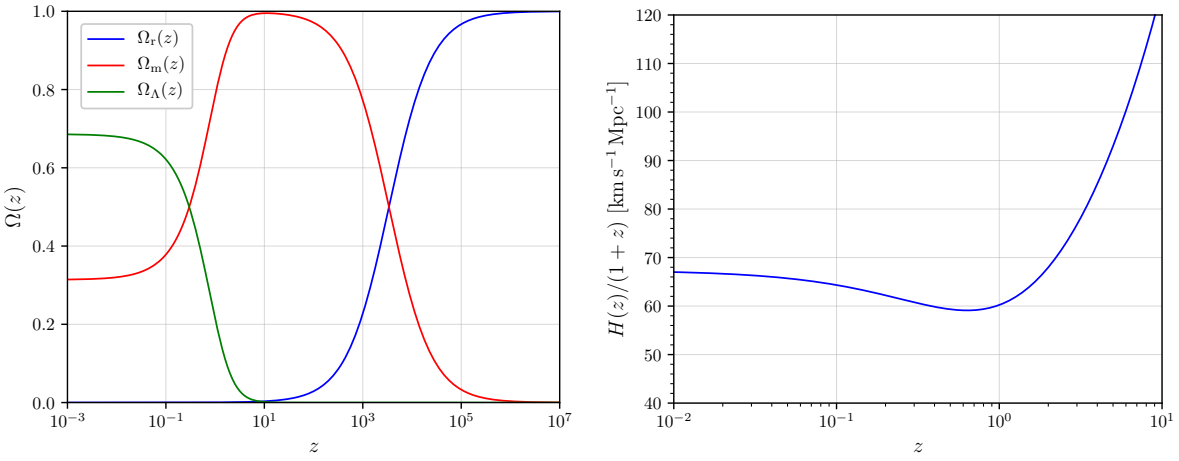

Figure 2.1 – Left panel: Evolution of the abundances with the redshift. **Right panel :** Late time evolution of the Hubble parameter with the redshift. These two figures have been made using the Planck18 cosmology.

model with $\Omega_K = 0$, however, it is possible to derive a differential equation for the evolution of Ω_K assuming $\Omega_\Lambda = 0$

$$\frac{\mathrm{d}\Omega_K}{\mathrm{d}t} = 2\Omega_K H\,(\epsilon - 1) \tag{2.27}$$

where $\epsilon = -\dot{H}/H^2 = 1 - \ddot{a}/\dot{a}^2$. There are not specific physically well-motivated reasons, a priori, for Ω_K to be equal to 0 as an initial condition. In standard cosmology, $\epsilon = 3(1+w)/2$ and since $w > 0$ for radiation and matter, Ω_K should then increase up to today and has all the chances to be larger than the constraint $\Omega_{K,0} = 0.0007^{+0.0037}_{-0.0037}$ (95% confidence level interval – see Planck18) if the initial value is not fined tuned. Now, let us assume that we have a period of accelerated expansion in the very early universe. During that period $\epsilon < 1$ and Ω_K is a decreasing function of time. Consequently, even if Ω_K was a priori arbitrary, assuming sufficiently long inflation, it may have had time to become extremely small before entering the radiation era. In other words, this process gives a physical dynamical explanation for the smallness of Ω_K as measured today without requiring a fine-tuning of the initial conditions. One could remark that the most efficient configuration corresponds to $\epsilon = 0$, nevertheless, that would impose $H = \text{cst.}$ and give the Universe a stable de Sitter geometry and a never-ending accelerated expansion. Therefore we need to have $1 > \epsilon > 0$. One can then wonder about the time necessary for inflation to match all the constraints. This time is parametrized by $N = \ln(a(t_e)/a(t_i))$ and referred to as the number of e-folds where t_e and t_i are the cosmic times a the end and start of inflation respectively. The value of N is constrained to be larger than ~ 50 (THE PLANCK COLLABORATION 2020).

A simple model for inflation is driven by a single scalar field ϕ called the inflaton, that minimally couples to gravity through the matter action given by

$$\mathcal{S}_\mathrm{M} = -\int \left[\frac{1}{2} g^{\mu\nu}\partial_\mu\phi\partial_\nu\phi + V(\phi)\right]\zeta \tag{2.28}$$

where $V(\phi)$ is the inflaton potential and ζ the volume form defined in Eq. (2.1). In an homogenous and isotropic universe, for the FLRW metric, the stress energy tensor

and the equation of motion for this field yield

$$\rho_\phi = \frac{\dot\phi^2}{2} + V(\phi) \quad \text{and} \quad p_\phi = \frac{\dot\phi^2}{2} - V(\phi), \tag{2.29}$$

$$\ddot\phi + 3H\dot\phi + \frac{\mathrm{d}V(\phi)}{\mathrm{d}\phi} = 0 \quad \text{and} \quad H^2 = \frac{8\pi G_\mathrm{N}}{3}\left[\frac{\dot\phi^2}{2} + V(\phi)\right] \tag{2.30}$$

where ρ_ϕ and p_ϕ are respectively the energy density and pressure of the field. The parameter ϵ introduced above in the differential equation for Ω_K can be written here under the form

$$\epsilon_\phi = \frac{3\dot\phi^2}{\dot\phi^2 + 2V(\phi)} \tag{2.31}$$

and $\epsilon_\phi \sim 0$, as required to have an accelerated expansion, only if $\dot\phi^2 \ll V(\phi)$. If we also require that $\ddot\phi \ll H\dot\phi$, these two constraints form the slow roll conditions for the field ϕ. They are essentially equivalent to impose that the potential at the initial value of ϕ is flat and that the field rolls slowly from its initial position towards a minimum of V. The parameter ϵ_ϕ is referred to as the slow roll parameter. The end of inflation happens at $\epsilon_\phi \sim 1$ when the inflaton eventually goes all the way down the potential and gains enough kinetic energy. If we assume that the potential is quadratic close to $\phi = 0$, and goes as $V(\phi) = m_\phi^2\phi^2/2$, once at the bottom, the field satisfies the equation of motion of an harmonic oscillator with a friction term,

$$\ddot\phi + 3H\dot\phi + m_\phi^2\phi = 0\,. \tag{2.32}$$

When close to the minimum of potential we can assume that H^{-1} becomes negligible in comparison to the typical time of oscillations $\sim m_\phi^{-1}$. Then $\ddot\phi = -m_\phi^2\phi$, which implies $\dot\phi^2 = -m_\phi^2\phi^2$ and the perfect oscillator solution, $\phi \propto \cos(m_\phi t)$. The continuity equation for ϕ yields $\dot\rho_\phi + 3H\rho_\phi = -3p_\phi = -3H(\dot\phi^2 - m_\phi^2\phi^2)/2 \sim 0$ in average, on Hubble time scales, and $\rho_\phi \sim a^{-3}$ decreases with time. In practice, because the inflation leads to standard cosmology we assume that the inflaton field decays in all the standard model particles during its oscillation with enough energy so that they acquire a state of *thermodynamic equilibrium*. This transition is called the *reheating* phase and it will not be further detailed here. After reheating, standard cosmology sets in. To complete the picture, however, we now need to develop the statistics of the particle content in the early Universe in order to understand what happened after reheating, in a period that is rich in cosmological events and interesting physics – and cannot simply be reduced to the simple model of a radiation dominated period. It will be the occasion to detail the concept of thermodynamic equilibrium that has been mentioned before.

2.2 phase-space distributions in general relativity

2.2.1 Geometry of phase space for a single particle

The best way to understand the behaviour of particles in the early Universe is to describe their distribution in phase space. Let us describe here the general framework. First and foremost, let us give a definition of phase space. To this end, consider a particle on a curve whose commoving coordinates are given by $x^\mu = x^\mu(\lambda)$ with λ the affine parameter that traces the position on the curve and maps it to a real

number (it can be taken as the proper time for timelike paths, which is however not appropriate to describe the motion of massless particles). The tangent vector field to this curve is then given by $\dot{x}^\mu = \mathrm{d}x^\mu/\mathrm{d}\lambda$[1]. If the particle is free falling, x^μ is the solution to the equation of motion given by the action, and associated Lagrangian (CHOQUET-BRUHAT 2014; W84),

$$\mathcal{S}_{\rm FF}[x] \equiv \int \left\{ L_{\rm FF} \equiv \frac{1}{2} g_{\mu\nu}\dot{x}^\mu \dot{x}^\nu \right\} \mathrm{d}\lambda \,. \tag{2.33}$$

The equation of motion obtain from the Euler-Lagrange equation is

$$\frac{\mathrm{d}}{\mathrm{d}\lambda}\left(\frac{\partial L_{\rm FF}}{\partial \dot{x}^\mu}\right) - \frac{\partial L_{\rm FF}}{\partial x^\mu} = 0 \,, \quad \textit{i.e.} \quad \frac{\mathrm{d}\dot{x}^\mu}{\mathrm{d}\lambda} + \Gamma^\mu_{\alpha\beta}\dot{x}^\alpha \dot{x}^\beta = 0 \tag{2.34}$$

also called the geodesic equation. Moreover it is straightforward to show that the general equality holds

$$\frac{\mathrm{d}}{\mathrm{d}\lambda}\left(L_{\rm FF} - \frac{\partial L_{\rm FF}}{\partial \dot{x}^\mu}\dot{x}^\mu\right) = 0 \,, \tag{2.35}$$

which implies, in the present case, the conservation of the quantity $g(u,u) = g_{\mu\nu}\dot{x}^\mu\dot{x}^\nu$ along the geodesics. In addition, we introduce the canonical momentum as $p_\mu = g_{\mu\nu}\dot{x}^\nu$. Because of the relation

$$g(p,p) = \mathrm{cst} = \frac{\mathrm{d}s^2}{\mathrm{d}\lambda^2}, \tag{2.36}$$

one can choose $\lambda = \tau/m$, with τ the proper time, for massive particles, so that, in the end, it yields the general mass-shell relation

$$g(p,p) = m^2 \,. \tag{2.37}$$

To go a little bit further, in mathematical terms, the couple (x^μ, p_μ) is said to live in the cotangent bundle $T^\star\mathcal{M}$ of the manifold $\mathcal{M}$ describing the space-time. Then $p^\mu = g^{\mu\nu}p_\nu$ and the 8 dimensional couple (x^μ, p^μ) lives in the tangent bundle $T\mathcal{M}$. In the following we follow the notations and the clear introduction made in EHLERS (2011) – hereafter referred to as E70, since these published notes are from a lecture given in 1970. See also BICHTELER (1967), MARLE (1969), and STEWART (1971). We call phase space and its on-shell hypersurfaces the following sets

$$\begin{aligned} \mathcal{P} &= \{(x,p) \,|\, x \in \mathcal{M} \,,\, p \in T_x\mathcal{M} \,,\, g(p,p) \geq 0\} \\ \mathcal{P}_m &= \{(x,p) \,|\, x \in \mathcal{M} \,,\, p \in T_x\mathcal{M} \,,\, g(p,p) = m^2\} \end{aligned} \tag{2.38}$$

It is also important to define volume elements on those spaces. Every set $P(x) = \{p \in T_x\mathcal{M}, g(p,p) \leq 0\}$ for $x \in \mathcal{M}$ has its own pseudo-Riemannian structure with the associated volume form

$$\theta = \frac{1}{4!}\sqrt{-g}\,\varepsilon_{\mu\nu\rho\sigma}\mathrm{d}p^\mu \wedge \mathrm{d}p^\nu \wedge \mathrm{d}p^\rho \wedge \mathrm{d}p^\sigma \,. \tag{2.39}$$

When restricted to the mass-shell hypersurface $P_m(x) = \{p \in T_x\mathcal{M}, g(p,p) = m^2\}$ it reduces by imposing the mas-shell condition Eq. (2.37) as

$$\theta_m \equiv 2\Theta(p^0)\delta\left[g(p,p) - m^2\right]\theta = \frac{1}{3!}\frac{\sqrt{-g}}{\hat{p}_0}\varepsilon_{ijk}\,\mathrm{d}p^i \wedge \mathrm{d}p^j \wedge \mathrm{d}p^k \,. \tag{2.40}$$

where $\hat{p}_0(x^\mu, p^i)$ is the value of p_0 that satisfies the dispersion relation for a given (x^μ, p^i). We denote by Θ/δ the Heaviside/Dirac distribution. On the total phase space and its mass-shell hypersurface the volume forms are then respectively given by

$$\Omega \equiv \zeta \wedge \theta \quad \text{and} \quad \Omega_m \equiv \zeta \wedge \theta_m \,. \tag{2.41}$$

[1]For this discussion the dot notation refers to derivative with respect to λ and not the cosmic time.

2.2.2 Liouville's theorem and phase-space distribution function

From the previous geodesic equation, we can define a vector field on $\mathcal{P}_m$ that is called the Liouville vector L_m and which describes the geodesic flow in phase space,

$$L_m \equiv p^\alpha \frac{\partial}{\partial x^\alpha} - \Gamma^i_{\mu\nu} p^\mu p^\nu \frac{\partial}{\partial p^i} \,. \tag{2.42}$$

An important property related to the Liouville vector is that the volume form is conserved along the geodesic flow. This is often referred to as the Liouville theorem. The proof relies on $\mathrm{d}\Omega_m = 0$ and Cartan's formula

$$\mathfrak{L}_{L_m}(\Omega_m) = \mathrm{d}(i_{L_m}\Omega_m) + i_{L_m}(\mathrm{d}\Omega_m) \tag{2.43}$$

where i_L is the interior product, $\mathfrak{L}_{L_m}$ is the Lie derivative along L_m. Usually one denotes $\omega_m = i_{L_m}\Omega_m$ that can be proven to satisfy $\mathrm{d}\omega_m = 0$ as well. This yields the aforementioned property under the form $\mathfrak{L}_{L_m}(\Omega_m) = 0$. Let us now introduce the phase-space distribution function. One can prove that for any hypersurface Σ (oriented 6-dimensional submanifold with boundary) of $\mathcal{P}_m$, the ensemble average number of occupied states in Σ, denoted $\overline{N}[\Sigma]$, can be written according to a single function f_m called the one-point phase-space distribution function (PSDF) as

$$\overline{N}[\Sigma] = \int_\Sigma f_m \omega_m \,. \tag{2.44}$$

The number of collisions in any bounded region $D \subset \mathcal{P}_m$ is given by the value of the previous quantity at the boundaries ∂D according to

$$\overline{N}[\partial D] = \int_{\partial D} f_m \omega_m = \int_D \mathrm{d}(f\omega_m) = \int_D \mathrm{d}f_m \wedge \omega_m \,. \tag{2.45}$$

The different equalities come from Stokes' theorem and the fact that $\mathrm{d}\omega_m = 0$. Moreover as Ω_m is a 7-form in a 7-dimensional manifold it follows that for any vector field X and function h in that manifold $\mathrm{d}h \wedge i_X(\Omega_m) = X(h)\Omega_m$. In our case, it yields

$$\overline{N}[\partial D] = \int L_m(f_m)\Omega_m \tag{2.46}$$

proving that the Liouville vector represents, as a matter of fact, the phase-space density of collisions. When there is a balance between particle entering and leaving the region then the Liouville operator is equal to 0. The corresponding equation is called Liouville's equation $L_m(f_m) = 0$. The interest behind the definition of the PSDF is that it fully describes the system. Furthermore, one can also define its corresponding moments,

$$M^{\alpha_1 \ldots \alpha_n} \equiv \int f_m p^{\alpha_1} \ldots p^{\alpha_n} \theta_m \,. \tag{2.47}$$

In E70 the following useful Lemma is proven. If h is a differentiable function with continuous derivatives on $\mathcal{P}_m$ then it satisfies the equality

$$\nabla_\mu \left(\int h p^\mu \theta_m \right) = \int L_m(h)\theta_m \,. \tag{2.48}$$

The proof follows the same principles as the derivation we sketched to show that the Liouville operator corresponds to the phase-space density of collisions. With the help of a second lemma, based on this first one, E70 even more generally shows that

$$\nabla_\mu M^{\alpha_1 \ldots \alpha_{n-1}\mu} = \int L_m(f_m) p^{\alpha_1} \ldots p^{\alpha_{n-1}} \theta_m \,. \tag{2.49}$$

In the following now we take into account the fact that particles are quantum objects that occupy a volume $h^3 = (2\pi)^3$ (in natural units) of phase space and that they can have a number g_m of internal degrees of freedom. Therefore we slightly change the definition of the PSDF to make explicit these dependencies. For the rest of the study we use the redefinition $f_m \to g_m f_m/(2\pi)^3$. Consequently, the first and second moments that correspond to the number density current and the stress-energy density tensor, are written

$$n^\mu \equiv M^\mu = \frac{g_m}{(2\pi)^3}\int f_m p^\mu \theta_m \quad \text{and} \quad T^{\mu\nu} \equiv M^{\mu\nu} = \frac{g_m}{(2\pi)^3}\int f_m p^\mu p^\nu \theta_m \,. \tag{2.50}$$

Thus, according to Eq. (2.49), both satisfy $\nabla_\mu n^\mu = 0$ and $\nabla_\mu T^{\mu\nu} = 0$ for a balanced number of collisions in a volume of phase space. Moreover we also decompose the stress-energy tensor and extract two key quantities, the energy density and the mean kinetic pressure

$$\rho \equiv T^{00} = \frac{g_m}{(2\pi)^3}\int f_m \left(p^0\right)^2 \theta_m \quad \text{and} \quad P \equiv \frac{1}{3}\mathrm{Tr}\left\{T^{ij}\right\} = \frac{g_m}{3(2\pi)^2}\int f_m p^2 \theta_m \tag{2.51}$$

where we introduced the 3-momentum norm $p = (-g_{ij}p^i p^j)^{1/2}$.

The Liouville equation is here described for a single particle and then used to characterise a entire population through the one-point PSDF. To be more precise, one should describe the phase space for all particles through the complete PSDF depending on all degrees of freedom. In that case the Liouville theorem holds for a system driven by Hamiltonian dynamics. However the treatment in a relativistic framework is beyond the scope of this simple introduction.

In the next section, we discuss the unbalanced case leading to the Boltzmann equation, that is Liouville equation with a collision term. Let us mention also that this introduction to the PSDF is rather abstract and that a more pedestrian derivation of the Liouville operator and subsequently of the Boltzmann equation is given in DEBBASCH et al. (2009a,b). There the authors detail every geometrical property of the phase space. Moreover, they also show the relations between the contra-variant on-shell PSDF as introduced here (which depends on p^i and the covariant (which depends on p_i) and off-shell counterparts.

2.2.3 Boltzmann's equation

In this section we briefly introduce the general expression of the Boltzmann equation. In a system where several species coexist together, we label by a Roman letter the distribution function of each species. For instance, for species denoted a the PSDF is labelled $f_a \equiv f_{m_a}$.The phase-space density of collisions is denoted by an operator $\hat{C}$ on f_a and depends on the PSDF of all other species interacting with a. With this definition Boltzmann equation takes the form

$$L_m(f_a) = \hat{C}(f_a)\,. \tag{2.52}$$

In full generality, the collision term depends on the two-point PSDF. In turn, the Hamiltonian treatment for the full PSDF (depending on all degrees of freedom) gives an equation for the two-point PSDF that depends on the three-point PSDF, so on and so forth. This is referred to as the Bogoliubov-Born-Green-Kirkwood-Yvon hierarchy. Under the assumption of "molecular chaos", *i.e.* the momenta of colliding

particles are uncorrelated and do not depend on their position, the two-point PSDF can be written as the product of two one-point PSDFs. Here we work under this approximation that justifies Eq. (2.52).

Let us now give an expression for $\hat{C}$. Consider a generic interaction between two sets of particles $I = Y \to Z$. We are interested on its impact for particles of the given species a. For clarity, we illustrate all our notations on the process $a+a+c \to a+b+b$. Note that for fermionic species, particles and antiparticles are labelled differently. There Y, Z and I can be represented as three sets $Y = \{a, a, c\}$, $Z = \{a, b, b\}$ and $I = Y \cup Z = \{a, a, a, c, b, b\}$. Then, we index all particles in the sets Y or Z. As a is at least present once, one of them is labelled a_1. The only requirement is that all other particles are indexed with numbers that do not repeat for identical particles. The sets of the indexed particles are called $\mathcal{Y}$, $\mathcal{Z}$ and $\mathcal{I} = \mathcal{Y} \cup \mathcal{Z}$. For instance if $a_1 \in \mathcal{Y}$ then $\mathcal{Y} = \{a_1, a_2, c_1\}$ and $\mathcal{Z} = \{a_3, b_1, b_2\}$ are two valid sets. If $a_1 \in \mathcal{Z}$ one can choose $\mathcal{Y} = \{a_2, a_3, c_1\}$ and $\mathcal{Z} = \{a_1, b_1, b_2\}$. Whenever necessary we specify in which set is a_1 by marking it with a star, $\mathcal{Y}_\star$ or $\mathcal{Z}_\star$. For a set of indexed particles $\mathcal{X} = \mathcal{Y}, \mathcal{Z}, \mathcal{I}$ we introduce $\overline{\mathcal{X}} = \mathcal{X} \backslash \{a_1\}$. For instance, if $a_1 \in \mathcal{Y}_\star$, one has $\overline{\mathcal{Y}_\star} = \{a_2, c_1\}$ and $\overline{\mathcal{Z}} = \{a_3, b_1, b_2\} = \mathcal{Z}$. This notation will turn useful because the Liouville equation characterises the evolution of one species, whose phase-space volume is not integrated over. Eventually, the number of particles of species a in an set of particles $X = Y, Z, I$ is denoted $\xi_a(X)$.

With all these definitions we can now introduce physical quantities without ambiguities. Firstly, the total phase-space volume element associated with the interaction $Y \to Z$ at fixed value of the momentum p_{a_1} is defined by

$$\mathrm{d}\overline{\Pi} \equiv (2\pi)^4 \delta^{(4)} \left(\sum_{\kappa \in \mathcal{Y}} p^\mu_\kappa - \sum_{\kappa' \in \mathcal{Z}} p^\mu_{\kappa'} \right) \bigwedge_{\kappa'' \in \overline{\mathcal{I}}} \left\{ \frac{\theta_{\kappa''}}{2(2\pi)^3} \right\} \tag{2.53}$$

and secondly the phase space function is introduced as

$$\mathcal{F}_{\mathcal{Y};\mathcal{Z}} \equiv \prod_{\kappa \in \mathcal{Y}} f_\kappa(x^\mu, p^i_\kappa) \prod_{\kappa' \in \mathcal{Z}} (1 + \varepsilon_{\kappa'} f_{\kappa'}(x^\mu, p^i_{\kappa'})) \tag{2.54}$$

where ε is a factor differentiating bosons and fermions. For outgoing fermions, the available phase space is reduced due to Pauli blocking, which is subsequently encoded by setting $\varepsilon = -1$. For bosons, on the contrary, it is enhanced, therefore $\varepsilon = +1$. As a shorthand notation f_κ is to be understood as the PSDF for the species which the particle labelled κ belongs to. The collision operator for $Y \to Z$ takes the form

$$\hat{C}_{Y \to Z}(f_a)(x^\mu, p^i_{a_1}) = \frac{1}{2 g_a \mathcal{S}} \int \left[\xi_a(Z) W_{\mathcal{Y};\mathcal{Z}_\star} \mathcal{F}_{\mathcal{Y};\mathcal{Z}_\star} - \xi_a(Y) W_{\mathcal{Y}_\star;\mathcal{Z}} \mathcal{F}_{\mathcal{Y}_\star;\mathcal{Z}} \right] \mathrm{d}\overline{\Pi} \tag{2.55}$$

where W represents the strength of the interaction and $\mathcal{S}$ is a combinatorial prefactor. Indeed, labelling the particles and subsequently their momentum, when integrating over $\mathrm{d}\overline{\Pi}$, the phase space of identical particles is counted multiple times. Hence the introduction of

$$\mathcal{S} \equiv \prod_{r \in \hat{I}} \left[\xi_r(Y)! \, \xi_r(Z)! \right] . \tag{2.56}$$

where $\hat{I}$ represents the set of all species in I. In our example $\hat{I} = \{a, b, c\}$. Furthermore the coefficients $\xi_a(Z)$ and $\xi_a(Y)$ are introduced because we do not actually integrate over p_{a_1} and because the choice of particle a_1 is arbitrary; every other particle of species a in the same set Y or Z contributes the same. Eventually, the last

ingredient is the expression of the interaction strength. With the choice of normalisation in Eq. (2.53) it can be written

$$W_{\mathcal{Y};\mathcal{Z}} = \prod_{\kappa\in\mathcal{I}} \sum_{s_\kappa} |\mathcal{M}_{\mathcal{Y}\to\mathcal{Z}}|^2 \tag{2.57}$$

with s_κ the different spin configurations of the particle κ. The product simply means that we sum over all possible spin configurations. In particular, here we sum over the spin states of the particle a_1 too which is why we divided the total by g_a. The matrix elements of the interaction $\mathcal{M}_{\mathcal{Y}\to\mathcal{Z}}$ is computed from quantum field theoretical methods. As specified with the notations, $W_{\mathcal{Y};\mathcal{Z}_\star} \neq W_{\mathcal{Y}_\star;\mathcal{Z}}$ a priori, since they do not have the same dependence in the momenta. In $W_{\mathcal{Y};\mathcal{Z}_\star}$ the momentum p_{a_1} is in the outgoing side while for $W_{\mathcal{Y}_\star;\mathcal{Z}}$ it is in the incoming side.

Now, if CP (Charge-Parity) symmetry (or equivalently time inversion symmetry by the CPT theorem – PESKIN et al. 1995; S. WEINBERG 1995; SCHWARTZ 2014) is conserved in the interaction, as it will be in all the cases we consider, then the matrix element is the same for the forward and backward processes. Therefore, the collision term can be slightly simplified by defining the sum of the forward and backward contributions

$$\begin{aligned}\hat{C}_{Y\leftrightarrow Z}\left(f_a\right)\left(x^\mu, p^i_{a_1}\right) &= \hat{C}_{Y\to Z}\left(f_a\right)\left(x^\mu, p^i_{a_1}\right) + (1-\delta_{YZ})\hat{C}_{Z\to Y}\left(f_a\right)\left(x^\mu, p^i_{a_1}\right) \\ &= \frac{1}{2g_a\mathcal{S}}\int \mathrm{d}\overline{\Pi}\left\{\xi_a(Y) W_{\mathcal{Y}_\star;\mathcal{Z}}\left[(1-\delta_{YZ})\mathcal{F}_{\mathcal{Z},\mathcal{Y}_\star} - \mathcal{F}_{\mathcal{Y}_\star;\mathcal{Z}}\right]\right. \\ &\qquad \left. -\xi_a(Z) W_{\mathcal{Y};\mathcal{Z}_\star}\left[(1-\delta_{YZ})\mathcal{F}_{\mathcal{Z}_\star;\mathcal{Y}} - \mathcal{F}_{\mathcal{Y};\mathcal{Z}_\star}\right]\right\} .\end{aligned} \tag{2.58}$$

where $\delta_{YZ} = 1$ if $Y = Z$ and 0 otherwise. Indeed in the case $Y = Z$ the collision operator $\hat{C}_{Y\to Y}$ as defined in Eq. (2.55) already includes the backward process. The total collision operator is finally expressed as a sum over all possible interactions

$$\hat{C}\left(f_a\right)\left(x^\mu, p^i_{a_1}\right) = \sum_{(Y,Z)} \hat{C}_{Y\leftrightarrow Z}\left(f_a\right)\left(x^\mu, p^i_{a_1}\right) . \tag{2.59}$$

Eventually, let us mention the the Boltzmann equation introduced above is derived from the classical theory, and then applied to the evolution of quantum species. There are still ambiguities in the Boltzmann approach between decays and 2-body processes. For instance you can have $a + b \to c$ on the one hand, $c \to d + e$ on the other hand, but also $a + b \to (\text{offshell } c) \to d + e$. The full quantum equation takes care of these possible double-counting issues in principle. A more precise (and much more involved) description of a quantum system is possible through the Kadanoff-Baym equation, which is based on the density matrix. However, in a cosmological context, this framework is mostly relevant to study leptogenesis and baryogenesis (BUCHMULLER et al. 2000; FROSSARD et al. 2013). For the study of thermal DM, the Boltzmann equation is appropriate.

2.2.4 H-theorem

In this section, the main ingredients for the proof of the H-theorem are displayed. Let us start by defining the total entropy current density of a system of several species as the sum of the different entropy current densities,

$$S^\mu \equiv \sum_a \left\{ S^\mu_a = -\frac{g_a}{(2\pi)^3}\int \left[f_a \ln f_a - \varepsilon_a(1+\varepsilon_a f_a)\ln(1+\varepsilon_a f_a)\right] p^\mu \theta_a \right\} . \tag{2.60}$$

where the usual definition of the scalar entropy is given by the 0-th component of this 4-vector. Using the Lemma of Eq. (2.48) and setting the function $h = f/(1+\varepsilon f)$ in order to gain space in the equations[2], one obtains the covariant derivative as

$$\begin{aligned}\nabla_\mu S^\mu_a &= -\frac{g_a}{(2\pi)^3}\int L_m\left(f_a \ln f_a - \varepsilon_a(1+\varepsilon_a f_a)\ln(1+\varepsilon_a f_a)\right)\theta_a \\ &= -\frac{g_a}{(2\pi)^3}\int L_m\left(f_a\right)\ln\left(\frac{f_a}{1+\varepsilon_a f_a}\right)\theta_a = -\frac{g_a}{(2\pi)^3}\int L_m\left(f_a\right)\ln\left(h_a\right)\theta_a\,.\end{aligned} \tag{2.61}$$

With the Boltzmann equation, the Liouville vector can be replaced by the collision operator to get

$$\nabla_\mu S^\mu = -\sum_a \frac{g_a}{(2\pi)^3}\int \hat{C}\left(f_a\right)(x^\mu, p^i_{a_1})\ln\left(h_a(x^\mu,p^i_{a_1})\right)\theta_{a_1}\,. \tag{2.62}$$

where we made explicit the momentum dependence in this last expression.

As the collision operator for a given interaction $Y \leftrightarrow Z$ has been given in the previous section it can be used to further develop the computation. However, in order to keep the discussion short we only treat the case of a single species with particles interacting through $a+a \to a+a$. Afterward we will argue on why the theorem holds for arbitrary interactions and species. Consequently, one first set $Y = Z = \{a,a\}$, $\mathcal{S}=4$, $\xi_a(\mathcal{Y}) = \xi_a(\mathcal{Z}) = 2$. For simplicity we also index the particles as $\mathcal{Z}_\star = \mathcal{Y}_\star = \{a_1,a_2\}$ and $\mathcal{Z} = \mathcal{Y} = \{a_3,a_4\}$. The collision operator becomes

$$\hat{C}_{Y\leftrightarrow Z}\left(f_a\right)(x^\mu,p^i_{a_1}) = \frac{1}{4g_a}\int W_{\{a_1,a_2\};\{a_3,a_4\}}\left[\mathcal{F}_{\{a_3,a_4\};\{a_1,a_2\}} - \mathcal{F}_{\{a_1,a_2\};\{a_3,a_4\}}\right]\mathrm{d}\overline{\Pi}\,. \tag{2.63}$$

and the derivative of the entropy is

$$\nabla_\mu S^\mu_a = -\frac{1}{2}\int W_{\{a_1,a_2\};\{a_3,a_4\}}\left[\mathcal{F}_{\{a_3,a_4\};\{a_1,a_2\}} - \mathcal{F}_{\{a_1,a_2\};\{a_3,a_4\}}\right]\ln\left(h_a(x,p_{a_1})\right)\mathrm{d}\Pi \tag{2.64}$$

with the notation of the total phase-space volume form $\mathrm{d}\Pi = \mathrm{d}\overline{\Pi}\wedge\theta_{a_1}/(2(2\pi)^3)$. Notice now that changing $p_{a_1}\to p_{a_2}$ leaves the expression invariant. Changing $p_{a_1}\to p_{a_3}$ or $p_{a_1}\to p_{a_4}$ transforms the expression on its opposite. Therefore we average over four copies of $\nabla_\mu S^\mu_a$ and make the proper changes of variables to get

$$\begin{aligned}\nabla_\mu S^\mu_a = -\frac{1}{8}\int \mathrm{d}\Pi\, W_{a_1a_2;a_3a_4} f_a(x^\mu,p^i_{a_1})f_a(x^\mu,p^i_{a_2})f_a(x^\mu,p^i_{a_3})f_a(x^\mu,p^i_{a_4}) \\ \times\left[\frac{1}{h_a(x^\mu,p^i_{a_1})h_a(x^\mu,p^i_{a_2})} - \frac{1}{h_a(x^\mu,p^i_{a_3})h_a(x^\mu,p^i_{a_4})}\right]\ln\left(\frac{h_a(x^\mu,p^i_{a_1})h_a(x^\mu,p^i_{a_2})}{h_a(x^\mu,p^i_{a_3})h_a(x^\mu,p^i_{a_4})}\right)\,.\end{aligned} \tag{2.65}$$

Because of the inequality $(x-y)\ln(x/y)\geq 0$, valid for all $(x,y)\in\mathbb{R}^2$ that satisfies $xy>0$, this equation implies $\nabla_\mu S^\mu_a \geq 0$. This is exactly the result of the H-theorem, *i.e.* the second principle of thermodynamics: the entropy current density can only increase. It is therefore proven here for the specific configuration of a single species with $2\to 2$ interactions. As a matter of fact for any number of species and any interaction $I = Y\leftrightarrow Z$ the momenta can always be shuffled around so that every term in the derivative of S^μ satisfies

$$\nabla_\mu S^\mu \propto -\int\left[\prod_{\kappa\in\mathcal{I}} f_q(x^\mu,p^i_\kappa)\right]\ln\left(\frac{\prod_{\kappa\in\mathcal{Y}} h_\kappa(x^\mu,p^i_\kappa)}{\prod_{\kappa'\in\mathcal{Z}} h_{\kappa'}(x^\mu,p^i_{\kappa'})}\right)\left[\frac{1}{\prod_{\kappa\in\mathcal{Y}} h_\kappa(x^\mu,p^i_\kappa)} - \frac{1}{\prod_{\kappa'\in\mathcal{Z}} h_{\kappa'}(x^\mu,p^i_{\kappa'})}\right]\mathrm{d}\Pi \tag{2.66}$$

[2]When $\varepsilon = 0$ we recover the non relativistic case.

with a positive coefficient of proportionality. From similar arguments one then gets the conclusion $\nabla_\mu S^\mu \geq 0$ in full generality which proves the H-theorem.

2.2.5 Thermodynamic equilibrium between species

Let us focus first on the equilibrium distribution of an isolated species $f_a^{\rm eq}$. It is defined such that it conserves entropy, i.e. $\nabla_\mu S^\mu\left[f_a^{\rm eq}\right] = 0$. The condition for equality is obtained from Eq. (2.65) and can be written as

$$\ln h_a^{\rm eq}(x^\mu, p^i_{a_1}) + \ln h_a^{\rm eq}(x^\mu, p^i_{a_2}) = \ln h_a^{\rm eq}(x^\mu, p^i_{a_3}) + \ln h_a^{\rm eq}(x^\mu, p^i_{a_4})\,. \tag{2.67}$$

Because of the energy momentum conservation the solution $h_a^{\rm eq}$ can be parametrised as $\ln h_a^{\rm eq}(x^\nu, p^\nu) = \alpha_a(x^\nu) - \beta_{a,\mu}(x^\nu)p^\mu$. Inverting the relation between h_a and f_a gives

$$f_a^{\rm eq}(x^\nu, p^i) = \left[e^{\beta_{a,\mu}(x^\nu)p^\mu - \alpha_a(x^\nu)} - \varepsilon_a\right]^{-1}\,. \tag{2.68}$$

This expression in called the Maxwell-Juttner distribution (JÜTTNER 1911). In order for f_a to vanish at large p the vector $\beta_{a,\mu}$ needs to be time-like and future directed, therefore it can be parametrised by $\beta_{a,\mu} = \beta_a u_{a,\mu}$ with $u_{a,\mu}u_a^\mu = 1$. In the rest frame of u_a^μ one can then simplify $\beta_{a,\mu}p^\mu = \beta_a \hat{p}_0$. The physical meaning of α_a and β_a can be found by deriving the thermodynamic equalities associated associated to $f_a^{\rm eq}$. One then shows that α_a is in fact the chemical potential at position x per units of temperature while β_a is the inverse temperature. In the end, setting the chemical potential $\mu_a = \alpha_a/\beta_a$, we recover the general expression of the Fermi-Dirac and Bose-Einstein distributions.

Replacing f_a by the equilibrium distribution in Eq. (2.62) gives that $L_m(f_a^{\rm eq}) = 0$. As shown in BERNSTEIN (1988) and E70 there is no general solution to that equation for massive particles in the FLRW metric; this is a purely geometric property. Therefore there is no universal solution for α_a and β_a. Nevertheless, consider a species a of mass m_a described by its equilibrium distribution. Then one can still derive that in FLRW if $m_a = 0$ its temperature goes as $T \propto a^{-1}$ and if $m_a \to \infty$ it goes as $T_a \propto a^{-2}$.

In the Early Universe multiple species coexist and interact. Then the conservation of the stress-energy tensor, as well as the general H-theorem give

$$\nabla_\mu\left(\sum_a T_a^{\mu\nu}\right) = 0 \quad \text{and} \quad \nabla_\mu\left(\sum_a S_a^\mu\right) \geq 0\,. \tag{2.69}$$

The equilibrium PSDF are defined by $\nabla_\mu S^\mu = 0$. This implicit definition imposes that all species satisfy the equilibrium distribution of Eq. (2.68) with the addition that for every interaction $Y \leftrightarrow Z$

$$\sum_{a\in Y}\mu_a = \sum_{a'\in Z}\mu_{a'} \quad \text{and} \quad \sum_{a\in Y}\beta_a = \sum_{a'\in Z}\beta_{a'} \tag{2.70}$$

This two equalities are referred respectively to as the *chemical* and *kinetic* or *thermal* equilibrium. The combination of the two is called the *thermodynamic* equilibrium. However, for the same reason as for the single species treatment, there are no general solutions to these equations when dealing with massive particles. Nevertheless, in the equilibrium approximation, as long as particle interact sufficiently between

themselves, they still acquire a state of quasi thermodynamic equilibrium.

We end here the first part of this statistical physics analysis. In the following section, we use the formulae established here and put them in a physical context with several particle species in interaction.

2.3 Thermal history of the early Universe

In this section, the different ingredients introduced in the previous section concerning the statistical description of particle species are applied to the history of the early Universe. However, first, we discuss the locally inertial frame that is convenient for computations. Afterwards, we describe the thermochemical evolution of the Early Universe and conclude by addressing the thermal history of WIMPs.

2.3.1 Locally inertial frame

The geometry of space-time has not been specified hitherto in Sect. 2.2. In the following, at every position x_p^μ we will work in the locally inertial frame (LIF) with *new* coordinates $y^\mu(x^\nu)$ and associated canonical momentum $q^\mu = \mathrm{d}y^\mu/\mathrm{d}\lambda$. We introduce the comoving momentum norm as $q = (\delta_{ij}q^iq^j)^{1/2}$ and we define the energy of a particle as

$$E(q) \equiv q^0 = q_0 = (m^2 + \delta_{ij}q^iq^j)^{1/2} = (m^2+q^2)^{1/2}\,. \tag{2.71}$$

Let us consider a (n,m) tensor T with component $\tilde{T}^{\mu_1..\mu_n}_{\mu_{n+1}..\mu_{m+n}}$ in the LIF and $T^{\mu_1..\mu_n}_{\mu_{n+1}..\mu_{m+n}}$ in the *original* coordinate system x^μ. One can relate both components by the usual law for coordinate transformations,

$$\tilde{T}^{\mu_1..\mu_n}_{\mu_{n+1}..\mu_{m+n}} = \frac{\partial y^{\mu_1}}{\partial x^{\nu_1}}...\frac{\partial y^{\mu_n}}{\partial x^{\nu_n}}\frac{\partial x^{\nu_{n+1}}}{\partial y^{\mu_{n+1}}}...\frac{\partial x^{\nu_{n+m}}}{\partial y^{\mu_{n+m}}}T^{\nu_1..\nu_n}_{\nu_{n+1}..\nu_{m+n}} \tag{2.72}$$

For a metric in the diagonal form it is always possible to transform it into a Minkowski metric (up to second order corrections) by setting

$$\begin{aligned} \partial_{x^\mu}y^\nu &= \begin{cases} \sqrt{|g_{\mu\mu}|} & \text{if } \mu=\nu \\ 0 & \text{if } \mu\neq\nu \end{cases} \\ \text{and}\quad y^\mu &= y_p^\mu + \partial_{x^\nu}y^\mu\left[(x^\nu - x_p^\nu) + \frac{1}{2}\Gamma^\nu_{\rho\sigma}(x^\rho-x_p^\rho)(x^\sigma-x_p^\sigma)\right] + \dots \end{aligned} \tag{2.73}$$

This definition of the new coordinates is not unique however as it can be rescaled by a Lorentz transformation. In the interesting case for us, when the *original* coordinate system is Cartesian in a FLRW Universe with no curvature then the metric is $\mathrm{d}s^2 = \mathrm{d}t^2 - a^2\mathrm{d}x^i\mathrm{d}x^j$ and according to Eq. (2.72) we can relate q^μ to the canonical momentum $p^\mu = \mathrm{d}x^\mu/\mathrm{d}\lambda$ with

$$q^0 = p^0 \quad \text{and} \quad q^i = a(t_p)p^i \tag{2.74}$$

This transformation being position dependent, we specify that in the previous equation the scale factor has to be evaluated at $x_p^0 = t_p$[3]. Moreover with the definition

[3]In order to get the Christoffel symbols to vanish in the new set of coordinates we can simply write the new coordinates in terms of the old ones in a second order expansion as

$$\begin{aligned} y^0 &= (t-t_p) + \frac{1}{2}a^2(t_p)H(t_p)\delta_{ij}(x^i-x_p^i)(x^j-x_p^j) + \dots \\ y^i &= a(t_p)\left(1+H(t_p)t_p\right)(x^i-x_p^i) + \dots \end{aligned} \tag{2.75}$$

of the 3-momentum norm $p = (-g_{ij}p^i p^j)^{1/2}$ one can check that $p = q$ and $\hat{p}_0 = p^0 = E(q) = E(p)$. In addition, from now on we also use another, more intuitive notation for the phase space volume element. We define

$$\mathrm{d}^3\mathbf{p} = \hat{p}_0\theta_m = \frac{1}{3!}\sqrt{-g}\varepsilon_{ijk}\,\mathrm{d}p^i \wedge \mathrm{d}p^j \wedge \mathrm{d}p^k \tag{2.76}$$

so that in the LIF it reduces to

$$\mathrm{d}^3\mathbf{q} = \frac{1}{3!}\varepsilon_{ijk}\,\mathrm{d}q^i \wedge \mathrm{d}q^j \wedge \mathrm{d}q^k\,. \tag{2.77}$$

In conclusion, all the equations can be written in the LIF without loss of generality (remembering then to make the proper transformation when necessary) as it is often more convenient in practice. Besides, in order to go from the LIF to the frame of coordinates x^μ corresponding the the Cartesian FLRW, one can simply replace $\mathrm{d}^3\mathbf{q} \to \mathrm{d}^3\mathbf{p}$, $q \to p$ and therefore $E(q) \to E(p)$ in the expressions.

2.3.2 The effective energy and entropy densities

We are now fully equipped to address the thermodynamics of the early Universe. After the end of inflation, the inflaton field arguably releases its energy in the form of radiation during a period called *reheating*. This very large energy density is then turned into all accessible standard-model states called the primordial plasma (depending on the effective reheating temperature T_r), and to exotic particles with sufficient couplings and kinetically allowed masses such that $m < T_\mathrm{r}$. This is called thermal production. Then rapid scatterings between particles $p_i + p_j \leftrightarrow p'_i + p'_j$ ensures thermal equilibrium, while rapid annihilations and creations of particle and antiparticle pairs $p_i + \overline{p}_i \leftrightarrow X$ (where X represents any other set of particles in the plasma) ensures chemical equilibrium.

When assumed in thermodynamic equilibrium all species have their number density, pressure and density given by the equilibrium equation derived from the equilibrium expression in Eq. (2.68). Therefore the equilibrium distribution becomes

$$f^\mathrm{eq}(q) = \left[e^{\beta(E(q)-\mu)} - \varepsilon\right]^{-1}\,. \tag{2.78}$$

where we recall that μ is the chemical potential here. Nevertheless, we mentioned that there is no universal solution for the temperature and the chemical potential as functions of time for massive particles. This has been studied by BERNSTEIN (1988) who showed that if all particles interact frequently in the thermal bath we can then be certain that the corrections to the equilibrium distribution remain small. Therefore, in the following we assume that all SM species can be described simply by their equilibrium distribution unless stated otherwise.

A first remark is that because the photon number is not necessarily conserved, for instance in interactions such as

$$e^- + \gamma \to e^- + \gamma + \gamma\,, \tag{2.79}$$

their chemical potential is $\mu_\gamma = 0$ in order to satisfy Eq. (2.70). Moreover, every fermion and anti-fermion ψ and $\bar{\psi}$ in the SM annihilates into photons according to

$$\psi + \bar{\psi} \to \gamma + \gamma \tag{2.80}$$

which implies $\mu_\psi = -\mu_{\bar{\psi}}$. Therefore, for fermions with $\mu_\psi \neq 0$ it can be shown that, when $m \ll T$, the difference in number density between the particle and the anti-particle is given by the following expression,

$$n_\psi - n_{\bar{\psi}} = \frac{g}{6\pi^2} T^3 \left[\pi^2 \left(\frac{\mu_\psi}{T} \right) + \left(\frac{\mu_\psi}{T} \right)^3 \right] . \tag{2.81}$$

At early times, when $m_e \ll T$, one can approximate $\mu_e \sim 0$. In the following, we neglect the chemical potential of SM particles with respect to the temperature as long as their mass satisfies $m \ll T$. Then, the number density, energy density and pressure at equilibrium can be written under the form

$$\begin{aligned} n^{\rm eq} &= \frac{gT^3}{2\pi^2} \sum_{n=1}^{\infty} \varepsilon^{n+1} \frac{x^2}{n} K_2(xn) = \frac{g}{2\pi^2} \frac{1}{\beta^3} \sum_{n=1}^{\infty} (-\varepsilon)^{n+1} \left\{ \frac{2x}{n^2} K_1(xn) + \frac{x^2}{n} K_0(xn) \right\} \\ \rho^{\rm eq} &= \frac{gT^4}{2\pi^2} \sum_{n=1}^{+\infty} \varepsilon^{n+1} \left\{ \left(\frac{6x}{n^3} + \frac{x^3}{n} \right) K_1(xn) + \frac{3x^2}{n^2} K_0(xn) \right\} \\ P^{\rm eq} &= \frac{gT^4}{2\pi^2} \sum_{n=1}^{\infty} (-\varepsilon)^{n+1} \frac{x^2}{n^2} K_2(xn) = \frac{gT^4}{2\pi^2} \sum_{n=1}^{+\infty} \varepsilon^{n+1} \left\{ \frac{2x}{n^3} K_1(xn) + \frac{x^2}{n^2} K_0(xn) \right\} \end{aligned} \tag{2.82}$$

where $K_j(z)$ is the modified cylindrical Bessel function of order j and

$$x = m/T \, . \tag{2.83}$$

In the scenario $x \to 0$ of massless particles, also called ultra-relativistic (UR) limit, these expressions simplify and give

$$n^{\rm eq} = \frac{gT^3}{\pi^2} \zeta(3) A, \quad \rho^{\rm eq} = \frac{g\pi^2 T^4}{30} B \quad \text{and} \quad P^{\rm eq} = \frac{\rho^{\rm eq}}{3} \tag{2.84}$$

with $A = 1$ and $B = 1$ for bosons and $A = 3/4$ and $B = 7/8$ for fermions. The full proof is given in App. B.1. Note that at the same time we have proven that the equation of state for radiation is given by $w = 1/3$. We can also evaluate the expression in the opposite limit, $x \to \infty$, for what is then called non-relativistic particles (NR). Including the contribution of the chemical potential yields

$$n^{\rm eq} = g \left(\frac{mT}{2\pi} \right)^{3/2} e^{-(m-\mu)/T}, \quad \rho^{\rm eq} = m n^{\rm eq} \quad \text{and} \quad P^{\rm eq} = n^{\rm eq} T \ll \rho^{\rm eq} \, . \tag{2.85}$$

Non-relativistic species are pressureless which yields the equation of state for the matter component of the Universe $w \sim 0$. After the inflation phase, the temperature of the plasma decreases and most species become, as the Universe expands, non-relativistic. Then, if they stay in thermodynamic contact with the plasma their number and energy densities are thus exponentially suppressed.

Collisions and annihilations ensuring thermodynamic equilibrium are called *rapid* if the associated interaction rate, generically denoted Γ, is larger than the expansion rate H. One can then discriminate between the interactions that have time to happen with those that are frozen due to the expansion. To this end, H can be evaluated in the Early Universe thanks to the first Friedmann equation. Indeed, using the fact that only UR species contribute to the total energy density at this epoch,

$$\rho_{\rm tot} \equiv \sum_i \rho_i^{\rm eq} \simeq \sum_{i \in \mathcal{R}} \rho_i^{\rm eq} . \tag{2.86}$$

where we tag by the letter i every species present in the plasma and where $\mathcal{R}$ formally represents the set of UR species. The common notation is to introduce $g_{\rm eff}(T)$, the effective relativistic degrees of freedom for energy density at temperature T so that

$$H^2 = \frac{4\pi^3 G_{\rm N}}{45}\left\{g_{\rm eff}(T) \equiv \frac{30\rho}{\pi^2 T^4}\right\} T^4. \tag{2.87}$$

In essence, the history of the early Universe is encoded in the evolution of $g_{\rm eff}(T)$. Its variations are related to variations of ρ and thus to species appearing into or vanishing from the plasma, either because they are at thermodynamic equilibrium and become NR or for any other possible reason – at the QCD phase transition when all quarks and gluons combine into protons, neutrons, etc. Furthermore, the total entropy being a conserved quantity if the expansion is adiabatic, it is convenient, in many computations, to use its associated density. More precisely, for a volume V of entropy $S(V)$, the entropy density is simply given as $s \equiv S(V)/V$. As shown in App. B.1 it can be written, for a given species at equilibrium with $\mu = 0$,

$$s^{\rm eq} = \frac{\rho^{\rm eq} + P^{\rm eq}}{T} = \frac{gT^3}{2\pi^2}\sum_{n=1}^{+\infty}\varepsilon^{n+1}\left\{\left(\frac{8x}{n^3}+\frac{x^3}{n}\right)K_1(xn) + \frac{4x^2}{n^2}K_0(xn)\right\}. \tag{2.88}$$

Because both the energy density and the pressure go to zero for NR species, it is useful to introduce another relativistic effective degree of freedom, $h_{\rm eff}(T)$, so that the total entropy density is

$$s = \sum_i s_i^{\rm eq} \equiv \frac{2\pi^2}{45} h_{\rm eff}(T) T^3. \tag{2.89}$$

According to the expressions of $\rho_i^{\rm eq}$ and $s_i^{\rm eq}$ shown previously thus $g_{\rm eff}$ and $h_{\rm eff}$ can also be written in terms of Bessel functions as

$$g_{\rm eff}(T) = \sum_{i\neq\nu} g_i \frac{15}{\pi^4}\left(\sum_{n=1}^{\infty}\varepsilon_i^{(n+1)}\left\{\left(\frac{6x_i}{n^3}+\frac{x_i^3}{n}\right)K_1(x_i n) + \frac{3x_i^2}{n^2}K_0(x_i n)\right\}\right) + \Delta g_\nu^4, \tag{2.90}$$

$$h_{\rm eff}(T) = \sum_{i\neq\nu} g_i \frac{45}{4\pi^4}\left(\sum_{n=1}^{\infty}\varepsilon^{(n+1)}\left\{\left(\frac{8x_i}{n^3}+\frac{x_i^3}{n}\right)K_1(x_i n) + \frac{4x_i^2}{n^2}K_0(x_i n)\right\}\right) + \Delta g_\nu^3, \tag{2.91}$$

where the sum on i runs over all possible species of the SM, except for neutrinos. Neutrino contribution is given by the last term Δg_ν^n and cannot be computed directly using Eq. (2.82) because they decouple from the plasma at $T \sim 1$ MeV. Therefore when electrons become NR, at $T \sim m_e = 511$ keV, they transfer their entropy to the photons, but no longer to neutrinos, which are left colder. Neutrinos then acquire a new temperature $T_\nu = (4/11)^{1/3}T$, computed from entropy conservation, different from T. This changes the number of effective degrees of freedom in the photon bath. For further details on the decoupling process see below, in Sect. 2.3.3 the specific case of DM decoupling – the basic principles are the same for neutrinos. Therefore their contribution is, more precisely,

$$\Delta g_\nu^n = g_\nu \frac{7}{8}\left(3\Theta(T-m_e) + N_{\rm eff}\left(\frac{T_\nu}{T}\right)^n \Theta(m_e - T)\right) \tag{2.92}$$

with Θ the Heaviside distribution. In practice, the Heaviside step is numerically smoothed out by a regulating function. Moreover, $N_{\rm eff} = 3.045$ is an effective number

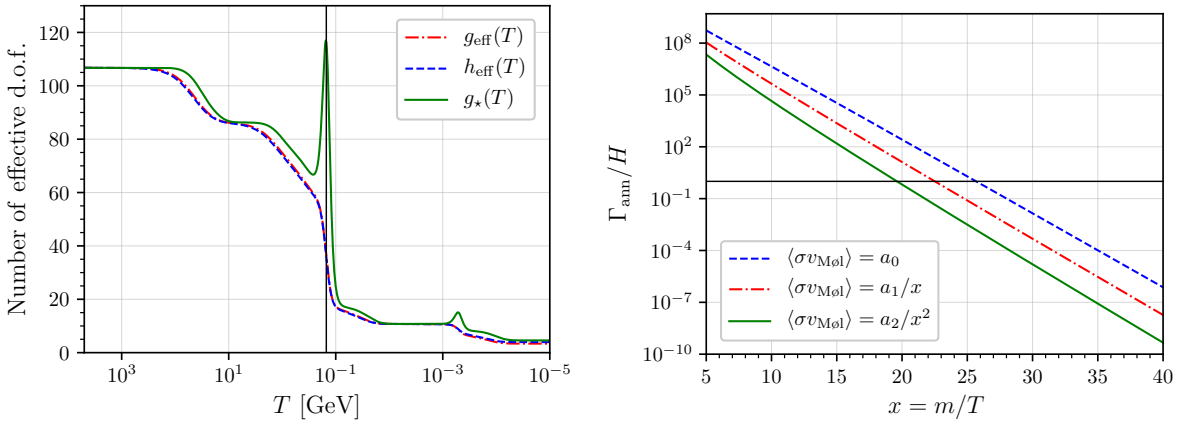

Figure 2.2 – Left panel: Evolution of the number of effective degree of freedom with the temperature. Note that the x-axis is reversed so that high temperature (and therefore early times) are on the left. The peak for $g_\star^{1/2}$ is due to the divergence of the derivative of $h_{\rm eff}$ at the QCD phase transition that is unphysical. It is regularised numerically through simple smooth functions. **Right panel:** Evolution of the DM annihilation rate over the Hubble rate for various temperature dependences of the thermally average cross-section. In this example $a_0 = a_1 = a_2 = 3 \times 10^{-26}$ cm^2 s^{-1} and the DM mass is 100 GeV. When the ratio is much larger than 1 chemical equilibrium is maintained, when it becomes much lower than 1 the chemical equilibrium is lost.

of neutrinos. This value, different from 3, takes into account the fact that all three flavours did not decouple exactly at the same time and that the high-momentum tails of their distributions remained coupled to the plasma up to electron-position annihilation (Mangano et al. 2005; Salas et al. 2016). In the left panel of Fig. 2.2 the evolution of these effective degrees of freedom with temperature is represented, taking into account all the SM species. It is not important to leave a possible WIMP contribution out for this graph since we are interested in DM particles that decouple from the plasma when NR (a condition for being a CDM candidate). Eventually, let us introduce the evolution of cosmic time with respect to the temperature

$$\frac{{\rm d}t}{{\rm d}T} = -\frac{1}{s}\sqrt{\frac{\pi}{45 G_{\rm N}}}\left\{g_\star^{1/2}(T) \equiv \frac{h_{\rm eff}(T)}{\sqrt{g_{\rm eff}(T)}}\left(1 + \frac{{\rm d}\ln h_{\rm eff}(T)}{3\,{\rm d}\ln T}\right)\right\} \tag{2.93}$$

that plays an important role for the study of the early Universe. The evolution of $g_\star$ is represented in the left panel of Fig. 2.2 alongside $h_{\rm eff}$ and $g_{\rm eff}$.

2.3.3 Qualitative history of WIMPs in the early Universe

In this section, we assume that DM is made of one species χ of mass m_χ for clarity that can be, for now, a scalar, a Dirac fermion, a Majorana fermion, or a vector. In all generality, we denote $\overline{\chi}$ the anti-particle even if in the case of a Majorana fermion for instance the bar notation can be redundant as they are their own anti-particles. Besides, we address here two different configurations: the usual WIMP scenario and the FIMP (Feebly Interacting Massive Particle) scenario. Let us start with the former. In the standard picture, after inflation, WIMPs are produced from the plasma, and reach instantaneously thermodynamic equilibrium. This imposes that their mass be lower than the thermal energy of the primeval bath, and that they have strong enough couplings to particles from the plasma. At chemical equilibrium, production from the

plasma is balanced by annihilation of $\bar{\chi}\chi$ pairs. However, as the Universe expands and the temperature drops, WIMPs become NR, and the plasma is no longer energetic enough to produce them efficiently. As long as chemical equilibrium holds, this results in exponentially quenching the WIMP population, according to Eq. (2.85). The rate at which annihilation occurs, denoted by $\Gamma_{\rm ann}$ below, is given approximately by

$$\Gamma_{\rm ann} \propto n_\chi \langle \sigma_{\chi\bar{\chi}} v_{\rm Møl} \rangle \propto \sum_{q=0} a_q x^{-q-3/2} e^{-x} \tag{2.94}$$

with n_χ the number density of WIMPs and $\langle \sigma_{\chi\bar{\chi}} v_{\rm Møl} \rangle$ the thermal average of the annihilation cross-section – detailed in Sect. 2.4. Here we simply assume the partial wave decomposition of the cross-section in terms of $x = m_\chi/T (\propto 1/v^2$ for NR interacting particles) so that $\langle \sigma_{\chi\bar{\chi}} v_{\rm Møl} \rangle \simeq \sum_q a_q x^{-q}$. The first term, $q = 0$, is called the s-wave term while the second, $q = 1$, is called the p-wave term, and is NR velocity supressed. Assuming similar amplitudes a_q, the annihilation rate is dominated by the lowest non-vanishing q term[4]. Annihilation ceases depleting the WIMP population when the probability of WIMP encounters drops to zero, i.e. when the expansion rate gets roughly larger than the annihilation rate,

$$\Gamma_{\rm ann} \lesssim H \propto \sqrt{g_{\rm eff}\,(T)} x^{-2}. \tag{2.95}$$

From this time on particles χ and $\bar{\chi}$ can no longer interact and the annihilation process stops (rigorously, it never completely stops but is rather tremendously reduced). By tuning the cross section to values typical of weak interactions, this occurs before DM particles are completely exponentially suppressed and the number density of WIMPs freezes out. Hence the subsequent denomination of *freeze-out* mechanism and also "weakly-interacting" massive particles. The right panel of Fig. 2.2 shows the evolution of $\Gamma_{\rm ann}/H$ for different behaviours of the cross-section. At high temperature, small x, the ratio is larger than 1 (marked by the black vertical line) but decreases and eventually drops below 1.

Now let us explain the basic principle of kinetic decoupling. In the standard picture, even when WIMPs have chemically decoupled they can still be in kinetic equilibrium with the plasma. They keep the same temperature T with the approximate functional form for the PSDF thanks to scattering interactions of the type: $\chi + \psi \leftrightarrow \chi + \psi$, with any particle ψ of the plasma. If not strongly velocity-suppressed, those processes are still efficient for a while since they occur at a rate given by

$$\Gamma_{\rm scatt} = n_\psi \langle \sigma_{\chi\psi\leftrightarrow\chi\psi} v_{\rm Møl} \rangle \propto x^{-3} \langle \sigma_{\chi\psi\leftrightarrow\chi\psi} v_{\rm Møl} \rangle . \tag{2.96}$$

Here there is no exponential suppression in $\Gamma_{\rm scatt}$ with the temperature while the plasma is relativistic as there is in $\Gamma_{\rm ann}$. In the most common scenario, $\Gamma_{\rm scatt} \gg \Gamma_{\rm ann}$ and kinetic decoupling occurs at later times when $\Gamma_{\rm scatt} \sim H$ - see BINDER et al. (2017) for the treatment when this is not true. Thus, even though the number density of particles in the plasma (represented by $n_\psi \propto x_\chi^{-3}$ here) decreases slower than n_χ, it still decreases faster than H and at some point, the scattering processes can no longer keep up with the expansion rate of the Universe. Then DM stops interacting and starts to stream freely. It acquires its own temperature denoted T_χ. The complete history of the WIMP evolution is summarised in Fig. 2.3.

[4] If $a_1 \gg a_0$, the p-wave term can dominates over the s-wave term even if the later is non null.

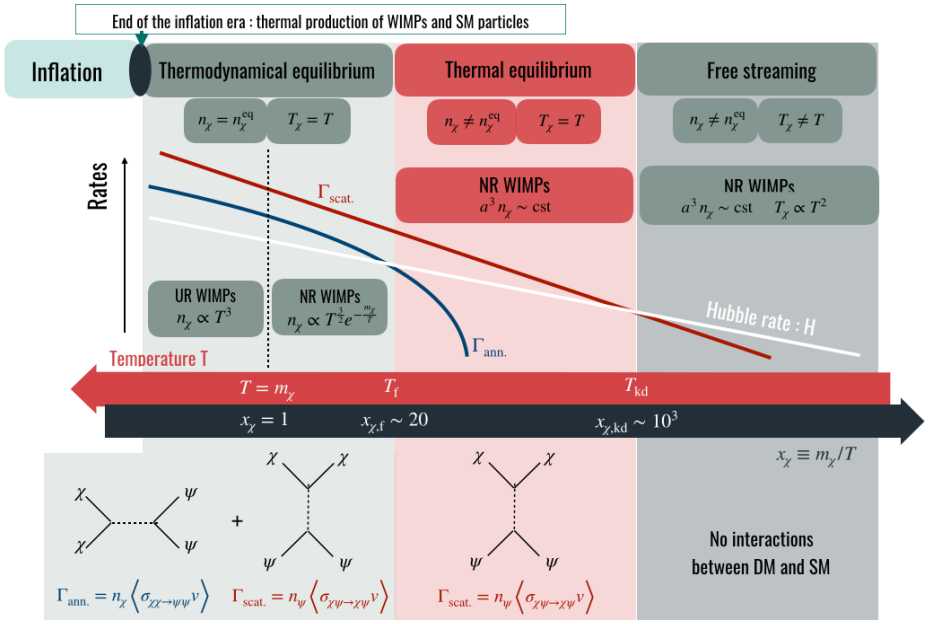

Figure 2.3 – Representation of the standard WIMPs thermal history.

Let us finally briefly mention the FIMP configuration. It occurs when DM particles do not interact enough with the rest of the primordial plasma and are not produced very quickly in thermodynamic equilibrium with the SM particles. Nonetheless, either creation processes (not balanced by annihilations processes due to the initial lack of DM particles) or decays of more massive particles can lead to an increase in n_χ and a possible increase in $\Gamma_{\rm ann}$. If $\Gamma_{\rm ann}$ grows fast enough DM reaches the state of thermodynamic equilibrium before chemically decoupling and we then recover the previous scenario. However, if $\Gamma_{\rm ann}$ stays lower than H, because of too small couplings to the SM particles, one talks of FIMP DM and this scenario is referred to as a *freeze-in* (L. J. Hall et al. 2010; Bernal et al. 2017). This scenario is analogue to the production mechanism relevant to sterile neutrinos: The Dodelson-Widrow mechanism – active-sterile oscillation in vacuum – (Dodelson et al. 1994) or the resonant Shi-Fuller mechanism – resonant Mikheyev-Smirnov-Wolfenstein oscillation – (Shi et al. 1999). The freeze-in mechanism was also already discussed in the context of scalar DM (McDonald 2002), or sneutrinos (Asaka et al. 2006).

In the last sections of this chapter, we now detail the mathematics and the different physical interactions behind the chemical and kinetic decouplings of WIMPs. Then we illustrate the impact for the halo minimal mass discussed in Chapter 3 within a simplified particle model.

2.4 Chemical and kinetic decoupling of WIMPs

In this section, we detail the production mechanism of thermal DM and its loss of equilibrium with the rest of the primordial plasma. For that, we assume that DM is made of one or several WIMP fermionic species that are thermally produced in the early Universe along with all the SM particles either during reheating or slightly after by the conversion from SM particles. All particles that are directly interacting both

with WIMPs and with SM particles are called mediators. They can be SM mediators or exotic mediators coming from a dark sector.

We denote by $\{\chi_i\}_i$ the set of WIMPs with associated masses $\{m_i\}_i$. This set also contains the anti-particles if DM is made of Dirac fermions. For instance, for one Dirac fermion we denote $\chi_1 = \overline{\chi}_0$. By convention, the lightest of all the WIMPs is tagged 0 and has mass m_0. Moreover in this section n_i represents the number density of χ_i and f_i its PSDF. Interactions involving WIMPs can be put into one of the following four broad categories based on the decomposition of EDSJO et al. (1997)

- Annihilation and creation interactions, e.g. $\chi_i + \chi_j \leftrightarrow Y$
- Elastic scatterings, e.g. $\chi_i + X \leftrightarrow \chi_i + X$
- Decays and inverse decays, e.g. $\chi_i \leftrightarrow \chi_j + Y$
- Non elastic scatterings, e.g. $\chi_i + X \leftrightarrow \chi_j + Z$

where X, Y, and Z are arbitrary sets of incoming and outgoing particles different from WIMPs. Therefore, the collision operator can be divided into four subsequent parts. Only the first category, however, corresponds to processes changing the total number of WIMPs and is relevant for chemical decoupling. For the thermal contact, they all contribute although, in the kinetic decoupling context, we are only interested in the lightest WIMP and the dominant contribution comes from elastic scatterings.

2.4.1 Chemical decoupling: general set-up

The study of the chemical decoupling is nothing more than the study of the evolution of the number density of WIMPs when it starts to diverge from its equilibrium value. Conveniently, using Eq. (2.48) we have already seen that

$$\nabla_\mu n_a^\mu = \frac{g_a}{(2\pi)^3} \int L_m(f_a)\theta_a \tag{2.97}$$

so that, combined to the Boltzmann equation, it yields

$$\nabla_\mu n_a^\mu = \left\{ \hat{\mathcal{C}}(f_a) \equiv \frac{g_a}{(2\pi)^3} \int \hat{C}(f_a)(x^\mu, p^i_{a_1})\theta_{a_1} \right\} . \tag{2.98}$$

Here we introduce $\hat{\mathcal{C}}$ as the 0^{th} moment of the collision operator. In the Cartesian FLRW metric, the covariant derivative of the density vector flow depends only on its 0^{th} component[5] and it yields the equation for the evolution of the density in terms of the Hubble rate

$$\nabla_\mu n_a^\mu = \frac{\mathrm{d}n_a}{\mathrm{d}t} + 3Hn_a \, . \tag{2.99}$$

The Hubble rate H acts as a dilution term thus, if $\hat{\mathcal{C}} = 0$, this equation simply gives $n_a \propto (1+z)^3$. The main objective is to evaluate the 0^{th}-moment of the collision operator to recast it under a form that only depends on the number densities of the different species, no longer on the PSDFs. If this is possible, all equations on the number densities will then form a closed system of differential equations that can be numerically solved. To this end, let us consider an arbitrary interaction between two sets of

[5]Note that the 0^{th} component of a four-vector in the Cartesian FLRW and in the LIF are the same.

particles $Y \leftrightarrow Z$ and show how this quantity can be generically simplified. Here we are only interested in the case where $Y \neq Z$ since elastic scattering are not relevant. Therefore, assuming the CP invariance of the interactions, according to Eq. (2.58) we can write the zeroth-order collision operator as

$$\hat{\mathcal{C}}_{Y\leftrightarrow Z}\left(f_a\right) = \frac{1}{\mathcal{S}}\int \mathrm{d}\Pi\left\{\xi_a(Y) W_{\mathcal{Y}_\star;\mathcal{Z}}\left[\mathcal{F}_{\mathcal{Z},\mathcal{Y}_\star} - \mathcal{F}_{\mathcal{Y}_\star;\mathcal{Z}}\right] - \xi_a(Z) W_{\mathcal{Y};\mathcal{Z}_\star}\left[\mathcal{F}_{\mathcal{Z}_\star;\mathcal{Y}} - \mathcal{F}_{\mathcal{Y};\mathcal{Z}_\star}\right]\right\} . \quad (2.100)$$

where $\mathrm{d}\Pi = \mathrm{d}\overline{\Pi}\wedge\theta_{a_1}/(2(2\pi)^3)$. As a matter of fact, since the particle that is labelled a_1 is completely equivalent to all the other particles of species a in this expression, there is no use of the $\star$ notation and we can simplify the expression as

$$\hat{\mathcal{C}}_{Y\leftrightarrow Z}\left(f_a\right) = \frac{\Delta\xi_a(Y,Z)}{\mathcal{S}}\int \mathrm{d}\Pi\, W_{\mathcal{Y};\mathcal{Z}}\left[\mathcal{F}_{\mathcal{Z},\mathcal{Y}} - \mathcal{F}_{\mathcal{Y};\mathcal{Z}}\right] \quad (2.101)$$

where $\Delta\xi_a(Y,Z) = \xi_a(Y) - \xi_a(Z)$ counts the net difference between created and annihilated particles in the process. In the following, because this should hold true for interactions in the early Universe, we assume that all particles are in thermal equilibrium with the plasma. However as we have seen there is no general equilibrium parametrisation for the distribution function of massive species. The solution is then to use the *pseudo-potential* approximation that consists in writing the different PSDF under the form

$$f(q) = \left[e^{\beta E(q)+\alpha+\phi(q)} - \varepsilon\right]^{-1} . \quad (2.102)$$

where ϕ is a correction to the equilibrium distribution. As proven in Bernstein (1988) the value of ϕ is constrained by the rate of elastic collisions. If this rate is high enough one can safely approximate $\phi \sim 0$ and this is what is assumed in the following. An essential property of this PSDF, which is useful for simplifying the expressions is

$$1 + \varepsilon_\kappa f_\kappa(q_\kappa) = e^{\alpha_\kappa+\beta E_\kappa(q)} f_\kappa(q_\kappa) . \quad (2.103)$$

Moreover the Dirac delta distribution in $\mathrm{d}\Pi$ enforces the conservation of energy

$$\sum_{\kappa\in\mathcal{Y}} E_\kappa(q_\kappa) = \sum_{\kappa'\in\mathcal{Z}} E_{\kappa'}(q_{\kappa'}) . \quad (2.104)$$

Using these two equalities alongside Eq. (2.101) allows factoring out the pseudo-chemical potentials

$$\hat{\mathcal{C}}_{Y\leftrightarrow Z}(f_a) = \frac{\Delta\xi_a(Y,Z)}{\mathcal{S}}\left[e^{\alpha_Y-\alpha_Z} - 1\right]\int \mathrm{d}\Pi\, W_{\mathcal{Y},\mathcal{Z}}\mathcal{F}_{\mathcal{Y};\mathcal{Z}} \quad (2.105)$$

with the definitions of the total potentials

$$\alpha_Y \equiv \sum_{r\in Y}\alpha_r \quad \text{and} \quad \alpha_Z \equiv \sum_{r'\in Z}\alpha_{r'} . \quad (2.106)$$

The integral term can take different forms according to the process and this is what we detail in the following. Let us first give a convenient way to massage it. We introduce the volume element which reduces to the Lorentz-invariant phase space in the LIF

$$\mathrm{d}\Pi_{\mathcal{Y},\mathcal{Z}} = (2\pi)^4\delta^{(4)}\left(\sum_{\kappa\in\mathcal{Y}} q^\mu_\kappa - \sum_{\kappa'\in\mathcal{Z}} q^\mu_{\kappa'}\right)\prod_{\kappa\in\mathcal{Z}}\left\{\frac{1}{2E(q)}\frac{\mathrm{d}^3\mathbf{q}_\kappa}{(2\pi)^3}\right\} . \quad (2.107)$$

Besides, we also introduce the Y-momentum volume element and the Y-energy product so that we can write $\mathrm{d}\Pi = \mathrm{d}\Pi_{\mathcal{Y},\mathcal{Z}}\mathrm{d}\mathcal{P}_\mathcal{Y}/\mathcal{E}_\mathcal{Y}$ with

$$\mathrm{d}\mathcal{P}_\mathcal{Y} = \prod_{\kappa\in\mathcal{Y}}\left\{\frac{\mathrm{d}^3\mathbf{q}_\kappa}{(2\pi)^3}\right\} \quad \text{and} \quad \mathcal{E}_\mathcal{Y} = \prod_{\kappa\in\mathcal{Y}}\left\{\frac{1}{2E_\kappa(q_\kappa)}\right\}. \tag{2.108}$$

Eventually we separate the symmetry factor into two parts $\mathcal{S}_Y$ and $\mathcal{S}_Z$ for the two sets respectively, so that $\mathcal{S} = \mathcal{S}_Y\mathcal{S}_Z$. Now we can introduce a generic notation for a quantity that represents a differential rate of interactions with a dimension of [length]$^{-3(\#Y-1)}\cdot$[time]$^{-1}$ and its *thermal* average as

$$\begin{aligned}\mathrm{d}\mathcal{R}_{\mathcal{Y};\mathcal{Z}} &\equiv \left(\prod_{\kappa\in\mathcal{Y}}\frac{1}{g_\kappa}\right)\frac{1}{\mathcal{S}_Z\mathcal{E}_\mathcal{Y}}W_{\mathcal{Y};\mathcal{Z}}\,\mathrm{d}\Pi_{\mathcal{Y},\mathcal{Z}} \\ &\text{and} \quad \langle\mathcal{R}_{\mathcal{Y};\mathcal{Z}}\rangle \equiv \left(\prod_{\kappa\in\mathcal{Y}}\frac{g_\kappa}{n_\kappa}\right)\int \mathrm{d}\mathcal{P}_\mathcal{Y}\,\mathrm{d}\mathcal{R}_{\mathcal{Y};\mathcal{Z}}\mathcal{F}_{\mathcal{Y};\mathcal{Z}}\,.\end{aligned} \tag{2.109}$$

The bracket notation represents the fact that the integral is weighted by the phase space distribution functions. Consequently, the 0^{th}-moment of the collision operator can be written explicitly, as a function of the thermally averaged collision rate, the number density of the species in Y, the chemical potentials and a combinatorial pre-factor as follows

$$\hat{\mathcal{C}}_{Y\leftrightarrow Z}(f_a) = \frac{\Delta\xi_a(Y,Z)}{\mathcal{S}_Y}\left[e^{\alpha_Y-\alpha_Z}-1\right]\left(\prod_{\kappa\in\mathcal{Y}}n_\kappa\right)\langle\mathcal{R}_{\mathcal{Y};\mathcal{Z}}\rangle\,. \tag{2.110}$$

We are now equipped to detail the expression of the zeroth moment of the collision operator in meaningful examples. In practice we limit ourselves to two classes of processes $2\leftrightarrow n$ and $1\leftrightarrow n$ with $n\geq 2$.

Interactions $2\leftrightarrow n$. In this case we write the process as $b+c\to Z$ where b and c can represent any species and Z is a set of unknown species. In that specific configuration we can start by writing the interaction rate as follows

$$\mathrm{d}\mathcal{R}_{bc\to Y} = \frac{1}{4E_c(q_c)E_b(q_b)}\frac{1}{g_cg_b}\frac{1}{\mathcal{S}_Z}W_{\{bc\};\mathcal{Z}}\,\mathrm{d}\Pi_{\{bc\},\mathcal{Z}}\,. \tag{2.111}$$

This expression is already very similar to the expression of a cross-section. Hence, the idea to write it in terms of $\sigma_{bc\to Z}$. In order to do so, let us make use of the Møller velocity $v^{bc}_{\text{Møl}} = [(\eta_{\mu\nu}q_b^\mu q_c^\nu)^2 - m_b^2m_c^2]^{1/2}/(E_b(q_b)E_c(q_c))$ between the two incoming particles, where $\eta_{\mu\nu}$ is the Minkowski metric. The differential cross-section is given, with our notations, as a function of the differential interaction rate $\mathrm{d}\mathcal{R}_{bc\to Z}$ and $v^{bc}_{\text{Møl}}$, by

$$\mathrm{d}\sigma_{bc\to Z} = \frac{1}{4E_b(q_b)E_c(q_c)v^{bc}_{\text{Møl}}}\frac{1}{g_bg_c}\frac{1}{\mathcal{S}_Z}W_{\{bc\};\mathcal{Z}}\mathrm{d}\Pi_{\{bc\},\mathcal{Z}} = \frac{1}{v^{bc}_{\text{Møl}}}\,\mathrm{d}\mathcal{R}_{\{bc\};\mathcal{Z}}\,. \tag{2.112}$$

The common notation is not to use the quantity denoted $\mathcal{R}_{bc\to Y}$ but rather to define the *thermal* average product of the cross-section and relative Møller velocity (referred to as the thermal cross-section for short in the following). In the end, the total zeroth moment collision operator is given by

$$\hat{\mathcal{C}}_{bc\leftrightarrow Y} = \frac{\Delta\xi_a(\{bc\},Z)}{\mathcal{S}_{\{bc\}}}\left\{\left\langle\sigma_{bc\to Y}v^{bc}_{\text{Møl}}\right\rangle = \left\langle\mathcal{R}_{\{bc\},\mathcal{Z}}\right\rangle\right\}n_bn_c\left[e^{\alpha_b+\alpha_c-\alpha_Z}-1\right]. \tag{2.113}$$

From this formula it is possible to quickly deduce the expression for any interaction $2 \leftrightarrow n$ with $n \geq 2$. Moreover note that if Z does not contain any particle of species a then $\Delta\xi_a(\{bc\}, Z)/\mathcal{S}_{\{bc\}} = 1$ whether or not b and c are actually both equal or not to a.

Interactions $1 \leftrightarrow n$. These interactions correspond to decay and inverse decay processes. Let us consider $y \leftrightarrow Z$. We can start, similarly to what has been done above, by writing the differential interaction rate

$$\mathrm{d}\mathcal{R}_{y\to Z} = \frac{1}{2E_y(q_y)}\frac{1}{g_y}\frac{1}{S_Z}W_{y;\mathcal{Z}}\,\mathrm{d}\Pi_{y,\mathcal{Z}} = \frac{m_y}{E_y(q_y)}\mathrm{d}\Gamma_{y\to\mathcal{Z}} \tag{2.114}$$

which appears to directly depend on $\Gamma_{y\to\mathcal{Z}}$, the usual decay rate. Then, it is possible to define a thermally averaged decay rate in a manner similar to the thermal cross-section and the zeroth moment collision operator becomes

$$\hat{\mathcal{C}}_{y\leftrightarrow Z} = \Delta\xi_a(\{y\}, Z)\left\{\langle\Gamma_{y\to Z}\rangle = \langle\mathcal{R}_{y;\mathcal{Z}}\rangle\right\} n_y\left[e^{\alpha_y-\alpha_Z}-1\right]. \tag{2.115}$$

Note that the thermal average decay rate can be evaluated completely as shown in BÉLANGER et al. (2018) when there are only two particles in the final state.

In summary, Bolzmann's equation can be integrated to give an equation on the number density of WIMPs. This equation therefore implies the integral of the collision operator, which depends on thermally averaged interaction rates and on the number density of species involved in these interactions.

2.4.2 Chemical decoupling : WIMPs (co-)annihilation equation

Now that these general considerations have been introduced let us resume the study of the zeroth moment of the Boltzmann equation for the set of WIMP species introduced above. However, we should have as many Boltzmann equations as species are involved, which can be an issue for a numerical solver. This section is therefore devoted to the introduction of a simple ordinary differential equation driving the total WIMPs number density.

Evolution of the total number density

Let us introduce the co-annihilation equation that describes the evolution of the total number density of all the WIMPs species,

$$n_\chi \equiv \sum_i n_i\,. \tag{2.116}$$

If we assume that they have all decayed today in the less massive species χ_0, which makes then the entire DM component of the Universe, the value of $n_0(t_0)$ and $n_\chi(t_0)$ are the same. Note that here we cannot describe co-annihilation with a species that does not end decaying to WIMPs, or that gets suppressed only after DM freezes out, nor can we describe relativistic exotic degrees of freedom. For simplicity, let us furthermore consider in the following that the only interactions that change the total number of WIMPs and have an impact on n_χ are the annihilations/creations of a pair of WIMPs. Because WIMPs are assumed to be non-relativistic when they chemically decouple, the collision operator can be written such that the total number of

DM particles satisfies

$$\begin{aligned}\frac{\mathrm{d}n_\chi}{\mathrm{d}t} + 3Hn_\chi = &\sum_{i,j}\sum_{Z} \langle\sigma_{ij\to Z} v_{\text{Møl}}\rangle^{\text{eq}} \frac{n_i^{\text{eq}} n_j^{\text{eq}}}{(n_\chi^{\text{eq}})^2}\left[(n_\chi^{\text{eq}})^2 - e^{\alpha_Z} n_\chi^2\right] \\ &+ \sum_{i,j}\sum_{y}(1+\delta_{\chi_i\chi_j})\langle\Gamma_{y\to ij}\rangle^{\text{eq}} \frac{n_y^{\text{eq}}}{(n_\chi^{\text{eq}})^2}\left[(n_\chi^{\text{eq}})^2 e^{-\alpha_y} - n_\chi^2\right]\end{aligned} \tag{2.117}$$

where the sum over Z spans all the possible set of outgoing particles in $\chi_i + \chi_j \to Z$ and the sum on y runs over all mediators decaying into $\chi_i + \chi_j$. The prefactor $\delta_{\chi_i\chi_j}$ is one if $\chi_i = \chi_j$ and zero otherwise. We introduced n_i^{eq}, the equilibrium number densities of the WIMP species at zero chemical potential. Besides, the equilibrium values of the cross-section and the decay rates are respectively given in Eq. (B.48) and Eq. (B.54) and this equation is more generally proven in App. B.2.

Interaction mediators can be either SM particles or exotic particles from a dark sector. One issue is that these particles can be produced (*e.g.* by the annihilation of DM) and be part of the initial or final states of the interactions. Then, they either have to be in thermodynamic equilibrium, so that their pseudo-potential is zero (which is the case when they are SM particles) or it is necessary to solve an equation for their pseudo-chemical potential – which implies the resolution of a coupled system of equations. In the following, we always rely on the assumption that all such particles involved are in thermodynamic equilibrium with the thermal bath (thanks to frequent interactions with light SM particles for instance) when it is possible. Two options can be considered.

- The mediators have a mass greater than $2m_0$. As chemical decoupling is expected to occur at $T \sim m_0/20$ these mediators have an exponentially suppressed number density and their decay into WIMPs is sub-dominant with respect to light SM particle annihilation (as long as the coupling SM/mediator is larger or roughly similar to the coupling WIMPs/mediator). We could worry that if the mediator is too massive its chemical equilibrium with the rest of the thermal bath should, however, be broken. Nevertheless, in that configuration, such mediators cannot be produced by DM annihilation (plasma not energetic enough) and similarly to the decay, their number density is too low to produce DM via $2 \leftrightarrow 2$ interactions efficiently. Consequently, they cannot be amongst the final/initial states of the relevant DM annihilation/creation processes. In conclusion, for mediators with mass greater than $2m_0$ even if their chemical equilibrium with the primordial plasma is lost, Eq. (2.117) is not impacted.
- The mediators have a mass lower than $2m_0$. These are more likely to be still at chemical equilibrium with the bath, which we thus assume, and they are not massive enough to decay into WIMPs. Therefore the decay term can still be neglected if the aforementioned condition, in brackets, on the coupling is satisfied and the pseudo chemical potential of the mediators may be set to zero. In that case, however, we need to be careful because those mediators, if they are not part of the SM, can be a part of DM if they do not have time to decay into light SM particles (and they would not be in chemical equilibrium then).

Henceforth, under the simplifying hypothesis of thermodynamical equilibrium $\alpha_Y = 0$ and $\alpha_y = 0$ in Eq. (2.117) and following BINÉTRUY et al. (1984), GRIEST et al.

(1991), and EDSJO et al. (1997) we can rewrite the previous equation with the definition of the effective thermally averaged annihilation cross-section and decay rates as

$$\begin{aligned}\langle\sigma v_{\text{Møl}}\rangle_{\text{eff}}^{\text{eq}} &\equiv \sum_{i,j}\sum_{Z}\frac{n_i^{\text{eq}}n_j^{\text{eq}}}{(n_\chi^{\text{eq}})^2}\langle\sigma_{ij\to Z}\rangle^{\text{eq}}\\ \frac{1}{n_\chi^{\text{eq}}}\langle\Gamma\rangle_{\text{eff}}^{\text{eq}} &\equiv \sum_{i,j}\sum_{y}(1+\delta_{\chi_i\chi_j})\langle\Gamma_{y\to ij}\rangle^{\text{eq}}\frac{n_y^{\text{eq}}}{(n_\chi^{\text{eq}})^2}\end{aligned} \tag{2.118}$$

even though the latter is usually negligible in most scenarios – as decay terms are only important here when DM is mainly produced by the decay of a heavy particle that is not in thermal equilibrium with the plasma. Then the total DM number density is driven by the equation

$$\frac{\mathrm{d}n_\chi}{\mathrm{d}t}+3Hn_\chi=\left\{\langle\sigma v_{\text{Møl}}\rangle_{\text{eff}}^{\text{eq}}+\frac{\langle\Gamma\rangle_{\text{eff}}^{\text{eq}}}{n_\chi^{\text{eq}}}\right\}\left[(n_\chi^{\text{eq}})^2-n_\chi^2\right] \tag{2.119}$$

first derived in LEE et al. (1977) with no co-annihilation and no decay processes. Under this form it is easier to highlight the competition between the Hubble rate H and the collisional rate $\Gamma_{\text{ann}} \equiv n_\chi(\langle\sigma v_{\text{Møl}}\rangle_{\text{eff}}^{\text{eq}} + \langle\Gamma\rangle_{\text{eff}}^{\text{eq}}/n_\chi^{\text{eq}})$ that was discussed in Sect. 2.3.3. Indeed, when Γ_{ann} dominates, the equation drives the number density towards the equilibrium value. However, when the Hubble rate dominates, we recover the equation for the dilution of the number density of matter in the expanding Universe.

Majorana vs. Dirac fermions

So far we have not introduced a difference between DM particles that are Majorana or Dirac fermions. As a matter of fact, there is one but it is subtle to include in that framework. Indeed, consider that DM particles are made of the minimal possible amount of Dirac particles. Then, we necessarily have two species, χ_0 and its antiparticle $\chi_1 = \overline{\chi}_0$. If we assume a simple coupling to SM fermions ψ in order to use the definition of Eq. (2.118) we need to sum over four configurations $(i = 0/1, j = 0/1)$. For Dirac fermions, cross-sections where $i = j$ are not permitted (annihilation processes involve the particle and its antiparticle). It yields the sum over two terms that are actually identical (as the configuration where i represents χ and j represents $\overline{\chi}$ is exactly similar to the reversed one) so that

$$\langle\sigma v_{\text{Møl}}\rangle_{\text{eff,Dirac}}^{\text{eq}}=\frac{1}{4}\left[\left\langle\sigma_{\chi\overline{\chi}\to\psi\overline{\psi}}v_{\text{Møl}}\right\rangle^{\text{eq}}+\left\langle\sigma_{\overline{\chi}\chi\to\psi\overline{\psi}}v_{\text{Møl}}\right\rangle^{\text{eq}}\right]=\frac{1}{2}\left\langle\sigma_{\chi\overline{\chi}\to\psi\overline{\psi}}v_{\text{Møl}}\right\rangle^{\text{eq}} \tag{2.120}$$

The factor $1/4$ in front comes from the fact that $n_{\chi_0}^{\text{eq}}n_{\overline{\chi}_0}^{\text{eq}}/(n_\chi^{\text{eq}})^2 = 1/4$ since $n_\chi^{\text{eq}} = n_{\chi_0}^{\text{eq}} + n_{\overline{\chi}_0}^{\text{eq}}$ and we assume symmetric DM, so that the two terms that are added are equal. For a minimal content of Majorana particles there is only one species and for a similar coupling to a single SM species it yields

$$\langle\sigma v_{\text{Møl}}\rangle_{\text{eff,Majorana}}^{\text{eq}}=\left\langle\sigma_{\chi\chi\to\psi\overline{\psi}}v_{\text{Møl}}\right\rangle^{\text{eq}}=2\,\langle\sigma v_{\text{Møl}}\rangle_{\text{eff,Dirac}}^{\text{eq}}\,. \tag{2.121}$$

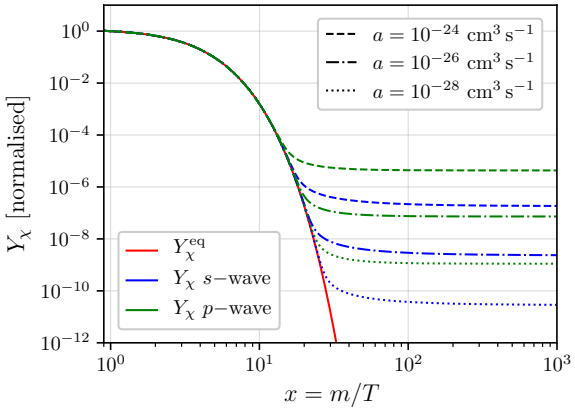

Figure 2.4 – Evolution of the comoving number density Y_χ with the parameter $x = m_0/T$ and a mass $m_0 = 100$ GeV at chemical decoupling. In red is represented the equilibrium solution. In blue is the solution for s-wave cross-section $\langle \sigma v_{\rm Møl} \rangle = a$ with a taking three different values. In green the case of a p-wave cross-section with $\langle \sigma v_{\rm Møl} \rangle = a/x$. The p-wave cross-section being suppressed by a factor of x, the decoupling occurs before for the green curves and yields to a higher residual quantity of DM.

Resolution of the annihilation equation

The goal is now to review the method that, in practice, is used to solve Eq. (2.119). Moreover we also need to make the link between the final number density evaluated and the observed abundance of DM that can be used to put constraints on the particle model used to compute the cross-sections. A common parametrisation is to use a *pseudo*-comoving number density, usually written as the ratio of the number density over the total entropy density. More precisely we denote

$$Y_\chi \equiv \frac{n_\chi}{s} \,. \tag{2.122}$$

This definition is convenient since when the number of DM particles in the Universe becomes almost a constant $n_\chi \propto a^{-3}$ by dilution in the expanding Universe after chemical decoupling. Therefore, as when there is no production of entropy, $s \propto a^{-3}$ as well, the ratio becomes almost a constant. Massaging Eq. (2.119), using the expressions of s and H with the temperature and the definition of $g_\star$ of Eq. (2.93) the differential equation on Y_χ is then

$$\frac{{\rm d}Y_\chi}{{\rm d}x} = \sqrt{\frac{\pi}{45 G_{\rm N}}} \frac{m_0}{x^2} g_\star^{1/2}(T) \, \langle \sigma v_{\rm Møl} \rangle_{\rm eff}^{\rm eq} \left[\left(Y_\chi^{\rm eq} \right)^2 - Y_\chi^2 \right] \,. \tag{2.123}$$

From now on we forget about a possible DM production from the decay of a massive particle and therefore we do not take into account the decay term of Eq. (2.119). The equilibrium value of the comoving number density is given by the ratio of the equilibrium number density to the entropy density

$$Y_\chi^{\rm eq} = \frac{n_\chi^{\rm eq}}{s} = \frac{45}{4\pi^4 h_{\rm eff}(T)} \sum_i g_i \left(\frac{m_i}{T} \right)^2 K_2 \left(\frac{m_i}{T} \right) \,. \tag{2.124}$$

Finding a solution to the ODE Eq. (2.123) is not trivial and requires a numerical evaluation. However it is still possible to estimate the value of the temperature (or equivalently x) at the moment of freeze-out. For that, we search when Y_χ becomes

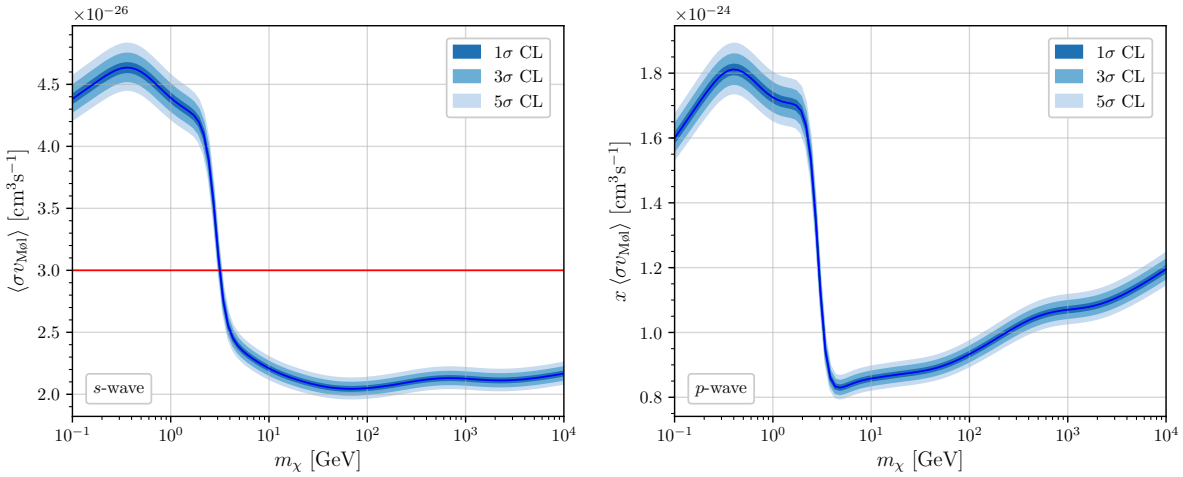

Figure 2.5 – Constraints on the cross-section by the comparison to the abundance measured in Planck18 with the different confidence level. For simplicity, only the uncertainty on the observed abundance is taken into account – not the uncertainties on ρ_c and T_0. **Left panel:** Case of a s-wave cross-section, i.e. $\langle\sigma v_{\text{Møl}}\rangle_{\text{eff}}^{\text{eq}} = \text{cst}$. The conventional value is represented in red. **Right panel:** Case of a p-wave cross-section, i.e. $\langle\sigma v_{\text{Møl}}\rangle = \text{cst.}/x$. Here we represented the value of the constant by multiplying the thermally averaged cross-section by x on the y-axis.

sufficiently different from Y_χ^{eq}. Following Gondolo et al. (1991) we define the freeze-out temperature as $Y_\chi(x_f) = (\delta+1)Y_\chi^{\text{eq}}(x_f)$ with δ a fixed parameter that can be approximated as $\delta = 1.5$. This leads to the implicit equation

$$\frac{\sqrt{45\pi}m_0}{4\pi^4\sqrt{G_{\text{N}}}}\frac{K_2(x_f)}{h_{\text{eff}}(T_f)}g_\star^{1/2}(T_f)\,\langle\sigma v_{\text{Møl}}\rangle_{\text{eff}}^{\text{eq}}\,\delta(\delta+2) = \frac{K_1(x_f)}{K_2(x_f)} - \frac{1}{x_f}\frac{\mathrm{d}\ln h_{\text{eff}}(T)}{\mathrm{d}\ln T}\bigg|_{T=T_f} \tag{2.125}$$

which is roughly equivalent to (but more precise) asking $\Gamma_{\text{ann}} = H$. In practice the temperature of chemical decoupling does not vary much between different models and unless the couplings are extremely low – in which case we are closer to a freeze-in scenario – or extremely large – in which case the number density of DM is too much depleted to account for the observed abundance today. Typically it is given by $x_{\text{cd}} = m_0/T_{\text{cd}} \sim 20$.

In Fig. 2.4 we show the solution of Eq. (2.123) obtained with a implicit Euler solver. We assume the presence of only one Majorana DM species of mass 100 GeV and the thermal cross-section $\langle\sigma v_{\text{Møl}}\rangle_{\text{eff}}^{\text{eq}} = \sum_n a_n x^{-n}$. This partial wave decomposition has already been mentioned in Sect. 2.3.3. More particularly we recall that a_0 is called the s-wave term and a_1 the p-wave term. In the figure we represent the solution for a pure s-wave term and a pure p-wave term for different values of $a = a_0 = a_1$. Because at temperatures of interest $x \gg 1$ for a same value of a the s-wave scenario gives a larger thermally averaged cross-section and therefore a lower final DM density subsequent to a later decoupling. We have used typical values for a in particular 10^{-26} cm^3·s^{-1} ($\sim 10^{-1}$ pb) and 10^{-24} cm^3·s^{-1} ($\sim 10^{1}$ pb) , which roughly correspond to what is expected to obtain the observed abundance today. See the following discussion about Fig. 2.5. Moreover we recover the previous statement, that the chemical decoupling temperature satisfies $x_{\text{cd}} \sim 20 - 25$.

The total abundance today

Eventually, the most important quantity is the value of Y_χ today that we denote $Y_\chi(t_0) = Y_\chi(x_0)$. In theory we could obtain it by solving Eq. (2.123) up to now. However, because we know that after chemical decoupling $Y_\chi^{\rm eq}$ is negligible in comparison to Y_χ, it is possible to simplify the equations. In practice we define a truncation temperature as $Y_\chi(x_t) = 10^3 Y_\chi^{\rm eq}(x_t)$. After that point we approximate the evolution equation as

$$\frac{{\rm d}Y_\chi}{{\rm d}x} = -\sqrt{\frac{\pi}{45 G_{\rm N}}} \frac{m_0}{x^2} g_\star^{1/2}(T) \, \langle \sigma v_{\rm Møl} \rangle_{\rm eff}^{\rm eq} \, Y_\chi^2 \tag{2.126}$$

that can be solved analytically. A separation of variables yields

$$Y_\chi(t_0) = Y_\chi(x_t) \left\{ 1 + Y_\chi(x_t) \sqrt{\frac{\pi}{45 G_{\rm N}}} \int_{x_t}^{x_0} \left(\frac{g_\star^{1/2}(T)}{x^2} \, \langle \sigma v_{\rm Møl} \rangle_{\rm eff}^{\rm eq} \right) {\rm d}x \right\}^{-1} \tag{2.127}$$

However, the evaluation of $\langle \sigma v_{\rm Møl} \rangle_{\rm eff}^{\rm eq}$ up to today is not possible numerically a priori and requires to know the leading orders in the partial wave expansion, the s-wave term and the p-wave term. The latter cannot always be efficiently derived from a given particle model, but this is not an issue since, if the s-wave term is zero, we can simply consider $Y_\chi^0 \simeq Y_\chi(x_t)$ in a good approximation. The theoretical abundance of Majorana (C)DM particles is then

$$\begin{aligned} \Omega_{{\rm c},0}^{\rm th} h^2 &= \frac{m_0 n_\chi(t_0)}{\rho_c} h^2 = \frac{m_0 s(t_0) Y_\chi(t_0)}{\rho_c} h^2 \\ &= \frac{16\pi^3 Y_\chi(t_0)}{135} h_{\rm eff}(T_0) \left(\frac{T_0}{\rm GeV} \right)^3 \left(\frac{m_0}{\rm GeV} \right) \left(\frac{\rm GeV}{m_{\rm pl}} \right)^2 \left(\frac{\rm Mpc}{\rm km} \right)^2 \left(\frac{\rm GeV}{100\,{\rm s}^{-1}} \right)^2 \\ &= 2.764 \times 10^8 \times Y_\chi(t_0) \left(\frac{m_0}{\rm GeV} \right) \end{aligned} \tag{2.128}$$

where we have used for the last equality $T_0 = 2.72548$ K (FIXSEN 2009) and $h_{\rm eff}(T_0) = 3.94$ (assuming massless neutrinos). Comparing the theoretical value to the observed one, $\Omega_{{\rm c},0} h^2 = 0.1200 \pm 0.0012$ from Planck18, is useful to put constraints on the underlying particle physics model. In Fig. 2.5 we considered the s-wave and p-wave scenarios, that is $\langle \sigma v_{\rm Møl} \rangle_{\rm eff}^{\rm eq} = \sum_n a_n x^n$ with $a_0 \neq 0$ and $a_0 = 0$ respectively on the left and right panel. Interestingly, when $m_\chi > 10$ GeV the value of a_0 or a_1 that gives the correct abundance is approximately a constant of the mass. In practice the conventional adopted value to make quick comparisons is, for the s-wave case,

$$\langle \sigma v_{\rm Møl} \rangle_{\rm eff}^{\rm eq} \sim 3 \times 10^{-26} \, {\rm cm}^3 \, {\rm s}^{-1} \, , \tag{2.129}$$

given in red on the figure, even though the real curve is slightly above or below depending on the dark matter mass. This result is in agreement with STEIGMAN et al. (2012). Note that we truncated the range in mass at 10 TeV since higher masses – over $\mathcal{O}(100)$ TeV – would break the unitarity of the underlying particle physics theory (GRIEST et al. 1990).

2.4.3 Kinetic decoupling

From the Boltzmann to the Fokker-Planck equation

The thermal or kinetic equilibrium is mostly maintained through elastic scattering processes $\chi(q_1) + \psi(q_2) \leftrightarrow \chi(q_3) + \psi(q_4)$ where χ is the DM particle and ψ a particle

in the relativistic bath such as light SM fermions. The aim is therefore to derive an equation for the DM temperature T_χ to evaluate when it departs from the bath temperature T. As derived in App. B.3.3 the temperature of a non-relativistic species with an isotropic distribution is given by

$$T_\chi = \frac{m_\chi}{6}\left\langle v_{\rm rel}^2\right\rangle_{\rm NR} = \frac{g_\chi}{m_\chi n_\chi}\int q^2 f_\chi(x^\mu, q^i)\frac{{\rm d}^3\mathbf{q}}{(2\pi)^3}\,. \tag{2.130}$$

Therefore integrating the second moment of the Boltzmann equation (with $q^2 = \delta_{ij}q^i q^j$) should give an equation for T_χ. More precisely one can check that

$$g_\chi\int L_m(f_\chi)\frac{q^2}{m_\chi}\frac{{\rm d}^3\mathbf{q}}{(2\pi)^3} = g_\chi\int L_m(f_\chi)\frac{p^2}{m_\chi}\frac{{\rm d}^3\mathbf{p}}{(2\pi)^3} = 3m_\chi n_\chi\left[\frac{\partial T_\chi}{\partial t} + 2HT_\chi\right]\,. \tag{2.131}$$

where p is the canonical momentum in FLRW and q the canonical momentum in the LIF. Therefore, the only missing part is the same integral but on the collision operator. This turns out to require several approximations in order to obtain an analytical formulation. According to Bertschinger (2006) and Binder et al. (2016) the collision-operator for the elastic scattering can be written

$$C(f_\chi)(q_1^j) = \frac{E_\chi(q_1^j)}{2}\delta_{ik}\frac{\partial}{\partial q_1^i}\left[\gamma(T,q_1^j)\left\{E_\chi(q_1^j)T\frac{\partial f_\chi}{\partial q_1^k} + q_1^j f_\chi(q_1^j)\left(1+\varepsilon_\chi f_\chi(q_1^j)\right)\right\}\right] \tag{2.132}$$

This results follows from an expansion at small momentum transferred $\delta q^j = q_3^j - q_1^j$, as expressed in terms of the initial and final momenta of the DM particle, q_1 and q_3, respectively. Moreover, $\gamma(T, q_1^j)$ corresponds to the momentum relaxation rate. Assuming that DM is non-relativistic so that DM particles have a negligible velocity in the plasma frame, it only depends on the temperature and can be written

$$\gamma(T) = \frac{1}{3m_\chi^3\pi^2 T}\sum_\psi g_\psi\int {\rm d}\omega\frac{e^{\omega/T}}{\left(e^{\omega/T}-\epsilon_\psi\right)^2}\sigma_{\rm T}^{\chi\psi}(s)\overline{p}_{\chi\psi}^4(s)s \tag{2.133}$$

where $\omega = E_\psi$ is the scattered particle energy in the center-of-mass frame, such that $s \simeq m_\chi^2 + 2\omega m_\chi + m_\psi^2$. Moreover

$$\overline{p}_{\chi\psi}^2(s) = \frac{1}{4s}\left[s-(m_\chi+m_\psi)^2\right]\left[s-(m_\chi-m_\psi)^2\right] \tag{2.134}$$

is the 3-momentum norm of the incoming particles in the the centre-of-mass frame and $\epsilon_\psi = \epsilon_\chi = -1$ when dealing with fermionic particles. Besides, we introduced the transfer cross-section $\sigma_{\rm T}^{\chi\psi}$,

$$\begin{aligned}\sigma_{\rm T}^{\chi\psi} &\equiv \int(1-\cos\overline{\theta})\frac{{\rm d}\sigma_{\chi\psi\to\chi\psi}}{{\rm d}\overline{\Omega}}{\rm d}\overline{\Omega}\\ &= \frac{1}{128\pi s\overline{p}_{\chi\psi}^4(s)}\frac{1}{g_\chi g_\psi}\int {\rm d}t(-t)\left(\sum_{\rm spins}|\mathcal{M}_{\chi\psi\to\chi\psi}|^2\right)\end{aligned} \tag{2.135}$$

where $\overline{\theta}$ is the angle between q_1^j and q_3^j in the centre-of-mass frame and t in this integral does not refer to time but to the Mandelstam variable $t = (q_1^\mu - q_3^\mu)^2$. As a matter of fact, the transfer cross-section corresponds to a weighted version of the usual cross-section where the collisions transferring more momentum are favoured ($\cos\theta \sim -1$ corresponds to particles leaving the collision with the opposite direction

they initially have). The collision term has the form of a Fokker-Planck operator and, under the assumption of non-relativistic DM and using isotropy, it can be written in term of the momentum norm q

$$C(f_\chi)(q) = \gamma(T)\frac{1}{2}\left[m_\chi T\frac{\partial^2}{\partial q^2} + \left(q + \frac{2m_\chi T}{q}\right)\frac{\partial}{\partial q} + 3\right] f_\chi \,. \tag{2.136}$$

The second moment ot the collision operator is then

$$g_\chi \int C(f_\chi)\frac{q^2}{m_\chi}\frac{\mathrm{d}^3\mathbf{q}}{(2\pi)^3} = 3m_\chi n_\chi \gamma(T)(T - T_\chi) \tag{2.137}$$

which can be combined with Eq. (2.131) to get the equation for the DM temperature

$$\frac{\mathrm{d}T_\chi}{\mathrm{d}t} + 2HT_\chi = \gamma(T)(T - T_\chi)\,. \tag{2.138}$$

Here, as in the annihilation equation, there is competition between the Hubble rate H and the momentum relaxation rate γ. In the limit $\gamma \gg H$ the equation admits the simple solution $T_\chi = T$ which means thermal equilibrium is reached. On the contrary, when $\gamma \ll H$ the solution is $T_\chi \propto a^{-2}$ that is the expected behaviour for the temperature of a massive species.

The temperature evolution

Similarly to the number density of DM particles, which is more efficiently tracked through its comoving expression, it is convenient to express an effective pseudo-temperature that would tend to a constant after kinetic decoupling. Since we expect $T_\chi \propto a^{-2}$ asymptotically after kinetic decoupling, we can again use the entropy density as a weighting factor, to a power giving the correct asymptotic scaling in a. An additional factor of m_χ allows use to define the following dimensionless pseudo-temperature (BRINGMANN et al. 2007). Let us introduce,

$$y_\chi \equiv \frac{m_\chi T_\chi}{s^{2/3}} \tag{2.139}$$

which depends on the mass of the DM particle, and the entropy density. Massaging Eq. (2.138) with the expression of the entropy density in terms of effective degree of freedoms allows to rewrite it under the form

$$\frac{\mathrm{d}\ln y_\chi}{\mathrm{d}\ln x} = -\frac{\sqrt{g_{\mathrm{eff}}(T)}g_\star^{1/2}(T)}{h_{\mathrm{eff}}(T)}\frac{\gamma(T)}{H}\left(1 - \frac{y_\chi^{\mathrm{eq}}}{y_\chi}\right)\,. \tag{2.140}$$

The structure of this equation suggests to numerically solve for $\ln y_\chi$, which we do with an implicit Euler solver once again. The equilibrium value y_χ^{eq} is simply obtained for $T_\chi = T \propto a^{-1}$ when thermal equilibrium is maintained. After decoupling y_χ reaches a plateau at the value y_χ^∞. The kinetic decoupling temperature is thus defined at the intersection of the plateau with the equilibrium value, y_χ^{eq},

$$T_{\mathrm{kd}} \equiv \frac{y_\chi^\infty}{m_\chi}s^{2/3}(T_{\mathrm{kd}})\,. \tag{2.141}$$

In Fig. 2.6 is shown an example of solution for a DM particle of mass $m_\chi = 100$ GeV and pseudo-scalar and scalar mediated tree-level interactions. The mass of the

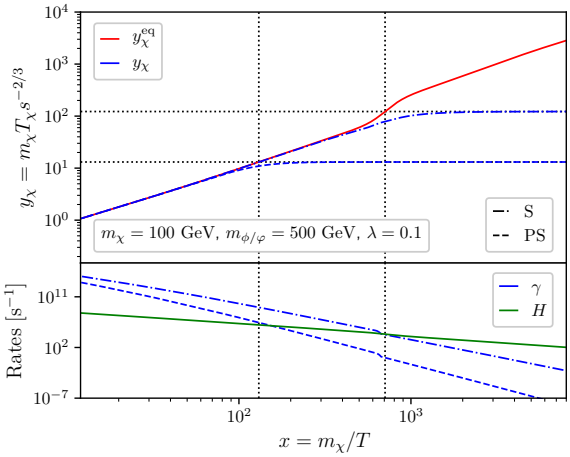

Figure 2.6 – Upper panel: Evolution of the comoving temperature (blue) with the ratio $x = m_\chi/T$ for a single Majorana DM species of mass $m_\chi = 100$ GeV in two scenarios (dash-dotted and dashed) referred as scalar and pseudo-scalar and detailed in Sect. 2.5. The particle mediator has a mass of 500 GeV and couples to SM and DM particles with the same coupling constant $\lambda = 0.1$. The red curve corresponds to the equilibrium value. **Lower panel**: Evolution of the corresponding scattering (blue) and Hubble (green) rate.

mediating particle is 500 GeV and we set a universal coupling constant $\lambda = 0.1$ as defined in the following section. In the upper panels, we represented the evolution of the comoving temperature with $x = m_\chi/T$ in blue and the equilibrium value in solid red. In the lower panel, we show the evolution of $\gamma(T)$ and the Hubble rate H. When the interaction rate dominates, equilibrium is maintained and $y_\chi = y_\chi^{\rm eq}$. On the contrary, when γ drops below H the equilibrium is lost and the plateau is quickly reached. The dash-dotted lines report the position of the asymptotes and the subsequent temperature of kinetic decoupling. We observe a bump on the red curve occurring at $x \simeq 7 \times 10^2$ (roughly where the decoupling of the scalar-mediated interaction happens). Translated in terms of temperatures for $m_\chi = 100$ GeV this yields $T \simeq 150$ MeV which is the temperature of the QCD phase transition. By tremendously decreasing the value of s_χ the transition changes the growing rate of y_χ since one can show that $y_\chi \propto h_{\rm eff} x$. The difference between the pseudo-scalar and scalar mediated processes mainly comes from their different behaviour when the incoming particles have a small relative velocity. This difference is similar and related to the difference between the s-wave and p-wave terms obtained for chemical decoupling. Here the pseudo-scalar interaction is velocity suppressed and therefore equilibrium is lost faster than for the scalar case where the interaction is not. More details on these velocity effects are given in the following section.

2.5 Consistent determination of the halo minimal mass

In the previous sections, we have detailed the evaluation of the chemical and kinetic decoupling for WIMPs. In this final section, we evaluate the subsequent minimal cosmological mass that halo may have. This quantity is directly related to the temperature of kinetic decoupling via two processes called free-streaming and acoustic damping, which are detailed in Sect. 3.6. Moreover, the minimal mass of collapsing DM structures directly impacts their population in the MW such as their total number. This is more particularly detailed in Chapter 4 when introducing the SL17

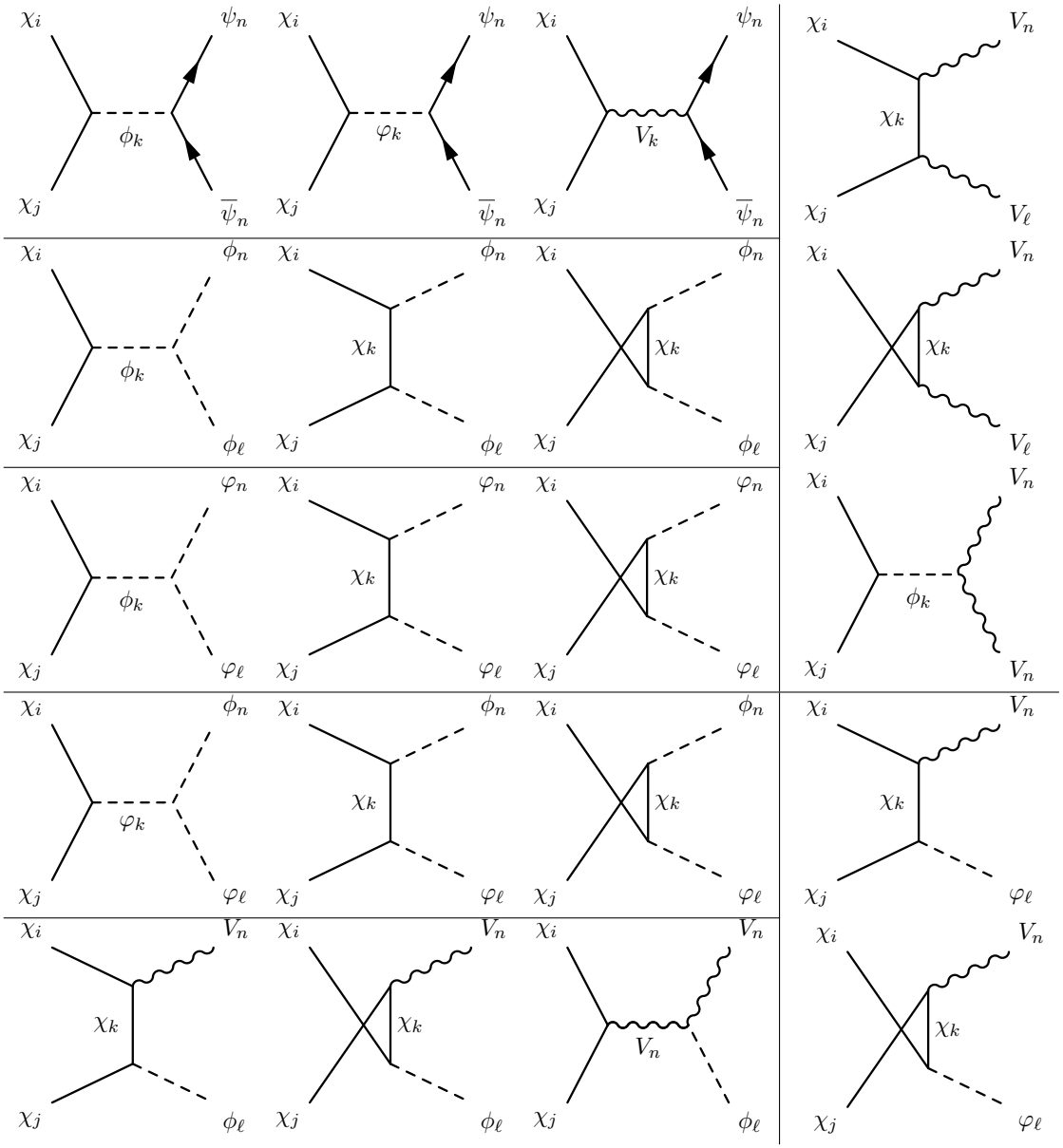

Table 2.1 – All the tree-level diagrams involved in DM annihilation and creation. Every box corresponds to a different final product. Note that the u-channel diagrams are only involved when the incoming or/and the outgoing particles are identical.

model. In this section we assume, for now, that given $T_{\rm kd}$ it is possible to evaluate the minimal cosmological mass $M_{\rm min}$.

2.5.1 Lagrangian of the WIMP simplified model

We consider a model of fermionic DM, Majorana or Dirac particles denoted χ_i interacting with standard model fermions ψ_i through scalar, pseudo-scalar, vector and axial-vector interactions. We denote by ϕ_k, φ_k and V_k^μ all the possible neutral scalar, pseudo-scalar, and vector mediators. A generic CP-conserving Lagrangian density for

the interactions between the SM and the DM particles is then

$$\begin{aligned}\mathcal{L}_{\rm int}^{\chi,\rm SM} =& -\overline{\chi}_i\delta_\chi(A_k^{ij}\phi_k + i\gamma^5 B_k^{ij}\varphi_k)\chi_j - \overline{\psi}_i(\mathcal{A}_k^i\phi_k + i\gamma^5\mathcal{B}_k^i\varphi_k)\psi_i \\ &+ \overline{\chi}_i\gamma^\mu\delta_\chi(X_k^{ij} - Y_k^{ij}\gamma^5)V_k^\mu\chi_j + \overline{\psi}_i\gamma^\mu\left(\mathcal{X}_k^i - \mathcal{Y}_k^i\gamma^5\right)V_k^\mu\psi_i\end{aligned} \tag{2.142}$$

where the summation over k, i, j is implicit. The factor $\delta_\chi = 1/2$ (resp 1) for Majorana (resp. Dirac) DM particles is set in order to conserve similar Feynman rules in both cases despite the different combinatorial factors arising in the evaluation of the S-matrix. For Majorana DM particles $\overline{\chi} = \chi$ and the coupling via the vector interaction is not permitted, hence $X_k^{ij} = 0$ in that case. The mediating particles can also interact between themselves with

$$\mathcal{L}_{\rm int}^{\phi\varphi\rm V} = -\frac{w}{\mathcal{S}_{ijk}}G_{ijk}\phi_i\phi_j\phi_k - \frac{w}{\mathcal{S}_{jk}}H_{ijk}\phi_i\varphi_j\varphi_k - wI_{ij}\phi_i V_j^\mu V_{j,\mu}\,. \tag{2.143}$$

The symmetry factors are $\mathcal{S}_{ijk} = n_\phi!$ (resp. $\mathcal{S}_{jk} = n_\varphi!$) where n_ϕ (resp. n_φ) is the number of identical fields ϕ (resp. φ) in the first and second terms. The factor w is a normalisation factor with an energy dimension. Such terms can arise from Higgs-like mechanisms. Indeed with the Higgs doublet of the SM, $H = (h^+, h^0)^T$, after the spontaneous breaking of the $SU(2)_L$ symmetry, the field acquires a vacuum expectation value (VEV) $\langle H\rangle = (0, w/\sqrt{2})$. Then the quadratic term of the Higgs potential, namely $\lambda(H^\dagger H)^2$, produces $\lambda w h^3$. The term $(D^\mu H)^\dagger(D_\mu H)$ gives $\lambda w h Z^\mu Z_\mu$. In addition, ϕ^4 or φ^4 interactions can also be produced in the same way and could be added for completeness. In this work they are omitted for simplicity. As pointed out in KAHLHOEFER et al. (2016) this theory is, a priori, non-renormalizable. In particular, the axial-vector interaction violates unitarity at large energy. One solution would be to consider the V particle as the gauge boson of a new symmetry $U'(1)$. However, this brings further complications in the model to provide a mass to V and it is not consistently taken into account in this analysis. Here we also neglect the couplings of the vector mediator to the other gauge bosons through kinetic mixing. Therefore, we should keep in mind that if the mass of one of the vector mediators is sufficiently close to the mass of the Z boson $m_Z \simeq 91$ GeV electroweak constraints may be spoiled through an enhanced mixing (BABU et al. 1997).

With N_χ DM particles, N_ϕ, N_φ, N_V mediators and N_ψ SM particles/antiparticle couples, the Lagrangian density $\mathcal{L}_{\rm int}^{\chi,\rm SM}$ contains $(N_\chi^2 + N_\psi)(N_\phi + N_\varphi + 2N_V)$ free couplings. The total set of free parameters also contains the $N_\phi + N_\varphi + N_V$ free masses and the couplings of $\mathcal{L}_{\rm int}^{\phi\varphi\rm V}$. For simplicity therefore we can focus on special cases. One can assign values separately for the couplings between the DM particle χ and the interaction mediators on the one hand, and for the couplings between the SM fermions and the same mediators on the other hand. For the latter, all couplings would be fixed if we considered SM mediators, a possibility that we discard here. However, we may still envisage simplifying assumptions. We can consider that couplings to the scalar mediation sector is of Yukawa type, with $A \sim B \sim \lambda_\psi \propto m_\psi$ to respect minimal flavour violation principles (D'AMBROSIO et al. 2002) – we can also allow for different normalisation factors between up-type and down-type quarks, or between quarks and leptons (like in supersymmetric models). More simply, we can assign universal couplings to all SM fermions (also for vector and axial interactions), and other universal couplings to DM particles.

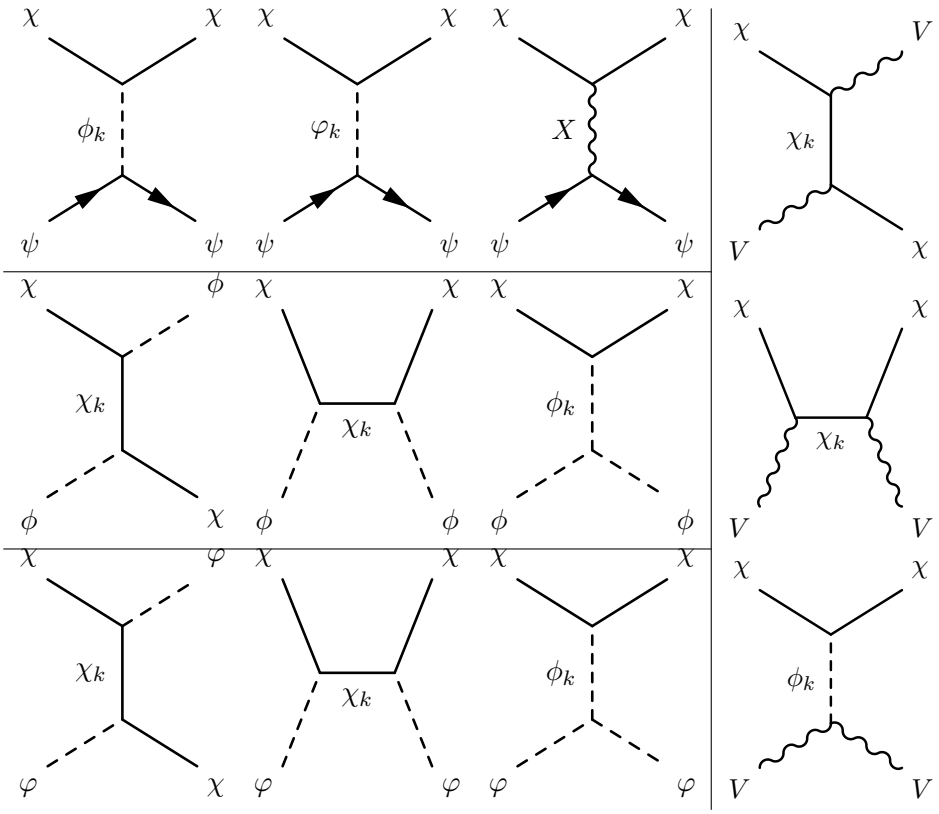

Table 2.2 – Diagrams involved in the scattering of DM particles on the thermal bath, which do not change the number of particles. Every box corresponds to a different particle with which the DM particle scatters. Note that DM can also scatter off the SM antifermions, which is not represented here to gain space.

2.5.2 Cross-sections and velocity dependencies

After the derivation of the master equations of chemical and kinetic decouplings, one needs to determine both the cross-section for annihilation processes and the transfer cross-section for elastic scatterings. We recall that for a generic interaction $i + j \to k + \ell$ they are respectively given by

$$\begin{aligned} \sigma_{ij\to k\ell} &= \frac{1}{64\pi s\overline{p}_{ij}^2}\frac{1}{g_i g_j S_{k\ell}}\int \mathrm{d}t \left(\sum_{\text{spins}} |\mathcal{M}_{ij\to k\ell}|^2\right) \\ \sigma_{\mathrm{T}}^{ij} &= \frac{1}{128\pi s\overline{p}_{ij}^4}\frac{1}{g_i g_j S_{ij}}\int \mathrm{d}t(-t) \left(\sum_{\text{spins}} |\mathcal{M}_{ij\to ij}|^2\right) \end{aligned} \tag{2.144}$$

where $\overline{p}_{ij}(s)$ is the centre of mass momentum given by $\overline{p}_{ij}(s) = (s - (m_i - m_j)^2)(s - (m_i + m_j)^2)/(4s)$. The factor S_{ij} is 2 if the two particles are the same and 1 otherwise. We restrict the analysis to the tree-level diagrams. All the relevant processes for chemical decoupling are represented in Tab. (2.1). All the relevant processes for kinetic decoupling are represented in Tab. (2.2). Note that here we do not take into account the possible scatterings on the mediators via the exchange of a DM particle in the t-channel or s-channel. Indeed we assume that mediators are only present in the thermal bath if lighter than the DM particles, in which case these diagrams are suppressed by the mass of the DM particles in comparison to the scattering on SM fermions. Moreover, the DM particles can also scatter on the anti-fermions of the

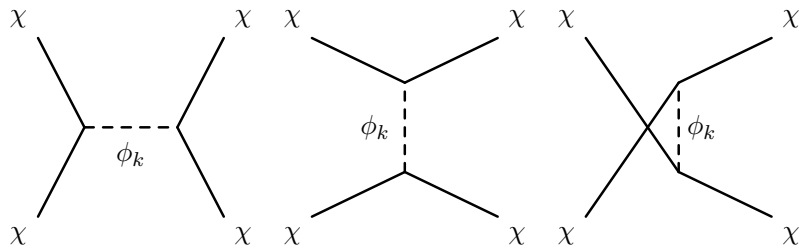

Table 2.3 – Diagrams involved in the self-interaction with scalar mediators.

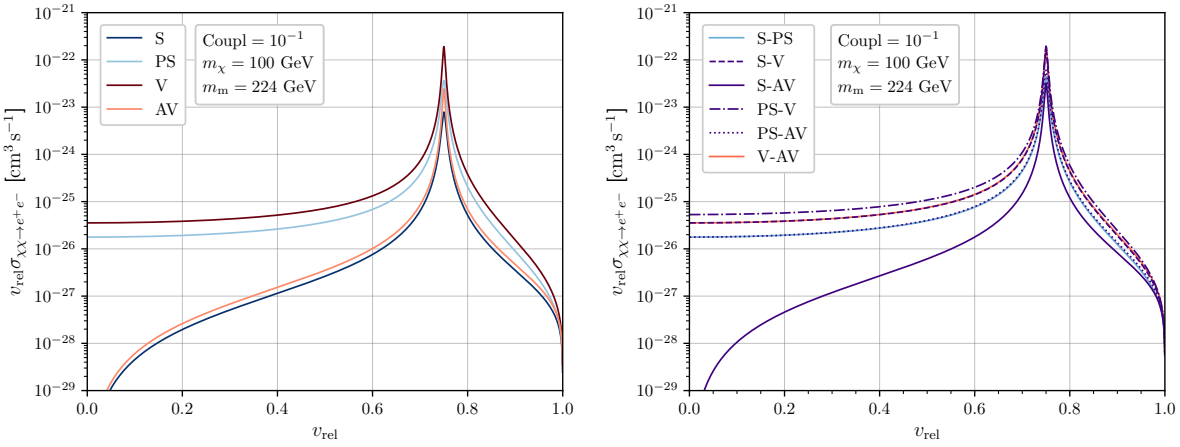

Figure 2.7 – Annihilation cross-section of DM into e^+e^- multiplied by the relative velocity of the incoming particles. In the left panel, only one mediator contributes while on the right there is a mixture of two. We denote S=scalar, PS=pseudo-scalar, V=vector and AV=axial-vector. All mediators have the same mass $m = 224$ GeV, chosen so that the resonance happens at $v_{\rm rel} = 0.75$ for clarity. The couplings involved are all equal to 0.1.

SM. The amplitudes are the same as for the scattering on the fermions except for the term implying a vector mediator, for which the signs of interference contributions may be changed. Therefore, one needs to be careful and consider these two scattering processes on their own. Indeed, even if a global sign of the amplitude is irrelevant, if several mediators of different nature are involved the interference terms with the vector mediators can potentially switch signs.

As detailed in Chapter 1, self-interactions in DM models can help solve some of the small-scale tensions. Therefore we also evaluate, within our model, the corresponding transfer cross-section divided by the DM mass. The diagrams involved are represented in Tab. (2.3) for scalar mediators. The contribution of the other mediators adds in the same way. For Majorana DM all three diagrams play a role. For Dirac DM we need to distinguish $\chi\overline{\chi} \to \chi\overline{\chi}$ which involves the s and t-channel diagrams and $\chi\chi \to \chi\chi$ which involves the t and u-channel.

The velocity dependence can be evaluated through the Lorentz-invariant relative velocity. Indeed, one can relate the energy in the centre of mass defined by the Mandelstam variable s to $v_{\rm rel}$ with the expression

$$s = (m_i + m_j)^2 + 2m_i m_j(\gamma_{\rm rel} - 1) \quad \text{with} \quad \gamma_{\rm rel} = \left(1 - v_{\rm rel}^2\right)^{-1/2} \tag{2.145}$$

It appears to be useful to develop the expression of the thermally averaged cross-section and transfer cross-section involved in chemical and kinetic decoupling. One

can always write the expansion

$$\sigma v_{\rm rel} = \sum_{n=0}^{\infty} a_n v_{\rm rel}^{2n} \,. \tag{2.146}$$

and the leading order can be evaluated with some lengthy mathematical developments detailed in App. B.3.3. In practice, it is painful to go to high order, but it turns out that terms beyond $n = 1$ usually add negligible corrections, which can safely be neglected in most cases. Then, using the non-relativistic definition of the temperature and Eq. (B.98) one can evaluate the s-wave and p-wave terms of the usual partial wave decomposition in the ratio $x = m_\chi/T$

$$\langle \sigma v_{\rm rel} \rangle = a_0 + 6a_1 \frac{T_\chi}{m_\chi} = a_0 + 6a_1 x \,, \tag{2.147}$$

with the assumption of thermal equilibrium $T_\chi = T$. For non-relativistic species we recall that $v_{\rm rel} \simeq v_{\rm Møl}$ so we can use both indifferently.

For the transfer cross-section a similar expansion is possible. If interested in its behaviour for direct detection, where the relative velocity between the incoming particle is small, one can also develop in series of $v_{\rm rel}$. However, for kinetic decoupling, a better parameter to develop on is $\overline{p}_{\chi\psi}/m_\chi$. Indeed, the velocity of SM particles in the primordial plasma is large (~ 1). The incoming centre-of-mass momentum, on the contrary, is limited by the temperature and a rough scaling gives $\overline{p}_{\chi\psi}/m_\chi \sim |T^2 - m_\psi^2|^{1/2}/m_\chi \ll 1$ when kinetic decoupling occurs. Therefore we can write

$$\sigma_T = \sum_{n=0}^{\infty} b_n v_{\rm rel}^{2n} \quad \text{or} \quad \sigma_T = \sum_{n=0}^{\infty} c_n \left(\frac{\overline{p}_{\chi\psi}}{m_\chi} \right)^{2n} . \tag{2.148}$$

In Fig. 2.7 we show the evolution, with the relative velocity, of the total tree-level cross-section for the annihilation of DM particles into e^+e^-. In the left panel, there is only one mediator while in the second panel there is a combination of two, with the same mass. The couplings involved are all set to 0.1. At low velocity the scalar and vector-mediated interactions have a cross-section that drops to 0, which is the sign that the corresponding s-wave term is 0, that is $a_0 = 0$ in Eq. (2.146). On the contrary, for the pseudo-scalar and axial-vector mediator, the product of the relative velocity with the cross-section goes to a constant at vanishing velocity. This is the sign that the s-wave term is non zero. On the right-hand side, the combination of propagators by pairs shows that only for the case where we add two mediators that induce a zero s-wave term on their own we recover a final 0 s-wave term. This configuration is the addition of a vector with a scalar mediator. Nevertheless, this is, a priori, non-trivial since the interference in the amplitude squared can either cancel or add new terms.

In the left panel of Fig. 2.8 we show the evolution of the tree-level cross-section for the annihilation of DM into scalar and pseudo-scalar mediators and a combination of both. The couplings are set to 0.1 except for G_{ijk} and H_{ijk} that are set to 0. The difference between Majorana and Dirac is here induced by the fact that there is no u-channel contribution in $\sigma_{\chi\overline{\chi}\to\phi\varphi}$ when DM is made of Dirac particles. As shown by the vanishing-velocity behaviour, only the annihilation into two scalars misses the s-wave term. This is further shown in Sect. 2.5.4 where we treat in more details the scalar and pseudo-scalar configurations. In the right panel of the same figure, we represented the self-interaction transfer cross-section. The masses and couplings are chosen so that the Sommerfeld effect due to bound state formation is on the verge

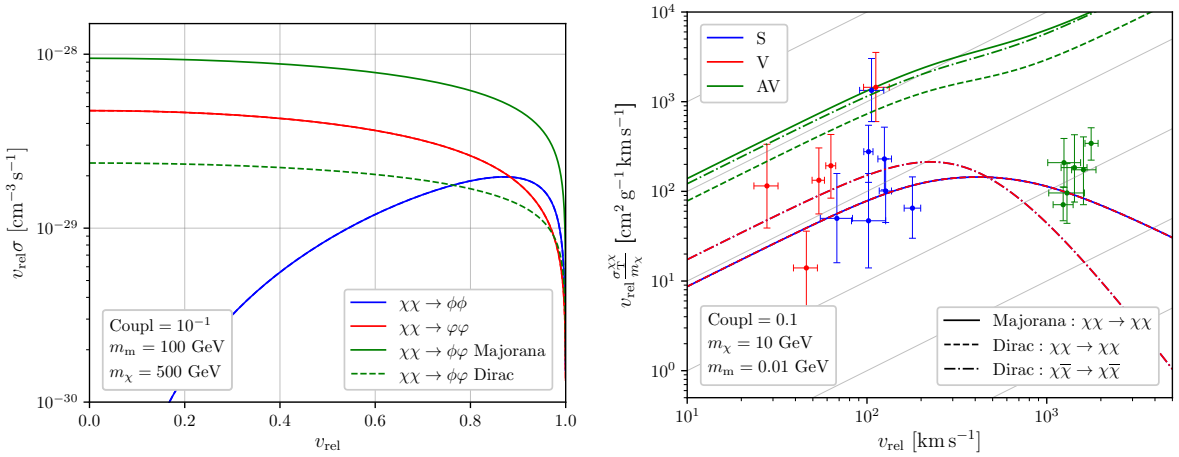

Figure 2.8 – Left panel: Annihilation cross-section of DM into scalar and pseudo-scalars multiplied by the relative velocity of the incoming particles. For the annihilation into one scalar and one pseudo-scalar the Dirac and Majorana DM particle scenarios have to be distinguished since the latter has a u-channel contribution the former misses. The couplings G_{ijk} and H_{ijk} are set to 0 and we only consider the coefficients A_k^{ij} and B_k^{ij} equal to 0.1. **Right panel:** Self-interaction transfer cross-section at low velocity. Notice that in the x-axis $v_{\rm rel}$ is given in km s^{-1} contrary to the other figures. Each curve corresponds to a single mediator that is either scalar (S) in blue, vector (V) in red or axial-vector (AV) in green. The pseudo-scalar mediator gives much lower values that are not represented here. The Majorana and Dirac case are separated as they involve different Feynman diagrams. The scalar and vector-mediated interactions have the same cross-section in several configurations and the blue solid curve, blue dashed and green dashed curves are superposed. Similarly the blue and green dash-dotted curves are also superposed. For Majorana DM particles vector interactions are impossible and therefore not computed. The dots represent the values obtained from observations by Kaplinghat et al. (2016) from dwarf galaxies (red), LSBs (blue) and clusters (green). The masses and couplings are chosen at the verge of Sommerfeld enhancement effects. The grey lines represents constant values of $\sigma_{\rm T}^{\chi\chi}$.

of being important (Arkani-Hamed et al. 2009; Iengo 2009; Cassel 2010; Feng et al. 2010). Indeed its strength is parametrised by $\epsilon_\phi \equiv 4\pi m_{\rm m}/(\lambda^2 m_\chi)$ for $m_{\rm m}$ the mediator mass and λ the coupling constant. Sommerfeld effects start being relevant when $\epsilon_\phi \lesssim 1$. However, our goal is to give a simple application of this "toy" model. These constraints are thus not considered in a first approach. Here $\epsilon_\phi = 1.3$ and in this configuration, the scalar, vector and axial-vector mediated transfer cross-sections are on the right order of magnitude to match the observationally derived values in Kaplinghat et al. (2016) and represented by the coloured dots. The three distinct groups are obtained from three classes of astrophysical objects: dwarf galaxies in red, Low Surface Brightness spiral galaxies (LSBs) in blue and clusters in green, which exhibit different typical velocity dispersions. As mentioned in Chapter 1, the need for self-interactions to solve the core-cusp issue is only present on small scales. This translates as asking for a self-interaction cross-section that decreases with the velocity. Namely the values inferred in Kaplinghat et al. (2016) give the rough scaling $\sigma_{\rm T} \propto 1/v_{\rm rel}$. The scalar and vector-mediated interactions show a velocity evolution that is consistent with this requirement. The axial-vector however tends to predict too large cross-sections at large velocity. Eventually, the pseudo-scalar mediator provides such a small cross-section that it is not represented in the figure for clarity.

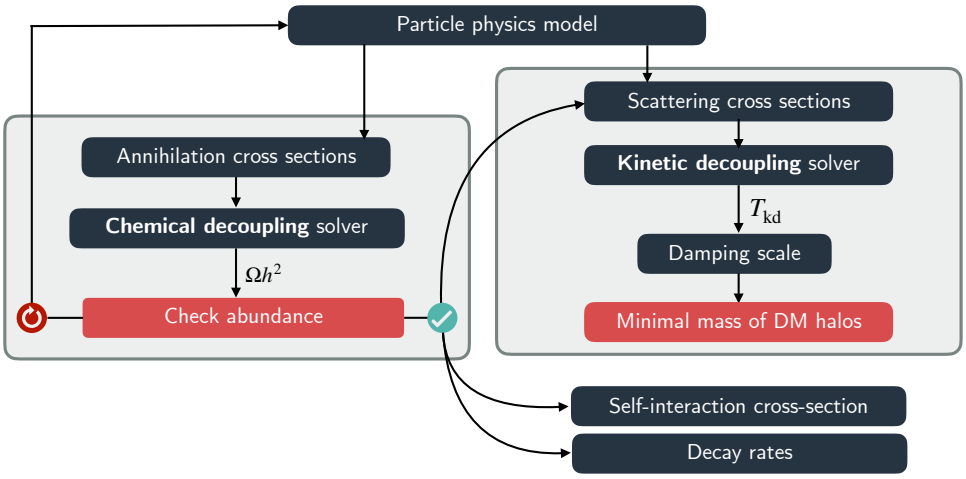

Figure 2.9 – Representation of the operations performed in order to obtain a consistent minimal mass for DM halos.

2.5.3 A consistent evaluation : the method

We have developed, from scratch, a C++ code that is able to evaluate, for any parameters in the simplified Lagrangian, the chemical decoupling temperature, the abundance of DM today, the kinetic decoupling temperature, and the minimal halo mass. The structure of this entire code is given in App. A.5.

First, for every model we constrain the couplings by the total abundance of DM observed today – assuming that WIMPs are the only source of DM. As mentioned in Sect. 2.4.2 this value is fixed according to the result of Planck18. When a single effective coupling constant is considered as a free parameter, we precisely determine its appropriate value by a simple bisection method[6]. Once the couplings are determined we move on to the evaluation of the kinetic decoupling temperature and of different properties of the model. The total procedure is shown in Fig. 2.9 and is illustrated in the context of a single scalar and single pseudo-scalar mediator in the following subsection.

Several properties of the constrained model need to be further checked in order to ensure theoretical consistency. They are the following

- In order to remain consistent with the perturbative treatment at tree level we ask that the coupling constant be lower than $\sqrt{4\pi}$.
- The amplitudes are evaluated with a Breit-Wigner functional form that has a width given by the decay rate of the mediator, according to the optical theorem. However, this is an approximation, only valid in the limit $\Gamma \ll m$: we ask that $\Gamma < 0.1m$. This further sets another upper bound on the couplings.
- When the mediators are less massive than the DM particles they can be present in the plasma at chemical decoupling, in which case we assume that they are in thermodynamic contact with the SM particles in order not to have to solve for their number density – c.f. the discussion in Sect. 2.4.2. Nevertheless, in that

[6]The amplitudes for the processes described above feature products of DM-mediators and SM-mediators couplings. We can basically promote this whole product as a free parameter, which allows us to actually account for more diverse situations.

case, one should at least verify that they decay fast, much faster than ~ 1 s. This ensures that they do not contribute to the effective number of degree of freedom during BBN and obey the associated constraints.

- For a large mass hierarchy between the DM particles and the mediators, one can have bound-state formation and Sommerfeld enhancement of the cross-sections. As we do not treat these phenomena in the current version of the code we should ask that whenever Sommerfeld enhancement is relevant (in particular for annihilation and creation of DM particles), the couplings be less than $(4\pi m_{\rm m}/m_\chi)^{1/2}$ with $m_{\rm m}$ the mediator mass.
- In this study of chemical decoupling it is assumed that DM is still in thermal contact with the plasma. Therefore, we need to ask that both events are sufficiently far apart and occurring in the right order, firstly chemical and then kinetic decoupling. We choose to set the criterion $x_{\rm kd} > 5x_{\rm cd}$ even though one should probably ask for a greater difference in order to ensure no contamination. Precise study of what happens in simultaneous chemical and kinetic decoupling is treated in BINDER et al. (2018, 2021).

We should again emphasize here that our goal is to allow for an accurate resolution of the chemical and kinetic decouplings whenever our sets of assumptions are valid. It is rather to give a general idea of the relations between the parameters of the model and the minimal halo mass (and the subsequent properties for indirect detection). However, even outside from the validity range of our assumptions, we still carry on the study to try to infer as generic as possible a physical understanding, even if more approximate in that case.

2.5.4 The scalar and pseudo-scalar examples

In order to illustrate the method, we perform the full computation in two specific cases, both involving a single Majorana DM particle χ of mass m_χ. Firstly, we consider a unique pseudo-scalar mediator φ of mass m_φ coupling to the DM particles and to e^+e^-. We define the associated effective coupling constant

$$\lambda \equiv \sqrt{B_0^{00}\mathcal{B}_0^e}\,. \tag{2.149}$$

Secondly, we consider a single scalar ϕ with mass m_ϕ, which similarly couples only to the DM particles and e^+e^-, such that we also introduce

$$\lambda \equiv \sqrt{A_0^{00}\mathcal{A}_0^e}\,. \tag{2.150}$$

Besides, for simplicity, we do not consider the couplings between the scalar and pseudo-scalar particle themselves. This actually amounts to suppress bi-quadratic and quartic terms from the fundamental scalar Lagrangian.

Taking this effective coupling as the only free coupling of the problem, annihilation cross sections trivially scale like $\propto \lambda^4$. In order to further understand the velocity dependencies of the relevant cross sections, we fully provide them in Tab. (2.4) and Tab. (2.5) up to second order in relative velocity. This makes explicit the velocity dependence that we first illustrated in Fig. 2.7 and Fig. 2.8 in terms of the s-wave and p-wave contributions. Besides, we show the first order in velocity of the transfer cross-section for the scattering against SM fermions in Tab. (2.6).

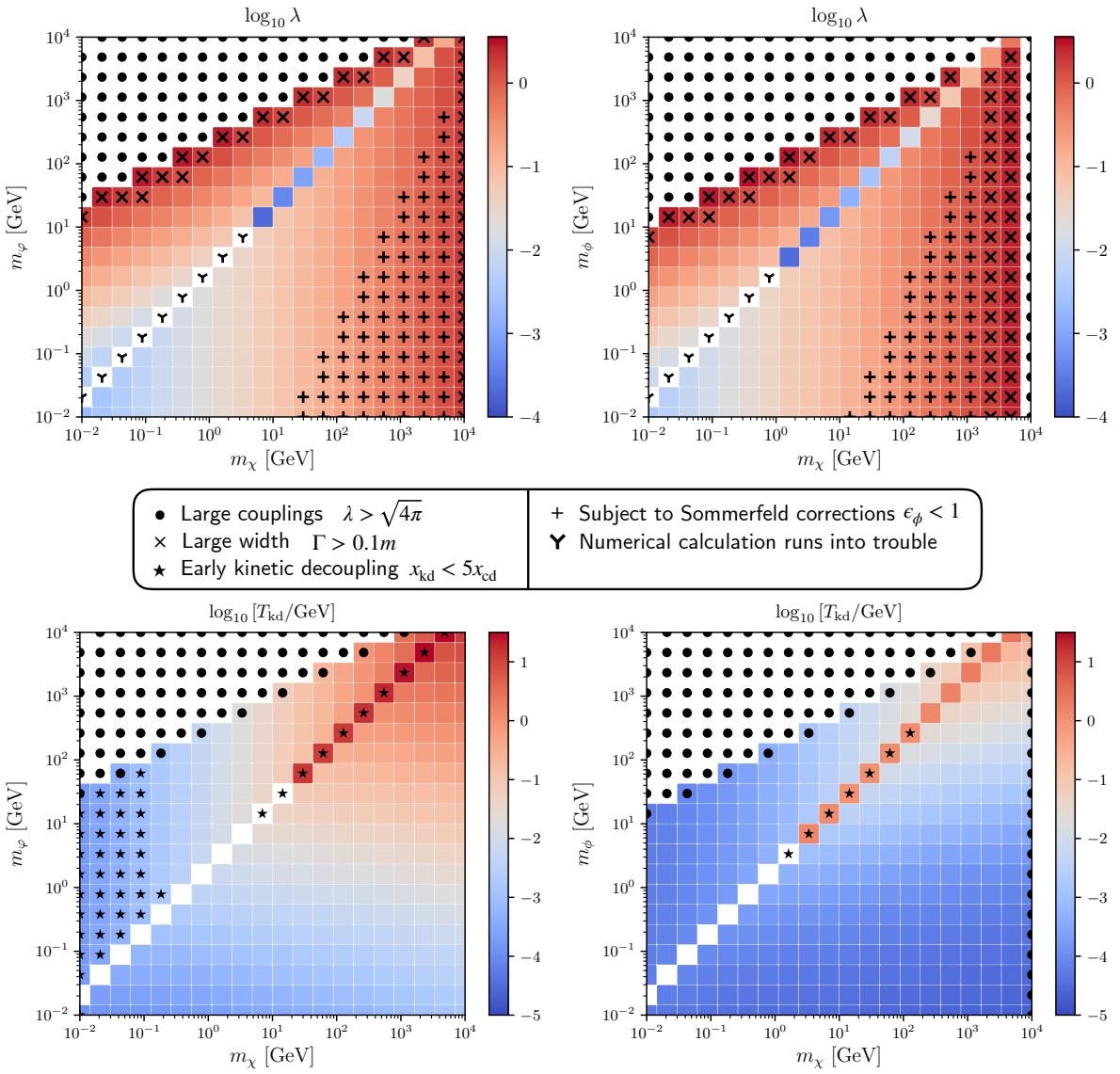

Figure 2.10 – Constrained effective universal coupling (upper panels) and kinetic decoupling temperature (bottom panels) in terms of the DM and mediator masses. Here the dark sector is made of a single Majorana DM particle and a single mediator pseudo-scalar (left panels) or scalar (right panels).

We recover the well-known scaling relation of the DM abundance with the annihilation cross section

$$Y_\chi(t_0) \sim \frac{1}{g_\star^{1/2}\,\langle\sigma v_{\rm Møl}\rangle_{\rm eff}^{\rm eq}}\,. \tag{2.151}$$

Let us focus on the constrained value of the effective coupling constant. According to the tables of cross-sections, after some simplifications one finds that it satisfy

$$\lambda \propto \begin{cases} \sqrt{m_\chi} & \text{if} \quad m_\chi \gg m_{\rm m} \\ m_{\rm m}/\sqrt{m_\chi} & \text{if} \quad m_\chi \ll m_{\rm m}\,, \end{cases} \tag{2.152}$$

where $m_{\rm m}$ represents the mediator mass, either m_ϕ or m_φ. Here we used that the s-channel annihilation into fermions is only open if $m_\chi \gtrsim m_\psi$ (in the non-relativistic regime).

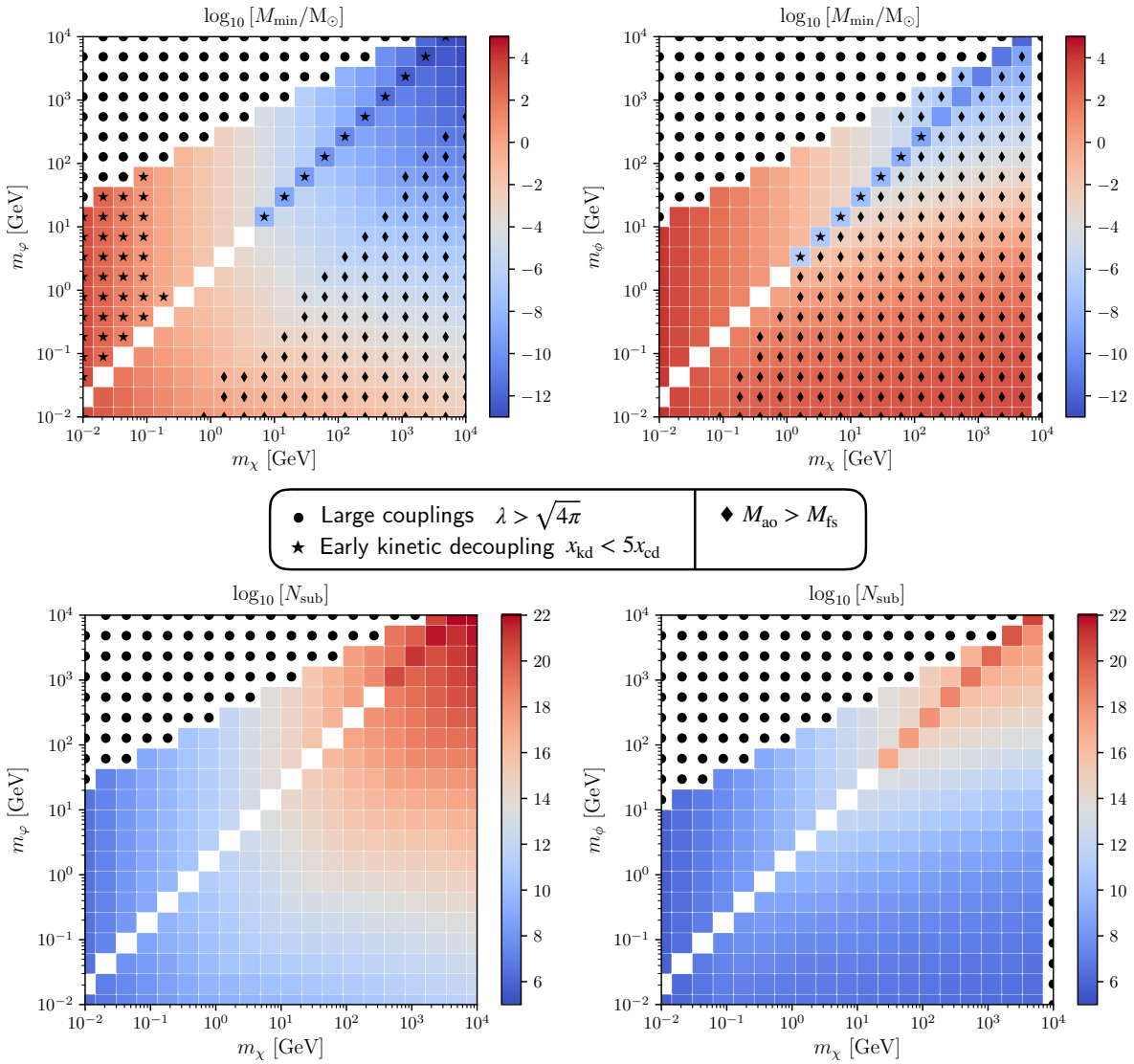

Figure 2.11 – Minimal mass of the halos (upper panel) and the unevolved number of subhalos in a 10^{12} $M_\odot$ host (lower panels). All black marks in Fig. 2.10 should also be reported here but are not for clarity.

The minimal halo mass is the *maximum* between the mass set by the scale of acoustic oscillations ($M_{\rm ao}$) and that set by the free-streaming scale ($M_{\rm fs}$). As detailed in Sect. 3.6 one has the following scaling relations[7]

$$\begin{aligned} M_{\rm fs} &\sim (m_\chi T_{\rm kd})^{-3/2} \\ M_{\rm ao} &\sim T_{\rm kd}^{-3} \end{aligned} \tag{2.153}$$

Therefore, as we expect the rough scaling $T_{\rm kd} \propto m_\chi$, it should imply that $M_{\rm min} \propto m_\chi^{-3}$ anyway. Eventually, the total number of subhalos in a given host object should scale as $N_{\rm sub} \propto M_{\rm min}^{1-\alpha}$ with $\alpha \sim 1.95$ as discussed both in Chapter 3 and Chapter 4. Therefore one can expect the approximate scaling $N_{\rm sub} \propto m_\chi^3$.

In Fig. 2.10 and Fig. 2.11, we show the result for the entire chain of analysis from the tuning of the effective coupling to get the correct abundance to the number of

[7]Note that here we use the simple prescription $k_{\rm ao} \sim a_{\rm kd}\sqrt{3}H_{\rm kd}$, would we consider $k_{\rm d} \sim 1.8(m_\chi/T_{\rm kd})^{1/2}a_{\rm kd}H_{\rm kd}$ one would have $M_{\rm ao} \sim (m_\chi T_{\rm kd})^{-3/2}$ similarly than for the free-streaming mass.

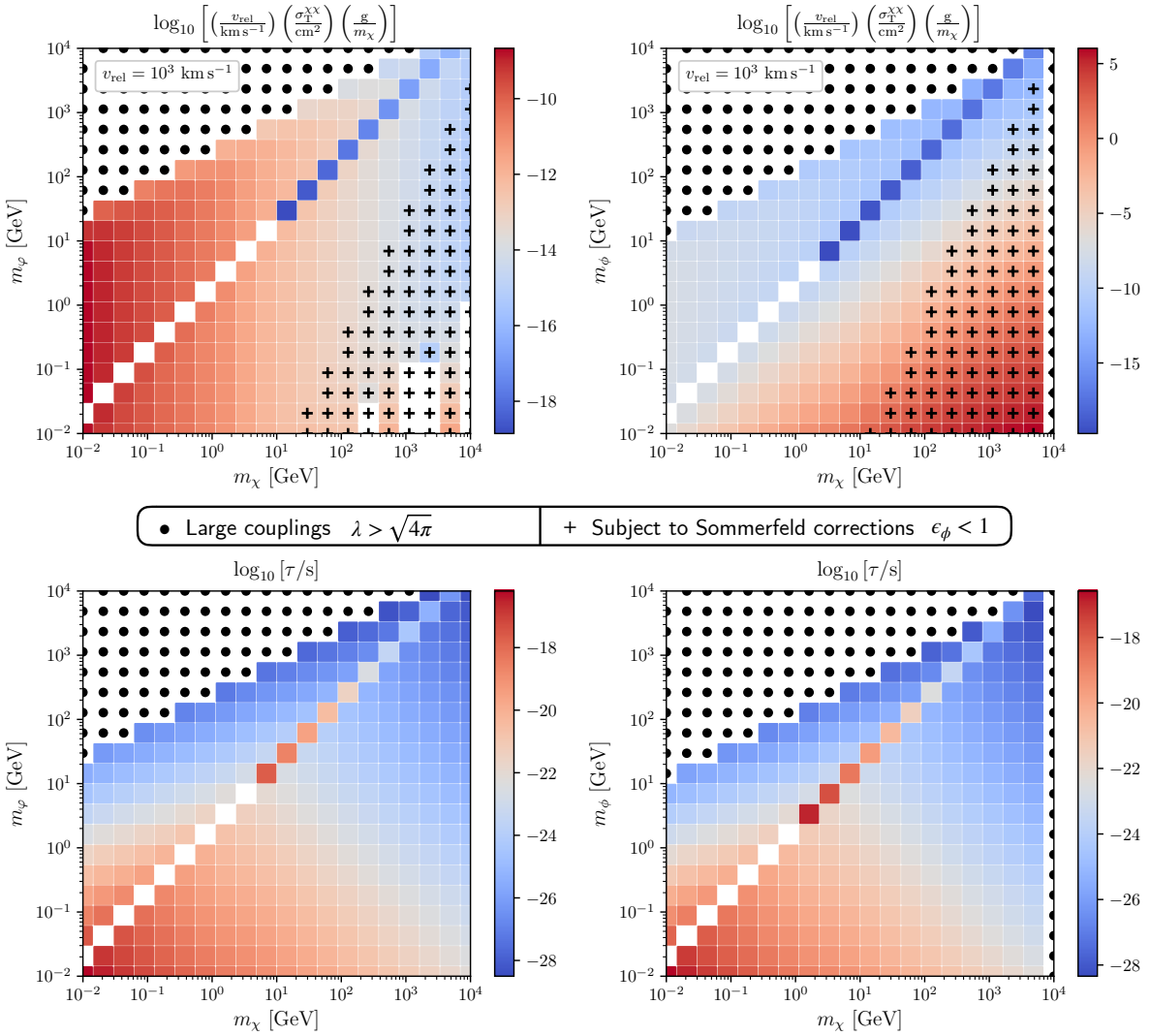

Figure 2.12 – Self-interaction transfer cross-section at $v_{\rm rel} = 10^3$ km s^{-1} (upper panels) and decay time of the mediator (lower panels) for a pseudo-scalar (left panels) and scalar (right panels) mediator. All black marks in Fig. 2.10 should also be reported here but are not for clarity.

unevolved subhalos in a 10^{12} $M_\odot$ host. By unevolved we mean, cosmological, before taking into account any dynamical effects modifying the halo properties. The tuned value of the effective coupling λ in the upper panels Fig. 2.10 follows the scaling of Eq. (2.152). The diagonal lines, where the mediator mass is twice the mass of the DM particle, correspond to annihilation on the pole. There, the annihilation cross-section is subsequently enhanced and a small value of λ is required in order to obtain the correct abundance. In some cases, the numerical calculation runs into trouble – with a dedicated warning – (represented by black *tri-branch star* symbol) as the correct coupling is so low that the mediator width becomes too narrow to properly perform the integrals numerically. The black crosses show when the decay rate of the mediator is larger than 10% of its mass. This constraint could be alleviated if the coupling of the mediator to WIMPs was different from its coupling to the SM particles. The other black symbols show where the resolution may fail because of the different constraints mentioned in the previous subsection (see the legend). Eventually, the couplings in

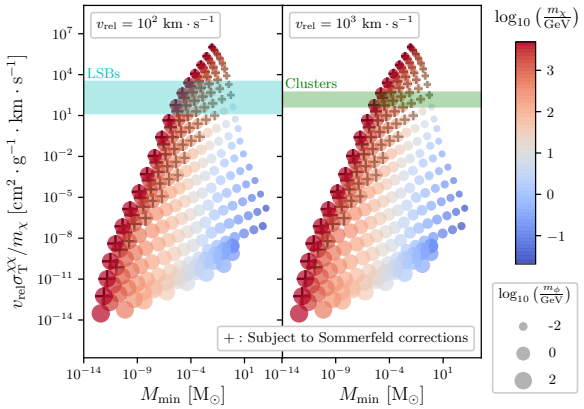

Figure 2.13 – Scatter plot showing the correlation between the self-interaction transfer cross-section and the minimal halo mass for the scalar propagator. The two panels correspond to $v_{\rm rel} = 10^2$ km·s^{-1} (left) and $v_{\rm rel} = 10^3$ km·s^{-1} (right). The colours span the range of DM mass and the circle sizes represent the logarithm of the scalar mediator mass (between 10^{-2} and 10^3 GeV). As the left panels correspond to typical velocities in galaxies we show a cyan band corresponding to the constraints derived in KAPLINGHAT et al. (2016) for Low Surface Brightness galaxies. Similarly in the right panel, the velocity is typical of clusters and therefore we show the associated constraint in green. Here we kept all the points that do not satisfy the Sommerfeld limit (that is they can be in the Sommerfeld enhanced regime). However, we removed all those not satisfying the other constraints (non-perturbative effective couplings, kinetic decoupling close to chemical decoupling).

the pseudo-scalar scenario are lower than in the scalar scenario. Indeed, the latter exhibits an annihilation cross-section that is velocity suppressed[8] – since the DM particles are non-relativistic at chemical decoupling – which forces the coupling to higher values in order to compensate.

In the lower panel of Fig. 2.10 the corresponding kinetic decoupling temperature is represented. A first remark is that for m_χ lower than the mediator mass it is roughly independent of the mediator mass. This can be derived from the scaling in λ extracted from Eq. (2.152), which, once put in the expression of $\sigma_{\rm T}^{\chi\psi}$ given in Tab. (2.6), yields

$$\sigma_{\rm T}^{\chi\psi} \propto \begin{cases} \left(\frac{m_\chi}{m_\varphi}\right)^4 F_{\rm m}\left(\frac{m_\psi}{m_\chi}\right) & \text{if} \quad m_\chi \gg m_{\rm m} \\ F_{\rm m}\left(\frac{m_\psi}{m_\chi}\right) & \text{if} \quad m_\chi \ll m_{\rm m} \end{cases} \tag{2.154}$$

with $m_{\rm m}$ the mediator mass and where we introduced here

$$F_\phi(x) = \frac{x^2}{(1+x)^2} \quad \text{and} \quad F_\varphi(x) = \frac{1}{(1+x)^2}\left(\frac{\overline{p}_{\chi\psi}}{m_\chi}\right)^4 . \tag{2.155}$$

Moreover, this also shows that when $m_\chi \gg m_{\rm m}$, the larger the mediator the earlier the decoupling and the greater the kinetic decoupling, which also corresponds to the observed behaviour. The black stars represent configurations where kinetic decoupling is close to chemical decoupling (or even happens before). In the scalar scenario, this situation only occurs on the pole where the coupling constant is low and therefore the kinetic decoupling early. In the pseudo-scalar case, however, this also happens for other points at small DM mass and large mediator coupling. This is

[8] For the $\chi\chi \to \phi\phi$ annihilation the velocity independent terms produced by the t and u-channels are actually cancelled by the interference term, as shown in Tab. (2.4).

due to the velocity suppression of the scattering transfer cross-section with a pseudo-scalar mediator, thus giving an earlier kinetic decoupling than with a scalar mediator.

The upper panels of Fig. 2.11 represent the subsequent minimal halo mass obtained using the results of Sect. 3.6. The black diamonds correspond to the points where the acoustic mass dominates over the free-streaming mass. This happens for late decouplings. As the kinetic temperature does not exactly scale as $T_{\rm kd} \sim m_\chi$, in particular, due to the dependence on the mediator mass, the true behaviour of $M_{\rm min}$ departs from the simple scaling $\propto m_\chi^{-3}$. However, the global trend is conserved when the mediator mass is close to the DM mass and therefore the decoupling does not occur too late so that the dominant halo mass still is the free-streaming mass. Eventually, as the kinetic decoupling temperature is generally colder in the scalar scenario, the subsequent minimal halo mass is larger. The lower panels of Fig. 2.11 show the evolution of the unevolved number of subhalos in a 10^{12} $\mathrm{M}_\odot$ host and obtained using the recipes of SL17 presented in Chapter 5. The global trend $N_{\rm sub} \sim m_\chi^3$ is also respected when the mass difference between the mediator and the DM particle is not too large. Indeed this number spans 18 orders of magnitudes for a DM mass which spans 6. Moreover, it reaches values up to 10^{22} that prohibits a full description of the DM structuring in Galaxy-like objects with numerical simulations. This justifies the use of analytical models like SL17. Besides, the imprint of the velocity dependence of the cross-sections can be seen here as a difference of 2 to 3 orders of magnitude between the scalar and pseudo-scalar cases at equivalent masses. The latter, which has the earlier kinetic decoupling, gives the largest number of subhalos. Interestingly enough, it is also the pseudo-scalar case that can be probed by indirect DM searches, since it yields an s-wave annihilation.

The upper panels of Fig. 2.12 show the behaviour of the self-interacting transfer cross-section at $v_{\rm rel} = 10^3$ km·s^{-1} (the typical velocity in galaxy clusters). For pseudo-scalar interactions, the values are too low to have an impact. However, in the scalar case, some configurations exhibit values in the interesting range for the core-cusp issue as already discussed in the context of Fig. 2.8. Fig. 2.13 additionally presents a scatter plot of all points obeying most of the required constraints (see the legend for details), shown in the plane self-interacting cross-section (actually $v_{\rm rel}\,\sigma_{\rm T}/m_\chi$, more suited to observational constraints) vs. minimal halo mass. The preferred values (with uncertainties) of cross-sections to potentially solve the core-cusp issue on different scales, as constrained by current observations (KAPLINGHAT et al. 2016), are reported as shaded cyan and green bands. This figure points out that it should be possible to obtain a consistent theory with a single scalar mediator to address the core-cusp issue while accounting for observational constraints on different scales. The inclusion of Sommerfeld enhancement should increase the self-interaction at small velocity, therefore further making it easier to obtain the desired hierarchy between dwarf galaxies and clusters. We remind however that such high couplings are probably already excluded by detection constraints. Forgetting about the Sommerfeld enhancement and this latter issue, one sees that this simple model roughly correlates the self-interaction to the maximal subhalo mass. If the self-interaction was the answer to the core-cusp problem, in this simple model it would then restrict the range of minimal subhalo mass to $10^{-8} M_\odot \lesssim M_{\rm min} \lesssim 10^{-1} M_\odot$. Eventually, let us point out that the lower panels of Fig. 2.12 show the decay time of the mediator that should be sufficiently small to avoid any impact on BBN.

$\chi\chi \to \phi\phi$	$\phi\ (s)$	$\chi\ (t)$	$\chi\ (u)$
$\phi\ (s)$	$\frac{\lambda^4 w^2}{2048\pi m_\chi^4} v_{\rm rel}^2$		
$\chi\ (t)$	$-\frac{5\lambda^4 w^2}{1536\pi m_\chi^4} v_{\rm rel}^2$	$\frac{\lambda^4}{128\pi m_\chi^2}$	
$\chi\ (u)$	$-\frac{5\lambda^4 w^2}{1536\pi m_\chi^4} v_{\rm rel}^2$	$\frac{\lambda^4}{64\pi m_\chi^2}\left[-1+\frac{3}{2}v_{\rm rel}^2\right]$	$\frac{\lambda^4}{128\pi m_\chi^2}$

$\chi\chi \to \varphi\varphi$	$\phi\ (s)$	$\chi\ (t)$	$\chi\ (u)$
$\phi\ (s)$	$\frac{\lambda^4 w^2}{2048\pi m_\chi^4} v_{\rm rel}^2$		
$\chi\ (t)$	0	$\frac{\lambda^4}{128\pi m_\chi^2}\left[1-\frac{1}{3}v_{\rm rel}^2\right]$	
$\chi\ (u)$	0	$\frac{\lambda^4}{64 m_\chi^2}\left[1-\frac{5}{6}v_{\rm rel}^2\right]$	$\frac{\lambda^4}{128\pi m_\chi^2}\left[1-\frac{1}{3}v_{\rm rel}^2\right]$

$\chi\chi \to \phi\varphi$	$\varphi\ (s)$	$\chi\ (t)$	$\chi\ (u)$
$\varphi\ (s)$	$\frac{\lambda^4 w^2}{256\pi m_\chi^4}\left[1-\frac{3}{4}v_{\rm rel}^2\right]$		
$\chi\ (t)$	$\frac{\lambda^2 w}{64\pi m_\chi^3}\left[-1+\frac{2}{3}v_{\rm rel}^2\right]$	$\frac{\lambda^4}{64\pi m_\chi^2}\left[1-\frac{1}{3}v_{\rm rel}^2\right]$	
$\chi\ (u)$	0	$\frac{\lambda^4}{64 m_\chi^2}\left[1-\frac{5}{6}v_{\rm rel}^2\right]$	$\frac{\lambda^4}{32\pi m_\chi^2}\left[1-\frac{1}{2}v_{\rm rel}^2\right]$

Table 2.4 – Velocity dependence of the three different squared tree-level diagrams of $v_{\rm rel}\sigma_{\chi\chi\to\varphi\varphi}$, $v_{\rm rel}\sigma_{\chi\chi\to\phi\phi}$, $v_{\rm rel}\sigma_{\chi\chi\to\phi\varphi}$ and the associated interferences. Each row and column is identified with a particle symbol and a letter (s,t,u) that correspond to the mediating particle and the channel. The squared terms are on the diagonal and the interference terms are off the diagonal. The DM mass is m_χ, the pseudo-scalar mass m_φ and the scalar mass m_ϕ. We considered here the expansion to third order in relative velocity and to zeroth order in m_φ/m_χ and m_ϕ/m_χ, thus assuming $m_\chi \gg m_\varphi, m_\phi$. The effective coupling λ is assumed universal and w is the VEV-like term. The widths of the mediators are neglected in front of their mass.

$\chi\chi \to \psi\overline{\psi}$	$\phi\ (s)$	$\varphi(s)$
	$m_\chi \gg m_\phi, m_\varphi$	
$\phi\ (s)$	$\frac{\lambda^4 (m_\chi^2-m_\psi^2)^{3/2}}{128\pi m_\chi^5} v_{\rm rel}^2$	
$\varphi\ (s)$	0	$\frac{\lambda^4 (m_\chi^2-m_\psi^2)^{1/2}}{32\pi m_\chi^3}\left[1-\frac{1}{8}\frac{4m_\chi^2-5m_\psi^2}{m_\chi^2-m_\psi^2}v_{\rm rel}^2\right]$
	$m_\chi \ll m_\phi, m_\varphi$	
$\phi\ (s)$	$\frac{\lambda^4 (m_\chi^2-m_\psi^2)^{3/2}}{8\pi m_\chi m_\phi^4} v_{\rm rel}^2$	
$\varphi\ (s)$	0	$\frac{\lambda^4 m_\chi (m_\chi^2-m_\psi^2)^{1/2}}{2\pi m_\varphi^4}\left[1+\frac{1}{8}\frac{m_\psi^2}{m_\chi^2-m_\psi^2}v_{\rm rel}^2\right]$

Table 2.5 – Velocity dependence of the annihilation cross-section in SM fermions $v_{\rm rel}\sigma_{\chi\chi\to\psi\psi}$ and their interferences. See the table above for more explanations. The fermion mass is m_ψ. Moreover, we consider the two limits $m_\chi \gg m_\phi, m_\varphi$ and $m_\chi \ll m_\phi, m_\varphi$. The width of the mediators are neglected in front of their mass.

$\chi\psi \to \chi\psi$	$\phi\ (t)$	$\varphi\ (t)$
$\phi\ (t)$	$\frac{\lambda^4}{\pi}\frac{m_\chi^2 m_\psi^2}{m_\phi^4 (m_\chi+m_\psi)^2}$	
$\varphi\ (t)$	0	$\frac{\lambda^4}{2\pi}\frac{m_\chi^4}{m_\varphi^4 (m_\chi+m_\psi)^2}\left(\frac{\overline{p}_{\chi\psi}}{m_\chi}\right)^4$

Table 2.6 – Leading order expansion of the scattering transfer cross-sections $\sigma_{\rm T}^{\chi\psi}$ in terms of the ratio $\overline{p}_{\chi\psi}/m_\chi$. We assume no hierarchy between the DM and mediator mass. The width of the mediators are neglected in front of their mass.

2.6 Conclusion

2.6.1 Discussion of the preliminary results

In this chapter, we started by the introduction of the mathematics behind the ΛCDM model and then introduced the notion of phase space and of the associated distribution function. Then we showed that the PSDF is driven by the Boltzmann equation, and from there, we gave an overview of the thermodynamics describing the evolution of particle species in the early universe.. We then detailed on the computation of the chemical and kinetic decouplings. In the last section, we moved on to the study of a simplified DM model and determined the minimal halo mass implied by its intimate properties. After making explicit the Lagrangian and our method for the analysis we showed specific realisations for scalar and pseudo-scalar mediated interactions. There we derived the velocity dependencies of the cross-sections and used appropriate series expansions to provide some generic scaling relations. We summarized the comparison of the two configurations in Tab. (2.7). It is well-known that a scalar (respectively pseudo-scalar) mediation leads to a p-wave (s-wave) annihilation cross-section, not suited (well suited) for indirect searches, while well suited (not suited) for direct searches. Less known is the fact that s-wave annihilation (in this very minimalistic setup) is also related to smaller minimal halo masses, which should increase the potential of indirect searches. Finally, we looked at the self-interaction transfer cross-section and recovered that, up to Sommerfeld corrections, the scalar mediator can be compatible with observationally favoured values. We further identified the portion of the parameter space that could be consistent with a DM solution to the core-cusp problem. This includes the associated minimal halo masses, which provides a well-defined target range for more dedicated studies.

We now discuss the impact of the minimal mass and subhalo number on DM searches. Firstly, they may have some impact on the indirect detection methods. Indeed, one shows in Sect. 5.1.4 that the luminosity of a subhalo is roughly proportional to its mass. In practice it goes as $m^{1-\varepsilon}$ with $\varepsilon \sim 0.1$ a small correction related to concentration (or time of collapse). Moreover, the subhalo mass function approximately goes as a power law, $m^{-\alpha}$ with $\alpha \leq 2$ for conventional primordial power spectra.. Therefore, the integrated luminosity goes as $M_{\rm max}^{2-\varepsilon-\alpha} - M_{\rm min}^{2-\varepsilon-\alpha}$ and at most yields a dependence going in $M_{\rm min}^{-\varepsilon}$. Assuming a realistic value $\alpha \sim 1.95$ – c.f. Chapter 3 – it is already possible to anticipate differences in the amplification of the annihilation rate (the so-called subhalo boost factor for a velocity independent annihilation cross-section (SILK et al. 1993; BERGSTRÖM et al. 1999; LAVALLE et al. 2008)) for a velocity-independent (s-wave) annihilation cross-section – c.f. the discussion in SL17 where a factor 2 difference in the MW is shown between $M_{\rm min} = 10^{-10}$ $\mathrm{M}_\odot$ and $M_{\rm min} = 10^{-6}$ $\mathrm{M}_\odot$ for $\alpha = 2$. Between, $M_{\rm min} = 10^{-12}$ and $M_{\rm min} = 10^{3}$ one can very roughly expect a factor 5 difference with $\alpha \sim 1.95$. However, we also show in Chapter 5 that the perspective of detecting sub-halos as point-like sources with gamma-ray instruments does not depend on the minimal cut-off mass of the subhalos because only massive enough subhalos can be found above the sensitivity reach of current and future experiments. According to IBARRA et al. (2019), the smallest subhalos could change by a factor of a few the probability that we under-evaluate the constraints of direct detection with a subhalo passing through the Earth, though without taking into account the range of minimal masses that we determined earlier in this chapter (scalar interactions and p/s-wave annihilation/scattering). Having a link between the subhalo distribution and the particle physics properties can then help reveal further

	$\langle\sigma v_{\text{Møl}}\rangle_{\text{eff}}^{\text{eq}}$	$\sigma_{\text{T}}^{\chi\psi}$	λ	T_{kd}	$M_{\text{min}} \sim m_\chi^{-3}$	$N_{\text{sub}} \sim m_\chi^3$
pseudo-scalar	v-indep.	v-dep. (v^4)	lower	higher	lower	higher
scalar	v-dep. (v^2)	v-indep.	higher	lower	higher	lower

Table 2.7 – Summary - Comparison between pseudo-scalar and scalar interactions. The label *higher* and *lower* are indicative of a direct comparison at equivalent masses.

correlations between the fundamental theoretical ingredients and the subsequent direct detection constraints (including a proper treatment of structuring on small scales). In the same analysis, the authors point out that, what could be an additional promising probe, the capture of DM particles by the Sun, should not be impacted by the presence of subhalos – though this relies on assumptions on their local abundance which are plagued by large uncertainties. Let us also mention that very small clumps with mass $\lesssim 10^{-13}$ $\text{M}_\odot$ could also be probed locally by laser interferometers like LISA as they could modify the arm length if passing through (Adams et al. 2004). However, classical clumps are too large to have a significant impact so that the method is better suited for PBHs or to superdense clumps with a different formation scenario (V. Berezinsky et al. 2010). Nevertheless, because of dynamical mass loss effects induced by gravitational tides in the MW, subhalos can be pruned very significantly, especially due to the crossing of the baryonic disc and to individual stellar encounters – as discussed in Chapter 5. This could lead, if subhalos are resilient to tidal stripping (which is still debated), to a crowded population of tiny remnants. The probability to observe such objects may anyway remain too low to be relevant. Eventually, the most promising probe in the next decades may come from pulsar timing arrays which could, in principle, be used on subhalos with masses as low as 10^{-13} $\text{M}_\odot$ (Ramani et al. 2020). In summary, although a clear signature due to small-scale clumps may be difficult to find, if we detected one (at least), it would be a powerful tool to constrain the underlying particle physics model and the CDM scenario as a whole.

The next step is to perform the same analysis with the vector and axial-vector mediators. Furthermore, we also want to link all the possible interactions to the corresponding effective operators in order to relate this simplified model to the already existing constraints from the CMB (Gluscevic et al. 2018) or direct detection (Cirelli et al. 2013). Yet another interesting step, but which goes beyond our current interest and effort, would be to more deeply account for collider constraints, using for instance the results of Abdallah et al. (2015).In the same vein, it would be interesting to flag more precisely the violation of unitarity produced by the axial-vector couplings and set the corresponding limitations on the model. In the following, we discuss how to connect the simplified model phenomenology with an example of UV-complete theory.

2.6.2 Connection to the CP-odd sector of the NMSSM

In the introduction of the chapter, we had mentioned that simplified models could also be mapped to UV complete models. This is something we started to study in the context of the light CP-odd sector of the NMSSM. Indeed in that model, DM couples to a pseudo-scalar that can itself mix with pseudo-scalar mesons. Then DM can annihilate into fermions via the direct coupling of the CP-odd Higgs or into photons and gluons through its mixing via the mesons and triangle diagrams. The

entire framework we have implemented is fully described in DOMINGO (2017). Here I broadly summarise the main features of the model and show very preliminary results.

The idea is to consider configurations where the lightest pseudo-scalar particle called A_1 is lighter than 2 times the charm mass which means $m_{A_1} \lesssim 3$ GeV. The value of m_{A_1} is obtained through the diagonalization of the two pseudo-scalar states (one doublet component and one singlet state). Its interaction Lagrangian density with quarks, leptons, photons and gluons is

$$\begin{aligned}\mathcal{L}_{A_1} = -\frac{iP_{11}}{\sqrt{2}v}A_1 \left\{ \frac{m_u}{\tan\beta}\overline{u}\gamma^5 u + \tan\beta \sum_{\substack{\psi=d,s\\ \mu,e}} m_\psi \overline{\psi}\gamma^5\psi \right\} \\ - \frac{\alpha}{4\pi}C_\gamma A_1 F_{\mu\nu}\tilde{F}^{\mu\nu} - \frac{\alpha_s}{4\pi}C_g A_1 G^a_{\mu\nu}\tilde{G}_{a\,\mu\nu}\end{aligned} \tag{2.156}$$

where $\tan\beta$ is the ratio of the two Higgs VEVs and P_{11} is the element relating A_1 to the doublet component of the NMSSM (ELLWANGER et al. 2010). In the first line we recognise pseudo-scalar interactions as already set in our simplified model, thus already taken into account in our numerical codes. In the second line however there are effective couplings to photons and gluons parametrised by C_γ and C_g – they result from triangle loops of leptons, charginos and heavy quarks. See App. B.4 for the expressions and their computation. At the exception of the chargino contribution, the simplified model introduced above formally takes into account such terms. However they are not at tree-level and therefore they were not hitherto considered.

In addition, the particle A_1 mixes with pseudo-scalar mesons. This effect can be evaluated through the chiral Lagrangian. One then obtains a new physical eigenstate $\tilde{A}_1$ that is a combination of different pseudo-scalar states written

$$\tilde{A}_1 = O_{AA}A_1 + \sum_\varphi O_{A\phi\varphi} \tag{2.157}$$

where the sum runs over $\varphi = \pi^0, \eta, \eta'$. In the left panel Fig. 2.14 we show the evolution of the mixing parameters $O_{A\varphi}$ obtained in our numerical code. They are consistent with the results shown in DOMINGO (2017) and appear to be small except near the masses of the mesons. In the following we must ask that the A_1 does not contaminate their masses too much and therefore we avoid the resonances. The mesons also couple to photons through the Wess-Zumino-Witten terms. One denotes $C_\gamma[\varphi]$ the corresponding coupling to $F^{\mu\nu}\tilde{F}^{\mu\nu}$. In the end, $\tilde{A}_1$ couples to photons through A_1 and the pions. For large masses, $m_{A_1} \gtrsim 1$ GeV, the validity of the description with the chiral Lagrangian breaks down but we do not consider these cases for now.

In order to implement this framework within our numerical tools we simply need to evaluate the annihilation and scattering cross-sections corresponding to the couplings to photons and gluons. This amounts to add two new terms

$$-\mathcal{L}^{\chi,\mathrm{SM}}_{\mathrm{int}} \ni \mathcal{D}^\gamma_{A_1} A_1 F^{\mu\nu}\tilde{F}^{\mu\nu} + \mathcal{D}^g_{A_1} A_1 G^a_{\mu\nu}\tilde{G}_{a\,\mu\nu}\,. \tag{2.158}$$

Then, to evaluate the DM annihilation into photons in the s-channel, we plug an effective coupling constant

$$\mathcal{D}^\gamma_{A_1}(s) = O_{AA}C_\gamma(s) + \sum_\varphi O_{A\varphi}C_\gamma[\varphi]\,, \tag{2.159}$$

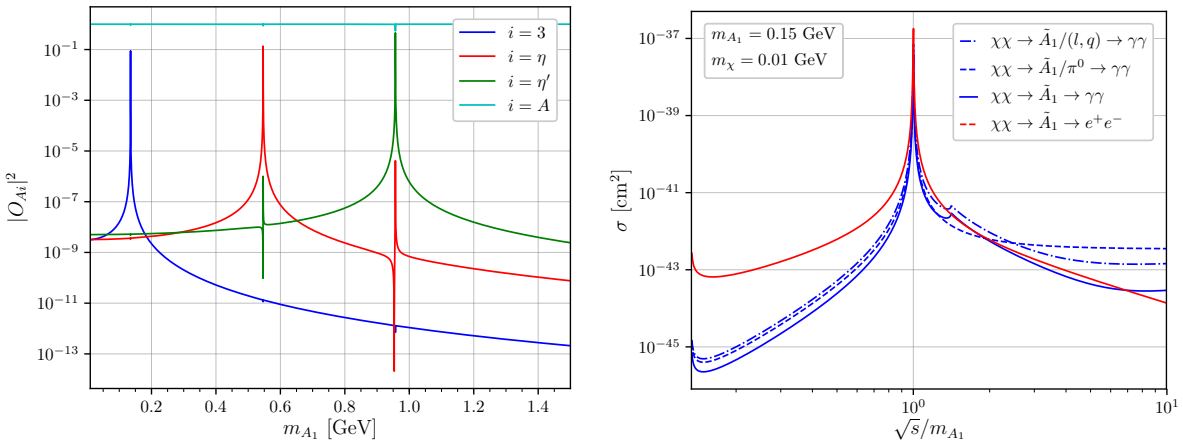

Figure 2.14 – Left panel: Evolution of the mixing parameters with the mass of A_1 for $\tan\beta = 10$ and $P_{11} = 0.03$. Except for resonances at the mass of the mesons they remain low. The parameter $i = 3$ refers to π^0. **Right panel**: Annihilation cross-section of the DM particle χ for the same parameters P_{11} and $\tan\beta$ and a coupling between A_1 and χ being 0.1. For simplicity we did not incorporate here the effect of the chargino loops.

which depends on s, the Mandelstam variable. The cross-sections for the annihilation into photons are shown as the blue curves in the right panel of Fig. 2.14. We represented the total cross-section as well as the contribution of the triangle loops (dash-dotted) and the mixing to the π^0 (dashed). Note that the total is not the sum of the two components due to interferences. For comparison, we show the annihilation into e^+e^- in solid red. We could now scan the parameter space in order to constrain the model with the abundance. Then we may try to evaluate the scattering cross-section and the kinetic decoupling in such models. In conclusion, we demonstrated here how our numerical tools and simplified model could be generically adapted to probe more complex theories (with the addition of effective couplings in that case). This project is part of a larger collaboration on new supergravity models (MOULTAKA et al. 2019).

III

Cosmological halo mass function

"If there were an answer I could give you to how the universe works, it wouldn't be special. It would just be machinery fulfilling its cosmic design. It would just be a big, dumb food processor. But since nothing seems to make sense, when you find something or someone that does, it's euphoria"

Janet character in The Good Place

Contents

To understand the distribution of CDM halos and subhalos in the Universe today, it is necessary to dive into their formation mechanism. In the standard picture, the DM density field was primarily imprinted by quantum fluctuations at the time of inflaton decay. Their evolution in the first stages of the Universe was mainly dictated by the particle properties of CDM. They started to grow efficiently after matter-radiation equality (linearly in time), subsequently leading to the non-linear collapse of structures. The over-dense regions became denser and denser, so much that at some point they collapsed into bounded objects, which we call halos, and virialised. Several authors have investigated the detailed physics behind this evolution, first with analytical developments (e.g. MO et al. (2010), and references therein), which provide deeper insights on the physical phenomena before entering (or independent of) the highly non-linear stages, not to mention complementary considerable effort to study galaxy formation (e.g. VOGELSBERGER et al. (2019)). One of the main results in the field is the halo mass function obtained via the Extended Press-Schechter (EPS) or Excursion Set Theory (EST) (PRESS et al. 1974; BOND et al. 1991). One subtlety, however, comes from the approximate self-similar structuration of the halos. Large halos contain smaller ones that contain even smaller ones, so on and so forth. The lower limit to this Russian doll construction is set by the minimal halo mass, itself depending on the nature of DM as already mentioned in Chapter 2. The EPS framework is particularly efficient to describe the population of halos in the Universe. However, the distribution of subhalos in a given host halo is harder to evaluate. Using an algorithmic tool called merger trees (LACEY et al. 1993) that is built upon the EPS formalism, the upper limit of the subhalo mass function can be approximated. The result, which seems to be rather insensitive to the considered cosmology, has been compared to simulations and proven to be reliable (GIOCOLI et al. 2008b; Y. LI et al. 2009; BENSON 2012; JIANG et al. 2014, 2016). Unfortunately, the low mass range of subhalo is poorly constrained and one usually makes naive extrapolations below the resolved masses. Here we show a slight modification of the previous methods that is better motivated in the low mass range. The main objective is to provide a correct description of the full cosmological subhalo distribution in the MW, dwarf galaxies, or galaxy clusters. Indeed, the subhalo model SL17 —-(STREF et al. 2017) – which is at the core of this thesis, has been built for the MW at $z = 0$ and the total number of subhalo is calibrated on numerical simulations: here we want to pave the way to go beyond these restrictions. In the longer term, the idea would be to provide a generic analytic model of subhalos, complementary to approaches like HIROSHIMA et al. (2018) which would have many possible applications, for instance for the study of the 21cm line and more generally for indirect searches; and which could also apply to DM candidates beside WIMPs. So far, the results presented in Sect. 3.5 are preliminary but the development of the different numerical tools is advanced enough to make a comparison with the literature in Chapter 4 after the SL17 model is introduced.

The first sections of this chapter are devoted to the CDM halo formation history from the primordial fluctuations (Sect. 3.1, Sect. 3.2) to the collapse and virialisation (Sect. 3.3). Then, we introduce the EPS formalism (Sect. 3.4) and discuss merger trees and the subhalo mass function in Sect. 3.5. Eventually, in Sect. 3.6, we connect with Chapter 2 by defining the minimal mass of halos in the CDM paradigm introduced by free-streaming and acoustic damping and by relating it to the DM properties.

3.1 Relativistic theory of perturbations

In the first two sections the linear evolution of the matter density field is detailed with the linearised Einstein's equation at first order. This first part introduces more particularly the main equations and initial conditions.

3.1.1 Notations and gauge choice

Here we present the notations and some features of the relativistic perturbations. However, the aim is simply to introduce and summarise the main results of what is a lengthy derivation. The issues around gauge transformation and Scalar-Vector-Tensor decomposition are thus not mentioned for instance. We assume from the start that it is possible to work in the conformal Newtonian gauge with the metric

$$\mathrm{d}s^2 = a^2(\eta)\left[(1+2\psi)\mathrm{d}\eta^2 - (1-2\phi)\delta_{ij}\mathrm{d}x^i\mathrm{d}x^j\right] \tag{3.1}$$

and where the parameters ψ and ϕ represent, in the appropriate limit, the classical Newtonian potential. We denote by η the conformal time. For a complete treatment of perturbation theory in general relativity see the reviews and books Green et al. (2005), Mo et al. (2010), Knobel (2012), and Baumann (a, b). The metric tensor is written $g_{\mu\nu} = \overline{g}_{\mu\nu} + \delta g_{\mu\nu}$ where $\overline{g}_{\mu\nu}$ corresponds to the homogeneous and isotropic FLRW metric introduced in Sect. 2.1.2. More generally, the inhomogeneous quantities are distinguished from the homogeneous ones by putting a bar on top of the latter: they are referred to as the background values. The associated Christoffel symbols can be found in App. C.1. We have seen that the stress-energy tensor for a perfect fluid in a homogeneous and isotropic universe can be written, with $\overline{\rho}$ the homogeneous energy density and $\overline{P}$ the homogeneous pressure,

$$\overline{T}^{\mu}{}_{\nu} = (\overline{\rho} + \overline{P})\overline{u}^{\mu}\overline{u}_{\nu} - \overline{P}\delta^{\mu}_{\nu}\,. \tag{3.2}$$

In contrast, the full stress energy tensor is denoted

$$T^{\mu}{}_{\nu} = \overline{T}^{\mu}{}_{\nu} + \delta T^{\mu}{}_{\nu} = (\rho + P)u^{\mu}u_{\nu} - P\delta^{\mu}_{\nu} - \Pi^{\mu}{}_{\nu} \tag{3.3}$$

with $\rho = \overline{\rho} + \delta\rho$, $P = \overline{P} + \delta P$, $u_\mu = \overline{u}_\mu + \delta u_\mu$. The last term, $\Pi^{\mu}{}_{\nu}$, is the traceless anisotropic 4-tensor and it satisfies $\Pi^{i}{}_{j} = -T^{i}{}_{j} + \delta^{i}_{j}T^{k}{}_{k}/3$, $\Pi^{0}{}_{0} = 0$ and $\Pi^{0}{}_{i} = 0$. Its non zero components, $\Pi^{i}{}_{j}$ form a 3-tensor (*i.e.* it transforms as a tensor in a 3D manifold). Using that $\overline{g}_{\mu\nu}\overline{u}^{\mu}\overline{u}^{\nu} = g_{\mu\nu}u^{\mu}u^{\nu} = 1$ yields $\delta u^0 = -a^{-1}\psi$. The comoving (or coordinate) velocity v^i is given such that $\delta u^i \equiv v^i/a$ with $v^i = \mathrm{d}x^i/\mathrm{d}\eta$. At first order,

$$u^{\mu} = a^{-1}\left(1-\psi, v^i\right) \quad \text{and} \quad u_{\mu} = a\left(1+\psi, -v_i\right) \tag{3.4}$$

and these two expressions can be used to express the stress-energy tensor

$$T^{i}{}_{j} = \begin{pmatrix} \overline{\rho} + \delta\rho & (\overline{\rho} + \overline{P})v^i \\ -(\overline{\rho} + \overline{P})v_j & -(\overline{P} + \delta P)\delta^{i}_{j} - \Pi^{i}{}_{j} \end{pmatrix}. \tag{3.5}$$

Eventually we introduce both the density contrast δ and the comoving gauge density contrast Δ with the following definitions

$$\overline{\rho}\delta \equiv \rho \quad \text{and} \quad \overline{\rho}\Delta \equiv \delta\rho + \overline{\rho}'v = \delta\rho - 3\overline{\rho}\mathcal{H}(1+w)v\,, \tag{3.6}$$

where v is defined so that $v_i = \partial_i v$. Moreover, $w = \overline{P}/\overline{\rho}$ is the equation of state and the second equality for Δ is obtained using the continuity equation at the zero-th order

of perturbation theory, given in Eq. (2.20).

Now that all the key quantities have been defined we can derive the equations that they satisfy. However, let us first discuss shortly some more notational intricacies. This next part is not of crucial importance to understand structure formation. However it gives a better insight into the equations and the way they are derived.

3.1.2 Intermezzo: a few words on geometry and Fourier space

Following BAUMANN (b), it is possible to rewrite the tensors with respect to the orthonormal frame defined by the tetrad

$$e_0^\mu = a^{-1}(1-\psi)\delta_0^\mu, \quad e_i^\mu = a^{-1}(1+\phi)\delta_i^\mu \tag{3.7}$$

that satisfies $g_{\mu\nu}e_\alpha^\mu e_\beta^\mu = \eta_{\alpha\beta}$ where $\eta_{\alpha\beta}$ is the usual Minkowski metric. These vectors have been chosen as the perturbed component of velocity of a co-moving observer at rest. Tensor components defined in that new frame are identified by a hat on their indices, *e.g.* $\hat{\mu}$. For a given (2, 0) tensor J for instance, its components satisfy $J^{\mu\nu} = J^{\hat{\alpha}\hat{\beta}}e_{\hat{\alpha}}^\mu e_{\hat{\beta}}^\nu$. Let us consider δq^i a 3-vector that is an order 1 quantity, then

$$\delta q^i = \delta q^{\hat{\alpha}} e_{\hat{\alpha}}^i = a^{-1}\delta q^{\hat{i}} \quad \text{and} \quad \delta q_{\hat{i}} = a^{-1}\delta q_i\,. \tag{3.8}$$

In order to simplify the problem, for 3-vectors and 3-tensors that have no time components such as Π_{ij} and v_i, it is common to work in this new frame. However, for simplicity we drop the hat notation, keeping in mind that it should be here. It amounts to say that we reduce the problem to the Minkowski metric. For the comoving velocity and symmetric, traceless 3-tensors, which are order 1 quantities, one simply scales out the expansion rate by doing so.

Another way of reformulating the same idea, following KNOBEL (2012), is to directly scale out the expansion rate in the spatial coordinates so that the metric reduces to $h_{ij} = a^{-2}g_{ij}$ (not Minkowski at first order). Then, similarly to above, for any order 1 quantity δq it is possible to write $h_{ij}\delta q = \bar{h}_{ij}\delta q = \delta_{ij}\delta q$ and there is no difference between lower and upper indices. In the following we work with the Laplace operator of the velocity that is therefore defined as $\theta \equiv \nabla^2 v = \delta^{il}\partial_i v_l = \partial_i v^i$.

Eventually, let us introduce the Fourier transform. We define in the 3D-space, with $\mathbf{k}$ the co-moving Fourier mode,

$$\delta q(\mathbf{k}) = \int \delta q(\mathbf{x}) e^{-i\mathbf{k}\mathbf{x}}\sqrt{h}\,\mathrm{d}^3\mathbf{x}\,. \tag{3.9}$$

It can be shown that $\sqrt{h} = 1 + \mathrm{Tr}(\delta h)/2$ at first order, with the decomposition $h = \mathbf{1} + \delta h$. Therefore, the Fourier transform of order 1 quantities can simply be expressed as the usual Fourier transform in 3D Euclidean space with co-moving Fourier modes

$$\delta q(\mathbf{k}) = \int \delta q(\mathbf{x}) e^{-i\mathbf{k}\mathbf{x}}\,\mathrm{d}^3\mathbf{x} \quad \text{and} \quad \delta q(\mathbf{x}) = \frac{1}{(2\pi)^3}\int \delta q(\mathbf{k}) e^{i\mathbf{k}\mathbf{x}}\,\mathrm{d}^3\mathbf{k} \tag{3.10}$$

3.1.3 First order equations

In order to set a realistic framework, let us assume that the Universe is filled with different species that are supposed to interact only gravitationally between themselves. All quantities related to a given species called a are labelled by the same

letter (*e.g.* $\delta_a, \theta_a, \ldots$). Because the total stress-energy tensor is given by a sum of the different components

$$T^{\mu\nu} = \sum_a T_a^{\mu\nu} \tag{3.11}$$

and because this equality has to be valid at all orders, the global density, the pressure and the stress-anisotropy tensor are also given by a simple sum over all the species

$$\overline{\rho} = \sum_a \overline{\rho}_a, \quad \overline{P} = \sum_a \overline{P}_a, \quad \delta\rho = \sum_a \delta\rho_a, \quad \delta P = \sum_a \delta P_a, \quad \Pi^{ij} = \sum_a \Pi_a^{ij}\,. \tag{3.12}$$

This equation holds for $(\overline{\rho} + \overline{P})\theta$ - as a direct consequence of the sum of the stress anisotropy tensor. Therefore one can write as well,

$$(\overline{\rho} + \overline{P})\theta = \sum_a (\overline{\rho}_a + \overline{P}_a)\theta_a\,. \tag{3.13}$$

The continuity and Euler equations come from the conservation of all the stress-energy tensors $\nabla_\mu T_a^{\mu\nu} = 0$ (as we assume that different species interact only gravitationally between themselves). Using the 0^{th} component of this expression we get the continuity equation

$$\delta_a' + (1+w_a)(\theta_a - 3\phi') = 3\mathcal{H}\left(w_a - \frac{\delta P_a}{\delta\rho_a}\right)\delta_a \tag{3.14}$$

with the definition of the matter density contrast $\delta_a \equiv \delta\rho_a/\overline{\rho}_a$. We recall that the prime notation represents the derivative with respect to the conformal time η. The i^{th} components give the Euler equation (the generalisation in general relativity of the usual Euler equation of hydrodynamics)

$$v_{a,i}' + \mathcal{H}v_{a,i} - 3\mathcal{H}\frac{\overline{P}_a'}{\overline{\rho}_a'}v_{a,i} = -\frac{\partial_i \delta P_a}{\overline{\rho}_a(1+w_a)} - \partial_i\psi - \frac{\partial_j \Pi_{a,i}^j}{\overline{\rho}_a(1+w_a)}\,. \tag{3.15}$$

Traditionally these three equations are gathered in a single one which is written in terms of the variable θ_a. To this end, one simply needs to apply the operator $\delta^{il}\partial_l$ on both sides of Eq. (3.15). This gives

$$\theta_a' + \mathcal{H}\left(1 - 3\frac{\overline{P}'}{\overline{\rho}_a'}\right)\theta_a = -\frac{\nabla^2\delta P_a}{\overline{\rho}(1+w_a)} - \nabla^2\psi - \frac{\delta^{il}\partial_l\partial_j\Pi_{a,i}^j}{\overline{\rho}_a(1+w_a)}\,. \tag{3.16}$$

Let us now introduce the anisotropic pressure σ[1] as

$$\Pi_{a,ij} = \left(\overline{\rho}_a + \overline{P}_a\right)\left(\partial_i\partial_j - \frac{1}{3}\delta_{ij}\nabla^2\right)\sigma_a\,. \tag{3.18}$$

In Fourier space the following implicit definition can be inverted in order to write σ_a in terms of Π_a, more precisely,

$$\frac{3}{2}\left[\frac{1}{3}\delta^{ij} - \frac{k^i k^j}{k^2}\right]\left[\frac{1}{3}\delta_{ij} - \frac{k_i k_j}{k^2}\right] = 1 \quad \text{yields} \quad \sigma_a = \frac{3}{2}\left[\frac{1}{3}\delta^{ij} - \frac{k^i k^j}{k^2}\right]\frac{\Pi_{a,ij}}{\overline{\rho}_a + \overline{P}_a}\,. \tag{3.19}$$

[1]This quantity is defined in (Baumann b). In Green et al. (2005) the notation π is used, however in order to avoid confusion with the mathematical number we will not work with this convention. Eventually (Mo et al. 2010) have a slightly different definition denoted Π. Moreover, notice that for this equation the total anisotropic pressure σ must satisfy

$$(\overline{\rho} + \overline{P})\sigma = \sum_a (\overline{\rho}_a + \overline{P}_a)\sigma_a\,. \tag{3.17}$$

Massaging Eq. (3.16) with this new notation, in Fourier space, one can write the Fourier transformed Euler equation as

$$\theta_a' + \mathcal{H}\left(1 - 3\frac{\overline{P}_a'}{\overline{\rho}_a'}\right)\theta_a = \frac{k^2\delta P_a}{\overline{\rho}_a(1+w_a)} + k^2\psi - \frac{2}{3}k^2\sigma_a\,. \tag{3.20}$$

The continuity and Euler equations tell how the content of the Universe evolves with time, however, they do not provide information on the evolution of space-time itself (*i.e.* on the evolution of the potentials ψ and ϕ in this specific case). This, in turn, is given by the perturbed Einstein equation. At first order the component of Einstein's tensor can be decomposed as $G_{\mu\nu} = \overline{G}_{\mu\nu} + \delta G_{\mu\nu}$. The 0^{th} order equation $\overline{G}_{\mu\nu} = 8\pi G_{\text{N}}\overline{T}_{\mu\nu}$ must still hold and it gives the Friedmann equations. The first order reduces to $\delta G_{\mu\nu} = 8\pi G_{\text{N}}\delta T_{\mu\nu}$. See App. C.1 for the details of the different components of this tensorial equation. They can be summarised as

$$\begin{aligned}
&\phi - \psi = 12\pi G_{\text{N}}a^2(\overline{\rho} + \overline{P})\sigma \quad \text{(spatial traceless)}\\
&\phi' + \mathcal{H}\psi = 4\pi G_{\text{N}}a^2(\overline{\rho} + \overline{P})\theta/k^2 \quad \text{(0-}i^{\text{th}}\text{ component)}\\
&k^2\phi = -4\pi G_{\text{N}}a^2\overline{\rho}\Delta \quad \text{(Poisson)}\\
&\phi'' + (2\mathcal{H}' + \mathcal{H}^2)\psi + \mathcal{H}(\psi' + 2\phi') = 4\pi G_{\text{N}}a^2\left[\delta P + (\overline{\rho} + \overline{P})\nabla^2\sigma\right] \quad \text{(spatial trace)}\,.
\end{aligned} \tag{3.21}$$

All the important equations have now been introduced. They form a system that cannot be solved analytically without making some approximations. In the next part we say a few words about the initial conditions and we subsequently focus on the evolution of the perturbations.

3.2 Evolution of the perturbations

3.2.1 Initial conditions

Initial conditions are imposed by the inflation model. Let us follow LESGOURGUES et al. (2013) and look at the easiest deviation that can be considered from the homogeneous background and that is predicted in the most common scenarios. It consists in assuming that there is a local time shift $\delta\eta(\mathbf{x})$ of order 1 in perturbation theory between the quantities of interest and their background value, in particular,

$$\begin{aligned}
\rho_a(\eta,\mathbf{x}) &= \overline{\rho}_a(\eta + \delta\eta(\mathbf{x}),\mathbf{x}) \simeq \overline{\rho}_a(\eta,\mathbf{x}) + \overline{\rho}_a'(\eta,\mathbf{x})\delta\eta(\mathbf{x})\\
P_a(\eta,\mathbf{x}) &= \overline{P}_a(\eta + \delta\eta(\mathbf{x}),\mathbf{x}) \simeq \overline{P}_a(\eta,\mathbf{x}) + \overline{P}_a'(\eta,\mathbf{x})\delta\eta(\mathbf{x})\,.
\end{aligned} \tag{3.22}$$

which imposes the initial condition

$$\delta\rho_a = -3\mathcal{H}(\overline{\rho}_a + \overline{P}_a)\delta\eta(\mathbf{x})\,. \tag{3.23}$$

If we write the pressure as a function of the energy density ρ_a and S_a the entropy, we can develop $P_a = P_a(\rho_a, S_a)$ as

$$P_a(\rho_a, S_a) = P_a(\overline{\rho}_a, \overline{S}_a) + c_a^2\delta\rho_a + \tau_a\delta S_a + \mathcal{O}(\delta\rho_a^2 + \delta S_a^2) \tag{3.24}$$

with the definition of the sound speed

$$c_a^2 \equiv \left.\frac{\partial P_a}{\partial\rho_a}\right|_{S_a} \quad \text{and with} \quad \tau_a \equiv \left.\frac{\partial P_a}{\partial S_a}\right|_{\rho_a}\,. \tag{3.25}$$

Therefore, combining Eq. (3.22) and Eq. (3.23) gives

$$\delta P_a = \frac{\overline{P}'_a}{\overline{\rho}'_a}\delta\rho_a + \mathcal{O}\left(\delta\rho_a^2\right) \tag{3.26}$$

and the subsequent identifications $c_a^2 = \overline{P}'_a/\overline{\rho}'_a$ and $\delta S_a = 0$. Perturbations are thus called isentropic. Moreover, when the equation of state is $w_a = \text{cst.}$ for every species, it can then be identified with the sound speed. Indeed, differentiating w_a with respect to the conformal time yields

$$w'_a = 0 = -\frac{\overline{\rho}'_a}{\overline{\rho}_a}\left[\frac{\overline{P}_a}{\overline{\rho}_a} - \frac{\overline{P}'_a}{\overline{\rho}'_a}\right] \quad \text{and} \quad w_a = \frac{\overline{P}'_a}{\overline{\rho}'_a}\,, \tag{3.27}$$

which leads to $w_a = c_a^2$. Besides, it is also possible to define an effective sound speed for the entire fluid as a weighted sum of the sound speeds for each species

$$c_s^2 \equiv \sum_a c_a^2 \frac{\overline{\rho}_a + \overline{P}_a}{\overline{\rho} + \overline{P}}\,. \tag{3.28}$$

In the context of isentropic perturbations it becomes

$$c_s^2 = \frac{\sum_a c_a^2(\overline{\rho}_a + \overline{P}_a)}{\sum_a(\overline{\rho}_a + \overline{P}_a)} = \frac{\sum_a c_a^2\delta\rho_a\delta\eta(\mathbf{x})}{\sum_a \delta\rho_a\delta\eta(\mathbf{x})} = \frac{\sum_a \delta P_a}{\sum_a \delta\rho_a} = \frac{\delta P}{\delta\rho} \tag{3.29}$$

where we used Eq. (3.23). However notice that even though $c_a^2 = w_a$ for every species, $w \equiv \overline{P}/\overline{\rho} \neq c_s^2$ in general – if there are more than one species. Now, to see how these initial conditions can be translated into constrains on the unknown variables $(\delta\rho_a, \theta_a, \dots)$ of our system of equations, one can define a non adiabatic pressure fluctuation

$$\begin{aligned}\delta P_{\text{nad}} &\equiv \delta P - c_s^2\delta\rho = \sum_a c_a^2\delta\rho_a - \sum_a c_a^2\frac{\overline{\rho}_a + \overline{P}_a}{\overline{\rho} + \overline{P}}\delta\rho \\ &= \sum_a c_a^2\left(\overline{\rho}_a + \overline{P}_a\right)\left[\frac{\delta\rho_a}{\overline{\rho}_a + \overline{P}_a} - \frac{\delta\rho}{\overline{\rho} + \overline{P}}\right].\end{aligned} \tag{3.30}$$

Remark that in the case of isentropic perturbation one has initially $\delta P_{\text{nad}} = \tau\delta S = 0$[2]. However, the initial condition does not impose that δP_{nad} remains equal to zero as time goes. When δP_{nad} is initially zero and remains so we say that perturbations are isentropic and their evolution is adiabatic.

If we consider a Universe made of two components, radiation labelled by the letter r and matter labelled by the letter m, then (using the fact that $w_{\text{r}} = 1/3$, $w_{\text{m}} = 0$ and $c_{\text{r}}^2 = w_{\text{r}}$) it yields the expression of the homogeneous energy density and pressure

$$\begin{aligned}\overline{\rho} &= \overline{\rho}_{\text{r}} + \overline{\rho}_{\text{m}} = \frac{\overline{\rho}_{\text{eq}}}{2}\left[\left(\frac{a_{\text{eq}}}{a}\right)^3 + \left(\frac{a_{\text{eq}}}{a}\right)^4\right] \\ \overline{P} &= \overline{P}_{\text{r}} = \frac{1}{3}\overline{\rho}_{\text{r}} = \frac{1}{3}\frac{\overline{\rho}_{\text{eq}}}{2}\left(\frac{a_{\text{eq}}}{a}\right)^4\end{aligned} \tag{3.31}$$

with the effective sound speed being

$$c_s^2 = c_{\text{r}}^2\frac{1 + w_{\text{r}}}{1 + w_{\text{r}} + y} = \frac{1/3}{1 + 3y/4} \tag{3.32}$$

[2]This last equation is similar to the definition of the dimensionless entropy in Green et al. (2005).

and where $y \equiv \overline{\rho}_{\rm m}/\overline{\rho}_{\rm r} = a/a_{\rm eq}$. Similarly, the non adiabatic pressure fluctuation is

$$\delta P_{\rm nad} = c_{\rm r}^2 \frac{\overline{\rho}_{\rm m}}{\overline{\rho}+\overline{P}}\left[\frac{\delta\rho_r}{\overline{\rho}_{\rm r}+\overline{P}_{\rm r}} - \frac{\delta\rho_{\rm m}}{\overline{\rho}_{\rm m}}\right] = \frac{y/4}{1+3y/4}\left[\frac{3}{4}\frac{\delta\rho_{\rm r}}{\overline{\rho}_{\rm r}} - \frac{\delta\rho_{\rm m}}{\overline{\rho}_{\rm m}}\right]. \tag{3.33}$$

In the end, having isotropic initial fluctuations with adiabatic evolution implies the relation between the radiation and matter density contrasts $3\delta\rho_r/\overline{\rho}_{\rm r} = 4\delta\rho_{\rm m}/\overline{\rho}_{\rm m}$.

3.2.2 Evolution of the potentials

Henceforth we continue the analysis in the case of an anisotropic-free fluid. One has, from the spatial traceless component of Einstein's equation, the equality $\psi = \phi$. This quantity is thus referred to as *the* gravitational potential. In order to study its evolution one can use Poisson's equation in terms of the density contrast δ Eq. (C.11) and a combination of the other linearised Einstein equations [Eq. (C.20), Eq. (C.10) and Eq. (C.3)] under the form

$$k^2\phi + 3\mathcal{H}(\phi' + \mathcal{H}\phi) = -\frac{3}{2}\mathcal{H}^2\delta \quad \text{and} \quad \phi'' + 3(1+w)\mathcal{H}\phi' + wk^2\phi = 0\,. \tag{3.34}$$

with the approximation $c_s^2 \sim w$ – even though that does not strictly hold when there are more than one species. In the super-Hubble limit, $k \ll \mathcal{H}$, the terms proportional to $\mathcal{H}^2$ are dominant in Poisson's equation and therefore $\delta \sim -2\phi$. Moreover the right hand side equation shows that supper-Hubble modes of ϕ are a constant that only depends on the value of w. Consequently these modes have a fixed value $\phi_{\rm RD}$ in the radiation dominated era, where $w \simeq w_{\rm r} = 1/3$, and another fixed but different value $\phi_{\rm MD}$ in the matter-dominated era where, $w \simeq w_{\rm m} = 0$. With the assumption of adiabatic perturbations $\delta_{\rm r} = 4\delta_{\rm m}/3$ in the early radiation dominated era, thus, on super Hubble scales, $\delta_{\rm r} \simeq -2\phi_{\rm RD}$ and $\delta_{\rm m} \simeq -3\phi_{\rm RD}/2$.

One can then relate $\phi_{\rm RD}$ to $\phi_{\rm MD}$ thanks to the comoving curvature perturbation. In the Newtonian gauge the latter takes the form

$$\mathcal{R} \equiv -\phi + \mathcal{H}v\,. \tag{3.35}$$

A straightforward computation made in BAUMANN (a) and reproduced in App. C.2 shows that for isentropic initial conditions with an adiabatic evolution and a zero anisotropic stress-energy tensor, the derivative of $\mathcal{R}$ reduces to

$$\mathcal{R}' = -3\frac{k^2}{\mathcal{H}}\frac{\overline{\rho}}{\overline{\rho}+\overline{P}}(\mathcal{R} - \mathcal{H}v) \quad \text{and gives the scaling} \quad \frac{{\rm d}\ln\mathcal{R}}{{\rm d}\ln a} \sim \left(\frac{k}{\mathcal{H}}\right)^2. \tag{3.36}$$

Therefore, for the super-horizon modes, the curvature perturbation is a constant of the scale factor. This property is important since inflation has increased the value of $\mathcal{H}$ so much that, initially, all modes are assumed to be super-Hubble. Consequently, all modes start with an initially constant $\mathcal{R}$ before they re-enter the horizon. Moreover, massaging $\mathcal{R}$ as a function of the potential and the equation of state only and using its conservation on super-Hubble scales yields

$$\mathcal{R} = -\left(\frac{5+3w_{\rm r}}{3+3w_{\rm r}}\right)\phi_{\rm RD} = -\left(\frac{5+3w_{\rm m}}{3+3w_{\rm m}}\right)\phi_{\rm MD}\,. \tag{3.37}$$

Plugging the values $w_{\rm r} = 1/3$ and $w_{\rm m} = 0$ yields $\phi_{\rm MD} = (9/10)\phi_{\rm RD}$. For sub-Hubble scales, $k \gg \mathcal{H}$, computations are more involved. Let us just mention that in the

radiation era ϕ decreases and that its *growing* mode becomes constant in the matter-dominated era. The important message of this section is that on super-Hubble scales the potential is frozen and so are $\delta_{\rm r}$ and $\delta_{\rm m}$ with it. In the following we focus on the evolution of the DM perturbations.

3.2.3 Evolution of the DM perturbations

We assume that the Universe is only made of matter, still labelled here by the generic letter m, and radiation r. For the evolution of perturbations in the radiation dominated era it is necessary to study the evolution of $\theta_{\rm m}$ and $\delta_{\rm m}$ simultaneously with the continuity and Euler equations

$$\delta'_{\rm m} + \theta_{\rm m} - 3\phi' = 0 \quad \text{and} \quad \theta'_{\rm m} + \mathcal{H}\theta_{\rm m} = k^2\phi \tag{3.38}$$

In practice, combining these two equations yields

$$\delta''_{\rm m} + \mathcal{H}\delta_{\rm m} = -k^2\phi + 3\mathcal{H}\phi' + 3\phi'' \tag{3.39}$$

and, in the sub-Hubble limit, only the first term of the right hand side is important. Moreover it is possible to neglect the radiation contribution to the potential (S. Weinberg 2002) and consider that it is only sourced by matter. Therefore, thanks to the Poisson equation, the evolution of $\delta_{\rm m}$ is driven by

$$\delta''_{\rm m} + \mathcal{H}\delta'_{\rm m} = 4\pi G_{\rm N} a^2 \overline{\rho}_{\rm m} \Delta_{\rm m} \,. \tag{3.40}$$

Now, as shown in App. C.1, Δ and δ are related by the equation $\Delta = \delta + 2\phi + 2\phi'/\mathcal{H}$. Because $\phi \propto \mathcal{H}^2\Delta/k^2$ by Poisson's equation, for sub-Hubble scales it yields $\Delta \simeq \delta$. Thus, the equation on $\delta_{\rm m}$ can be written only in terms of its derivatives. By a change of variable $\eta \to y = a/a_{\rm eq}$ it transforms into the Mezáros equation

$$\frac{{\rm d}^2\delta_{\rm m}}{{\rm d}y^2} + \frac{2+3y}{2y(1+y)}\frac{{\rm d}\delta_{\rm m}}{{\rm d}y} - \frac{3}{2y(1+y)}\delta_{\rm m} = 0 \tag{3.41}$$

whose growing mode solution for the radiation dominated era goes as $\delta_{\rm m} \propto \ln y \propto \ln a$. Therefore DM perturbations grow during DM on sub-Hubble scales, however the growth is logarithmic and consequently rather slow.

In the matter-dominated era, Poisson's equation yields

$$\Delta_{\rm m} \sim \delta_{\rm m} = \frac{-k^2\phi}{4\pi G_{\rm N} a^2 \overline{\rho}_{\rm m}} \,. \tag{3.42}$$

As the *growing* mode of the potential is a constant of time in the matter-dominated era and in the sub-Hubble limit, this shows that the growing mode of the DM perturbation follows $\delta_{\rm m} \propto a$. In more details, when taking into account dark energy it is possible to use Eq. (3.40) that we introduced for the radiation dominated era[3].

[3]This equation can also be found often written in terms of the cosmic time t instead of the conformal time η. Going from one to the other is straightforward using the relation $a{\rm d}\eta = {\rm d}t$ one finds

$$\delta''_{\rm m} = \frac{{\rm d}^2\delta_{\rm m}}{{\rm d}\eta^2} = a\frac{\rm d}{{\rm d}t}\left(a\frac{{\rm d}\delta_{\rm m}}{{\rm d}t}\right) = a^2\frac{{\rm d}^2\delta_{\rm m}}{{\rm d}t^2} + a^2 H\frac{{\rm d}\delta_{\rm m}}{{\rm d}t}$$

which gives a similar equation with a factor of 2 in front of the Hubble drag term,

$$\ddot{\delta}_m + 2H\dot{\delta}_m = 4\pi G_{\rm N}\overline{\rho}\Delta_{\rm m} \,.$$

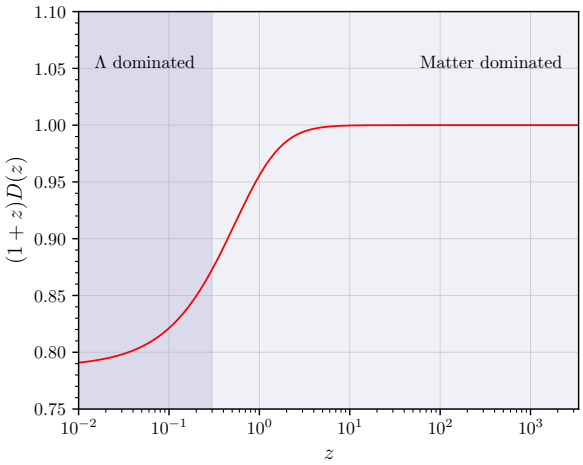

Figure 3.1 – Evolution of the growth factor with the redshift in the matter and Λ dominated era for the Planck 2018 cosmology Planck18. Here we assume $\Omega_{\rm r}(z) = 0$ which should not hold down to the equivalence between matter and radiation.

The growing mode solution is usually parametrised by $\delta_{\rm m} \propto D(t)$ where D is called the growth function and satisfies

$$D(t) \equiv \frac{5}{2}\Omega_{\rm m,0}\frac{H(t)}{H_0}\int_0^t \frac{H_0^3 {\rm d}t'}{a^2(t')H^2(t')} \quad \text{and} \quad \ddot{D}(t) + 2H\dot{D}(t) = 4\pi G_{\rm N} a^2 \overline{\rho}_{\rm m} D(t)\,. \tag{3.43}$$

It can be approximated by the following fitting formula given in CARROLL et al. (1992)

$$D(z) \simeq \frac{5}{2(1+z)}\Omega_{\rm m}(z)\left\{\Omega_{\rm m}^{4/7}(z) - \Omega_\Lambda(z) + \left[1+\frac{\Omega_{\rm m}(z)}{2}\right]\left[1+\frac{\Omega_\Lambda(z)}{70}\right]\right\}^{-1}, \tag{3.44}$$

assuming no radiation ($\Omega_{\rm r}(z) \sim 0$). The evolution of $(1+z)D(z)$ is represented in Fig. 3.1 for the Planck cosmology. Let us point out that, for z in the matter dominated era, the abundances are such that $\Omega_{\rm m} \sim 1$ and $\Omega_\Lambda \sim 0$ so that the growth factor satisfies $(1+z)D(z) \to 1$. The conclusion is, as expected, the same as the simple estimation from Eq. (3.42). However, when Ω_Λ dominates the increase of $D(z)$ drops and perturbation stop growing, they are frozen by the cosmological constant.

In summary, DM perturbations entering the horizon grow as $\ln a$ during the radiation-dominated era, as a during the matter-dominated era and stop growing in a dark energy-dominated era. As over-dense regions get denser and denser they develop a gravitational instability that prompts their collapse and triggers the formation of halos. This is the subject of the next section.

3.3 Collapse model and halo formation mechanism

In this section we describe the process of over-densities collapsing to form halos. This is non-linear physics and, in general, our understanding of this process relies mostly on cosmological simulations. However, provided that several simplifications are made, it is possible to extract analytical solutions (S. WEINBERG 1972; KNOBEL 2012).

3.3.1 Non-linear spherical collapse

In this section we consider an isolated spherical over-dense region of size $R(t)$ at time t that has density $\rho(t) = \overline{\rho}(t) + \delta\rho(t)$ where $\overline{\rho}(t)$ stands as the homogeneous background density. Because over-densities are essentially frozen during the radiation domination era; as shown in the previous section, we study its evolution during a matter-dominated Universe when the cosmological constant is negligible. The matter is assumed to be homogeneously distributed inside the over-dense region and, being isolated during all its evolution, it conserves a constant mass M. Following Mo et al. (2010) we assume that the different shells forming the spherical region never cross. Then a particle at radius R from the centre on a radial trajectory has energy per units of mass

$$E = \frac{1}{2}\left(\frac{\mathrm{d}R}{\mathrm{d}t}\right)^2 - \frac{G_\mathrm{N}M}{R}\,. \tag{3.45}$$

Because this energy is required to be negative to have a bound object collapsing we introduce $\mathcal{E} = -E > 0$. Moreover, during the matter domination era, we know that the background density evolves as

$$\overline{\rho}(t) = \frac{1}{6\pi G_\mathrm{N} t^2}\,. \tag{3.46}$$

Then, it is convenient to introduce a pseudo-conformal time τ that is defined by the differential equality $\mathrm{d}t = R/\sqrt{2\mathcal{E}}\,\mathrm{d}\tau$. We separate variables so that between two instants, corresponding to τ and τ_i where the corresponding radii are R and R_i, Eq. (3.45) yields

$$\tau - \tau_i = \int_{R_i}^{R} \frac{\mathrm{d}R'}{\sqrt{G_N M R'/\mathcal{E} - R'^2}}\,. \tag{3.47}$$

Note that we choose the positive square root only in order to have an increasing solution. Furthermore, considering only negative energies restricts solutions to be bounded by $R < G_\mathrm{N}M/\mathcal{E}$. We can solve the above integral by making the change of variable $R \to X = 1 - 2\mathcal{E}R/(G_\mathrm{N}M)$, which yields the simplification

$$\tau - \tau_i = -\int_{X_0}^{X} \frac{\mathrm{d}X'}{1 - X'^2} = \arccos\left(1 - \frac{2\mathcal{E}R}{G_\mathrm{N}M}\right) - \arccos\left(1 - \frac{2\mathcal{E}R_i}{G_\mathrm{N}M}\right)\,. \tag{3.48}$$

In addition, we show in App. C.3 that in a matter-dominated Universe at an initial time t_i, the argument of the second arccosine is negligible since $2\mathcal{E}R_i/(G_\mathrm{N}M) \sim 4\delta_i/9 \ll 1$ – a precise treatment of the initial conditions of the overdensity is given in Mo et al. (2010) – chapter 5.1. Thus, the final solution in terms of τ is given by

$$R(\tau) = \frac{G_\mathrm{N}M}{2\mathcal{E}}(1 - \cos(\tau - \tau_i)) \quad \text{and} \quad t(\tau) = \frac{G_\mathrm{N}M}{(2\mathcal{E})^{3/2}}(\tau - \tau_i - \sin(\tau - \tau_i))\,. \tag{3.49}$$

Without loss of generality we can further redefine $\tau - \tau_i \to \tau$. Therefore, we can now give an expression of the overdensity δ as a function of the conformal time τ. Using Eq. (3.49), Eq. (3.46) and the expression of the mass we get

$$\delta(\tau) = \frac{\delta\rho(\tau)}{\overline{\rho}(\tau)} = \frac{9}{2}G_\mathrm{N}M\frac{t^2(\tau)}{R^3(\tau)} - 1 = \frac{9}{2}\frac{[\tau - \sin\tau]^2}{[1 - \cos\tau]^3} - 1 \tag{3.50}$$

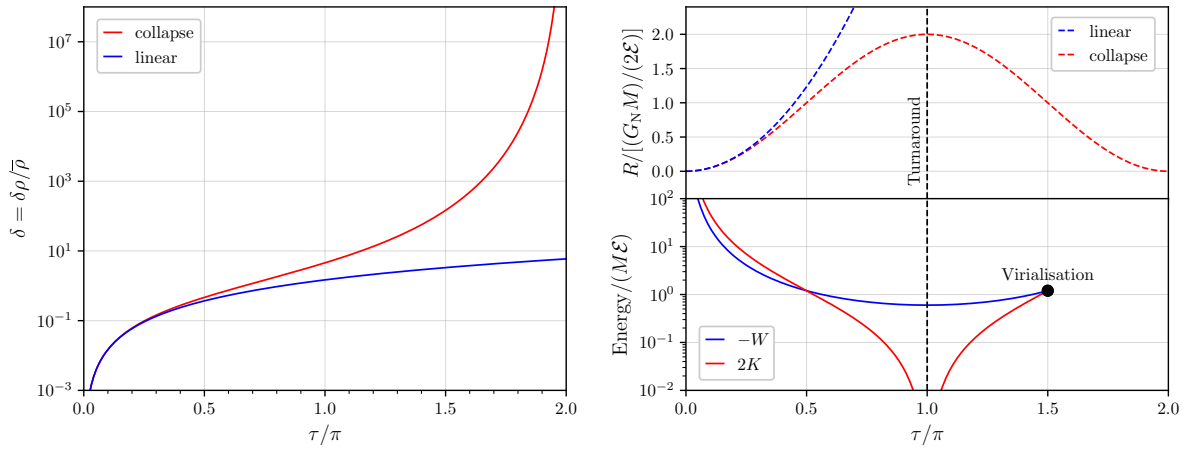

Figure 3.2 – Left panel: Evolution of the overdensity with τ in the spherical collapse model and from the linear approximation. **Right panel:** Evolution of the radius R and of the gravitational and kinetic energy with τ. After turnaround at $\tau = \pi$, virialisation occurs when the virial relation is satisfied ($2K + W = 0$).

When developing in series this expression around $\tau = 0$, it yields

$$\delta(\tau) \sim \frac{3}{20}\tau^2 \sim \frac{3\mathcal{E}}{10}\left(\frac{6t}{G_N M}\right)^{2/3} . \tag{3.51}$$

Besides, δ increases from 0 to infinity when τ goes from 0 to 2π: the overdensity diverges. In the same time the radius $R(\tau)$ increases from $\tau = 0$ to $\tau = \pi$ with a maximum of $R(\pi) = G_N M/\mathcal{E}$ and then decreases back to 0. The size of the region grows and then shrinks, the transition between these two phases is called the turnaround. The evolution of δ and R is represented in Fig. 3.2.

Before going further, let us mention that this computation is also often made by considering a spherical homogeneous sphere in a fully general relativistic treatment and its evolution is examined by using Friedman equations. Indeed according to the Birkhoff theorem, the background and the region evolve independently. Moreover, the over-dense region is an independent isotropic and homogeneous region that has a positive curvature. Its geometry can then be described using the FLRW metric in the same way we do for the Universe with $K = 1$. We introduce a scale factor $\mathcal{A}$ associated with it. If $\mathcal{A}(t_0) = 1$ is set as a definition, then it satisfies $R(t) = \mathcal{A}(t)R_0$. Using Friedmann's equations, the evolution of the scale factor is

$$\left(\frac{\dot{\mathcal{A}}}{\mathcal{A}}\right)^2 = \frac{8\pi G_N}{3}\rho - \frac{1}{R_0^2\mathcal{A}^2} \quad \text{which implies} \quad \left(\frac{\mathrm{d}R}{\mathrm{d}t}\right)^2 = \frac{2G_N M}{R} - 1 \tag{3.52}$$

where where we have used the conservation of the mass M. With this approach we find back the exact same equations when taking $-2E = 1$ *i.e.* by rescaling the time variable in this new FLRW metric. In fact, this does not impact the physical interpretation because the only relevant time is that defining the background evolution, and, irrespective of the time normalisation, because the initial condition is always set by demanding $R = R_i \sim 0$ at initial time $t = t_i$.

3.3.2 Initial kinetic and potential energy of over-densities

The over-dense region starts shrinking when $\tau = \pi$ and the model predicts that it goes back to a singularity when $\tau = 2\pi$. This is, of course, non-physical and would prevent the existence of halos by forming black holes. As matter of fact, after the *turn-around* point, the region virialises and reaches a state of equilibrium before the singularity. According to the virial theorem, a self-gravitating system in steady-state has its potential energy W equal to minus two times its kinetic energy K. It is therefore interesting to search for the radius R at which this condition is satisfied. However, while the potential energy is straightforward to compute, the kinetic energy is not. The idea is thus to compute the initial total energy when the over-density is still in the linear regime and deduce the kinetic energy from its conservation. In the following we follow, in part, a derivation presented in Okoli et al. (2016).

Kinetic energy. The computation first starts with the expression of the initial velocity field for particles inside the region of interest that is still assumed to be spherical, though not necessarily homogeneous in this first part. Consider a non relativistic particle species at *physical* position $\mathbf{r}(t)$. Because of expansion $\mathbf{r}(t) = a(t)\mathbf{x}$ (with $\mathbf{x}$ the comoving coordinate) and the velocity field evolves as $\mathbf{u}(t) = H\mathbf{r} + \mathbf{v}$ where $\mathbf{v} = a(t)\dot{\mathbf{x}}$ is the comoving/peculiar velocity. Using Eq. (3.15) in the non-relativistic limit, with no anisotropy tensor and pressure-less matter, the linearized equation for the peculiar velocity can be re-written under the form

$$\frac{\partial \mathbf{v}}{\partial t} + H\mathbf{v} = -\frac{1}{a}\nabla\Phi(\mathbf{x}, t)\,, \tag{3.53}$$

where $\Phi = \phi + a\ddot{a}\sum_i (x^i)^2/2$. The Poisson equation can then be written $\nabla^2\Phi = 4\pi G_{\rm N}\bar{\rho}a^2\delta$. Therefore, $\Phi(\mathbf{x}, t) = D(t)/a(t)\Phi_i(\mathbf{x})$ since $D(t_i) = a(t_i)$ for t_i a time in the matter-dominated era when the perturbation still has not grown significantly. Written differently, the peculiar velocity satisfies,

$$\frac{\partial(a\mathbf{v})}{\partial t} = -\frac{D(t)}{a(t)}\nabla_{\mathbf{x}}\Phi_i(\mathbf{x}) \tag{3.54}$$

This equation can be solved for $\mathbf{v}$ at time t as

$$\mathbf{v} = -\frac{\nabla_{\mathbf{x}}\Phi_i(\mathbf{x})}{a(t)}\int^t \frac{D(t')}{a(t')}\mathrm{d}t' = -\frac{1}{4\pi G_{\rm N}\bar{\rho}a^2(t)}\dot{D}(t)\nabla_{\mathbf{x}}\Phi_i(\mathbf{x}) \tag{3.55}$$

where we use the differential equation Eq. (3.43) satisfied by the growth function D for the second equality. At the initial time t_i in the matter-dominated era, the Hubble rate satisfies $H_i = \dot{a}(t_i)/a(t_i) = \dot{D}(t_i)/D(t_i)$. Moreover the Friedmann equation gives $H_i^2 = 8\pi G_{\rm N}\bar{\rho}(t_i)/3$, which yields

$$\mathbf{v}_i = -\frac{2}{3H_i}\frac{1}{a(t_i)}\nabla_{\mathbf{x}}\Phi_i(\mathbf{x}) = -\frac{2}{3H_i}\nabla_{\mathbf{r}}\Phi_i(\mathbf{r})\,. \tag{3.56}$$

Therefore the total initial velocity field can be formulated under the simple form

$$\mathbf{u}_i = H_i\mathbf{r} - \frac{2}{3}H_i\nabla_{\mathbf{r}}\Phi_i(\mathbf{r})\,. \tag{3.57}$$

Furthermore, the total kinetic energy of the system at initial time can be written

$$K_i = \frac{1}{2}\int_{\mathcal{V}_i}\rho_i(\mathbf{r})\mathbf{u}_i^2(\mathbf{r})\mathrm{d}^3\mathbf{r} \tag{3.58}$$

where $\mathcal{V}_i$ represents the volume of the over-dense region. Replacing $\mathbf{u}_i$ by its expression, expanding at first order and using the Poisson equation $\nabla_{\mathbf{r}}\Phi_i(\mathbf{r}) = 3H_i^2\delta_i(\mathbf{r})/2$ the kinetic energy becomes

$$\begin{aligned} K_i &= \frac{1}{2}\overline{\rho}_i \int_{\mathcal{V}_i} \left(H_i^2 r^2 + \frac{2}{3} r^2 \nabla_{\mathbf{r}}\Phi_i(\mathbf{r}) - \frac{4}{3}\mathbf{r}.\nabla_{\mathbf{r}}\Phi_i(\mathbf{r}) \right) \mathrm{d}^3\mathbf{r} \\ &= \frac{1}{2}\overline{\rho}_i \int_{\mathcal{V}_i} \left(H_i^2 r^2 + \frac{4}{3} r^2 \nabla_{\mathbf{r}}\Phi_i(\mathbf{r}) \right) \mathrm{d}^3\mathbf{r} - \frac{1}{3}\overline{\rho}_i \oint_{\mathcal{S}_i} r^2 \nabla_{\mathbf{r}}\Phi_i(\mathbf{r}) \mathrm{d}^2\mathbf{s} \end{aligned} \tag{3.59}$$

where $\mathcal{S}_i$ represents the surface area of the region at time t_i. Moreover, as the system is spherical it is possible to introduce an initial radius R_i and then, at first order on the surface area, we have

$$\begin{aligned} \nabla_{\mathbf{r}}\Phi_i(\mathbf{r})|_{\mathcal{S}_i} &= \frac{\mathbf{r}}{r}\frac{G_{\mathrm{N}}\overline{\rho}_i}{R_i} \int_{\mathcal{V}_i} \delta_i(\mathbf{r}) \mathrm{d}^3\mathbf{r} \\ \text{so that} \quad \oint_{\mathcal{S}_i} r^2 \nabla_{\mathbf{r}}\Phi_i(\mathbf{r}) \mathrm{d}^2\mathbf{s} &= 4\pi G_{\mathrm{N}} R_i^2 \overline{\rho}_i \int_{\mathcal{V}_i} \delta_i(\mathbf{r}) \mathrm{d}^3\mathbf{r} \,. \end{aligned} \tag{3.60}$$

Using, once again, the Poisson equation to get rid of the Laplace operator the final expression of the initial kinetic energy for a spherical system at first order becomes

$$K_i = \frac{4\pi G_{\mathrm{N}}}{3}\overline{\rho}_i^2 \int_{\mathcal{V}_i} \left[r^2 + \delta_i(\mathbf{r}) \left(2r^2 - R_i^2 \right) \right] \mathrm{d}^3\mathbf{r} \,. \tag{3.61}$$

Potential energy. The potential energy is much simpler to compute as we do not need the initial velocity of particles to do so. The only important quantity is the density of matter inside the object. The most general expression of the gravitational potential energy is

$$W_i = -\frac{G_{\mathrm{N}}\overline{\rho}_i^2}{2} \iint_{\mathcal{V}_i} \frac{\left[1 + \delta_i(\mathbf{r}_1)\right]\left[1 + \delta_i(\mathbf{r}_2)\right]}{|\mathbf{r}_1 - \mathbf{r}_2|} \mathrm{d}^3\mathbf{r}_1 \mathrm{d}^3\mathbf{r}_2 \,. \tag{3.62}$$

In order to be consistent with the computation of the kinetic energy and slightly simplify this expression we expand it at first order in δ_i. Moreover, using symmetry considerations (invariance under exchange of $\mathbf{r}_1$ and $\mathbf{r}_2$ inside the integral) it can now directly be written under the form

$$W_i = -\frac{4\pi G_{\mathrm{N}}\overline{\rho}_i^2}{3} \int_{\mathcal{V}_i} \left[1 + 2\delta_i(\mathbf{r})\right] \left(\frac{3R_i^2 - r^2}{4} \right) \mathrm{d}^3\mathbf{r} \,. \tag{3.63}$$

3.3.3 Virialisation of an homogeneous sphere

Firstly, we compute the total energy E_{tot} as the sum of the initial kinetic and potential energy. With the previous expressions it is straightforward to show that

$$E_{\mathrm{tot}} = -\frac{10}{3}\pi G_{\mathrm{N}} R_i^5 \overline{\rho}_i^2 \int_{\mathcal{V}_i} \delta_i(\mathbf{r}) \left(1 - \frac{r^2}{R_i^2} \right) \frac{1}{R_i^3} \mathrm{d}^3\mathbf{r} \,. \tag{3.64}$$

In order to keep things simple in this section we come back to the assumption of the non-spherical homogeneous collapse, that is, the over-dense region is homogeneous and of total mass M. Consequently, we can simply write $\delta_i(\mathbf{r}) = \delta_i$ and perform the integral over the entire volume. The total energy is then

$$E_{\mathrm{tot}} = -\frac{\delta_i}{(1+\delta_i)^2}\frac{G_{\mathrm{N}}M^2}{R_i} = -\frac{3M\mathcal{E}}{5} \,, \tag{3.65}$$

using the fact, for the second equality, that $\delta_i = 3/20\tau^2$ and $R_i = G_{\rm N}M\tau^2/(4\mathcal{E})$ at first order for $\tau \to 0$. In addition, when the sphere is homogeneous, the expression of the potential energy in Eq. (3.62) can be simplified and gives the compact expression, valid even when δ is no longer small,

$$W = -\frac{3}{5}\frac{G_{\rm N}M^2}{R}\,. \tag{3.66}$$

Eventually, using $E_{\rm tot} = K + W$ the virialisation condition, $2K + W = 0$ now becomes $2E_{\rm tot} = W$. This equation translates into an equation on R that takes the form

$$\frac{6M\mathcal{E}}{5} = \frac{3}{5}\frac{G_N M^2}{R} \quad \text{and yields} \quad R = \frac{G_N M}{2\mathcal{E}} = R(\tau = 3\pi/2)\,. \tag{3.67}$$

The evolution of K and W is represented in the right panel of Fig. 3.2. Therefore, after turnaround we can expect virialisation to occur at $\tau = 3\pi/2$. However, this model is very simplistic and in reality the halo is considered formed when $\tau \simeq 2\pi$. As we cannot trust our non-linear model of δ around this point and because we do not know how to properly treat non-linearities we define the collapsed density of the over-dense region as the linear overdensity at $\tau = 2\pi$. This collapsed region becomes what is usually called a (dark matter-dominated) halo. In other words we say that a halo is collapsed and virialised at $t_{\rm vir} \equiv 2\pi G_{\rm N}M/(2\mathcal{E})^{3/2}$ when its linear overdensity reaches

$$\delta_c \equiv \frac{3\mathcal{E}}{10}\left(\frac{6t_{\rm vir}}{G_{\rm N}M}\right)^{2/3} = \frac{3}{20}(12\pi)^{3/2} \simeq 1.686\,. \tag{3.68}$$

Let us repeat that this critical overdensity is not the true overdensity of the collapsing object that becomes close to infinite, it is an extrapolation of the linear one. Eventually, we can remark that this expression is a fixed number that does not depends on any characteristic of the overdensity (such as its mass). This is of particular interest for counting halos and understanding their distribution, as detailed in the next section.

3.4 Excursion set theory and halo mass function

In the following, we rely on the review of Knobel (2012) for the introduction of the power spectrum and the PS formalism (Press et al. 1974). Useful references for the power spectrum and transfer function definitions are C.-P. Ma et al. (1995), Dodelson (2003), and Peter et al. (2013). Then we refer to Bond et al. (1991) and Zentner (2007) for more details on the excursion set theory. The aim of this section is to summarise the previous developments that can be used to learn more about the population of halos in the Universe assuming that they have no internal dynamics. The specific study of the subhalo population in galaxies where dynamical effects play an important role is treated in Chapter 4. In the first part, we introduce the probabilistic treatment of the density contrast and define the matter power spectrum and the associated transfer function. Then we briefly develop the PS formalism and show why it fails to be the right and complete description of the halo population. Eventually, using the excursion set formalism, we show how a revised treatment can be performed and the kind of information that can be brought out of it.

3.4.1 Density contrast

The CMB data show that after inflation, the matter density contrast $\delta_{\rm m} = \delta\rho_{\rm m}/\overline{\rho}_{\rm m}$ presumably behaves as an approximately homogeneous and isotropic Gaussian random field[4]. The latter can be entirely described by its two point correlation function

$$\xi(\mathbf{x}_1, \mathbf{x}_2) \equiv \langle \delta_{\rm m}(\mathbf{x}_1)\delta_{\rm m}(\mathbf{x}_2)\rangle \quad \forall \mathbf{x}_1,\, \mathbf{x}_2\,. \tag{3.69}$$

Using the hypothesis of homogeneity and isotropy it is possible to go further and write $\xi(\mathbf{r}) = \langle \delta_{\rm m}(\mathbf{x}+\mathbf{r})\delta_{\rm m}(\mathbf{x})\rangle = \xi(r)$. If ξ is a continuous function at $r = 0$, using the spectral representation theorem it is possible to define a Fourier transformed expression as

$$\mathcal{P}(\mathbf{k}) = \int \xi(\mathbf{r}) e^{-i\mathbf{kr}} \mathrm{d}^3\mathbf{r} \quad \text{with} \quad \langle \delta_{\rm m}(\mathbf{k})\delta^*_{\rm m}(\mathbf{k}')\rangle\, \delta^{(3)}(\mathbf{k}-\mathbf{k}') = \mathcal{P}(\mathbf{k}) \tag{3.70}$$

where $\mathcal{P}$ is called the matter power spectrum. The fact that ξ must be real and rotationally invariant imposes $\mathcal{P}(\mathbf{k}) = \mathcal{P}^*(-\mathbf{k}) = \mathcal{P}(k)$. Taking the inverse Fourier transform yields

$$\xi(r) = \frac{1}{(2\pi)^3}\int \mathcal{P}(k) e^{i\mathbf{kr}} \mathrm{d}^3\mathbf{k} = \int_0^\infty \Delta^2_{\rm m}(k) \frac{\sin(kr)}{kr} \mathrm{d}\ln k \tag{3.71}$$

where we defined $\Delta^2_{\rm m} = k^3\mathcal{P}(k)/(2\pi^2)$ as the dimensionless matter power spectrum[5]. The fact that $\delta_{\rm m}$ is a Gaussian field means that it satisfies a multivariate Gaussian probability distribution. Since $\langle \delta_{\rm m}(\mathbf{x})\rangle = 0$ for all $\mathbf{x} \in \mathbb{R}^3$ by definition, if we consider N arbitrary points $(\mathbf{x}_1, ..., \mathbf{x}_N)$ the probability density of the fields is

$$p_\delta(\delta_{\rm m}(\mathbf{x}_1), ..., \delta_{\rm m}(\mathbf{x}_N)) = \frac{1}{(2\pi)^{N/2}\sqrt{\det C}} \exp\left(-\frac{1}{2}\sum_{ij} \delta_{\rm m}(\mathbf{x}_i) C^{-1}_{ij} \delta_{\rm m}(\mathbf{x}_j)\right) \tag{3.72}$$

where $C_{ij} = \xi(|\mathbf{x}_i - \mathbf{x}_j|)$ is the covariance matrix that characterises the field completely. If we look more precisely at a single point $\mathbf{x}$, then the PDF of the field becomes simply

$$p_\delta(\delta_{\rm m}) = \frac{1}{\sqrt{2\pi}\sigma} \exp\left(-\frac{\delta^2_{\rm m}}{2\sigma^2}\right) \tag{3.73}$$

with $\sigma^2 = \xi(0)$. Besides, to properly evaluate the statistics of the density contrast field $\delta_{\rm m}$, it is necessary to assume (approximate) ergodicity. In other words, since one has only one realisation of the Universe, one considers that the ensemble average over several realisations gives the same result as a volume average. As a matter of fact, if $\xi(r) \to 0$ when $r \to \infty$ the zero mean homogeneous Gaussian random field is indeed ergodic (ADLER 1981). Therefore the power spectrum is sufficient to know everything about the statistics of the density contrast.

3.4.2 Power spectrum and transfer function

The matter power spectrum appearing in the definition of the two-points correlation function is to be evaluated during the matter-dominated era and later, when structures can actually form. However, in practice, we have access to the prediction

[4] This remains an approximation as the distribution is limited by the lower boundary $\delta \geq -1$.

[5] The notation Δ^2_m is standard but must not be mistaken with the co-moving gauge density contrast.

of inflationary models right after inflation that we denote as time $t_{\rm inf}$. To be more precise, at that epoch, for modes that are super-Hubble, the comoving curvature perturbation $\mathcal{R}$ is simply related to the primordial potential by $\mathcal{R} = -3\phi(t_{\rm inf})/2$ as shown in Eq. (3.37). It is then possible to predict the curvature power spectrum defined as

$$\mathcal{P}_{\mathcal{R}}(k) \equiv \langle \mathcal{R}(k)\mathcal{R}(k)\rangle = \frac{9}{4}\langle \phi(k,t_{\rm inf})\phi(k,t_{\rm inf})\rangle \tag{3.74}$$

In the ΛCDM model the curvature power spectrum is parametrised by

$$\mathcal{P}_{\mathcal{R}}(k) = \frac{2\pi^2}{k^3}\mathcal{A}_S\left(\frac{k}{k_0}\right)^{n_{\rm s}-1} \tag{3.75}$$

with $k_0 = 0.05$ Mpc^{-1} fixed by convention. In Planck18 the best fit is found for a spectral amplitude $\ln(10^{10}\mathcal{A}_S) = 3.044 \pm 0.014$ and a spectral index $n_s = 0.9649 \pm 0.0042$.

The transfer function is a generic function that makes the connection between $t_{\rm inf}$ and a later time t taking into account the different growth of different modes as well as damping effects. We introduce t_m, a time in the matter-dominated phase of the Universe when the cosmological constant and curvature of the universe are still negligible. The transfer function is then implicitly defined by

$$\phi(k,t) \equiv \mathcal{K}\phi(k,t_{\rm inf})T(k,t_m)\frac{D_1(t)}{a(t)}\frac{a(t_m)}{D_1(t_m)} \tag{3.76}$$

with the introduction of a *new*[6] growth function

$$D_1(t) \equiv \frac{\phi(k,t)}{\phi(k,t_m)}a(t)\,. \tag{3.77}$$

The last part of the equation is introduced such that at $t = t_m$ there is no dependence on the growth function on the left-hand side. However at time t_m, when matter dominates, $D_1(t_m) = a(t_m)$ therefore this convention has no impact and the last fraction is 1. Then, since nothing else is dependent on t_m, the transfer function only depends on k, and we write $T(k) \equiv T(k,t_m)$. For modes k well inside the horizon at a time t, after the radiation era, Poisson's equation gives the relation between the matter fluctuations and the potential as

$$\delta_{\rm m}(k,t) \simeq \Delta_{\rm m}(k,t) = -\frac{k^2}{4\pi G a^2(t)\bar{\rho}_{\rm m}(t)}\phi(k,t)\,. \tag{3.78}$$

If we neglect the cosmological constant impact, the background density evolves as

$$\bar{\rho}_{\rm m}(t) = \Omega_{\rm m,0}\frac{3H_0^2}{8\pi G_{\rm N}}a^{-3}(t) \quad \text{that yields} \quad \delta_{\rm m}(k,t) = -\frac{2}{3}\frac{k^2 a(t)}{\Omega_{\rm m,0}H_0^2}\phi(k,t)\,. \tag{3.79}$$

For isentropic perturbations entering the horizon in the matter-dominated era (i.e. with $k \ll k_{\rm eq}$), the amplitude of the metric perturbation satisfies $\phi(k,t_m) = (9/10)\phi(k,t_{\rm inf})$ as seen in Sect. 3.2.2. Therefore, in this configuration we choose $\mathcal{K} = 9/10$ in order to have the correct normalisation. Indeed, the transfer function is also well defined for modes entering the horizon at late time. Since those modes

[6] In the sense that we have already introduced a growth function in Eq. (3.43). We will show below that, in fact, for sub-Hubble modes the two definitions coincide.

were super-horizon at the matter-radiation equality, $\phi(k,t) = \mathcal{K}\phi(k,t_{\rm inf})D_1(t)/a(t)$[7]. Therefore this yields the convenient property of the transfer function,

$$\lim_{k\to 0} T(k) = 1\,. \tag{3.80}$$

Note that for isocurvature perturbations, modes entering the horizon in the matter-dominated era satisfy $\phi(k,t_m) = (1/5)\phi(k,t_{\rm inf})$, and the normalisation factor has to be set to $\mathcal{K} = 1/5$ to respect the same property at small k. Using the transfer function and the new growth function, we obtain

$$\delta_{\rm m}(k,t) = -\frac{2}{3}\mathcal{K}\frac{k^2 D_1(t)}{\Omega_{\rm m}^0 H_0^2}T(k)\phi(k,t_{\rm inf})\,. \tag{3.81}$$

Remark that for sub-Hubble scales $\delta_{\rm m}(t) \propto D_1(t)$. Therefore $D_1(t) = D(t)$, with $D(t)$ the growth function introduced in Eq. Eq. (3.43), because $D_1(t)$ is normalised such that $D_1(t) = a(t)$ in the matter-dominated era — when the potential is constant. Giving it a new definition simply allows us to match with the usual definitions in the literature. The matter power spectrum, for isentropic initial conditions with adiabatic evolution is then related to the curvature power spectrum by the relation (NAKAMA et al. 2018),

$$\mathcal{P}(k,t) = \frac{4}{25}\left[\frac{k^2 D_1(t)}{\Omega_{\rm m,0}H_0^2}T(k)\right]^2 \mathcal{P}_{\mathcal{R}}(k)\,. \tag{3.82}$$

The transfer function for a given mode mainly depends on the moment it crossed the horizon. Three physical processes have an important imprint on its shape: the collisional damping of baryon at recombination (also called Silk damping – SILK 1968), the collisional damping of DM at kinetic decoupling, and the collision-less damping of DM after kinetic decoupling (free-streaming). In practice, we use the parametrisation given by EISENSTEIN et al. (1998) that takes into account the baryonic effect. Let us point out that in this work, the authors give a different definition of the transfer function, using the matter fluctuations in the synchronous gauge, but because the transfer function only addresses sub-horizon scales, gauge choice has no importance and it can be shown that it is perfectly equivalent to the definition above. For the DM-induced effects, we give more details in Sect. 3.6.

3.4.3 Filters and window functions

In the standard derivation of the halo mass function, the next step is to introduce filtered moments of the density contrast. Indeed, we are interested in averages on volumes of typical length R, and we ask the question of whether it is possible to form there a halo of mass M. Therefore, the smoothed density contrast on scale R is defined as the convolution product

$$\delta_R(\mathbf{x}) \equiv \int \delta(\mathbf{y})W_R(|\mathbf{x}-\mathbf{y}|)\mathrm{d}^3\mathbf{y} \tag{3.83}$$

where W_R is called the window function of size R, or the filter. The definition of this function is not unique and in practice 3 different choices are made: the Gaussian filter, the real-space top hat, and the k-space top hat. As we will see, the latter is the only convenient choice in the excursion set formalism. In Fourier space this equation becomes

$$\delta_R(\mathbf{k}) = \hat{W}_R(k)\delta(\mathbf{k}) \tag{3.84}$$

[7]Indeed $\mathcal{K}\phi(k,t_{\rm inf}) = \mathcal{K}\phi_{\rm RD} = \phi_{\rm MD} = \phi(k,t_m)$, by the choice of $\mathcal{K}$, on these scales. The definition of $D_1(t)$ being equivalent to $\phi(k,t) = \phi(k,t_m)D_1(t)/a(t)$ the result is immediate.

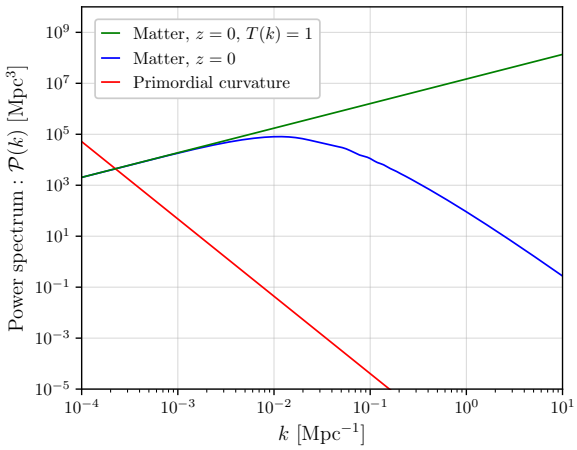

Figure 3.3 – Power spectra of the primordial curvature perturbations (red), matter today without transfer function (green) and matter today (blue). For this plot we used the Planck18 cosmology, the transfer function given in (EISENSTEIN et al. 1998) and the exact growth function from Eq. (3.43).

and the three different definitions are

$$\begin{aligned}
\hat{W}_R(k) &= \frac{3}{(kR)^3}\left[\sin(kR) - kR\cos(kR)\right] \quad \text{(real-space top hat)} \\
\hat{W}_R(k) &= \exp\left(-\frac{(kR)^2}{2}\right) \quad \text{(Gaussian)} \\
\hat{W}_R(k) &= \Theta(1 - kR) \quad (k\text{-space top hat})\,.
\end{aligned} \tag{3.85}$$

Only the first two have a corresponding definition in real space

$$\begin{aligned}
W_R(r) &= \Theta(R - r)\frac{3}{4\pi R^3} \quad \text{(real-space top hat)} \\
W_R(r) &= \left(\frac{1}{2\pi R^2}\right)^{3/2}\exp\left(-\frac{r^2}{2R^2}\right) \quad \text{(Gaussian)}
\end{aligned} \tag{3.86}$$

and can be associated with a volume $V(R)$ without ambiguity that is equal to $4\pi R^3/3$ for the real-space top hat window, and to $(2\pi)^{3/2}R^3$ for the Gaussian window. Nevertheless, it is possible to assign a volume to the k-space top-hat window in real space by the normalisation requirement $W_R(0)V(R) = 1$ so that $V(R) = 6\pi^2 R^3$. The typical mass associated to R for a given window is then

$$M = \bar{\rho}_{\mathrm{m},0} V(R) \tag{3.87}$$

where $\bar{\rho}_{\mathrm{m},0}$ is the background matter density today. Note that since δ_R is a linear combination of δ it then follows the same Gaussian statistics with variance

$$\sigma_R^2 \equiv \langle \delta_R(0)\delta_R(0)\rangle = \int \Delta^2_{\mathrm{m}}(k)|\hat{W}_R(k)|^2 \mathrm{d}\ln k\,. \tag{3.88}$$

One can see that, if there were no transfer function, the power law power spectrum for the curvature perturbations $\mathcal{P}_{\mathcal{R}}(k) \propto k^{n_s-4}$ would yield $\mathcal{P}(k) \propto k^{n_s}$ and $\Delta^2_{\mathrm{m}} \propto k^{n_s+3}$. Moreover, the variance would be $\sigma_R^2 \propto R^{-(n_s+3)}$ or put differently, with respect to the mass, $\sigma_M^2 \propto M^{-(n_s+3)/3}$. Consequently, if $n_s \sim 1$, the variance of the density field decreases with the mass (or size) of the region. The evolution of σ_{M} with the mass at redshift $z = 0$ is represented in Fig. 3.4 and shows, more accurately, that it decreases with M also in a model where the transfer function is taken into account.

3.4.4 The Press-Schechter formalism and cloud-in-cloud problem

The objective here is to compute the halo mass function, *i.e.* the mass distribution of halos in the Universe. The main idea of Press-Schechter (PS) (PRESS et al. 1974) was to say that any region with radius R with a density contrast δ_R that is equal to the critical threshold δ_c collapses into a halo. It is reasonable to assume that δ_R decreases with the radius of the region of interest so that if $\delta_R > \delta_c$ then it exists $R' > R$ such that $\delta_{R'} = \delta_c$. Looking at a specific scale R, all the points in space with $\delta_R > \delta_c$ should correspond to larger and larger halos with increasing δ_R. Therefore the fraction of halos with a mass greater than a given mass M is

$$\begin{aligned} F(M) &= \int_{\delta_c}^{+\infty} \frac{1}{\sqrt{2\pi}\sigma_M} \exp\left(-\frac{\delta_M^2}{2\sigma_M^2}\right) \mathrm{d}\delta_M \\ &= \frac{1}{2}\mathrm{erfc}\left(\frac{\delta_c}{\sqrt{2}\sigma_M}\right) . \end{aligned} \tag{3.89}$$

Unfortunately this approach does not take into account the fact that even though δ_R might be less than δ_c, it is possible that δ'_R with $R' > R$ may satisfy $\delta'_R > \delta_c$. Said differently, the PS formalism is based upon the averaged expectation, and does not correctly account for the fact that delta is truly a random variable, and independent from scale to scale. Whatever delta on a given scale, there's always a non-zero probability for delta to either larger or smaller at a different scale, irrespective of its size (except for asymptotic cases). There the larger volume R' collapses and creates a halo that is not counted by the PS formalism. Let us highlight, one more time, that in the PS computation it is implicitly assumed that only over-dense region at small scales ends up in larger collapsed objects. Therefore they are missing the under-dense regions that belong to larger over-densities. This effect is called the cloud-in-cloud problem and it can be seen directly from the formula above. At very small scales the variance of the density field goes to infinity,

$$\lim_{R\to 0} \sigma_R = \lim_{M\to 0} \sigma_M = \infty . \tag{3.90}$$

This can be shown very easily in the case of a constant transfer function since a rough scaling of the variance is $\sigma^2(M) \propto M^{-(3+n_s)/3}$ with $n_s \sim 1$. If we plug this result into Eq. (3.89) it yields that $F(0) = 1/2$, which would mean that the fraction of halos with a mass greater than 0 is $1/2$. Of course, this makes no physical sense, one should recover $F(0) = 1$. As already mentioned, this issue is a direct consequence of the cloud-in-cloud problem and Press and Schechter argued that it could be fixed simply by multiplying $F(M)$ by the missing factor 2. Even if this is true, the argument is not satisfying. We introduce, in the next section, the excursion set formalism that gives a complete answer.

3.4.5 The excursion set theory

The excursion set theory (BOND et al. 1991) – hereafter called EST – provides a way of counting correctly the number of formed halos. The formalism is much more involved than PS but we will see that it predicts the same result, with the correct normalisation. The basic idea is to compute the largest scale R for which $\delta_R = \delta_c$ so that the under-dense regions in over-dense larger ones are not forgotten. Moreover, this formalism does much more since it allows for a better understanding of the statistical properties of halos.

As seen above, one has $\sigma_R \to 0$ when $R \to \infty$, $\sigma_R \to \infty$ when $R \to 0$ and the function $R \mapsto \sigma_R^2$ is strictly decreasing. In the EST approach it is usual to define $S = \sigma_R^2$ and make use of the bijection between R and S to identify S to a given scale, writing $\delta_R = \delta(S)$. Note that in this picture the one to one correspondence is made at a specific redshift, chosen to be zero. Without fixing a time/redshift the definition of $S(R)$ would be ambiguous. Therefore, let us consider a given position and a large R. The value of S is then close to 0 and thus, from the Gaussian probability distribution, so is δ_R. Now if we decrease R, then S is higher and the value of δ_R can also depart from 0 more easily (in a statistical sense). In other words, lowering R increases the probability for δ_R to be above the threshold δ_c. For a given patch, the largest value of R for which δ_R becomes larger than δ_c is called the first up-crossing and corresponds to a halo of size R. The problem of counting halos amounts to determining the probability of having a first up-crossing at a given R, within an infinitesimal range $\mathrm{d}R$, or said otherwise at a given S within a range $\mathrm{d}S$. Starting from a large scale corresponding to a small S_0 with $\delta(S_0) = \delta_0 < \delta_c$, a change in the smoothing scale leads to $\delta(S_1) = \delta_1$ with $\delta S = S_1 - S_0 > 0$. With a k-space top hat window filter, increasing the window size only amounts to adding a set of new Fourier modes that are completely independent. As we shall see below, the transition probability for $\Delta\delta = \delta_1 - \delta_0$ (the change in critical density coming from a change δS) is actually a Gaussian with zero mean and a variance δS[8]. Now, starting from δ_0 and δ_1, when increasing the value of S by increments of δS, one has an evolution of δ by independent steps $(\delta_2, \delta_3, ...)$ describing a random walk. In addition, because all the steps are independent, this walk is more specifically a Markov Chain.

In order to study the behaviour of the walk one can go to the continuous limit and describe it as a Brownian diffusion. To this end, let us consider the density of trajectories $p(\delta, S)$ at position δ at *time* S. This density is normalised as a probability distribution, that is, its L_1 norm is 1 on $\mathbb{R}$. By the Gaussian character of the transitions the density of the chains at position δ at *time* $S + \delta S$ is related to the density at position $\delta - x$ at *time* S by the equation

$$p(\delta, S + \delta S) = \int \frac{1}{\sqrt{2\pi\delta S}} \exp\left(-\frac{x^2}{2\delta S}\right) p(\delta - x, S)\mathrm{d}x \tag{3.91}$$

From this relation one can compute the derivative of p with respect to S,

$$\begin{aligned}
\frac{\partial p}{\partial S} &= \lim_{\delta S \to 0} \frac{1}{\delta S}\left[\int \frac{1}{\sqrt{2\pi\delta S}} \exp\left(-\frac{x^2}{2\delta S}\right)\left[p(\delta - x, S) - p(\delta, S)\right]\mathrm{d}x\right] \\
&= \lim_{\delta S \to 0} \frac{1}{\delta S}\left[\int \frac{1}{\sqrt{2\pi\delta S}} \exp\left(-\frac{x^2}{2\delta S}\right)\left[\frac{x^2}{2}\frac{\partial^2 p}{\partial\delta^2} - x\frac{\partial p}{\partial\delta} + \mathcal{O}(x^3)\right]\mathrm{d}x\right] \\
&= \lim_{\delta S \to 0}\left[\frac{\langle x^2\rangle}{\delta S}\frac{1}{2}\frac{\partial^2 p}{\partial\delta^2} + \frac{\langle\mathcal{O}(x^3)\rangle}{\delta S}\right]
\end{aligned} \tag{3.92}$$

and as $\langle x^n\rangle \propto \delta S^{n/2}$ and $\langle x^2\rangle = \delta S$ it yields the equation of diffusion

$$\frac{\partial p}{\partial S} = \frac{1}{2}\frac{\partial^2 p}{\partial\delta^2}\,. \tag{3.93}$$

[8]The independence property is crucial for the following derivation and in the original EST framework it is necessary to work with a k-space top-hat window function which is not the filter with the best physical meaning. Therefore several studies have gone further and tried to find ways to include the possibility of a non-Gaussian random field and correlated steps, allowing them to use the other filters (Verechtchaguina et al. 2006; Maggiore et al. 2010; Musso et al. 2014). However, this is beyond the scope of this introduction.

In order to find a solution, we need initial and boundary conditions. The initial condition comes from the prescription that the walk starts at δ_0 for $S = S_0$ giving $p(\delta, S_0) = \delta_{\rm D}(\delta - \delta_0)$. Furthermore, once a trajectory reaches $\delta = \delta_c$ it has to be removed from the sample because it corresponds to a collapsed object; this gives the second condition $p(\delta_c, S) = 0$. One says that the trajectories are described by a diffusion equation with an absorbing wall at $\delta = \delta_c$. A general solution is given in CHANDRASEKHAR (1943). Let us here sketch a quick proof. First, let us start with the usual method to solve the diffusion equation and define the Fourier transform of the density p as

$$\hat{p}(\omega, S) = \int \mathrm{d}\gamma\, p(\delta, S) e^{-i\omega\delta} \quad \text{with} \quad p(\delta, S) = \frac{1}{2\pi}\int \mathrm{d}\omega\, \hat{p}(\omega, S) e^{i\omega\delta}\,. \tag{3.94}$$

Fourier transforming the master equation allows for a simple solution

$$\hat{p}(\omega, S) = A(\omega)\exp\left(-\frac{\omega^2}{2}S\right) \quad \text{with} \quad A(\omega) = \exp\left(-i\omega\delta_0 + \frac{\omega^2}{2}S_0\right) \tag{3.95}$$

where the value of A is determined thanks to the initial condition. Fourier transforming back the expression yields

$$\begin{aligned} p(\delta, S) &= \frac{1}{2\pi}\int_{-\infty}^{+\infty} \mathrm{d}\omega\, \exp\left(-\frac{\omega^2}{2}\Delta S\right) e^{i\omega\Delta\delta} \\ &= \frac{1}{\sqrt{2\pi\Delta S}}\exp\left(-\frac{(\Delta\delta)^2}{2\Delta S}\right) \end{aligned} \tag{3.96}$$

with $\Delta S = S - S_0$ and $\Delta\delta = \delta - \delta_0$. This is the usual solution for a diffusion equation with an initial condition concentrated in one point. However, here one can see that the absorption condition is not satisfied as $p(\delta_c, S) \neq 0$. In order to take the absorption into account one notices that removing all the trajectories reaching $\delta = \delta_c$ is the same than subtracting the contribution of a new source in $\delta = 2\delta_c - \delta_0$ (as if the absorbed trajectories were in fact absorbed by this source)[9]. Therefore, the total solution is

$$p(\delta, S) = \frac{1}{\sqrt{2\pi\Delta S}}\left[\exp\left(-\frac{(\Delta\delta)^2}{2\Delta S}\right) - \exp\left(-\frac{\left(2\left[\delta_c - \delta_0\right] - \Delta\delta\right)^2}{2\Delta S}\right)\right] \tag{3.97}$$

and one can easily check that the subtraction does not change the initial condition.

The fraction of halos formed with variance less than $S(M)$ (i.e. with mass greater that the associated mass M) is simply the complementary of the fraction of halos that have not collapsed

$$F(S) = 1 - \int_{-\infty}^{\delta_c} \mathrm{d}\delta\, p(\delta, S) = \mathrm{erfc}\left(\frac{\delta_c - \delta_0}{\sqrt{2\Delta S}}\right)\,. \tag{3.98}$$

For $S_0 = 0$ and $\delta_0 = 0$ it yields the results of PS with the correct normalisation, as expected. However, this is much more powerful since now we can evaluate the probability distribution of first up-crossing at scale S knowing that we started from scale $S_0 \neq 0$ at $\delta_0 \neq 0$. This is given by

$$f(S\,|\,\delta_0, S_0) \equiv \frac{\mathrm{d}F}{\mathrm{d}S} = -\int_{-\infty}^{\delta_c}\mathrm{d}\delta\frac{\partial p}{\partial S} = \frac{\delta_c - \delta_0}{\sqrt{2\pi}\Delta S^{3/2}}\exp\left(-\frac{(\delta_c - \delta_0)^2}{2\Delta S}\right)\,. \tag{3.99}$$

[9] This is actually nothing else but the method of images in classical electrostatics – see JACKSON (2003) (3rd edition - p57).

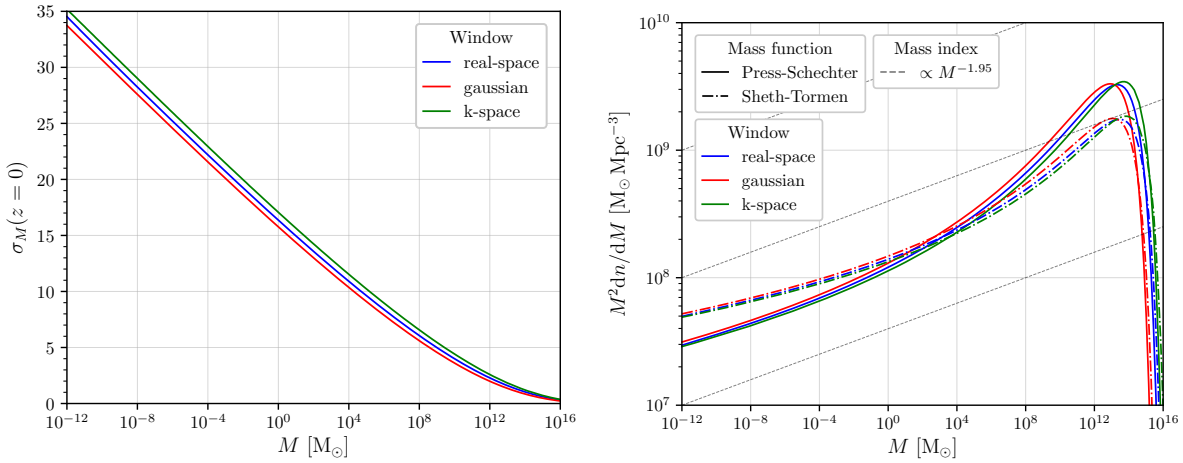

Figure 3.4 – Right panel: The smoothed variance of the matter density field in a window (written in terms of mass) of size M. **Left panel:** Press-Schechter and Sheth-Tormen mass functions for the different window filters. The tilted dashed black lines are a guide for the eyes and represent the halo mass function proportional to $M^{-1.95}$.

Once translated into the fraction of mass in halos between M and $M + \mathrm{d}M$, in the region of scale S_0 and density contrast δ_0, one has

$$f(M \,|\, \delta_0, S_0) \left|\frac{\mathrm{d}S}{\mathrm{d}M}\right| \mathrm{d}M = \frac{\delta_c - \delta_0}{\sqrt{2\pi}\Delta S^{3/2}} \exp\left(-\frac{(\delta_c - \delta_0)^2}{2\Delta S}\right) \left|\frac{\mathrm{d}S}{\mathrm{d}M}\right| \mathrm{d}M \,. \tag{3.100}$$

In the next section, we show in more details how this formulation, once generalised, can tell us much more about the statistics of halos than the PS formalism. Taking now $S \to 0$ (infinitely large region) with null density contrast $\delta_0 = 0$ we recover the PS case and it is possible to get the halo mass function of the entire Universe. Using the fact that $S = \sigma^2$ it yields

$$\begin{aligned} \frac{\mathrm{d}n}{\mathrm{d}M} &= \frac{\bar{\rho}_\mathrm{m}}{M} f(M) \left|\frac{\mathrm{d}S}{\mathrm{d}M}\right| \\ &= \sqrt{\frac{2}{\pi}} \frac{\bar{\rho}_\mathrm{m}}{M^2} \frac{\delta_c}{\sigma} \left|\frac{\mathrm{d}\ln\sigma}{\mathrm{d}\ln M}\right| \exp\left(-\frac{\delta_c^2}{2\sigma^2}\right) \\ &= \frac{\bar{\rho}_\mathrm{m}}{M^2} \frac{\mathrm{d}\ln\nu}{\mathrm{d}\ln M} \nu f_\mathrm{PS}(\nu) \end{aligned} \tag{3.101}$$

where we introduced the usual notation of the peak height $\nu = \delta_c/\sigma$ with the definition of the function f_PS being simply

$$f_\mathrm{PS}(\nu) = \sqrt{\frac{2}{\pi}} e^{-\nu^2/2} \,. \tag{3.102}$$

Using the scale invariant power spectrum (thus neglecting the transfer function), the PS mass function scales as $\propto M^{(n_s-9)/6} \exp(CM^{(n_s+3)/3})$($\propto M^{-4/3} \exp(CM^{4/3})$ for $n_s \sim 1$) where C is a constant.

3.4.6 A few words on ellipsoidal collapse

This last expression is valid in the spherical collapse model. When one accounts for ellipsoidal perturbations, the critical density becomes a function of the ellipticity e

and prolateness p, which we shall properly define later on.. Let us consider a particle in the universe at the initial comoving coordinate $\mathbf{x}_i$. Using Eq. (3.55) and $\mathbf{v} = a\mathbf{x}$ one has the equation of evolution for its comoving position,

$$\frac{\mathrm{d}\mathbf{x}}{\mathrm{d}t} = -\frac{\dot{D}(t)}{4\pi G_{\mathrm{N}}\overline{\rho}(t)a^3}\nabla\Phi_i(\mathbf{x})\,. \tag{3.103}$$

In the matter-dominated era the factor $\overline{\rho}(t)a^3$ is a constant and if we assume that, at first order, $\nabla\Phi_i(\mathbf{x}) = \nabla\Phi_i(\mathbf{x}_i)$, with the additional fact that $D(t) \gg D(t_i)$ one can write the Zel'dovich approximation (ZEL'DOVICH 1970)

$$\mathbf{x}(t) = \mathbf{x}_i - \frac{D(t)}{4\pi G_{\mathrm{N}}\overline{\rho}(t)a^3(t)}\nabla\Phi_i(\mathbf{x}_i) \tag{3.104}$$

which is equivalent to consider that particles go on straight line trajectories. Because of mass conservation the matter density satisfies the following relation $\rho(\mathbf{x},t)a^3(t)\mathrm{d}^3\mathbf{x} = \rho(\mathbf{x}_i,t_i)a^3(t_i)\mathrm{d}^3\mathbf{x}_i$. From the formula of change of variable, one can relate $\mathrm{d}^3\mathbf{x}$ and $\mathrm{d}^3\mathbf{x}_i$ through the Jacobian matrix according to

$$\mathrm{d}^3\mathbf{x} = \det\left(\frac{\partial\mathbf{x}}{\partial\mathbf{x}_i}\right)\mathrm{d}^3\mathbf{x}_i \quad \text{with} \quad \left(\frac{\partial\mathbf{x}}{\partial\mathbf{x}_i}\right)_{jk} = \delta_{jk} - D(t)\frac{\partial^2}{\partial x_j\partial x_k}\left[\frac{\Phi_i}{4\pi\overline{\rho}(t)a^3(t)}\right](\mathbf{x}_i)\,. \tag{3.105}$$

where $\partial_{x_j}\partial_{x_k}\left[\Phi_i/(4\pi G_{\mathrm{N}}\overline{\rho}(t))a^3(t)\right](\mathbf{x}_i)$ is called the deformation tensor. If λ_1, λ_2 and λ_3 are the eigenvalues of this tensor, then $1 - D(t)\lambda_1$, $1 - D(t)\lambda_2$ and $1 - D(t)\lambda_3$ are the eigenvalues of $(\partial\mathbf{x}/\partial\mathbf{x}_i)$. Then the mass conservation takes the form

$$\rho(\mathbf{x},t) = \rho(\mathbf{x}_i,t_i)\frac{a^3(t)}{a^3(t_i)}\frac{1}{[1-D(t)\lambda_1]\,[1-D(t)\lambda_2]\,[1-D(t)\lambda_3]}\,. \tag{3.106}$$

Choosing the initial time when the perturbations are negligible, one obtains

$$1 + \delta(\mathbf{x},t) = \frac{\rho(\mathbf{x},t)}{\overline{\rho}(t)} = \frac{1}{[1-D(t)\lambda_1]\,[1-D(t)\lambda_2]\,[1-D(t)\lambda_3]}\,. \tag{3.107}$$

Now considering the ordered eigenvalues $\lambda_1 \geq \lambda_2 \geq \lambda_3$, ellipticity and prolateness of the halos are defined by the two following parameters

$$e \equiv \frac{\lambda_1 - \lambda_3}{2(\lambda_1 + \lambda_2 + \lambda_3)} \quad \text{and} \quad p \equiv \frac{\lambda_1 + \lambda_3 - 2\lambda_2}{2(\lambda_1 + \lambda_2 + \lambda_3)}\,. \tag{3.108}$$

An ellipsoidal halo collapses preferentially in the direction of the largest eigenvalue as gravity enhances the non-sphericity. In particular, it leads to the "Zel'dovich pancakes" formation (SHANDARIN et al. 1989). According to SHETH et al. (2001), the critical overdensity for ellipsoidal collapse δ_{ec} can be obtained by solving

$$\delta_{\mathrm{ec}}(e,p) = \delta_{\mathrm{c}}\left\{1 + \beta\left[5(e^2 - |p|p)\left(\frac{\delta_{\mathrm{ec}}(e,p)}{\delta_{\mathrm{c}}}\right)^2\right]^{\gamma}\right\} \tag{3.109}$$

with $\gamma = 0.615$ and $\beta = 0.47$ and $\delta_{\mathrm{c}} \simeq 1.686$ the spherical collapse model critical density. They obtain this relation by fitting the ellipsoidal collapse model – summarised in (MO et al. (2010) - chapter 5.3). In the end they provide the scaling of δ_{ec} with ν and the redshift z instead of e and p

$$\delta_{\mathrm{ec}}(\nu,z) = \delta_{\mathrm{c}}\frac{D(z=0)}{D(z)}\left[1 + \beta\nu^{-2\gamma}\right]\,. \tag{3.110}$$

With this expression of the barrier the solution of the diffusion equation on $p(\delta, S)$ has no simple solution. However they also provide a fit of $f_{\rm ST}(\nu)$ that can be used to replace $f_{\rm PS}$ in the halo mass function

$$f_{\rm ST}(\nu) = A\left(1+\frac{1}{\nu^{2q}}\right)\sqrt{\frac{2}{\pi}}e^{-\frac{\nu^2}{2}}\,, \tag{3.111}$$

with $A = 0.3222$ and $q = 0.3$ (the usual PS result being $q = 0$ and $A = 0.5$). In Fig. 3.4 we show the Press-Schechter and Sheth-Tormen mass functions for different window filters multiplied by the mass squared. While this plot covers 28 orders of magnitudes in mass, the total variation on the y-axis is less than 2 orders of magnitude. Therefore the halo mass function is roughly proportional to $M^{-\alpha}$ with $\alpha \in [1.9, 2.0]$. The diagonal black lines show $M^{-1.95}$ in order to guide the eyes. The difference between Press-Schechter and Sheth-Tormen results is small but the latter is able to better reproduce the results from simulations. In addition, even small changes at small mass could have dramatic impacts on observables sensitive to the low mass range as the number of small halos drastically dominates – see the discussion in the conclusion of Chapter 2.

3.5 Subhalo mass function from merger trees

3.5.1 From the excursion set theory to merger trees

In this section, we are interested in the evolution of halos. We mainly follow the review of Zentner (2007) and use similar notations, which are also the same as Lacey et al. (1993, 1994) who studied this problem in great details.

First and foremost we need to add the scale factor a (or equivalently the redshift z) into the problem. In the standard picture the value of δ_c is fixed and σ_R changes with time. Here we adopt the other point of view where the only quantity dependent on the scale factor is the threshold. Indeed, increasing the fluctuations or decreasing the threshold is equivalent. More precisely, we introduce an effective collapse threshold that decreases with time as $\omega(z) = \delta_c D(z=0)/D(z)$, where $D(z)$ is the linear growth factor introduced in Eq. (3.43), while $S = S(z=0)$ is a constant. We just expressed in Eq. (3.99) the probability distribution to have a first up-crossing of the threshold δ_c knowing that we started in a region of size S_0 and density contrast δ_0. Actually, this expression can be generalised to the generic two-barrier crossing problem: it gives the probability to have a first up-crossing of the barrier ω_2 in a region of size S_2 knowing that it has already first up-crossed the barrier ω_1 in a region of size S_1 as

$$f(\omega_2, S_2\,|\,\omega_1, S_1)\,{\rm d}S_2 = \frac{\Delta\omega}{\sqrt{2\pi}\Delta S^{3/2}}\exp\left(-\frac{(\Delta\omega)^2}{2\Delta S}\right){\rm d}S_2\,, \tag{3.112}$$

with $\Delta\omega = \omega_2 - \omega_1$. One of the most interesting quantity we can compute is the averaged number of halos formed at time t_2 and of mass M_2 that are contained in a halo of mass M_1 formed at time $t_1 > t_2$,

$$\frac{{\rm d}N(M_2\,|\,M_1)}{{\rm d}M_2} = \frac{M_1}{M_2}f(\omega_2, S_2\,|\,\omega_1, S_1)\left|\frac{{\rm d}S_2}{{\rm d}M_2}\right|\,. \tag{3.113}$$

Now, from Eq. (3.112) one can simulate the formation history of a given halo. The easiest way is to proceed is by going backwards in time. Consider a host halo of mass M_1 at time z_1 that we call the parent or the host. At time $z_2 = z_1 + \Delta z$ one can draw

the masses $M_2^{(1)}, M_2^{(2)}, M_2^{(3)}, ...$ of the progenitor halos that merged to form the host. At the next step, $z_3 = z_1 + 2\Delta z$ the previously defined progenitors become parents and one can draw new smaller progenitors for them as well as new progenitors for the original host ... and so on and so forth. This way one builds a tree; the branches being all new progenitors that subdivide as z increases. This iterative procedure may seem straightforward to implement to produce a realistic merging history but it is not. The reason is that the algorithm drawing the progenitor masses needs to satisfy several conditions. Firstly, one needs to introduce a mass cut-off $M_{\rm res}$ not too small to converge in a reasonable amount of time. Nevertheless, the algorithm needs to take into account the mass included in subhalos smaller than the cut-off. This is referred to as accreted mass. Secondly, all progenitors must be treated equally at each step. Thirdly, the total mass needs to be conserved and the mass distribution given by Eq. (3.113) at each redshift must be satisfied (this is called the consistency test). In practice, in order to satisfy all these conditions, several algorithms have been proposed (COLE 1991; LACEY et al. 1993; PARKINSON et al. 2007; ZHANG et al. 2008; JIANG et al. 2014). Here we have compared the algorithms of SOMERVILLE et al. (1999) (hereafter labelled – SK99) and COLE et al. (2002) (hereafter labelled - C00). Both have the advantage of treating left-over mass (not contained in progenitors) as accreted mass and being fast to execute. In Fig. 3.5 are shown the comparison of the averaged number of subhalos formed at two redshifts $z_2 = 0.2$ and $z_2 = 1$ in a halo of mass $M_1 = 10^{12}$ $\mathrm{M}_\odot$. One can see that the consistency test is not exactly verified for SK99. As a matter of fact, this behaviour is expected as the algorithm does not satisfy the second point (all subhalos treated equally); it discards progenitors drawn from the halo mass function that gives a total mass exceeding that of the host halo. As detailed in ZHANG et al. (2008) and JIANG et al. (2014), the C00 algorithm is not perfect and suffers from several drawbacks (as all merger trees do) too, essentially because it underestimates the mass of the most massive progenitors at large redshift. However, it is simple to implement and behaves rather well in the self-consistency test. Most importantly, it compares well with results from simulations. An improvement of the C00 algorithm is given in PARKINSON et al. (2007). However they calibrate their recipe on the Millennium Simulation. Our goal is to be as much as possible independent of simulations, therefore we make the choice of using the original C00 algorithm in the following, which we shortly explain below.

Let us give more details on this algorithm. Consider a small *time* step $\Delta\omega$. From Eq. (3.113) one can compute the average mass fraction of a halo of mass M_1 at ω_1 that was in progenitors of mass M_2 at $\omega_2 = \omega_1 + \Delta\omega$ as

$$\left.\frac{\mathrm{d}^2N(M_2,\omega_2|M_1,\omega_1)}{\mathrm{d}M_2\mathrm{d}\omega}\right|_{\omega_2=\omega_1}\Delta\omega\mathrm{d}M_2 = \frac{M_1}{M_2}\frac{\Delta\omega}{\sqrt{2\pi}(S_2-S_1)^{3/2}}\left|\frac{\mathrm{d}S_2}{\mathrm{d}M_2}\right|\mathrm{d}M_2 \tag{3.114}$$

The mean number of progenitors of masses $M_{\rm res} < M_2 < M_1/2$ into the parent of mass M_1 after one step is then

$$\begin{aligned} P(M_1) &= \Delta\omega\int_{M_{\rm res}}^{M_1/2}\mathrm{d}M_2\left.\frac{\mathrm{d}^2N(M_2\,|\,M_1)}{\mathrm{d}M_2\mathrm{d}\omega}\right|_{\omega_2=\omega_1} \\ &= \Delta\omega\frac{M_1}{\sqrt{2\pi}}\int_{M_{\rm res}}^{M_1/2}\frac{1}{M_2\,(S_2-S_1)^{3/2}}\left|\frac{\mathrm{d}S_2}{\mathrm{d}M_2}\right|\mathrm{d}M_2\,. \end{aligned} \tag{3.115}$$

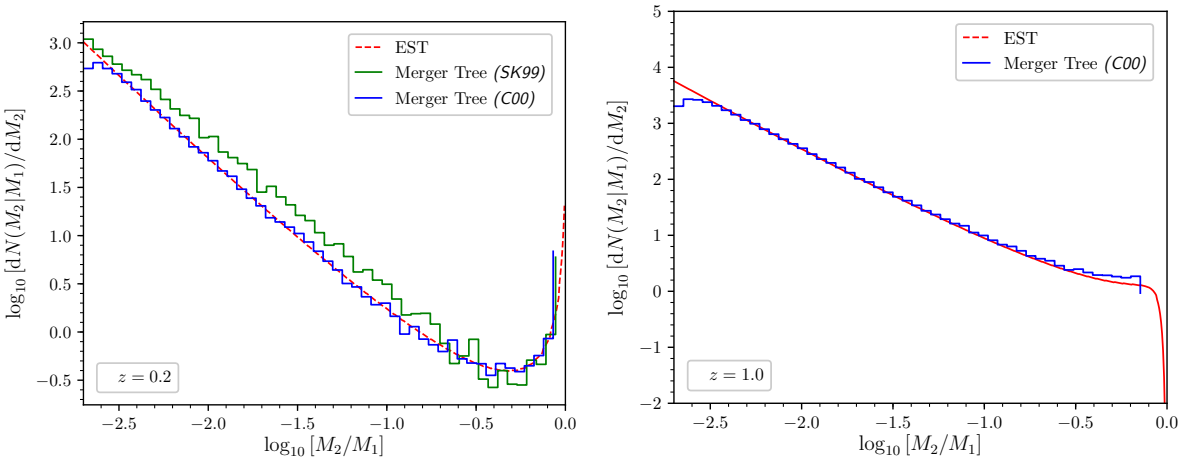

Figure 3.5 – Consistency test for the SK99 (green) and C00 (blue) algorithms for one and two redshifts respectively. The red dashed curves represent the expected value for the excursion set theory (EST). The close the algorithm get to the red curve the better it is.

Besides, one can also evaluate the fraction of mass that is made of unresolved subhalos (that are below the mass resolution cut-off),

$$F(M_1) = \Delta\omega \int_{S_{\rm res}}^{+\infty} \frac{1}{\sqrt{2\pi}(S_2 - S_1)^{3/2}} \mathrm{d}S_2 = \Delta\omega \sqrt{\frac{2}{\pi(S_{\rm res} - S_1)}}\,. \tag{3.116}$$

One first chooses $\Delta\omega$ such that $P \ll 1$ in order to ensure that the probability to have more than two progenitors on that time step is negligible. Then one draws R from a uniform distribution in $[0,1]$. If $R < P$ then this means that at that time step one has found a progenitor in the range $[M_{\rm res}, M_1/2]$. One defines the cumulative distribution of M_2 within the range $[M_{\rm res}, M_1/2]$ as

$$\mathcal{F}(M_2\,|M_1) = \frac{1}{P(M_1)} \int_{M_{\rm res}}^{M_2} \mathrm{d}M_2' \left.\frac{\mathrm{d}^2 N(M_2'\,|\,M_1)}{\mathrm{d}M_2' \mathrm{d}\omega}\right|_{\omega_2=\omega_1} \tag{3.117}$$

Then one draws a value y from a uniform distribution in $[0,1]$ and the value of M_2 is defined as the solution of $\mathcal{F}(M_2\,|M_1) = y$. Here we have exactly two progenitors of mass M_2, $M_1(1-F) - M_2$ and it remains $M_1 F$ accreted mass (from unresolved progenitors). When $R > P$ one only has one progenitor (the main progenitor) of mass $M_1(1-F)$ and it remains $M_1 F$ accreted mass (from unresolved progenitors).

3.5.2 Unevolved subhalo mass function

The unevolved subhalo mass function (hereafter USMF) is what we call the *cosmological* subhalo mass function (in the sense that a subhalo mass is defined as a smaller scale collapsing on a flat homogeneous background, not subject to any tidal stripping effect). Here we show how it can be obtained from merger-tree simulations. The mass function in a parent halo of mass M is denoted $\Phi(m, M)$ in the following. In Giocoli et al. (2008b), Y. Li et al. (2009), and Jiang et al. (2014) the authors have looked at the p-th order USMFs denoted USMF$[p]$. The 1st order USMF is defined as the mass function of all subhalos that have directly merged into the parent halo. The 2-nd order is the mass function of the sub-subhalos (the subhalos of the 1$^{\rm st}$-order

subhalos), etc. We denote the USMF[p] as $\phi_p = \mathrm{d}N_p/\mathrm{d}m$. Assuming universality, all the orders are related by the recursion relation

$$\phi_p(m, M) = \int_0^M \phi_1(m, m')\phi_{p-1}(m', M)\mathrm{d}m' \,. \tag{3.118}$$

This equation just mathematically means that at order p all the halos of mass m are contained in larger halos of order $p-1$ of mass m' and they are distributed according to $\phi_1(m, m')$ in each of them. The total USMF is given by the sum

$$\Phi(m, M) \equiv \sum_{p=1}^{\infty} \phi_p(m, M) \,. \tag{3.119}$$

Because of the recursion relation, Φ can also be written as a function of ϕ_1,

$$\begin{aligned}
\Phi(m, M) &= \phi_1(m, M) + \sum_{p=2}^{\infty} \phi_p(m, M) = \phi_1(m, M) + \sum_{p=2}^{\infty} \int_0^M \phi_1(m, m')\phi_{p-1}(m', M)\mathrm{d}m' \\
&= \phi_1(m, M) + \int_0^M \phi_1(m, m') \sum_{p=2}^{\infty} \phi_{p-1}(m', M)\mathrm{d}m' \\
&= \phi_1(m, M) + \int_0^M \phi_1(m, m')\Phi(m', M)\mathrm{d}m'
\end{aligned} \tag{3.120}$$

Since $\phi_1(m > m', m') = 0$ one can massage the last equation by truncating the integral from below and we get the implicit relation

$$\Phi(m, M) = \phi_1(m, M) + \int_m^M \phi_1(m, m')\Phi(m', M)\mathrm{d}m' \,. \tag{3.121}$$

Unfortunately, this equation does not allow to easily solve for ϕ_1 or Φ knowing one or the other. It can be used for numerical tests or in very simple scenarios. If we assume, for instance, that USMF[1] is self-similar and has a power-law dependence that is $\phi_1(m, M) \propto (m/M)^\lambda$ with $\lambda \in \mathbb{R}$, then, the total USMF necessarily goes as $\Phi(m, M) \propto (m/M)^{-2}$ and the index of -2 can be viewed as a critical exponent. However, this theoretical result does not provide any practical insights on the value of λ.

The total number of halos contained in a host with $M = 10^{12}$ $\mathrm{M}_\odot$ with a mass over a given threshold is given in Fig. 3.6. This figure was obtained by running the C00 algorithm with $M_{\mathrm{res}} = 10^{-4}M$ over 350 Monte-Carlo realisations. The blue line represents the average total number of unevolved halos while the red lines are the average of the successive orders of USMF. The sum of the different orders gives back the total number.

3.5.3 Merger Trees and fitting function

In the following we evaluate with C00 the USMF[1] on five decades of mass and fit $\eta(m, M) = m\phi_1(m, M)$ with the functional form proposed by (JIANG et al. 2014) – which is an extension of another function proposed by GIOCOLI et al. (2008b) –

$$\eta(m, M) = \left[\gamma_1(M)\left(\frac{m}{M}\right)^{\alpha_1(M)} + \gamma_2(M)\left(\frac{m}{M}\right)^{\alpha_2(M)}\right] \exp\left(-\beta(M)\left(\frac{m}{M}\right)^{\zeta(M)}\right) \,. \tag{3.122}$$

As mentioned in JIANG et al. (2014) – and relying on Y. LI et al. (2009) – some kind of universality appears, the coefficients do not depend on the host mass for 10^{10} $\mathrm{M}_\odot$

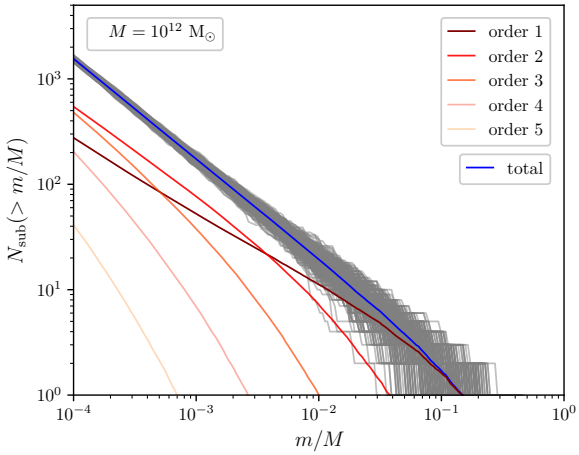

Figure 3.6 – Left panel: The cumulative number of subhalos in a host halo of mass 10^{12} M$_\odot$. First-order halos are represented in dark red, second-order sub(sub)halos in lighter red and so on. The total number of subhalos in over 350 realisations is represented by the grey lines, the blue line is the total average.

$< M < 10^{15}$ M$_\odot$ and they also should not vary with the cosmology. Here we can impose the theoretical bounds

$$0 \leq \gamma_1\,, \quad 0 \leq \gamma_2\,, \quad -1 \leq \alpha_1 \leq 0\,, \quad -1 \leq \alpha_2 \leq 0\,, \quad 0 \leq \beta \quad \text{and} \quad 0 \leq \zeta \tag{3.123}$$

on the coefficients. In their fit, however, the aforementioned authors do not constrain the shape of the mass function at small masses, which is not a problem, a priori, as they are interested in the large-mass tail. Because we want to recover a mass function valid over many orders of magnitude in mass (up to ~ 30!) we have to design another method to extrapolate the results at low masses. Let us first assume the purely theoretical approximation, that there is no minimal mass limit for the halos (that they can be of vanishingly small size). Obviously, this cannot be the case in reality, either because of the damping effects detailed in Sect. 3.6 or to another extent, because we can no longer talk about subhalos under the typical distance between two particles. Furthermore, we also make the assumption that every halo of order p is entirely made of halos of order $p+1$. In the strict infinitely small size limit, this should hold true. Therefore if we integrate the USMFs on the mass over the entire range between 0 and the host mass, this yields

$$\frac{1}{M}\int_0^M \phi_p(m,M) m\,\mathrm{d}m = 1 \quad \forall p \geq 1\,. \tag{3.124}$$

One can check, as a consistency test, that this normalisation condition is conserved by Eq. (3.118). If we assume that ϕ_{p-1} and ϕ_1 are normalised to 1 then ϕ_p is too because of the relation

$$\begin{aligned}
\frac{1}{M}\int_0^M \phi_p(m,M) m\mathrm{d}m &= \frac{1}{M}\int_0^M \left[\int_0^M \phi_1(m,m') m\mathrm{d}m\right] \phi_{p-1}(m',M)\mathrm{d}m' \\
&= \frac{1}{M}\int_0^M \left[\int_0^{m'} \phi_1(m,m') m\mathrm{d}m\right] \phi_{p-1}(m',M)\mathrm{d}m' \\
&= \frac{1}{M}\int_0^M m'\phi_{p-1}(m',M)\mathrm{d}m' = 1
\end{aligned} \tag{3.125}$$

Cosmo.	$M/M_\odot$	γ_1	α_1	α_2	β	ζ	γ_2
Planck18	10^9	0.01954	-0.9452	-0.5609	20.39	3.333	0.4618
Planck18	10^{12}	0.01894	-0.9402	-0.5783	24.57	3.586	0.4568
Planck18	10^{15}	0.02228	-0.9191	-0.5719	21.48	3.473	0.4949
Jiang+14	10^{12}	0.02340	-0.9313	-0.5670	22.36	3.456	0.4634
Jiang + 14		0.13	-0.83	-0.02	5.67	1.19	1.33
Giocoli + 08		0.18	-0.80	0	12.27	3.00	0

Table 3.1 – Results of the fit for the Planck18 cosmology and the same cosmology than that of JIANG et al. (2014) – here Jiang+14. For comparison in the bottom two panels we put the results obtained by Jiang+14 and GIOCOLI et al. (2008b) – here Giocoli+08.

where we used the fact that $\phi_p(m' > m, m) = 0$ (subhalos cannot be larger than the host). In the end, it amounts to say that, instead of letting γ_1 and γ_2 be free parameters, one of them is actually constrained. More specifically, from the normalisation condition of Eq. (3.124), we get

$$\gamma_2 = \frac{1 - \gamma_1 \beta^{-\frac{1+\alpha_1}{\zeta}} \gamma\left(\frac{1+\alpha_1}{\zeta}, \beta\right)}{\beta^{-\frac{1+\alpha_2}{\zeta}} \gamma\left(\frac{1+\alpha_2}{\zeta}, \beta\right)}, \tag{3.126}$$

where $\gamma : (z, s) \mapsto \gamma(z, s)$ is the lower incomplete gamma function. With this requirement, we theoretically constrain the slope of the mass function in the small mass range. In Tab. 3.1, we give the results for the Planck18 cosmology and the cosmology used in JIANG et al. (2014), for $M_{\rm res} = 10^{-5} M$ and discarding all the subhalos with a mass between $[M_{\rm res}, 2M_{\rm res}]$ in order to minimise possible boundary effects. In addition, these fits are also represented in Fig. 3.7. The red curves corresponding to USMF[1] are the fitted functions while the other orders, in lighter red, are here evaluated with Eq. (3.118). In the lower right panel of the same figure we compare the results of the literature in dark and light red with our own for the three different host masses – in light, medium and dark blue. We also show results for unconstrained fits for which the value of γ_2 is not fixed by the normalisation condition (dashed curves). With the simple C00 algorithm we obtain results that differ at most by 50% from the fits in the literature. Moreover, the necessity of the constrain on γ_2 appears here as the unconstrained fits all give $\alpha_2 = -0.9999$ at the limit of the available range of values.

All these fits remain roughly similar whatever the mass of the host. Henceforth, for simplicity, we introduce a standardised mass function by considering $(\gamma_1 = 0.019, \alpha_1 = -0.94, \alpha_2 = -0.58, \beta = 24, \zeta = 3.4; \gamma_2 = 0.464)$. We keep three digits for γ_2 in order to have a correct normalisation at the sub-per cent level. This standardised USMF matches with cosmological simulation results (DIEMAND et al. 2006, 2007; DIEMAND et al. 2008; SPRINGEL et al. 2008; ZHU et al. 2016) where the mass function exhibits a power-low dependency with a mass index $\alpha \lesssim 2$. Note that in terms of our parameters, $\alpha \simeq 1 - \alpha_1$. Consequently, we get a prediction for $\alpha \simeq 1.94$ for the Planck18 cosmology — this is slightly different from similar predictions in the literature which are not constrained by Eq. (3.124). This may have deep consequences on the subhalo abundance in host halos, because this would predict a net domination of the smallest scales in the overall subhalo mass fraction.

The next step is to evaluate the evolved subhalo mass function (ESMF), after taking into account the dynamics inside the host. This is treated by the SL17 model, detailed

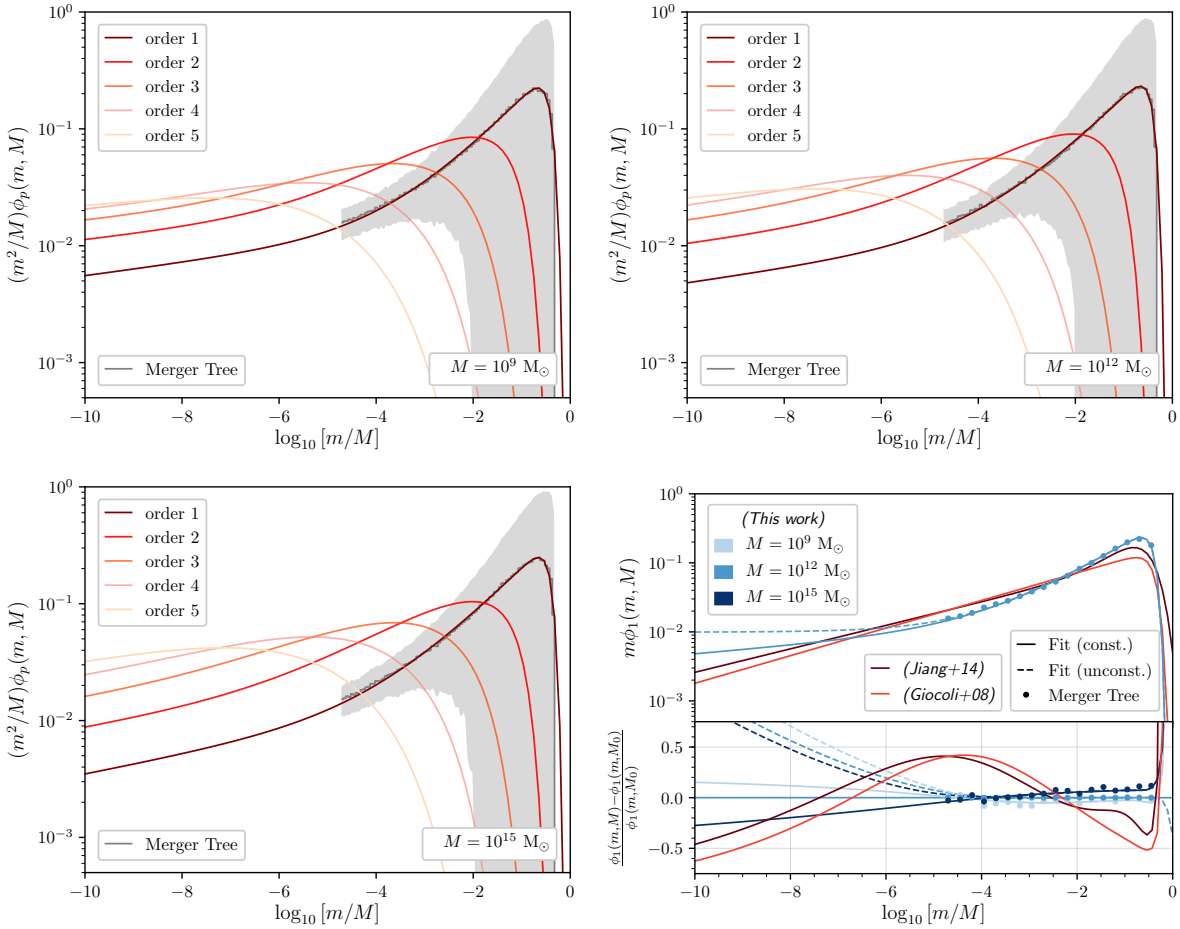

Figure 3.7 – Upper and bottom left panels: Unevolved subhalo mass function at different orders. The first order (red curve) is fitted on simulations (grey) and all further orders are obtained using Eq. (3.118) and the universality approximation (that is, the fitted coefficients do not depend on the host mass). The grey shaded area represents the 1σ fluctuations between Monte-Carlo realisations. Note that on every mass decade the number of realisation is different for optimisation: from 100 realisations at low mass to 10000 realisations at large masses. **Lower right panel:** Comparison of our constrained fit (solid blue) and unconstrained fit (dashed blue) obtained for a host mass $M_0 = 10^{12}$ M$_\odot$ with the similar fits provided in Jiang et al. (2014) (dark red) and Giocoli et al. (2008b) (light red). Note that we do not use the same cosmology but this should have little impact. The main difference may come from the Merger Tree algorithm that is used. The result of the merger tree is here shown with blue round markers. In the lower panel, we show the residuals of the upper panel as well as the difference between the two different host halo masses $M = 10^9, 10^{15}$ M$_\odot$ (light blue) and (dark blue) for the constrained (solid) and unconstrained fits (dashed). The three solid blue lines and the blue round markers are relatively close, thus showing the self-similarity.

in Chapter 4. In its original construction, the SL17-USMF is a power law normalised to the typical subhalo mass fraction measured in cosmological simulations. This also translates in terms of total number of subhalos. With the USMF that we have just predicted from merger-tree calculations, and from given cosmological parameters, the total number of subhalo is now a theoretical prediction, and a calibration on numerical simulations is no longer required (except to test the validity or precision of merger-tree approaches themselves). This is an important improvement for the model. For clarity, however, we delay the rest of this discussion to Sect. 4.2.

3.6 Power spectrum cut-off and minimal halo mass

So far DM has been treated as a perfect fluid. However, it is not necessarily a good description depending on the scale of interest. This section is focused on this issue. Indeed, when DM is collision-less (such as for WIMPs after kinetic decoupling), its behaviour on small scales can depart from the fluid approximation. From this effect comes a limit on the minimal mass that DM halos can have and that is called the free-streaming mass. Besides, because of interactions between the DM and radiation fluids at kinetic decoupling, a second lower bound on the masses exists and is referred to as the acoustic mass here. The main goal of this section is to summarise the key concepts and show how the minimal mass of halos can be derived.

3.6.1 The Euler equation for collision-less dust

We have hitherto considered the different component of matter in the Universe as fluids. However, the fluid description is valid for species exhibiting a mean free path smaller than the scale of interest. When DM becomes collision-less, as discussed in Chapter 2, discrepancies arise on the smallest scales. In this section, we follow the discussion of MO et al. (2010) and we first show that the fluid description remains valid on sub-horizon scales as long as the particle diffusion can be neglected. Indeed, let us consider a non-relativistic particle in the expanding universe. Its Lagrangian can be written as the difference of the kinetic energy and potential energy,

$$L(\mathbf{x},\dot{\mathbf{x}},t)=\frac{1}{2}m(a\dot{\mathbf{x}}+\dot{a}\mathbf{x})^2-m\phi(\mathbf{x},t) \tag{3.127}$$

Using $\mathbf{x}\equiv(x^1,x^2,x^3)$ as the argument of the Lagrangian amounts to work in the 3D-euclidean space where distances are rescaled by the scale factor. The canonical momentum associated with this Lagrangian is the physical 3-momentum $\tilde{\mathbf{p}}\equiv(\tilde{p}_1,\tilde{p}_2,\tilde{p}_3)$ given by $\tilde{\mathbf{p}}=\partial L/\partial\dot{\mathbf{x}}=ma^2\dot{\mathbf{x}}+ma\dot{a}\mathbf{x}$. However it is more convenient to work with the momentum $\hat{\mathbf{p}}=ma^2\dot{\mathbf{x}}$ that only depends on the peculiar velocity $\mathbf{v}=a\dot{\mathbf{x}}$. In fact, this momentum can be canonically associated with a canonical transformation of this Lagrangian. Indeed one can subtract a total derivative to the Lagrangian without changing the action of the system and one introduces therefore $\hat{L}=L-\mathrm{d}S/\mathrm{d}t$ where $S=ma\dot{a}\mathbf{x}^2/2$. This corresponds to a change of variables in parameter space $(x^i,\tilde{p}_i)\to(x^i,\hat{p}_i)$ where $\hat{p}_i$ has the desired expression. More precisely the new Lagrangian is

$$\hat{L}(\mathbf{x},\dot{\mathbf{x}},t)=\frac{1}{2}ma^2\dot{\mathbf{x}}^2-m\Phi(\mathbf{x},t) \tag{3.128}$$

where $\Phi=\phi+a\dot{a}\mathbf{x}^2/2$. Let us look now at the transformation from the Hamiltonian point of view. The original Hamiltonian is

$$\tilde{K}(\mathbf{x},\tilde{\mathbf{p}},t)=\mathbf{x}\cdot\tilde{\mathbf{p}}-L(\mathbf{x},\dot{\mathbf{x}},t)=\frac{1}{2ma^2}\tilde{\mathbf{p}}^2-\frac{\dot{a}}{a}\mathbf{x}\cdot\tilde{\mathbf{p}}+m\phi(\mathbf{x},t)\,. \tag{3.129}$$

The subtraction of the time derivative of S in the Lagrangian corresponds to a canonical transformation through a type 2 generating function – following the same notations as BINNEY et al. (2008), appendix D and problem 9.3 –

$$S_2(\mathbf{x},\hat{\mathbf{p}},t)=S+\mathbf{x}\cdot\hat{\mathbf{p}}=\frac{1}{2}ma\dot{a}\mathbf{x}^2+\mathbf{x}\cdot\hat{\mathbf{p}} \tag{3.130}$$

and the canonically transformed Hamiltonian is

$$\hat{K}(\mathbf{x},\hat{\mathbf{p}},t)=\tilde{K}(\mathbf{x},\tilde{\mathbf{p}},t)+\frac{\partial S_2}{\partial t}=\frac{1}{2ma^2}\hat{\mathbf{p}}^2+m\Phi(\mathbf{x},t) \tag{3.131}$$

In the end, one can introduce the PSDF associated with $\hat{\mathbf{p}}$ as $f(\mathbf{x}, \hat{\mathbf{p}}, t)$. According to Liouville's theorem for a collision-less gas, it is possible to write the collision-less Boltzmann equation (that is also called the Vlasov equation in that context) for f as

$$\frac{\partial f}{\partial t} + \left\{f, \hat{K}\right\} = 0 \quad \text{with} \quad \left\{f, \hat{K}\right\} \equiv \sum_i \left[\frac{\partial \hat{K}}{\partial \hat{p}_i}\frac{\partial f}{\partial x^i} - \frac{\partial \hat{K}}{\partial x^i}\frac{\partial f}{\partial \hat{p}_i}\right] . \tag{3.132}$$

Note that here we keep the index of $\hat{p}_i$ down as the canonical momentum is formally defined with down indices. We introduce the momentum amplitude $\hat{q} = (\delta^{ij}\hat{p}_i\hat{p}_j)^{1/2}$. In Mo et al. (2010) – chapter 4.1.4 – the authors introduce also the average valued of a any quantity Q as

$$\langle Q \rangle \equiv \frac{g}{a^3 n}\int f(\mathbf{x}, \hat{\mathbf{p}}, t) Q \frac{\mathrm{d}^3\hat{\mathbf{p}}_\star}{(2\pi)^3} , \tag{3.133}$$

where n is the number density of particles and $\mathrm{d}^3\hat{\mathbf{p}}_\star \equiv \mathrm{d}\hat{p}_1\mathrm{d}\hat{p}_2\mathrm{d}\hat{p}_3$[10]. Using the Vlasov equation they show that for a collision-less dust one recovers the traditional Jean's equation in the expanding universe, involving the average of the peculiar velocity $\mathbf{v} = \hat{\mathbf{p}}/(ma)$,

$$\frac{\partial \langle \mathbf{v} \rangle}{\partial t} + H \langle \mathbf{v} \rangle + \frac{1}{a}\left[\langle \mathbf{v} \rangle . \nabla_{\mathbf{x}}\right] \langle \mathbf{v} \rangle = -\frac{1}{a}\nabla_{\mathbf{x}}\Phi - \frac{\nabla_{\mathbf{x}} P_{\mathrm{eff}}}{\overline{\rho} a (1+\delta)} . \tag{3.134}$$

However, instead of a pressure term, here one obtains an effective pressure P_{eff} that is given according to its divergence by

$$(\nabla_{\mathbf{x}} P_{\mathrm{eff}})_i = \overline{\rho}\sum_j \frac{\partial}{\partial x^j}\left[(1+\delta)\sigma_{ij}^2\right] \quad \text{with} \quad \sigma_{ij}^2 = \langle v_i v_j \rangle - \langle v_i \rangle \langle v_j \rangle , \tag{3.135}$$

which shows that, indeed, the velocity dispersion induces an effective pressure in the fluid. If this term is negligible we recover the same equation as for a pressureless fluid. On large scales, this should be true and all the treatment of DM perturbation and background evolution holds even after it decouples from the plasma and can no longer strictly speaking be considered as a fluid. However, this is not satisfied on small scales where the velocity dispersion and the fluid approximation breaks down. In particular, particles that are in small over-densities can *free-stream* out due to the velocity dispersion-induced pressure and therefore smear it out. This effect is called *free-streaming* damping and we detail it in the next section in order to extract the impacted length scales. It is specifically relevant for DM after kinetic decoupling.

3.6.2 Free-streaming damping effect

In order to study the evolution of small perturbations when the fluid approximation does not hold, as we cannot solve the Vlasov equation analytically we decompose the PSDF into a background part and a first order perturbation $f = f_0 + f_1$. As f_0 represent the background it does not depend on $\mathbf{x}$ and the dependence on momentum is only

[10] Note that the momentum p^μ introduced in Sect. 2.2.1, reduces, in the non relativistic limit, to $p^\mu = (m, p^i = m\dot{x}^i)$. Therefore one has $p^i = \hat{p}_i/a^2$ and subsequently $\hat{q} = ap$ where $p = (-g_{ij}p^i p^j)^{1/2}$. Moreover, this relation also highlights that $\mathrm{d}^3\mathbf{p} = \mathrm{d}^3\hat{\mathbf{p}}_\star/a^3$, explaining the factor $1/a^3$ in the definition of the average value $\langle Q \rangle$.

through the norm $\hat{q} = (\delta^{ij}\hat{p}_i\hat{p}_j)^{1/2}$. A straightforward derivation done in (MO et al. 2010 – chapter 4.1.4) shows that in Fourier space, with k^i the conjugate variable to x^i,

$$\begin{aligned} f_1(\mathbf{k},\hat{\mathbf{p}},\xi) = f_1(\mathbf{k},\hat{\mathbf{p}},\xi_{\rm kd})\exp\left(-i\frac{\mathbf{k}\cdot\hat{\mathbf{p}}}{m}(\xi-\xi_{\rm kd})\right) \\ + im\left(\mathbf{k}\cdot\nabla_{\hat{\mathbf{p}}}f_0\right)\int_0^{\xi}\mathrm{d}\xi' a^2(\xi')\Phi(\mathbf{k},\xi')\exp\left(-i\frac{\mathbf{k}\cdot\hat{\mathbf{p}}}{m}(\xi-\xi')\right) \end{aligned} \tag{3.136}$$

They introduce $\mathrm{d}\xi = \mathrm{d}t/a^2$ and the variable $\xi_{\rm kd} = \xi(t_{\rm kd})$ representing the initial value of ξ i.e. the value at kinetic decoupling. The solution for f_1 can be plugged into the Fourier transform of the density contrast $\delta(\mathbf{k},t)$ to obtain the first order equation

$$\begin{aligned} \delta(\mathbf{k},t) = \frac{gm}{\bar{\rho}a^3}\int f_1(\mathbf{k},\hat{\mathbf{p}},\xi_{\rm kd})\exp\left(-i\frac{\mathbf{k}\cdot\hat{\mathbf{p}}}{m}(\xi-\xi_{\rm kd})\right)\frac{\mathrm{d}^3\hat{\mathbf{p}}_\star}{(2\pi)^3} \\ + i\frac{gm^2}{\bar{\rho}a^3}\int\left(\mathbf{k}\cdot\nabla_{\hat{\mathbf{p}}}f_0\right)\int_{\xi_{\rm kd}}^{\xi}\mathrm{d}\xi' a^2(\xi')\Phi(\mathbf{k},\xi')\exp\left(-i\frac{\mathbf{k}\cdot\hat{\mathbf{p}}}{m}(\xi-\xi')\right)\frac{\mathrm{d}^3\hat{\mathbf{p}}_\star}{(2\pi)^3} \end{aligned} \tag{3.137}$$

Using an integration by part in the last integral

$$\begin{aligned} \delta(\mathbf{k},t) = \frac{gm}{\bar{\rho}a^3}\int f_1(\mathbf{k},\hat{\mathbf{p}},\xi_{\rm kd})\exp\left(-i\frac{\mathbf{k}\cdot\hat{\mathbf{p}}}{m}(\xi-\xi_{\rm kd})\right)\frac{\mathrm{d}^3\hat{\mathbf{p}}_\star}{(2\pi)^3} \\ - \frac{gmk^2}{\bar{\rho}a^3}\int_{\xi_{\rm kd}}^{\xi}\mathrm{d}\xi'\xi' a^2(\xi')\Phi(\mathbf{k},\xi')\mathcal{G}_0\left(\frac{\mathbf{k}}{m}(\xi-\xi')\right) \end{aligned} \tag{3.138}$$

with $k = (\delta_{ij}k^ik^j)^{1/2}$. Moreover we introduced $\mathcal{G}_n$ the kernel function

$$\mathcal{G}_n(\mathbf{s}) \equiv \int f_0(\hat{q})\hat{q}^n e^{-i\mathbf{s}\cdot\hat{\mathbf{p}}}\frac{\mathrm{d}^3\hat{\mathbf{p}}_\star}{(2\pi)^3} = \int_0^\infty\frac{\mathrm{d}\hat{q}}{2\pi^2}f_0(\hat{q})\frac{\hat{q}^{n+1}}{s}\sin(\hat{q}s)\,. \tag{3.139}$$

The second equality comes from the simple dependence of f_0 with $\hat{q}$. In order to go further in the analysis it is necessary to have more information on f_0 and f_1 at the initial time. Let us assume that f_0 is given by the Maxwell-Boltzmann distribution

$$f_0(\hat{q}) = \exp\left(\frac{\mu-m}{T_0}\right)\exp\left(-\frac{\hat{q}^2}{2ma^2T_0}\right)\,, \tag{3.140}$$

where T_0 here represent the temperature of the species background and not the temperature of the plasma. As introduced in Chapter 2, $T_0 \propto a^{-2}$ for a massive species and then the PSDF f_0 is in fact independent on time. At initial time, we further assume that f_1 can be approximated by its first order expansion in μ and T_0,

$$\frac{f_1(\mathbf{k},\hat{\mathbf{p}},\xi_{\rm kd})}{f_0(\hat{q})} = \delta\left(\frac{\mu}{T_0}\right) + \left(\frac{m}{T_0}+\frac{\hat{q}^2}{2ma^2T_0}\right)\frac{\delta T_0}{T_0} + \mathcal{O}\left(\left(\frac{\delta\mu}{\mu}\right)^2 + \left(\frac{\delta T_0}{T_0}\right)^2\right)\,. \tag{3.141}$$

According to GREEN et al. (2005), considering the adiabatic evolution, up to kinetic decoupling, allows us to write

$$\frac{f_1(\mathbf{k},\hat{\mathbf{p}},\xi_{\rm kd})}{f_0(\hat{q})} = \frac{\hat{q}^2}{3ma_{\rm kd}^2T_{\rm kd}}\delta(\mathbf{k},t_{\rm kd}) + \mathcal{O}\left(\left(\frac{\delta\mu}{\mu}\right)^2 + \left(\frac{\delta T_0}{T_0}\right)^2\right) \tag{3.142}$$

with $T_{\rm kd} = T_0(t_{\rm kd}) = T_0(\xi_{\rm kd})$ and $a_{\rm kd} = a(t_{\rm kd})$. Inserting this relation into Eq. (3.138), gives a relation for the density contrast as

$$\begin{aligned} \delta(\mathbf{k},t) = \frac{g\delta(\mathbf{k},\xi_{\rm kd})}{3T_{\rm kd}\bar{\rho}a^3}\mathcal{G}_2\left(\frac{\mathbf{k}}{m}(\xi-\xi_{\rm kd})\right) \\ - \frac{gmk^2}{\bar{\rho}a^3}\int_{\xi_{\rm kd}}^{\xi}\mathrm{d}\xi'\xi' a^2(\xi')\Phi(\mathbf{k},\xi')\mathcal{G}_0\left(\frac{\mathbf{k}}{m}(\xi-\xi')\right)\,. \end{aligned} \tag{3.143}$$

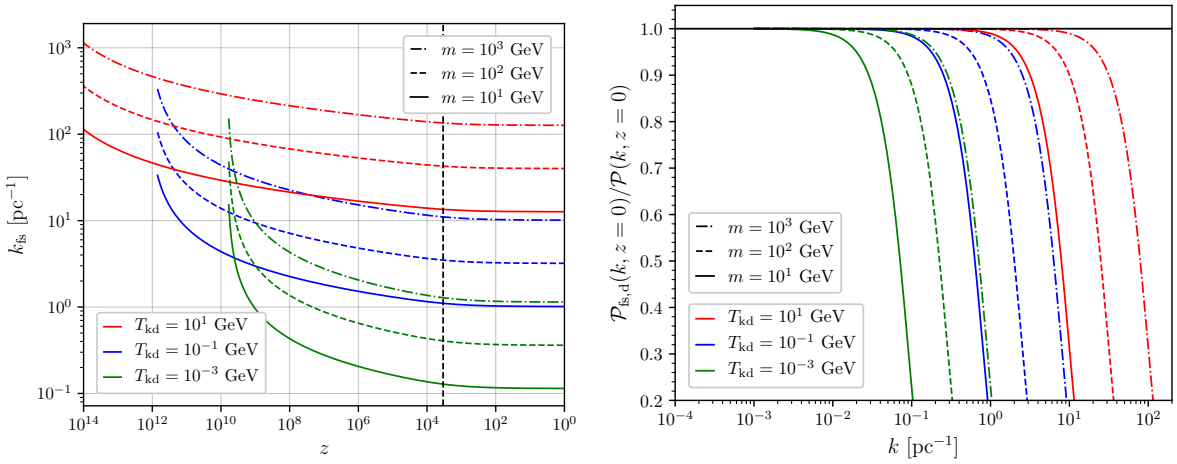

Figure 3.8 – Right panel: Evolution of the comoving free-streaming Fourier scale with the redshift for different kinetic decoupling temperatures and different DM mass. **Left panel:** Ratio of the matter power spectrum damped due to free-streaming and acoustic oscillation matter over the perfect CDM power spectrum.

Moreover, it is also possible to neglect the gravitational potential, as a good approximation, in order to simplify the expression. Evaluating $\mathcal{G}_2$ and $\overline{\rho}$ using the expression of f_0, yields the following ratio between the density contrast at time t and the density contrast at the moment of kinetic decoupling $t_{\rm kd}$:

$$\frac{\delta(\mathbf{k},t)}{\delta(\mathbf{k},t_{\rm kd})} = \left[1 - \frac{2}{3}\left(\frac{k}{k_{\rm fs}}\right)\right] e^{-\left(\frac{k}{k_{\rm fs}}\right)^2} \quad \text{with} \quad k_{\rm fs}(t) \equiv \left[a_{\rm kd}\sqrt{\frac{T_{\rm kd}}{2m}}\int_{t_{\rm kd}}^{t}\frac{\mathrm{d}t}{a^2(t')}\right]^{-1}. \tag{3.144}$$

In the end, this equation, valid for $k < k_{\rm fs}$, shows that Fourier modes greater than $k_{\rm fs}$ are damped. Indeed, these are scales for which the velocity dispersion is no longer negligible. In practice the effect is taken into account in the transfer function that is modified according to

$$T(k) \to T(k)\left[1 - \frac{2}{3}\left(\frac{k}{k_{\rm fs}}\right)^2\right] e^{-\left(\frac{k}{k_{\rm fs}}\right)^2}. \tag{3.145}$$

3.6.3 The free-streaming length and mass

A common approach is also to define the free-streaming length at time t as the proper distance that DM particles travelled from kinetic decoupling to today. Then it is possible to roughly evaluate the free-streaming scale as the inverse of this distance. The free-streaming length is defined as

$$\lambda_{\rm fs}(t) \equiv a(t)\int\sqrt{\delta_{ij}\mathrm{d}x^i\mathrm{d}x^j} \tag{3.146}$$

and one can show, using the 4-momentum $p^\mu = m\mathrm{d}x^\mu/\mathrm{d}\tau$ that

$$\begin{aligned}\lambda_{\rm fs}(t) &= a(t)\int_{t_{\rm kd}}^{t}\sqrt{\delta_{ij}p^ip^j}\frac{\mathrm{d}\tau}{\mathrm{d}t'}\mathrm{d}t' = a(t)\int_{t_{\rm kd}}^{t}\frac{p(t')}{a(t')E[p(t')]}\mathrm{d}t' \\ &= a(t)\int_{t_{\rm kd}}^{t}\frac{v(t')}{a(t')}\mathrm{d}t' = a(t)v_{\rm kd}a_{\rm kd}\int_{t_{\rm kd}}^{t}\frac{\mathrm{d}t'}{a^2(t')}\end{aligned} \tag{3.147}$$

The last equality comes from the fact $v \propto 1/a$ and with $v_{\rm kd}$ being the velocity of the particles at kinetic decoupling. Therefore the free-streaming length and the Fourier mode are related by the relation

$$\lambda_{\rm fs} = a(t)\frac{v_{\rm kd}}{k_{\rm fs}}\sqrt{\frac{2m}{T_{\rm kd}}} \tag{3.148}$$

In practice $v_{\rm kd}$ is distributed according to the PSDF f_0. Then its PDF is

$$p_{v_{\rm kd}}(v_{\rm kd}) = \sqrt{\frac{2}{\pi}}\left(\frac{m}{T_{\rm kd}}\right)^{3/2} v_{\rm kd}^2 e^{-\frac{mv_{\rm kd}^2}{2T_{\rm kd}}} \tag{3.149}$$

and its average $\overline{v_{\rm kd}} = \sqrt{8T_{\rm kd}/(\pi m)}$. BERTSCHINGER (2006) has numerically solved the Boltzmann hierarchy in a general relativistic set-up and has found that at kinetic decoupling the average velocity must be corrected by a numerical factor so that $\overline{v_{\rm kd}} = \sqrt{6T_{\rm kd}/(5m)}$. In the end, it yields that $\overline{\lambda_{\rm fs}} \sim a(t)/k_{\rm fs}$. A simple expression for the minimal mass of subhalos accessible due to free streaming damping is given by the mass enclosed in the comoving scale $k_{\rm fs}$ today

$$M_{\rm fs} \equiv \frac{4\pi}{3}\overline{\rho}_{\rm m}(t_0)\left(\frac{\pi}{k_{\rm fs}(t_0)}\right)^3 = \frac{4\pi}{3}\overline{\rho}_{\rm m}(t_0)\overline{\lambda_{\rm fs}}^3(t_0)\left(\frac{\pi}{\overline{v_{\rm kd}}}\sqrt{\frac{T_{\rm kd}}{2m}}\right)^3 . \tag{3.150}$$

The last term inside the parentheses in the right hand side is an $\mathcal{O}(1)$ number.

The expression of $k_{\rm fs}$ can be numerically evaluated first by replacing the integral on time by an integral on the scale factor, and by making explicit the dependence on the Hubble parameter

$$\int_{t_{\rm kd}}^{t}\frac{{\rm d}t}{a^2(t')} = \int_{a_{\rm kd}}^{a}\frac{{\rm d}a}{a^3 H(a)} . \tag{3.151}$$

As performed in GONDOLO et al. (2012), the integral can be done in two parts. Introduce the scale factor (resp. time) $a_\star$ (resp. $t_\star$) such that at that time the universe has a temperature $T_\star$ much smaller than the electron-positron annihilation temperature but also higher than the temperature at the matter-radiation equivalence $T_{\rm eq}$. Then, for late times, $t > t_\star$,

$$\int_{t_{\rm kd}}^{t}\frac{{\rm d}t}{a^2(t')} = \int_{a_{\rm kd}}^{a_\star}\frac{{\rm d}a}{a^3 H(a)} + \int_{a_\star}^{a}\frac{{\rm d}a}{a^3 H(a)} . \tag{3.152}$$

Replacing H by its expression in terms of degrees of freedom Eq. (2.87) in the first part and by its expression for a Universe made of matter and radiation Eq. (2.24) in the second part yields the final expression

$$\begin{aligned}\int_{t_{\rm kd}}^{t}\frac{{\rm d}t}{a^2(t')} &= \frac{\sqrt{2}}{a_{\rm eq}^2 H_{\rm eq}}\left\{\left[\ln\left(\frac{B(T)-1}{B(T)+1}\right)\right]_{T_{\rm kd}}^{T} + K_{\rm fs}(T_{\rm kd})\right\} \\ &\text{with}\quad K_{\rm fs}(T_{\rm kd}) \equiv \frac{\sqrt{g_{\rm eff}(T_\star)}}{h_{\rm eff}^{2/3}(T_\star)}\int_{T_\star}^{T_{\rm kd}}\left[\frac{g_\star^{1/2}(T')}{h_{\rm eff}^{1/3}(T')} - 1\right]\frac{{\rm d}T'}{T'} \\ &\text{and}\quad B(T) \equiv \sqrt{1+\frac{T_{\rm eq}}{T}} ,\end{aligned} \tag{3.153}$$

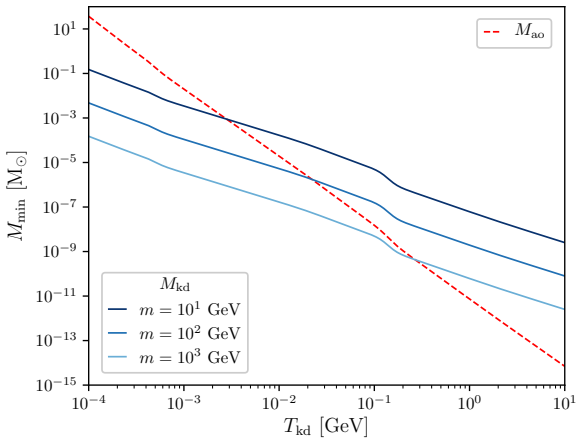

Figure 3.9 – Minimal halo mass due to acoustic oscillations from Eq. (3.160) (dashed red) and free-streaming damping (solid blue) for different DM particle masses.

provided that $T_\star \gg T_{\rm eq}$. Here T represents the temperature of photons at time t. Eventually, in order to evaluate $k_{\rm kd}$ one also needs the scale factor at kinetic decoupling, $a_{\rm kd}$, which can be obtained as

$$a_{\rm kd} = \frac{T_{\rm eq}}{T_{\rm kd}} \left(\frac{h_{\rm eff}(T_{\rm eq})}{h_{\rm eff}(T_{\rm kd})} \right)^{1/3} a_{\rm eq} \,. \tag{3.154}$$

After matter-radiation equality when $T \ll T_{\rm eq}$, assuming also that $T_{\rm kd} \gg T_{\rm eq}$ for simplicity, one can expand the expression of Eq. (3.153) as

$$\int_{t_{\rm kd}}^{t} \frac{{\rm d}t}{a^2(t')} \simeq \frac{\sqrt{2}}{a_{\rm eq} H_{\rm eq}^2} \left[\ln\left(\frac{T_{\rm eq}}{4T_{\rm kd}} \right) + K_{\rm fs}(T_{\rm kd}) - 2\sqrt{\frac{T}{T_{\rm eq}}} \right] \tag{3.155}$$

which tends to a constant at small temperature, i.e. at large time. Therefore one roughly has $\overline{\lambda_{\rm fs}}(t > t_{\rm eq}) \propto a(t)$ and $k_{\rm fs}(t > t_{\rm eq}) = {\rm cst}$. Consequently, the free-streaming mass can often be found written under the forms

$$M_{\rm fs} = \frac{4\pi}{3} \overline{\rho}_{\rm m}(t_{\rm eq}) \left(\frac{\pi a_{\rm eq}}{k_{\rm fs}(t_{\rm eq})} \right)^3 = \frac{4\pi}{3} \overline{\rho}_{\rm m}(t_{\rm eq}) \overline{\lambda_{\rm fs}}^3(t_{\rm eq}) \left(\frac{\pi}{\overline{v_{\rm kd}}} \sqrt{\frac{T_{\rm kd}}{2m}} \right)^3 \tag{3.156}$$

using the fact that $\rho_{\rm m}(t_0) = \rho_{\rm m}(t_0) a_0^3 = \rho_{\rm m}(t_{\rm eq}) a_{\rm eq}^3$. In the right panel of Fig. 3.8 the evolution of the comoving free-streaming Fourier scale $k_{\rm fs}(t)$ is represented with the redshift. It shows that, indeed, after matter radiation equality the free-streaming length reaches an asymptotes. In Fig. 3.9 the free-streaming mass is plotted in blue for different DM masses. It can go as low as 10^{-11} M$_\odot$ in the most extreme cases shown.

3.6.4 Acoustic damping effect and minimal mass

Before kinetic decoupling, the WIMPs are coupled to the relativistic plasma and therefore they cannot be treated as separate fluids. All the modes which enter the horizon scale in that period are subject to Jean's oscillations due to the competition between pressure induced by the plasma and gravity. Moreover, because the decoupling is not instantaneous, viscosity is responsible for a damping of the sub-horizon modes when their oscillation frequency becomes higher than the scattering

rate. This corresponds to the Silk damping for baryons (SILK 1968). The exact analysis of viscosity in an imperfect fluid in a general relativistic framework is beyond the scope of this short review – see BOEHM et al. (2001), HOFMANN et al. (2001), BOEHM et al. (2005), and LOEB et al. (2005). Following the authors of GREEN et al. (2005), similarly to the free-streaming damping, it is possible to define a collisional damping scale k_d such that

$$\frac{\delta(\mathbf{k}, t_\mathrm{kd})}{\delta(\mathbf{k}, t_i)} = e^{-\left(\frac{k}{k_\mathrm{d}}\right)^2} \tag{3.157}$$

with t_i the initial time, and where they give the approximation

$$k_\mathrm{d} \simeq 1.8 \left(\frac{m}{T_\mathrm{kd}}\right)^{1/2} a_\mathrm{kd} H_\mathrm{kd} \,. \tag{3.158}$$

The total impact on the overdensity field is given by

$$\frac{\delta(\mathbf{k}, t)}{\delta(\mathbf{k}, t_i)} = \frac{\delta(\mathbf{k}, t)}{\delta(\mathbf{k}, t_\mathrm{kd})} \frac{\delta(\mathbf{k}, t_\mathrm{kd})}{\delta(\mathbf{k}, t_i)} = \left[1 - \frac{2}{3}\left(\frac{k}{k_\mathrm{fs}}\right)^2\right] e^{-\left(\frac{k}{k_\mathrm{fs}}\right)^2 - \left(\frac{k}{k_\mathrm{d}}\right)^2} \tag{3.159}$$

The total effect on the matter power spectrum is shown in the left panel of Fig. 3.8. In the following, however, we use the same prescription as GONDOLO et al. (2012) by considering an acoustic damping scale set by the sound horizon scale at kinetic decoupling uniquely. This roughly amounts to slightly overestimate k_d by not considering the term $(m/T_\mathrm{kd})^{1/2}$ which is of the order $\sim 10^{-1} - 10^{-2}$. More precisely, as the sound speed is $c_s = 1/\sqrt{3}$ in a relativistic plasma, the comoving sound horizon scale is $k_\mathrm{ao} \sim \sqrt{3}\mathcal{H}_\mathrm{kd} \sim a_\mathrm{kd}\sqrt{3}H_\mathrm{kd}$. The corresponding acoustic mass is

$$M_\mathrm{ao} \equiv \frac{4\pi}{3}\bar{\rho}_\mathrm{m}(t_\mathrm{kd}) \left(\frac{\pi a_\mathrm{kd}}{k_\mathrm{ao}}\right)^3 = \frac{4\pi}{3}\bar{\rho}_\mathrm{m}(t_\mathrm{kd}) \left(\frac{1}{\sqrt{3}H_\mathrm{kd}}\right)^3 . \tag{3.160}$$

which amounts to define a minimal halo mass as

$$M_\mathrm{min} = \max\left[M_\mathrm{ao}, M_\mathrm{fs}\right] \tag{3.161}$$

The evolution of M_ao with the kinetic decoupling temperature is plotted as the dashed red line on Fig. 3.9. We can explain the different behaviours in these plots with the mass and the temperature. Indeed for the free-streaming mass, the dominant term in front of the free-streaming mode k_fs is $a_\mathrm{kd}^{-1}(T_\mathrm{kd}/m)^{-1/2}$ with $a_\mathrm{kd} \sim 1/T_\mathrm{kd}$. Therefore $M_\mathrm{fs} \sim (mT_\mathrm{kd})^{-3/2}$. Similarly for the acoustic mass, if one considers k_d given by Eq. (3.158) then it yields $M_\mathrm{ao} \sim (mT_\mathrm{kd})^{-3/2}$. However for $k_\mathrm{ao} \sim a_\mathrm{kd}\sqrt{3}H_\mathrm{kd}$ there is no direct dependence on the mass and one finds $M_\mathrm{ao} \sim T_\mathrm{kd}^{-3}$. This is exactly what is observed in the figure.

3.7 Conclusion

In this chapter, we have detailed the formation and cosmological distribution of DM halos. We have shown the first-order equations governing the evolution of the density contrasts for matter and radiation as well as their velocity. Then, we briefly have mentioned the initial conditions and, with some approximations, we have derived the main behaviours, in particular that of the matter density contrast; the latter grows logarithmically in the radiation dominated era and linearly in the matter-dominated

era. Afterwards, we have shown a simple model to explain the formation of halos through their collapse and virialisation. From there we have dived into the statistical properties of the density contrast field. We haves shown how to characterise the field of density fluctuations through the matter power spectrum and how to evaluate the matter power spectrum from the primordial curvature perturbations. Eventually, we have reviewed the Press-Schechter formalism and its extension, the Excursion Set Theory and we have detailed the construction of Merger Trees as a theoretical framework to predict the (sub)halo mass function. So far all these results were already known in the literature. Nevertheless, with our own implementation of a Merger Tree algorithm, we have evaluated the first order unevolved subhalo mass function USMF[1] while ensuring its consistent normalisation through a fitting procedure that is slightly tweaked in comparison to the literature. Inserting this USMF[1] in the SL17 model we have recovered a population of subhalos in the MW that is consistent with simulations – and with its original calibration procedure; this is detailed in Chapter 4. In the end, we have connected the formation history of halos to Chapter 2 by introducing the free-streaming and acoustic damping of small over-densities. With several approximations, we have shown how to evaluate the minimal mass of halos from the DM mass and the temperature of the photon bath at kinetic decoupling.

Having revisited the entire formation history of halos is an asset to now improve the SL17 model in different directions. First, as already mentioned, the evaluation of the USMF for Merger Trees allows to properly normalise the SL17 model without directly relying on cosmological simulations. However Merger Trees are much more than the USMF, since they reproduce the complete cosmological history of the halos. As done in Cole et al. (2002), Bosch et al. (2005), Zentner et al. (2005), Giocoli et al. (2008a), Benson (2012), Jiang et al. (2016), and Hiroshima et al. (2018), they could theoretically be used to more precisely predict the evolved distribution of subhalos today – in comparison to what is done with the recipe of the SL17 model – and at higher redshifts. However, Merger Trees are only efficient to describe the large mass range of subhalos and extrapolation to the total population is not trivial if we want to avoid, as much as possible, relying on cosmological simulations. This calls for further work as it may have several interesting applications. For instance, for the use of the 21-cm cosmological signal/s to probe the dark ages of the universe, where subhalos could have a strong impact (Lopez-Honorez et al. 2016).

IV

Effect of baryonic tides on the Galactic subhalo population

"Petite furie, je me bats pour toi
Pour que dans dix mille ans de ça
On se retrouve à l'abri, sous un ciel aussi joli
Que des milliers de roses
Je viens du ciel et les étoiles entre elles
Ne parlent que de toi
D'un musicien qui fait jouer ses mains
Sur un morceau de bois
De leur amour plus bleu que le ciel autour"

Francis Cabrel, Petite Marie

Contents

In the previous chapter, we have summarised the entire evolution of halos from their formation seeded by primordial fluctuation through their virialisation and up to today. However, the extended Press-Schechter formalism only informs about the statistical count of halos and says nothing about their structural properties and their spatial distribution (with the exception of the bias parameter that we do not discuss). In this section, we enter deeper into the descriptions of halos, from their internal properties to the study of global populations. In particular, we address the structuring of DM in the MW and, more specifically, study the population of subhalos (i.e the halos inside the Galactic halo) throughout the analytical and dynamically constrained SL17 model (STREF et al. 2017). In this article, as a first-order description of the complex Galactic DM distribution, it is assumed that all subhalos of the MW are stripped and potentially destroyed due to two dynamical effects called smooth stripping and disc shocking. However, several other dynamical processes can impact on the subhalo population. Many studies have been carried out on this topic (TAYLOR et al. 2001; BOSCH et al. 2005; PENARRUBIA et al. 2005; ZENTNER et al. 2005; PEÑARRUBIA et al. 2010; JIANG et al. 2016; DELOS 2019b; OGIYA et al. 2019). This chapter focuses on a specific process: the subhalo-star encounters in the Galactic disc. They have been studied with (semi-)analytical models in V. BEREZINSKY et al. (2005), GREEN et al. (2007), SCHNEIDER et al. (2010), and V. S. BEREZINSKY et al. (2014) and with numerical simulations in ANGUS et al. (2007) and DELOS (2019a). It has been shown that they can have serious consequences on individual subhalos but the global impact on the total population of the MW has never been evaluated accurately. Our goal is therefore to implement subhalo-star encounters as a new feature of the SL17 model.

Because the SL17 model is purely analytical, we keep on with the same philosophy to include the impact of stars. It has the main advantage of producing results in a matter of seconds (ideal for large scans of the parameter space) and making the model easily scalable to any other Galaxy-like objects. Nonetheless, inherently to the non-linear aspect of the issue, the derivation we propose relies on several assumptions that we carefully justify.

In several of the aforementioned in-depth (semi-)analytical analysis of the stellar encounter process, the authors evaluate the fraction of disrupted subhalos by comparing the total binding energy of each clump of DM with the kinetic energy kick they receive during the encounter. However as mentioned in GREEN et al. (2007) and BOSCH et al. (2018b) this procedure does not provide a satisfactory criterion to claim the disruption since it does not relate directly to the capacity of a subhalo to survive. We provide here another method to evaluate the disruption efficiency. Moreover most of these studies rely on a computation that has been developed for the encounter of two galaxies and performed in GERHARD et al. (1983) – hereafter GF83 – based itself on SPITZER (1958). Then it has been adapted to the encounter between a cluster of stars and black hole (B. J. CARR et al. 1999) and for the encounter of sub-halos with stars later on. While this simple formula provides the correct scaling and the right asymptotic behaviour is some limits it was made to describe, originally, the encounter of two extended objects. Because a star has a typical size much smaller than the typical size of a subhalo it can be considered negligible, which allows us to improve the computation as we aim to prove.

This chapter is divided as follows. In the first two parts Sect. 4.1 and Sect. 4.2 we recall the main features of the SL17 model by detailing the description of individual (sub)halos and then their global, constrained, distribution in the MW. Then we move on to the impact of the individual stellar encounters on the subhalo population. In

Sect. 4.3 we start by studying the encounter of one star with one subhalo, refining the original and usual analytical computations. In Sect. 4.4 we analytically integrate the effect of several encounters on a single subhalo. Eventually, in Sect. 4.5 we show, for the first time, a complete evaluation of the consequences for the constrained total subhalo population in the MW.

4.1 Properties of individual halos and subhalos

In this section we are interested in the internal properties of halos. We start by focusing on their mass density profile parametrised by a scale radius and scale density and later introduce the virial mass and concentration. Eventually we address briefly the interdependence of these different parameters.

4.1.1 Mass density profile, mass profile and gravitational potential

Because virialisation is a non-linear process, it is challenging to analytically and accurately predict the structure of halos; therefore, one relies on numerical simulations. The density profile of a subhalo is a result of several processes that can be internal – phase mixing, relaxation – or due to interactions with the environment – accretion, mergers. Cosmological simulations have shown that the shape of dark halos presents a self-similar structure over a large range of scales. Such a halo shape should then describe all systems down to all existing layers of inhomogeneities like subhalos and sub-subhalos, etc. This result is due to Navarro et al. (1996) who showed, more particularly, that dark halos are spherical with a mass density well fitted by

$$\rho(x) = \rho_{\rm s} \times \left\{ g(x) = \frac{1}{x(1+x)^2} \right\} \tag{4.1}$$

where $\rho_{\rm s}$ is called the scale density and the scaled variable $x = r/r_{\rm s}$ represents the ratio of the distance r from the centre of the halo over the scale radius $r_{\rm s}$. The function g is implicitly defined as the dimensionless mass density. This profile is now called the NFW profile. A more general version is

$$g(x) = \frac{1}{x^{\gamma}(1+x^{\alpha})^{(\beta-\gamma)/\alpha}} \tag{4.2}$$

that we refer to as the (α, β, γ) model. The NFW profile is recovered for $(\alpha, \beta, \gamma) = (1, 3, 1)$. This model is convenient as varying the parameters allows describing a variety of different relevant shapes. Indeed the NFW profile is cuspy, that is $\rho(r) \to \infty$ when $r \to 0$ but today some observations points toward possible cored profiles – in dwarf galaxies for instance Oh et al. (2015) where $\rho(r) \to \text{cst.}$ when $r \to 0$. As γ provides the inner slope of the profile, taking $\gamma \to 0$ allows to recover a core. The other parameters β and α control respectively the outer slope and the transition regime between the centre and the outskirts. In this work we use $(\alpha, \beta, \gamma) = (1, 3, 0)$ just called cored profile in the next chapter and $(\alpha, \beta, \gamma) = (2, 5, 0)$ called the Plummer profile (Plummer 1911). Since the original work that introduced the NFW profile, other propositions have been made, providing better fit to simulations, such as the Einasto profile (Springel et al. 2008), given by

$$g(x) = \exp\left(-\frac{2}{\alpha} \left[x^{\alpha} - 1 \right] \right) . \tag{4.3}$$

This profile is cored, however, simulations show that the parameter α is ~ 0.17. Thus, it effectively behaves as a core only when $x \lesssim 10^{-3}$. All in all, cosmological simulations tend to favour little to no cores. The different dimensionless mass density profiles are represented in the right panel of Fig. 4.1. In this plot, the range of radii does not allow to see the cored feature of the Einasto profile when $\alpha = 0.17$ as it is too small.

From the density profile several other quantities can be derived. First the mass profile, representing the mass contained in the ball delimited by the spherical shell at radius r, is

$$m(r) = \int_{|\mathbf{r}'|<r} \rho(r')\mathrm{d}^3\mathbf{r}' = 4\pi\rho_\mathrm{s} r_\mathrm{s}^3 \left\{ \mu(x) \equiv \int_0^x g(x')x'^2\mathrm{d}x' \right\} . \tag{4.4}$$

In the case of an NFW profile, in particular, the result is

$$\mu(x) = \ln(1+x) - \frac{x}{1+x} . \tag{4.5}$$

One could worry that here $\mu(x \to \infty) \to \infty$, making the mass of the dark halo ill-defined. In practice one can associate a finite size to halos: either their virial radius if they are isolated or a smaller one if, throughout their history, they have been pruned by interactions with their environment. Moreover one can also compute the internal gravitational potential Φ of an isolated dark halo (provided that it only contains DM). Indeed from Poisson equation one has $\Delta\Phi = 4\pi G_\mathrm{N}\rho$. Inverting this equation yields

$$\Phi(r) = -G_\mathrm{N} \int_r^\infty \frac{m(r')}{r'^2}\mathrm{d}r' . \tag{4.6}$$

4.1.2 Virial parameters

A subhalo of mass M is considered formed once it is virialised – see Sect. 3.3 . An interesting quantity is the value of the true overdensity at virialisation, not only the extrapolated value from the linear approximation. We can compute that, within the spherical top-hat collapse model, the overdensity at turn-around δ_{ta} is given by evaluating δ at the turn-around conformal time $\tau_\mathrm{ta} = \pi$ corresponding to $t_\mathrm{ta} = \pi G_\mathrm{N} M/(2\mathcal{E})$ according to Eq. (3.49) and, $\delta_\mathrm{ta} = \delta(\tau_\mathrm{ta}) = 9\pi^2/16 - 1$ according to Eq. (3.50). However while the spherical collapse model predicts virialisation at $\tau = 3\pi/2$, cosmological simulations predict a virialisation time closer to $\tau_\mathrm{vir} = 2\pi$, corresponding to $t_\mathrm{vir} = \pi G_\mathrm{N} M/\mathcal{E} = 2t_\mathrm{ta}$ where δ diverges. Therefore, in order to extract the value of the overdensity at virialisation we rely on the fact that the virial theorem always imposes that the radius of the structure at virialisation $R(t_\mathrm{vir})$ must be half the radius at turnaround. Thus, because in the matter domination era $\overline{\rho} \propto t^{-2}$, it yields $\overline{\rho}(t_\mathrm{vir}) = \overline{\rho}(t_\mathrm{ta})/4$. Moreover, since the density inside the structure is $\rho = 3M/(4\pi R^3)$, consequently $\rho(t_\mathrm{vir}) = 8\rho(t_\mathrm{ta})$ because of the evolution of R between these two instants. Therefore introducing the density contrast as $\Delta \equiv \delta + 1$, for simplicity, at virialisation it satisfies

$$\Delta_\mathrm{vir} = \frac{\rho(t_\mathrm{vir})}{\overline{\rho}(t_\mathrm{vir})} = 32\Delta_\mathrm{ta} = 18\pi^2 , \tag{4.7}$$

which is once again independent of the mass of the structure. Naturally this simple approximation needs to be corrected when we take into account that $\Omega_\mathrm{m} \neq 1$.

Under the hypothesis that the curvature of the universe is null, $\Omega_{\rm K} = 0$, (BRYAN et al. 1998) give the fitting formula

$$\Delta_{\rm vir}(z_{\rm vir}) = 18\pi^2 + 82q(z_{\rm vir}) - 39q^2(z_{\rm vir}) \quad \text{where} \quad q(z) = \frac{\Omega_{\Lambda,0}}{\Omega_{\rm m,0}(1+z)^3 + \Omega_{\Lambda,0}}\,. \tag{4.8}$$

Moreover, $z_{\rm vir}$ is the redshift of virialisation of the structure corresponding to the cosmic time $t_{\rm vir}$. Our first evaluation of this parameter is the $0^{\rm th}$ order of this expression. For $\Omega_{\rm m,0} = 0.31$ and $\Omega_{\Lambda,0} = 0.68$, as soon as $z_{\rm vir} > 10$, the previous functional form exhibits a saturation plateau at $\Delta_{\rm vir} \simeq 18\pi^2 \sim 178$. The mass of the structure is then

$$M = \frac{4}{3}\pi\Delta_{\rm vir}(z_{\rm vir})\overline{\rho}(z_{\rm vir})R^3(z_{\rm vir}) \tag{4.9}$$

and because the $\Delta_{\rm vir}$ is close to the value 200 for the typical collapse redshift, it is common to introduce a density contrast $\Delta = 200$. The main advantage with this fixed number is that, by definition, it is independent of the cosmology. We associate to the constant contrast a slightly modified virial mass and virial radius related by

$$m_\Delta(z) \equiv \frac{4}{3}\pi\Delta\rho_c(z)r_\Delta^3(z)\,. \tag{4.10}$$

In the first part we keep the notation Δ as another prescription than 200 is mathematically equivalent. Then, if one takes $r_\Delta(z_{\rm vir}) = R(z_{\rm vir})$ we recover $m_\Delta(z_{\rm vir}) \simeq M$. The virial mass of a subhalo changes with time because of accretion or by the simple change of $r_{\rm s}(z)$. Eventually, a last quantity of interest, although it has no real physical meaning, is the virial concentration $c_\Delta(z)$. Formally we introduce the radius $r_{-2}(z)$ of a profile as

$$\left.\frac{{\rm d}\ln\rho}{{\rm d}\ln r}\right|_{r=r_{-2}(z)} = -2 \tag{4.11}$$

and the virial concentration is then $c_\Delta(z) = r_\Delta(z)/r_{-2}(z)$. Notice that the ratio $r_{-2}(z)/r_s(z)$ does not depend on $r_s(z)$ so that $r_{-2}(z) = \eta r_{\rm s}(z)$ where η is a fixed number depending only on the profile. Therefore, $\eta c_\Delta(z) = r_\Delta(z)/r_{\rm s}(z)$. In practice for an (α,β,γ) profile one has $r_{-2}(z) = r_{\rm s}(z)\left[(2-\gamma)/(\beta-2)\right]^{1/\alpha}$ which implies $r_{-2}(z) = r_{\rm s}(z)$ for NFW. The main advantage of defining the virial concentration is that it establishes a bijection between $(r_{\rm s}(z),\rho_{\rm s}(z))$ and $(m_\Delta, c_\Delta(z))$. Let us prove it. Firstly, we ask, for consistency,

$$m_\Delta(z) = m(r_\Delta(z)) = 4\pi\rho_{\rm s}(z)r_{\rm s}^3(z)\mu(\eta c_\Delta(z))\,. \tag{4.12}$$

where we have used the dimensionless mass $\mu(x)$. This relation can also be seen, in a way, as the definition of the scale parameters. Secondly, this last equation, combined to Eq. (4.10), then yields the relations

$$\rho_{\rm s}(z) = \frac{\Delta\rho_c(z)}{3}\frac{[\eta c_\Delta(z)]^3}{\mu\left(\eta c_\Delta(z)\right)} \quad \text{and} \quad r_{\rm s}(z) = \frac{1}{\eta c_\Delta(z)}\left[\frac{3m_\Delta(z)}{4\pi\Delta\rho_c(z)}\right]^{1/3}\,. \tag{4.13}$$

Remark that the scale density is only dependant on the virial concentration and not on the virial mass. However, concentration and mass are not entirely independent. Cosmological simulations show that they are anti-correlated which means that subhalos with a lower virial mass tend to have a higher concentration. This effect is called the mass-concentration relation. The next section is dedicated to summarising several approaches to theoretically predict it.

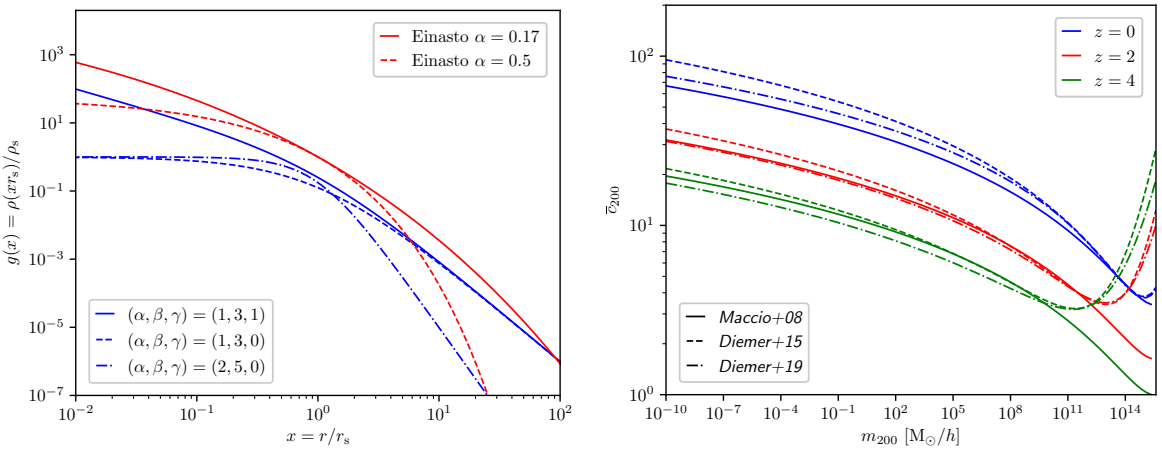

Figure 4.1 – Left panel: Several dimensionless mass density profiles used in this study, NFW (solid blue), cored $\alpha\beta\gamma$ (dashed blue), Plummer (PLUMMER 1911) (dash-dotted blue), Einasto $\alpha = 0.17$ (solid blue) and Einasto $\alpha = 0.5$ (dashed red). The latter is just represented to show the core in the Einasto profile which is not easy to see for $\alpha = 0.17$ in that range of x. **Right panel:** Mass-Concentration relation for different redshifts and given by three models called here Maccio+08 (MACCIO' et al. 2008), Diemer+15 and Diemer+19 (DIEMER et al. 2019). This figure has been produced using the COLOSSUS code (DIEMER 2018) with the Planck18 cosmology.

4.1.3 The virial mass-concentration relation

The anti-correlation of concentration with mass can be well understood by looking at the cosmological history of halos. Indeed halos with a small mass form rather early in the Universe, at a time when the average density is higher. Therefore, in comparison to halos formed at a later time, when the density is smaller, they tend to have lower scale radii and higher concentrations. However, it is difficult to translate this simple idea into a realistic model that can give predictions consistent with the results of simulations. Amongst the most popular models we can cite: BULLOCK et al. (2001b), MACCIO' et al. (2008), LUDLOW et al. (2014), DIEMER et al. (2015), OKOLI et al. (2016), and DIEMER et al. (2019).

An usual method to build models is to assume a behaviour, for the scale density and for the scale radius, similar to what is observed in simulations. Namely, they show that the central density of halos seems to become roughly independent of the redshift after a short period of evolution. In order to see what are the implications for the concentration, one first comment is that we can always relate the concentration at redshift z_1 to concentration at redshift z_2 thanks to the relation

$$\frac{c_\Delta^3(z_1)}{\mu(\eta c_\Delta(z_1))} = \frac{\rho_c(z_2)}{\rho_c(z_1)} \frac{\rho_s(z_1)}{\rho_s(z_2)} \frac{c_\Delta^3(z_2)}{\mu(\eta c_\Delta(z_2))} \,. \tag{4.14}$$

In what is maybe one of the simplest and earliest, yet rather accurate, model developed by BULLOCK et al. (2001b) and MACCIO' et al. (2008). They assume that the parameter which remains constant over time is the pseudo scale density defined as

$$\tilde{\rho}_s = 3\mu(\eta c_\Delta(z))\rho_s(z) \tag{4.15}$$

Replacing in Eq. (4.14), and considering $z_1 = z$ and $z_2 = z_c$ (the redshift of collapse) it yields the expression of the concentration with z as

$$c_\Delta(z) = \frac{1}{\eta}\left[\frac{\tilde{\rho}_s}{\Delta\rho_c(z_c)}\right]^{1/3}\left[\frac{\rho_c(z_c)}{\rho_c(z)}\right]^{1/3} . \tag{4.16}$$

Further assuming that $\tilde{\rho}_s/(\Delta\rho_c(z_c))$ is the same for all halos and is not really sensitive to z_c, one calls this constant ratio K^3. The last step consists in finding z_c for a given halo of mass $m_\Delta(z)$. The main assumption is to say that $m_\Delta(z_{\rm vir}) = m_\star$ is related to $m_\Delta(z)$ by a constant factor F such that $m_\star = F m_\Delta(z)$. Then we define $z_c(F, m_\Delta(z))$ as

$$\sigma_M(m_\star, z_c(F, m_\Delta(z))) = \delta_c \tag{4.17}$$

and the concentration can be obtained by a fit of the parameters F and K on numerical simulations. It is found that for the cosmology of The Planck Collaboration (2014) the best-fit is given by $F = 0.01$ and $K = 4.2$. In the more modern model of Diemer et al. (2019), they assume two phases for the halo evolution. In the first one , the halo grows rapidly with a constant concentration parameter $c_\Delta \sim 4$, which means that $r_s(z)$ follows the increase of $r_\Delta(z)$. In the second phase, which they call "pseudo"-evolution, the halo freezes: ρ_s and r_s become constants (an idea similar to what we have seen above). Using Eq. (4.14) they are then able to relate the concentration to the peak height $\nu(M, z) = \delta_c/\sigma_M(M, z)$ through an implicit function with parameters they fit to their simulations. We do not detail here all the other possible models, however let us just mention the one of Okoli et al. (2016) which is particular because it has the advantage of deriving a concentration from first principles using the ellipsoidal collapse model. Consequently, it almost does not depend on fits of numerical simulations. Several mass-concentration relations are plotted as an illustration for three different redshifts in the left panel of Fig. 4.1. At large redshift and large mass one observe an upturn in the more recent model. This has been interpreted to be due to the presence of unrelaxed halos in the cosmological simulations used to fit the concentration law. Taking only into account the relaxed halos, the upturn would vanish (Ludlow et al. 2014). In the following, however, because we are only interested in the redshift $z = 0$, we use a direct fit to simulations taken from Sánchez-Conde et al. (2014).

4.2 A model for the subhalo population in the Galaxy

More interesting than individual properties of subhalos are their total distribution in galaxies, dwarfs, galaxy clusters, etc. Indeed, we review in the conclusion of Chapter 2 the main potential impacts of the subhalo population on the detection experiments, namely boost factor of local density enhancements. Consequently, it is essential to properly model their distribution, especially in the MW. In Chapter 3 we already discussed the unevolved distribution of subhalos in a given host through the USMF but we are now interested in the *evolved* counterpart, taking into account dynamical effects. Several methods exist to describe the subhalo population, each has its advantages and drawbacks. Firstly, there are cosmological simulations. They provide the full knowledge of a consistent population in all the mock halos that they produce. The main drawback, however, is the limited resolution (Springel et al. 2008), while subhalos can have masses down to 10^{-12} $M_\odot$ as detailed in Sect. 3.6, cosmological simulations cannot resolve objects with masses $\lesssim 10^4$ $M_\odot$.Moreover, while they can provide MW-like objects for instance, these are not the MW, with its specific

properties and constraints. The second method is to use analytical models, based on cosmological principles and dynamical effects to produce a statistical parametrisation of the subhalo population. In that framework a fully consistent description of a precise constrained host object is possible, however, some assumptions and simplification are required in order to be able to build the models and use them with the aim to make predictions. This approach is detailed in this section through the model (STREF et al. 2017) previously called SL17 and which originally described the subhalo population of the MW. See complementary approaches, in particular with the already mentioned merger tree-based models in e.g. BOSCH et al. (2005), PENARRUBIA et al. (2005), BENSON (2012), ZAVALA et al. (2014), BARTELS et al. (2015), HIROSHIMA et al. (2018), and ISHIYAMA et al. (2020).

4.2.1 The general recipe and initial hypothesis

The SL17 model is inherently built according to the internal properties of dark halos that have been previously summarised. The construction follows the recipe:

- Start from a constrained mass model of the MW that includes baryons and a DM halo, cuspy or cored, (more specifically MCMILLAN (2017) is used) and assume that the latter is the sum of a smooth component and a subhalos component, as expected from the cosmological structure formation in the CDM scenario for the early ages of the Milky Way. These two components are supposed to still be present today.

- Assume that all subhalos are independent hard spheres on circular orbits so that they can be characterised by three quantities: their initial cosmological (or also said fictitious) mass m_Δ, their concentration c_Δ and their distance from the centre of the Galaxy R. The distribution of subhalos along these three variables is described by three PDFs, p_m, p_c and $p_\mathbf{R}$, normalised to unity.

- Assume that, initially, the concentration and mass functions are given by first cosmological principles and that they are independent of the position of the subhalos. Moreover, assume that the subhalos follow the same spatial distribution as the total DM halo (as if they were *large* particles of the halo). Eventually, subhalos initial radial extension is given by their virial radius r_Δ.

- Incorporate the fact that, with time, particles are stripped from the subhalos according to different physical processes (called tidal effects) and that, consequently, subhalos shrink. These tidal effects have two main causes that are detailed later on. They define a new radial extension of the subhalos that depends on their original mass concentration and position and that is called the tidal radius $r_\mathrm{t}(m_\Delta, c_\Delta, R) < r_\Delta$. In consequence their mass gets also smaller than their original virial cosmological mass and is called the tidal mass $m_\mathrm{t} = m(r_\mathrm{t}) < m_\Delta$. If some of them are pruned too much, according to a hand-selected criterion, they are assumed to be destroyed.

- Normalise the whole subhalo mass taking into account that all particles lost by subhalos due to tidal effects are incorporated in the smooth component so that the total constrained DM halo is conserved and that we have reached equilibrium today.

In more details, the total DM density of the MW at distance R from the Galactic centre (GC) can be written as

$$\rho_{\rm tot}(R) = \rho_{\rm sm}(R) + \rho_{\rm sub}(R) \tag{4.18}$$

where ρ represents the smooth DM component and $\rho_{\rm sub}$ describes the average mass density in the form of subhalos. More precisely it is convenient to write it as

$$\rho_{\rm sub}(R) = \int {\rm d}m_{\rm t} m_{\rm t} \frac{{\rm d}n_{\rm sub}}{{\rm d}m_{\rm t}} \tag{4.19}$$

where ${\rm d}n_{\rm sub}/{\rm d}m_{\rm t}$ is the position dependent *evolved* mass function, *i.e.* the final number density of subhalo with a mass $m_{\rm t}$ at the position R. In order to detail the expression of the integral one needs first to address the disruption criterion. According to the results of cosmological simulations (Tormen et al. 1998; Hayashi et al. 2003; Diemand et al. 2004; Diemand et al. 2008; Springel et al. 2008; Bosch 2017) we expect subhalos that are stripped too much (i.e. that have a too small tidal radius) to be destroyed. In the model this is implemented by the criterion

$$\begin{cases} r_{\rm t}/r_{\rm s} \geq \epsilon_{\rm t} & \Rightarrow \quad \text{the subhalo survives} \\ r_{\rm t}/r_{\rm s} < \epsilon_{\rm t} & \Rightarrow \quad \text{the subhalo is disrupted} \end{cases} \tag{4.20}$$

that relies on the value of $\epsilon_{\rm t}$, treated as a fixed input of the model. The lower this coefficient is, the more resilient subhalos are to tidal stripping. Cosmological simulations suggest that it should be taken ~ 1, which implies rather fragile subhalos. However, according to Bosch et al. (2018a,b) and Errani et al. (2020a,b) this is may come from a numerical bias due to the limited resolution. Therefore, typical values can be taken close to $\epsilon_{\rm t} \sim 0$. In practice we consider values in the range $\epsilon_{\rm t} \in [10^{-2}, 1]$.

The entire population is described by a joint PDF on all the cosmological masses m_Δ, concentrations c_Δ and positions R of all the N subhalos. In practice, we only use $\Delta = 200$ – since we have seen it is a good approximation of the real overdensity at virialisation. Henceforth, the subscript Δ is omitted and we write $m = m_{\Delta=200}$, $c = c_{\Delta=200}$ whenever there are no possible confusions. I particular one should be careful not to mistake the cosmological mass m with the function $m(r)$ of r that is the real physical mass enclosed in the ball of radius r of the subhalo (these two quantities are related by $m = m(r_{\Delta=200})$). Using the fact that all subhalos are independent of each other the joint PDF can be factored out into N one-point PDFs as follows

$$p(\{m_i\}_i, \{c_i\}_i, \{R_i\}_i) = \prod_{i=1}^{N} p_1(m_i, c_i, R_i)\,. \tag{4.21}$$

Initially, when tidal effects are not taken into account (when the distribution is the cosmological *unevolved* one), the one-point PDF is factorisable in

$$p_1^{\rm init.}(m, c, R) = p_{\mathbf{R}}(R) p_m(m) p_c(c\,|\,m)\,. \tag{4.22}$$

where $p_{\mathbf{R}}$ is the PDF on the position in the GC assuming isotropy, p_m the PDF on the cosmological mass and p_c the PDF on the concentration. After the inclusion of tidal effects, a population of subhalos is destroyed and their total number decreases to their number in the MW today, denoted $N = N_{\rm sub}$. Mathematically this is included

by an Heaviside function that truncates the population according to the disruption criterion. In practice the one-point PDF at late time becomes

$$p_1^{\rm late}(m,c,R) \equiv \frac{1}{K_{\rm t}} p_{\mathbf{R}}(R) p_m(m) p_c(c\,|\,m) \Theta\left[\frac{r_{\rm t}(m,c,R)}{r_{\rm s}(m,c)} - \epsilon_t\right], \tag{4.23}$$

where $K_{\rm t}$ is a normalisation factor – so that the PDF be normalised to one if integrated on the entire parameter space. For simplicity, and to show that tidal effects are accounted for, we denote in the following $p_1^{\rm late} = p_{\rm t}$. While $p_{\mathbf{R}}$ and p_m are independent, because of the Heaviside function, the total one point PDF, which takes into account tidal stripping, becomes an intricate combination of them.

The PDF on the position is given assuming that subhalos are distributed according to the total DM profile of the MW. Therefore, using simply the density profile of DM in the MW, denoted $\rho_{\rm MW}$, taken from McMillan (2017) yields,

$$p_{\mathbf{R}}(R) = \frac{\rho_{\rm MW}(R)}{M_{200}} \quad \text{with} \quad M_{200} = 4\pi \int_0^{R_{200}} \rho_{\rm MW}(R) R^2 {\rm d}R \tag{4.24}$$

where M_{200} is the virial mass of the total DM Galactic halo inside its virial radius R_{200}.

In the original version, the PDF on the cosmological mass takes the form of a simple power-law

$$p_m(m) = K_m \left(\frac{m}{m_0}\right)^{-\alpha}, \tag{4.25}$$

with K_m and m_0 being normalisation factors. Note that the cosmological mass is bounded from below: it cannot be lower than a given $m_{\rm min}$. As seen in Chapter 2 and Chapter 3, for thermal produced DM WIMPs, the value of $m_{\rm min}$ is fully determined by their microscopic behaviour in the early Universe. Nonetheless, in the SL17 model, it is regarded as a free input parameter. In this simple power-law scenario, the mass index α is taken in $[1.9, 2.0]$ to match with cosmological simulation results (Diemand et al. 2006, 2007; Diemand et al. 2008; Springel et al. 2008; Zhu et al. 2016). Testing the two extreme cases $\alpha = 1.9$ and $\alpha = 2.0$ generally allows bracketing some degree of theoretical uncertainties. Besides, one also needs to fix a maximal cosmological subhalo mass; we choose $m_{\rm max} = M_{200}/100$. In a new, updated version, the PDF of the cosmological mass can be evaluated through the Merger Tree-induced USMF ϕ_1, evaluated in Sect. 3.5. There one simply has

$$p_m(m) = \frac{1}{\tilde{N}_{\rm sub}} \phi_1(m, M_{200}) \quad \text{where} \quad \tilde{N}_{\rm sub} \equiv \int_{m_{\rm min}}^{M_{200}} \phi_1(m, M_{200}) {\rm d}m \tag{4.26}$$

is the total number of unevolved subhalos in the host Galaxy. Remark that in the low mass range it reduces to a power-law with a mass index $\alpha = 1.94$.

Eventually, the concentration is log-normal-distributed (Jing 2000; Bullock et al. 2001a; Wechsler et al. 2002; Maccio' et al. 2007, 2008),

$$p_c(c\,|\,m) = \frac{1}{K_c(m)} \frac{1}{c\sqrt{2\pi}\sigma_c} \exp\left[-\left(\frac{\ln c - \ln \bar{c}}{\sqrt{2}\sigma_c}\right)^2\right] \tag{4.27}$$

with the scatter σ_c and the mass dependent median concentration $\bar{c}(m)$. For simplicity the relation between mass and concentration is, here, taken from result of numerical simulations (Sánchez-Conde et al. 2014),

$$\bar{c}(m) = \sum_{n=0} a_n \left[\ln\left(\frac{m}{h^{-1}{\rm M}_\odot}\right)\right]^n \tag{4.28}$$

with $a_n = [37.5153, -1.5093, 1.636 \times 10^{-2}, 3.66 \times 10^{-4}, -2.89237 \times 10^{-5}, 5.32 \times 10^{-7}]$ and h the scaled Hubble parameter. The scatter, is found to be independent of the mass (MACCIO' et al. 2008) and the value is fixed at $\sigma_c = 0.14 \ln(10)$ as in (MACCIO' et al. 2008; DUTTON et al. 2014; SÁNCHEZ-CONDE et al. 2014). Because $c \in [1, +\infty[$ there is also a normalisation factor K_c given by

$$K_c(m) = \frac{1}{2}\mathrm{erfc}\left(-\frac{\ln \bar{c}(m)}{\sqrt{2}\sigma_c}\right) . \tag{4.29}$$

Let us recall that $p_m(m)$ is not the distribution of the physical mass of subhalos, it is the distribution of cosmological initial mass. The distribution of physical mass at a given position R from the GC takes into account the dynamical effects and is

$$p_{m_\mathrm{t}}(m_\mathrm{t} \,|\, R) = \int_1^\infty \mathrm{d}c \int \mathrm{d}m \, \frac{p_\mathrm{t}(m, c, R)}{p_\mathbf{R}(R)} \delta_\mathrm{D}\left[m_\mathrm{t} - m\left(r_\mathrm{t}(m, c, R)\right)\right] \tag{4.30}$$

with δ_D the Dirac distribution. From this expression it is possible to compute the expression of ρ_sub taking tidal effects into account as expressed in Eq. (4.19), with $\mathrm{d}n_\mathrm{sub}/\mathrm{d}m_\mathrm{t} = N_\mathrm{sub}\, p_{m_\mathrm{t}}(m_\mathrm{t} \,|\, R)$. In conclusion, this models allows to access the complete statistical knowledge of the subhalo population in the MW today. As shown, by this previous example, it can be used to compute any statistical quantity on the subhalo population that has been impacted by tidal effects. In the next section, we briefly introduce tidal effects, from the underlying physical mechanisms to the evaluation of the subhalo tidal radii.

4.2.2 The dynamical constraints on the subhalo

The first dynamical effect is tidal stripping. When a subhalo with a cosmological structure orbits inside a host halo, particles in the outskirts of the subhalo can be more attracted by the gravitational potential of the host than by the potential of the subhalo itself. In other words, outskirts particles are no longer bound to the subhalo. They leave the structure to become particles of the host halo. According to BINNEY et al. (2008), this effect prunes the subhalo until its extension becomes equal to the *smooth Jacobi radius* that is given by

$$r_{\mathrm{t,sm}}(R, m, c) \equiv R \left\{ \frac{m(r_{\mathrm{t,sm}}(R, m, c))}{3\hat{M}(R)F(R)} \right\}^{1/3} \quad \text{with} \quad F(R) = 1 - \frac{1}{3}\frac{\mathrm{d}\ln \hat{M}(R)}{\mathrm{d}\ln R} . \tag{4.31}$$

Here, $\hat{M}(R)$ is the mass of the MW contained in the ball of radius R, due to DM *and* baryons. Interestingly the ratio $r_{\mathrm{t,sm}}/r_\mathrm{s}$ is independent of the virial mass of the subhalo, it only depends on R and c. Indeed one can write

$$\frac{\mu(r_{\mathrm{t,sm}}/r_\mathrm{s})}{(r_{\mathrm{t,sm}}/r_\mathrm{s})^3} = \frac{3}{4\pi\rho_\mathrm{s}(c)}\frac{\hat{M}(R)}{R^3}F(R) \tag{4.32}$$

where the left hand side only depends on c and R.

The second dynamical effect is called tidal shocking by the stellar disc and it is due to baryons. Indeed, crossing the smooth gravitational potential of the Galactic disc induces an energetic and velocity shock for the particles of the subhalo. For

that we use the stellar mass density model of McMillan (2017) defined by a double exponential disc

$$\rho_\star(R,z) = \sum_{i=1}^{2} \left[\frac{\Sigma_i}{2z_i} \exp\left(-\frac{R}{R_i} - \frac{|z|}{z_i} \right) \right] \tag{4.33}$$

where the best-fit parameters are $(\Sigma_1, \Sigma_2) = (8.96, 1.83) \times 10^8$ $\mathrm{M}_\odot\,\mathrm{kpc}^{-2}$, $(R_1, R_2) = (2.5, 3.02)$ kpc and $(z_1, z_2) = (0.3, 0.9)$ kpc. In order to evaluate the impact of disc shocking, we use the impulsive approximation: we consider that the time scale of the crossing is small enough that particles can be considered frozen in the frame of the subhalo. In addition, for simplicity, we give an expression of velocity kick that is averaged over radial shells and only depends on the distance r from the centre of the subhalo as (Ostriker et al. 1972)

$$\Delta\mathbf{v}_\mathrm{d} = \frac{2g_\mathrm{d}}{\sqrt{3}v_z} r\hat{\mathbf{e}}_z \,. \tag{4.34}$$

This expression depends on $\hat{\mathbf{e}}_z$, the axis normal to the galactic plane, v_z the subhalo velocity along $\hat{\mathbf{e}}_z$ and g_d the gravitational acceleration due to the potential of the disc. It is straightforward to relate this velocity kick to a kinetic energy kick per unit of particle mass using

$$\Delta E_\mathrm{d} = \frac{1}{2}\left[(\mathbf{v}_\mathrm{d} + \Delta\mathbf{v}_\mathrm{d})^2 - \mathbf{v}^2 \right] = \frac{1}{2}(\Delta\mathbf{v}_d)^2 + \mathbf{v}.\Delta\mathbf{v}_\mathrm{d} \tag{4.35}$$

where we introduced $\mathbf{v}$ the initial velocity of the particle in the frame of the subhalo. Considering a isotropic initial velocity distribution the second term can be averaged out so that $\Delta E_\mathrm{d} \sim (\Delta\mathbf{v}_\mathrm{d})^2/2$. Nevertheless, we need to come back to the impulsive approximation as, for the innermost particle of a subhalo, it breaks down. There, the adiabatic invariance protects the particle from receiving a too high energy kick. A correction factor can therefore be introduced according to Gnedin et al. (1999) to give

$$\Delta E_\mathrm{d} = \frac{1}{2}\left(\Delta\mathbf{v}_\mathrm{d}\right)^2 A_1(\eta_\mathrm{d}) = \frac{4g_\mathrm{d}^2}{3v_z^2} r^2 A_1(\eta_\mathrm{d}) \tag{4.36}$$

where $A_1(\eta) = (1+\eta^2)^{-3/2}$ and η_d is the adiabatic parameter: a ratio of characteristic times. More precisely, $\eta = t_\mathrm{d}\omega$ with $t_\mathrm{d} = h_\mathrm{d}/v_z$ the crossing time of the disc. We use $h_d \simeq 0.9$ kpc. The quantity ω represents the orbital frequency of the particle approximated by $\omega = \sigma_\mathrm{sub}/r$ with σ_sub the velocity dispersion in the subhalo evaluated using Jean's equation. The functional form of A_1 reproduces the correct behaviour of adiabatic protection, that is, whenever it is efficient, for $\eta_\mathrm{d} \gg 1$, the energy kick is suppressed.

The tidal radius is then evaluated recursively. The number of disc crossings N_cross is evaluated with the assumption that the orbits are circular. The algorithm starts with $r_{\mathrm{t},0} = r_{\mathrm{t,sm}}$ given by Eq. (4.31) for a subhalo of given virial mass m and concentration c. For every crossing, it evaluates a new value of r_t with the requirement that if the kinetic energy kick in a shell is greater than the gravitational potential of the structure at that position, the entire shell is removed. More precisely, we make explicit the dependence in the radius and in the tidal extension r_t of the energy gain function by writing $\Delta E_\mathrm{d} = \Delta E_\mathrm{d}(r, r_\mathrm{t})$. We denote by $\Phi(r, r_\mathrm{t})$ the gravitational potential of the truncated structure – see Eq. (4.6) –

$$\Phi(r, r_\mathrm{t}) = -G_\mathrm{N} \int_r^{r_\mathrm{t}} \frac{m(r')}{r'^2} \mathrm{d}r' \,. \tag{4.37}$$

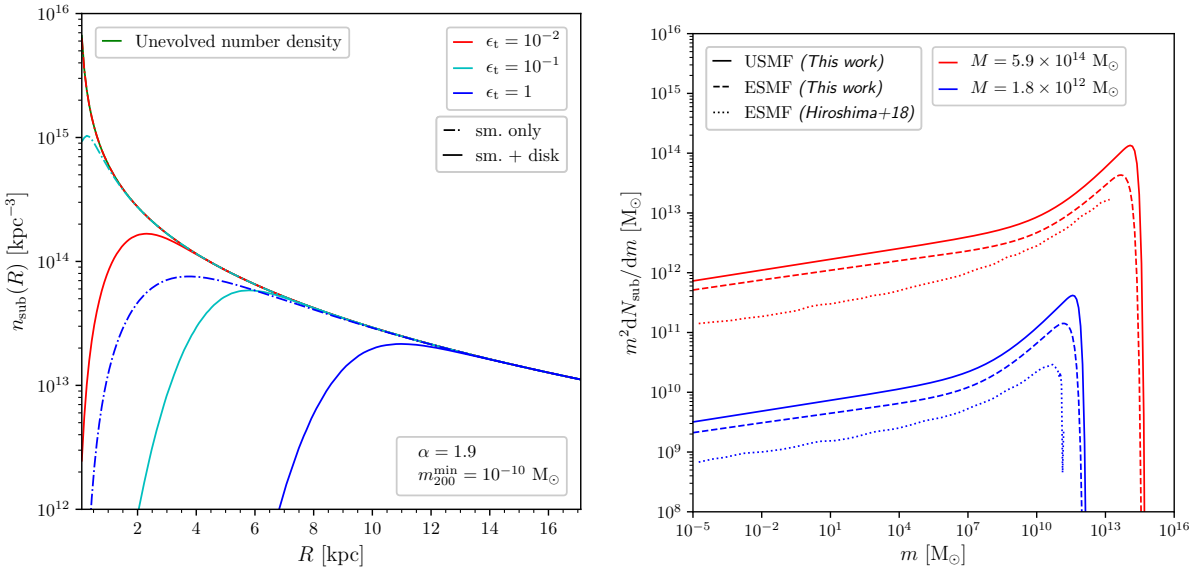

Figure 4.2 – Left panel: Number density of subhalo with respect to the distance from the GC for a minimal subhalo cosmological mass of $m_{200}^{\rm min}$=10^{-10} M$_\odot$ and a mass index $\alpha = 1.9$. The effect of the disc shocking is switched on in the case (sm. + disc) and switched off in the (sm. only) configuration. In comparison is shown the cosmological distribution) in green (superposed to the red dash-dotted curve). **Right panel :** Comparison of the ESMF (dashed lines) obtained from the standardised USMF (solid lines) of Sect. 3.5 with the results of HIROSHIMA et al. (2018) (dotted lines) – here Hiroshima+18. Only the smooth stripping is taken into account and subhalos are considered rather fragile $\epsilon_{\rm t} = 0.77$. The minimal cosmological subhalo mass is set to 10^{-5} M$_\odot$. The two colours, red and blue, correspond to two host masses.

The successive tidal radii, crossing after crossing are evaluated, for the crossing $i+1$, by solving $r_{{\rm t},i+1}$ in the equation

$$\Delta E_{\rm d}(r_{{\rm t},i+1}, r_{{\rm t},i}) = |\Phi(r_{{\rm t},i+1}, r_{{\rm t},i})| \quad \forall i \in [\![0, N_{\rm cross} - 1]\!] \,. \tag{4.38}$$

The tidal radius today is then $r_{\rm t} \equiv r_{{\rm t},N_{\rm cross}}$.

4.2.3 Total number of subhalos

This paragraph is devoted to the evaluation of the total number of subhalo, that is the normalisation of the mass function. In the first place, we review the original method of SL17 and then show the new method based on Merger Tree algorithms. For the rest of this document, nevertheless, the former, original method is used as it is built explicitly for the MW.

Original calibration for the MW

When the USMF is set by a simple power-law, the calibration of the model is made according to DM only simulations. This particular choice is motivated by the fact that the inclusion of baryonic feedback in simulation is still a difficult task based on tuned recipes of *subgrid physics*. Moreover, simulations offer MW-like object and not *the* MW; they have baryonic distributions that are not exactly the same as the MW. Therefore their effect on subhalos might differ. In particular we use DIEMAND et al.

	$m_{\rm min} = 10^{-10}\ {\rm M}_\odot$		$m_{\rm min} = 10^{-6}\ {\rm M}_\odot$	
$N_{\rm sub}$	$\epsilon_{\rm t} = 1$	$\epsilon_{\rm t} = 10^{-2}$	$\epsilon_{\rm t} = 1$	$\epsilon_{\rm t} = 10^{-2}$
$\alpha = 1.9$	4.4×10^{18}	4.6×10^{18}	1.1×10^{15}	1.2×10^{15}
$\alpha = 2.0$	2.4×10^{20}	2.5×10^{20}	2.3×10^{16}	2.5×10^{16}

Table 4.1 – Calibrated number of subhalos for various configurations of the model when smooth stripping and tidal shocking by the disc are taken into account. The MW halo is assumed to have an NFW profile and the mass densities are taken from McMillan (2017).

(2008). The result of this simulation can be converted as follows. First, we define the mass fraction in a given range, when there are no baryons as

$$\hat{f}_{\rm sub}(m_1, m_2) = \frac{4\pi N_{\rm sub}}{M_{200}} \int {\rm d}R\, R^2 \int_{m_1}^{m_2} {\rm d}m\, m \int_1^\infty {\rm d}c\, \hat{p}_{\rm t}(m, c, R)\,, \tag{4.39}$$

where $\hat{p}_{\rm t}$ is the one point PDF when baryonic tidal effects are omitted. Then, for $\epsilon_{\rm t} = 1$ (remember that this high value may be the result of numerical artefacts), the mass fraction in the DM only simulation is given by

$$\hat{f}_{\rm sub}^{\rm sim} = \hat{f}_{\rm sub}(2.2 \times 10^{-6} M_{200}, 8.8 \times 10^{-4} M_{200}) \simeq 11\% \tag{4.40}$$

Therefore this allows computing the ratio $K_{\rm t}^{\rm sim}/N_{\rm sub}^{\rm sim}$ as

$$\frac{K_{\rm t}^{\rm sim}}{N_{\rm sub}^{\rm sim}} = \frac{4\pi}{M_{200} \hat{f}_{\rm sub}^{\rm sim}} \int {\rm d}R\, R^2 \int_{m_1}^{m_2} {\rm d}m\, m \int_1^\infty {\rm d}c\, p_{\mathbf{R}}(R) p_m(m) p_c(c\,|\,m) \Theta\left[\frac{r_{\rm t,sm}}{r_{\rm s}}(c, R) - 1\right]. \tag{4.41}$$

where $N_{\rm sub}^{\rm sim}$ (resp. $K_{\rm t}^{\rm sim}$) is the number of subhalos from the simulation (resp. the normalisation factor of the simulation), with the specific parameters and configuration of the simulation. Now we want to get the value of $N_{\rm sub}$ and $K_{\rm t}$ for any set of parameters of the model. To this end, we assume that in the outskirts of the MW halo, subhalos do not experience tidal effects (or that they are negligible). The mass density DM in the form of subhalos is the same in the simulation and for any parameters of the model at $R = R_{200}$. We have seen how to write $\rho_{\rm sub}$ so that

$$\begin{aligned} \frac{N_{\rm sub}^{\rm sim}}{K_{\rm t}^{\rm sim}} \int {\rm d}m\, m \int_1^\infty {\rm d}c\, p_m(m) p_c(c\,|\,m) \Theta\left[\frac{r_{\rm t,sm}}{r_{\rm s}}(c, R_{200}) - 1\right] = \\ \frac{N_{\rm sub}}{K_{\rm t}} \int {\rm d}m\, m \int_1^\infty {\rm d}c\, p_m(m) p_c(c\,|\,m) \Theta\left[\frac{r_{\rm t}}{r_{\rm s}}(m, c, R_{200}) - \epsilon_{\rm t}\right]. \end{aligned} \tag{4.42}$$

Because, as assumed, tidal effects are negligible in the outer regions

$$\Theta\left[\frac{r_{\rm t,sm}}{r_{\rm s}}(c, R_{200}) - 1\right] \sim \Theta\left[\frac{r_{\rm t}}{r_{\rm s}}(m, c, R_{200}) - \epsilon_{\rm t}\right] \tag{4.43}$$

and from the previous equation

$$N_{\rm sub} = \frac{K_{\rm t}}{K_{\rm t}^{\rm sim}} N_{\rm sub}^{\rm sim}\,. \tag{4.44}$$

Typical values of $N_{\rm sub}$ are given in Tab. 4.1 for a MW having an NFW profile in terms of the different parameters of the model that are the mass index, α, the minimal virial mass of subhalos $m_{\rm min}$ and the disruption parameter $\epsilon_{\rm t}$. The value of $m_{\rm min}$ is treated as

a free parameter in the range $\sim [10^{-12}\mathrm{M}_\odot, 10^{-4}\mathrm{M}_\odot]$. In all configurations, the number of subhalos is huge, which justify the use of such a statistical model. Moreover, for $\alpha = 2.0$ the values are higher than for $\alpha = 1.9$ because while the total mass of the MW must be the same there are more of the small subhalos. Therefore the difference between $\alpha = 2.0$ and $\alpha = 1.9$ is more pronounced when $m_{\rm min}$ is smaller. Eventually, because most subhalos are in the outer regions of the Galaxy, where tidal effects are not very efficient to destroy them, $N_{\rm sub}$ is not very sensitive to the disruption parameter. This effect is enhanced by the fact that disrupted subhalos have small concentration, and therefore large virial mass (by the anti-correlation between mass and concentration), subsequently, they are less numerous from the start. In Fig. 4.2 we show the subhalo number density given by

$$n_{\rm sub}(R) = \int \mathrm{d}m_{\rm t} \frac{\mathrm{d}n_{\rm sub}}{\mathrm{d}m_{\rm t}}\,, \tag{4.45}$$

in the central part of the MW. Two configurations are considered, with and without the disc shocking effects. For comparison, the cosmological (unevolved) distribution is also represented. For fragile subhalos (disruption parameter $\varepsilon_{\rm t} = 1$) we find a strong suppression due to the disc shocking effect toward the centre of the Galaxy in comparison to the cosmological distribution and to smooth stripping only. The effect is less important with smaller and smaller values of $\varepsilon_{\rm t}$.

Normalisation using Merger Trees

When the USMF is given by the Merger Trees algorithm, there is no need for a calibration procedure. Indeed, one directly has the total number of evolved subhalos by $N_{\rm sub} \equiv \tilde{N}_{\rm sub} K_{\rm t}$ – we recall that $\tilde{N}_{\rm sub}$ is the number of unevolved subhalos given in Eq. (4.26). According to Tab. (4.2), we recover here the same mass fraction $\hat{f}_{\rm sub} \sim 11\%$ for a MW-sized halo, which gives confidence in the Merger Tree method. Subsequently, we also compare the associated evolved subhalo mass function (ESMF),

$$\frac{\mathrm{d}N_{\rm sub}}{\mathrm{d}m} = 4\pi \int p_{\mathbf{R}}(R) n_{\rm sub}(R) R^2 \mathrm{d}R, \tag{4.46}$$

with Hiroshima et al. (2018) in the left panel of Fig. 4.2. We consider only the smooth stripping effects and rather fragile subhalos with $\epsilon_{\rm t} = 0.77$ and $m_{\rm min} = 10^{-5}$ $\mathrm{M}_\odot$. The behaviours of the ESMFs are similar, only the overall normalisation differs. However, the model presented in Hiroshima et al. (2018) is built differently than the SL17 model and contains more physical ingredients; it takes into account the evolution of the subhalos from their accretion to today and the non-circularity of their orbits, based on recipes calibrated on numerical simulations. Therefore let us emphasize that this new normalisation procedure is a preliminary result which should pave the way towards further improvements of the SL17 model – where the philosophy is to avoid relying on cosmological simulations whenever possible.

4.3 Encounter of a single subhalo with a single star

So far the outer edge stripping of subhalos from the host halo and disc shocking have been taken into account. In fact, another dynamical effect has to be considered, the individual stellar encounters. This is addressed now. We first focus on the encounter between one subhalo and a single star. The goal is to evaluate the variation

$m_{\rm min} = 10^{-6}\ {\rm M}_\odot$, $\epsilon_{\rm t} = 1$	$\hat{f}_{\rm sub}$	$N_{\rm sub}$
$M = 10^{9}\ {\rm M}_\odot$	11 %	2.5×10^{12}
$M = 10^{12}\ {\rm M}_\odot$	11 %	1.7×10^{15}
$M = 10^{15}\ {\rm M}_\odot$	11 %	1.1×10^{18}

Table 4.2 – Mass fraction of subhalos in the range $[2.2 \times 10^{-6}M, 8.8 \times 10^{-4}M]$ obtained with the standardised USMF from Chapter 3 for three different host masses and for fragile subhalos destroyed whenever $r_{\rm t} < r_{\rm s}$. The corresponding total number of subhalos is also shown assuming the minimal subhalo cosmological mass of $10^{-6}\ {\rm M}_\odot$.

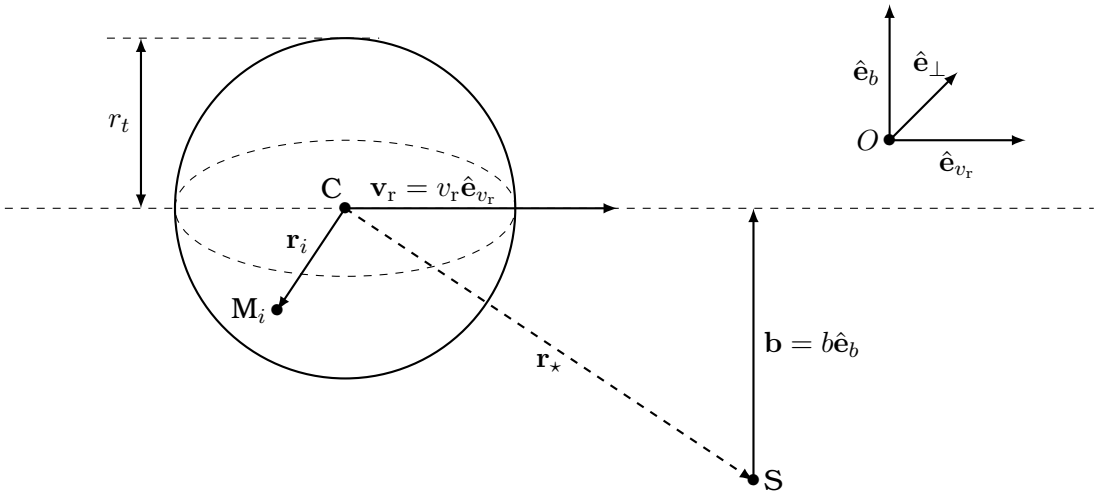

Figure 4.3 – The geometry of the problem. The clump is represented as a sphere with centre C and radius r_t. The star is at point S and the encounter happens with the impact parameter $\mathbf{b}$.

in kinetic energy felt by the particles in the subhalo. We start by giving a complete parametrisation of the problem and then move on to the computation of the *kinetic energy kick*, that we compare to the literature.

4.3.1 General set-up and velocity kick

We follow the original work of SPITZER (1958) and GERHARD et al. (1983) , hereafter GF83. The geometry of the problem is summarised in Fig. 4.3. The star is assumed to be a point-like object with a mass $m_\star$. The subhalo has an original extension $r_{\rm t}$ and its mass is $m_{\rm t} = m(r_{\rm t})$. The centre of mass of the subhalo is labelled by the letter C. The centre of mass of the entire system, associated with 3-fixed axes, defines a Galilean frame $\mathcal{R}$. Let O be a fixed random point in that frame. Particles inside the subhalos all have the same mass $m_{\rm p}$. Consider one of them with a position tagged by the letter M_i. Using Newton's second law its equation of motion in $\mathcal{R}$ can be written

$$\frac{{\rm d}^2\mathbf{OM}_i}{{\rm d}t^2} = -\frac{G_{\rm N} m_\star}{|\mathbf{SM}_i|^3}\mathbf{SM}_i + \sum_{j\neq i}\frac{G_{\rm N} m_{\rm p}}{|\mathbf{M}_i\mathbf{M}_j|^3}\mathbf{M}_i\mathbf{M}_j \tag{4.47}$$

The position of the centre of mass of the subhalo is obtained as

$$\mathbf{OC} = \frac{m_{\rm p}}{m_{\rm t}}\sum_i \mathbf{OM}_i \tag{4.48}$$

so that, deriving twice by the time and applying Eq. (4.47) on the left hand side yields

$$\frac{\mathrm{d}^2\mathbf{OC}}{\mathrm{d}t^2} = -G_{\mathrm{N}}\frac{m_{\mathrm{p}}m_\star}{m_{\mathrm{t}}}\sum_i \frac{\mathbf{SM}_i}{|\mathbf{SM}_i|^3}\,. \tag{4.49}$$

A practical parametrisation is to introduce the positions with respect to the centre of mass of the subhalo, $\mathbf{r}_i = \mathbf{CM}_i$ and $\mathbf{r}_\star = \mathbf{CS}$. The velocity of the DM particle M_i with respect to the centre of mass is denoted $\mathbf{v}_i = \mathrm{d}\mathbf{r}_i/\mathrm{d}t$ and can be written

$$\frac{\mathrm{d}\mathbf{v}_i}{\mathrm{d}t} = \frac{\mathrm{d}^2\mathbf{CM}_i}{\mathrm{d}t^2} = \frac{\mathrm{d}^2\mathbf{OM}_i}{\mathrm{d}t^2} - \frac{\mathrm{d}^2\mathbf{OC}}{\mathrm{d}t^2}\,. \tag{4.50}$$

Then, we introduce $\mathrm{d}\mathbf{u}_i/\mathrm{d}t$ describing the motion of the particle itself and $\mathrm{d}\mathbf{u}_c/\mathrm{d}t$ describing the motion of the centre of mass of the subhalo in $\mathcal{R}$ and write these two components in terms of the variables $\{\mathbf{r}_j\}_j$ and $\mathbf{r}_\star$

$$\begin{aligned}
\frac{\mathrm{d}\mathbf{u}_i}{\mathrm{d}t} &\equiv \frac{\mathrm{d}^2\mathbf{OM}_i}{\mathrm{d}t^2} = -\frac{G_{\mathrm{N}}}{|\mathbf{r}_i-\mathbf{r}_\star|^3}(\mathbf{r}_i-\mathbf{r}_\star) + \sum_{j\neq i}\frac{G_{\mathrm{N}}m_{\mathrm{p}}}{|\mathbf{r}_i-\mathbf{r}_j|^3}(\mathbf{r}_j-\mathbf{r}_i)\\
\frac{\mathrm{d}\mathbf{u}_c}{\mathrm{d}t} &\equiv \frac{\mathrm{d}^2\mathbf{OC}}{\mathrm{d}t^2} = -\frac{m_\star}{m_{\mathrm{t}}}\sum_i \frac{G_{\mathrm{N}}m_{\mathrm{p}}}{|\mathbf{r}_j-\mathbf{r}_\star|^3}(\mathbf{r}_i-\mathbf{r}_\star)\,.
\end{aligned} \tag{4.51}$$

Because the subhalo contains a large amount of particles it can be described by continuous functions and in particular by its mass density. Therefore taking the continuous limit yields, for a particle at a position $\mathbf{r}$

$$\begin{aligned}
\frac{\mathrm{d}\mathbf{u}}{\mathrm{d}t} &= -\frac{G_{\mathrm{N}}m_\star}{|\mathbf{r}-\mathbf{r}_\star|^3}(\mathbf{r}-\mathbf{r}_\star) + G_{\mathrm{N}}\int\frac{\rho(\mathbf{r}')}{|\mathbf{r}'-\mathbf{r}|^3}(\mathbf{r}-\mathbf{r}')\mathrm{d}^3\mathbf{r}'\\
\frac{\mathrm{d}\mathbf{u}_c}{\mathrm{d}t} &= -\frac{G_{\mathrm{N}}m_\star}{m_{\mathrm{t}}}\int\frac{\rho(\mathbf{r}')}{|\mathbf{r}'-\mathbf{r}_\star|^3}(\mathbf{r}'-\mathbf{r}_\star)\mathrm{d}^3\mathbf{r}'\,.
\end{aligned} \tag{4.52}$$

The two integrals can be further simplified if we assume that the subhalo keeps a spherical symmetry during the encounter

$$\begin{aligned}
\frac{\mathrm{d}\mathbf{u}}{\mathrm{d}t} &= -\frac{G_{\mathrm{N}}m_\star}{|\mathbf{r}-\mathbf{r}_\star|}(\mathbf{r}-\mathbf{r}_\star) + \frac{G_{\mathrm{N}}m(r)}{r^3}\mathbf{r}\\
\frac{\mathrm{d}\mathbf{u}_c}{\mathrm{d}t} &= \frac{G_{\mathrm{N}}m_\star m(r_\star)}{m_{\mathrm{t}}r_\star^3}\mathbf{r}_\star\,.
\end{aligned} \tag{4.53}$$

In order to evaluate, from this expression, the net change in velocity for a particle during the encounter one needs to rely on two assumptions. The first one is the *impulse approximation* already discussed for the disc shocking effect. Here it amounts to neglect the second term of $\mathrm{d}\mathbf{u}/\mathrm{d}t$ corresponding to self-gravity. In other words, it amounts to neglect the internal dynamics of the subhalo in comparison to the other dynamical effects. This approximation will be justified in Sect. 4.4.2. The second one is the *high-speed encounter limit* that allows, if the relative velocity between the centre of mass of the subhalo and the star is high enough, to consider that the relative trajectories are straight lines. It ensures that the frame where the subhalo is fixed, let us say $\mathcal{R}'$, is not rotating with respect to the frame $\mathcal{R}$ and that the derivative of the velocity $\mathbf{v}$ computed previously in $\mathcal{R}$ is the same in $\mathcal{R}'$. We only consider encounters that happen in this regime – as it will be justified in Sect. 4.4.1 they almost all fall in this category for the purpose of the study in the MW. Now let us define the change in velocity, also called the *velocity kick*, as

$$\delta\mathbf{v} \equiv \int_{-\infty}^{\infty}\frac{\mathrm{d}\mathbf{v}}{\mathrm{d}t}\mathrm{d}t = \int_{-\infty}^{\infty}\left\{\frac{\mathrm{d}\mathbf{u}}{\mathrm{d}t} - \frac{\mathrm{d}\mathbf{u}_c}{\mathrm{d}t}\right\}\mathrm{d}t = \delta\mathbf{u} - \delta\mathbf{u}_c\,. \tag{4.54}$$

In the high speed encounters regime, $\mathbf{r}_\star(t) = -\mathbf{b} - \mathbf{v}_\mathrm{r} t$ where $\mathbf{b}$ is the impact vector directed from S to C at the time of closest approach and $\mathbf{v}_\mathrm{r}$ is the constant relative velocity. Performing the integration over time yields

$$\begin{aligned} \delta\mathbf{u} &= -2\frac{G_\mathrm{N} m_\star}{v_\mathrm{r}} \frac{\mathbf{r} + \mathbf{b} - \hat{\mathbf{e}}_{v_\mathrm{r}}(\mathbf{r}.\hat{\mathbf{e}}_{v_\mathrm{r}})}{r^2 - (\mathbf{r}.\hat{\mathbf{e}}_{v_\mathrm{r}})^2 + b^2 + 2\mathbf{r}.\mathbf{b}} \\ \delta\mathbf{u}_c &= -2\frac{G_\mathrm{N} m_\star}{v_\mathrm{r} b} I(b, r_\mathrm{t}) \hat{\mathbf{e}}_b \end{aligned} \tag{4.55}$$

with the unitary vectors $\hat{\mathbf{e}}_{v_\mathrm{r}} = \mathbf{v}_\mathrm{r}/v_\mathrm{r}$ and $\hat{\mathbf{e}}_b = \mathbf{b}/b$. Moreover we also introduced the dimensionless function I that can be written

$$I(b, r_\mathrm{t}) \equiv \frac{b^2 v_\mathrm{r}}{m_\mathrm{t}} \int_0^\infty \frac{m\left(\sqrt{b^2 + v_\mathrm{r}^2 t^2}\right)}{\left(b^2 + v_\mathrm{r}^2 t^2\right)^{3/2}} \mathrm{d}t \tag{4.56}$$

where we assume implicitly that $m(r > r_\mathrm{t}) = m_\mathrm{t}$. We have found convenient to slightly transform this expression. First let us proceed to the change of variable $x^2 = b^2 + v_\mathrm{r}^2 t^2$ that yields

$$I(b, r_\mathrm{t}) = \frac{b^2}{m_\mathrm{t}} \int_b^\infty \frac{m(x)}{x^2\sqrt{x^2 - b^2}} \mathrm{d}x \,. \tag{4.57}$$

Then remark that if $b \geq r_\mathrm{t}$ the expression simplifies a lot as

$$I(b \geq r_\mathrm{t}, r_\mathrm{t}) = b^2 \int_b^\infty \frac{1}{x^2\sqrt{x^2 - b^2}} \mathrm{d}x = 1 \,. \tag{4.58}$$

When $b \leq r_\mathrm{t}$ let us use the fact that $\mathrm{d}m(x)/\mathrm{d}x = 4\pi\rho(x)x^2$ for $x < r_\mathrm{t}$ to write that in full generality the factor I satisfies,

$$\begin{aligned} I(b, r_\mathrm{t}) &= \frac{b^2}{m_\mathrm{t}} \int_b^{r_\mathrm{t}} \frac{m(x)}{x^2\sqrt{x^2 - b^2}} \mathrm{d}x + b^2 \int_{r_\mathrm{t}}^{+\infty} \frac{1}{x^2\sqrt{x^2 - b^2}} \mathrm{d}x \\ &= \frac{b^2}{m_\mathrm{t}} \left\{ \left[m(x) \frac{\sqrt{x^2 - b^2}}{x b^2} \right]_b^{r_\mathrm{t}} - \int_b^{r_\mathrm{t}} 4\pi\rho(x) x \frac{\sqrt{x^2 - b^2}}{b^2} \mathrm{d}x \right\} + \int_{r_\mathrm{t}}^{+\infty} \frac{b^2}{x^2\sqrt{x^2 - b^2}} \mathrm{d}x \\ &= -\frac{4\pi}{m_\mathrm{t}} \int_b^{r_\mathrm{t}} \rho(x) x \sqrt{x^2 - b^2} \mathrm{d}x + \frac{1}{r_\mathrm{t}} \left\{ \sqrt{r_\mathrm{t}^2 - b^2} + \frac{b^2}{r_\mathrm{t} + \sqrt{r_\mathrm{t}^2 - b^2}} \right\} \\ &= 1 - \Theta\left(r_\mathrm{t} - b\right) \frac{4\pi}{m_\mathrm{t}} \int_b^{r_\mathrm{t}} \rho(x) x \sqrt{x^2 - b^2} \mathrm{d}x \,. \end{aligned} \tag{4.59}$$

In a first approach, we can say that the function I is a weighted average of the mass enclosed between $r = 0$ and $r = b$ inside the subhalo. Indeed, one can also check that when $b = 0$ one has $I(b = 0, r_\mathrm{t}) = 0$. As a matter of fact, I represents more particularly, the weighted fraction of particles that contribute to $\delta\mathbf{u}_c$. Indeed, when $b > r_\mathrm{t}$, panel (b) of Fig. 4.4, the star does not penetrate the structure and therefore the velocity kicks from all particles add up to make the centre of mass' velocity kick and that is why $I = 1$. On the contrary, when $b < r_\mathrm{t}$, panel (a) of Fig. 4.4, the star penetrates the structure and all the outer shell particles, at $r > b$, do not contribute to the centre of mass velocity kick; albeit all receiving a velocity kick their sum averages out to 0. Consequently only the inner part of the subhalo contained in $r < b$ has a substantial contribution. When $b = 0$ there is no inner part and $I = 0$.

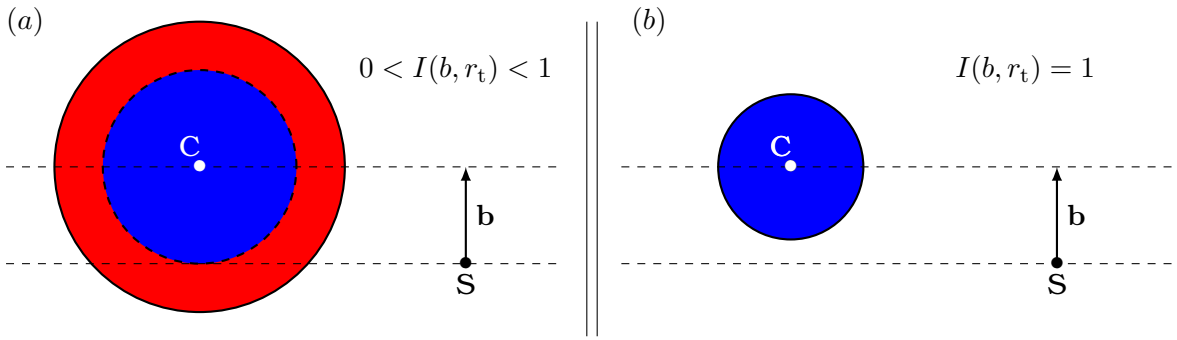

Figure 4.4 – Two different geometrical configurations. In the left panel (a) the sum of the velocity kick of particles in the red area gives no contribution to the velocity kick felt by the centre of mass of the subhalo in $\mathcal{R}$. On the contrary, in both panels (a) and (b) the particles in the blue areas contributes. Consequently, the factor I is less than 1 in (a) and is equal to 1 in (b).

Eventually as for the the disc shocking effect, we can also introduce a kinetic energy kick per units of particle mass as

$$\delta E = \frac{1}{2}(\delta \mathbf{v})^2 + \mathbf{v}.\delta \mathbf{v}\,. \tag{4.60}$$

Similarly, if the initial velocity distribution is isotropic then the second term can be averaged out which yields the expression of the averaged value

$$\overline{\delta E} = \frac{1}{2}(\delta \mathbf{v})^2 = \frac{1}{2}\left(\frac{2G_{\rm N}m_\star}{v_{\rm r}b}\right)^2\left[I^2 + \frac{b^2(1-2I) - 2I\mathbf{r}.\mathbf{b}}{(\mathbf{r}+\mathbf{b})^2 - (\mathbf{r}.\hat{\mathbf{e}}_{v_{\rm r}})^2}\right]\,. \tag{4.61}$$

Before following up on this result by defining an angle averaged version, we first recap the original computation of GF83 in order to make comparisons. Moreover, in this first part, we forget about the effect of the energy dispersion that is induced by the initial velocity in the term $\mathbf{v}.\delta\mathbf{v}$. A careful treatment of the dispersion effects will be made when accounting for the encounters with many stars.

4.3.2 Comparison with the original result

The result of Eq. (4.55) can be compared to GF83. Because the authors of the latter reference were considering the encounter of two extended objects (more specifically two galaxies with Plummer density profiles) they could not obtain an expression as simple as with a point star. Therefore they derived an expression in two limiting cases that correspond to $b \ll r$ and $b \gg r_{\rm t}$ in our notations. Then they interpolated their result between the two asymptotic behaviours.

Assuming a Plummer density for the star $\rho_\star(r) = \rho_\star(1 + (r/\varepsilon_\star)^2)^{-5/2}$ with $\rho_\star$ and $\varepsilon_\star$ being the scale density and scale radius of the star, it can be shown that Eq. (4.52) amputated from the self gravitating term is transformed into

$$\frac{\mathrm{d}\mathbf{v}}{\mathrm{d}t} = -\frac{G_{\rm N}m_\star}{|\mathbf{r}-\mathbf{r}_\star|}(\mathbf{r}-\mathbf{r}_\star) + G_{\rm N}\frac{m_\star}{m_t}\int_0^{r_t}\mathrm{d}r\left(\frac{r}{r_\star}\right)^2\rho(r)\left[\frac{r+r_\star}{|r+r_\star|}h_+^\star(r) - h_-^\star(r)\right] \tag{4.62}$$

with the definition of the function

$$h_\pm^\star(r) = \frac{1 + \frac{\varepsilon_\star^2}{r(r\pm r_\star)}}{\sqrt{1 + \frac{\varepsilon_\star^2}{(r\pm r_\star)^2}}}\,. \tag{4.63}$$

When $\varepsilon_\star \to 0$, $h^\star_\pm(r) \to 1$ and we come back to our first derivation. However here, the derivative of the velocity can no longer be simplified to define the analytic equivalent of $I(b, r_t)$ as we did. Other approximations are needed to pursue the derivation when the scale radius of the star $\varepsilon_\star$ cannot be neglected in front of the other typical scale of the problem – that are the scale radius r_s of the subhalo and the impact parameter b. The latter having the theoretical possibility to go to 0 we will make sure that, either taking it small will not affect our result, or that in practice it is never small enough to be an issue.

Therefore let us focus on the details of GF83 computation where we make the replacement $\varepsilon_\star = 0$ to match with our configuration. First, let us look at the limit $b \to 0$. Using $I(b = 0, r_t) = 0$ one recovers their asymptotic expression

$$\delta\mathbf{v} \underset{b\to 0}{\sim} -\left(\frac{2G_\mathrm{N}m_\star}{v_\mathrm{r} b}\right)\frac{\hat{\mathbf{e}}_r - c_{v_\mathrm{r}}\hat{\mathbf{e}}_{v_\mathrm{r}}}{r(1-c^2_{v_\mathrm{r}})}b\,. \tag{4.64}$$

where we introduced $\hat{\mathbf{e}}_r = \mathbf{r}/r$ and $c_{v_\mathrm{r}} = \hat{\mathbf{e}}_r.\hat{\mathbf{e}}_{v_\mathrm{r}} \in [-1, 1]$ and with the typical velocity kick $\delta V \equiv 2G_\mathrm{N}m_\star/(bv_\mathrm{r})$. However, one major issue is that for $c_{v_\mathrm{r}} = \pm 1$ the velocity kick diverges. This can be physically interpreted by saying that at $b = 0$ the star goes through the centre of the clump. Therefore a segment of particles meet the point star during the encounter and get an infinite velocity kick. This effect which concerns only a negligible amount of particles is a direct consequence of taking $\varepsilon_\star \to 0$ since this parameter otherwise acts as a regulator. In any case, they choose to simplify the denominator in a way that remove the divergence arguing that if angles are parametrised in an appropriate way one has the average value $\langle c^2_{v_\mathrm{r}}\rangle = 1/3$ and the velocity kick is approximately given by

$$\delta\mathbf{v} \underset{b\to 0}{\sim} -\left(\frac{2G_\mathrm{N}m_\star}{v_\mathrm{r} b}\right)\frac{3}{2}\frac{\hat{\mathbf{e}}_r - c_{v_\mathrm{r}}\hat{\mathbf{e}}_{v_\mathrm{r}}}{b}\left(\frac{b}{r}\right)^2 \tag{4.65}$$

where the dependence in the ratio r/b has been made explicit.

In a second time they also give the asymptotic behaviour when $r/b \to 0$. Making a development of Eq. (4.55) at first order yields

$$\delta\mathbf{v} = -\left(\frac{2G_\mathrm{N}m_\star}{v_\mathrm{r} b}\right)\left[\left(1 - I - 2\frac{r}{b}c_b\right)\hat{\mathbf{e}}_b + \frac{r}{b}(\hat{\mathbf{e}}_r - c_{v_\mathrm{r}}\hat{\mathbf{e}}_{v_\mathrm{r}}) + \mathcal{O}\left(\left(\frac{r}{b}\right)^2\right)\right]. \tag{4.66}$$

In GF83 because of the non integrability of Eq. (4.62), the computation is made through a method equivalent to assuming $I(b, r_t) = 1$ in the equation above, i.e. the implicitly assume $b > r_t$. However, in our case it is possible to have $b < r_t$ and $b \gg r$ at the same time for the inner-most particles, in which case $I(b, r_t) < 1$ and the original expression is missing a term. This could make a substantial difference for certain encounters. Remark, that in contrast with the asymptotic limit when $b \to 0$ this expression is never divergent for any value of the scalar products c_{v_r} and c_b.

Eventually, they completed their computation by providing with an interpolation formula between the two asymptotes under the form

$$\delta\mathbf{v} = -\left(\frac{2G_\mathrm{N}m_\star}{v_\mathrm{r} b}\right)\left[\left(1 - I - 2\frac{r}{b}c_b\right)\lambda_2\left(\frac{r}{b}\right)\hat{\mathbf{e}}_b + \frac{r}{b}(\hat{\mathbf{e}}_r - c_{v_\mathrm{r}}\hat{\mathbf{e}}_{v_\mathrm{r}})\lambda_1\left(\frac{r}{b}\right)\right]. \tag{4.67}$$

with λ_1 and λ_2 two functions that follows the conditions: $\lambda_1(x) \to 1$, $\lambda_2(x) \to 1$ when $x \to 0$ and $\lambda_1(x) \sim 3x^{-2}/2$, $\lambda_2(x)/\lambda_1(x) \to 0$ when $x \to \infty$. They chose to use the

parametrisation $\lambda_1(x) = (2x^2/3+1)^{-1}$ and $\lambda_2(x) = \lambda_1^2(x)$. If we conserve the factor I and average over angles their expression (see next paragraph for more details), the averaged squared velocity kick becomes

$$\left\langle (\delta \mathbf{v})^2 \right\rangle_{\rm GF} = \left(\frac{2G_{\rm N} m_\star}{v_{\rm r} b}\right) \left\{ [I-1]^2 + 6\left(\frac{r}{b}\right)^2 \frac{9+4\left(\frac{r}{b}\right)^4}{\left[3+2\left(\frac{r}{b}\right)^2\right]^4} \right\} . \tag{4.68}$$

Taking the limit $I(b, r_t) = 1$ in the previous expression yields the original GF83 result when $\epsilon_\star \to 0$. As shown in the next section, Eq. (4.68) appears to be an excellent approximation of the velocity kick squared. Nevertheless the replacement $\langle c_{v_{\rm r}}^2 \rangle = 1/3$ done in Eq. (4.65) can be more justified.

4.3.3 Angle averaged velocity squared

Taking the average value of $\delta \mathbf{v}$ on entire shells is actually very useful because it reduces the dimensionality of the problem and it remains consistent with the fact that the subhalo is assumed to conserve its spherical symmetry throughout the encounter. Therefore one defines, for any function q of the angles, its averaged value

$$\langle q \rangle \equiv \frac{1}{4\pi} \oint \mathrm{d}\Omega \, q(\theta, \varphi) \tag{4.69}$$

with $\mathrm{d}\Omega = \mathrm{d}\cos\theta \mathrm{d}\varphi$ so that θ and φ that can represent different geometrical angles chosen so that the computation is made as convenient as possible.

Issues of this method

Computing the integral over angles appears to be not trivial. Let us try to evaluate the average value of $(\delta \mathbf{v})^2$ that is the only quantity appearing in the mean kinetic energy kick. If we consider a radius $r < b$ the computation can be done analytically from Eq. (4.61),

$$\left\langle (\delta \mathbf{v})^2 \right\rangle_{r<b} = \left(\frac{2G_{\rm N} m_\star}{v_{\rm r} b}\right)^2 \left[I^2 - 2I + \frac{b}{r} \frac{\arcsin\left(\frac{r}{b}\right)}{\sqrt{1-\left(\frac{r}{b}\right)^2}} \right] . \tag{4.70}$$

However, this function diverges when $r/b \to 1$ even if that has no physical meaning. Indeed the problem is identical to the issue that was pointed out in Eq. (4.64) for the GF83 computation when $c_{v_{\rm r}} \pm 1$. The divergence comes from the fact that at $r = b$ particles in the $-\hat{\mathbf{e}}_b$ direction are in contact with the star and since the star is considered to be a point with a diverging potential the velocity kick for those particles goes to infinity. As was mentioned then, one can expect that this only affects a rather negligible number of particles but, because of the averaging process, this divergence appears now on the entire shell $r = b$. The problem becomes even more important when $r > b$. Indeed the same computation in this range gives

$$\left\langle (\delta \mathbf{v})^2 \right\rangle_{r>b} = \left(\frac{2G_{\rm N} m_\star}{v_{\rm r} b}\right)^2 \left\{ I \left[I - 1 + \frac{b}{r} \sqrt{\left(\frac{r}{b}\right)^2 - 1} \right] + \fint_0^{r/b} \mathrm{d}x \, \frac{x}{\sqrt{\left(\frac{r}{b}\right)^2 - x^2}} \frac{1}{|1-x^2|} \right\} \tag{4.71}$$

where the barred integral represents the Cauchy principal value. However for any parameter $y > 1$ one can straightforwardly show that

$$\fint_0^y \mathrm{d}x \, \frac{x}{\sqrt{y^2 - x^2}} \frac{1}{|1-x^2|} = +\infty \tag{4.72}$$

and the energy kick is not properly defined. As for the case, $r = b$ this divergence occurs because $r > b$ necessarily defines a star-crossing shell, that is, a shell for which some particles end up inside the star at one point or another of the crossing. Once again, those particles meeting the star, or passing in its vicinity, are a small fraction of the total amount of particles and for simplicity, their behaviour may here be assumed of little importance for the rest of the computation. One could argue that actually, the divergence is the signature that the angle-averaged procedure is in fact impossible and should not be used. However, even if a complete computation taking into account the angle dependence could be made for an individual halo, this would make the numerical evaluation so long that it would realistically make impossible the study of the stellar encounter effect on the entire subhalo population. That is why, in the following, we rely on an ansatz.

Definition of several ansatzes

In order to get rid of the divergence one can adopt several ansatz which may be physically motivated. The first solution would be to truncate the average and perform it on the plane $(\hat{\mathbf{e}}_{v_\mathrm{r}}, \hat{\mathbf{e}}_\perp = \hat{\mathbf{e}}_{v_\mathrm{r}} \times \hat{\mathbf{e}}_b)$ perpendicular to $\hat{\mathbf{e}}_b$ since no particles in it ever is in the vicinity of the star and assume that the radial behaviour of $(\delta\mathbf{v})^2$ can be extrapolated in the other direction. Doing so it defines a first ansatz

$$\begin{aligned}\left\langle |\delta\mathbf{v}|^2 \right\rangle_\perp &\equiv \frac{1}{2\pi}\oint \mathrm{d}\Omega\, (\delta\mathbf{v})^2 \delta_\mathrm{D}\left[\cos\widehat{(\hat{\mathbf{e}}_r, \hat{\mathbf{e}}_b)}\right] \\ &= \left(\frac{2G_\mathrm{N}m_\star}{v_\mathrm{r} b}\right)^2 \left[I^2 + \frac{1-2I}{\sqrt{1+\left(\frac{r}{b}\right)^2}}\right]\end{aligned} \tag{4.73}$$

where δ_D represents the Dirac distribution (noted here with the tag $_D$ in order to make the distinction with the other occurrences of δ which represents variations in this chapter) and the cosine imposes that we fix r in the plane perpendicular to $\hat{\mathbf{e}}_b$. Another possibility is to extrapolate Eq. (4.61) for the particles in the direction $\hat{\mathbf{e}}_b$ for $r > 0$, to all other directions. The result is then

$$\left\langle (\delta\mathbf{v})^2 \right\rangle_\parallel \equiv \left(\frac{2G_\mathrm{N}m_\star}{v_\mathrm{r} b}\right)^2 \left[I^2 - \frac{2I}{1+\frac{r}{b}} + \frac{1}{(1+\frac{r}{b})^2}\right]. \tag{4.74}$$

Eventually a last option is to give an averaged value of c_b and c_{v_r} and replace them directly in Eq. (4.61) in the same way that what was done in GF83 to replace c_{v_r} by the average value $\langle c_{v_\mathrm{r}}^2 \rangle = 1/3$. However, there are several ways to make this substitution. Since we have an analytical formula for small values of r/b we can ask for our approximation to match the exact result of Eq. (4.70) at first order in the r/b expansion, in order to constrain the value of c_{v_r} and c_b. It gives the following system

$$2c_b(I-1) = 0 \tag{4.75}$$

$$(1-c_{v_\mathrm{r}}^2)(2I-1) + 4c_b^2(1-I) = 2/3\,. \tag{4.76}$$

The first equation directly gives $c_b = 0$ while the second cannot be solved in a general way as we do not want c_{v_r} to be a function of I. However since $I(b \geq r_t, r_t) = 1$ it is consistent to require that $(1 - c_{v_\mathrm{r}}^2) = 2/3$. Doing so, it no longer describes well the limit $b \to 0$ when $r/b \to 0$. Nevertheless, in practice, it corresponds to particles at a position $r \ll b \ll r_t$, too far in the centre to be of interest for us (as we will only look at radii

above $r = 10^{-2} r_{\rm s}$). Interestingly, this solution is also compatible with a direct average over angles since, defining $c_{v_{\rm r}} = \cos\theta$ and $c_b = \sin\theta\cos\varphi$, it yields

$$\left\langle (1 - c_{v_{\rm r}}^2) \right\rangle = \frac{2}{3} \quad \text{and} \quad \langle c_b \rangle = 0\,. \tag{4.77}$$

Therefore we have proven that averaging the terms $c_{v_{\rm r}}$ and c_b directly is indeed not a bad approximation. Consequently, because it relies on similar assumptions, the result will be equivalent to Eq. (4.68), which should then give a good evaluation of the squared velocity kick too. However the latter relies on an interpolation that we do not need here. Following our development to the end, the total expression of the velocity kick becomes

$$\left\langle (\delta \mathbf{v})^2 \right\rangle_\sim \equiv \left(\frac{2G_{\rm N} m_\star}{v_{\rm r} b} \right)^2 \left[I^2 + \frac{3(1-2I)}{3 + 2(\frac{r}{b})^2} \right] . \tag{4.78}$$

which is also an expression more compact than Eq. (4.68).

A comparison of all these approximations is made in the left panel of Fig. 4.5 for $b < r_{\rm t}$. Firstly, we check that all our different ansatz have a consistent behaviour. The only "irregularity" is observed for $\langle \delta \mathbf{v} \rangle_\perp$ in dash-dotted blue which drops to 0 at a finite radius. Secondly, as expected, the GF83 computation not corrected by the factor $I(b, r_t)$ is not efficient to actually describe what happens at small and large radii; it misses the correct asymptotic behaviours. This is a direct consequence of the absence of the I term which has a finite value in $]0, 1[$ in this configuration. We can easily check with Eq. (4.61) that

$$\begin{aligned} \lim_{r\to 0} (\delta \mathbf{v})^2 &= \left(\frac{2G_{\rm N} m_\star}{v_{\rm r} b} \right)^2 [I - 1]^2 \neq 0 \\ \lim_{r\to \infty} (\delta \mathbf{v})^2 &= \left(\frac{2G_{\rm N} m_\star}{v_{\rm r} b} \right)^2 I^2 \neq 0 \end{aligned} \tag{4.79}$$

which translate the fact that the velocity kick of the centre of mass of the clump in $\mathcal{R}$ is only obtained as the sum of the individual velocity kicks of only a fraction of the particles – see the discussion in Sect. 4.3.1 about the meaning of the function I.

4.3.4 The integrated kinetic energy kick

It is common in the literature to work with the total integrated kinetic energy kick of the subhalo over its binding energy. For comparison we therefore introduce

$$\delta E_{\rm int} = 2\pi \int_0^{r_t} r^2 \rho(r) (\delta \mathbf{v})^2 {\rm d}r \tag{4.80}$$

and the binding energy

$$U = 4\pi G_{\rm N} \int_0^{r_{\rm t}} m(r) \rho(r) r {\rm d}r \tag{4.81}$$

The ratio of these two quantities is represented in the left panel of Fig. 4.5 with respect to the impact parameter. It scales as b^{-4} when $b \gg r_{\rm s}$ and as a constant (up to a small logarithmic correction) when $b \ll r_{\rm s}$. Therefore one recovers the behaviour found in

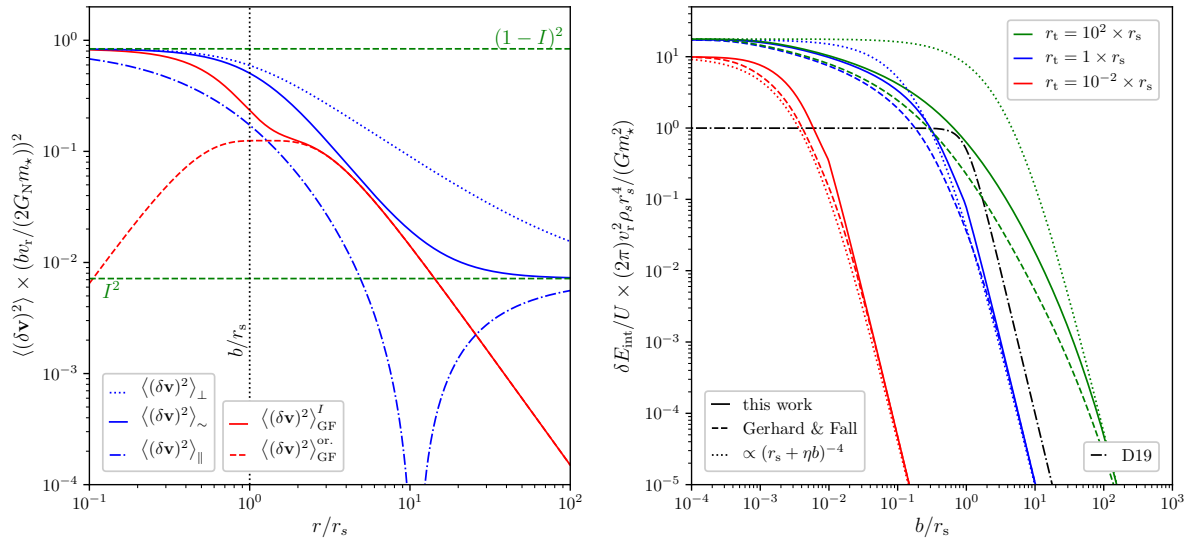

Figure 4.5 – Left panel: Angle-averaged velocity squared in the plane perpendicular to $\hat{\mathbf{e}}_b$ (dotted blue), in the direction $+\hat{\mathbf{e}}_b$ (dash-dotted blue) and from Eq. (4.78) (solid blue). These results are compared to the original prediction by GF83 (dashed red) and to the corrected version in Eq. (4.68) (solid red). The tidal radius of the subhalo is set to $r_{\rm t} = 100 \times r_{\rm s}$ and $b = r_{\rm s}$. The green dashed lines correspond to the asymptotic behaviours. **Right panel:** Ratio of the total kinetic energy integrated on the entire profile over the binding energy for various values of the tidal radius. The solid curves are obtained with our ansatz of Eq. (4.78), dashed curve are obtained using GF83 result and the dotted lines correspond to a comparison with the usually adopted shape $\propto (\eta b + \mathbf{r}_{\rm s})^{-4}$. Comparison is made with the characteristic binding energy introduced in DELOS (2019a) (here denoted D19)

MOORE (1993) and used in the context of dark matter subhalos in GREEN et al. (2007) and DELOS (2019a) – as well as in GOERDT et al. (2007) in the large b limit –:

$$\frac{\delta E_{\rm int}}{U} \sim \frac{G_{\rm N} m_\star^2}{v_r^2 \rho_{\rm s} (\eta b + r_{\rm s})^4} \tag{4.82}$$

with η a parameter. Albeit GREEN et al. (2007) provide an estimate for η it is ill-defined in the case of an NFW profile. Here we find $\eta = 213$ for $r_{\rm t}/r_{\rm s} = 10^{-2}$, $\eta = 3.57$ for $r_{\rm t}/r_{\rm s} = 1$ and $\eta = 0.228$ for $r_{\rm t}/r_{\rm s} = 10^2$. The dash-dotted curve corresponds to the characteristic binding energy introduced in DELOS (2019a) (referred to as D19) and assumes a slightly different shape $\delta E_{\rm int} \propto 1/(b^4 + r_{\rm s}^4)$. If the tidal radius is not smaller than the scale radius our solution provides better agreement with Eq. (4.82) than the GF83 solution. The agreement is similar if the tidal radius is smaller the scale radius.

4.4 Encounters of a single subhalo with a population of star

When a subhalo crosses the stellar disc it encounters many stars. The goal of this section is to study the integrated effect of all these encounters . We start by describing the stellar population before performing a full statistical analysis and analyse the impact on the subhalo profile.

4.4.1 The stellar population

What matters for a subhalo that crosses the stellar disc is the impact parameters of its encounters with stars and the masses of the latter. Here we assume that the stellar disc is infinite, infinitely thin and homogeneous with surface density $\Sigma_\star(R)$. Consider a subhalo following a straight line trajectory making an angle θ with respect to the perpendicular of the disc. The number of encountered stars with an impact parameter between b and $b + \mathrm{d}b$ is

$$\mathrm{d}\mathcal{N} = \frac{\Sigma_\star(R)}{\overline{m_\star}} \frac{2\pi b\,\mathrm{d}b}{\cos(\theta)} \,. \tag{4.83}$$

Here we define $\overline{m_\star}$ as the average stellar mass of a star in the disc. As a matter of fact, this distribution cannot be physically valid in all configurations as it diverges when $\theta = \pi/2$, which corresponds to subhalo with an orbit within the disc. Nonetheless, it is also possible to consider a non-homogeneous and finite disc to obtain a finite distribution. However, the computation is much more involved and done in App. D.2. Comparing Eq. (4.83) to the more accurate expression of Eq. (D.18) shows that it is a good approximation as long as $\cos(\theta) \gg b/R_\mathrm{d}$ where R_d is the typical length scale of the variations in $\Sigma_\star(R)$. This condition is satisfied for the vast majority of subhalos so Eq. (4.83) is used in the following.

As already mentioned, our previous computation for the energy kick in Sect. 4.3 relies on several assumptions. The first implicit one is that the encounter is isolated. It bounds the impact parameter to, at maximum, half the distance between stars. We consider then an axisymmetric distribution of stars parametrised by the mass density $\rho_\star(R, z)$ where R is the radius from the GC in the galactic plane and z the height. Henceforth, the previously introduced surface density is given by

$$\Sigma_\star(R) = \int_{-\infty}^{+\infty} \rho_\star(R, z)\mathrm{d}z \tag{4.84}$$

and we introduce the maximal impact parameter at R as

$$\begin{aligned} b_\mathrm{max}(R) &\equiv \frac{1}{2\Sigma_\star(R)} \int_{-\infty}^{+\infty} \rho_\star(R, z) \left(\frac{\rho_\star(R, z)}{\overline{m_\star}}\right)^{-1/3} \mathrm{d}z \\ &= \frac{\overline{m_\star}^{1/3}}{\Sigma_\star(R)} \int_0^{+\infty} \rho_\star^{2/3}(R, z)\,\mathrm{d}z \,. \end{aligned} \tag{4.85}$$

In order to be consistent with SL17 we use the stellar mass density model of McMillan (2017) defined by a double exponential disc and introduced in Eq. (4.33). With the stellar mass distribution function of Chabrier (2003) that we call $p_{m_\star}(m_\star)$ in the following we find $\overline{m_\star} \simeq 0.17\,\mathrm{M}_\odot$, thus giving $b_\mathrm{max}(8\,\mathrm{kpc}) \simeq 1.1\,\mathrm{pc}$.

Furthermore, the expression of δE also relies on the *high-speed encounter* assumption which ensures that the subhalo keeps a straight line trajectory with respect to the star. This is satisfied only if the kinetic energy T, in the centre of mass frame of the system $\{\mathrm{star} + \mathrm{subhalo}\}$, is much larger than the potential energy $|W|$ with

$$T = \frac{1}{2}\frac{m_\star\, m_\mathrm{t}}{m_\star + m_\mathrm{t}} v_\mathrm{r}^2 \quad \text{and} \quad W = -G\, m_\star \left[\frac{m(r_\star)}{r_\star} + \Theta(r_\mathrm{t} - r_\star) \int_{r_\star}^{r_\mathrm{t}} \frac{\rho(r)}{r}\,\mathrm{d}^3\mathbf{r}\right] . \tag{4.86}$$

One can easily check that W is minimal when $r_\star = b$. Therefore the condition defines a minimal impact parameter b_min. As a matter of fact, for an average star of mass

$\overline{m_\star} \simeq 0.17\,\mathrm{M}_\odot$ the minimal impact parameter $b_{\min}$ is always much smaller than $b_{\max}$ unless the relative velocity becomes smaller than 0.1 km s^{-1}. Such small velocities are very unlikely in the MW since the typical subhalo velocity is of order 100 km s^{-1}. Nevertheless, in order to be sure that the condition is satisfied we impose in our numerical codes $T \geq 10W$ – even though this condition gives $b_{\min} = 0$ kpc in most configurations. Therefore we may discard some extremely rare encounters making the result conservative in the sense that we do not take into account values of δE that would not be evaluated with all the assumption satisfied. The total number of encounter is then

$$\mathcal{N} = \frac{\Sigma_\star}{\overline{m_\star}} \frac{\pi}{\cos(\theta)} \left(b_{\max}^2 - b_{\min}^2 \right) . \tag{4.87}$$

At $8\,\mathrm{kpc}$, we find $\mathcal{N} \simeq 2346 \times (0.5/\cos(\theta))$.

Eventually we also need to introduce the distribution of relative velocity. For that we assume that subhalos follow a Maxwell-Boltzmann distribution with dispersion $\sigma(R)$ – which can be evaluated using Jean's dispersion as shown in App. D.1. In addition we assume that stars have a circular velocity $v_\star(R)$. Then we get the relative speed distribution under the form

$$f_{v_\mathrm{r}}(v_\mathrm{r}) = \sqrt{\frac{2}{\pi}} \frac{v_\mathrm{r}}{\sigma\, v_\star} \sinh\left(\frac{v_\mathrm{r}\, v_\star}{\sigma^2} \right) e^{-(v_\star^2 + v_\mathrm{r}^2)/(2\,\sigma^2)} \tag{4.88}$$

with the corresponding average value

$$\overline{v_\mathrm{r}} = \sigma \sqrt{\frac{2}{\pi}} \left\{ e^{-X^2} + \frac{\sqrt{\pi}}{2} (1 + 2\,X^2) \frac{\mathrm{erf}(X)}{X} \right\} \tag{4.89}$$

and with the introduction of $X = v_\star/(\sqrt{2}\,\sigma)$. In particular at 8 kpc, $\overline{v_\mathrm{r}} \simeq 334\,\mathrm{km/s}$. This concludes the description of the stellar population. We now move on to the evaluation of total energy kick received after multiple encounters during one crossing of the disc.

4.4.2 Total energy kick and scatter

We develop here a statistical analysis of the total energy kick and scatter. We discuss in detail some subtleties of the computation and justify the impulsive approximation. Then we evaluate the profile change of a subhalo when it crosses the disc and we compare our main results to the literature.

The random walk in velocity space

When crossing the stellar disc a subhalo encounters a number $\mathcal{N}$ of subhalos, every encounter occurring with a different impact parameter. Therefore a particle inside receives a sequence of velocity kicks that we denote $\{\delta \mathbf{v}_j\}_{1 \leq j \leq \mathcal{N}}$. We make the assumption that the subhalo does not have time to relax between the encounters (to be consistent with the impulse approximation), hence the total velocity kick given by the sum of all the velocities

$$\Delta \mathbf{v} = \sum_{i=1}^{\mathcal{N}} \delta \mathbf{v}_i \, . \tag{4.90}$$

Then the total kinetic energy per particle mass becomes

$$\Delta E = \frac{1}{2} (\Delta \mathbf{v})^2 + \mathbf{v} \cdot \Delta \mathbf{v} \tag{4.91}$$

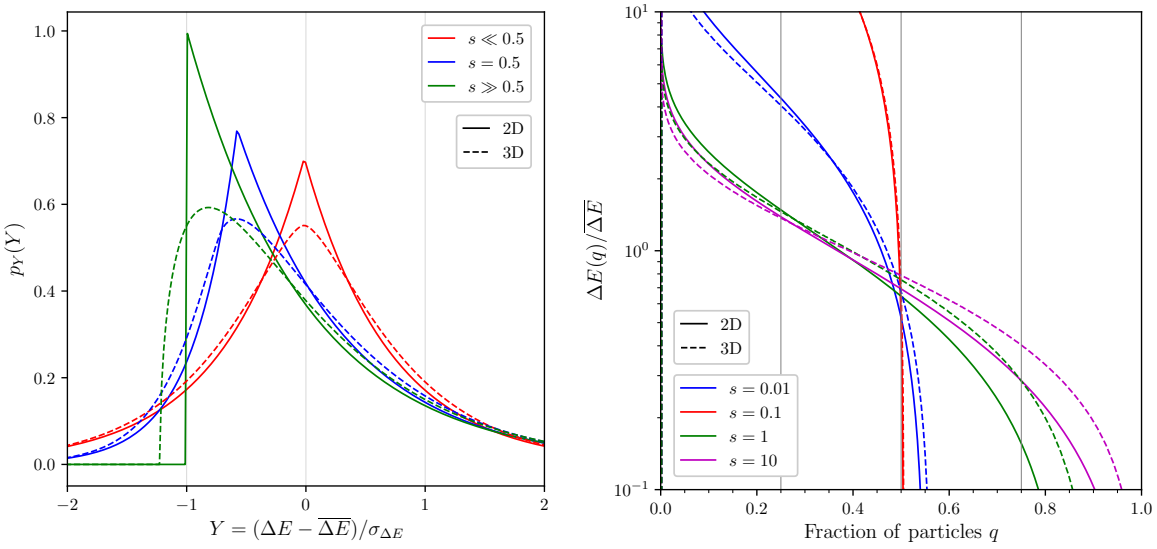

Figure 4.6 – In both panels, the solid curves are obtained assuming $\Delta\mathbf{v}$ constructed out of a 2D isotropic random walk in velocity space and dashed curve are for a 3D isotropic random walk. **Left panel:** Probability density function of the centred reduced total energy kick for different values of the parameter s. We denoted by $\sigma_{\Delta E}$ the standard deviation of ΔE. **Right panel:** The maximal energy that at least a fraction q of the particles gain over the average energy kick with respect to q for different value of s. The inset is a zoom on the region $0.2 < q < 0.8$ for $s > 0.5$.

All the encounters are characterised by the statistical distribution of impact parameters and stellar masses. Therefore all vectors $\delta\mathbf{v}_i$ and thus $\Delta\mathbf{v}$ are random variables. In the following, we first show how it is possible to evaluate a PDF for $\Delta\mathbf{v}$. The sequence $\{\delta\mathbf{v}_j\}_{1\leq j\leq\mathcal{N}}$ behaves like a random walk in velocity space. In a first approach, from Eq. (4.55), every $\delta\mathbf{v}_i$ is confined in the same plane, perpendicular to the relative velocity vector $\hat{\mathbf{e}}_{v_r}$ and therefore, the random walk must be two-dimensional. Nevertheless, as the stars have their own velocity, the relative velocity vector varies from one encounter to another if the velocity of the subhalo is not high enough. Thus, the perpendicular plane is actually not necessarily fixed and the random walk is not strictly two dimensional. In order to bracket the uncertainty, we parametrise the dimension by d that takes the value $2, 3$. When $\mathcal{N}$ is large enough the random walk can then be approximated as a Brownian motion by using the Central Limit (CL) theorem. The PDF for $\Delta\mathbf{v}$ is then

$$p_{\Delta\mathbf{v}}(\Delta\mathbf{v}) = \frac{1}{(2\pi)^d\sqrt{\det C}}\exp\left[-\frac{1}{2}\left(\Delta\mathbf{v}-\overline{\Delta\mathbf{v}}\right)^T C^{-1}\left(\Delta\mathbf{v}-\overline{\Delta\mathbf{v}}\right)\right] \tag{4.92}$$

with C the covariance matrix which can be written (for an isotropic random walk) as

$$C = \frac{\mathcal{N}}{d}\mathrm{diag}\left[\overline{(\delta v)^2}\right], \tag{4.93}$$

and only depends on the second moment of $\delta\mathbf{v}$ defined by

$$\overline{\delta v^2} = \int \mathrm{d}m_\star p_{m_\star}(m_\star)\int_{b_{\min}}^{b_{\max}}\mathrm{d}b\, p_b(b)(\delta\mathbf{v})^2 \tag{4.94}$$

with the approximation $(\delta\mathbf{v})^2 \simeq \langle(\delta\mathbf{v})^2\rangle_\sim$ defined in Eq. (4.78) and with the impact parameter distribution $p_b(b) = (\mathrm{d}\mathcal{N}/\mathrm{d}b)/\mathcal{N}$. Moreover $p_{m_\star}(m_\star)$ is the stellar mass PDF.

In practice, in order to improve the numerical speed, the simplification $p_{m_\star}(m_\star) = \delta_{\rm D}\left(m_\star - \overline{m_\star}\right)$ is considered. Moreover, by isotropy, the average value of $\Delta\mathbf{v}$ is then necessarily 0. Consequently, the previous general Gaussian distribution takes the form

$$p_{\Delta\mathbf{v}}(\Delta\mathbf{v}) \simeq \left(\frac{d}{2\pi\mathcal{N}\overline{(\delta\mathbf{v})^2}}\right)^{d/2} \exp\left(-\frac{d(\Delta\mathbf{v})^2}{2\mathcal{N}\overline{(\delta v)^2}}\right) . \tag{4.95}$$

A straightforward first evaluation for ΔE is obtained by considering the average value of $\Delta\mathbf{v}$ using the PDF derived above as

$$\overline{\Delta E} = \frac{1}{2}\overline{(\Delta\mathbf{v})^2} = \frac{1}{2}\mathcal{N}\overline{\delta v^2} . \tag{4.96}$$

However one may wonder about the impact of the second term in Eq. (4.91). In order to properly take it into account the solution is to derive the full PDF for ΔE. A general way to write the probability distribution of energy kick is

$$p_{\Delta E}(\Delta E) = \int \mathrm{d}^3\mathbf{v}\, p_{\mathbf{v}}(\mathbf{v}) \int \mathrm{d}^d\Delta\mathbf{v}\, p_{\Delta\mathbf{v}}(\Delta\mathbf{v})\delta_{\rm D}\left[\Delta E - \frac{(\Delta\mathbf{v})^2}{2} + \mathbf{v}\cdot\Delta\mathbf{v}\right] . \tag{4.97}$$

We only consider isotropic initial velocity distributions $p_{\mathbf{v}}(\mathbf{v}) = p_{\mathbf{v}}(v)$. Therefore it is convenient to first perform the integral over the direction of $\mathbf{v}$. A straightforward notation is to introduce the probability of ΔE knowing $\Delta\mathbf{v}$

$$p_{\Delta E}(\Delta E\,|\,\Delta\mathbf{v}) = \int \mathrm{d}^3\mathbf{v}\, p_{\mathbf{v}}(\mathbf{v})\, \delta_{\rm D}\left[\Delta E - \frac{(\Delta\mathbf{v})^2}{2} + \mathbf{v}\cdot\Delta\mathbf{v}\right] . \tag{4.98}$$

In this integral we can parametrise $\mathbf{v}.\Delta\mathbf{v} = v|\Delta\mathbf{v}|\cos\theta$ in the Dirac distribution and integrate over the angle θ so that

$$p_{\Delta E}(\Delta E\,|\,\Delta\mathbf{v}) = \frac{2\pi}{|\Delta\mathbf{v}|}\int_0^{+\infty} \mathrm{d}v\, v p_{\mathbf{v}}(v)\Theta\left[v - \frac{|(\Delta\mathbf{v})^2 - 2\Delta E|}{2|\Delta\mathbf{v}|}\right] \tag{4.99}$$

In the end the total distribution of ΔE is given as

$$\begin{aligned} p_{\Delta E}(\Delta E) &= \int \mathrm{d}^d\Delta\mathbf{v}\, p_{\Delta E}(\Delta E\,|\,\Delta\mathbf{v}) p_{\Delta\mathbf{v}}(\Delta\mathbf{v}) \\ &= \frac{4\pi^{1+d/2}}{\Gamma(d/2)}\int_0^{\infty} \mathrm{d}|\Delta\mathbf{v}||\Delta\mathbf{v}|^{d-2} p_{\Delta\mathbf{v}}(\Delta\mathbf{v}) \\ &\qquad \times \int_0^{+\infty} \mathrm{d}v\, v p_{\mathbf{v}}(v)\Theta\left[v - \frac{|(\Delta\mathbf{v})^2 - 2\Delta E|}{2|\Delta\mathbf{v}|}\right] , \end{aligned} \tag{4.100}$$

where we use, in the second integral, the fact that the distribution in velocity kick is isotropic: $p_{\Delta\mathbf{v}}(\Delta\mathbf{v}) = p_{\Delta\mathbf{v}}(|\Delta\mathbf{v}|)$. For some numerical applications it can be interesting now to invert the two integrals. It amounts to re-write the total PDF as

$$p_{\Delta E}(\Delta E) = \int_0^{+\infty} \mathrm{d}^3\mathbf{v}\, p_{\Delta E}(\Delta E\,|\,v) p_{\mathbf{v}}(v) \tag{4.101}$$

with the probability of ΔE knowing v being

$$p_{\Delta E}(\Delta E\,|\,v) \equiv \frac{\pi^{d/2}}{v\Gamma(d/2)}\Theta\left[v - \eta(\Delta E)\right]\int_{|\Delta\mathbf{v}|_-(v,\Delta E)}^{|\Delta\mathbf{v}|_+(v,\Delta E)} p_{\Delta\mathbf{v}}(\Delta\mathbf{v})|\Delta\mathbf{v}|^{d-2}\mathrm{d}|\Delta\mathbf{v}| \tag{4.102}$$

and with the definition $\eta(x) = \sqrt{\max\{-2x, 0\}}$. The Heaviside function Θ naturally appears from the computation and it simply enforces the physical positivity of the final kinetic energy $E_f \equiv \Delta E + v^2/2$. Besides, we introduced the integral boundaries for $|\Delta\mathbf{v}|$ as

$$\begin{aligned} |\Delta\mathbf{v}|_-(v, \Delta E) &= \begin{cases} -v + \sqrt{v^2 + 2\Delta E} & \text{if} \quad \Delta E \geq 0 \\ +v - \sqrt{v^2 + 2\Delta E} & \text{if} \quad \Delta E < 0 \end{cases} \\ |\Delta\mathbf{v}|_+(v, \Delta E) &= +v + \sqrt{v^2 + 2\Delta E}\,. \end{aligned} \tag{4.103}$$

The interest behind this new expression for the probability of ΔE is to isolate the PDF on the initial velocity $\mathbf{v}$ that is, in general, non-analytical and not necessarily perfectly known. As a matter of fact, we will see in the following that this formulation allows deriving generic and interesting properties regardless of the initial velocity PDF. Using Eq. (4.95) and Eq. (4.102), the expression of $p_{\Delta E}(\Delta E \,|\, v)$ can then be written under the form

$$p_{\Delta E}(\Delta E \,|\, v) = \frac{\Theta\left[v - \eta(\Delta E)\right]}{2v\Gamma(d/2)} \sqrt{\frac{d}{2\mathcal{N}\overline{(\delta\mathbf{v})^2}}} \delta\Gamma\left[\frac{d-1}{2}; \frac{d|\Delta\mathbf{v}|_-^2}{2\mathcal{N}\overline{(\delta\mathbf{v})^2}}, \frac{d|\Delta\mathbf{v}|_+^2}{2\mathcal{N}\overline{(\delta\mathbf{v})^2}}\right] \tag{4.104}$$

with the notation of the Gamma function difference being

$$\delta\Gamma\left[z; a, b\right] = \Gamma\left(z, a\right) - \Gamma\left(z, b\right) = \int_a^b t^{z-1} e^{-t} \mathrm{d}t\,. \tag{4.105}$$

In practice let us look at $d = 2$ and a Maxwellian distribution of initial velocity

$$p_{\mathbf{v}}(v) = \frac{1}{(2\pi\sigma_{\rm sub}^2(r))^{3/2}} e^{-\frac{v^2}{2\sigma_{\rm sub}^2(r)}}\,. \tag{4.106}$$

with dispersion $\sigma_{\rm sub}$ that is evaluated through the Jean's equation c.f. App. D.1. As shown in App. D.3.3, the total integration reduces to the simple expression

$$p_{\Delta E}(\Delta E) = \frac{1}{2\sigma_{\rm sub}^2\sqrt{1+s^2}} \exp\left(\frac{\Delta E}{2\sigma_{\rm sub}^2} - \frac{|\Delta E|}{2\sigma_{\rm sub}^2}\frac{\sqrt{1+s^2}}{s}\right) \tag{4.107}$$

with the parameter $s^2 = \mathcal{N}\overline{\delta v^2}/(8\sigma_{\rm sub}^2) = \overline{\Delta E}/(4\sigma_{\rm sub}^2)$ that is a normalised ratio of the dispersion of $|\Delta\mathbf{v}|^2$ (or also the average in that case) and the dispersion of the initial velocity $|\mathbf{v}|$. The associated scatter is larger than the average value and is given by

$$\sigma_{\Delta E} = \overline{\Delta E}\sqrt{1 + \frac{1}{2s^2}} > \overline{\Delta E}\,. \tag{4.108}$$

This distribution is plotted in the left panel of Fig. 4.6 in terms of the associated centred reduced variable. When $\sigma_{\rm sub}$ is large, s is small and the distribution is symmetric with respect to the average while it shifts toward lower values for small $\sigma_{\rm sub}$. This can be understood as the dominant dispersion comes from the uncertainty on the initial velocity that, because of the Maxwell-Boltzmann distribution, is symmetric. When s grows, however, the PDF is peaked on negative values, so that energies lower than the average are more probable. In order to properly take into account the dispersion in energy kick and the shift in the distribution, one should evaluate, after each disc crossing, a new density profile for the subhalo by properly removing the particles with a final velocity greater than the escape velocity – this

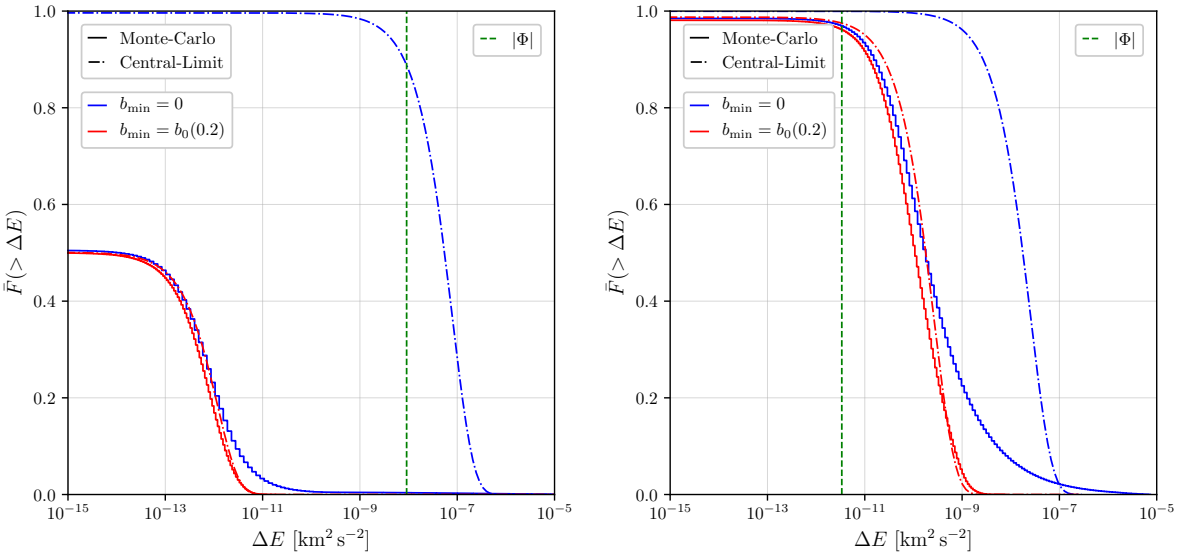

Figure 4.7 – Complementary cumulative distribution function of the energy kick received after one crossing of the disc due to the encounter with stars ΔE. In blue is shown the true value (solid) and the approximation using the CL theorem (dashed-dotted) for $b_{\rm min} \sim 0$. In red are similar curve imposing a lower cut-off on the distribution of impact parameters $b_{\rm min} \to b_0(Q = 0.2)$. The vertical green dashed line is the value of the gravitational potential ψ. **Left panel:** In the inner part of the subhalo $r/r_{\rm s} = 0.01$ **Right panel:** In the outskirts of the subhalo $r/r_{\rm s} = 2.34$.

possibility is discussed in App. D.3. However, this requires extensive numerical resources to evaluate the impact of one disc crossing on a single subhalo and could not be applicable in the framework of SL17. Therefore, in the following, we focus on defining *one* energy kick value as an estimate of the energy kick felt by all particles in each given shell.

Let us introduce $\Delta E(q)$ the maximal total energy kick that is received by at least a fraction q of the particles – the full expression is discussed in App. D.3.3 for a Maxwellian distribution of initial velocity. In particular the median energy gain is $\text{Med}(\Delta E) \equiv \Delta E(q = 0.5)$. One can show that for any value of s,

$$\frac{1}{2} < \frac{\text{Med}(\Delta E)}{\overline{\Delta E}} < \ln(2) \tag{4.109}$$

so mean and median are always close. The ratio $\Delta E(q)/\overline{\Delta E}$ is plotted in the right panel of Fig. 4.6 for different values of the parameter s. If s is large enough ($s \leq 0.5$), *i.e.* if the effect of the encounters is relevant, then $\Delta E(0.25 < q < 0.75)$ and $\overline{\Delta E}$ stay close to each other as $\Delta E(q)/\overline{\Delta E} \in [0.1, 2]$. The fact that at large values of s the PDF of the left panel of Fig. 4.6 is no longer symmetric with respect to the average is the reason why $\text{Med}(\Delta E) < \overline{\Delta E}$ in all configurations. Subsequently, it is both physically meaningful and convenient to define *the* energy kick received by all particles in a given shell as being $\text{Med}(\Delta E)$ and it can be well approximated by $\Delta E \sim \kappa\overline{\Delta E}$, choosing $\kappa \sim 0.7$.

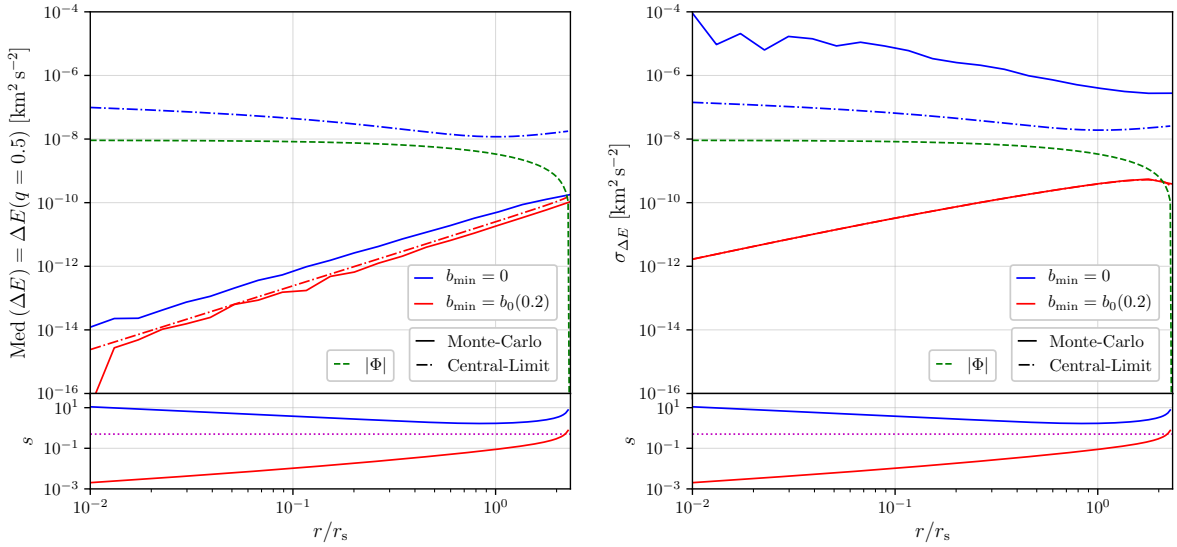

Figure 4.8 – Left panel: Median energy kick received by at least half of the particles in terms of the radius. *Upper panel:* In blue is shown the true value (solid) and the approximation using the CL theorem (long-sort dashed) for $b_{\min} \sim 0$. In red are similar curve imposing a lower cut-off on the distribution of impact parameters $b_{\min} \to b_0(Q = 0.2)$. The green dashed curve is the value of the gravitational potential of the subhalo. *Lower panel:* Value of the parameter s in the two configurations with (blue) and without (red) the cut-off on the impact parameters. The magenta dotted curve is the limit $s = 0.5$. **Right panel:** Same figure for the energy kick standard deviation. Note that the dash-dotted and solid red curve are not distinguishable (one has good convergence of the CL theorem when the impact parameter range is truncated for the dispersion).

Issues with the Central Limit

So far, all the results are built on the fact that the number of encountered stars per crossing $\mathcal{N}$ is large enough to apply the CL theorem as if it were infinite. As a matter of fact, according to the position inside the subhalo, this does not necessarily hold. Indeed, when $b_{\min}$ is close to 0, as the velocity kick $(\delta\mathbf{v})^2 \propto b^{-4}$ for the innermost particles, it gets tremendously large. In the meantime, because $p_b(b) \propto b$, in the majority of the disc crossings, on a total of $\mathcal{N} \sim 10^2 - 10^5$ encounters, none of them has an impact parameter $b \ll b_{\max}$. Therefore, when applied blindly, the CL theorem overestimates the energy kick felt by the particles in the innermost part of the subhalo – here we keep on omitting the protection by adiabatic invariance that will be discussed later on. More details on the CL theorem and the limit of its application in a physical context are given in App. A.2.2. In order to illustrate and quantify the effect let us look at a striking example and focus on a small subhalo where it is more pronounced. More precisely, consider a typical subhalo before its first crossing of the stellar disc, with a typical mass $m_t = 1.6 \times 10^{-9}$ M$_\odot$, scale radius $r_s = 7.1 \times 10^{-7}$ kpc and tidal radius $r_t = 2.34192 \times r_s$ at a distance $R = 8$ kpc for the GC. All these values are consistent with a subhalo that has only been smoothly stripped in the SL17 model. Its relative velocity with the stars is given by the average value $\overline{v_r}(8\,\mathrm{kpc}) = 334$ km s^{-1} and its inclination is given by $\cos\theta = 0.5$ so that it encounters $\mathcal{N} \sim 2346$ stars. The goal is to determine the true PDF for ΔE and compare it to Eq. (4.107). However, even though the number of encounters is not high enough to have proper convergence of the CL distribution it is still too high to allow for a full analytical computation. Indeed, that would require evaluating $\mathcal{N}$ convolutions of the PDF for $\delta\mathbf{v}$, which is far

from being achievable, even numerically and with the use of Fourier transforms. A Monte-Carlo (MC) algorithm is, therefore, better suited for the task and with a total of 5×10^5 draws we achieve convergence to the true PDF of ΔE. In Fig. 4.7 is represented the complementary cumulative distribution function (CCDF) of ΔE

$$\overline{F}(> \Delta E) \equiv \int_{\Delta E}^{+\infty} p_{\Delta E}(\Delta E') \mathrm{d}\Delta E' \tag{4.110}$$

for two radii, one in the inner part of the subhalo $r = 10^{-2} \times r_\mathrm{s}$ and in the outskirts $r = 2.34 \times r_\mathrm{s}$. The blue solid curves show the true distribution from the MC algorithm while the blue dash-dotted lines are the expectations from the CL theorem. As predicted the difference between these two curves is less pronounced in the outskirts, however, the approximated distribution is tremendously shifted toward much higher values of ΔE in the centre. For the same subhalo, Fig. 4.8, clearly shows that the expectation from the CL theorem for Med(ΔE), in dashed blue, overshoots the gravitational potential on the entire range of radii, while the true value, in solid blue, only crosses it on the outskirts. Therefore it seems that using Eq. (4.92) is impossible.

Unfortunately, even though the MC algorithm is efficient to treat the aforementioned example, it is too greedy in terms of CPU-time to be used for the study of the full subhalo population. Because only encounters with small impact parameters are responsible for the convergence issue while they have very small chances to occur, the solution is to truncate the impact parameter range from below. We detail the method in the following. For one crossing of the disc, we denote by b_0 the minimal impact parameter. From the PDF of impact parameter, the PDF of b_0 is given by

$$p_{b_0}(b_0) = \frac{2\mathcal{N}}{(1-\beta^2)^{\mathcal{N}}} \frac{b_0}{b_\mathrm{max}^2} \left[1 - \left(\frac{b_0}{b_\mathrm{max}}\right)^2\right]^{\mathcal{N}-1} \tag{4.111}$$

with $\beta \equiv b_\mathrm{min}/b_\mathrm{max} \ll 1$. We define $b_0(Q)$ so that in only a fraction Q of the disc crossings the subhalo experiences an encounter with impact parameter lower than $b_0(Q)$. It is given by

$$b_0(Q) = b_\mathrm{max} \left[1 - (1-\beta^2)(1-Q)^{1/\mathcal{N}}\right]^{1/2} . \tag{4.112}$$

Consequently, the best way to recover a *pseudo*-convergence so that the CL distribution of Eq. (4.92) approximate as good as possible the real distribution is to replace b_min by $b_0(Q)$. We estimated that setting $Q \sim 0.2$ gives correct results. Examples are shown by the red curves in Fig. 4.7. Convergence is not exact but the new CL result is now much closer to the true CCDF in solid blue. In Fig. 4.8 we show the evolution of the median energy kick and its dispersion in terms of the radius inside the substructure. As the energy kick becomes sizeable when it is of the same order as the gravitational potential it is when $s \gtrsim 1$ that the effect of stars become important. This can be understood easily as the inequality $\sigma < |\Phi|$ obtained from the expression of σ_sub given by Jean's equation implies directly $\Delta E \sim |\Phi| \Rightarrow s > 0.5$. While the CL result with the truncation (in dashed red) provides a good estimation of the true median (solid blue) in the left panel, the dispersion is not at all well recovered in the right panel: the true energy kick has a much higher dispersion. That was expected as the non-convergence issue we are trying to solve here is symptomatic of the large discrepancy between the median and the average and thus of the large dispersion. The take-home message is that defining a precise energy kick for the entire population of particles in one shell of a subhalo is not trivial and the chosen definition needs to be considered with care. Hereafter we stick to the median as it is a well, physically grounded, prescription.

Validity of the impulse approximation

While we have already discussed the high-speed encounter limit we have not yet mentioned the validity of the impulse approximation which amounts to consider that particles in the subhalo do not have to reorganise during an encounter. The justification is provided by comparing the orbital time scale of the particles to the time scale of the encounter $t_{\rm col} \sim b/v_{\rm r}$. At a distance r for the centre of the subhalo the typical orbital frequency of the particles is $\omega(r) = \sigma_{\rm sub}/r$ and the encounter can be considered impulsive if $t_{\rm col}\omega(r) \ll 1$ for any value of r. In practice, in an NFW subhalo $\omega(r \to 0) \to \infty$ therefore the approximation cannot hold perfectly. However what is important is to evaluate at which radius it exactly breaks down. Let us consider an encounter with $b = b_{\rm max}$ and $v_{\rm r} = \overline{v_{\rm r}}$. Then we find $t_{\rm col}\omega(10^{-3}r_{\rm s}) < 1$ whatever the mass of the subhalo (with a concentration fixed at the median value). The equality is reached at 8 kpc if $v_{\rm r} \sim 20$ km s^{-1}, which has less than 0.02 % to occur according to the PDF for $v_{\rm r}$ given in Eq. (4.89). In conclusion, the impulse approximation is valid for the vast majority of encounters down to radii as small as $10^{-3}r_{\rm s}$.

We can compare this configuration to that of the disc shocking effect. In the latter case, the typical time of encounter is much longer as it corresponds to the total crossing of the disc $t_{\rm cross} \sim h_{\rm d}/v_z$ with $h_{\rm d} \simeq 0.9$ kpc the width of the disc and v_z the velocity in the perpendicular direction. Because $h_{\rm d} \gg b_{\rm max}$ the impulse approximation breaks down for larger radii and has to be taken into account.

4.4.3 The impact on the subhalo profile

In this section, we aim at giving a rough estimation of the impact of the star encounters on the subhalo profile. Here we go beyond the stripping criterion of SL17 described by Eq. (4.38) – which simply consists of truncating the halo where the kinetic energy kick is equal to the gravitational potential – in order to justify that it gives a good first approximation. We start with the assumption that right after the encounter a subhalo is stripped of its particles with a final velocity greater than the escape velocity at their original position r. In practice, we should also take into account the fact that the system relaxes after some time and acquire a new structure, however, this is beyond the scope of this analysis.

Let us start with the initial phase space distribution function (PSDF) that we denote $f(\mathbf{v}, \mathbf{r})$. Because we assume isotropy it only depends on the norm of the velocity and radius such that $f(\mathbf{v}, \mathbf{r}) = f(v, r)$. Note, however, that a generalisation of the following equations to a non isotropic system would be straightforward. The PSDF is normalised such that

$$\rho(r) = \int_{v<v_{\rm es}(r)} f(v,r)\mathrm{d}^3\mathbf{v} = 4\pi \int_0^{v_{\rm es}(r)} f(v,r)v^2\mathrm{d}v\,, \tag{4.113}$$

where we introduced $v_{\rm es}(r)$ the escape velocity which is given in terms of the gravitational potential as

$$v_{\rm es}(r) = \sqrt{2|\Phi(r)|}. \tag{4.114}$$

The probability distribution of initial velocity that we introduced earlier is then given by $p_v(v\,|\,r) = 4\pi v^2 f(v,r)/\rho(r)$. Note that here we make explicit the dependence in r. Our goal is thus to define a final PSDF, after crossing of the disc, $\tilde{f}(v_f, r)$ in order

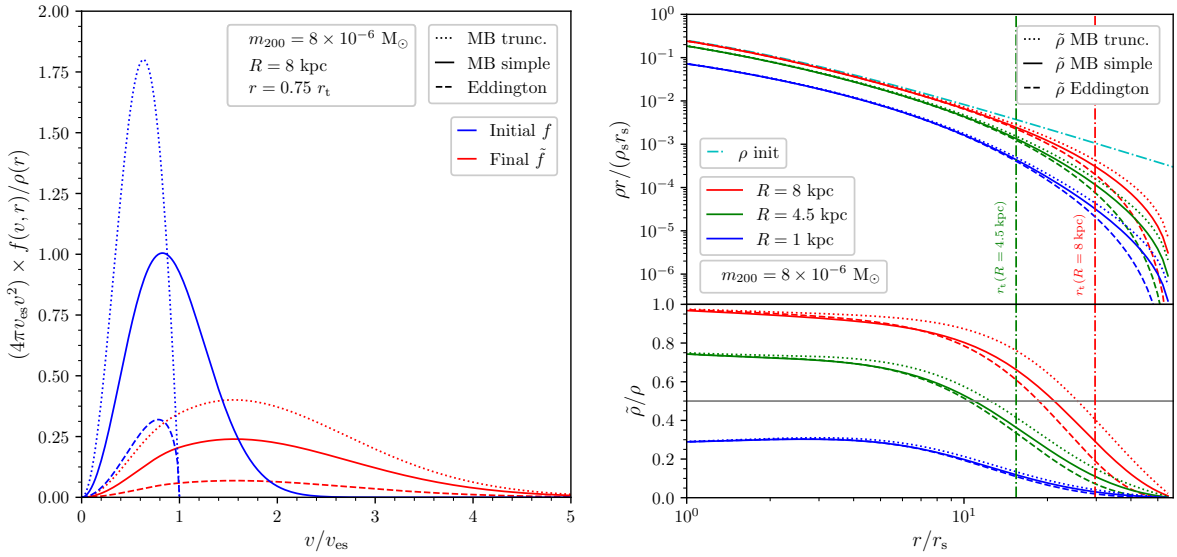

Figure 4.9 – Left panel: Final PSDF (in red) in terms of the velocity at a given radius r inside a subhalo of mass $m_{200} = 8 \times 10^{-6}$ M$_\odot$ with median concentration that crosses the disc at 8 kpc from the GC for three different initial PSDF (in blue). The value of r is chosen as 75% of the tidal radius fixed by the virial radius r_{200} here. Eddington is given by Eq. (4.121), MB by Eq. (4.122) and MB truncated by Eq. (4.123). The normalisation was chosen such that the integral between $v = 0$ and $v = v_{es}$ of these curve should be 1 to recover the correct value of the density profile at position r. The only correctly normalised distribution is MB truncated. The MB simple PSDF is normalised on the range $v \in [0, \infty[$ and the Eddington PSDF is not normalised at all. The later two, therefore, under-predict the value of the density. **Right top panel:** The initial profile in cyan and the new profiles computed with the different initial PSDF for an NFW subhalo crossing the disc at three distances from the GC. **Right bottom panel:** The ratio of the new profile over the initial profile. The dash-dotted lines correspond to the tidal radius evaluated in the SL17 recipe by when choosing a typical kinetic energy kick of every shell at the median value.

to access the final density profile

$$\tilde{\rho}(r) = \int_{v_f < v_{es}(r)} \tilde{f}(v_f, r) \mathrm{d}^3\mathbf{v}_f = 4\pi \int_0^{v_{es}(r)} \tilde{f}(v_f, r) v_f^2 \mathrm{d}v_f \,. \tag{4.115}$$

To this end, because for a fixed initial velocity v the final velocity v_f is directly related to the energy kick, we can deduce, from Eq. (4.104), the PDF of final velocity for a given initial velocity, as

$$p_{v_f}(v_f \,|v, r) = \frac{1}{2\Gamma(d/2)} \frac{v_f}{v} \sqrt{\frac{d}{2\mathcal{N}(\delta\mathbf{v})^2}} \delta\Gamma\left[\frac{d-1}{2}; \frac{(v-v_f)^2 d}{2\mathcal{N}(\delta\mathbf{v})^2}, \frac{(v+v_f)^2 d}{2\mathcal{N}(\delta\mathbf{v})^2}\right] \tag{4.116}$$

Therefore the final PSDF can be evaluated as

$$\tilde{f}(v_f, r) = \frac{1}{4\pi v_f^2} \int p_{v_f}(v_f \,|\, r) f(v, r) \mathrm{d}^3\mathbf{v} \tag{4.117}$$

where $p_{v_f}(v_f \,|\, r)$ acts as a kernel function linking the final to the initial PSDF. Integrating over the final velocity, according to Eq. (4.115), it yields the final density,

$$\tilde{\rho}(r) = \int f(v, r) \left\{ F_{v_f}(\leq v_{es(r)} \,|\, v, r) \equiv \int_{v_f < v_{es}(r)} p_{v_f}(v_f \,|\, r) \right\} \mathrm{d}^3\mathbf{v} \tag{4.118}$$

where $F_{v_f}(\leq v_f \,|\, v, r)$ is the complementary distribution function (CDF) of the PDF p_{v_f}. In that sense F_{v_f} is the kernel distribution which relates the final to the initial density. The only thing that we need to evaluate now is the initial PSDF f. To be consistent with SL17 we assume that the initial profile exhibits a sharp truncation at the tidal radius. Unfortunately, finding the initial PSDF for such objects is involved (Lacroix et al. 2018). The main method, for an isotropic system, is to rely on the Eddington formalism. One introduces the opposite gravitational potential $\Psi = |\Phi|$ and the opposite total energy $\mathcal{E} = \Psi - v^2/2$. Then the PSDF is only dependent on $\mathcal{E}$ and the Eddington inversion formula gives

$$f(\mathcal{E}) = \frac{1}{\sqrt{8}\pi}\left\{\frac{1}{\sqrt{\mathcal{E}}}\frac{\mathrm{d}\rho}{\mathrm{d}\Psi}\bigg|_{\Psi=0} + \int_0^{\mathcal{E}} \frac{\mathrm{d}\Psi}{\sqrt{\mathcal{E}-\Psi}}\frac{\mathrm{d}^2\rho}{\mathrm{d}\Psi^2}\right\} \tag{4.119}$$

with the relation between Ψ and ρ given by Poisson's equation $\Delta\Psi = -4\pi G_{\mathrm{N}}\rho$. When $\Psi = 0$ at finite radius the derivative of ρ with respect to Ψ does not vanish and the first term $\propto 1/\sqrt{\mathcal{E}}$ is divergent and non physical. In order to keep things simple in the following we naïvely remove this term and compute the associated initial profile as

$$\rho(r) = 4\pi\sqrt{2}\int_0^{\Psi(r)}\left\{\hat{f}(\mathcal{E}) \equiv \int_0^{\mathcal{E}} \frac{\mathrm{d}\Psi'}{\sqrt{\mathcal{E}-\Psi'}}\frac{\mathrm{d}^2\rho}{\mathrm{d}\Psi'^2}\right\}\sqrt{\Psi(r)-\mathcal{E}}\mathrm{d}\mathcal{E}\,. \tag{4.120}$$

Two major caveats can then be pointed out. Firstly, the reconstructed density is defined up to a constant that is taken as 0 here. Moreover, modifying the PSDF, from f to $\hat{f}$, modifies the profile and one should then use the proper gravitational potential given by Poisson's equation. For simplicity here, the gravitational potential is evaluated with respect to the original profile. Furthermore, this is slightly discordant with the fact that the kernel F_{v_f} is evaluated for a strict NFW profile. Regardless of these issues the PSDF, in terms of velocity, can then be evaluated as

$$f(v, r) = \hat{f}\left(\Psi(r) - \frac{v^2}{2}\right)\,. \tag{4.121}$$

Nevertheless, in order to parametrise our uncertainty due to the aforementioned caveats we introduce two other simple PSDF. First we consider the Maxwell-Boltzmann distribution Eq. (4.106) and we simply set

$$f(v, r) = \frac{\rho(r)}{(2\pi\sigma^2_{\mathrm{sub}}(r))^{3/2}}\exp\left(-\frac{v^2}{2\sigma^2_{\mathrm{sub}}}\right)\,. \tag{4.122}$$

Even though this distribution is realistic, its main downside is that the velocity of particles can be initially higher than the escape velocity, especially in the outskirts where the velocity dispersion given by Jean's equation tend to the gravitational potential. Consequently, close to the truncation radius, this PSDF is not correctly normalised and it under-evaluates the density; Eq. (4.113) is not satisfied. The second option we investigate is to set a cut-off in the velocity-space and renormalise to obtain

$$f(v, r) = \frac{\rho(r)}{K(r)}\left[\exp\left(-\frac{v^2}{2\sigma^2_{\mathrm{sub}}}\right) - \exp\left(-\frac{v^2_{\mathrm{es}}(r)}{2\sigma^2_{\mathrm{sub}}}\right)\right] \tag{4.123}$$

where we set the normalisation factor $K(r)$ to specifically satisfy Eq. (4.113). Nevertheless, such a prescription is also not perfect because the velocity dispersion is no longer σ_{sub} (it gives a lower velocity dispersion). All in all, even if the three initial

PSDF we introduced are all approximate, they allow us to bracket the theoretical uncertainty on the initial velocity distribution.

In the left panel of Fig. 4.9 we represent the evolution of the PSDF with respect to the velocity at a fixed position in a typical subhalo after one disc crossing. We observe, as expected, that the stars naturally shift the distributions to higher values of velocity. In the right panel, we show the corresponding new profile density in the top part and the comparison to the initial profile at the bottom for the different initial PSDF introduced. We plotted the result for a subhalo crossing the disc at three different distances from the GC. We can remark that even in the most conservative case of the initial truncated Maxwell-Boltzmann distribution of Eq. (4.123) the density decreases toward the outskirts. At R =8 kpc and R =4.5 kpc the vertical dash-dotted lines represent the tidal radius obtains from the SL17 recipe using a typical kinetic energy kick equal to the median. In both cases, they correspond to positions where the new densities are already below 50% of the initial one. At R =1 kpc the tidal radius is evaluated to be 0 as a sizeable part of the central particles are ejected (the blue curves being below the 50% threshold in the bottom panel). In order to determine the true final profile one also should integrate the effect of relaxation after the shock. Nevertheless, this simple analysis is enough to justify the SL17 recipe and the use of the median as a typical energy kick and to compare it to more realistic effects on the density profile.

4.4.4 Results and comparisons with previous works

In conclusion, the energy kick induced by star encounters on a total disc crossing is defined as $\Delta E \sim \mathrm{Med}(\Delta E) = \kappa \mathcal{N} \overline{\delta v^2}/2$ with $\kappa \sim 0.7$ and $\overline{\delta v^2}$ given by the integral in Eq. (4.94) truncated from below by imposing the cut-off $b_{\min} \to b_0(Q = 0.2)$. The total impact of star encounters during several disc crossings on one subhalo can be evaluated by replacing the value of ΔE in Eq. (3.118) by the value of the median discussed above.

Using this method we compared, in the left panel of Fig. 4.10, the evolution, with time, of the bound mass fraction of a given subhalo with initial radius given by the virial radius to the simulation results of ANGUS et al. (2007) – hereafter AZ07. As they considered a subhalo at $z \sim 26$ with concentration ($c_{\rm vir} = 2$)) and virial mass $m_{\rm vir} = 10^{-6}$ $\mathrm{M}_\odot$ in order to use our formalism we roughly rescaled its size to $z \sim 0$ by assuming that the scale radius and scale density remain constant – which should hold approximately – see the discussion on the mass concentration relation. We found a concentration $c_{200} = 84.7$, a mass $m_{200} = 8 \times 10^{-6}$ $\mathrm{M}_\odot$ and a tidal radius $r_{200} = 0.42$ pc. In the same figure, we also show the evolution of the bound mass fraction for a subhalo of the same virial mass but median concentration picked in SÁNCHEZ-CONDE et al. (2014). We consider that the subhalo enters the galactic disc with an inclination $\cos\theta = 1/2$ and has a relative velocity with the stars $\overline{v_{\rm r}}(8\,\mathrm{kpc}) = 334$ km.s^{-1}. Even if stripping becomes less and less efficient with time in our work, all three results are still in good agreement. Moreover, while we have derived an analytical estimate for the number of star encounters per crossing and for the number of crossings, the authors of AZ07 used a refined model of the Galaxy to evaluate these two quantities with better precision. In addition, the discrepancies can be further understood as we assume a sharp and fixed truncation in radius (parametrised by $r_{\rm t}$) without change of the density profile at every crossing such as it realistically should be (GOERDT et al. 2007; DELOS 2019a).

In the right panel of Fig. 4.10 we show the time it takes to completely destroy a subhalo with a mass m_{200} (and median concentration) trapped and immobile in the

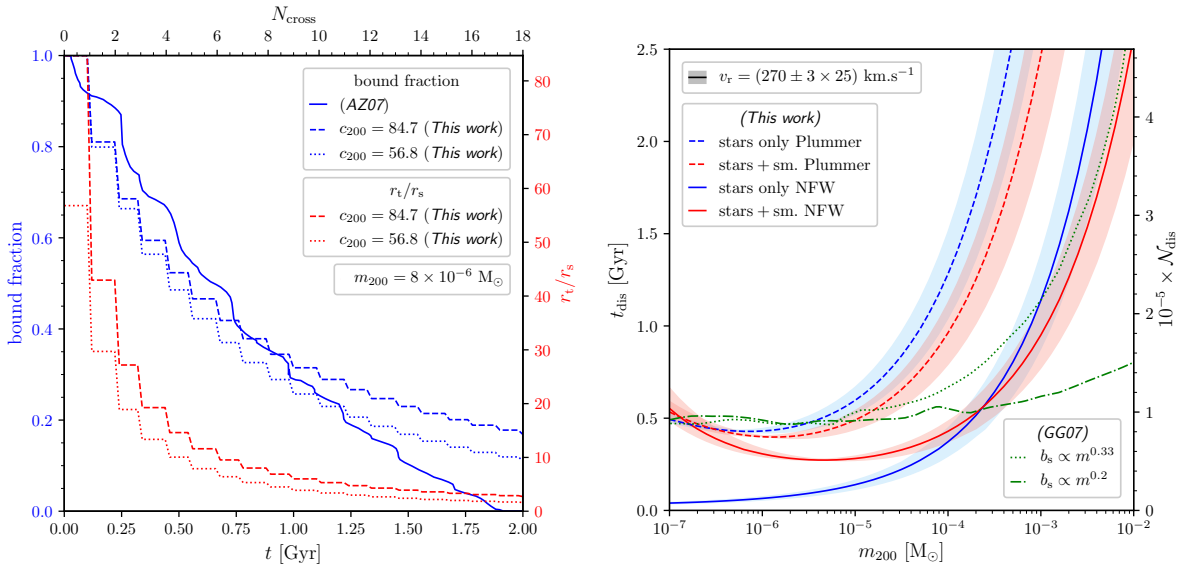

Figure 4.10 – Left panel: Evolution of the mass fraction (blue) and tidal radius (red) of a subhalo of initial virial mass $8 \times 10^{-6}\ M_\odot$. This mass corresponds to the rescaled virial mass today studied in AZ07 (Angus et al. 2007) assuming fixed scale density and scale radius. The initial radius of the structure is fixed to r_{200} and the energy kick induced by star encounters at each crossing is fixed by $\Delta E = \kappa \mathcal{N} \overline{\delta v^2}/2$ with $\kappa \sim 0.7$ and $\overline{\delta v^2}$ given by the integral in Eq. (4.94). The concentration $c_{200} = 84.7$ correspond to that of AZ07 rescaled to today assuming fixed scale radius and scale density. The concentration $c_{200} = 56.8$ is the median concentration from Sánchez-Conde et al. (2014). **Right panel:** Evolution with mass of the disruption time for a subhalo trapped at 8 kpc of the GC in the stellar disc. Two cases are considered: stars only where the initial radius is the virial radius today (blue) and stars+smooth where the initial radius is the Jacobi radius. Comparison is made with GG07 (Green et al. 2007) and the two model they consider (green)

Galactic disc at 8 kpc of the GC. For comparison with Green et al. (2007) – hereafter GG07 we also considered both NFW and Plummer density profiles for the subhalo and we assumed stars flying by with a velocity in the range $v_{\rm r} \sim (270 \pm 3 \times 25)$ km.s^{-1}. We focus on two cases, one where the initial radius of the subhalo is given by its virial radius at $z \sim 0$ and one where the initial radius is set from the smooth stripping. Comparing the first scenario to GG07 we observe that the orders of magnitude and the general behaviour of $t_{\rm dis}$ with the mass are similar. Let us point out, nevertheless, that the comparison is somewhat biased as they considered subhalos at $z \sim 26$ similarly to AZ07 and therefore there can be a mismatch between the definition of mass and virial radius for the same substructures. Another caveat of the method is that we make the crude approximation that the profile and the gravitational potential of the subhalo do not evolve during its entire time in the disc before being completely destroyed, which may artificially lower the value of $t_{\rm dis}$. Eventually, we note here that it is quicker to destroy subhalos with an NFW profile and a virial mass $m \lesssim 10^{-4}$ M$_\odot$ than it is for a Plummer profile of the same mass.

In this analysis above, we considered resilient subhalos by choosing $\epsilon_{\rm t} = 10^{-2}$ as disruption parameter. However this choice appears not to have a strong impact as when the number of encountered stars becomes large ($\mathcal{N} > 10^4$), there is a sudden transition between two distinct behaviours of the energy kick with the radius owing to the dependence of $b_{\rm min}$ in $\mathcal{N}$: from $\Delta E \propto (r/r_{\rm s})^2$, as plotted in Fig. 4.8, to $\Delta E \propto$ cst. larger than the gravitational potential. Therefore subhalos experience a rapid

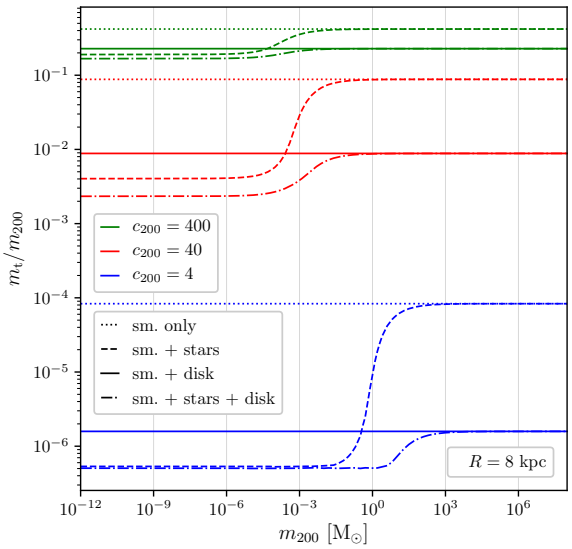

Figure 4.11 – The ratio of the physical mass m_t over the cosmological virial mass m_{200} with respect to m_{200} for several configurations of tidal effects and three different concentrations. Are considered a scenario when only smooth stripping is included, with no effects from baryons (dotted), a scenario where only the star encounters (resp. disc shocking) are taken into account on top of the smooth stripping (dashed, resp. solid) and a scenario where all encounter are included (dash-dotted).

transition with $\mathcal{N}$ between having a new tidal radius r_t close to the initial boundaries and complete dispersal of all their particles (even in the inner shells).

4.5 Effect on the total population of subhalo

In this section, we incorporate the effect of stars into the SL17 model in addition to smooth stripping and disc shocking. Firstly, we describe how we compute the combined effect of individual encounters and disc shocking. Then, in a second step, we show our results for the impact on the subhalo mass function and the total number density.

4.5.1 Combination of the different stripping effects

Let us now discuss the inclusion of the gravitational shocking by individual stars into that framework. In the impulsive approximation limit, the total energy kick is the combination $\Delta\mathbf{v} + \Delta\mathbf{v}_d$ for which a PDF could be formally derived. Because of adiabatic corrections for the disc shocking however this is not possible. Nevertheless one can always write the total energy gain as

$$\begin{aligned}\Delta E_{tot} &= \frac{1}{2}(\Delta\mathbf{v} + \Delta\mathbf{v}_d)^2 + \mathbf{v}\cdot(\Delta\mathbf{v} + \Delta\mathbf{v}_d) \\ &= \Delta E + \Delta E_d + \Delta\mathbf{v}\cdot\Delta\mathbf{v}_d\,.\end{aligned} \tag{4.124}$$

In order to circumvent our ignorance of the true distribution for $\Delta\mathbf{v}_d$ with adiabatic corrections, we make the assumption that $\Delta\mathbf{v}.\Delta\mathbf{v}_d \sim 0$ that is exact in the case of a subhalo with a normal incidence on the disc (in the 2D random walk configuration,

$\Delta \mathbf{v}$ is parallel to the disk and $\Delta \mathbf{v}_{\rm d}$ is perpendicular to it). Therefore one approximate the total energy kick as being

$$\Delta E_{\rm tot} \simeq \frac{1}{2}\left[0.7\mathcal{N}\overline{\delta v^2} + |\Delta \mathbf{v}_{\rm d}|^2 A_1(\eta_{\rm d})\right] \tag{4.125}$$

More details on the total distribution of $\Delta E_{\rm tot}$ are given in App. D.4 and support this definition. Moreover, for efficiency, $\overline{(\delta v)^2}$ is evaluated assuming a *typical* subhalo entering the galactic disc with an average inclination $\cos\theta = 1/2$ and an average relative velocity with the stars $\overline{v_{\rm r}}(R)$ given in Eq. (4.89). In the following, we recompute the tidal radius of subhalos by replacing the value of the kinetic energy kick in Eq. (3.118), which only took into account the smooth and disk shocking effect, by the above definition. We show how tidal stripping is impacted by single encounters with stars.

4.5.2 Results

We consider four different configurations for the evaluation of the tidal effects. *(i) smooth only:* the tidal radius is entirely defined by Eq. (4.31). *(ii) smooth+stars:* on top of the smooth effect only the individual encounters with stars are included. *(iii) smooth+disc:* on top of the smooth effect only the disc shocking effect is included. *(iv) smooth+stars+disc:* all effects are taken into account. In Fig. 4.11 we show the evolution of the final tidal mass in terms of the original cosmological mass for the different stripping configurations and for three concentrations at a distance $R = 8$ kpc from the GC. The dominant effect of baryons on small subhalos with initial mass $m_{200} \lesssim 1$ $\mathrm{M}_\odot$ are the individual encounters. On the contrary, for larger subhalos, baryonic stripping is mostly due to the disc shocking.

The total mass function for the different stripping cases and for different input parameters of the subhalo model are plotted in Fig. 4.12 for a minimal cosmological mass $m_{200}^{\rm min} = 10^{-10}$ $\mathrm{M}_\odot$. While baryonic effects are mild and even negligible in the outer region of the disc, *e.g.* at a distance $R = 15$ kpc, they have more and more impact close to the GC. At $R = 1$ kpc the mass functions are strongly suppressed and offset toward small masses, especially because of stellar encounters. Indeed, in the resilient subhalo scenario (with a disruption parameter $\epsilon_{\rm r} = 10^{-2}$), they reduce by 6 orders of magnitude the mass function for $10^{-10} < m_{\rm t} \lesssim 10^{-6}$ $\mathrm{M}_\odot$ (in comparison to the smooth only case) and populate the mass range much below the minimal cosmological mass. The disc shocking effects only induce an equivalent reduction of 4 orders of magnitude. In the fragile case ($\epsilon_{\rm r} = 1$) disc shocking effects disrupt all subhalos and so do stellar encounters at low masses. At $R = 8$ kpc one notice a similar effect with almost 2 (resp. 4) orders of magnitude suppression due to stellar encounters and a 1 (resp. 2) order(s) of magnitude suppression due to disk shocking at low masses for resilient subhalos (resp. fragile). The causes for the strength of stellar encounters in the centre are two-fold: close to the GC subhalos cross the disc more often and the stellar density is higher, reducing the interstellar distances and the impact parameters, therefore, enhancing the kinetic energy kicks.

In Fig. 4.13 we show the number density of subhalo at every position from the GC. As seen above, stellar encounters strongly impact the low mass range that is also the most populated therefore the effects can be important. We recover the conclusions that further than 12 kpc from the GC the baryonic effects are negligible. At 8 kpc effects are already sizeable. Although the number density for a population of resilient

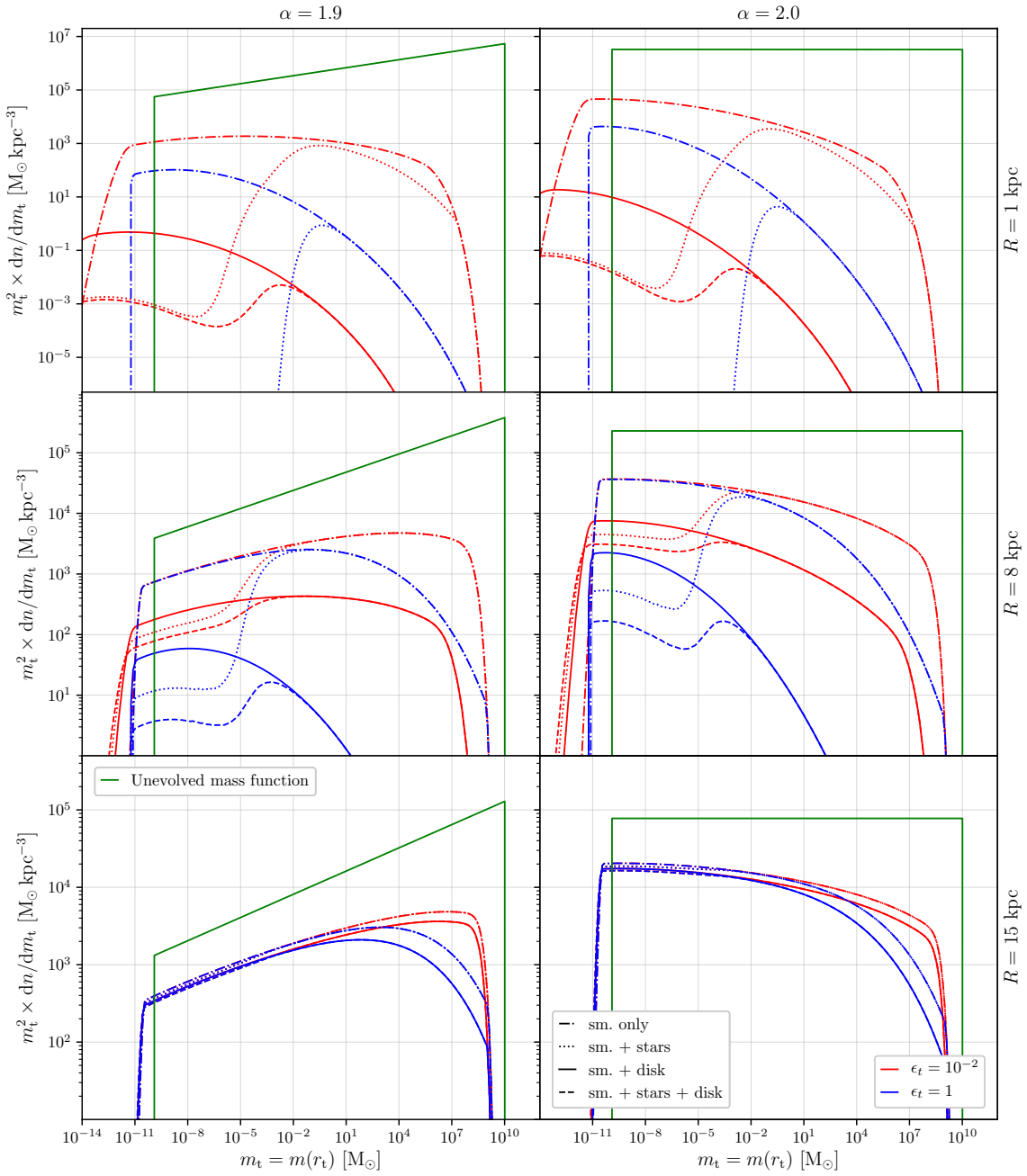

Figure 4.12 – Mass functions taking into account four different stripping configurations, at different distances from the GC, R= 1, 8, 15 kpc and for two different values of the mass index $\alpha = 2.0$ on the left and $\alpha = 1.9$ on the right. The minimal cosmological mass is set to $m_{200}^{\rm min} = 10^{-10}$ $M_\odot$. The red (resp. blue) curves correspond to the resilient (resp. fragile) subhalos configuration. The green curve is the unevolved mass function where $r_t = r_{200}$. Notice that at $R = 1$ kpc there are no solid and dashed blue curves as disk shocking effects destroy all the population of subhalos if they are fragile.

subhalos would still be non-impacted, fragile subhalos would have a population reduced by one order of magnitude in comparison to the scenario with disc shocking and smooth stripping only (as seen with the dashed and solid curves). The difference grows toward the GC and at $R = 1$ kpc fragile subhalos are all destroyed and resilient subhalos have a population divided by 100 because of star encounters.

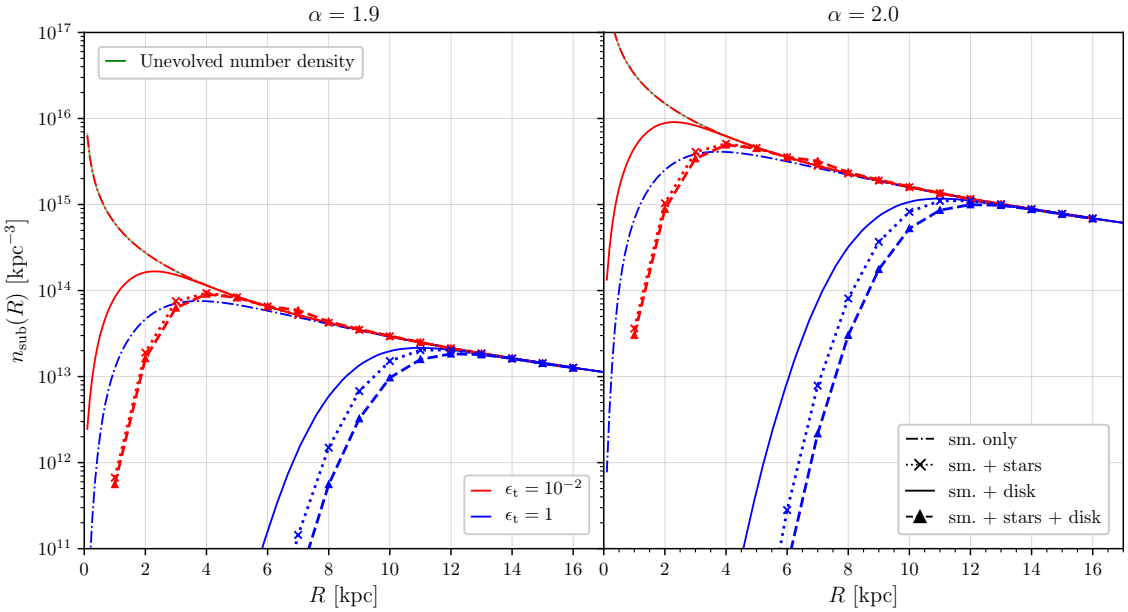

Figure 4.13 – Number density of subhalos taking into account four different stripping configurations, at different distances from the GC, R= 1, 8, 15 kpc and for two different values of the mass index $\alpha = 2.0$ on the left and $\alpha = 1.9$ on the right. The minimal cosmological mass is set to $m_{200}^{\rm min} = 10^{-10}$ M$_\odot$. The red (resp. blue) corresponds to the resilient (resp. fragile) subhalos configuration. The green curve is the cosmological number density without tidal effects. Notice that at $R = 1$ kpc there is no blue circle marker as disk shocking effect destroy all the population of subhalo if they are fragile.

4.6 Conclusion and further developments

4.6.1 Discussion on stellar encounters

In conclusion, we have refined the theoretical analysis of dynamical effects induced on particles of one subhalo during the encounter with a star. In particular, we have derived a new solution for the estimated velocity kick received by particles in every shell of the subhalo. Conveniently this solution is chosen to remove the divergences produced by the potential of the point-like star, therefore it also may underestimate the impact of very penetrative encounters. In the following, we have studied the properties of the stellar encounters for a subhalo crossing the stellar disc (neglecting the effect of the central bulge) and computed the impact of successive encounters. In order to use the SL17 recipe for the evaluation of tidal effects on the total subhalo population, we have given specific attention to the definition of a typical kinetic energy kick received by particles in every shell of the subhalo. To this end we have performed Monte-Carlo simulations in a given specific configuration that we have compared to analytical estimates: they show that a careful treatment of the impact parameter distribution is necessary in order to not overestimate the kinetic energy. Then, choosing the typical energy kick as the median energy kick in every shell is interesting as it is easy to evaluate and because it is physically motivated. However, the MC simulation also evidenced that the dispersion around the median can be important and therefore this choice remains an approximation and there is no perfect solution. Besides, the model exhibits another caveat as it considers that subhalos conserve an isotropic distribution with their original density profile and with a sharp truncation at their tidal radius. This has been shown to

not be the case, in part because after a shock subhalos enter a relaxation phase. We cannot take it into account in our analytical model and simulations indicate that subhalos possibly adopt a universal profile different from NFW (HAYASHI et al. 2003; DELOS 2019a). Nevertheless, a quick comparison with previous studies based on numerical simulation seems to still be in good agreement. Consequently, for the aim of this study, we can be confident in the global effect of stars on the total population: namely, stellar encounters have a sizeable effect in the inner 10 kpc on subhalos with mass $\lesssim 1$ $M_\odot$. However the precise impact can vary from one subhalo to another (depending on their orbit, their velocity, ...) and the global theoretical uncertainty should be evaluated in more details – with dedicated simulations for instance. Eventually, let us mention that the validity of the disruption criterion can be questioned (ERRANI et al. 2020a,b) and one could imagine the possibility of creating undisrupted small bound remnants through tidal stripping.

From an observational point of view, the star encounters, because they tend to reduce the number density of subhalos and change the mass function, can have consequences for the local DM searches. Many of the possible impacts have already been mentioned in the conclusion of Chapter 2 – *e.g.* the probability that a subhalo passes through the Earth and produces a sizeable effect on the direct detection constraints. The modification of the mass density profile could also play a role. Note that the effect of stars should not, however, drastically impact the boost factor in most of the directions in the sky, as it only concerns a rather limited region around the GC where the smooth component dominates. In the next chapter, in particular, because we assume resilient subhalos, the star encounter effects can be neglected for simplicity. Especially since the research of point-like subhalos mostly involves large structures that are too massive ($m > 10^3$ $M_\odot$) to be impacted by the stellar encounters, as it will be shown.

4.6.2 Prospects for further developments

Direct follow-ups of this study could concern the capture of subhalos by stars or the heating of the disc due to subhalos and the comparison to numerical simulation. Indeed here we only treated the effect of stars on subhalo, conversely, the effect of subhalos on stars may give rise to interesting signatures. Moreover, the disruption of halos by stellar encounters may create dark streams that could also be studied (ZHAO et al. 2005; SCHNEIDER et al. 2010). In addition, because this works relies on several assumptions and hand-selected criteria, it would be of interest to compare this analysis to a more refined analytical description of the star encounters on a specific subhalo and against dedicated numerical simulations.

Other upgrades of the SL17 model would consist in introducing a more realistic history of the subhalos as mentioned in the conclusion of Chapter 5. We have already started to go in that direction with the determination of the USMF thanks to Merger Tree algorithms. In more details, we could now also take into account the fact that their mass evolves with time through accretion before they are themselves accreted in addition to the non-trivial evolution of their scale radius and scale density (parametrised by the evolution of the mass-concentration relation with the redshift). Besides, the non-circularity of subhalo orbits could also be considered. Let us briefly mention that we have also already paved the way to the latter by computing, with the

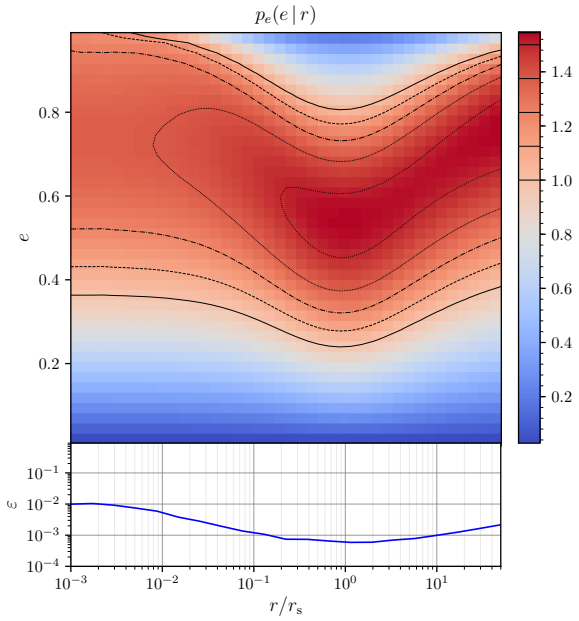

Figure 4.14 – Probability distribution of eccentricity at given position r from the centre of an infinitely large NFW halo. The black curves are iso-contours. The bottom panel shows an evaluation of the numerical error.

Eddington formalism, the probability for a particle at a distance r from the centre of a spherical self-gravitating structure with profile ρ to have a given eccentricity e (or given perihelion and aphelion). Indeed it can be given as

$$p(e\,|\,r) \equiv \frac{1}{\rho(r)} \int f(\mathcal{E}) \delta_{\rm D}\left[h_e(\mathcal{E}, L) - e\right] \mathrm{d}^3\mathbf{v} \tag{4.126}$$

where $\mathcal{E} = \Psi(r) - v^2/2$ with $\Psi(r)$ the gravitational potential and $L = |\mathbf{r} \times \mathbf{v}|$ the angular momentum. The function $h_e(\mathcal{E}, L)$ is the value of the eccentricity fixed by the energy and the angular momentum: the perihelion and aphelion, $r_{\rm min}(\mathcal{E}, L)$ and $r_{\rm max}(\mathcal{E}, L)$, are implicitly given as solutions of

$$\frac{1}{r^2} + \frac{2}{L}\left[\mathcal{E} - \Psi(r)\right] = 0 \quad \text{and} \quad h_e(\mathcal{E}, L) \equiv \frac{r_{\rm max}(\mathcal{E}, L) - r_{\rm min}(\mathcal{E}, L)}{r_{\rm max}(\mathcal{E}, L) + r_{\rm min}(\mathcal{E}, L)} \tag{4.127}$$

In Fig. 4.14 the PDF is represented for an infinite NFW profile – thus avoiding the finite size issues of the Eddington formalism discussed in Sect. 4.4. Because of the implicit definition of h_e, the numerical evaluation is complex, therefore the bottom panel shows the numerical error by checking that the normalisation is correct with

$$\varepsilon \equiv \left| \int_0^1 p_e(e\,|\,r) \mathrm{d}e - 1 \right| . \tag{4.128}$$

Considering, instead of a particle, a subhalo in the MW density profile[1], this would represent the probability distribution for a subhalo at a given position from the GC to have a given eccentricity. From this figure we remark that the distribution is peaked above 0.5, thus the circular orbit approximation ($e = 1$) should already give good results. Let us emphasize that this study is only preliminary and that it needs more work to be properly included in the SL17 model. Nonetheless, this is one step towards a possible future improvement.

[1]Note that the gravitational effect of baryons should be also included and that it could be done by spherisizing their distribution as shown in App. D.1.

V

Detectability of point-like subhalos with gamma-ray telescopes

"I would prefer to stay up and watch the stars than go to sleep. I started learning. I started going to the library and reading. But it was initially just watching the stars from my bedroom that I really did. There was just nothing as interesting in my life as watching the stars every night."

Vera Rubin

Contents

In recent years, the Fermi-LAT collaboration has produced catalogues of gamma-ray point sources (ABDO et al. 2010; NOLAN et al. 2012; ACERO et al. 2015; FERMI-LAT COLLABORATION 2019), amongst which some of them are classified as unidentified. That is to say, they cannot be hitherto associated with a known astrophysical object. In the fourth and last catalogue, 1525 point sources are reported as such. Assuming that DM can self annihilate, this is of particular interest as it raises the question, whether or not, some of these point sources can be DM subhalos that should populate the MW. In this study we make use of the SL17 model detailed in Sect. 4.2 to answer the question. Similar studies have been done in the literature. One class of analysis is based on the MW-like object produced in cosmological numerical simulations; they evaluate the detectability of the DM subhalos within these mock Galaxies – although their DM and baryonic distribution can still significantly depart from the real MW – (PIERI et al. 2011; CALORE et al. 2017). The second class of methods is to search for unidentified point sources in the data, looking for specific features that would point toward annihilating DM – such as spectral properties – (BELIKOV et al. 2012; BERTONI et al. 2015; MIRABAL et al. 2016; SCHOONENBERG et al. 2016; HOOPER et al. 2017; CORONADO-BLAZQUEZ et al. 2019; CORONADO-BLÁZQUEZ et al. 2019; GLAWION et al. 2019). Eventually, the last class of methods is based on a statistical description of the DM subhalo population such as we will present. We can mention the Clumpy code (CHARBONNIER et al. 2012; HÜTTEN et al. 2016) which goal was to make comparison with the cosmological simulations (KELLEY et al. 2019). However, these analyses did not evaluate the detectability of the individual objects over a consistent and realistic foreground. This was further investigated in CALORE et al. (2019a), also based on the SL17 model.

Here we go further by proposing a fully consistent and analytic model for the intricate gamma-ray analysis. Indeed, our DM distribution is based on SL17, which is itself built using the realistic baryonic distribution model of MCMILLAN (2017). Evaluating the baryonic diffuse emission of gamma-ray (that we call GDE or sometimes DGE, for galactic diffuse emission, in the following) with the same model we implicitly take into account its spatial correlations with the subhalo distribution. Note that here, however, we do not incorporate the contribution of the stellar encounters discussed in the previous chapter; we will show that it is a valid approximation. The diffuse DM sourced gamma-ray emission is also important. Because past and current observations have not resulted in an unambiguous detection, this diffuse emission is used to set constraints on the annihilation cross-section, requiring that the DM diffuse signal be lower than the baryonic background/foreground fluctuations. For future instruments, the hope to detect it and consequently discover DM is still alive (CIRELLI et al. 2010; FERMI-LAT COLLABORATION 2010; S. BLANCHET et al. 2012; BRINGMANN et al. 2012; FERMI-LAT COLLABORATION 2012a; ESSIG et al. 2013; CIRELLI et al. 2015; FORNASA et al. 2015; LEFRANC et al. 2015; SILVERWOOD et al. 2015; CHANG et al. 2018). Let us point out that an additional level of intricacy is given by the fact that the diffuse DM contribution is also impacted by the unresolved subhalo population that boosts the annihilation strength (ANDO et al. 2019). In conclusion, specific attention has to be paid to the sensitivity levels both to the point-sources and to the DM diffuse emission to assess if the detection of point-sources has a non-negligible probability to happen before the detection of the latter. We actually show that this consistent treatment tends to yield rather pessimistic results for the detection of point-like subhalos. Nevertheless, in hypothetical situations where some subhalos are detectable, we evaluate the position of the most visible ones and their internal properties.

The entire chapter is based on the work published in FACCHINETTI et al. (2020) and develops as follows. In Sect. 5.1 we derive the emissivity properties of DM and in particular we introduce the notion of J-factor. In Sect. 5.2 we describe the statistics of this quantity in the MW. In Sect. 5.3 we detail the background baryonic models and we establish the sensitivity of Fermi-LAT-like and CTA-like instruments. Let us point out already that our main goal is here to give a proof of principle of the method and obtain the right orders of magnitudes without being necessarily accurate. Therefore, in this chapter, we introduce a simplified *realistic* (yet not necessarily accurate) model for the background that is, in part fitted on data but with angular distributions in the sky that are based on a constrained baryonic distribution in the MW (the same distribution used to implement the tidal effects). This way we account for the correlation between tidal effects and background model. We do not consider a full data analysis mainly because DM can be hidden in the data and disentangling background from signal is beyond the scope of this analysis. Finally we conclude, in Sect. 5.4, on the detectability of DM subhalos as point sources. In this chapter, for notational simplifications, we write $m = m_{200}$ and $c = c_{200}$. Here we refer to both background and foreground contributions as background. We consider two density profiles for the total Galactic halo, an NFW profile and a Cored profile given respectively according to Eq. (4.2) by $(\alpha = 1, \beta = 3, \gamma = 1)$ and $(\alpha = 1, \beta = 3, \gamma = 0)$ and with the parameter fits of MCMILLAN (2017). The subhalos profile is always NFW. The parameters of the SL17 model are mostly chosen to be $\alpha = 1.9$, $m_{\rm min} = 10^{-10}$ $\mathrm{M}_\odot$ and $\epsilon_{\rm t} = 10^{-2}$ so that subhalos are resilient in order to maximise their detectability. Nevertheless, in the first sections we also consider a few other configurations for comparisons.

5.1 Gamma-rays from subhalos

This section is focused on the introduction of subhalo luminosity, gamma-fluxes and J-factors that are of great importance in the following. In the first paragraph, we also introduce some geometrical notations that are necessary to introduce all the other quantities.

5.1.1 Geometry and integrals in the Galaxy

As the Solar System is within the MW at a distance $R_\odot = 8.2$ kpc for the GC we introduce a convenient coordinate system represented in Fig. 5.1. In order to describe the position of any point M a convenient choice is to use the distance-longitude-latitude triplet (also called Galactic coordinates) $\mathbf{s} = (s, l, b)$. This coordinate system is related Cartesian orthonormal frame attached to the solar system $(\hat{\mathbf{e}}_x, \hat{\mathbf{e}}_y, \hat{\mathbf{e}}_z)$, where $\hat{\mathbf{e}}_y$ points to the GC and $\hat{\mathbf{e}}_x$ is also within the Galactic plane. The precise relation is given by the vectorial equality

$$\mathbf{s} = s\left(\cos b \sin l\, \hat{\mathbf{e}}_x + \cos b \cos l\, \hat{\mathbf{e}}_y + \sin b\, \hat{\mathbf{e}}_x\right) . \tag{5.1}$$

The GC is therefore located at $\mathbf{R}_\odot = R_\odot \hat{\mathbf{e}}_y$. The vector between the GC and a point at position s in the Galactic coordinates is $\mathbf{R} = \mathbf{s} - \mathbf{R}_\odot$. Thus, the distance squared can be written in terms of s and $R_\odot$ as follows

$$R^2(s, l, b) = (\mathbf{s} - \mathbf{R}_\odot)^2 = s^2 + R_\odot^2 - 2sR_\odot \left\{\cos\psi = \cos b \cos l\right\} \tag{5.2}$$

where we have introduced the angle $\psi = \widehat{(\mathbf{s}, \hat{\mathbf{e}}_y)}$. As a matter of fact, because the SL17 model is spherically symmetric, the spatial dependence of the DM sourced gamma

rays is fully specified by ψ. In addition, for any line of sight parametrised by the unit vector $\hat{\mathbf{n}} = (l_0, b_0)$, there is another convenient coordinate system represented by $\mathbf{s} = (s, \theta, \varphi)$ where $\theta = \widehat{(\mathbf{s}, \hat{\mathbf{n}})}$ is called the polar angle and φ is the azimuthal angle. The volume element, in that coordinate system, takes the form $\mathrm{d}^3\mathbf{s} = s^2 \mathrm{d}\Omega \mathrm{d}s = s^2 \sin\theta \mathrm{d}\theta \mathrm{d}\varphi \mathrm{d}s$. Moreover, the expression of the radius to the GC R can also be re-written

$$R^2(s, \theta, \varphi) = s^2 + R_\odot^2 - 2sR_\odot \left(\cos\psi \cos\theta - \sin\psi \cos\theta \sin\varphi\right) \tag{5.3}$$

Nevertheless, while for numerical applications it is important to choose the proper system, it can also be extremely convenient to introduce definitions that are independent on the coordinate choice. In the following, pointing directions in the sky are defined by 3-dimensional unitary vectors in S^2 the 2-sphere. For instance, any position vector is decomposed as its norm and direction as $\mathbf{s} = s\hat{\mathbf{n}}$. Consequently, instead of writing $R(s, l, b)$ or $R(s, \theta, \varphi)$ we denote $R(s, \hat{\mathbf{n}})$. Subsequently, the solid angle element in direction $\hat{\mathbf{q}} \in S^2$ is called $\mathrm{d}^2\Omega_{\hat{\mathbf{q}}}$. When a choice of coordinate is made and $\hat{\mathbf{q}}$ is parametrised by the angles (θ, φ) or (l, b) the solid angle element becomes $\mathrm{d}^2\Omega_{\mathbf{q}} = \sin\theta \mathrm{d}\theta \mathrm{d}\varphi = \cos b \mathrm{d}b \mathrm{d}l$ such that $\mathrm{d}^3(s\hat{\mathbf{q}}) = s^2 \mathrm{d}s \mathrm{d}^2\Omega_{\mathbf{q}}$. For a given sky patch, $\mathcal{P} \subset S^2$ and a function $g(s, \mathbf{q})$ defined on $\mathbb{R} \times \mathcal{P}$ what is commonly called the integral over the solid angles corresponding to $\mathcal{P}$ is

$$\int_{\mathbf{q} \in \mathcal{P}} g(s, \mathbf{q}) \mathrm{d}^2\Omega_{\mathbf{q}} \,. \tag{5.4}$$

When $g = 1$ then the integral gives $\delta\Omega(\mathcal{P})$, the solid angle covered by the patch $\mathcal{P}$. One specific class of patches of interest are the cones. For a given direction $\hat{\mathbf{n}}$ and an angle $\alpha \in [0, \pi]$ we call cone centred in $\hat{\mathbf{n}}$ and of angular aperture α, the set

$$\mathcal{C}(\hat{\mathbf{n}}, \alpha) = \{\hat{\mathbf{q}} \in S^2 \,|\, \alpha > |\widehat{(\hat{\mathbf{q}}, \hat{\mathbf{n}})}|\} \tag{5.5}$$

with solid angle $\delta\Omega(\mathcal{C}(\hat{\mathbf{n}}, \alpha)) = 2\pi(1 - \cos\alpha)$. Because it is often interesting to integrate over small regions, if the angle α is smaller than the typical angular variations of g then the following approximation holds,

$$\int_{\mathbf{q} \in \mathcal{C}(\hat{\mathbf{n}}, \alpha)} g(s, \hat{\mathbf{q}}) \mathrm{d}^2\Omega_{\hat{\mathbf{q}}} \simeq \delta\Omega(\mathcal{C}(\hat{\mathbf{n}}, \alpha)) g(s, \hat{\mathbf{n}}) \,. \tag{5.6}$$

5.1.2 General definition of the differential flux

We can now write the gamma-ray flux induced by DM annihilation along the line of sight $\hat{\mathbf{n}} = \mathbf{s}/s$ (equivalently along ψ, (θ, φ) or all corresponding coordinates pairs (l, b) in Galactic coordinates if a coordinate system is chosen):

$$\begin{aligned} \frac{\mathrm{d}\phi_{\gamma,\chi}(E, \hat{\mathbf{n}})}{\mathrm{d}E \mathrm{d}\Omega} =& \frac{1}{4\pi} \int_0^{s_{\mathrm{m}}(\hat{\mathbf{n}})} \mathrm{d}s \int \mathrm{d}^3\mathbf{v}_1 \frac{f_\chi\left[\mathbf{R}(s, \hat{\mathbf{n}}), \mathbf{v}_1\right]}{m_\chi} \\ & \int \mathrm{d}^3\mathbf{v}_2 \, \frac{f_\chi\left[\mathbf{R}(s, \hat{\mathbf{n}}), \mathbf{v}_2\right]}{m_\chi} \sum_f \frac{\mathrm{d}N_\gamma^f(E)}{\mathrm{d}E} \frac{v_{\mathrm{rel}}(\mathbf{v}_1, \mathbf{v}_2) \sigma_f\left[v_{\mathrm{rel}}(\mathbf{v}_1, \mathbf{v}_2)\right]}{2\delta_\chi} \end{aligned} \tag{5.7}$$

where $s_{\mathrm{m}}(\hat{\mathbf{n}}) \simeq R_{200} + R_\odot \cos\psi$ is the distance to the virial border of the halo in the direction $\hat{\mathbf{n}}$ and $\mathbf{R}(s, \hat{\mathbf{n}}) = s\hat{\mathbf{n}} - \mathbf{R}_\odot$. The function $(\mathbf{R}, \mathbf{v}) \mapsto f(\mathbf{R}, \mathbf{v})$ is the Galactic PSDF normalised such that

$$\int f_\chi(\mathbf{R}, \mathbf{v}) \, \mathrm{d}^3\mathbf{v} = \rho_\chi(\mathbf{R}) \,. \tag{5.8}$$

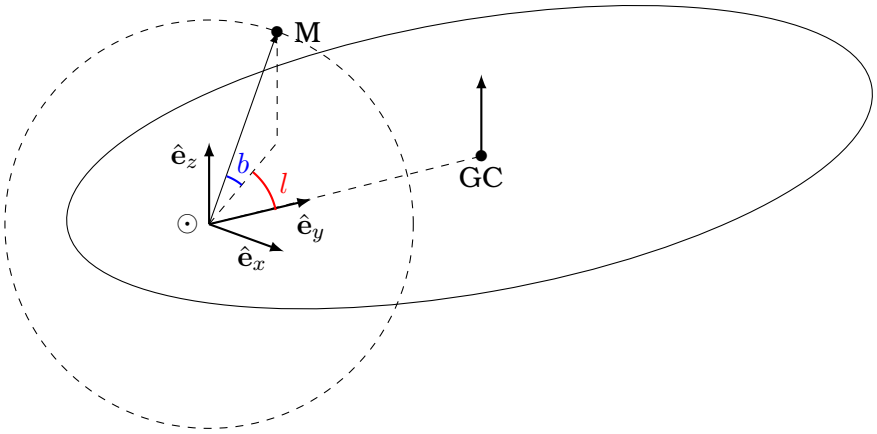

Figure 5.1 – Representation of the Galactic coordinate system and of the Cartesian coordinate attached to the solar system

where ρ_χ denotes any DM mass density profile under consideration. The different properties of the DM particles are encoded in the mass m_χ, the annihilation cross-section σ_f in SM particles $f\bar{f}$ and the associated differential photon flux $\mathrm{d}N_\gamma^f/\mathrm{d}E$ – which we tabulate from Cirelli et al. (2011). The parameter δ_χ is 1 (2) for scalar DM or Majorana (Dirac) fermionic DM and $v_{\rm rel}(\mathbf{v}_1, \mathbf{v}_2) = |\mathbf{v}_2 - \mathbf{v}_1|$ because velocities are non relativistic. The total annihilation cross-section σ is then decomposed according to the branching ratios

$$B_f = \mathrm{Br}\left(\chi\chi \leftrightarrow f\bar{f}\right) = \frac{\sigma_f}{\sigma} \tag{5.9}$$

In addition, we define the average annihilation cross-section as

$$\langle\sigma v\rangle\,(\mathbf{R}) \equiv \int \mathrm{d}^3\mathbf{v}_1 \frac{f_\chi\,(\mathbf{R},\mathbf{v}_1)}{\rho_\chi\,(\mathbf{R})} \int \mathrm{d}^3\mathbf{v}_2\, \frac{f_\chi\,(\mathbf{R},\mathbf{v}_2)}{\rho_\chi\,(\mathbf{R})} v_{\rm rel}\sigma(v_{\rm rel})\,. \tag{5.10}$$

For a s-wave annihilation cross-section $\sigma(v_{\rm rel})v_{\rm rel} = \mathrm{cst.}$ and therefore, the average value does not depend on the position along the line of sight s. For other velocity dependences a common parametrisation is to define a function S so that $\sigma(v_{\rm rel})v_{\rm rel} = (\sigma v)_0 S(v_{\rm rel}/2)$ where $(\sigma v)_0$ is a normalisation constant. In the s-wave case the natural convention is to set $S = 1$ such that $\langle\sigma v\rangle = (\sigma v)_0$. An example of non trivial S factor is obtained, for instance, with Sommerfeld enhancement (Arkani-Hamed et al. 2009; Iengo 2009; Cassel 2010; Feng et al. 2010; Boddy et al. 2017), such as discussed in the addendum Sect. 5.6. With these definitions we introduce the spectral function

$$\mathcal{S}_\chi \equiv \frac{(\sigma v)_0}{2\delta_\chi m_\chi^2} \sum_f \frac{\mathrm{d}N_\gamma^f(E)}{\mathrm{d}E} B_f \tag{5.11}$$

that carries almost all the WIMP-model-dependent information. In the end, the total differential flux is then given by

$$\begin{aligned} \frac{\mathrm{d}\phi_{\gamma,\chi}(E,\hat{\mathbf{n}})}{\mathrm{d}E\mathrm{d}\Omega} =& \frac{\mathcal{S}_\chi}{4\pi} \int_0^{s_{\rm m}(\hat{\mathbf{n}})} \mathrm{d}s\, \rho_\chi^2\left[\mathbf{R}(s,\hat{\mathbf{n}})\right] \langle S(v)\rangle\left[\mathbf{R}(s,\hat{\mathbf{n}})\right] \\ & \text{with} \quad \langle S(v)\rangle\,(\mathbf{R}) = \int \mathrm{d}^3\mathbf{v}_1 \frac{f_\chi\,(\mathbf{R},\mathbf{v}_1)}{\rho_\chi\,(\mathbf{R})} \int \mathrm{d}^3\mathbf{v}_2\, \frac{f_\chi\,(\mathbf{R},\mathbf{v}_2)}{\rho_\chi\,(\mathbf{R})} S\left(\frac{v_{\rm rel}}{2}\right)\,. \end{aligned} \tag{5.12}$$

In the following, only on the case of an s-wave annihilation cross-section is considered. However would we need to incorporate velocity effects, this could be added straightforwardly by replacing $\rho_\chi^2 \to \rho_\chi^2 \langle S(v) \rangle$. Furthermore the DM particle is assumed to be a Majorana fermion and for simplification, only two annihilations channels for bottom quarks $f = b$ and tau leptons $f = \tau^-$ are investigated, assuming that DM only annihilates entirely in one or in the other, $(B_b = 0, B_\tau = 1)$ or $(B_b = 1, B_\tau = 0)$.

5.1.3 The J-factor: several definitions

For every direction $\hat{\mathbf{q}}$ in the sky we introduce the quantity

$$j(\hat{\mathbf{q}}) \equiv \frac{1}{4\pi} \int_0^{s_{\rm m}(\hat{\mathbf{q}})} \mathrm{d}s \, \rho_\chi^2 \left[\mathbf{R}(s\hat{\mathbf{q}})\right] \quad \text{such that} \quad \frac{\mathrm{d}\phi_{\gamma,\chi}(E,\mathbf{q})}{\mathrm{d}E\mathrm{d}\Omega} = S_\chi j(\hat{\mathbf{q}}) \,. \tag{5.13}$$

Consider now a sky patch $\mathcal{P}$. A first version of the usual J-factor (BERGSTROM et al. 1998) is given by

$$J(\mathcal{P}) \equiv \int_{\hat{\mathbf{q}} \in \mathcal{P}} j(\hat{\mathbf{q}}) \mathrm{d}^2\Omega_{\hat{\mathbf{q}}} \quad \text{with} \quad \frac{\mathrm{d}\phi_{\gamma,\chi}(E,\mathcal{P})}{\mathrm{d}E} = \mathcal{S}_\chi J(\mathcal{P}) \tag{5.14}$$

the integrated flux on $\mathcal{P}$. Note that this J-factor has no dimension of steradians (in comparison to other definitions found in the literature) and consequently may slightly differ from other conventions. Now the average flux in $\mathcal{P}$ is given by

$$\left\langle \frac{\mathrm{d}\phi_{\gamma,\chi}(E,\mathcal{P})}{\mathrm{d}E\mathrm{d}\Omega} \right\rangle_{\mathcal{P}} = \mathcal{S}_\chi \left\{ \mathcal{J}(\mathcal{P}) \equiv \frac{J(\mathcal{P})}{\delta\Omega(\mathcal{P})} \right\} . \tag{5.15}$$

If we had at our disposal an instrument that was equally efficient for every line-of-sight contained in this patch, this quantity would be the true collected flux. However real instruments are more complex and it is necessary to be more precise and make explicit the energy-dependence of the angular resolution and effective collection area. To this end, we introduce new versions of the average J-factor, closer to what matters from an experimental point of view. Consider that $\theta_{\rm r}(E)$ is the resolution angle of the instrument. If $\mathcal{P} = \mathcal{C}(\hat{\mathbf{n}}, \theta_{\rm r})$ is the cone centred on $\hat{\mathbf{n}}$ and angular size the resolution angle, also called the resolution solid angle, we introduce shorthand notations

$$J_{\hat{\mathbf{n}}}(\theta_{\rm r}) \equiv J(\mathcal{P} = \mathcal{C}(\hat{\mathbf{n}}, \theta_{\rm r})) \quad \text{and} \quad \mathcal{J}_{\hat{\mathbf{n}}}(\theta_{\rm r}) \equiv \mathcal{J}(\mathcal{P} = \mathcal{C}(\hat{\mathbf{n}}, \theta_{\rm r})) \tag{5.16}$$

and we further define

$$\begin{aligned} \overline{J_{\hat{\mathbf{n}}}}(\Delta E) &\equiv \frac{1}{\overline{\mathcal{A}\mathcal{S}_\chi}(\Delta E)} \frac{1}{\Delta E} \int_{\Delta E} \mathrm{d}E \, \mathcal{A}(E) \mathcal{S}_\chi(E) J_{\hat{\mathbf{n}}} \left[\theta_{\rm r}(E)\right] \\ \overline{\mathcal{J}_{\hat{\mathbf{n}}}}(\Delta E) &\equiv \frac{1}{\overline{\mathcal{A}\mathcal{S}_\chi}(\Delta E)} \frac{1}{\Delta E} \int_{\Delta E} \mathrm{d}E \, \mathcal{A}(E) \mathcal{S}_\chi(E) \mathcal{J}_{\hat{\mathbf{n}}} \left[\theta_{\rm r}(E)\right] \,. \end{aligned} \tag{5.17}$$

When ΔE is in the argument of a function the notation $\Delta E \equiv (E_{\rm min}, E_{\rm max})$ is used, *i.e.* it refers to the dependence in both $E_{\rm min}$ and $E_{\rm max}$. When in integral boundaries it refers to the segment $\Delta E \equiv [E_{\rm min}, E_{\rm max}]$. Otherwise $\Delta E = E_{\rm max} - E_{\rm min}$. Besides, in the denominator we introduced

$$\begin{aligned} \overline{\mathcal{A}\mathcal{S}_\chi}(\Delta E) &\equiv \frac{1}{\Delta E} \int_{\Delta E} \mathrm{d}E \, \mathcal{A}(E) \mathcal{S}_\chi(E) \\ &= \frac{\langle \sigma v \rangle}{2 m_\chi^2} \left\{ \overline{\mathcal{N}_\gamma \mathcal{A}}(m_\chi, \Delta E) \equiv \sum_f B_f \frac{1}{\Delta E} \int_{\Delta E} \mathrm{d}E \, \mathcal{A}(E) \frac{\mathrm{d}N_\gamma^f}{\mathrm{d}E} \right\} . \end{aligned} \tag{5.18}$$

The quantity $\mathcal{A}$ is an effective experimental collection area. As a matter of fact $\mathcal{A}$ should depend both on the energy (as explicitly written) and on the pointing direction. However, in order to keep the analysis simple, we assume a flat maximal angular acceptance within each resolution solid angles. In addition $\mathcal{N}_\gamma$ is the number of photons per annihilation in the energy range $[E_{\rm min}, E_{\rm max}]$. These experiment-averaged definitions allow us to formulate the observational sensitivity more accurately. When the resolution angle is broadly independent of the energy in $[E_{\rm min}, E_{\rm max}]$, then the definitions have been set such that $\overline{J} \simeq J$ and $\overline{\mathcal{J}} \simeq \mathcal{J}$. Furthermore, if $\mathcal{J}_{\hat{\mathbf{n}}}$ is roughly independent of $\theta_{\rm r}$ then $\overline{\mathcal{J}_{\hat{\mathbf{n}}}} \simeq \mathcal{J}_{\hat{\mathbf{n}}}$ whatever the dependence in energy of $\theta_{\rm r}$. This assumption, which relies on Eq. (5.6), is particularly reasonable away from the GC where the angular variations of ρ_χ^2 are less important.

5.1.4 Subhalo luminosity

After this general introduction of the J-factors this section is focused on the subhalos and define their intrinsic luminosity. This quantity tells the capacity of their inner region (below a given radius r) to produce gamma rays regardless of the particle physics properties. It is defined as a function of r, m, c and of the subhalo density profile by

$$\ell(r,m,c) \equiv \int_0^r \rho^2(r')\,{\rm d}^3\mathbf{r}' = 3\left\{\ell_\infty(m,c) = \frac{4\pi}{3} r_{\rm s}^3 \rho_{\rm s}^2\right\} \int_0^{r/r_{\rm s}} x'^2 g^2(x'){\rm d}x' \,. \tag{5.19}$$

Recall that g is the dimensionless mass density profile. Here ℓ_∞ is the value of the intrinsic luminosity such that for an NFW profile $\ell_\infty = \lim_{r\to\infty} \ell(r)$. More precisely for this particular profile, the intrinsic luminosity function is analytical and takes the form

$$\ell(r,m,c) = \frac{1}{3}\left[1 - \frac{1}{(1+r/r_{\rm s})^3}\right] , \tag{5.20}$$

which yields $\ell(2r_{\rm s}, m, c) = 0.963\ell_\infty(m,c) \simeq \ell_\infty(m,c)$. Next we also introduce the tidal luminosity of a subhalo, given by the luminosity emitted by the entire structure

$$\ell_{\rm t}(R,m,c) \equiv \ell\left(r_\ell(R,m,c), m, c\right) \,. \tag{5.21}$$

where, because the volume inside $2r_{\rm s}$ produces 96% of the total luminosity, we defined the luminosity radius r_ℓ as

$$r_\ell(R,m,c) \equiv \min\left[r_{\rm t}(R,m,c), 2\,r_{\rm s}(m,c)\right] \tag{5.22}$$

In other words, this definition introduces the effective size of the subhalo. Subsequently, we introduce the notion of point-like structure base on this effective size and we show how the intrinsic luminosity can then be related to the definition of the J-factor.

5.2 Statistical description of J-factors

This section is devoted to transpose the statistical description of subhalo in term of their mass, concentration and position into the statistical distribution of the J-factors as it is the key astrophysical quantity related to the DM distribution in the context of gamma-ray searches.

5.2.1 Point-like subhalos and their properties

First, the notion of point-like subhalo is introduced. This is a purely geometrical construction that does not depend on whether the subhalo is resolved or unresolved. It only depends on the resolution angle $\theta_{\rm r}$ and on the subhalo size. Then we evaluate the number of point-like clumps in the MW and compute their J-factor.

Definition of a point-like subhalo

For a given resolution angle $\theta_{\rm r}$ a subhalo of scale radius $r_{\rm s}$ is assumed to be point-like if its luminosity radius r_ℓ introduced in Eq. (5.22) is contained in the corresponding resolution solid angle – see *e.g.* BUCKLEY et al. (2010) and CHARBONNIER et al. (2012). In mathematical term it amounts to ask

$$\frac{\min(r_{\rm t}, 2r_{\rm s})}{s} \leq \sin\theta_{\rm r}\,. \tag{5.23}$$

More importantly, for the description within the SL17 model, $r_{\rm s}$ can be related to (m, c) – *c.f.* Eq. (4.13) – in order to transform the expression into a bound on the mass

$$m \leq m_{\rm pt}^{\rm max}(\mathbf{s}, c, \theta_{\rm r}) \equiv \frac{4\pi}{3}(200\rho_c)\left\{\frac{cs\sin\theta_{\rm r}}{\min\left[x_{\rm t}(R(\mathbf{s}), c), 2\right]}\right\}^3\,. \tag{5.24}$$

We recall that $x_t = r_{\rm t}/r_{\rm s}$. Here we introduced the maximal mass $m_{\rm pt}^{\rm max}$ for a subhalo to be point-like. It only depends on $\mathbf{s}$, c and $\theta_{\rm r}$. Note that this inequality relies on the fact that x_t is independent of the cosmological mass – *c.f.* Eq. (4.32) – (had we consider the impact of stellar encounter this would no longer be the case and make the analysis considerably more complex). Therefore the less massive, the more concentrated and the farther a subhalo is, the more chances it has to be point-like. The bound can also be rewritten in terms of virial radius

$$r_{200}(m) \leq \frac{cs\sin\theta_{\rm r}}{\min(x_{\rm t}, 2)} \simeq \frac{cs\theta_{\rm r}}{2} \quad \Leftrightarrow \quad r_{\rm s}(m, c) \lesssim \frac{s\theta_{\rm r}}{2}\,. \tag{5.25}$$

For resolution angles satisfying $\sin\theta_{\rm r} \sim \theta_{\rm r} \lesssim 1$, the scale radius of a point-like subhalo has to be much smaller than its distance to the observer.

Statistics from SL17 and number of point-like subhalos

Let us now incorporate the contribution of the SL17 model and built averages and probabilities for all the quantities related to subhalo emission of gamma rays. In SL17 a subhalo is characterised by three quantities its virial mass m_i, concentration c_i and distance to the GC R_i. Here however it is more convenient to characterise the subhalo position not by its distance to the GC but by its distance to the observer s_i and its direction $\hat{\mathbf{n}}_i$ (which can be written in terms of two angles depending on the chosen coordinate system). Henceforth the position-dependence is now written in terms of $\mathbf{s}_i = s_i\hat{\mathbf{n}}_i$ – making use of the relation $R(s_i, \hat{\mathbf{n}}_i)$ in Eq. (5.2). We introduce both $\xi_i = (s_i, m_i, c_i)$ and $\zeta_i = (\hat{\mathbf{n}}_i, \xi_i)$ two 3 and 5-dimensional vectors encoding all the information of the subhalo. Consider a quantity Q that is a function of all subhalo parameters $Q : \{\zeta_i\}_i \mapsto Q(\{\zeta_i\}_i)$, we call the average value of Q the quantity

$$\langle Q\rangle \equiv \int_{\mathcal{Z}^{N_{\rm sub}}} Q(\{\zeta_i\}_i) \prod_{i=1}^{N_{\rm sub}} \left[p_{\rm t}\left(\zeta_i\right) {\rm d}^5\zeta_i\right] \tag{5.26}$$

where $p_{\rm t}$ is the one-point PDF for the subhalo distribution given in Eq. (4.23). Moreover, the volume element of the parameter space is

$$\mathrm{d}^5\zeta = \mathrm{d}^3\mathbf{s}\mathrm{d}m\mathrm{d}c = \mathrm{d}^2\Omega_{\hat{\mathbf{n}}}\mathrm{d}^3\xi \quad \text{with} \quad \mathrm{d}^3\xi = s^2\mathrm{d}s\mathrm{d}m\mathrm{d}c \tag{5.27}$$

and the total integration space $\mathcal{Z}$ is the set of all possible values for the 5-dimensional vector ζ. In practice we can start by introducing all the possible values of ξ, in a fixed direction $\hat{\mathbf{n}}$, as the set of all the allowed values for the mass, the concentration and the distance to the observer s,

$$\Xi(\hat{\mathbf{n}}) \equiv \{(s,m,c)\,|\,s < s_{\rm m}(\hat{\mathbf{n}}),\, 1 \leq c,\, m_{\rm min} \leq m \leq m_{\rm max}\}\,. \tag{5.28}$$

For a given sky patch we then introduce the total parameter space for ζ, as

$$\mathcal{Z}(\mathcal{P}) \equiv \bigcup_{\hat{\mathbf{q}}\in\mathcal{P}} \{\hat{\mathbf{q}}\} \times \Xi(\hat{\mathbf{q}}) = \left\{(\hat{\mathbf{q}},\xi) \in \mathbb{R}^5\,|\,\hat{\mathbf{q}} \in \mathcal{P},\, \xi \in \Xi(\hat{\mathbf{q}})\right\}\,. \tag{5.29}$$

Two specific kind of sky patches are used: $\mathcal{P} = S^2$ and $\mathcal{P} = \mathcal{C}(\hat{\mathbf{n}},\alpha)$, that are the full sky and the cone centred in $\hat{\mathbf{n}}$ and of angular aperture α. In particular the total integration space introduced in Eq. (5.26) is $\mathcal{Z} = \mathcal{Z}(S^2)$. When dealing with the conic patches we set the shorter notation $\mathcal{Z}(\hat{\mathbf{n}},\alpha) = \mathcal{Z}(\mathcal{C}(\hat{\mathbf{n}},\alpha))$. Eventually the sets of parameters restricted to the point-like subhalo in the direction $\hat{\mathbf{n}}$ and in the patch $\mathcal{P}$ are respectively

$$\begin{aligned}\Xi_{\rm pt}(\hat{\mathbf{n}}) &= \{(s,m,c) \in \Xi(\hat{\mathbf{n}})\,|\,m \leq m_{\rm pt}^{\rm max}(s\hat{\mathbf{n}},c,\theta_{\rm r})\}\\ \mathcal{Z}_{\rm pt}(\mathcal{P}) &= \{(\hat{\mathbf{n}},\xi) \in \mathcal{Z}(\mathcal{P})\,|\,\xi \in \Xi_{\rm pt}(\hat{\mathbf{n}})\}\end{aligned} \tag{5.30}$$

According to the definition of $J_{\hat{\mathbf{n}}}$ and $\mathcal{J}_{\hat{\mathbf{n}}}$, the most interesting patches are the cones of aperture $\alpha = \theta_{\rm r}$ therefore we mostly deal with $\mathcal{Z}_{\rm pt}(\hat{\mathbf{n}},\theta_{\rm r})$ in the following. Note also that because of the integration properties given in Eq. (5.6), because, for the considered instruments $\theta_{\rm r} \ll 1$ it is always possible to write, for a function $h(\zeta)$

$$\begin{aligned}\int_{\mathcal{Z}(\hat{\mathbf{n}},\theta_{\rm r})} h(\zeta)\mathrm{d}^5\zeta &\simeq \delta\Omega_{\rm r}\int_{\Xi(\hat{\mathbf{n}})} h(\hat{\mathbf{n}},\xi)\mathrm{d}^3\xi\\ \int_{\mathcal{Z}_{\rm pt}(\hat{\mathbf{n}},\theta_{\rm r})} h(\zeta)\mathrm{d}^5\zeta &\simeq \delta\Omega_{\rm r}\int_{\Xi_{\rm pt}(\hat{\mathbf{n}})} h(\hat{\mathbf{n}},\xi)\mathrm{d}^3\xi\end{aligned} \tag{5.31}$$

where $\delta\Omega_{\rm r} \equiv \delta\Omega(\mathcal{C}(\hat{\mathbf{n}},\theta_{\rm r})) = 2\pi(1-\cos\theta_{\rm r}) \simeq \pi\theta_{\rm r}^2$ is the resolution solid angle. This trick is numerically convenient as it reduces a 5-dimensional integral to a 3-dimensional integral much faster to evaluate. In summary, an integral on a variable ζ is an integral over all the parameters of the subhalos while an integral over the variable ξ means that the direction of the subhalo is fixed and the integral is only over the remaining three parameters (distance to the observer, cosmological mass and concentration).

In order illustrate all these rather abstract definitions let us evaluate the number of point-like subhalos around a direction $\hat{\mathbf{n}}$ is a cone $\mathcal{C}(\hat{\mathbf{n}},\theta_{\rm r})$. For a subhalo i, similarly to a Heaviside function, $\Theta\left[\hat{\mathbf{n}}_i \in \mathcal{C}(\hat{\mathbf{n}},\theta_{\rm r})\right]$ is defined as a measure which is 1 only if the centre of the subhalo is in the cone and 0 otherwise. The function $\Theta\left[m_i \leq m_{\rm pt}^{\rm max}(s_i,c_i,\theta_{\rm r})\right]$ is similar but is 1 when the subhalo i is point-like. Therefore the product of the two measures the size of the parameter space where the subhalo is point-like and in the right patch of the sky. Consequently, averaging over the subhalo distribution now gives the number of point-like subhalos in $\mathcal{C}(\hat{\mathbf{n}},\theta_{\rm r})$ as

$$\begin{aligned}N_{\rm sub}^{\rm pt}(\hat{\mathbf{n}},\theta_{\rm r}) &\equiv \left\langle \sum_i \Theta\left[\hat{\mathbf{n}}_i \in \mathcal{C}(\hat{\mathbf{n}},\theta_{\rm r})\right]\Theta\left[m_i \leq m_{\rm pt}^{\rm max}(s_i,c_i,\theta_{\rm r})\right]\right\rangle\\ &= N_{\rm sub}\int_{\mathcal{Z}_{\rm pt}(\hat{\mathbf{n}},\theta_{\rm r})} \mathrm{d}^5\zeta\, p_t(\zeta)\,.\end{aligned} \tag{5.32}$$

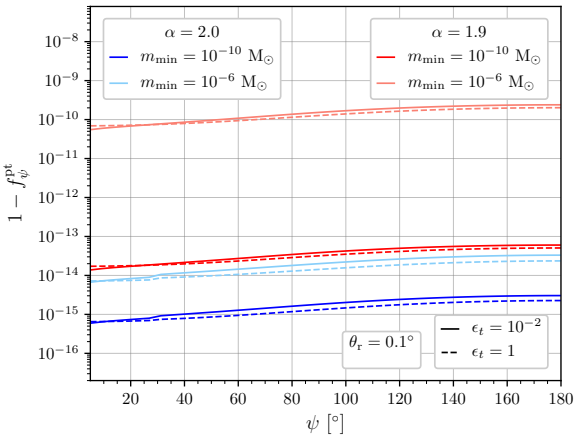

Figure 5.2 – Fraction of point like subhalos in a resolution angle $\theta_{\rm r} = 0.1°$ with respect to the direction in the sky and for different parameters of the subhalo model. We observe that $1 - f_\psi^{\rm pt} \ll 1$ which reflects the fact that the vast majority of the subhalos can be considered as point-like. The highest of the curves corresponds to the situation $m_{\rm min} = 10^{-6}$ M$_\odot$ and $\alpha = 1.9$ where the smallest subhalos are the less numerous.

where we used the fact that all subhalos are independent for the second equality. Let us then compare this number of point-like subhalos with the total number of subhalos. With the previous definitions the latter can be written as

$$N_{\rm sub}^{\rm tot}(\hat{\mathbf{n}}, \theta_{\rm r}) \equiv \left\langle \sum_i \Theta\left[\hat{\mathbf{n}}_i \in \mathcal{C}(\hat{\mathbf{n}}, \theta_{\rm r})\right] \right\rangle = N_{\rm sub} \int_{\mathcal{Z}(\hat{\mathbf{n}}, \theta_{\rm r})} {\rm d}^5\zeta \, p_t(\zeta) \, . \tag{5.33}$$

In order to properly illustrate the comparison we introduce $f_{\hat{\mathbf{n}}}^{\rm pt}(\theta_{\rm r})$ (equivalently written $f_\psi^{\rm pt}(\theta_{\rm r})$) the fraction of point-like subhalos lying in the cone $\mathcal{C}(\hat{\mathbf{n}}, \theta_{\rm r})$ in any direction $\hat{\mathbf{n}}$ (or ψ) in the sky,

$$f_{\hat{\mathbf{n}}}^{\rm pt}(\theta_{\rm r}) \equiv \frac{N_{\rm sub}^{\rm pt}(\hat{\mathbf{n}}, \theta_{\rm r})}{N_{\rm sub}^{\rm tot}(\hat{\mathbf{n}}, \theta_{\rm r})} \tag{5.34}$$

The value of $1 - f_\psi^{\rm pt}(\theta_{\rm r})$ is plotted in Fig. 5.2 for different subhalo models. In every direction ψ the fraction is very close to 1; the vast majority of subhalos appear as point-like. This can be easily understood as all the extended structure can only be close to the observer; on the size of the MW, almost all subhalos are distant enough.

J-factor for a single point-like object

Consider a point-like subhalo located at a distance $s_i \gg r_{\rm t}$ in the direction $\hat{\mathbf{n}}_i$, contained in the cone with aperture the resolution angle $\mathcal{C}(\hat{\mathbf{n}}_i, \theta_{\rm r})$. This subhalo occupies a volume δV_i and has a mass $m_{{\rm t},i}$. The total DM density at the position of the subhalo is the sum of the smooth component in δV_i and the subhalo contribution. Therefore at any position $s\hat{\mathbf{n}}$ in the volume δV_i one can write the DM density as

$$\rho_\chi\left[\mathbf{R}(s, \hat{\mathbf{n}})\right] = \rho_{\rm sm}\left[\mathbf{R}(s, \hat{\mathbf{n}})\right] + \rho_i\left(|s_i\hat{\mathbf{n}}_i - s\hat{\mathbf{n}}|\right) \, . \tag{5.35}$$

The J-factor of the subhalo i depends on the square of the DM density, so that

$$J_i^{\rm pt} \equiv \frac{1}{4\pi} \int_{\hat{\mathbf{q}} \in \mathcal{C}(\hat{\mathbf{n}}_i, \theta_{\rm r})} {\rm d}^2\Omega_{\hat{\mathbf{q}}} \int_{s\hat{\mathbf{q}} \in \delta V_i} {\rm d}s \, \rho_{\rm sm}^2\left[R(s, \hat{\mathbf{q}})\right] = J_i^{\rm pt,sub} + J_i^{\rm pt,sm} + J_i^{\rm pt,cross} \tag{5.36}$$

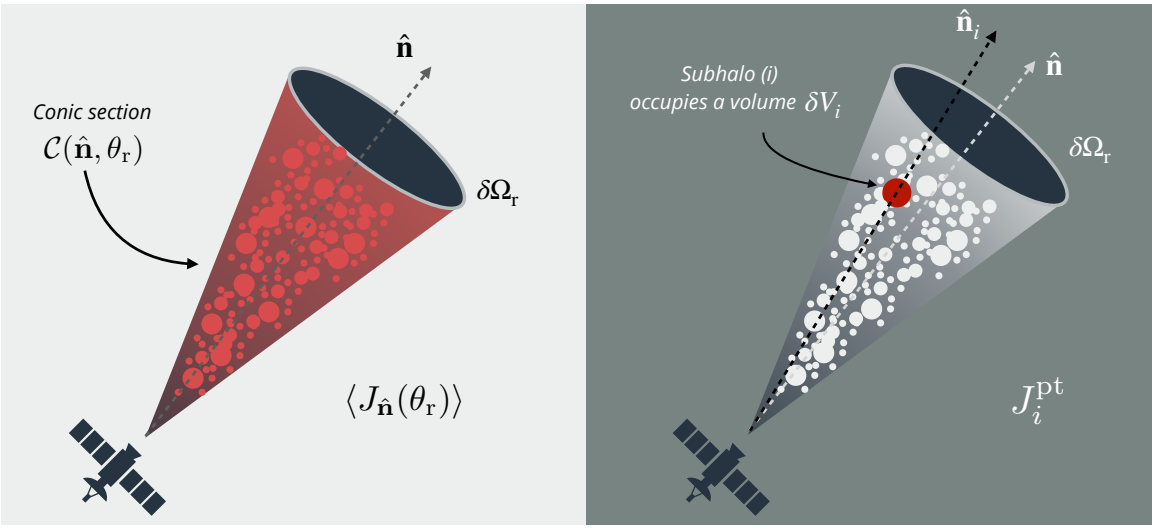

Figure 5.3 – Representation of the total diffuse DM J-factor averaged over the subhalo population (left) and point-like subhalo J-factor (right) in a resolution solid angle. Circles represent subhalos. This is a schematic view as the subhalo size must vary over orders of magnitudes and the satellite is excessively large.

where the different J-factor components are

$$\begin{aligned} J_i^{\rm pt,sub} &= \frac{1}{4\pi}\int_{\hat{\mathbf{q}}\in\mathcal{C}(\hat{\mathbf{n}}_i,\theta_{\rm r})} {\rm d}^2\Omega_{\hat{\mathbf{q}}} \int_{s\hat{\mathbf{q}}\in\delta V_i} {\rm d}s\, \rho_i^2(|s_i\hat{\mathbf{n}}_i - s\hat{\mathbf{q}}|) \\ J_i^{\rm pt,sm} &= \frac{1}{4\pi}\int_{\hat{\mathbf{q}}\in\mathcal{C}(\hat{\mathbf{n}}_i,\theta_{\rm r})} {\rm d}^2\Omega_{\hat{\mathbf{q}}} \int_{s\hat{\mathbf{q}}\in\delta V_i} {\rm d}s\, \rho_{\rm sm}^2\left[R(s,\hat{\mathbf{q}})\right] \\ J_i^{\rm pt,cross} &= \frac{1}{2\pi}\int_{\hat{\mathbf{q}}\in\mathcal{C}(\hat{\mathbf{n}}_i,\theta_{\rm r})} {\rm d}^2\Omega_{\hat{\mathbf{q}}} \int_{s\hat{\mathbf{q}}\in\delta V_i} {\rm d}s\, \rho_{\rm sm}\left[R(s,\hat{\mathbf{q}})\right] \rho_i(|s_i\hat{\mathbf{n}}_i - s\hat{\mathbf{q}}|) \end{aligned} \tag{5.37}$$

and the expressions can be simplified as

$$\begin{aligned} J_i^{\rm pt,sub} = J^{\rm pt,sub}(\zeta_i) = \frac{\ell_{\rm t}(\zeta_i)}{4\pi s_i^2}\,, \quad J_i^{\rm pt,sm} \simeq \frac{\rho_{\rm sm}^2\left[R(s_i,\hat{\mathbf{n}}_i)\right]\delta V_i}{4\pi s_i^2} \\ \text{and} \quad J_i^{\rm pt,cross} \simeq \frac{\rho_{\rm sm}\left[R(s_i,\hat{\mathbf{n}}_i)\right] m_{{\rm t},i}}{2\pi s_i^2}\,. \end{aligned} \tag{5.38}$$

The expression of $J_i^{\rm pt,sub}$ is exact and relates, for a point subhalo, its J-factor to its intrinsic luminosity. The two other expressions are approximated under the assumption that the smooth component is roughly a constant on the size of the subhalo so that $\rho_{\rm sm}^2\left[\mathbf{R}(s\hat{\mathbf{q}})\right] \simeq \rho_{\rm sm}^2\left[\mathbf{R}(\mathbf{s}_i)\right]$. Because at the border of the subhalo the density is always such that $\rho_i(r_{\rm t,i}) > \rho_{\rm sm}\left[R(\mathbf{s}_i)\right]$ – due to the smooth tidal stripping – it yields $J_{\hat{\mathbf{n}}_i,i}^{\rm pt,sub} \gg J_{\hat{\mathbf{n}}_i,i}^{\rm pt,cross} \gg J_{\hat{\mathbf{n}}_i,i}^{\rm pt,sm}$. Consequently, only the subhalo part is significant and in good approximation (at the sub-percent level)

$$J_i^{\rm pt} = J_i^{\rm pt,sub}\,. \tag{5.39}$$

By definition, for a point source, $J_i^{\rm pt} = \overline{J_i^{\rm pt}}$ where $\overline{J}$ is defined in Eq. (5.17).

5.2.2 Diffuse emission from the smooth and subhalo components

In the paragraph above, we evaluated the J-factor of point-like subhalos. Let us now look at the total J-factor for the diffuse DM component in a given direction $\hat{\mathbf{n}}$.

Similarly than for the total DM density around a subhalo given in Eq. (5.35), the total DM density at any point $s\hat{\mathbf{n}}$ of the Galaxy is

$$\rho_\chi\left[\mathbf{R}(s,\hat{\mathbf{n}})\right] = \rho_{\rm sm}\left[\mathbf{R}(s,\hat{\mathbf{n}})\right] + \sum_i \rho_i\left(|s_i\hat{\mathbf{n}}_i - s\hat{\mathbf{n}}|\right) . \tag{5.40}$$

where here there is a sum over all the possible subhalos. The J-factor can also be decomposed in a smooth contribution, a subhalo contribution and a cross product term as $J_{\hat{\mathbf{n}}}(\theta_{\rm r}) = J^{\rm sm}_{\hat{\mathbf{n}}}(\theta_{\rm r}) + J^{\rm sub}_{\hat{\mathbf{n}}}(\theta_{\rm r}) + J^{\rm cross}_{\hat{\mathbf{n}}}(\theta_{\rm r})$ where the different elements are

$$\begin{aligned}
J^{\rm sub}_{\hat{\mathbf{n}}}(\theta_{\rm r}) &= \frac{1}{4\pi}\sum_{i,j}\int_{\hat{\mathbf{q}}\in\mathcal{C}(\hat{\mathbf{n}},\theta_{\rm r})} {\rm d}^2\Omega_{\hat{\mathbf{q}}}\int_0^{s_{\rm m}(\hat{\mathbf{q}})} {\rm d}s\,\rho_i\left(|\mathbf{s}_i - s\hat{\mathbf{q}}|\right)\rho_j\left(|\mathbf{s}_j - s\hat{\mathbf{q}}|\right)\\
J^{\rm sm}_{\hat{\mathbf{n}}}(\theta_{\rm r}) &= \frac{1}{4\pi}\int_{\hat{\mathbf{q}}\in\mathcal{C}(\hat{\mathbf{n}},\theta_{\rm r})} {\rm d}^2\Omega_{\hat{\mathbf{q}}}\int_0^{s_{\rm m}(\hat{\mathbf{q}})} {\rm d}s\,\rho^2_{\rm sm}\left[\mathbf{R}(s,\hat{\mathbf{q}})\right]\\
J^{\rm cross}_{\hat{\mathbf{n}}}(\theta_{\rm r}) &= \frac{1}{2\pi}\sum_{i}\int_{\hat{\mathbf{q}}\in\mathcal{C}(\hat{\mathbf{n}},\theta_{\rm r})} {\rm d}^2\Omega_{\hat{\mathbf{q}}}\int_0^{s_{\rm m}(\hat{\mathbf{q}})} {\rm d}s\,\rho_{\rm sm}\left[\mathbf{R}(s,\hat{\mathbf{q}})\right]\rho_i\left(|s_i\hat{\mathbf{n}}_i - s\hat{\mathbf{q}}|\right) .
\end{aligned} \tag{5.41}$$

In order to evaluate the properties of the diffuse emission, we are interested in the averaged value of the total J-factor over the distribution of subhalos. Consequently we need to evaluate the average of $J_{\hat{\mathbf{n}}}(\theta_{\rm r})$ according to Eq. (5.26). Let us detail what it gives for the three components above. First, the average contribution of the subhalo component is

$$\left\langle J^{\rm sub}_{\hat{\mathbf{n}}}(\theta_{\rm r})\right\rangle = \frac{1}{4\pi}\sum_{i,j}\int_{\hat{\mathbf{q}}\in\mathcal{C}(\hat{\mathbf{n}},\theta_{\rm r})} {\rm d}^2\Omega_{\hat{\mathbf{q}}}\int_0^{s_{\rm m}(\hat{\mathbf{q}})} {\rm d}s\,\left\langle\rho_i\left(|s_i\hat{\mathbf{n}}_i - s\hat{\mathbf{q}}|\right)\rho_j\left(|s_j\hat{\mathbf{n}}_j - s\hat{\mathbf{q}}|\right)\right\rangle . \tag{5.42}$$

As in the SL17 model subhalos are assumed not to overlap it yields for the cross-correlation of densities $\left\langle\rho_i\left(|s_i\hat{\mathbf{n}}_i - s\hat{\mathbf{q}}|\right)\rho_j\left(|s_j\hat{\mathbf{n}}_j - s\hat{\mathbf{q}}|\right)\right\rangle = \left\langle\rho^2_i\left(|s_i\hat{\mathbf{n}}_i - s\hat{\mathbf{q}}|\right)\right\rangle\delta_{ij}$. It is then possible to reduce the double sum

$$\begin{aligned}
\left\langle J^{\rm sub}_{\hat{\mathbf{n}}}(\theta_{\rm r})\right\rangle &= \frac{1}{4\pi}\sum_{i}\int_{\hat{\mathbf{q}}\in\mathcal{C}(\hat{\mathbf{n}},\theta_{\rm r})} {\rm d}^2\Omega_{\hat{\mathbf{q}}}\int_0^{s_{\rm m}(\hat{\mathbf{q}})} {\rm d}s\,\left\langle\rho^2_i\left(|\mathbf{s}_i - s\hat{\mathbf{q}}|\right)\right\rangle = \sum_i\left\langle J^{\rm sub}_{\hat{\mathbf{n}},i}(\mathbf{s}_i,\theta_{\rm r})\right\rangle\\
&\text{with}\quad J^{\rm sub}_{\hat{\mathbf{n}},i}(\mathbf{s}_i,\theta_{\rm r}) \equiv \frac{1}{4\pi}\int_{\hat{\mathbf{q}}\in\mathcal{C}(\hat{\mathbf{n}},\theta_{\rm r})} {\rm d}^2\Omega_{\hat{\mathbf{q}}}\int_0^{s_{\rm m}(\hat{\mathbf{q}})} {\rm d}s\,\rho^2_i\left(|s_i\hat{\mathbf{n}}_i - s\hat{\mathbf{q}}|\right) .
\end{aligned} \tag{5.43}$$

Here $J^{\rm sub}_{\hat{\mathbf{n}},i}(\mathbf{s}_i,\theta_{\rm r})$ is the contribution of subhalo i to the J-factor. As seen in Sect. 5.2.1, most subhalos are point-like, therefore it is possible to assume that they are all centred in the cone $\mathcal{C}(\hat{\mathbf{n}},\theta_{\rm r})$ so that the approximation $J^{\rm sub}_{\hat{\mathbf{n}},i}(\mathbf{s}_i,\theta_{\rm r}) \simeq J^{\rm pt,sub}_i$ holds . The average is then

$$\begin{aligned}
\left\langle J^{\rm sub}_{\hat{\mathbf{n}},i}(\theta_{\rm r},\mathbf{s}_i)\right\rangle &\simeq \left\langle\Theta\left[\hat{\mathbf{n}}_i\in\mathcal{C}(\hat{\mathbf{n}},\theta_{\rm r})\right]J^{\rm pt}_i\right\rangle \simeq \int_{\mathcal{Z}_{\rm pt}(\hat{\mathbf{n}},\theta_{\rm r})} {\rm d}^5\zeta_i\,p_{\rm t}(\zeta_i)J^{\rm pt}_i(\zeta_i)\\
&\text{so that}\quad \left\langle J^{\rm sub}_{\hat{\mathbf{n}}}(\theta_{\rm r})\right\rangle \simeq N_{\rm sub}\int_{\mathcal{Z}_{\rm pt}(\hat{\mathbf{n}},\theta_{\rm r})} {\rm d}^5\zeta\,p_{\rm t}(\zeta)\frac{\ell_{\rm t}(\zeta)}{4\pi s^2} .
\end{aligned} \tag{5.44}$$

This equation simply tells that the subhalo term of the diffuse emission is obtained by averaging the contribution of all point-like subhalos in the cone $\mathcal{C}(\hat{\mathbf{n}},\theta_{\rm r})$. Furthermore, let us focus now on the cross term and make the assumption that the smooth density is almost a constant on the size of the subhalo. Then one can approximate $\rho_{\rm sm}\left[\mathbf{R}(s,\mathbf{q}))\right]$ in the integral by $\rho_{\rm sm}\left[\mathbf{R}(s_i,\hat{\mathbf{n}}_i))\right]$ and define

$$J^{\rm cross}_{\hat{\mathbf{n}},i}(\theta_{\rm r},s_i,\hat{\mathbf{n}}_i) \equiv \frac{\rho_{\rm sm}\left[\mathbf{R}(s_i,\hat{\mathbf{n}}_i))\right]}{2\pi}\int_{\hat{\mathbf{q}}\in\mathcal{C}(\hat{\mathbf{n}},\theta_{\rm r})} {\rm d}\hat{\mathbf{q}}\int_0^{s_{\rm m}(\hat{\mathbf{q}})} {\rm d}s\,\rho_i\left(|s_i\hat{\mathbf{n}}_i - s\hat{\mathbf{q}}|\right) \tag{5.45}$$

the contribution of the cross term to the J-factor. For the same reasons than for the subhalo term the cross term can also be approximated by $J^{\rm sm}_{\hat{\mathbf{n}},i}(\theta_{\rm r}, s_i, \hat{\mathbf{n}}_i) \simeq J_i^{\rm pt,cross}$. The averaged value over the subhalo distribution is then

$$\begin{aligned}\left\langle J^{\rm cross}_{\hat{\mathbf{n}},i}(\theta_{\rm r}, \mathbf{s}_i)\right\rangle \simeq \left\langle \Theta\left[\hat{\mathbf{n}}_i \in \mathcal{C}(\hat{\mathbf{n}}, \theta_{\rm r})\right] J_i^{\rm pt,cross}\right\rangle \simeq \int_{\mathcal{Z}_{\rm pt}(\hat{\mathbf{n}},\theta_{\rm r})} {\rm d}^5\zeta_i\, p_{\rm t}(\zeta_i) J_i^{\rm pt,cross}(\zeta_i) \\ \text{so that} \quad \langle J^{\rm cross}_{\hat{\mathbf{n}}}(\theta_{\rm r})\rangle \simeq N_{\rm sub} \int_{\mathcal{Z}_{\rm pt}(\hat{\mathbf{n}},\theta_{\rm r})} {\rm d}^5\zeta\, p_{\rm t}(\zeta) \frac{\rho_{\rm sm}\left[R(s,\hat{\mathbf{n}})\right] m_{\rm t}(\zeta)}{2\pi s^2}\,.\end{aligned} \tag{5.46}$$

In summary, the total diffuse emission from DM as the sum of the averaged value of the subhalo and cross term in addition to the smooth term (that does not need to be averaged over as it does not depend on the subhalos)

$$\begin{aligned}\langle J_{\hat{\mathbf{n}}}(\theta_{\rm r})\rangle =& \frac{1}{4\pi}\int_{\hat{\mathbf{q}}\in\mathcal{C}(\hat{\mathbf{n}},\theta_{\rm r})} {\rm d}^2\Omega_{\hat{\mathbf{q}}} \int_0^{s_{\rm m}(\hat{\mathbf{q}})} {\rm d}s\, \rho^2_{\rm sm}\left[\mathbf{R}(s,\hat{\mathbf{q}})\right] \\ &+ N_{\rm sub}\int_{\mathcal{Z}_{\rm pt}(\hat{\mathbf{n}},\theta_{\rm r})} {\rm d}^5\zeta\, p_{\rm t}(\zeta) \frac{1}{4\pi s^2}\left[\ell_{\rm t}(\zeta) + 2\rho_{\rm sm}\left[R(s,\hat{\mathbf{n}})\right] m_{\rm t}(\zeta)\right]\end{aligned} \tag{5.47}$$

with the associated gamma-ray flux being $\mathcal{S}_\chi(m_\chi, E)\,\langle J_{\hat{\mathbf{n}}}(\theta_{\rm r})\rangle$ consistently with Eq. (5.12). The evolution of the diffuse J-factor (and its different components) with the pointing direction parametrised by the angle ψ is shown in Fig. 5.4. The smooth component dominates towards the centre[1] and the subhalo component dominates (or is at least of the same order of magnitude) towards the outskirts. The cross term is however negligible, an order of magnitude (at least) below the other two terms. The effect of subhalos, already discussed in the original paper SL17 is known as the subhalo boost. Moreover using the prescription in Eq. (5.17) we can also introduce the energy averaged diffuse J-factor according to

$$\overline{\langle J_{\hat{\mathbf{n}}}\rangle}(\Delta E) \equiv \frac{1}{\Delta E\,\overline{\mathcal{A}\mathcal{S}_\chi}(\Delta E)} \int_{\Delta E} {\rm d}E\, \mathcal{A}(E)\mathcal{S}_\chi(E)\,\langle J_{\hat{\mathbf{n}}}\left[\theta_{\rm r}(E)\right]\rangle\,. \tag{5.48}$$

and similarly the energy and resolution averaged diffuse J-factor $\overline{\langle \mathcal{J}_{\hat{\mathbf{n}}}\rangle}$ as

$$\overline{\langle \mathcal{J}_{\hat{\mathbf{n}}}\rangle}(\Delta E) \equiv \frac{1}{\Delta E\,\overline{\mathcal{A}\mathcal{S}_\chi}(\Delta E)} \int_{\Delta E} {\rm d}E\, \mathcal{A}(E)\mathcal{S}_\chi(E) \left\langle \frac{J_{\hat{\mathbf{n}}}\left[\theta_{\rm r}(E)\right]}{\delta\Omega_{\rm r}(E)}\right\rangle\,. \tag{5.49}$$

Now that all the properties of the J-factor averaged on the subhalo population have been derived, in the next section, we more particularly look at the probability distribution of J-factor for point-like subhalos. This is indeed crucial in order to evaluate the number of detectable point-like subhalo above a given sensitivity threshold.

5.2.3 Statistical properties of point-like subhalos

Consider a direction and resolution angle $\theta_{\rm r}$. The probability for a subhalo to be point-like and contained in the cone $\mathcal{C}(\hat{\mathbf{n}}, \theta_{\rm r})$ with a J-factor J can be written as

$$p_J^{\rm pt}(J, \hat{\mathbf{n}}, \theta_{\rm r}) \equiv \int_{\mathcal{Z}_{\rm pt}(\hat{\mathbf{n}},\theta_{\rm r})} {\rm d}^5\zeta\, p_{\rm t}(\zeta)\delta\left[J^{\rm pt,sub}(\zeta) - J\right]\,. \tag{5.50}$$

[1]Therefore, by pruning the subhalos toward the centre, the impact of stellar encounters would only very slightly enhance the smooth contribution.

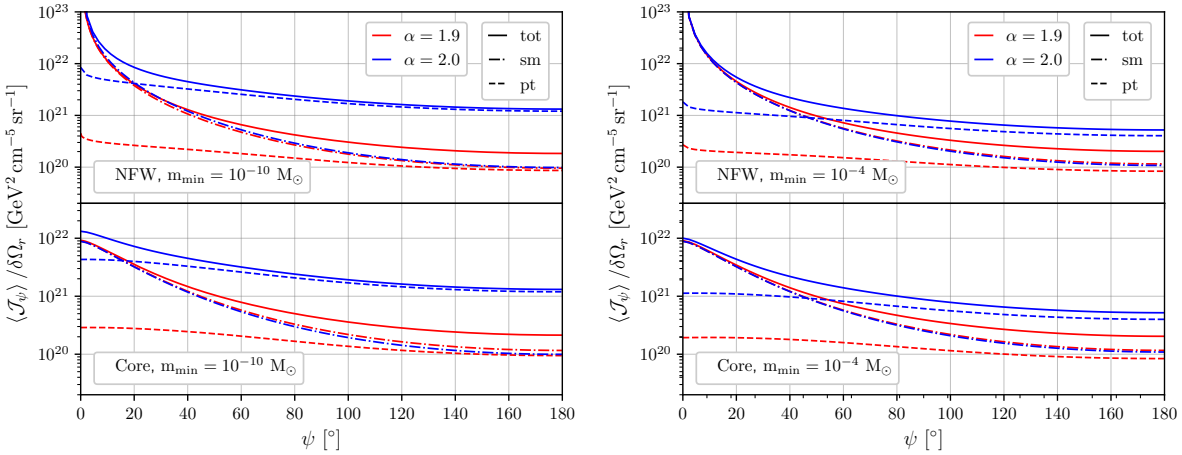

Figure 5.4 – Evolution of the diffuse J-factor, $\langle \mathcal{J}_\psi \rangle = \langle J_\psi \rangle / \delta\Omega_r$ with the angle ψ. Here are shown the contribution of the smooth component (dash-dotted lines) and of the point-like component (dashed lines). We consider both an NFW and a cored Galactic profile as well as two different minimal masses for the subhalo population, $m_{min} = 10^{-10}$ $M_\odot$ and $m_{min} = 10^{-4}$ $M_\odot$. Eventually two mass index are also represented $\alpha = 1.9$ and $\alpha = 2.0$.

One can then define the complementary cumulative distribution function (CCDF) as the integrated probability to have a J-factor larger than some threshold value as

$$\begin{aligned} P^{pt}_{>}(J, \hat{\mathbf{n}}, \theta_r) &\equiv \int_{J^0_{\hat{\mathbf{n}}}}^{\infty} dJ'\, p(J^0_{\hat{\mathbf{n}}}, \hat{\mathbf{n}}, \theta_r) \\ &= \int_{\mathcal{Z}_{pt}(\hat{\mathbf{n}}, \theta_r)} d^5\zeta\, p_t(\zeta) \Theta\left[J^{pt,sub}(\zeta) - J \right] . \end{aligned} \tag{5.51}$$

The total number of subhalos over the threshold value J in the resolution solid angle is then

$$N^{pt}_{>}(J, \hat{\mathbf{n}}, \theta_r) = N_{sub} P^{pt}_{>}(J, \hat{\mathbf{n}}, \theta_r) \tag{5.52}$$

where N_{sub} is the total number of subhalos in the MW. Note that $P^{pt}_{>}(0, \hat{\mathbf{n}}, \theta_r) < 1$ because it defines the probability in the cone of angle θ_r around the direction $\hat{\mathbf{n}}$ only. It only normalises to unity after integration over the full sky. In the right panel of Fig. 5.5 we represent the evolution of these two quantities for a resilient subhalo population defined by $(\alpha, m_{min}, \epsilon_t) = (1.9, 10^{-10} - 10^{-4}, 0.01)$ embedded in an NFW Galactic halo and for a resolution angle θ_r. By the spherical symmetry of the SL17 model, the line of sight $\hat{\mathbf{n}}$ is parametrised by the angle ψ – defined in Eq. (5.2) – and two directions are considered $\psi = 20°$ and $\psi = 90°$. On the same plot we also show the typical sensitivity of the Fermi-LAT instrument. This figure, shows; in particular, that the dependence of $P^{pt}_{J}(J, \hat{\mathbf{n}}, \theta_r)$ with the direction $\hat{\mathbf{n}}$ (or equivalently ψ here) is not trivial. We can remark that at $\psi = 20°$ the curves are higher in the region $J^0_{\hat{\mathbf{n}}} \in [10^{16}, 10^{19}]$ GeV^2 cm^{-5} than at $\psi = 90°$. This comes from the strength of the tidal effects in the inner part of the MW. There, because subhalos are resilient to disruption since $\epsilon_t = 10^{-2}$, a non negligible population of highly stripped subhalos with $r_t \simeq 10^{-2} r_s$, appear as point-like while being rather close. Not to mention that the surviving subhalos are also the most concentrated and therefore the most luminous. As a matter of fact the peak survives up to $\psi \sim 50°$ for $\theta_r = 0.1°$. In addition we can also observe a difference between $m_{min} = 10^{-10}$ and $m_{min} = 10^{-4}$, however one can show that the probability density at high J-factor scales as m_{min}.

Consequently, since $N_{\rm sub} \propto 1/m_{\rm min}$, this have not effect on the total number of visible subhalos (as it is defined below). On the right panel of Fig. 5.5 we show the number of point-like subhalo by unit of resolution solid angle above a given threshold in different directions. We also plot the difference between an NFW and a cored host halo. The cored profile predicts more visible subhalos, except in the range $J_0 \in [10^{18}, 10^{19}]$ GeV^2 cm^{-5}. The drop is a consequence of the sharp decrease, which appears roughly at $J \gtrsim 10^{18}$ GeV^2 cm^{-5} but at slightly smaller J-factors in the cored case.

Let us consider now a threshold that varies with the direction in the sky, we call it $J_0 : \hat{\mathbf{n}} \mapsto J_0(\hat{\mathbf{n}})$. Then, the probability for a subhalo to be point-like and over the threshold function on a sky patch $\mathcal{P}$ is given by

$$\begin{aligned} P^{\rm pt}_{>}(J_0; \mathcal{P}, \theta_{\rm r}) &= \frac{1}{\delta\Omega_{\rm r}} \int_{\hat{\mathbf{n}}\in\mathcal{P}} {\rm d}^2\Omega_{\hat{\mathbf{n}}}\, F^{\rm pt}_J(J_0(\hat{\mathbf{n}}), \hat{\mathbf{n}}, \theta_{\rm r}) \\ &\simeq \int_{\hat{\mathbf{n}}\in\mathcal{P}} {\rm d}^2\Omega_{\hat{\mathbf{n}}} \int_{\Xi_{\rm pt}(\hat{\mathbf{n}},\theta_{\rm r})} {\rm d}^3\xi\, p_{\rm t}(\hat{\mathbf{n}}, \xi) \Theta\left[J^{\rm pt,sub}(\hat{\mathbf{n}}, \xi) - J_0(\hat{\mathbf{n}})\right] \end{aligned} \tag{5.53}$$

where we recall $\delta\Omega_{\rm r} = \delta\Omega(\mathcal{C}(\hat{\mathbf{n}}, \theta_{\rm r})) = 2\pi(1 - \cos\theta_{\rm r})$. The second line is obtain using the approximation Eq. (5.6) and with the notation $\zeta = (\hat{\mathbf{n}}, s, m, c) = (\hat{\mathbf{n}}, \xi)$. By construction, when the patch $\mathcal{P} = S^2$ is the entire sky (the 2-sphere) and $J_0 = 0$, the probability is correctly normalised: $P^{\rm pt}_{>}(0; \pi/2, S^2) = 1$. Indeed this quantity is the probability for any subhalo (as $\theta_{\rm r} = \pi/2$ they are all point-like) to be anywhere in the sky and to have a positive J-factor, it has to be 1. The number of subhalos over the threshold function is, as in Eq. (5.52),

$$N^{\rm pt}_{>}(J_0; \mathcal{P}, \theta_{\rm r}) = N_{\rm sub} P^{\rm pt}_{>}(J_0; \mathcal{P}, \theta_{\rm r})\,. \tag{5.54}$$

Although the study is mainly focused on point-like substructures we also want to assess whether the detection of extended structure seems possible with the same techniques. Subsequently, we introduce, for a given subhalo, the general truncated J-factor in an apparent resolution angle $\theta_{\rm e}$ as

$$J_{\rm e}(\zeta, \theta_{\rm e}) \equiv \frac{\ell(r_e(\zeta, \theta_e), m, c)}{4\pi s^2} \quad \text{where} \quad r_{\rm e}(\zeta, \theta_e) \equiv \min\{r_{\rm t}, 2r_{\rm s}, s\sin(\theta_{\rm e})\}\,. \tag{5.55}$$

Henceforth, similarly to Eq. (5.53), we can also define a probability distribution for any subhalo to have a truncated J-factor $J_{\rm e}$ above a threshold function $J_0 : \hat{\mathbf{n}} \mapsto J_0(\hat{\mathbf{n}})$ and to be in the patch $\mathcal{P}$ as

$$P^{\rm e}_{>}(J_0; \mathcal{P}, \theta_{\rm e}) \equiv \int_{\hat{\mathbf{n}}\in\mathcal{P}} {\rm d}^2\Omega_{\hat{\mathbf{n}}} \int_{\Xi(\hat{\mathbf{n}})} {\rm d}^3\xi\, p_t(\hat{\mathbf{n}}, \xi) \Theta\left[J_{\rm e}(\theta_{\rm e}, \hat{\mathbf{n}}, \xi)) - J_0(\hat{\mathbf{n}})\right] \tag{5.56}$$

and the number of subhalos with truncated J-factor above the threshold function is

$$N^{\rm e}_{>}(J_0; \mathcal{P}, \theta_{\rm e}) = N_{\rm sub} P^{\rm e}_{>}(J_0; \mathcal{P}, \theta_{\rm e})\,. \tag{5.57}$$

Eventually, the probability to have any subhalo with a total J-factor above the threshold in $\mathcal{P}$ is obtained either by taking the limit $\theta_{\rm r} = \pi/2$ in Eq. (5.53) and considering all sources as point-like or taking the limit $\theta_{\rm e} = \pi$ in Eq. (5.56) such that $J_{\rm e}$ is always the total J-factor of the structure. Therefore

$$\begin{aligned} P^{\rm tot}_{>}(J_0; \mathcal{P}) &= P^{\rm e}_{>}(J_0; \mathcal{P}, \theta_{\rm e} = \pi) = P^{\rm pt}_{>}(J_0; \mathcal{P}, \theta_{\rm r} = \pi/2) \\ N^{\rm tot}_{>}(J_0; \mathcal{P}) &= N^{\rm e}_{>}(J_0; \mathcal{P}, \theta_{\rm e} = \pi) = N^{\rm pt}_{>}(J_0; \mathcal{P}, \theta_{\rm r} = \pi/2)\,. \end{aligned} \tag{5.58}$$

As a matter of fact, $N_{>}^{\rm pt/e/tot}(J_0;\mathcal{P},\theta_{\rm r})$ is actually an average value and the true number can fluctuate with a certain probability distribution. The probability to detect k subhalos is given by a binomial probability

$$P(k\,|\,N_{\rm sub}) = \binom{N_{\rm sub}}{k} p^k (1-p)^{N_{\rm sub}-k} \tag{5.59}$$

where, for shorthand notations $p = P_{>}^{\rm pt/e/tot}(J_0;\mathcal{P},\theta_{\rm r})$. Indeed, one subhalo has a probability p to satisfy all the requirements. Then in order for exactly k of them to be in that configuration one also needs $N_{\rm sub}-k$ that are not (which happens for each with a probability $1-p$). In addition, the binomial factor takes into account the fact that all subhalos are equivalent and the k visible one can be chosen amongst the total $N_{\rm sub}$ in different ways. Under the assumption that we expect to only deal with $k \ll N_{\rm sub}$ and $N_{\rm sub} \gg 1$, we can use the Poissonian limit

$$P(k\,|\,N_{\rm sub}) \simeq \frac{(N_{\rm sub}p)^k}{k!} e^{-N_{\rm sub}p} = \frac{N_{>}^k}{k!} e^{-N_{>}} \tag{5.60}$$

with $N_{>} = N_{>}^{\rm pt/e/tot}(J_0;\mathcal{P},\theta_{\rm r})$. We would like to define a confidence interval for the number of visible subhalo when knowing $N_{>}^{\rm pt/e/tot}(J_0;\mathcal{P},\theta_{\rm r})$. This happens to be non trivial because the Poisson distribution is not continuous. The cumulative distribution function, that is the probability to observe at least n point-like subhalos is given by

$$P(\geq k\,|\,N_{\rm sub}) \simeq 1 - \sum_{i=0}^{k-1} P(i\,|\,n)\,. \tag{5.61}$$

Nevertheless, if k is promoted to a real number x we can define the continous version of Eq. (5.61) as

$$P_x(x\,|\,N_{\rm sub}) \equiv e^{-N_{\rm vis}} \sum_{k=0}^{\lceil x\rceil-1} \frac{N_{>}^k}{k!} = \frac{\Gamma(\lceil x\rceil\,, N_{>})}{\Gamma(\lceil x\rceil)} \tag{5.62}$$

with Γ the gamma function (with, on the numerator, its incomplete version). The second equality is a pure mathematical identity. With this result it is then simpler to define a confidence interval. We define a non optimal, yet conservative, confidence interval at $100(1-c)\%$ that x be measured in the range $[N_c^-, N_c^+]$ by solving

$$\frac{c}{2} = \frac{\Gamma(N_c^- + 1, N_{>})}{\Gamma(N_c^- + 1)} = 1 - \frac{\Gamma(N_c^+, N_{>})}{\Gamma(N_c^+)}\,. \tag{5.63}$$

We define now four regions as strips, bounded in ψ:

- Region 1, $\mathcal{P}_1$: $5^\circ \leq \psi \leq 34^\circ$ with solid angle $\Delta\Omega_1 = 1.05$ sr
- Region 2, $\mathcal{P}_2$: $34^\circ \leq \psi \leq 48^\circ$ with solid angle $\Delta\Omega_2 = 1.04$ sr
- Region 3, $\mathcal{P}_3$: $48^\circ \leq \psi \leq 60^\circ$ with solid angle $\Delta\Omega_3 = 1.06$ sr
- Region 4, $\mathcal{P}_4$: $120^\circ \leq \psi \leq 132^\circ$ with solid angle $\Delta\Omega_4 = 1.06$ sr

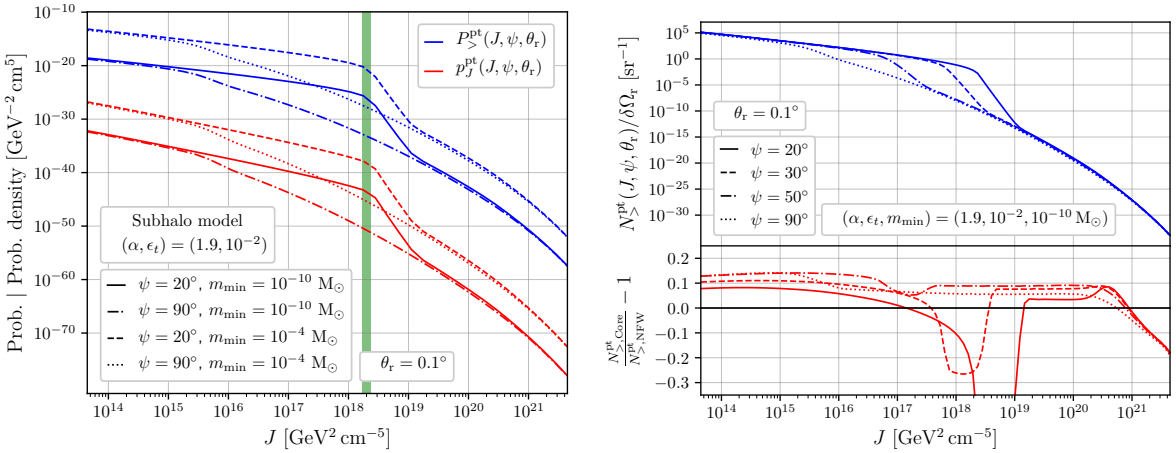

Figure 5.5 – Left panel: Probability distribution function $p^{\rm pt}_J(J,\psi,\theta_{\rm r})$ in red and the cumulative $P^{\rm pt}_>(J,\psi,\theta_{\rm r})$ in blue. Note that, from the symmetry of the SL17 model we have parametrised $\hat{\mathbf{n}}$ by the angle ψ. The resolution angle is chosen to be $\theta_{\rm r} = 0.1°$ and the line-of-sight are $\psi = 20°$ and $\psi = 90°$ (Galactic pole). In addition the subhalo configuration is $(\alpha, m_{\rm min}, \epsilon_{\rm t}) = (1.9, 10^{-10} - 10^{-4}, 0.01)$ and the host Galactic halo is assumed to have an NFW profile. The green line gives the typical sensitivity of a Fermi-LAT-like instrument calculated for an observation time of 10 yr. **Right panel:** The number of visible subhalo by units of the resolution solid angle in different directions and for the same subhalo configuration. The bottom plot represents the relative comparison between the numbers obtained for an Core profile of the host and an NFW profile (as represented in the upper panel).

In Fig. 5.6 we show the evolution of the number of subhalos above a constant J in $5° \leq \psi \leq 180°$ and in region 1. This is particularly interesting in the case of a simplified CTA-like instruments where the sensitivity to point-like sources can be assumed to be isotropic. Indeed, this is a reasonable assumption, justified later on, due to the isotropy of the cosmic rays distribution and if we neglect the sensitivity dependence of the instrument on the zenith angle, and the contribution of the GDE. In this scenario, the J-factor threshold for subhalos to be detectable is a constant. We plot $N^{\rm pt}_>$ (dashed blue curves), $N^{\rm e}_>$ (dash-dotted blue curves) and $N^{\rm tot}_>$ (solid blue curve) for different values of $\theta_{\rm r}$ and $\theta_{\rm e}$. The left panels are for a global NFW profile while the right panel are for a Cored profile. The shaded blue areas are the 68% confidence interval for $N^{\rm tot}_>$. Moreover, we compare our analytical formulas to the Monte-Carlo results of Hütten et al. (2016) with the red and grey curves, which correspond to two different subhalo models, and represent $N^{\rm e}_>$ for $\theta_{\rm e} = 0.8°$. Note that they integrate over a slightly different region of the sky given by $|b| > 10°$. Nevertheless, we are in good agreement with this previous study, especially because the dependence in J is similar and because the orders of magnitude are compatible. For a similar angle $\theta_{\rm r} = \theta_{\rm r}$ the curves $N^{\rm e}_>$ decrease less fast than the curves $N^{\rm pt}_>$ which is expected as the latter removes all the extended objects that are the only one which can make a substantial contribution at large J. The curve $N^{\rm tot}_>$ scales roughly as $1/J$ until it becomes close to 1, which is a direct consequence of the fact that the intrinsic luminosity of a subhalo approximately satisfies $\ell \propto m^{0.9}$ and because the cosmological mass distribution goes as $p_m(m) \propto m^{-1.9}$. Eventually, the confidence levels are wider in our case for small numbers of sources (blue shaded areas vs red and grey shaded areas) but this could be expected as our confidence interval is not optimal.

In figure Fig. 5.7 we show the ratios

$$\frac{N^{\rm pt}_{>}(J;\theta_{\rm r},\mathcal{P}_i))}{N^{\rm pt}_{>}(J;\theta_{\rm r},\mathcal{P}_j)}\,, \quad \frac{N^{\rm e}_{>}(J;\theta_{\rm e},\mathcal{P}_i))}{N^{\rm e}_{>}(J;\theta_{\rm e},\mathcal{P}_j)} \quad \text{and} \quad \frac{N^{\rm tot}_{>}(J;\mathcal{P}_i))}{N^{\rm tot}_{>}(J;\mathcal{P}_j)} \tag{5.64}$$

with the same colour and line style code as in Fig. 5.6. This plot allows identifying which region is best to favour the detection of subhalos, for an instrument with an isotropic sensitivity (because every region roughly covers the same solid angle). The higher the ratio is, the better it is to look in the region i instead of the region j. We can see that for the search of point-like sources the inner regions are the most efficient when $\theta_{\rm r} = 0.01^\circ$ or 0.1°. Indeed the light and medium blue dashed curves are all above 1. This is due to the presence of the bump in Fig. 5.5 at small angles ψ. For $\theta_{\rm r} = 1^\circ$ and for extremely large J (around 10^{18} GeV^2 cm^{-5} and above) it seems better to look toward the region 2, however such J correspond to very small values of $N^{\rm pt}_{>}$. Now for $N^{\rm e}_{>}$ (the dash-dotted curves) the differences between regions are less important even though for $\theta_{\rm e} = 0.01^\circ$ and 0.1° the same conclusion holds, the region 1 appears to be the most efficient. For $\theta_{\rm e} = 1^\circ$ (the curve is superposed to the curve for $N^{\rm tot}_{>}$ in solid dark blue) the region 3 is now the most appropriate for $J \gtrsim 10^{16}$ GeV^2 cm^{-5}. In conclusion in an isotropic background, the point-like sources have more probability to be detectable close to the GC. Let us now evaluate, in the next section the sensitivity of Fermi-LAT-like and CTA-like instruments to the point-sources.

5.3 Sensitivity of Fermi-LAT-like and CTA-like instruments

This section is devoted to the evaluation of the sensitivity of Fermi-LAT-like and CTA-like instruments within our model. The main point is that, in this study, we do not want to perform a full data-driven analysis, the philosophy is rather to develop a simple background model that can easily be implemented but which is still in good agreement with and calibrated on data. We call it *realistic* as physically motivated and partly fitted on data, even if not necessarily accurate. We avoid to perform a data analysis as disentangling the DM signal to the background is beyond the scope of this analysis. Besides, the angular dependence of this realistic model relies on the same baryonic distribution used to implement dynamical effects on the subhalo population. Thus, we account for the correlation between the subhalo properties and the background. Consequently, we first define the background and then move on to the statistical analysis.

5.3.1 A realistic background model

The Fermi-LAT background

For a Fermi-LAT-like telescope, which is a space-borne instrument, the true background includes different astrophysical contributions that can have either Galactic or extragalactic origins. The Galactic contributions form the GDE (or also DGE) and are mainly sourced by unresolved sources or by the interaction of cosmic rays with the interstellar gas and radiation such as Bremssthralung, inverse Compton and pion production processes. The extragalactic component provides an isotropic gamma-ray flux. Previous studies in the literature have tried to use very precise models of the GDE from cosmic ray modelling and template fitting techniques (FERMI-LAT COLLABORATION 2015a; GASKINS 2016; CALORE et al. 2019a; FERMI-LAT

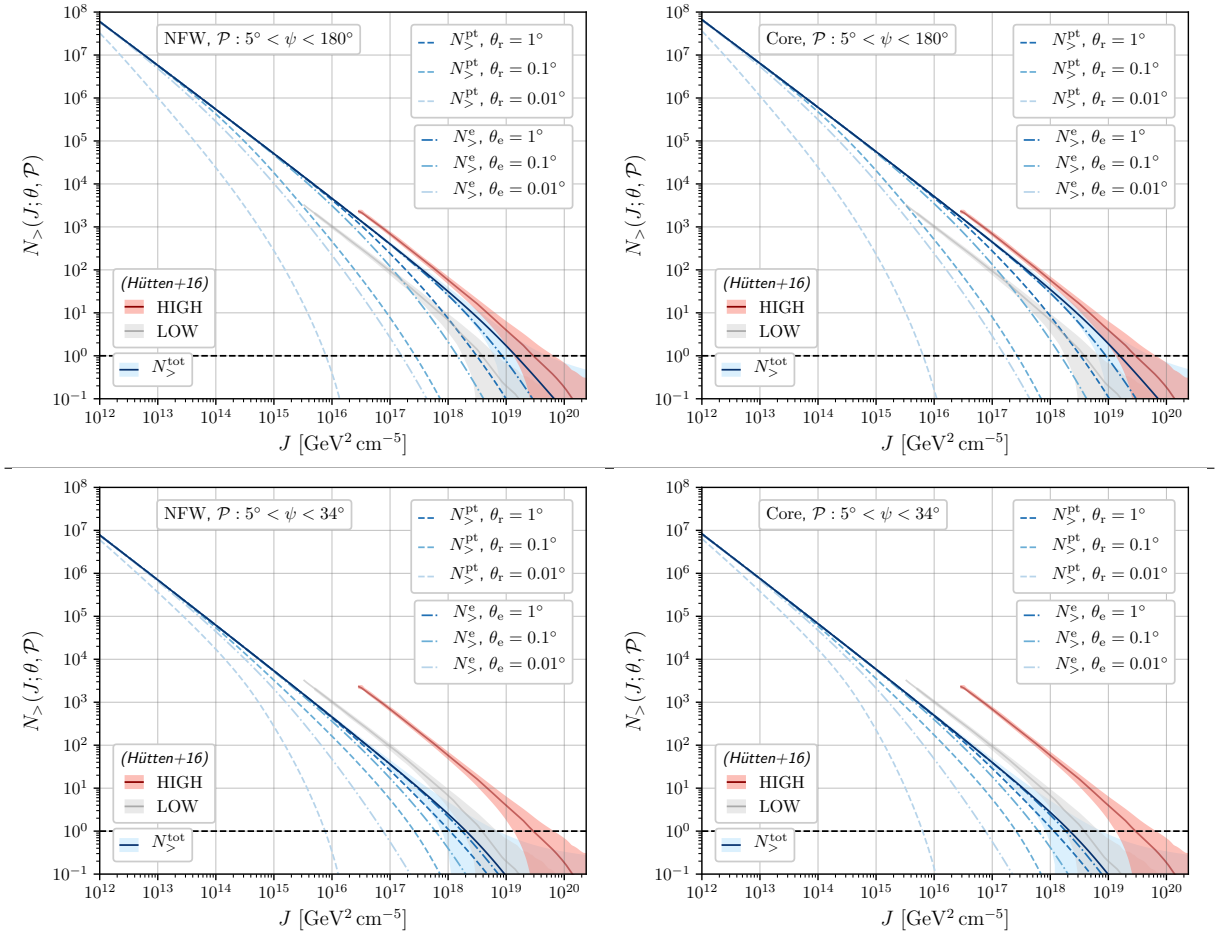

Figure 5.6 – Number of sources with a J-factor greater than a given uniform threshold. The red and grey solid curves are the result obtained by HÜTTEN et al. (2016) – here Hüten+16 – for their HIGH and LOW models counting all subhalos in the regions with $|b| > 10$ and considering $J = J(0.8°)$ with Monte-Carlo method. The darkest blue solid curve is our count of all sub-halos with total J-factor above the threshold. The shaded areas correspond to the 68% confidence limit. The dashed curves correspond to the number $N_{\rm pt}$ of point-like only subhalos with J-factor above the threshold for different resolution angles $\theta_{\rm r} = 1°, 0.1°, 0.01°$. The dash-dotted lines are the number $N_{\rm tot}$ of subhalos with a truncated J-factor denoted $J_{\rm e}$ in an apparent angle $\theta_{\rm r} = 1°, 0.1°, 0.01°$ greater than the threshold. We use our analytical model with an NFW profile (upper panel) and Core profile (lower panel) – with $\alpha = 1.9$, $m_{\rm min} = 10^{-10}$ M$_\odot$ and $\epsilon_{\rm t} = 10^{-2}$). Remark that because of a different normalisation of the J-factor (a difference of a factor 4π) we had to shift Hütten+16 results for proper comparisons.

COLLABORATION 2019). Here we restrict ourselves to the pion decay component which dominates the GDE (away from the GC and in the energy range $[1, 100]$ GeV) and is produced by proton-proton interactions.

In order to be consistent with the mass model, for the baryons, that is used to evaluate the tidal stripping of subhalos we pick the neutral hydrogen (atomic and molecular) distribution from MCMILLAN (2017). Then we define, at a given position $\mathbf{x}$ the number density of hydrogen in the intergalactic medium as

$$n_{\rm ism}(\mathbf{x}) = n_{\rm H}(\mathbf{x}) + 2n_{\rm H_2} = \frac{\rho_{\rm H}(\mathbf{x})}{m_{\rm H}} + 2\frac{\rho_{\rm H_2}(\mathbf{x})}{m_{\rm H_2}} \tag{5.65}$$

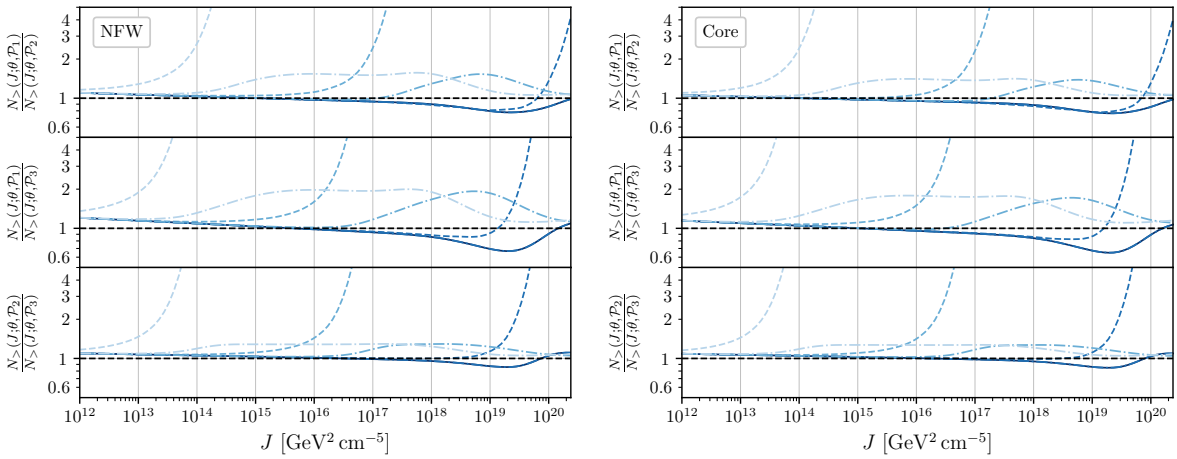

Figure 5.7 – Legends are identical to Fig. 5.6 and the subhalo model is the same. Ratio of the number of subhalos above the threshold in the three regions of interests. It shows that for small angular resolution $\theta_r \leq 0.1°$ point like subhalos are most likely to be found in Region 1 (central part of the galaxy). For $\theta_r = 1°$ it depends on the sensitivity of the instrument. In that configuration detectors with a high (resp. low) sensitivity in J have more chances to see point-like subhalos in Region 1 (resp. Region 3). For the number of sources with $J_e(\theta_e)$ above the threshold, given in Eq. (5.57), the conclusions are similar even though the difference between the regions is less pronounced. The optimal strategy for the angular resolution of CTA would then be to search for subhalos in Region 1.

where H and H_2 correspond to the atomic and molecular component respectively with m_H and m_{H_2} their masses. Integrating this distribution along a line of sight $\hat{\mathbf{n}}$ gives the corresponding gamma-ray flux as

$$\frac{\mathrm{d}^3\phi_\pi(E,\hat{\mathbf{n}})}{\mathrm{d}E\mathrm{d}^2\Omega} = \frac{f_\pi(E)}{4\pi}\int \mathrm{d}s\, n_{\rm ism}(s,\hat{\mathbf{n}})\,. \tag{5.66}$$

Usually the value of $\hat{\mathbf{n}}$ is parametrised by the longitude-latitude couple (l,b) as here there is no spherical symmetry that would allow to only use the angle ψ. Moreover, the spectral function $f_\pi(E)$ is calibrated on data from ACKERMANN et al. (2012b) and we use the parametrisation

$$f_\pi(E) = f_0(E)\left(\frac{E}{1\,\mathrm{GeV}}\right)^{-a(E)} \tag{5.67}$$

with the parameters being, in function of the energy range,

$$(f_0(E),a(E)) = \begin{cases} (6.69\times10^{-27}\ \mathrm{GeV^{-1}\,s^{-1}}, 2.27) & \text{if } 1\,\mathrm{GeV} \leq E < 1.4\,\mathrm{GeV} \\ (7.45\times10^{-27}\ \mathrm{GeV^{-1}\,s^{-1}}, 2.59) & \text{if } 1.4\,\mathrm{GeV} \leq E < 2.3\,\mathrm{GeV} \\ (8.31\times10^{-27}\ \mathrm{GeV^{-1}\,s^{-1}}, 2.72) & \text{if } 2.3\,\mathrm{GeV} \leq E < 100\,\mathrm{GeV}\,. \end{cases} \tag{5.68}$$

In the following we restrict the study to $E \in [1,100]$ GeV as below 1 GeV the pionic component can no longer be easily approximated by power laws. In the end we have the total background flux as

$$\frac{\mathrm{d}^3\phi_{\rm b}(E,\hat{\mathbf{n}})}{\mathrm{d}E\mathrm{d}^2\Omega} = \left\{\frac{\mathrm{d}^3\phi_{\rm GDE}(E,\hat{\mathbf{n}})}{\mathrm{d}E\mathrm{d}^3\Omega} \equiv \alpha_{\rm b}\frac{\mathrm{d}^3\phi_\pi(E,\hat{\mathbf{n}})}{\mathrm{d}E\mathrm{d}^2\Omega}\right\} + \frac{\mathrm{d}^3\phi_{\rm iso}(E)}{\mathrm{d}E\mathrm{d}^2\Omega}\,. \tag{5.69}$$

The introduction of a pre-factor $\alpha_{\rm b} \geq 1$ in front of the pionic component to enhance the GDE. This is done to roughly take into account the other neglected components

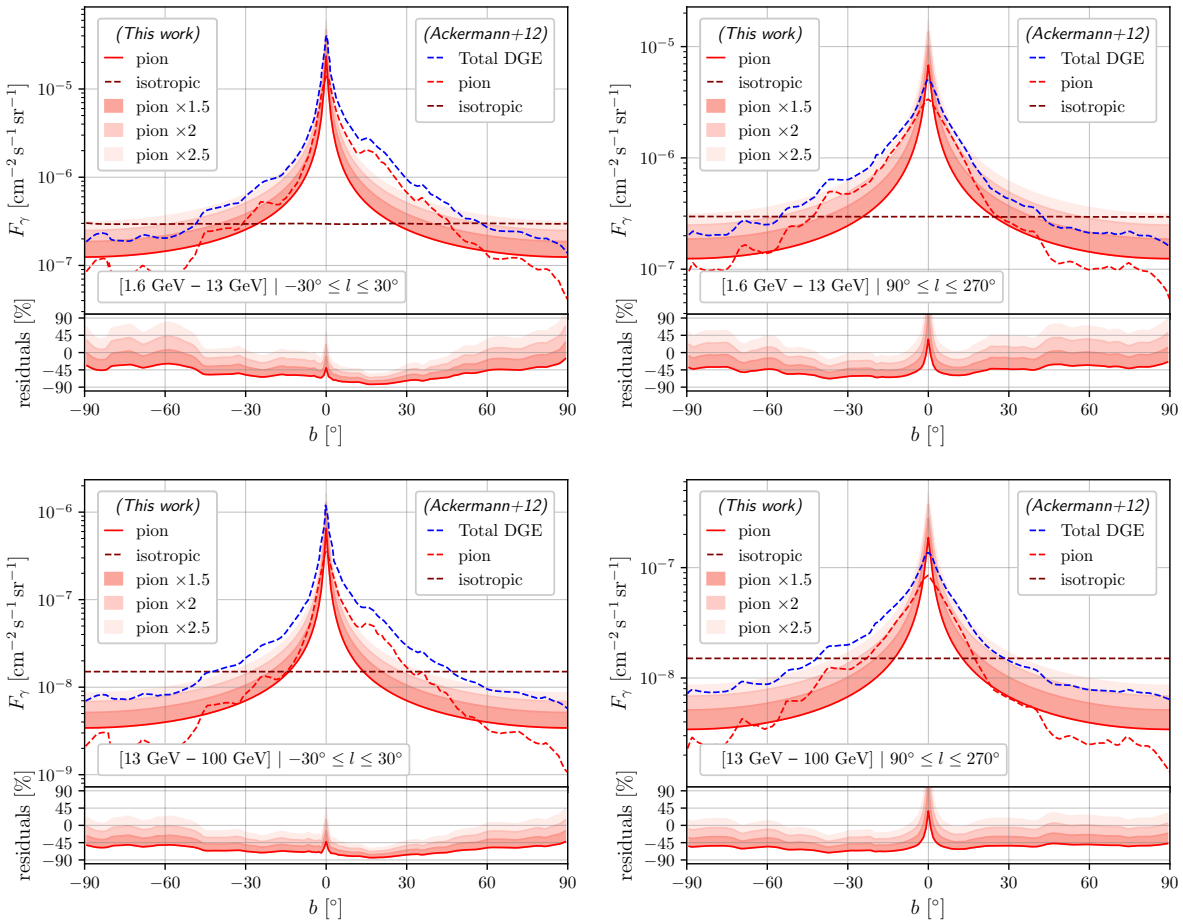

Figure 5.8 – Integrated gamma-ray flux vs. latitude. The gamma ray-flux is integrated over 2 ranges of longitudes $-30° \leq l \leq 30°$ and $-30° \leq l \leq 30°$ as well as 2 ranges of energy $E \in [1.6, 30]$ GeV and $E \in [13, 100]$ GeV. Comparison is made between our model (solid red) and the data taken from ACKERMANN et al. (2012b) – here called (Ackermann+12). The different shaded areas correspond to different values of the parameter α_b introduced in Eq. (5.69). Note that the isotropic component is the same in our model and in the data as we directly calibrated it on the data. The bottom panels represents the relative difference between our GDE and the total GDE (here called DGE) obtained from the data and for the different values of α_b.

that have a similar spatial dependence as well as to mimic additional systematic uncertainties. In Fig. 5.8 we show the dependence in latitude (integrated over fixed ranges of longitudes) of our background model, compared to the true background observed by the Fermi-LAT. The four plots correspond to 2 different energy ranges and two different longitudes ranges. The different shaded red areas show different values of α_b. As a good compromise to match our model to the true data as much as possible in the outskirts, we decide to set $\alpha_\mathrm{b} = 1.5$. This choice is also motivated by a direct comparison of the number of photons received in a given patch of the sky in Sect. 5.3. In any case, we can remark that our model, albeit not perfect, is fully consistent with the data.

Now we introduce our virtual Fermi-LAT instrument that does not have exactly the same characteristics as the true Fermi-LAT while still being comparable. Indeed here the goal is to reach an $\mathcal{O}(1)$ precision on our result and therefore we prefer taking simplified specifications. In particular, we restrict our search in the energy range $E \in [1, 100]$ GeV where the effective collection area is a constant (which is also con-

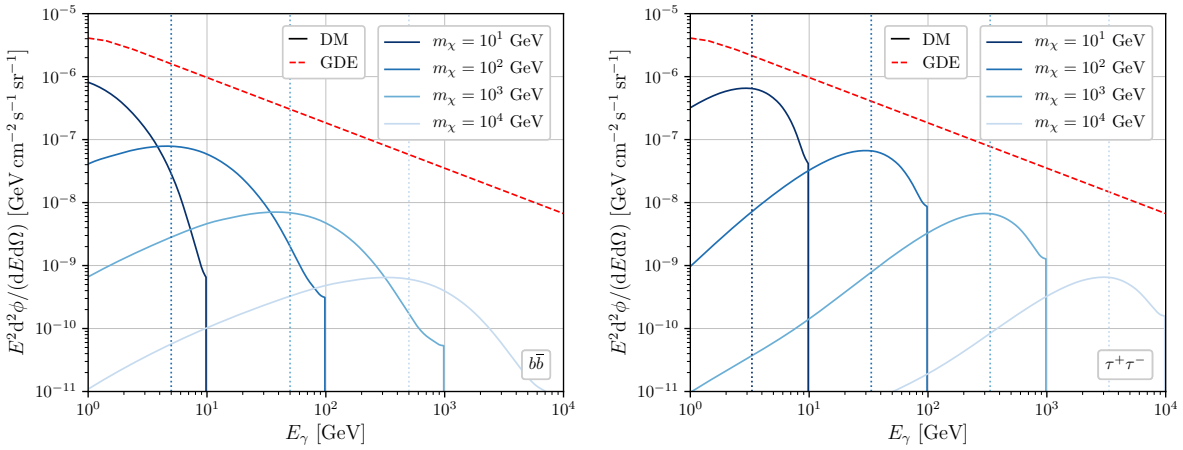

Figure 5.9 – Left panel : Spectrum of the gamma-ray flux in our GDE model with $\alpha_\mathrm{b} = 1.5$ (dashed red) and from DM annihilation (blue) into $b\bar{b}$ with $\langle\sigma v\rangle = 3 \times 10^{-26}$ cm^3 s^{-1} and for different particle masses. Here we averaged over on the patch $-80° < l < 80°$, $5° < |b| < 15°$ for an NFW Galactic profile. The vertical dashed lines represent $E = m_\chi/20$ and roughly goes through the maxima. **Right panel :** Same but for the $\tau^+\tau^-$ annihilation channel and with the vertical lines set at $E = m_\chi/3$.

venient as this is the limit of our pion model). This constant is taken to be $\mathcal{A} = 0.9$ m^2. Moreover, uniform coverage of the sky is assumed with a field of view spanning 1/5 of the full sky, i.e. $\simeq 2.3$ sr. This is consistent with the values found in W. ATWOOD et al. (2013) and BRUEL et al. (2018) and from the exposure quoted in FERMI-LAT COLLABORATION (2019). Eventually, instead of considering a proper point spread function with an energy dependence, we only limit our analysis to two benchmark resolution angles $\theta_\mathrm{r} = 0.1°$ and $\theta_\mathrm{r} = 1°$ which bracket the true point spread function of the Fermi-LAT.

5.3.2 The CTA background

For CTA-like instruments, that are imaging Cherenkov array telescopes (IACTs) and based on the ground, the gamma rays are not detected directly. It is rather the products of their interactions with atmospheric particles that are seen. Therefore while the Fermi-LAT-like background is also present in the CTA configuration, the data is polluted by cosmic-ray events that have the same signature as gamma-ray events and thus cannot always be distinguished. Consequently one also needs to properly take into account their contribution. In practice, the dominant components come from protons and electrons. We can parametrise the additional photon flux from electrons, which is isotropic, with the functions given in SILVERWOOD et al. (2015)

$$\frac{\mathrm{d}^3\phi_\mathrm{e}(E)}{\mathrm{d}E\mathrm{d}^2\Omega} = 1.17 \times 10^{-11} \left(\frac{E}{1\,\mathrm{TeV}}\right)^{-\Gamma_e(E)} \quad \mathrm{GeV}^{-1}\,\mathrm{cm}^{-2}\,\mathrm{s}^{-1}\,\mathrm{sr}^{-1} \tag{5.70}$$

with $\Gamma_e(E) = 3.0$ for $E <$ 1 TeV and $\Gamma_e(E) = 3.9$ for $E >$ 1 TeV. Similarly the photon flux from protons is given by a power law in terms of a false reconstructed photon energy,

$$\frac{\mathrm{d}^3\phi_\mathrm{p}(E)}{\mathrm{d}E\mathrm{d}^2\Omega} = 2.62 \times 10^{-8} \left(\frac{3E}{1\,\mathrm{TeV}}\right)^{-2.71} \quad \mathrm{GeV}^{-1}\,\mathrm{cm}^{-2}\,\mathrm{s}^{-1}\,\mathrm{sr}^{-1} \tag{5.71}$$

As a matter of fact, electron events cannot be distinguished from photon events. However, most of the proton events can. The efficiency of the rejection depends on the

energy, however here we follow SILVERWOOD et al. (2015) and assume that only a fraction $\epsilon_{\rm p} = 10^{-2}$ protons are mistaken for photons. Then the total background due to cosmic rays can be written

$$\frac{\mathrm{d}^2\phi_{\rm CR}(E)}{\mathrm{d}E\mathrm{d}\Omega} = \epsilon_{\rm p}\frac{\mathrm{d}^2\phi_{\rm p}(E)}{\mathrm{d}E\mathrm{d}\Omega} + \frac{\mathrm{d}^2\phi_{\rm e}(E)}{\mathrm{d}E\mathrm{d}\Omega}\,. \tag{5.72}$$

Besides, for CTA, the predictions for the sensitivity to the DM diffuse emission are done toward the centre of the Galaxy, therefore one needs a better model for this region that what we described in the Fermi case. In particular we assume that the total GDE in the central 5° is uniform as considered in LEFRANC et al. (2015) and given by

$$\frac{\mathrm{d}^2\phi_{\rm GDE}(E, <5^\circ)}{\mathrm{d}E\mathrm{d}\Omega} = 1.86\times10^{-4}\left(\frac{E}{1\,\mathrm{GeV}}\right)^{-2.57} \quad \mathrm{GeV}^{-1}\,\mathrm{cm}^{-2}\,\mathrm{s}^{-1}\,\mathrm{sr}^{-1} \tag{5.73}$$

This dependence is calibrated on the flux of the ON region (a very central region into $\psi < 1.36^\circ$) defined in SWSB15 – although they do not assume that the GDE flux is uniform as we do). We need to keep in mind, therefore, that the true flux should be slightly smaller in the outer part of the inner 5° region, by a factor of 2.5 approximately, which is of the same order than, or even below, the uncertainty on the effective collection area as shown below. Moreover, our goal not being to precisely model the background we simply check, in the end, that our results are realistic and consistent with SWSB15. In the left panel of Fig. 5.10 are shown the different gamma-ray flux components for CTA in direction of the GC. We also show the extrapolation of the model for $\psi > 5^\circ$ derived for the Fermi-LAT background. The latter appears to be sub dominant in front of the GDE and CR components given by SWSB15. In the right panel, the event rate from our work is compared to event rates obtained from Monte-Carlo simulations of the CTA performances from BERNLÖHR et al. (2013) and used in HÜTTEN et al. (2016). Our model is slightly underestimating the event rate but in view of the difference between the two black curves, it is still in good agreement with the literature. Moreover, we also plotted the total GDE toward the centre to show that it is almost negligible in comparison with the cosmic-ray contribution.

Eventually, similarly to the virtual Fermi-LAT instrument, let us introduce a virtual CTA-like instrument based on CTA characteristics (CTA CONSORTIUM 2019). We perform our analysis in the energy range $E \in [25, 10^4]$ GeV. In that range the effective collection area varies too much to be taken as a constant. Therefore, we compared several predictions made in BERNLÖHR et al. (2013) and *fitted* by hand

$$\log_{10}\mathcal{A}(E) = a\left[\log_{10}\left(\frac{E}{1\,\mathrm{GeV}} - 6\right)\right]^3 + b \tag{5.74}$$

with the parameters $a = 3.4\times10^{-2}$ and $b = 6.65$. In Fig. 5.11 the evolution of $\mathcal{A}(E)$ is represented in terms of the energy. Moreover here it is impossible to consider a uniform coverage of the sky as the field of view is $\theta_{\rm FoV} \sim 5^\circ$, thus covering a solid angle $\delta\Omega_{\rm FoV} = 0.024$ sr. With such a small value, one of the main goal of this study for CTA is to characterise the optimal pointing direction for a detection of a point-like subhalos. Eventually, similarly than for the Fermi-LAT case we do not consider the energy dependence of the point spread function and rather use two fixed resolution angles $\theta_{\rm r} = 0.1^\circ$ and $\theta_{\rm r} = 0.01^\circ$. Besides, for simplicity we also neglect the variation of sensitivity with the zenith angle.

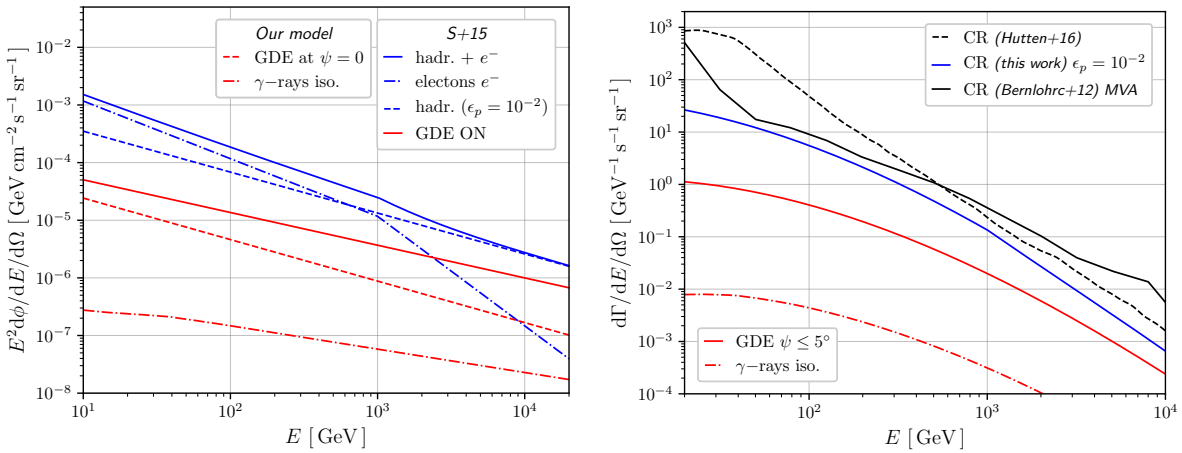

Figure 5.10 – Left panel: Gamma-ray fluxes reconstructed by CTA vs. the gamma-ray energy. In blue is represented the false CR-induced gamma-ray reconstructed signal in terms of the reconstructed gamma-ray energy taken from SWSB15 – here S+15. The red solid curve is the GDE flux in the ON region of SWSB15. We also show our own GDE model extrapolated to the GC ($\psi = 0$) with $\alpha_\mathrm{b} = 1.5$ and the isotropic gamma-ray component evaluated from Fermi-LAT data and extrapolated to high energies by a power law (dash-dotted). **Right panel:** Evolution of the differential event rate with the energy for different models. We compare our own model of false-CR induced reconstructed signal based on the CR model of SWSB15 (in solid blue on the left panel) and of our average effective collection area Eq. (5.74) (blue) to the MVA model of BERNLÖHR et al. (2013) (solid black) and HÜTTEN et al. (2016) (dashed black). The red solid line shows the event rate for the GDE of the ON region that we use for $\psi \leq 5°$ (also in solid red on the left panel). The red dashed-dotted line corresponds to the isotropic gamma-ray contribution.

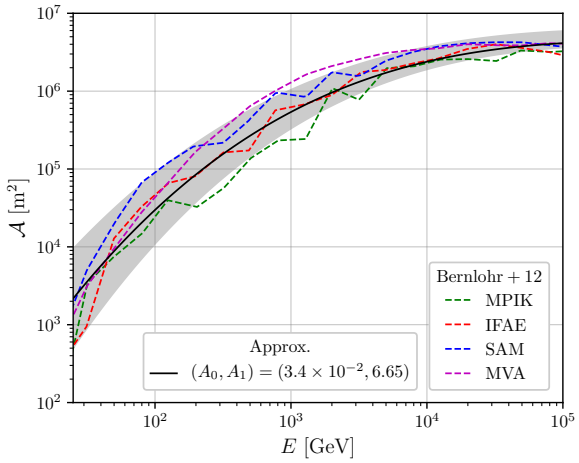

Figure 5.11 – Effective collection area for CTA-like instrument in terms of the energy. We compared our approximate model Eq. (5.74) in solid black to the different Monte Carlo results from BERNLÖHR et al. (2013) – denoted Bernlohr+12. The shaded grey shaded area is bracketed by the curves $(a, b) = (2.9 \times 10^{-2}, 6.8)$ and $(a, b) = (4 \times 10^{-2}, 6.6)$.

5.3.3 A simple criterion for the sensitivity

General framework

Before entering into an involved likelihood analysis for the sensitivity we first derive here some general properties from a much simpler criterion based on an On−Off study

(T.-P. Li et al. 1983). Assume that we look in one patch of the sky with the size of the resolution solid angle $\theta_{\rm r}$ and centred around a virtual point source in direction $\hat{\mathbf{n}}_i$ with $J-$factor $J_i^{\rm pt}$ – defined in Eq. (5.39). The number of photons received from this point-like structure in a time $\mathcal{T}(\hat{\mathbf{n}}_i)$, on an energy range ΔE, is given by

$$N_{\gamma,i}^{\rm pt}(\hat{\mathbf{n}}_i) = R_i^{\rm pt}(\hat{\mathbf{n}}_i)\mathcal{T}(\hat{\mathbf{n}}_i)\Delta E \tag{5.75}$$

with the definition of the energy-averaged event rate being

$$R_i^{\rm pt}(\hat{\mathbf{n}}_i) \equiv \overline{\mathcal{AS}_\chi} J_i^{\rm pt} = \frac{\langle\sigma v\rangle\, J_i^{\rm pt}}{2m_\chi^2}\overline{\mathcal{N}_\gamma \mathcal{A}}\,. \tag{5.76}$$

In the same sky patch and energy range and for the same observation time we also receive, on average, a number of background photons given by

$$N_{\gamma,\rm diff}^{\rm bg}(\hat{\mathbf{n}}_i, \Delta E) = R_{\rm diff}^{\rm bg}(E, \hat{\mathbf{n}}_i)\mathcal{T}(\hat{\mathbf{n}}_i)\Delta E \tag{5.77}$$

with the background differential rate being

$$\begin{aligned} R_{\rm diff}^{\rm bg}(\hat{\mathbf{n}}_i) &= \frac{1}{\Delta E}\int_{\Delta E} {\rm d}E \int_{\hat{\mathbf{q}}\in\mathcal{C}(\hat{\mathbf{n}}_i,\theta_{\rm r})} {\rm d}^2\Omega_{\hat{\mathbf{q}}} \frac{{\rm d}^3\phi_{\rm bg}(E,\hat{\mathbf{q}})}{{\rm d}E{\rm d}^2\Omega}\mathcal{A}(E) \\ &\simeq \frac{\delta\Omega_{\rm r}}{\Delta E}\int_{\Delta E} {\rm d}E \frac{{\rm d}^3\phi_{\rm bg}(E,\hat{\mathbf{n}}_i)}{{\rm d}E{\rm d}^2\Omega}\mathcal{A}(E)\,. \end{aligned} \tag{5.78}$$

where we used the approximation of Eq. (5.6) for the second equality and the fact that $\theta_{\rm r}$ is assumed not to depend on energy. Then, the criterion to have detection of the point-source is that it must detach from the Poissonian fluctuations of the background. Therefore, the source is detected if

$$N_{\gamma,i}^{\rm pt}(\hat{\mathbf{n}}_i) > n_\sigma\sqrt{N_{\gamma,\rm diff}^{\rm bg}(\hat{\mathbf{n}}_i)} \tag{5.79}$$

where n_σ gives a threshold of sensitivity. In practice, this number should be taken of order unity since this is the expected inequality in an On$-$Off analysis when the On and Off regions are identical. However, as this statistical criterion is rather simplistic, we consider it as an effective parameter that can be used to rescale the results obtained in this section to the results of the full likelihood analysis. From Eq. (5.79) the sensitivity in terms of a minimal value for J_i can be extracted. The subhalo is detectable if its J-factor is above the threshold

$$J_{\rm min}(\hat{\mathbf{n}}) \equiv \frac{n_\sigma}{\mathcal{T}(\hat{\mathbf{n}})}\frac{\sqrt{N_{\gamma,\rm diff}^{\rm bg}(\hat{\mathbf{n}})}}{\Delta E\overline{\mathcal{AS}_\chi}} = n_\sigma\frac{2m_\chi^2}{\langle\sigma v\rangle}\frac{1}{\sqrt{\mathcal{T}(\hat{\mathbf{n}})\Delta E}}\frac{\sqrt{R_{\rm diff}^{\rm bg}(\hat{\mathbf{n}})}}{\overline{\mathcal{N}_\gamma\mathcal{A}}}\,. \tag{5.80}$$

Here we can explicitly see that the spatial dependence of the minimal J-factor is due to the spatial variations of the background. Therefore, the most visible subhalo do not necessarily have to be the one with the highest intrinsic luminosity, they have to be the subhalos that have the largest luminosity in comparison to the threshold at their position. Moreover, the dependence in the observation time and on the annihilation cross-sections are rather trivial, and from Fig. 5.5, it may appear that a small change in $\langle\sigma v\rangle$ may give very different results for the number of visible subhalos. However if we assume no detection of the DM diffuse component, the constraints on $\langle\sigma v\rangle$, in a realistic context forbids this number to become arbitrarily large and, as a matter of fact, to remain below or close to 1 – see the discussion on the general case below. On the contrary, the dependence on m_χ is not trivial as it impacts the spectrum of photon produced by the DM annihilation.

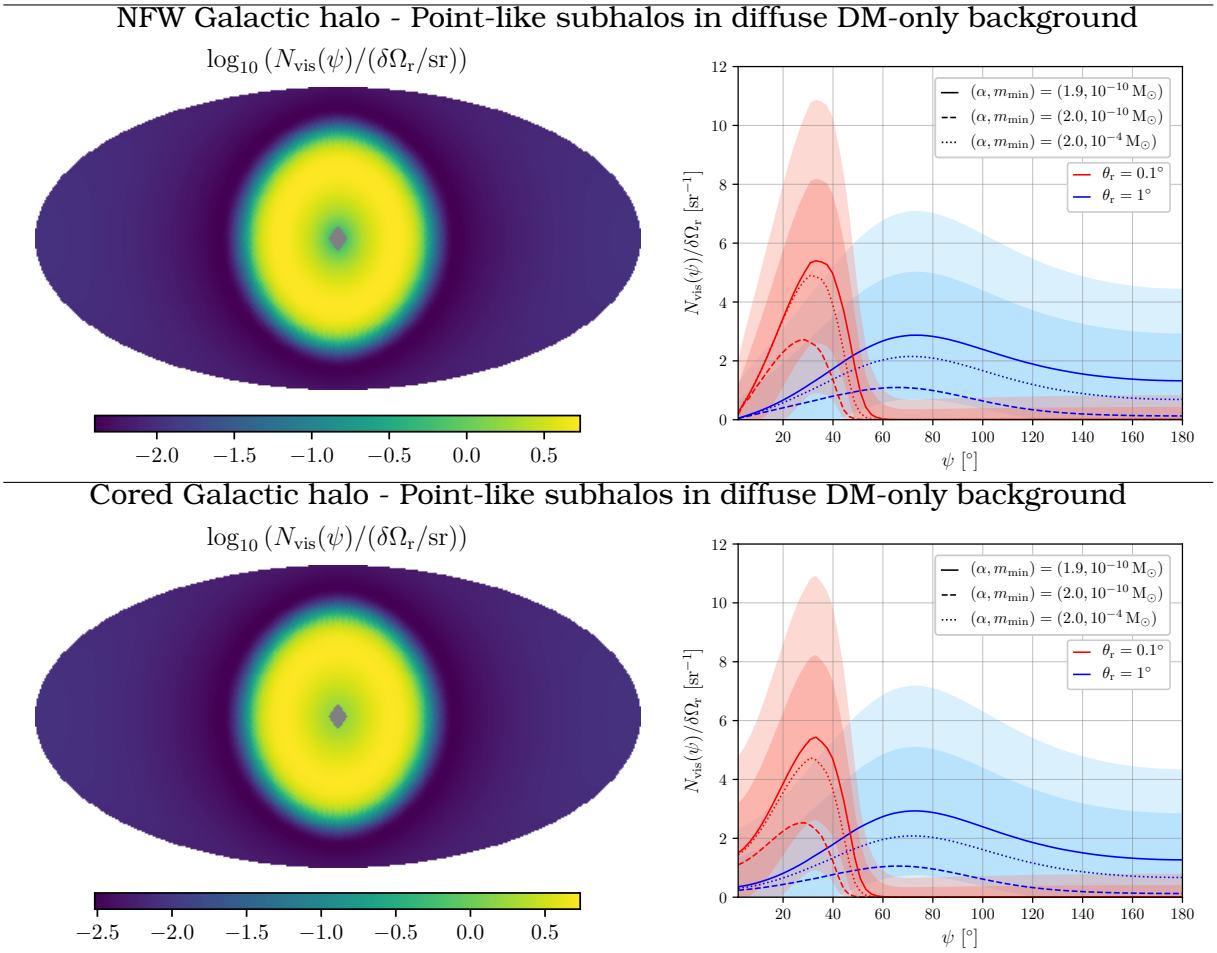

Figure 5.12 – Top left panel: Skymap of the effective number of subhalos per solid angle unit in a DM-only background—assuming a WIMP mass of 100 GeV annihilating to $\tau^+\tau^-$ with $\langle\sigma v\rangle = 3\times10^{-25}$ cm^3/s, a gamma-ray energy range 1-100 GeV, and a subhalo population configuration $(\alpha, m_{\rm min}/M_\odot, \epsilon_{\rm t}) = (1.9, 10^{-10}, 0.01)$ embedded in an NFW Galactic halo. **Top right panel**: Associated angular distribution (with 95% confidence band), with two angular resolutions $\theta_{\rm r} = 0.1°$ and $1°$, and several configurations for the subhalo population ranging in $(\alpha, m_{\rm min}/M_\odot) \in (1.9-2, 10^{-10}-10^{-4})$. **Bottom left and right panels:** Same as above for subhalos embedded in a cored Galactic halo.

The ideal DM-only configuration

With this first simple criterion, we can start looking at an idealised case, the DM-only configuration, where we assume that there is no baryon background. Although being completely unrealistic this simple exercise allows us to first evaluate where should be the most visible subhalos. Therefore, here, the only background component comes from the DM diffuse emission,

$$R^{\rm bg}_{\rm diff}(\hat{\mathbf{n}}) = R^{\rm DM}_{\rm diff}(\hat{\mathbf{n}}) \equiv \overline{\langle J_{\hat{\mathbf{n}}}\rangle}\frac{\langle\sigma v\rangle}{2m_\chi^2}\overline{\mathcal{N}_\gamma\mathcal{A}} \tag{5.81}$$

where $\overline{\langle J_{\hat{\mathbf{n}}}\rangle}(\Delta E)$ is defined in Eq. (5.47) and Eq. (5.48). Plugging this expression into Eq. (5.80) gives the simple expression of the sensitivity

$$J_{\rm min}(\hat{\mathbf{n}}) = \frac{n_\sigma}{\sqrt{\mathcal{T}(\hat{\mathbf{n}})}}\frac{1}{\sqrt{\Delta E}}\sqrt{\frac{2m_\chi^2\overline{\langle J_{\hat{\mathbf{n}}}\rangle}}{\langle\sigma v\rangle\,\overline{\mathcal{N}_\gamma\mathcal{A}}}}\,. \tag{5.82}$$

Here it is interesting to notice that, because we assume an energy-independent resolution angle, then $\overline{\langle J_{\hat{\mathbf{n}}}\rangle}(\Delta E) = \langle J_{\hat{\mathbf{n}}}\rangle \propto \delta\Omega_{\rm r} \propto \theta_{\rm r}^2$ from Eq. (5.6) and

$$J_{\rm min}(\hat{\mathbf{n}}) \propto \frac{\theta_{\rm r}}{\sqrt{\langle\sigma v\rangle\,\mathcal{T}(\hat{\mathbf{n}})}}\,. \tag{5.83}$$

Consequently, the dependence in $\langle\sigma v\rangle$ is through an inverse square root. A constant background (which does not depend on DM properties and thus on $\langle\sigma v\rangle$) would give, from Eq. (5.80), a dependency in the inverse. Indeed, this square root behaviour is a consequence of the fact that when one increases $\langle\sigma v\rangle$ in a DM-only configuration one decreases the sensitivity independently of the background but one also increases the background fluctuations. Moreover when $\theta_{\rm r}$ increases the sensitivity gets worse because it simply enhances the background. Eventually, let us mention that here as the diffuse DM J-factor only depends on ψ the pointing direction $\hat{\mathbf{n}}$ can be parametrised by ψ only.

In Fig. 5.12 we show skymaps for the number of visible point-like subhalos per units of the resolution solid angle. More precisely, in this figure, are called visible, all the point-like clumps with a J-factor above the sensitivity $J_{\rm min}$ and in the resolution solid angle such that

$$N_{\rm vis}(\hat{\mathbf{n}}) \equiv N_{>}^{\rm pt}(J_{\rm min}(\hat{\mathbf{n}}), \hat{\mathbf{n}}, \theta_{\rm r}) \tag{5.84}$$

In addition, we consider an NFW and cored Galactic profiles and a DM particle of mass $m_\chi = 100$ GeV which annihilates to $\tau^+\tau^-$ with the thermal cross-section $\langle\sigma v\rangle = 3\times10^{-26}$ cm^3 s^{-1}. Moreover $\Delta E = [1, 100]$ GeV, with an observation time of 10 yr and we look at the resolution angles $\theta_{\rm r} = 0.1^\circ, 1^\circ$. for a Fermi-LAT-like instrument. Although no baryon background is included, the baryonic tides are supposed to impact the subhalo distribution anyway and the subhalo model is specified by $(\alpha, m_{\rm min}, \epsilon_t) = (1.9, 10^{-10}\,M_\odot, 0.01)$. Eventually the statistical criterion is fixed to $n_\sigma = 3$. One needs to be careful here as with such parameters $N_\gamma^{\rm bg}$ and N_γ^i are small and can be below 1. Therefore the results must be treated with care and analysed at the qualitative level only; they can only be used to compare different configurations. The main conclusion however is that the optimal region to search for subhalos forms a ring peaked around $\psi \sim 30^\circ$ for $\theta_{\rm r} = 0.1^\circ$ and around $\psi \sim 50^\circ$ for $\theta_{\rm r} = 1^\circ$ as shown on the left panel. This change in angular distribution is due to two effects. Firstly changing $\theta_{\rm r}$ degrades the sensitivity and secondly, it changes the population of subhalos that can be considered as point-like. More generally decreasing $\theta_{\rm r}$ tends to shift the peak of the distribution toward small values of ψ. Moreover, the impact of changing the minimal mass or the mass index as well as the Galactic profile is shown by the different curves and in conclusion, the only real impact comes from the mass index. It could be surprising that a smaller mass index gives a higher number of visible subhalos since it corresponds to fewer substructures. However, a smaller mass index means a lower background as well as more massive subhalos (as the mass function is less steep) that are more visible. For the same mass index, lowering the minimal subhalo mass gives also less potentially visible subhalos – as this increases the background – while not really changing the number of subhalos that detach from the background (subhalos in the range 10^{-10}-10^{-4} M$_\odot$ are not enough massive for that). As mentioned earlier, even if the numbers have to be taken with care, for a thermal cross-section we only find a bit less than $\mathcal{O}(1)$ visible subhalos, which is not an optimistic first evaluation for a detection.

The general case

Here the general case is considered where the diffuse background has a component coming from DM and from baryons. We derive both the sensitivity to point sources but also the sensitivity to the DM diffuse component. Assuming that it is not detected we further deduce an interesting limit on the minimal possible value for the point source J-factor threshold. The total background emission rate is

$$\begin{aligned} R_{\rm diff}^{\rm bg}(\hat{\mathbf{n}}) &= R_{\rm diff}^{\rm DM}(\hat{\mathbf{n}}) + R_{\rm diff}^{\rm bg\backslash DM}(\hat{\mathbf{n}}) \\ &= \overline{\langle J_{\hat{\mathbf{n}}}\rangle}\frac{\langle\sigma v\rangle}{2m_\chi^2}\overline{\mathcal{N}_\gamma\mathcal{A}} + R_{\rm diff}^{\rm bg\backslash DM}(\hat{\mathbf{n}}) \end{aligned} \tag{5.85}$$

With a baryonic background, when there is no detection of the diffuse DM component it imposes that, in a sky patch $\mathcal{P}$ observed over a time $\widetilde{\mathcal{T}}(\mathcal{P})$ in the energy range $\widetilde{\Delta E}$, the cross-section is bounded from above. The number of received photon from the patch in question from the DM diffuse component and from the other astrophysical sources respectively are

$$\begin{aligned} \tilde{N}_{\gamma,\rm diff}^{\rm DM}(\mathcal{P}) &= \tilde{R}_{\rm diff}^{\rm DM}(\mathcal{P})\widetilde{\mathcal{T}}(\mathcal{P})\widetilde{\Delta E}(\mathcal{P}) \\ \tilde{N}_{\gamma,\rm diff}^{\rm bg\backslash DM}(\mathcal{P}) &= \tilde{R}_{\rm diff}^{\rm bg\backslash DM}(\mathcal{P})\widetilde{\mathcal{T}}(\mathcal{P})\widetilde{\Delta E}(\mathcal{P}) \end{aligned} \tag{5.86}$$

where the DM and background rate without DM diffuse emission rate are

$$\begin{aligned} \tilde{R}_{\rm diff}^{\rm DM}(\mathcal{P}) &= \frac{\langle\sigma v\rangle}{2m_\chi^2}\overline{\mathcal{N}_\gamma\mathcal{A}}\left\{J(\mathcal{P}) = \Delta E\int_{\hat{\mathbf{q}}\in\mathcal{P}}{\rm d}^2\Omega_{\hat{\mathbf{q}}}\,\overline{\langle\mathcal{J}_{\hat{\mathbf{q}}}\rangle}\right\} \\ \tilde{R}_{\rm diff}^{\rm bg\backslash DM}(\mathcal{P}) &= \frac{1}{\widetilde{\Delta E}(\mathcal{P})}\int_{\widetilde{\Delta E}(\mathcal{P})}{\rm d}E\int_{\hat{\mathbf{q}}\in\mathcal{P}}{\rm d}^2\Omega_{\hat{\mathbf{q}}}\frac{{\rm d}^3\phi_{\rm bg\backslash DM}(E,\hat{\mathbf{q}})}{{\rm d}E{\rm d}^2\Omega}\mathcal{A}(E)\,, \end{aligned} \tag{5.87}$$

and where $\overline{\langle\mathcal{J}_{\hat{\mathbf{q}}}\rangle}$ is defined in Eq. (5.49). No detection of the DM diffuse emission on the patch $\mathcal{P}$ implies that its emission is hidden in the Poissonian background, meaning

$$\tilde{N}_{\gamma,\rm diff}^{\rm DM}(\mathcal{P}) < \tilde{n}_\sigma\sqrt{\tilde{N}_{\gamma,\rm diff}^{\rm bg\backslash DM}(\mathcal{P})} \tag{5.88}$$

where $\tilde{n}_\sigma$ is an order 1 number and plays the same role as n_σ introduced above. From Eq. (5.86) and Eq. (5.87) we can transform this inequality as an upper bound for the annihilation cross-section, when there is no detection of the DM diffuse emission in all the observed patches. It takes the form

$$\langle\sigma v\rangle_{\rm max} = \tilde{n}_\sigma\frac{2m_\chi^2}{\overline{\mathcal{N}_\gamma\mathcal{A}}}\min_{\mathcal{P}}\left\{\frac{1}{\sqrt{\widetilde{\mathcal{T}}(\mathcal{P})\widetilde{\Delta E}}}\frac{\sqrt{\tilde{R}_{\rm diff}^{\rm bg\backslash DM}(\mathcal{P})}}{J(\mathcal{P})}\right\} \tag{5.89}$$

This result shows in particular that

$$\langle\sigma v\rangle_{\rm max} \propto \frac{1}{J(\mathcal{P})\sqrt{\tilde{\mathcal{T}}(\mathcal{P})}} \tag{5.90}$$

i.e., that the constraint on $\langle\sigma v\rangle$ gets more and more stringent with the observation time. Moreover, as it could be expected, it is also stricter in regionswith a large J-factor for the diffuse DM emission. Eventually, we now combine this new result with Eq. (5.80) in order to know what is the best sensitivity that can be reached for point

sources if no DM diffuse emission is ever detected in any observed patch $\mathcal{P}$. We call this quantity the critical minimal point J-factor and it is given by

$$J_{\rm min}^{\rm crit}(\hat{\mathbf{n}}) = \frac{n_\sigma}{\tilde{n}_\sigma} \max_{\mathcal{P}} \left\{ \sqrt{\frac{\widetilde{\mathcal{T}}(\mathcal{P})\widetilde{\Delta E}}{\mathcal{T}(\hat{\mathbf{n}})\Delta E}} \sqrt{\frac{R_{\rm diff}^{\rm bg\backslash DM}(\hat{\mathbf{n}})}{\tilde{R}_{\rm diff}^{\rm bg\backslash DM}(\mathcal{P})}} J(\mathcal{P}) \right\} \times \sqrt{1 + \frac{\tilde{n}_\sigma}{R_{\rm diff}^{\rm bg\backslash DM}(\hat{\mathbf{n}})} \min_{\mathcal{P}} \left\{ \frac{\sqrt{\tilde{R}_{\rm diff}^{\rm bg\backslash DM}(\mathcal{P})}}{\sqrt{\widetilde{\mathcal{T}}(\mathcal{P})\widetilde{\Delta E}}} \frac{\overline{\langle J_{\hat{\mathbf{n}}} \rangle}}{J(\mathcal{P})} \right\}}\,. \tag{5.91}$$

In particular, when $\langle \sigma v \rangle_{\rm max}$ is low enough, which amounts to take an observation time $\tilde{\mathcal{T}}(\mathcal{P})$ large, it yields the limit

$$J_{\rm min}^{\rm crit}(\hat{\mathbf{n}}) \underset{\tilde{\mathcal{T}}(\mathcal{P}^\star)\to\infty}{\sim} \frac{n_\sigma}{\tilde{n}_\sigma} \sqrt{\frac{\widetilde{\mathcal{T}}(\mathcal{P}^\star)\widetilde{\Delta E}}{\mathcal{T}(\hat{\mathbf{n}})\Delta E}} \sqrt{\frac{R_{\rm diff}^{\rm bg\backslash DM}(\hat{\mathbf{n}})}{\tilde{R}_{\rm diff}^{\rm bg\backslash DM}(\mathcal{P}^\star)}} J(\mathcal{P}^\star)\,, \tag{5.92}$$

where we introduced $\mathcal{P}^\star$ as the sky patch where the minimum in Eq. (5.89) is reached. Moreover, the true value is always above this asymptotic value, therefore it really corresponds to a lower bound on the minimal J-factor for point-like subhalos to be detectable (also called *visible* in the following). This last expression can be further simplified considering the same energy range $\Delta E = \widetilde{\Delta E}$. Moreover also assuming that $\mathcal{P}^\star = \mathcal{C}(\hat{\mathbf{m}}^\star, \theta_{\rm r})$ – that is the sky patch considered is just a cone of size the resolution angle – then the expression of the diffuse J-factor becomes $J(\mathcal{P}^\star) = \overline{\langle J_{\mathbf{m}^\star} \rangle}$ and the critical minimal point J-factor is

$$J_{\rm min}^{\rm crit}(\hat{\mathbf{n}}) \underset{\tilde{\mathcal{T}}(\hat{\mathbf{m}}^\star)\to\infty}{\sim} \frac{n_\sigma}{\tilde{n}_\sigma} \sqrt{\frac{\tilde{\mathcal{T}}(\hat{\mathbf{m}}^\star)}{\mathcal{T}(\hat{\mathbf{n}})}} \sqrt{R_{\rm diff}^{\rm bg\backslash DM}(\hat{\mathbf{n}})} \frac{\overline{\langle J_{\mathbf{m}^\star} \rangle}}{\sqrt{\tilde{R}_{\rm diff}^{\rm bg\backslash DM}(\hat{\mathbf{m}}^\star)}}\,. \tag{5.93}$$

The value of the critical J-factor is important as it gives the maximal number of subhalos that are *visible* if the DM diffuse emission is never detected. This expression tells that the only spatial dependence of the critical minimal J-factor comes from the known astrophysical background. In addition, as the diffuse J-factor quickly decreases from the centre, faster than the diffuse background $\tilde{R}_{\rm diff}^{\rm bg\backslash DM}$, thus $\hat{\mathbf{m}}^\star$ usually corresponds to a direction close to the GC. In the following, we also introduce

$$\eta_\sigma^{\rm eff}(\hat{\mathbf{m}}, \hat{\mathbf{n}}) \equiv \frac{n_\sigma}{\tilde{n}_\sigma} \sqrt{\frac{\tilde{\mathcal{T}}(\hat{\mathbf{m}})}{\mathcal{T}(\hat{\mathbf{n}})}} \tag{5.94}$$

as an effective normalisation parameter for the critical J-factor. In the next section, we show how it can be evaluated from the more realistic Likelihood analysis. As a matter of fact, and as seen in Fig. 5.13, this infinite observation time limit is a good approximation for realistic experiments. Indeed, in this figure we show with the dashed curves the evolution of the minimal J-factor for fixed values of $\langle \sigma v \rangle$ (red and green) and of $J_{\rm min}^{\rm crit}$ (blue) with the total observation time. There it is assumed that the same observation time is used to set the constraint on $\langle \sigma v \rangle$ and to evaluate $J_{\rm min}$ such that $\tilde{\mathcal{T}} = \mathcal{T}$. Then we also introduce the observation time T. For Fermi-LAT, it represents the total cumulative time of data collection by the instrument. Taking into account the fact that the satellite continuously observes the entire sky with a truncated field of view we set $\mathcal{T} = \tilde{\mathcal{T}} = T/5$. For CTA the field of view is so narrow that the instrument only uses its operating time on specific directions of interests.

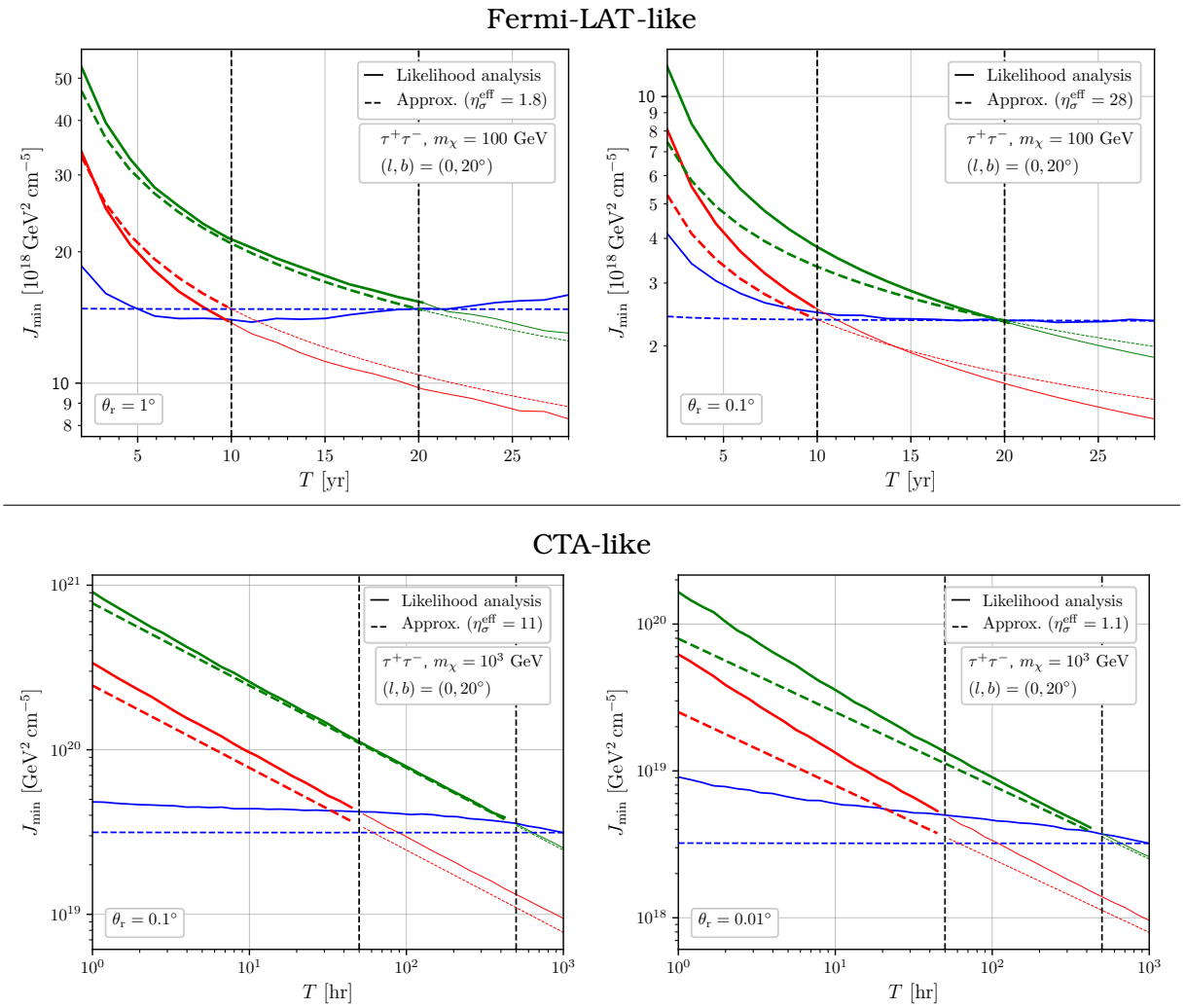

Figure 5.13 – Evolution of the minimal J-factor with the observation time T for the Fermi-LAT-like and the CTA-like instruments for a WIMP of mass 100 GeV annihilating into $\tau^+\tau^-$ in the direction $(l, b) = (0°, 20°)$. We assume an NFW Galactic DM profile. The red and green curves show the evolution of $J_{\rm min}$ at fixed $\langle\sigma v\rangle$. In red (resp. green) we assume a detection of the DM diffuse emission at T = 10 (resp. 20) yr for the Fermi-LAT configuration. In the CTA case we similarly assume a detection after $T = 50$ hr and 500 hr. We also set $(n_\sigma = 5, \tilde{n}_\sigma = 3)$ for Fermi and $(n_\sigma = 5, \tilde{n}_\sigma = 2.71)$ for CTA. The blue curves represent the critical minimal J-factor. By construction a subhalo with a J-factor under the blue curve cannot be detectable before the discovery of the diffuse DM emission for similar observation times. The dashed curve are the result from the simple criterion rescaled by $\eta_\sigma^{\rm eff}$ to the likelihood result in solid lines. The subhalo model is set by $\alpha = 1.9$, $m_{\rm min} = 10^{-10}$ $\mathrm{M}_\odot$ and $\epsilon_{\rm t} = 10^{-2}$.

Therefore T here only represents the observation time in the pointing direction which amounts to set $T = \tilde{\mathcal{T}} = \mathcal{T}$. Besides, the pointing direction for the constraint on $\langle\sigma v\rangle$ is fixed in the rough direction of the patches used in the likelihood analysis in order to make proper comparisons. Consequently we imposed $\mathbf{m}^\star$ as $(l, b) = (0°, 10°)$ for the Fermi-LAT-like configuration and $(l, b) = (0°, 1°)$ for the CTA-like configuration. The parameter $\eta_\sigma^{\rm eff}$ is also set to match the solid curves of the likelihood method. Remark then that the dashed blue lines for $J_{\rm min}^{\rm crit}$ appear, as predicted, to follow an asymptotic regime at observation times as low as $T = 2$ yr for $\theta_{\rm r} = 1°$ in the Fermi-LAT-like case and $T = 1$ hr in the CTA-like case

5.3.4 The likelihood analysis : general framework

In the following we perform a likelihood analysis to properly asses the sensitivity of the two types of instruments. The first part is focused on how the constraint on $\langle\sigma v\rangle$ is set from the DM diffuse emission. In a second part we detail the determination of the sensitivity to point-like sources.

The constraints on the annihilation cross-section

First, consider a Region of Interest (RoI) that is divided in N_S spatial bins, corresponding to different patches $\mathcal{P}_i$ in the sky. In addition we divide the total energy range of the instrument in N_E bins ΔE_j. Then in every bin the previous model for the known astrophysical background and for the DM emission allows to evaluate the average number of expected events. For the spatial bin i and energy bin j we write it under the form

$$\mu_{ij}\left[\langle\sigma v\rangle, \eta_k\right] = \Delta E_j \mathcal{T}(\mathcal{P}_i)\left\{\langle\sigma v\rangle\, M_j J(\Delta E_j, \mathcal{P}_i) + \sum_k \eta_k R^k_{\rm diff}(\Delta E_j, \mathcal{P}_i)\right\} \tag{5.95}$$

where the sum can run over all the possible background contributions. More precisely k can be CR, GDE or iso, where $R^{\rm CR}_{\rm diff}$ is the isotropic background from CR mistaken as photons, $R^{\rm GDE}_{\rm diff}$ is the baryonic Galactic diffuse emission and $R^{\rm iso}_{\rm diff}$ is the extragalactic baryonic emission. Using similar notations than in the previous discussion, with the straightforwardly adapted definitions, these terms are

$$\begin{aligned} J(\Delta E_j, \mathcal{P}_i) &= \int_{\hat{\mathbf{q}}\in\mathcal{P}_i} {\rm d}^2\Omega_{\hat{\mathbf{q}}}\, \overline{\langle \mathcal{J}_{\hat{\mathbf{q}}}\rangle}(\Delta E_j) \\ R^k_{\rm diff}(\Delta E_j, \mathcal{P}_i) &= \frac{1}{\Delta E_j}\int_{\Delta E_j} {\rm d}E \int_{\hat{\mathbf{q}}\in\mathcal{P}_i} {\rm d}^2\Omega_{\hat{\mathbf{q}}} \frac{{\rm d}^3\phi_{\rm k}(E,\hat{\mathbf{q}})}{{\rm d}E{\rm d}^2\Omega}\mathcal{A}(E)\,. \end{aligned} \tag{5.96}$$

The DM contribution is written in terms of the factor M_j which only depends on the DM particle mass and on the energy bin,

$$M_j = \frac{\overline{\mathcal{N}_\gamma \mathcal{A}}(m_\chi^2, \Delta E_j)}{2m_\chi^2} \tag{5.97}$$

In addition, $\mathcal{T}(\mathcal{P}_i)$ is the observation time in the bin i. Four different kind of analysis have to be done, whether we consider a Fermi-LAT-like or a CTA-like instrument and whether we want to set a constraint on $\langle\sigma v\rangle$ from the DM diffuse emission or evaluate the sensitivity to point-like sources. In all cases the method starts by drawing a mock number in every bin (ij) from a Poisson law as,

$$n_{ij} \sim {\rm Poiss}\left[\mu_{ij}(\langle\sigma v\rangle = 0, \eta_k = \eta_k^0)\right]\,. \tag{5.98}$$

For Fermi-LAT-like instruments $\eta^0_{\rm CR} = 0$ and $\eta^0_{\rm GDE} = \eta^0_{\rm iso} = 1$ while for CTA-like instruments $\eta^0_{\rm CR} = 1$, $\eta^0_{\rm GDE} = 1$ and $\eta_{\rm iso} = 0$ as the iso component is negligible in the centre in front of the CR component. The mock data is subsequently analysed with the following likelihood, inspired from Silverwood et al. (2015) – hereafter SWSB15 –

$$\mathcal{L}(\langle\sigma v\rangle, \alpha_{ij}, \eta_k) = \prod_{ij}\left[\frac{(\alpha_{ij}\mu_{ij})^{n_{ij}}}{\sqrt{2\pi\sigma_\alpha^2} n_{ij}!} e^{-\alpha_{ij}\mu_{ij}} e^{-\frac{(\alpha_{ij}-1)^2}{2\sigma_\alpha^2}} \prod_k \left(\frac{1}{\sqrt{2\pi\sigma^2_{\eta_k}}} e^{-\frac{(\eta_k-\overline{\eta}_k)^2}{2\sigma_k^2}}\right)\right]\,. \tag{5.99}$$

The variable α_{ij} are introduced to mimic systematic uncertainties of the instrument while σ_k and $\overline{\eta}_k$ set biases in the different component of the model. Note, however, that correlations between bins are not considered. The values of $\overline{\eta}_k$, σ_α and σ_k is discussed and justified later on. From now on, let us briefly detail the likelihood method. The first step is to define a null hypothesis H_0: *the value of* $\langle\sigma v\rangle$ *is equal to its best fit value*. The best fit value of the variables, denoted with a hat in what follows, are obtained by maximising the value of the likelihood. In other words, they must satisfy

$$\left.\frac{\partial\mathcal{L}}{\partial\langle\sigma v\rangle}\right|_{\widehat{\langle\sigma v\rangle},\hat{\alpha}_{ij},\hat{\eta}_k}=0\,,\quad \left.\frac{\partial\mathcal{L}}{\partial\alpha_{kl}}\right|_{\widehat{\langle\sigma v\rangle},\hat{\alpha}_{ij},\hat{\eta}_k}=0\quad\text{and}\quad \left.\frac{\partial\mathcal{L}}{\partial\eta_q}\right|_{\widehat{\langle\sigma v\rangle},\hat{\alpha}_{ij},\hat{\eta}_k}=0\,. \tag{5.100}$$

Then, the following step is to evaluate how much higher $\langle\sigma v\rangle$ can reasonably be from its best fit value in a statistical sense. To this end one first needs to introduce the likelihood ratio

$$\mathcal{R}(\langle\sigma v\rangle)\equiv\frac{\mathcal{L}(\langle\sigma v\rangle\,,\hat{\hat{\alpha}}_{ij}(\langle\sigma v\rangle),\hat{\hat{\eta}}_k(\langle\sigma v\rangle))}{\mathcal{L}(\widehat{\langle\sigma v\rangle},\hat{\alpha}_{ij},\hat{\eta}_k)} \tag{5.101}$$

where $\hat{\hat{\alpha}}_{ij}(\langle\sigma v\rangle)$ and $\hat{\hat{\eta}}_k(\langle\sigma v\rangle)$ are the best-fit values at fixed $\langle\sigma v\rangle$. The first noticeable property is that, by definition, $\mathcal{R}(\langle\sigma v\rangle)\leq 1$. Moreover when $\langle\sigma v\rangle$ is very different from its best-fit value $\mathcal{R}$ is expected to become small. Therefore the question becomes how small can $\mathcal{R}$ be. Wilk's theorem (WILKS 1938) tells that in the limit of an infinite number of bins and on the condition that the null hypothesis holds true, the value of $-2\ln\mathcal{R}(\langle\sigma v\rangle)$ satisfies a $\chi^2(1)$ distribution (COWAN et al. 2011): $2\ln\mathcal{R}(\langle\sigma v\rangle)\sim\chi^2(1)$. The probability distribution function of $\chi^2(k)$, for k a positive integer, is

$$p_{\chi^2(k)}(x)=\frac{1}{2^{/2}\Gamma(k/2)}x^{k/2-1}e^{-x/2} \tag{5.102}$$

We denote by t the number so that the probability to have $-2\ln\mathcal{R}(\langle\sigma v\rangle)>t$ is p_0 under the null hypothesis. Then, t satisfies

$$p_0=\int_t^\infty p_{\chi^2(k)}(y)\mathrm{d}y=\int_t^\infty\frac{1}{\sqrt{2\pi y}}e^{y/2}\mathrm{d}y=\sqrt{\frac{2}{\pi}}\int_{\sqrt{t}}^\infty e^{-x^2/2}\mathrm{d}x\,. \tag{5.103}$$

Setting a constraint at $\tilde{n}_\sigma$ amounts to ask that

$$p_0=1-\frac{1}{\sqrt{2\pi}}\int_{-\tilde{n}_\sigma}^{+\tilde{n}_\sigma}e^{-x^2/2}\mathrm{d}x=\sqrt{\frac{2}{\pi}}\int_{\tilde{n}_\sigma}^\infty e^{-x^2/2}\mathrm{d}x \tag{5.104}$$

which imposes $t=\tilde{n}_\sigma^2$. To summarise, the upper bound $\langle\sigma v\rangle_{\rm max}$ at $\tilde{n}_\sigma$ is set as the solution of $-2\ln\mathcal{R}(\langle\sigma v\rangle_{\rm max})=\tilde{n}_\sigma^2$. Instead of the $\tilde{n}_\sigma$ criterion, it is also common to simply fix the limit through p_0, in which case t is then implicitly given by

$$\mathrm{erfc}\left[\sqrt{\frac{t}{2}}\right]=p_0\,. \tag{5.105}$$

Typical values are $t(p_0=0.1)\simeq 2.71$ for a bound at 90% confidence level and $t(p_0=0.05)\simeq 3.85$ for a bound at 95% confidence level.

In practice, however, finding the best-fit values is not necessarily easy as it involves minimising a multivariate function. However, as pointed out in SWSB15, the

minimisation over the parameter α_{ij} is straightforward and it can be written as a function of $\langle\sigma v\rangle$ and η_k

$$\tilde{\alpha}_{ij}(\langle\sigma v\rangle, \eta_k) = \frac{1}{2}\left(1 - \sigma_\alpha^2 \mu_{ij} + \sqrt{\left(\sigma_\alpha^2 - 1\right)^2 + 4\sigma_\alpha^2 n_{ij}}\right) \tag{5.106}$$

Therefore, following App. A.3 we find the best-fit values using a Newton-Ralphson algorithm. In practice, the Hessian matrix involved in the process is at most 3 dimensional and the convergence is fast.

The sensitivity threshold to point-like sources

The analysis for the sensitivity to point-like structures is very similar to the analysis of the constraint on $\langle\sigma v\rangle$. Here, however, we consider a RoI that is centred around a central spatial bin tagged i_0 where we assume that a point-source is present. Therefore, we introduce a slightly modified expression for μ_{ij} by adding this point-source term as follows

$$\mu_{ij}\left[J, \eta_k; \langle\sigma v\rangle\right] = \Delta E_j \mathcal{T}(\mathcal{P}_i)\left\{\langle\sigma v\rangle\, M_j(J(\Delta E_j, \mathcal{P}_i) + \nu_i J) + \sum_k \eta_k R^k_{\rm diff}(\Delta E_j, \mathcal{P}_i)\right\} \tag{5.107}$$

where $\nu_i = \delta_{i,i_0}$. An important difference is that now, $\langle\sigma v\rangle$ is no longer considered as a free parameter which needs to be determined but it has a fixed value. That is to say we always evaluate the minimal J-factor at a given $\langle\sigma v\rangle$. The mock data is evaluated similarly, by drawing on a Poissonian distribution, except in the central bin where $n_{i_0 j} = \overline{\mu}_{i0j}$ and $J = \overline{J}$, the value of the J-factor emitted by the point-source. The goal is to find how large $\overline{J}$ should be to ensure the discovery. The likelihood for the analysis is the same than Eq. (5.99) at the difference that it now depends on J and not on $\langle\sigma v\rangle$: we denote $\mathcal{L} = \mathcal{L}(J, \alpha_{ij}, \eta_k; \langle\sigma v\rangle)$. The null hypothesis for a detection is H_0: *There is no point source in the central bin*. Consequently, we build a new likelihood ratio, that depends on $\overline{J}$ through the mock data

$$\mathcal{R}(\overline{J}) = \frac{\mathcal{L}(\hat{J}, \hat{\alpha}_{ij}, \hat{\eta}_k); \langle\sigma v\rangle)}{\mathcal{L}(J = 0, \hat{\hat{\alpha}}_{ij}(J = 0), \hat{\hat{\eta}}_k(J = 0); \langle\sigma v\rangle)} \tag{5.108}$$

where $\hat{\hat{\alpha}}_{ij}(J = 0)$ and $\hat{\hat{\eta}}_k(J = 0)$ are the best fit values in the null hypothesis. Under this form $\mathcal{R} > 1$ when $\overline{J} > 0$, since $\hat{J}$ should be driven toward the value of $\overline{J}$ in order to maximise the likelihood. According to Wilk's theorem we could define 5-σ detection by the requirement $2\ln\mathcal{R}(\overline{J}) \geq 25$ so that the minimal J-factor of a point-like source to be detected in direction $\hat{\mathbf{n}}$ of the central bin is

$$2\ln\mathcal{R}(J_{\rm min}(\hat{\mathbf{n}})) = 25\,. \tag{5.109}$$

However, rigorously, $2\ln\mathcal{R}(\overline{J})$ does not follow a $\chi^2(1)$ distribution as the null hypothesis enforces $J = 0$, at the boundary of its domain of definition – since a negative value of J makes no physical sense (Hütten et al. 2016). In that case, the distribution is slightly modified. However, the present criterion can just be taken as a definition that is also called the Test-Statistic (TS). Therefore rather than saying that we have a 5σ detection we rather say that we have a detection with a TS of 25, which is the typical value found in the literature (Calore et al. 2017; Fermi-LAT Collaboration 2019) and which should be sufficient to prevent false detections.

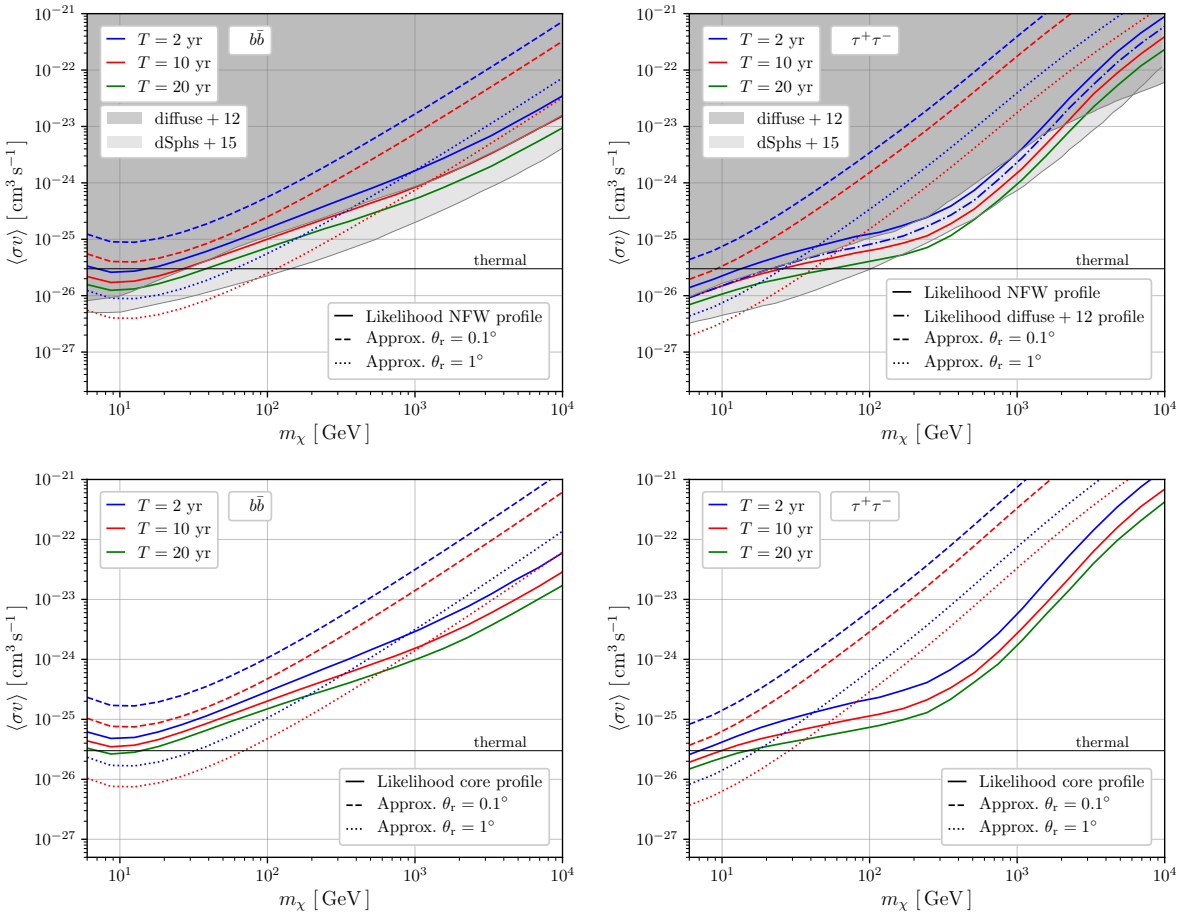

Figure 5.14 – 3σ constraint on the s-wave annihilation cross-section of DM in $b\bar{b}$ (right panels) and $\tau^+\tau^-$ (left panels) for a Fermi-LAT-like instrument. The upper panels correspond to a Galactic NFW profile and the lower panels to a Cored profile. We considered 3 different times of operation for the Fermi-LAT-like instrument $T = 2$, 10 or 20 yr, respectively shown in blue, red and green. The solid curves are obtained from the likelihood analysis while the dashed curves are given by the On-Off-like analysis for $\theta_r = 0.1°$ and $1°$. The dark shaded area is the limit obtained by the Fermi-LAT collaboration for $T = 2$ yr (FERMI-LAT COLLABORATION 2012a) with a Galactic DM density profile different from ours. Therefore the blue dashed line uses the same profile to make a direct comparison. The light shaded area is given by the same collaboration and using dwarf spheroidal galaxies as targets (instead of a region around the GC) and for a time of observation of 6 years (FERMI-LAT COLLABORATION 2015b). They also apply to the core profile scenario but are not displayed in the bottom panels for clarity.

5.3.5 The Fermi-LAT-like configuration

For a Fermi-LAT-like instrument the constraint on the annihilation cross-section is set in an RoI that covers two symmetric regions of the sky, above and below the GC, spanning $|l| < 80°$ and $5° < |b| < 15°$. This region is divided into 3200 bins that each cover roughly a solid angle $1° \times 1°$. The energy range $[1, 100]$ GeV is divided into 5 logarithmically spaced bins. Within our model by setting $\alpha_b = 1.5$ in Eq. (5.69), the GDE and isotropic components give an average of ~ 360000 photons collected in a total time $T = 2$ years of observations and in the total RoI. This number is in perfect agreement with the real number of photon collected by the Fermi-LAT collaboration (FERMI-LAT COLLABORATION 2012a). However, in their analysis, they have to discard all the $0.9° \times 0.9°$ areas around point sources. This suppresses by 25% the total

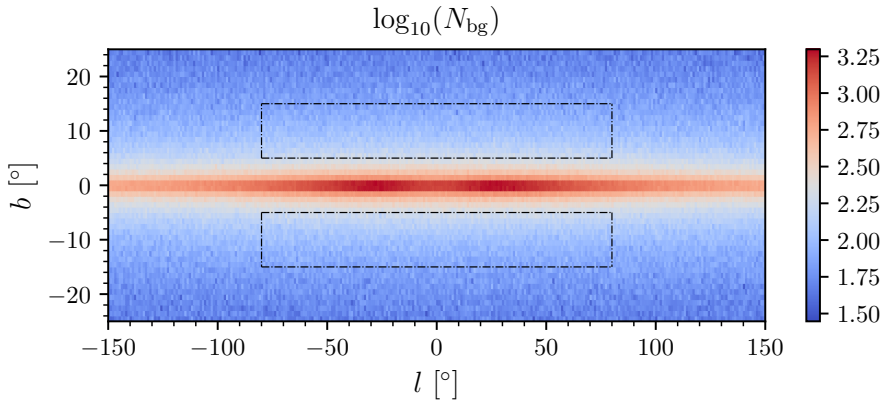

Figure 5.15 – Selected RoI to set constraints on $\langle\sigma v\rangle$ with the Fermi-LAT-like instrument and bases on Fermi-LAT Collaboration (2012a). In colour are represented one Monte Carlo draw for the number of background photons in bins of size $1^\circ \times 1^\circ$.

number of photons. In order to mimic this experimental constraint, when drawing the mock data we randomly mask 25% of the spatial bins. Then the total number of photon received roughly becomes 270000 as it is in the real collected data.

The data analysis is performed by setting $\sigma_\alpha = 0$ therefore fixing $\alpha_{ij} = 1$ because we do no assume systematics from the instrument. Moreover uncertainties on the isotropic gamma-ray component are neglected which amounts to set $\sigma_{\rm iso} = 0$, $\overline{\eta}_{\rm iso} = 1$ so that $\eta_{\rm iso} = 1$. On the contrary, however, because our GDE model is not perfect $\sigma_{\rm GDE}$ and $\overline{\eta}_{\rm GDE}$ are fixed such that the reconstruction of the best-fit is biased. This bias leaves room for a possible explanation of a fraction of the GDE component present in the mock data by DM emission; thus degrading the constraint on $\langle\sigma v\rangle$. In particular, we impose a constraint on these two quantities as

$$\sigma_{\rm GDE} \simeq \frac{1 - \overline{\eta}_{\rm GDE}}{3} \tag{5.110}$$

such that what corresponds to the data $\eta^0_{\rm GDE} = 1$ is at 3σ of the biased value. A 30% bias is authorised therefore $\overline{\eta}_{\rm GDE} = 0.7$ and $\sigma_{\rm GDE} = 0.11$. The results are shown in Fig. 5.15. The 3σ constraints on $\langle\sigma v\rangle$ are plotted for different total observation times of the Fermi-LAT ($T = 2$ yr, 10 yr and 20 yr) in blue, red and green respectively. The four panels correspond to two different annihilation channels ($\tau^+\tau^-$ and $b\bar{b}$) and two Galactic DM profiles (NFW/Core). The dashed curves are obtained thanks to the On-Off criterion in the direction $(l, b) = (0^\circ, 10^\circ)$. The first remark is that the spectral dependence of our curves follows the dark shaded area given by the Fermi-LAT collaboration. In particular, we should compare the dash-dotted blue curve of the top right panel which is obtained with the same Galactic DM profile than used by the Fermi-LAT collaboration. A slight deviation can be observed at large WIMP mass in the $\tau^+\tau^-$ channel. This deviation can be explained as in their data analysis they use photons above 100 GeV while we do not and the spectrum of photons produced in the $\tau^+\tau^-$ channel roughly decreases as E^{-1} with a bump around $E \sim m_\chi/3$ as shown in Fig. 5.9 and stated in Calore et al. (2017) – before being exponentially suppressed at larger energies. Therefore we do not probe the most sensitive region of energy for high masses. In the $b\bar{b}$ case, a similar bump occurs at $E \sim m_\chi/20$. This factor of 10 difference in the position of the bump with respect to the mass, allows keeping a good agreement up to $m_\chi = 10^4$ GeV. The second remark concerns the time evolution. The constraints go like $\propto 1/\sqrt{T}$ in the simple analysis and this also

approximately holds true in the likelihood analysis. This could be expected as we do not impose systematics. Let us also point out that the constraint from identified dwarf spheroidal galaxies is also an interesting limit. This method could allow to discover DM before the diffuse emission or the detection of several unassociated point-like sources. Eventually, the overall agreement with the Fermi-LAT results at $T = 2$ yr justifies the method which allows now evaluating the constraints at longer times.

In order to establish the sensitivity to point-like sources, we use two different RoIs according to the resolution angle. In the configuration where $\theta_{\rm r} = 0.1^\circ$ we consider a grid of 11×11 bins of size $0.2^\circ\times0.2^\circ$ and divide the energy range in 5 bins as for the constraints on the cross-section. When the resolution angle is $\theta_{\rm r} = 1^\circ$ then we reduce the analysis to a grid of 3×3 bins of size $2^\circ \times 2^\circ$. The analysis is performed with the same values of η_k, σ_k and σ_α in the likelihood than for the constraint. In Fig. 5.13 we can observe that this more involved analysis (solid curves) reproduces similar behaviours than the simple criterion (dashed curves) but with a correct overall normalisation.

5.3.6 The CTA-like configuration

For a CTA-like instrument, the constraint on the annihilation cross-section is set in the inner 5° of the Galaxy. The RoI is taken as in SWSB15, a circular region centred slightly above the galactic plane, divided into 28 bins and where the region $|b| < 0.3^\circ$ is truncated out. The energy range is $[25, 10^4]$ GeV and it is divided into 15 equal logarithmic bins. In the CTA-like case, for rapidity of convergence, and only for the constraint on the annihilation cross-section we do not really draw mock data according to the Poisson law but rather directly use the average value $n_{ij} \simeq \mu_{ij}(\langle\sigma v\rangle = 0, \eta_k = \eta_k^0)$, which is called the Asimov data set, in order to match the SWSB15 analysis. This should give the same results as an MC simulation but faster, avoiding the need for several mock data sets to obtain convergence. The analysis is performed without and with the GDE, which means that $\eta_{\rm GDE}$ is either set to 0 or stays a free parameter. When neglecting the GDE we set $\sigma_\alpha = 0$ in order to give the strongest possible constraint in the model, otherwise, the systematics is taken to be $\sigma_\alpha = 0.3\%$ or $\sigma_\alpha = 1\%$. The isotropic extragalactic gamma-ray component is neglected and we set $\sigma_{CR} = \sigma_{\rm GDE} \to \infty$, as we assume no constraints (in reality, the isotropic gamma-ray contribution in the inner 5° is negligible in comparison to the CR component). This amounts in reality to omit the Gaussian terms corresponding to $\eta_{\rm CR}$ and $\eta_{\rm GDE}$ (and renormalising correctly). Our results are shown in the upper panels of Fig. 5.16 for Cored (in red) and NFW (in blue) Galactic DM profile and for two annihilation channels $b\bar{b}$ (upper left panel) and $\tau^+\tau^-$ (upper right panel). In the bottom panel, we compare the results of SWSB15 represented by the shaded dark red and light red areas and obtained for an observation time $T = 100$ hr with an Einasto profile, to our own results obtained in similar configurations in solid dark and medium blue respectively. We observe small differences that can be explained by two factors. Firstly, our GDE model is supposed to be isotropic in the centre unlike in SWSB15 and overestimates the true value. Secondly, the final result is rather sensitive to the effective collection area. As we consider an idealised average dependence in energy this explain mostly the differences. Moreover two observation times $T = 100$ hr (solid curves) and $T = 500$ hr (dashed curves) are displayed. In the configuration without GDE and $\sigma_\alpha = 0$ as well as in the configuration with GDE and $\sigma_\alpha = 0.3\%$ the constraints go as $\langle\sigma v\rangle_{\rm max} \propto 1/\sqrt{T}$ as it was the case in the

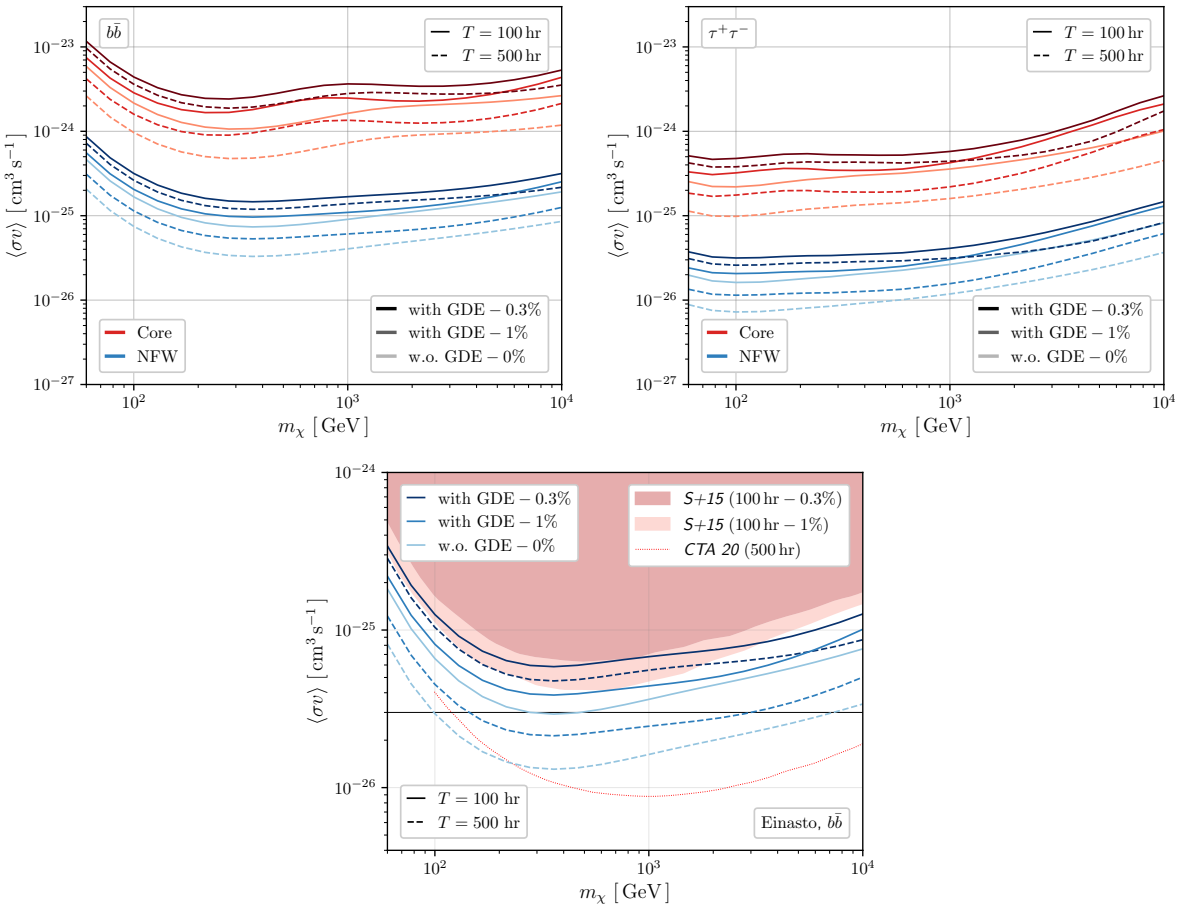

Figure 5.16 – Upper panels: 2.71σ constraint (90%) on the s-wave annihilation cross-section of DM in $b\bar{b}$ (right upper panel) and $\tau^+\tau^-$ (left upper panel) for a CTA-like instrument. The two Galactic DM profiles are considered, Cored (red) and NFW (blue). We evaluate three different configurations for the likelihood analysis with GDE ans 0.3% systematics (dark curves), with GDE and 1% systematics as well as no GDE and 0% systematics. The details on the method is described in Sect. 5.3.6. Moreover we also compared two observation time $T = 100$hr and $T = 500$ hr. **Lower panel:** Same than above but with the Einasto DM profile for the MW used in SWSB15 – here denoted S+15. The results obtained in SWSB15 for $T = 100$ hr are represented by the red shaded areas. Moreover we also show comparison with CTA20 (CTA Consortium 2020) results (light red curve).

Fermi-LAT-like instrument because the systematics are negligible in comparison to the fluctuations of the backgrounds. However for $\sigma_\alpha = 1\%$, this behaviour changes as for $T = 500$ hr the systematics become dominant and therefore fix the constraint.

The evaluation of the sensitivity to point source is limited to the region $\psi > 5°$ and is also determined with RoIs of 11×11 bins of size $0.2° \times 0.2°$ or $0.02° \times 0.02°$ whether $\theta_r = 0.1°$ or $0.01°$. The energy range is similarly divided into 15 equal logarithmic bins. Rigorously, in this region of research, the GDE is given by that of the Fermi-LAT configuration and the likelihood adapted in consequences. Indeed we set $\sigma_\alpha = 0.3\%$ and we introduce a bias in the GDE component with $\overline{\eta}_{\rm GDE} = 0.7$ and $\sigma_{\rm GDE} = 0.11$. However, in practice, the GDE appears to be completely negligible in front of the CR flux when $\psi > 5°$. Henceforth, for faster convergence, we consider only the CR isotropic background. In Fig. 5.13, already discussed after Eq. (5.94), the solid curves

$\frac{m_\chi}{[\mathrm{GeV}]}$	channel	bkg.	$\frac{T}{[\mathrm{yr}]}$	NFW			Core		
				$N^-_{95\%}$	$N_{\rm vis}$	$N^+_{95\%}$	$N^-_{95\%}$	$N_{\rm vis}$	$N^+_{95\%}$
				$\theta_{\rm r} = 0.1^\circ$					
100	$\tau^+\tau^-$	DM+b	10*	0	1.8×10^{-3}	0.6	0	9.0×10^{-3}	0.80
100	$\tau^+\tau^-$	b only	10*	0	2.4×10^{-3}	0.63	0	1.3×10^{-2}	0.85
100	$b\bar{b}$	DM+b	10*	0	0.26	2.0	0	1.2	4.2
1000	$b\bar{b}$	DM+b	10*	0	1.7×10^{-2}	0.92	0	7.1×10^{-2}	1.35
1000	$\tau^+\tau^-$	DM+b	10*	0	1.3×10^{-5}	0.34	0	9.8×10^{-5}	0.41
100	$b\bar{b}$	DM+ b	20†	...	...	...	0	1.8	5.3
100	$b\bar{b}$	DM+ b	20*	...	...	...	0	3.3	7.8
				$\theta_{\rm r} = 1^\circ$					
100	$\tau^+\tau^-$	DM+b	10*	0	5.0×10^{-2}	1.2	0	0.16	1.7
100	$\tau^+\tau^-$	b only	10*	0	5.4×10^{-2}	1.2	0	0.19	1.8
100	$b\bar{b}$	DM+b	10*	0	1.3	4.3	0	3.7	8.4
1000	$b\bar{b}$	DM+b	10*	0	0.20	1.8	0	0.57	2.9
1000	$\tau^+\tau^-$	DM+b	10*	0	4.2×10^{-3}	0.69	0	1.9×10^{-2}	0.93
100	$b\bar{b}$	DM+ b	20†	...	...	...	0.14	4.0	8.8
100	$b\bar{b}$	DM+ b	20*	...	...	...	1.2	6.0	12

* Using $\langle\sigma v\rangle_{\rm max}$ (10 yr) for the corresponding channel.
† Using $\langle\sigma v\rangle_{\rm max}$ (20 yr) for the corresponding channel.

Table 5.1 – Number of visible subhalos and 95% confidence interval assuming angular resolutions of $\theta_{\rm r} = 0.1^\circ$ and 1°, and different WIMP models. The subhalo sensitivity a,d the constraint on $\langle\sigma v\rangle$ are evaluated using the recipe for the Fermi-LAT-like instrument detailed in Sect. 5.3.5. The subhalo configuration is $(\alpha, m_{\rm min}/M_\odot, \epsilon_{\rm t}) = (1.9, 10^{-10}, 0.01)$, *i.e.* it describes a population of subhalos resilient to tidal stripping.

represent the evolution with the observation time of the minimal J-factor. Contrarily to the asymptotic behaviour reached in the Fermi-LAT configuration we observe a decrease at a large time for CTA. As a matter of fact, this is due to the systematics that affect more, at earlier times, the constraints $\langle\sigma v\rangle_{\rm max}$ than the sensitivity of point-like sources. Therefore at larger times $\langle\sigma v\rangle_{\rm max}$ becomes a constant and therefore $J^{\rm crit}_{\rm min}$ in blue recovers a behaviour in $\propto 1/\sqrt{T}$ as in Eq. (5.83).

5.4 Detectable point-subhalos and their characteristics

In summary, we have hitherto introduced the notion of J-factor and point like subhalos and we have evaluated the distribution of J within SL17. We also have defined a background/foreground model for Fermi-LAT-like and CTA-like instruments and from that, we have deduced, in Sect. 5.3, their sensitivity to point-like structure, written in terms of J-factor, as well as the constraint on the DM annihilation cross-section in order not to spoil the non-detection of the DM diffuse emission around the GC. We have already shown the evolution of these last two quantities with time. In this section, we insert the value $J_{\rm min}$ and in the probability distributions of Sect. 5.2.3 in order to evaluate the total number of detectable/visible point-like subhalos (and to a lesser extent of extended sources).

5.4.1 Results for the Fermi-LAT analysis

In Fig. 5.22, Fig. 5.23 and Fig. 5.24 we show 2D-plots of $N_{>}^{\rm pt}(J,\hat{\mathbf{n}},\theta_{\rm r})$ divided by $\delta\Omega_{\rm r}$ and defined in Eq. (5.52), with the parametrisation of $\hat{\mathbf{n}}$ by the angle ψ. That is, the number of point-sources above the threshold J in every direction ψ (we recall that knowing ψ is enough because of the spherical symmetry of the SL17 model). On top we also show the evolution of the sensitivity $J_{\rm min}(l,b)$ with $(l,b)=(0^\circ,\psi)$ and $(l,b)=(180^\circ,\psi-180^\circ)$ and for a 100 GeV WIMP annihilating into $\tau^+\tau^-$. Different configurations are considered. Firstly, we look at two different backgrounds for the sensitivity to point sources, one that is the sum of the baryonic sources and the DM diffuse source (solid curves) which has been discussed so far and one that only contains the baryonic sources (dash-dotted curves). In practice the latter simply amounts to neglect the term $\langle\sigma v\rangle\, M_j J(\Delta E_j,\mathcal{P}_i)$ in Eq. (5.107) for the likelihood analysis. Secondly, the value of $\langle\sigma v\rangle$ is fixed to its upper limit after 10 yr associated to two different observation times for the source search $T=10$ yr (blue curves) and $T=20$ yr (red-brownish curves). These numbers mean that, for the red curve, the diffuse DM emission has already been detected when the sensitivity to point-like subhalos is established. In addition we show an extreme case with a constant large $\langle\sigma v\rangle=10^{-24}$ cm^{-3} s^{-1} and a sensitivity to point sources evaluated at 10 yr (green). Note that the probability to detect subhalos above a constant threshold J peaks at $\psi=50^\circ$ for $\theta_{\rm r}=1^\circ$ and $\psi=20^\circ$ for $\theta_{\rm r}=0.1^\circ$. This is better seen in the middle panels that are just zoomed windows in $\psi\in[0^\circ,40^\circ]$. This is consistent with the discussion about the different regions done in Sect. 5.2.3. However, in the meantime, the closer to the GC we are, the worse the sensitivity is. This is amplified when taking into account the DM background in an NFW profiled host halo since it can have a large contribution toward the GC when $\langle\sigma v\rangle$ is large. See for instance the difference between the solid and dashed green curves. The number of visible point-like sources in the direction $\hat{\mathbf{n}}$ is $N_{\rm vis}(\hat{\mathbf{n}})=N_{>}^{\rm pt}(J_{\rm min}(\hat{\mathbf{n}}),\hat{\mathbf{n}},\theta_{\rm r})$. In conclusion, there is a cooperation between the two effects which tend to maximise $N_{\rm vis}(\hat{\mathbf{n}})$ where $N_{>}^{\rm pt}(J,\hat{\mathbf{n}},\theta_{\rm r})$ peaks, i.e. around 20° and 50° as emphasised by the projections of the bottom panels.

In Fig. 5.18 we present a summary plot for the dependence in position of the most detectable subhalos. We introduce $N_{\rm vis}(<\psi)=N_{>}^{\rm pt}(J_{\rm min}(\hat{\mathbf{n}}),\mathcal{P}(\psi),\theta_{\rm r})$ where $\mathcal{P}(\psi)$ is the region of angle ψ' such that $0<\psi'<\psi$. This quantity is the number of detectable point-like subhalo that are between the GC and the angle ψ. We look a two different WIMP masses and two background configurations. The annihilation cross-section is fixed to its 3σ limit after 10 yr (assuming no detection of the diffuse DM emission) and the sensitivity to point sources is also evaluated at 10 yr. The main conclusion is that if some were detectable, subhalos should be searched at $l=0^\circ$ in the bands $10^\circ\lesssim|b|\lesssim40^\circ$. This conclusion is also illustrated in the skymap Fig. 5.17 which shows the number of subhalo detectable in every direction of the sky per units of resolution solid angle for $\theta_{\rm r}=0.1^\circ$. According to the figures shown in App. E.1 the visible subhalos would then have a mass of 10^4-10^5 M$_\odot$ at $\theta_{\rm r}=0.1^\circ$ and 10^6-10^7 M$_\odot$ at $\theta_{\rm r}=1^\circ$[2]. Moreover they should be at a distance $s\sim8-10$ kpc from Earth.

The table Tab. (5.1) summarises the total number of visible point-like subhalos that we can expect to detect for different background configurations, different WIMP models, the two different Galactic profiles and the two benchmark resolution angles.

[2]Thus, they should not be impacted by the star encounters, as mentioned in the introduction of the chapter.

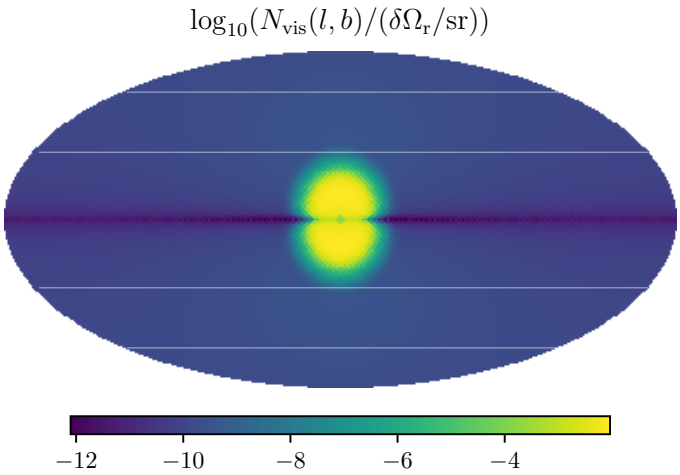

Figure 5.17 – Skymaps of the visible subhalos for a 100 GeV WIMP annihilating into $\tau^+\tau^-$ in the Fermi-LAT-like configuration. We also assume an NFW Galactic DM profile and the subhalo configuration is $(\alpha, m_{\rm min}/M_\odot, \epsilon_{\rm t}) = (1.9, 10^{-10}, 0.01)$. The annihilation cross-section is fixed to its 3σ upper bound after 10 years of observation given by the likelihood analysis for the Fermi-LAT-like recipe. The sensitivity is also fixed for 10 years of observation with a resolution angle fixed to $\theta_{\rm r} = 0.1°$. It is obtained with the likelihood analysis, including the full background, the GDE, the isotropic component and the DM diffuse emission. The horizontal lines are guides to indicate the latitudes $|b| = 30°, 60°$.

Different observation times are also compared. We give the average values as well as the confidence interval at 95%. The main conclusion is that the total number $N_{\rm vis}$ is less than 1 today (after 10 years of observation) as the DM diffuse emission still has not been detected in the two band RoI around the GC. The most optimistic scenario is found for $m_\chi = 100$ GeV and an annihilation into $b\bar{b}$, essentially because the constrain on the annihilation cross-section is slightly looser than for $\tau^+\tau^-$. Indeed $N_{\rm vis} < 3.7$ (1.3) for a cored (NFW) host halo. Nevertheless, the numbers are still compatible with 0 at a 95% confidence level. Furthermore, it seems that increasing $\theta_{\rm r}$ gives a slightly more visible subhalo which could make us think that extended subhalos may be easier to spot. However, this is not trivial as here we only evaluated the sensitivity to point-like subhalos and that of extended sources should be slightly degraded in comparison. Eventually, in the most optimistic configurations, several subhalos may become detectable after 20 years of observations, and even more if the diffuse emission DM was to be detected today. Therefore it motivates to push the observations even further as hopes for discoveries are still alive.

5.4.2 Results for the CTA analysis

For an instrument like CTA, as already mentioned, the operative time is smaller than for the Fermi-LAT and the field of view is also much more restricted. Therefore we always need to focus on specific directions of the sky and in regions with a reasonable size (in comparison to the field of view) in order to produce realistic results. Considering that CTA has an isotropic sensitivity to point source, in Fig. 5.20 we show the evolution of the number of subhalo above a constant threshold in J-factor with the angle ψ and in regions with the size the field of view. More precisely, we introduce simply

$$N^{\rm pt/e}_{>,{\rm FoV}}(J,\psi) \equiv N^{\rm pt/e}_{>}(J;\theta_{\rm r/e},\mathcal{P}_{\rm FoV}(\psi)) \tag{5.111}$$

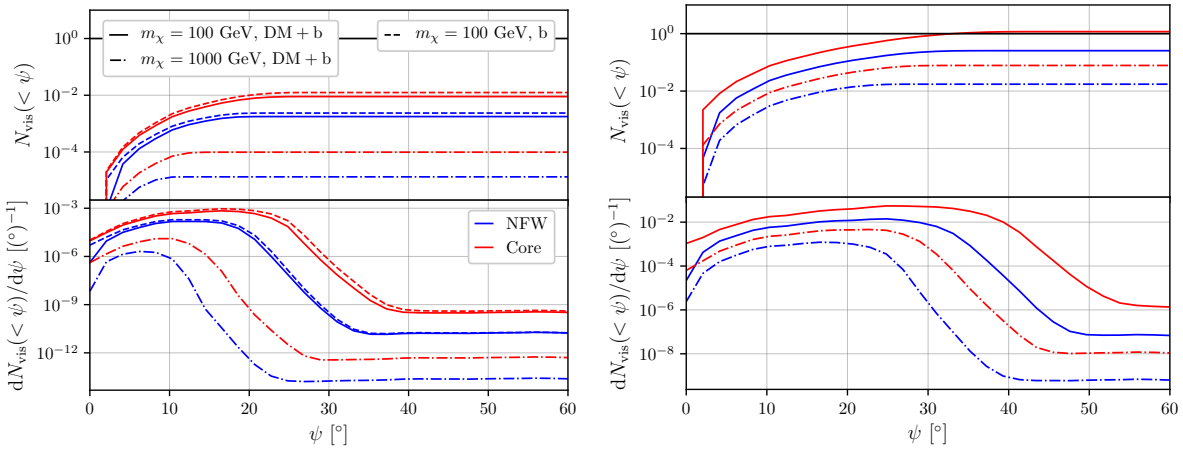

Figure 5.18 – Upper panels: Number of detectable point-like sources in the volume between the GC and the angle ψ. **Lower panel :** Angular distribution obtained from the derivation of the upper panel curves. We consider a 100 GeV and a 10^3 GeV WIMPs annihilating into $\tau^+\tau^-$ (left panel) and $b\bar{b}$ (right panel). The background is either sourced by baryons only or also by the DM diffuse emission. The annihilation cross-section is fixed at its 3σ upper limit assuming no detection of the diffuse DM component after 10 years of observations. The sensitivity to point sources is also set after 10 years of observation. The subhalo model is given by $\alpha = 1.9$, $m_{\rm min} = 10^{-10}$ $\mathrm{M}_\odot$ and $\epsilon_{\rm t} = 10^{-2}$.

for both point-like sources of extended sources and where $\mathcal{P}_{\rm FoV}(\psi)$ is the patch of the sky corresponding to the FoV around the direction $\hat{\mathbf{n}}$. However, this quantity is time consuming to evaluate numerically. Therefore it is approximated by

$$N^{\rm pt/e}_{>,\rm FoV}(J,\psi) \simeq \frac{\delta\Omega_{\rm FoV}}{\delta\Omega(\mathcal{P}^{\rm strip}_{\rm FoV}(\psi))} N^{\rm pt/e}_{>}(J;\theta_{\rm r/e},\mathcal{P}^{\rm strip}_{\rm FoV}(\psi)) \tag{5.112}$$

with $\mathcal{P}^{\rm strip}_{\rm FoV}(\psi)$ the strip between $\psi - \theta_{\rm FoV}$ and $\psi - \theta_{\rm FoV}$. Moreover in the numerator $\delta\Omega_{\rm FoV} \sim 0.024$ sr and in the denominator the solid angle of the strip is given by $\delta\Omega(\mathcal{P}^{\rm strip}_{\rm FoV}(\psi)) = 2\pi(\cos(\psi - \theta_{\rm FoV}) - \cos(\psi + \theta_{\rm FoV}))$. This figure is similar to Fig. 5.22, Fig. 5.23 and Fig. 5.24 but it is not presented as a 2D plot. The coloured line represent the contours of fixed J. The black lines are an example of the sensitivity J determined for a 10^3 GeV WIMP annihilating into $\tau^+\tau^-$ with two fixed annihilation cross-sections. While we have seen how to evaluate the sensitivity to point-like sources we must also detail how we evaluated to sensitivity to extended sources in order to plot the black lines of the lower panel. The chosen criterion goes as follows. If a source as an extension $\theta_{\rm e}$ then it is embedded in a square of $n \times n$ spatial bins with $n = \theta_{\rm e}/\theta_{\rm r}$. In practice the true total area covered by the source is $2\pi(1-\cos\theta_{\rm r}) \sim \pi\theta^2_{\rm e}$. The total area covered by the n^2 bins is $(2\theta_{\rm r} n)^2 = 4\theta^2_{\rm e}$. Therefore the the effective total number of bins in which the source shines is $\pi n^2/4$. After numerically verifying that the sensitivity is roughly proportional to the square root of the area it yields

$$J^{\rm ext}_{\rm min}(\theta_{\rm e},\hat{\mathbf{n}}) \sim J_{\rm min}(\hat{\mathbf{n}})\sqrt{\frac{\pi}{4}}\frac{\theta_{\rm r}}{\theta_{\rm r}} \tag{5.113}$$

where $J_{\rm min}(\hat{\mathbf{n}})$ is the point-like sensitivity evaluated in Sect. 5.3. In this analysis we only consider $\theta_{\rm e} = 10\theta_{\rm r}$ which is not enough to assess the detectability of all extended sources but gives a first indication. In Fig. 5.19 gives a practical example on how to evaluate $N^{\rm pt/e}_{>}(J;\theta_{\rm r/e},\mathcal{P})$ from the curve Fig. 5.6 when $\mathcal{P}$ is the region $5° \leq \psi \leq 180°$.

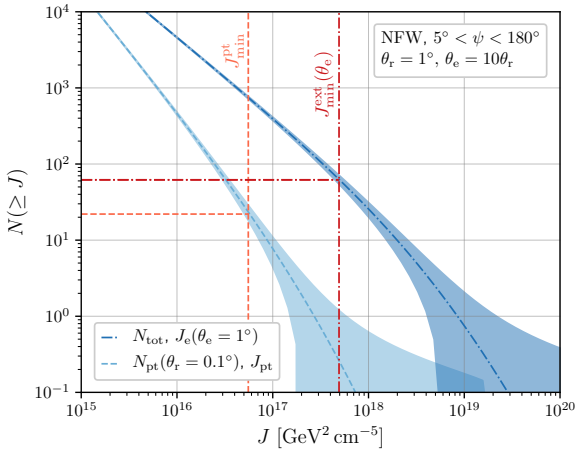

Figure 5.19 – Same than Fig. 5.6 but zoomed in and with examples of sensitivity to point sources and extended sources for $\theta_r = 0.1°$. The value of J^{pt}_{min} has been computed for a DM particle of mass $m_\chi = 10^3$ GeV annihilating via the channel $\tau^+\tau^-$, for 500 hr of observation and for an annihilation cross-section $\langle\sigma v\rangle = 10^{-23}$ cm^3 s^{-1}. The value of the J^{ext}_{min} is evaluated by Eq. (5.113). Note that here we also added the 95% confidence level bands that were only present for N_{tot} in Fig. 5.6 not to saturate the plot.

This method can be directly adapted to any sky patch.

The first remark on Fig. 5.20 is that the annihilation cross-section must be higher than the constraints set in Fig. 5.16 in order to have numbers greater than 1 for the specific WIMP model treated here – since the solid black curves representing $\langle\sigma v\rangle = 10^{-24}$ cm^3 s^{-1} are well below 1. This gives first indications that neither point-like subhalos nor extended subhalos may be detectable before the diffuse DM emission in the GC. The second remark concerns the position where we are most likely to detect these subhalos if it happens that they are. We find that the optimal region in the search of point-like clumps is $0 \lesssim \psi \lesssim 40°$ (around $\psi \sim 25°$). This is a similar conclusion to what we got in the Fermi-LAT-analysis, which is not surprising as the distribution of subhalo is the same in both cases and in the latter case the sensitivity was enhancing the probability of discovery in directions where the number of subhalo above constant threshold peaks. For extended objects the distribution is flatter and even if the region around $\psi \sim 50°$ ($\psi \sim 30°$) for $\theta_e = 1°$ ($\theta_e = 0.1°$) seems to be better suited, extended subhalos could be detected in any direction. Moreover, this plot is to be related to Fig. 5.6 and Fig. 5.7 where we already showed that Region 1 corresponding to $0° \leq \psi \leq 34°$ was the optimal region to detect point-like subhalos for an isotropic sensitivity. Besides, we also mentioned that if the threshold value of J is large enough $N^{pt/e}_{>}(J; \theta_{r/e}, \mathcal{P}_i)$ is maximal in the region 1 if $\theta_e = 1°$ and in the region 3 if $\theta_e = 0.1°$ but that the difference between region is not important. This is exactly what is shown again here but differently.

Eventually, in Fig. E.7 we show the limits set on the annihilation cross-section if we indeed do not detect a subhalo after 500 hr of observation in a patch of the size of the field of view at $\psi = 25°$ (solid lines). In comparison, the 2.71σ constraints obtained with the diffuse emission after 100 hr of observation of the GC with GDE and 0.3% of systematics is also plotted. The shaded areas correspond to the 68% and 95% confidence levels. For an NFW Galactic profile, the constraint set with the

subhalos is much larger than the constraint set by the diffuse DM emission, therefore it means that we should not detect a subhalo (point-like or extended) before the diffuse emission even with a five-time longer search of subhalos. For a cored profile the same conclusion holds even if the difference is less pronounced because the constraints on $\langle\sigma v\rangle$ from the diffuse are looser. For $\theta_{\rm r} = 0.01^\circ$ and point-like source searches (upper right panel) the confidence intervals shrink. Indeed, at such small resolution angles the number of point-like subhalo above a given J threshold J drops exponentially with J (c.f. the light dashed curves in Fig. 5.6). Therefore, the range of J corresponding to the range of fluctuations of the number of sources around 1 is smaller. Similar curves are plotted in App. E.2 for different configurations and for a uniform observation time of 100 hr in the 4 regions introduced in Sect. 5.2, which each cover a solid angle $\Delta\Omega \sim 1.05$ sr, that is 44 times larger than the field of view. Therefore spending 100 hr uniformly in all these regions may be unrealistic but allows to make comparisons. With such high exposure, the search of an extended object in a cored Galactic profile seems to get competitive with a 100 hr observation of the GC for the diffuse DM emission and the difference between regions is not discernible.

5.5 Conclusion

In this chapter, we have performed a fully consistent analysis of the detectability of point-like subhalos within a semi-analytical model. Our method is complementary to other work which relies on data analysis and/or a precise modelling of the background/foreground, cosmological simulation and/or Monte Carlo analysis. The main advantage of our work is to account with a rather simple, yet realistic model, for the correlation between the baryonic sourced background and the subhalo distribution which is impacted by the baryonic distribution in the MW through tidal stripping effects. This is especially true for the Fermi-LAT instrument which is sensitive to the pionic component and therefore to the distribution of hydrogen.

Three different questions have been addressed: *(i) Is it possible that some subhalos have been detected as unidentified sources in the Fermi-LAT catalogues? (ii) Can we expect to detect the subhalos as point-like sources before detecting the diffuse DM emission with the Fermi-LAT or CTA? (iii) If yes, then when, where and how much?* Let us summarise this entire analysis and try to extract the key points of the answer we have provided. We first have evaluated the emissivity of DM in gamma rays and introduced the notion of J-factor. In a second time, we have defined the notion of point like-subhalos and based on SL17 we have developed the statistical analysis of their J-factor. Then we have considered mock instruments resembling the Fermi-LAT and CTA for which we have given a consistent and realistic background model. Subsequently, we have derived the sensitivity to point-like subhalos and to the diffuse DM emission with a simple criterion and a more involved likelihood analysis. From there we extracted the constraints on $\langle\sigma v\rangle$ assuming no detection of the DM diffuse emission. We have shown that our results are completely consistent with the literature, which allowed us to extrapolate the constraints to any observation time. Moreover, we also established the existence of a critical constant (over time) J-factor. If a subhalo has a J-factor under the critical value it means that it will never be detectable before the discovery of the diffuse DM emission. We evidenced, with the likelihood analysis, that this critical value can slightly vary with time when the systematics of the instrument is introduced. Then, combining the statistical analysis of the J-factor and the sensitivity, we have extracted the total number of detectable subhalos in given patches of the sky for a

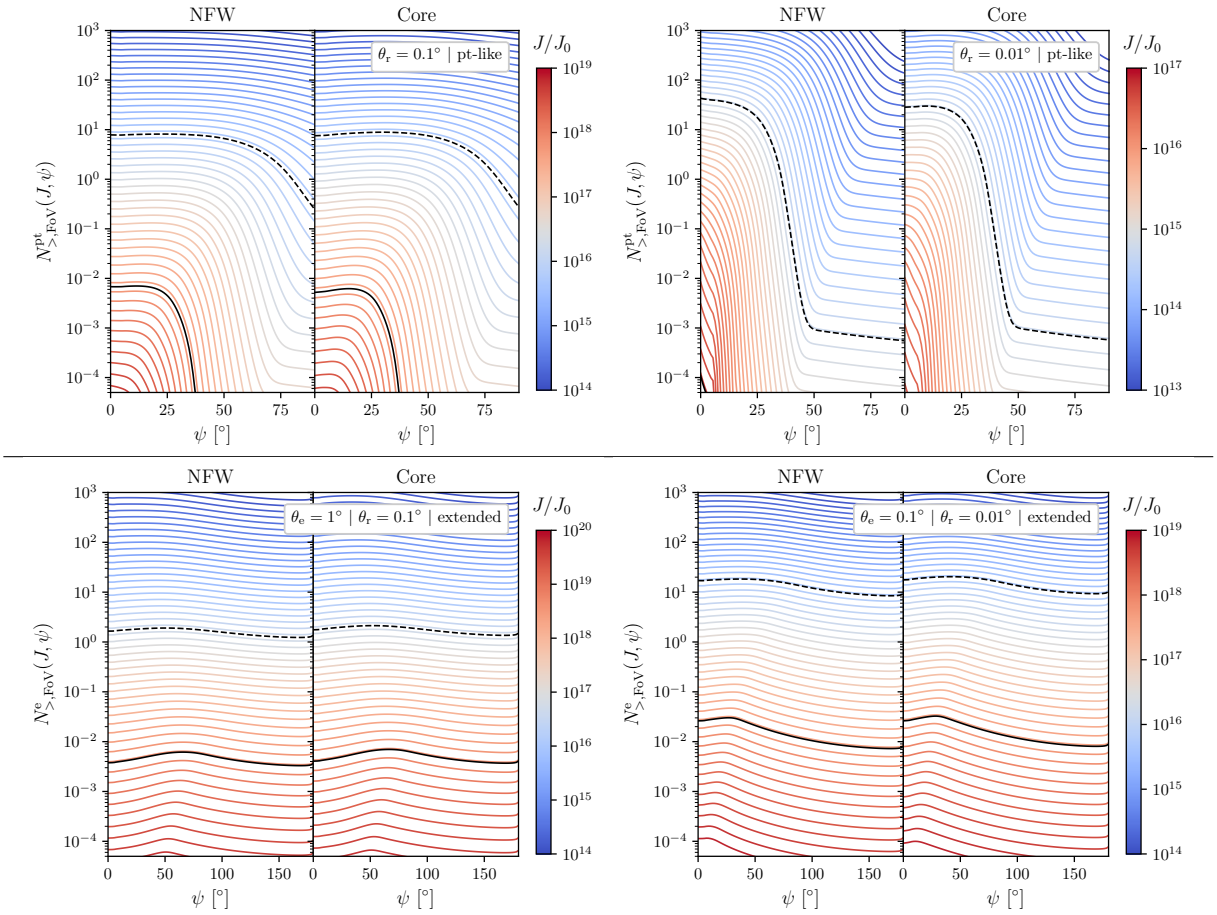

Figure 5.20 – Number $N_{\rm FoV}$ – defined in Eq. (5.111) – of sources above a given threshold in J-factor in terms of the pointing angle. The coloured level lines correspond to fixed value of J with $J_0 = 1$ GeV^2 cm^{-5}. The black lines correspond to the sensitivity of CTA for a DM particle of mass $m_\chi = 10^3$ GeV annihilating via the channel $\tau^+\tau^-$ and for 500 hr of uniform observation in the FoV. The solid line is for $\langle\sigma v\rangle = 10^{-24}$ cm^3 s^{-1} and the dashed one for $\langle\sigma v\rangle = 10^{-22}$ cm^3 s^{-1}. The upper panels are for the detection of point-like sources while the bottom panel are for the detection of extended sources with a size 10 times larger than the resolution. Note that the x-axis differs in both cases as for point-like sources the interesting range in between $\psi = 5^\circ$ and $\psi = 90^\circ$ only. The range of J-factor in the colour bar also differ.

time of observation assuming (or not) the detection of the DM diffuse emission first. In practice scanning a variety of WIMP masses and two annihilation channel as well as an NFW and a cored Galactic profile we have shown that it seems unlikely to have detected point-like subhalos as gamma-ray sources yet – which answers the question (i) – and if we do in the forthcoming future it should be a rather small number of $\mathcal{O}(1)$ even after 20 years of observation with the Fermi-LAT. For CTA it seems unlikely to ever discover a point-like subhalo unless a lot of observation time can be used for the search of point-sources or unless the annihilation cross-section is large $\langle\sigma v\rangle \gtrsim 10^{-23}$ cm^3 s^{-1} for a 10^3 GeV WIMP, in which case the DM diffuse emission should also be discovered quickly in the GC after a few hundred hours – this answers the question (ii). The most detectable subhalos should then mostly be rather massive and present toward the GC where the tidal effects have efficiently pruned them to become point-like while still large enough to provide a substantial gamma-ray emission. We evaluated that a good window of research would be $10^\circ \leq \psi \leq 40^\circ$ for both the Fermi-

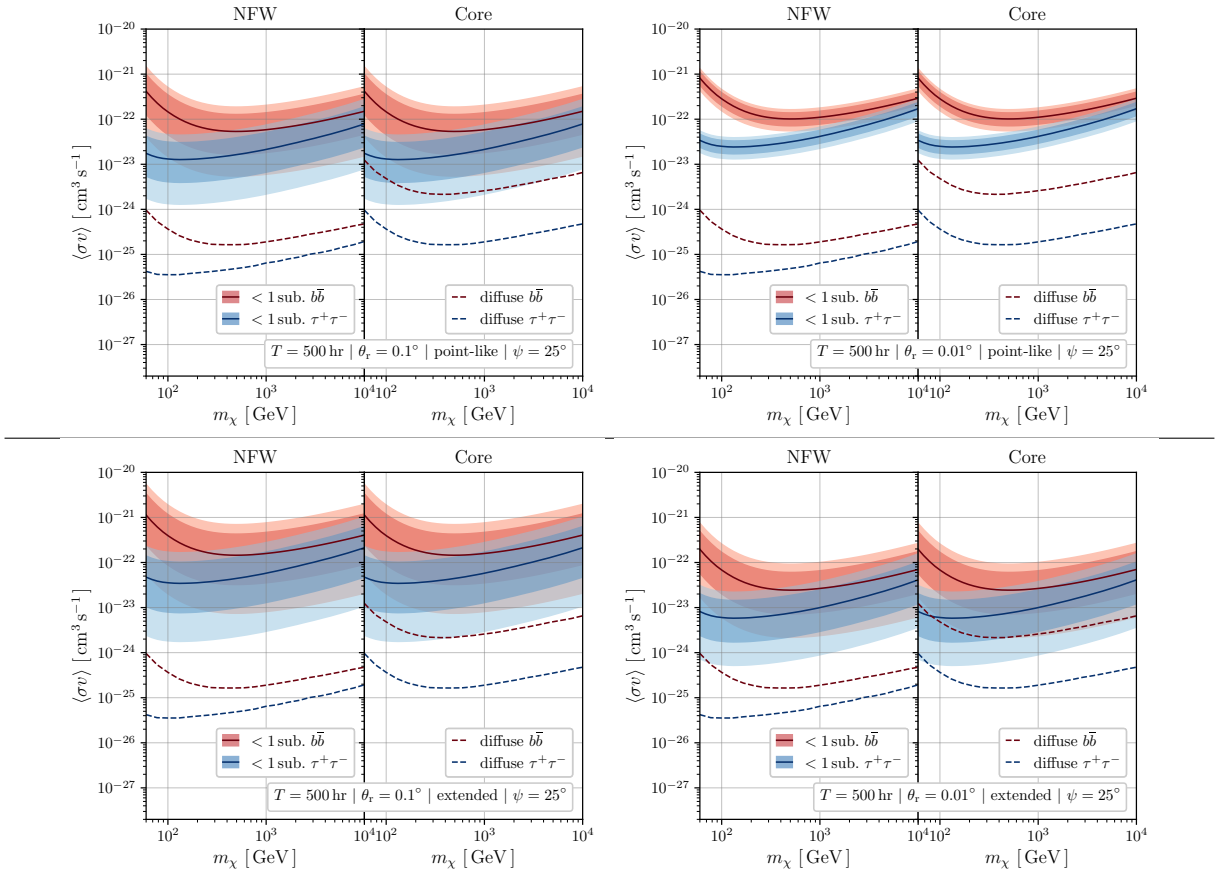

Figure 5.21 – Annihilation cross-section that is necessary to detect at least one subhalo (solid lines) with the shaded areas corresponding to the confidence levels at 68% and 95%. These curves can also be interpreted as the maximal value of the cross-section possible if no subhalos are discovered. The limit is set for a homogeneous observation of the sky over 500 hr in the FoV at $\psi = 25°$ (where detection is favoured as seen in Fig. 5.20). The comparison is made with the diffuse constraint already derived above also for an observation of 100 hr. The left panel is the limit for point-like sources and the right panel for extended objects where $\theta_e = 10 \times \theta_r$ (the extension is 10 times the angular resolution).

LAT and CTA – which answers the question (iii). In the general case, we also noticed that because a core Galactic profile tends to put a less strong constraint on $\langle\sigma v\rangle$ (as the DM density toward the GC is, by definition, not cuspy) it would be easier in that scenario to detect subhalos without the DM diffuse emission rather than in an NFW profile. As a side analysis, we have looked at estimations for the detectability of extended sources, especially in the case of CTA. It seems more probable to detect extended sources than a point-like structure although the cross-sections involved also seem to prevent a subhalo detection before the discovery of the diffuse DM emission.

In conclusion, we can wonder what it would take to obtain better results in terms of the number of detectable subhalos. First of all, we need to mention that, in fact, the chosen model for the subhalo population, that we used to extract the final numbers, has been chosen to be on the optimistic side with resilient subhalos. In a fragile subhalo scenario, the conclusions would be drastically more pessimistic as all the pruned, bright subhalos would have been destroyed around the GC. Another possibility would be to consider models that change the mass function by changing the primordial power spectrum and enhances the population of subhalos in the relevant

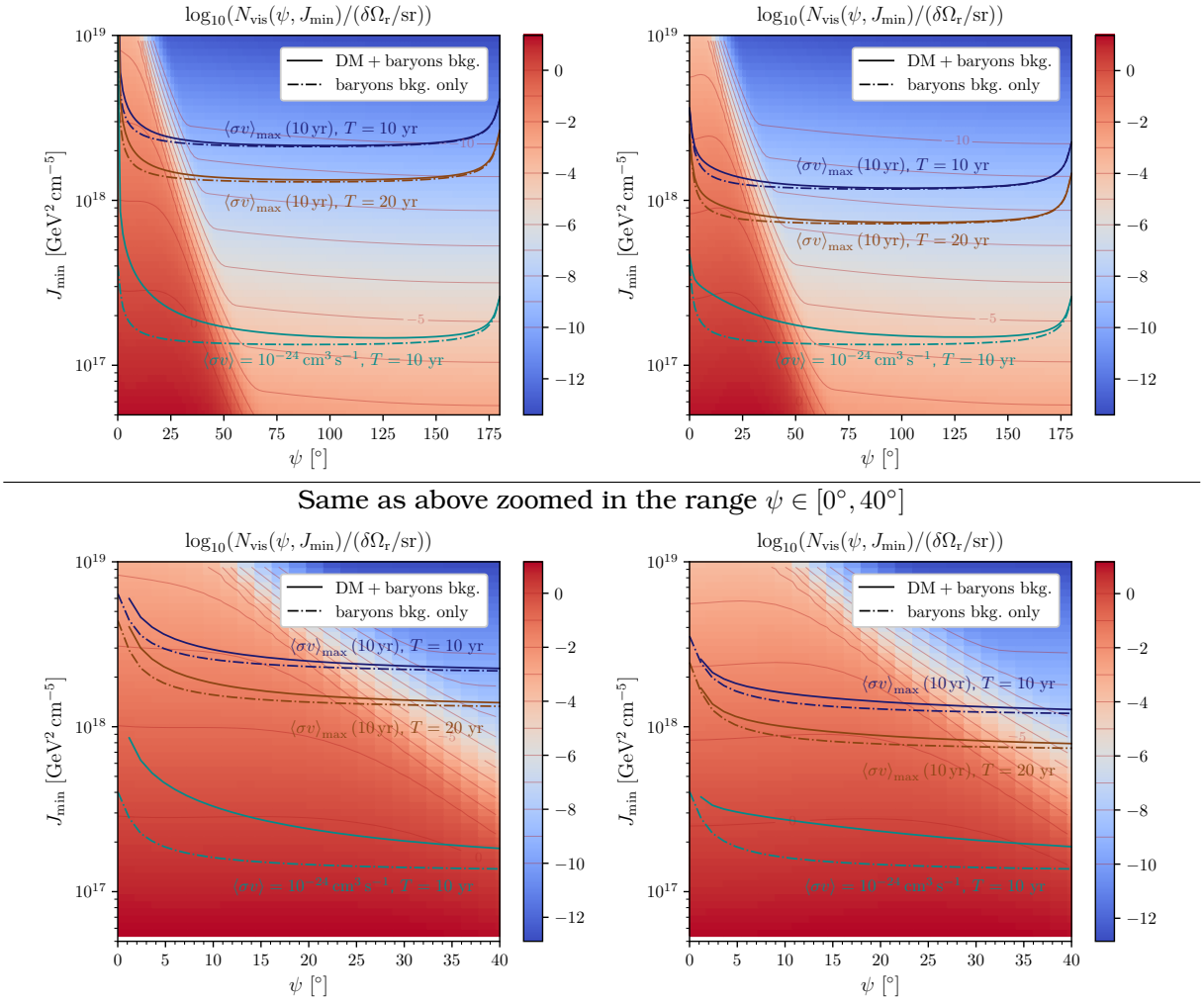

Figure 5.22 – Angular profile of visible point-like subhalos ($J > J_{min}^{(l,b)}$) assuming $\theta_r = 0.1°$ for a global NFW (left panels) or cored halo (right panels). Subhalo parameters are set to $(\alpha, m_{min}/M_\odot, \epsilon_t) = (1.9, 10^{-10}, 0.01)$. The J_{min} curves assume $\langle\sigma v\rangle$ fixed to its 3-σ limit for 10 yr or to an already excluded value of 10^{-24}cm^3/s for a 100 GeV WIMP annihilating into $\tau^+\tau^-$. Observation times of 10 and 20 yr are considered. **Top panels**: Angular distribution of subhalo J-factors (coloured), $J_{min}^{(l,b=\psi)}$ curves ($l = 0°, 180°$), and iso-$\log_{10} N_{vis}$. **Bottom panels**: Zoom in the $\psi \in [0° - 40°]$ range.

mass range for detection. A concrete physical realisation of such a model could come from primordial black holes (B. CARR et al. 2016) or ultra-compact mini halo, however, this is beyond the scope of this analysis.

5.6 Addendum: boost and Sommerfeld enhancement

When the annihilation cross-section of DM in gamma rays is velocity dependant, the generated flux may be strongly dependent on the subhalo distribution. For example, when it scales as the inverse of the velocity, subhalos, with a lower typical

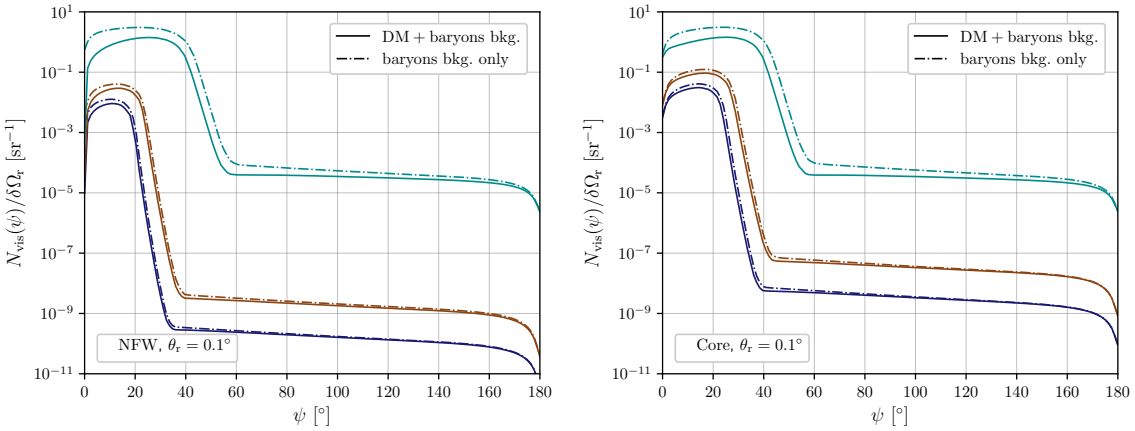

Figure 5.23 – 2-dimensional projection of Fig. 5.22 for a global NFW (left panel) or cored halo (right panel).

velocity than the host halo, can be the main source of the signal. In this section, we summarise the main results obtained in a collaboration that aims to classify different targets (clusters and dwarfs) for gamma-ray DM searches with velocity dependant annihilation cross-sections (LACROIX et al. in prep.). In particular, four cases are considered s/p-wave with/without Sommerfeld enhancement. Our contribution is twofold, the new normalisation procedure of the SL17 model already discussed in Chapter 3 and Chapter 4, which allow rescaling it to clusters and dwarfs, and the discussion on the impact of the subhalo population. Here we focus mainly on the second aspect and we start by characterising the velocity dependence of the cross-section before showing the impact of subhalos.

5.6.1 Velocity dependence of the cross-section

The Sommerfeld correction is a non-perturbative effect. In an annihilation process, it arises from the multiple self-interactions of the incoming non-relativistic DM particles through a light mediator and the formation of bound states. This is more particularly described by a Yukawa potential characterising the interactions between the incoming particles. One writes the modification of the cross-section with factors S_ℓ such that $\sigma v_{\rm rel} = a_0 S_s(v_{\rm rel}/2) + a_1 v_{\rm rel}^2 S_p(v_{\rm rel}/2) + \dots$ where a_0 and a_1 are the s and p-wave coefficients. However, these two S functions cannot be evaluated analytically for a Yukawa potential and one often relies upon the approximate Hulthén potential. It gives

$$\begin{aligned} S_s(v) &= \frac{\pi}{\epsilon_v} \frac{\sinh\left(2\pi \frac{6\epsilon_v}{\pi^2 \epsilon_\phi}\right)}{\cosh\left(2\pi \frac{6\epsilon_v}{\pi^2 \epsilon_\phi}\right) - \cos\left(2\pi \sqrt{\frac{6}{\pi^2 \epsilon_\phi} - \frac{36\epsilon_v^2}{\pi^4 \epsilon_\phi^2}}\right)} \\ S_p(v) &= \frac{\left(\frac{6}{\pi^2 \epsilon_\phi} - 1\right)^2 + \frac{144\epsilon_v^2}{\pi^4 \epsilon_\phi^2}}{1 + \frac{144\epsilon_v^2}{\pi^4 \epsilon_\phi^2}} \mathcal{S}_s(v_{\rm rel}) \end{aligned} \tag{5.114}$$

with the introduction of $\epsilon_v = \{v \equiv v_{\rm rel}/2\}/\alpha_\chi$ and $\epsilon_\phi = m_\phi/(\alpha_\chi m_\chi)$ where $\alpha_\chi = \lambda_\chi^2/(4\pi)$ is the equivalent of a fine structure constant. Here λ_χ is then the coupling constant of the mediator ϕ of mass m_ϕ to the DM particle of mass m_χ. For now on we use v instead of $v_{\rm rel}$ and we absorb the velocity dependence of the p-wave term in the Sommerfeld factor. That is, we redefine $\epsilon_v^2 S_p \to S_p$. For a simple phenomenological

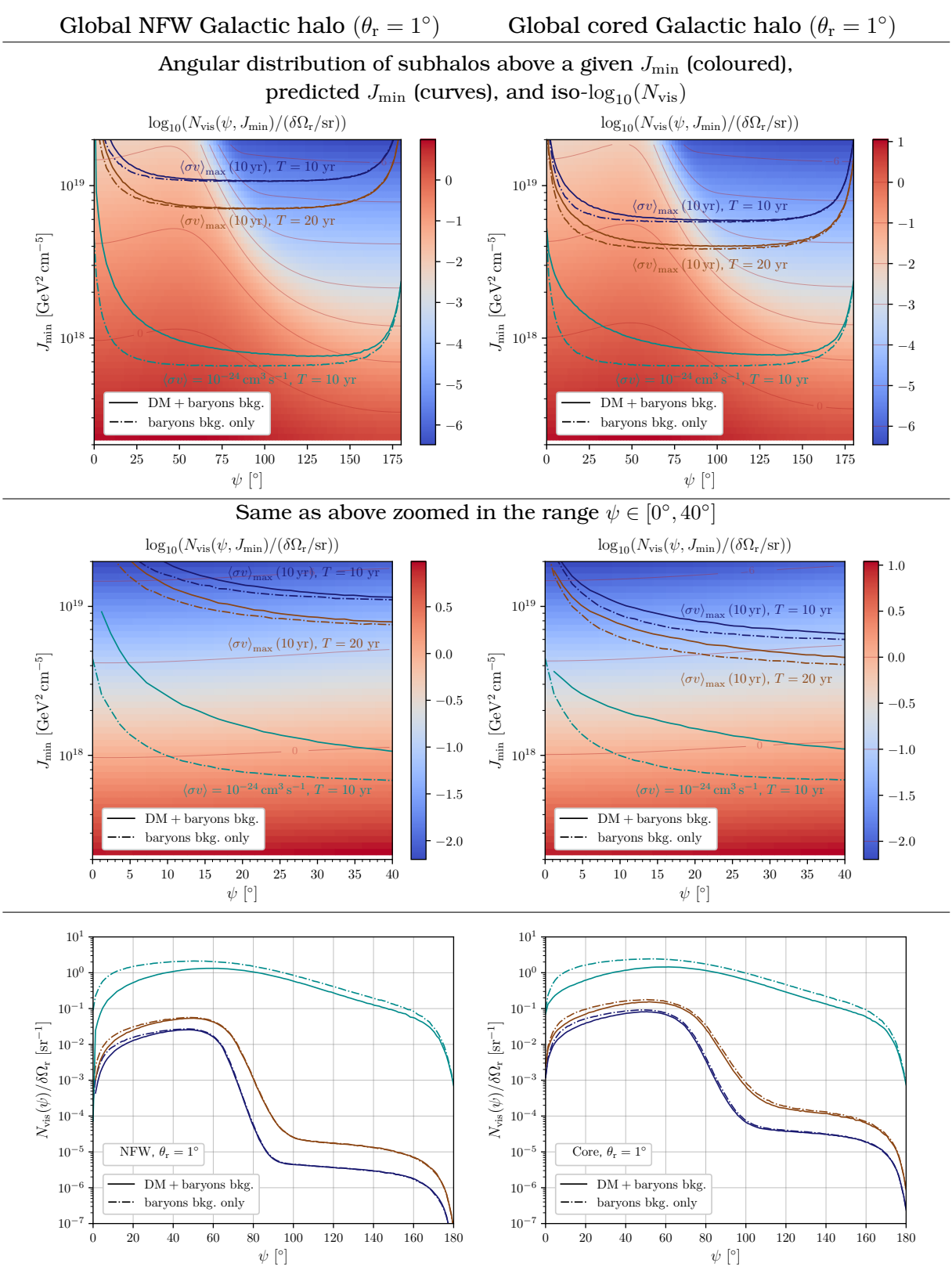

Figure 5.24 – Same as Fig. 5.22 and Fig. 5.23 for an angular resolution of $\theta_r = 1°$.

study and to understanding the different regimes in velocity one can reduce both

enhancement terms to the much simpler ansatz

$$S(\epsilon_v,\epsilon_\phi) \simeq \left(\epsilon_v^p + \frac{A_p}{\epsilon_v}\right)\left[1+\left(B_p^{\frac{1}{1+p}}\frac{\epsilon_v}{\epsilon_\phi}\right)^{-q}\right]^{-\frac{1+p}{q}} + \sum_{n=1}^{\infty}\left[(n^2-1)\epsilon_v\right]^p f_n^{\rm res}(\epsilon_v,\epsilon_\phi) \tag{5.115}$$

where we set $p = 0/2$ for the s/p-wave term. The two coefficients, A_p and B_p, can be set to recover the correct normalisation, in well defined limits, as

$$A_p = \frac{\pi}{2^p} \quad \text{and} \quad B_p = \frac{2^p 6^{1+p}}{\pi^{2p+1}}\,, \tag{5.116}$$

even though they are not really important for the discussion of the velocity effects. The parameter $q > 0$ does not play an important role as well and simply controls the transition between the two regimes where $\epsilon_v \gg \epsilon_\phi$ or $\epsilon_v \ll \epsilon_\phi$. Eventually, the function $f_n^{\rm res}$ resembles a Breit-Wigner distribution,

$$\begin{aligned} f_n^{\rm res}(\epsilon_v,\epsilon_\phi) &\simeq \frac{1}{\left(1-\frac{\pi n}{\sqrt{6}}\sqrt{\epsilon_\phi}\right)^2 + n^2\epsilon_v^2}\Theta\left[\epsilon_\phi-\epsilon_v\right] \\ &\sim \frac{1}{n^2\epsilon_v^2}\delta_{\rm D}\left[\epsilon_\phi - \frac{6}{\pi^2 n^2}\right]\Theta\left[\epsilon_\phi-\epsilon_v\right] \end{aligned} \tag{5.117}$$

and is, therefore, approximated by a Dirac distribution at first order of small ϵ_v and large n. In the following, we consider ϵ_ϕ less than 1 in order for Sommerfeld effects to possibly be important. One then distinguishes three different regimes in velocity for a fixed value of ϵ_ϕ that are:

- $1 \ll \epsilon_v$: No Sommerfeld enhancement, $S \simeq \epsilon_v^p$.
- $\epsilon_\phi \ll \epsilon_v \ll 1$: Coulomb regime, $S \simeq A_p \epsilon_v^{-1}$
- $\epsilon_v \ll \epsilon_\phi \ll 1$: Saturation/resonance regime.

In the last scenario resonances appear where $f_n^{\rm res}$ is close to its maximum, therefore for $\epsilon_\phi \sim 6/(\pi n)^2$. Otherwise, one simply gets the saturation behaviour dictated by the right hand term of Eq. (5.115). All in all, in the saturation/resonance regime, the enhancement factor goes as

$$S \simeq \begin{cases} [\pi^2\epsilon_\phi/6)]^{1-p}\epsilon_v^{p-2} \propto \epsilon_v^{p-2}/\epsilon_\phi^{p-1} & \text{(resonance)} \\ A_p B_p(\epsilon_v/\epsilon_\phi)^p/\epsilon_\phi \propto \epsilon_v^p/\epsilon_\phi^{1+p} & \text{(saturation)}\,. \end{cases} \tag{5.118}$$

The evolution of the enhancement factor with ϵ_ϕ is illustrated in Fig. 5.25. The dash-dotted and dashed lines show where the resonance peaks and the saturation minima are, according to our ansatz. We see that we recover the correct behaviour. Moreover one can also check that the value of the plateau corresponding to the Coulomb regime, for ϵ_ϕ small and $\epsilon_v < 1$ in the figure, the enhancement factor goes indeed as ϵ_v^{-1}.

In a DM structure, particles velocity spans a wide range of values, from 0 to the escape velocity. Thus, different regimes may play a role simultaneously. As there always are particles with a low velocity, the saturation/resonance regime should, a priori, always have an impact if $\epsilon_\phi < 1$. However the velocity distribution is peaked and some phase-space regions, if not populated enough, do not actually contribute

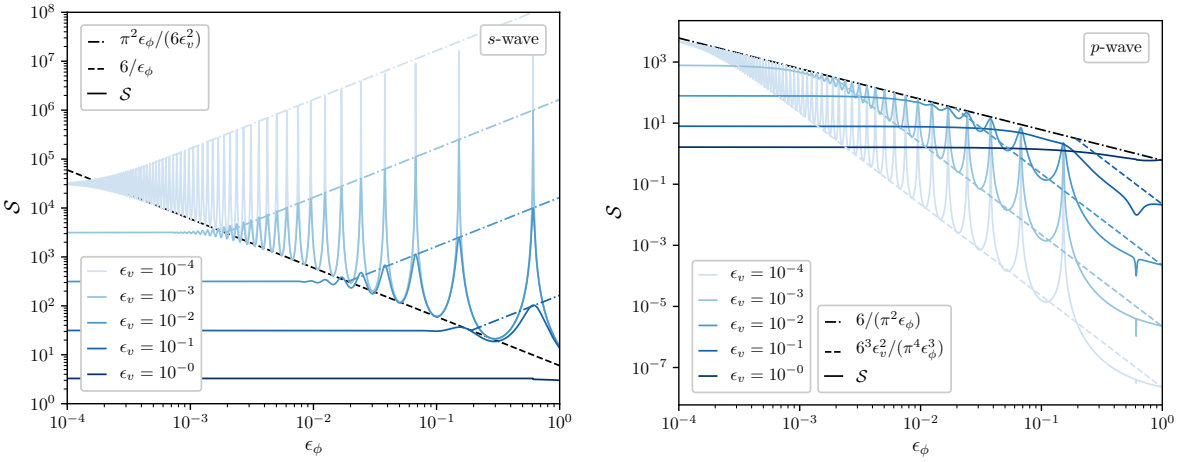

Figure 5.25 – Evolution of the Sommerfeld enhancement factor with the ratio ϵ_ϕ for fixed values of ϵ_v. **Left panel:** s-wave. **Right panel:** p-wave (note that we absorbed the v^2 dependence be redefining the enhancement factor). We also represent the scaling, induced by our simple ansatz, for the resonance peaks and the saturation minima with dash-dotted and dashed lines respectively.

significantly. In practice, we noticed that one can approximate the total Sommerfeld enhancement in a halo simply by looking at the circular velocity at the scale radius $\overline{v} \sim (G_{\rm N} m(r_{\rm s})/r_{\rm s})^{1/2}$. This special velocity is associated to the factor $\overline{\epsilon_v}$. Let us assume that $\bar{\epsilon}_v \equiv \epsilon_0 (m/m_0)^\nu$ where m is the cosmological mass and ϵ_0 and m_0 normalisation constants that do not need to be made explicit. According to the relations between the scale parameters and the virial parameters one finds $\nu \simeq 1/3$. This also defines a bijection between the mass and the parameter ϵ_ϕ. We introduce $m_\star(\epsilon_\phi) \equiv m_0 (\epsilon_\phi/\epsilon_0)^{1/\nu}$ and $\epsilon_\phi^\star(m) \equiv \overline{\epsilon_v} = \epsilon_0 (m/m_0)^\nu$ such that $m_\star(\epsilon_\phi^\star) = 1$. Therefore, we define $S(m, \epsilon_\phi) \equiv S(\overline{\epsilon_v}, \epsilon_\phi)$ and we translate the discussion of the different velocity regimes into a discussion of different mass regimes where

$$\begin{cases} m_\star(1) \ll m : & S \propto m^{\nu p} \quad \text{(no enhancement)} \\ m_\star(\epsilon_\phi) \ll m \ll m_\star(1) : & S \propto m^{-\nu} \quad \text{(Coulomb)} \\ m \ll m_\star(\epsilon_\phi) \ll m_\star(1) : & S \propto \begin{cases} m^{\nu(p-2)}/\epsilon_\phi^{p-1} & \text{(resonance)} \\ m^{\nu p}/\epsilon_\phi^{1+p} & \text{(saturation)} \,. \end{cases} \end{cases} \tag{5.119}$$

The value of $m_\star(\epsilon_\phi)$ sets the transition between the Coulomb and resonance/saturation regimes. The mass dependency can be summarised under a simple index s_m, such that $S \propto m^{-s_m} \epsilon_\phi^{-\gamma}$. In the left panel of Fig. 5.26 we show the different regimes associated to halos of three different masses; 10^6 $\mathrm{M}_\odot$, 10^{12} $\mathrm{M}_\odot$ and 10^{15} $\mathrm{M}_\odot$. The left curves represent the velocity distribution (not normalised) at the scale radius, obtained with the Eddington inversion method and assuming an infinite NFW profile. The solid horizontal lines mark the circular velocity at the scale radius. The dashed vertical lines give the associated value $\epsilon_\phi^\star(m)$. This highlights the fact tha,t because of the extension of the velocity distribution, several regimes can contribute at the same time. Besides, it also shows that, nonetheless, the velocity distribution is narrow enough to justify the identification between the circular velocity and the mass of the structure.

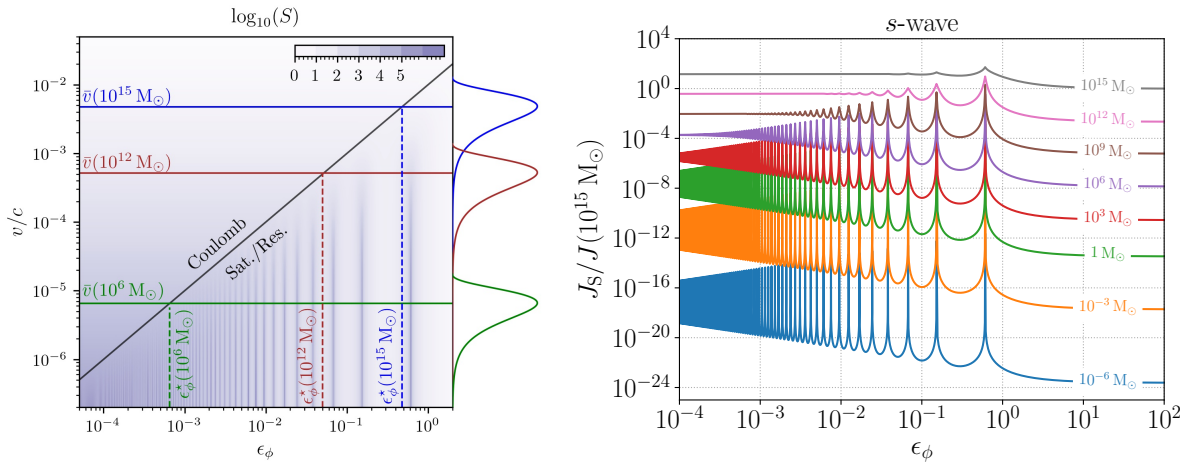

Figure 5.26 – Left panel: Saturation velocity as a function of ϵ_ϕ (solid black curve), delineating the transition between the Coulomb and saturation regimes. The Sommerfeld factor is represented as the third dimension (purple color scale), as a function of velocity v and ϵ_ϕ. The characteristic speeds of 10^{15}, 10^{12}, and $10^6\,\mathrm{M}_\odot$ halos are indicated, with the corresponding (unnormalized) full Eddington velocity distribution taken at the scale radius, along the right vertical axis for illustration. **Right panel:** Sommerfeld-enhanced J-factors as a function of ϵ_ϕ for DM halos of different masses, assuming an s-wave annihilation. Figure taken from Lacroix et al. (in prep.).

In the right panel of Fig. 5.26 we show the Sommerfeld-enhanced J-factor for several halos of different masses. Let us discuss the case of the three masses 10^6 $\mathrm{M}_\odot$, 10^{12} $\mathrm{M}_\odot$ and 10^{15} $\mathrm{M}_\odot$ reported on the left panel of the same figure. For 10^{15} $\mathrm{M}_\odot$ almost the whole phase space is within the Coulomb regime for all values of ϵ_ϕ. This is due to the large value $\epsilon_\phi^\star \simeq 0.5$. One barely witnesses any saturation peak except for the first one at $\epsilon_\phi \simeq 2/3$. The small but visible second and third peaks are due to a small fraction of phase space *leaking* on the saturation/resonance regime at slightly smaller values of ϵ_ϕ. For 10^{12} $\mathrm{M}_\odot$ one has $\epsilon_\phi^\star \simeq 0.05$. For higher values, the bulk of the phase space is in the saturation/resonance regime, hence the clear presence of the peaks. For lower values it goes to the Coulomb regime but some part of the phase space remains in the saturation/resonance regime for values of ϵ_ϕ slightly lower than 0.05. This explains, again, the presence of peaks down to $\epsilon_\phi \sim 10^{-2}$. Eventually, similar conclusions hold for 10^6 $\mathrm{M}_\odot$ with $\epsilon_\phi^\star \simeq 5 \times 10^{-4}$.

5.6.2 The impact of subhalos in a target halo

In order to understand the impact of subhalos on the J-factor of a target, one recalls the individual properties first. For a subhalo of mass m, without Sommerfeld enhancement, the J-factor goes as $J(m) \propto mc^3 \propto m^{1-3\varepsilon}$, where we assume here $c \propto m^{-\varepsilon}$ for simplicity. Adding the Sommerfeld enhancement is a priori non trivial – *c.f.* the expression in Eq. (5.12). Nonetheless, following our identification between circular velocity and cosmological mass one can approximate the enhanced J-factor by

$$J_S(m) \simeq J_0 S(m, \epsilon_\phi) J(m) \propto \epsilon_\phi^{-\gamma} \left(\frac{m}{m_0}\right)^{1-3\varepsilon-s_m} . \tag{5.120}$$

We now recall that the J-factor of a structure is its luminosity over its distance squared to the observer. Moreover, for non overlapping subhalos the luminosities

add. Therefore, the total impact of subhalos in a given host at a fixed distance from us is obtained by integrating the J-factor population as

$$J_S^{\rm sub}(\epsilon_\phi) = \int_{m_{\rm min}}^{m_{\rm max}} j_S(m,\epsilon_\phi) {\rm d}\ln m \quad \text{with} \quad j_S(m,\epsilon_\phi) \equiv m \frac{{\rm d}N_{\rm sub}}{{\rm d}m} J_S(m,\epsilon_\phi) \tag{5.121}$$

and with ${\rm d}N_{\rm sub}/{\rm d}m$ the evolved mass function that we take proportional to the power law $m^{-\alpha}$. We write the differential j-factor as $j_S(m,\epsilon_\phi) \propto \epsilon_\phi^{-\gamma} m^{-\beta}$ where $\beta \equiv \alpha - 2 + 3\varepsilon - s_m$. For most applications one can consider that $m_{\rm max} < m_\star(1)$ and the entire mass range is subject to enhancement (as long as $\epsilon_\phi < 1$). According to the value of s_m, the computation then relies on the associated indices

$$\begin{cases} \beta_{\rm c} &= \alpha - 2 + 3\varepsilon + \nu \quad \text{and} \quad \gamma_{\rm c} = 0 \\ \beta_{\rm res} &= \alpha - 2 + 3\varepsilon - \nu(p-2) \quad \text{and} \quad \gamma_{\rm res} = p - 1 \\ \beta_{\rm sat} &= \alpha - 2 + 3\varepsilon - \nu p \quad \text{and} \quad \gamma_{\rm sat} = 1 + p\,. \end{cases} \tag{5.122}$$

and the total J-factor can be decomposed as

$$J_S^{\rm sub}(\epsilon_\phi) = J_{S,{\rm c}}^{\rm sub}(\epsilon_\phi) + J_{S,{\rm res}}^{\rm sub}(\epsilon_\phi) + J_{S,{\rm sat}}^{\rm sub}(\epsilon_\phi)\,. \tag{5.123}$$

After integration these three terms take the form

$$\begin{aligned} J_{S,{\rm c}}^{\rm sub}(\epsilon_\phi) &\propto \Theta\left(m_{\rm max} - m_\star(\epsilon_\phi)\right) \frac{-\epsilon_\phi^{-\gamma_{\rm c}}}{\beta_{\rm c}} \left[\left(\frac{m}{m_0}\right)^{-\beta_{\rm c}}\right]_{\max\{m_\star(\epsilon_\phi), m_{\rm min}\}}^{m_{\rm max}} \\ J_{S,{\rm sat}}^{\rm sub}(\epsilon_\phi) &\propto \Theta\left(m_\star(\epsilon_\phi) - m_{\rm min}\right) \frac{-\epsilon_\phi^{-\gamma_{\rm sat}}}{\beta_{\rm sat}} \left[\left(\frac{m}{m_0}\right)^{-\beta_{\rm sat}}\right]_{m_{\rm min}}^{\min\{m_\star(\epsilon_\phi), m_{\rm max}\}} \\ J_{S,{\rm res}}^{\rm sub}(\epsilon_\phi) &\propto \sum_n \delta_{\rm D}\left[\epsilon_\phi - \frac{6}{(\pi n)^2}\right] \Theta\left(m_\star(\epsilon_\phi) - m_{\rm min}\right) \frac{-\epsilon_\phi^{-\gamma_{\rm res}}}{\beta_{\rm res}} \left[\left(\frac{m}{m_0}\right)^{-\beta_{\rm res}}\right]_{m_{\rm min}}^{\min\{m_\star(\epsilon_\phi), m_{\rm max}\}}\,. \end{aligned} \tag{5.124}$$

For a realistic value of the mass index $\alpha \simeq 1.95$ and with $\nu \simeq 1/3$ and $\varepsilon \simeq 0.05$ one has $\beta_{\rm c} > 0$, $\beta_{\rm sat} < 0$. For the resonance term, the sign depends on whether we are in the s-wave or p-wave scenario through the value of p. This means that all the subhalos contribute to the s-wave resonances, while only the subhalos with a mass above $m_\star(\epsilon_\phi)$ contribute to the p-wave resonances. We are mainly interested in the evolution of the J-factor with ϵ_ϕ. Using the bijection between the mass and ϵ_ϕ we can characterise three regions according to the value of the latter and to the values of $\epsilon_\phi^\star(m_{\rm min})$ and $\epsilon_\phi^\star(m_{\rm max})$. The behaviour of the three components is summarised in Tab. (5.2). Note that the J-factor may also be mostly dominated by the smooth component of the host halo, especially at large ϵ_ϕ, where the Sommerfeld correction is mild or null. The cross-term can, however, be safely neglected. Indeed it is already negligible without Sommerfeld enhancement in comparison to the smooth and subhalo contributions (and therefore often omitted in the literature). Furthermore, it corresponds to the annihilation of particles in subhalos with particles of the smooth distribution, occurring with a velocity of the order of the velocity dispersion in the host.

In Fig. 5.27 we show the Sommerfeld-enhanced J-factor (including or not the subhalo contribution), represented with respect to ϵ_ϕ for one galaxy cluster (Fornax), two dwarf spheroidal galaxies (Draco and Ursa Major II), and one dwarf irregular galaxy (IC10). In these plots one has $\epsilon_\phi > \epsilon_\phi^\star(m_{\rm min})$. Let us focus on Fornax which experiences a large subhalo boost, even when Sommerfeld enhancement is null

s-wave	$\epsilon_\phi < \epsilon_\phi^\star(m_{\rm min})$	$\epsilon_\phi^\star(m_{\rm min}) < \epsilon_\phi < \epsilon_\phi^\star(m_{\rm max})$	$\epsilon_\phi^\star(m_{\rm max}) < \epsilon_\phi < 1$
$J^{\rm sub}_{S,{\rm c}}(\epsilon_\phi)$	cst.	$\propto \epsilon_\phi^{-\beta_{\rm c}/\nu} \sim \epsilon_\phi^{-1.3}$	x
$J^{\rm sub}_{S,{\rm sat}}(\epsilon_\phi)$	x	$\propto \epsilon_\phi^{-1}$	$\propto \epsilon_\phi^{-1}$
$J^{\rm sub}_{S,{\rm res}}(\epsilon_\phi)$	x	$\propto \epsilon_\phi$	$\propto \epsilon_\phi$

p-wave	$\epsilon_\phi < \epsilon_\phi^\star(m_{\rm min})$	$\epsilon_\phi^\star(m_{\rm min}) < \epsilon_\phi < \epsilon_\phi^\star(m_{\rm max})$	$\epsilon_\phi^\star(m_{\rm max}) < \epsilon_\phi < 1$
$J^{\rm sub}_{S,{\rm c}}(\epsilon_\phi)$	cst.	$\propto \epsilon_\phi^{-\beta_{\rm c}/\nu} \sim \epsilon_\phi^{-1.3}$	x
$J^{\rm sub}_{S,{\rm sat}}(\epsilon_\phi)$	x	$\propto \epsilon_\phi^{-3-\beta_{\rm sat}/\nu} \sim \epsilon_\phi^{-1.3}$	$\propto \epsilon_\phi^{-3}$
$J^{\rm sub}_{S,{\rm res}}(\epsilon_\phi)$	x	$\propto \epsilon_\phi^{-1}$	$\propto \epsilon_\phi^{-1}$

Table 5.2 – Dependence in ϵ_ϕ of all the Sommerfeld-enhanced J-factors.

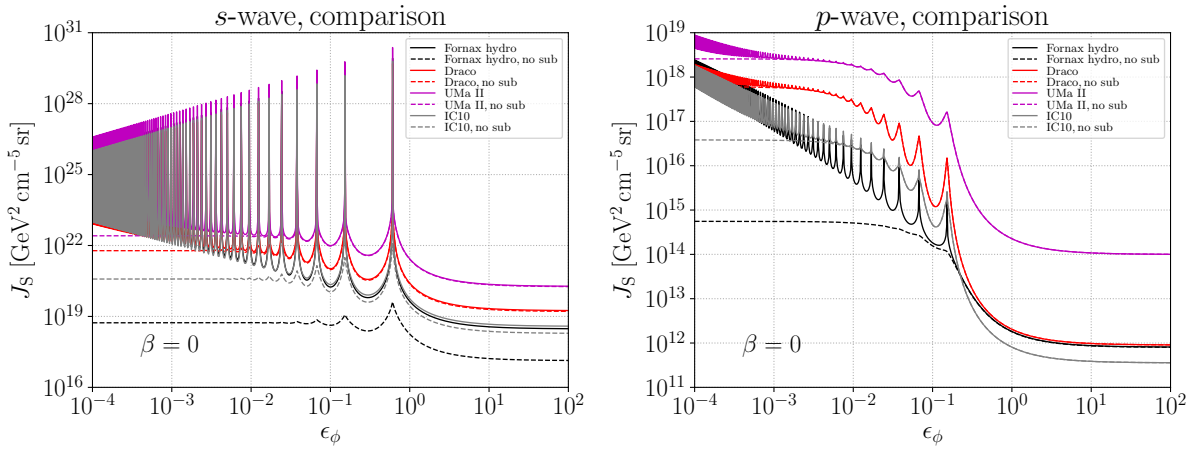

Figure 5.27 – Figures taken from LACROIX et al. (in prep.). Sommerfeld-enhanced J-factor for four different targets whether the subhalo contribution is included (solid lines) or not (dashed lines). Note that they are a factor 4π higher than what it would be with our own definition of the J-factor (and also have an extra unit of steradians). To fasten the numerical evaluation, the full phase-space distribution is not integrated over as is should be from Eq. (5.12). The computation relies on an approximation through typical velocities evaluated as moments of the PSDF, with the Eddington formalism, assuming no anisotropy. The latter being characterised by a parameter called β, hence the notation $\beta = 0$. More details are given in the original publication. **Left panel:** s-wave case. **Right panel:** p-wave case.

in the s-wave scenario. For this structure, at small ϵ_ϕ, when the host is already deeply in the Coulomb regime one can clearly witness the impact of the subhalos that further enhance the J-factor by several orders of magnitude. Moreover, one can approximate that $\epsilon_\phi^\star(m_{\rm max}) \sim 0.05$. Then, the subhalo behaviour is dominated by the regime $\epsilon_\phi^\star(m_{\rm min}) < \epsilon_\phi < \epsilon_\phi^\star(m_{\rm max})$. We can verify that the scaling, with ϵ_ϕ, of the peaks and minima is consistent with the corresponding values given in Tab. (5.2).

In conclusion, the presence of subhalos in a Sommerfeld-enhanced scenario can tremendously boost the J-factor in different targets for gamma-ray searches and especially in galaxy clusters. We have shown here an simple analytical model for the subhalo contribution of the J-factor dependence with ϵ_ϕ. This allows us to better understand the results of the extensive numerical computation that yield the curves of Fig. 5.27. Further developments and details can be found in LACROIX et al. (in prep.).

VI

Conclusion

Although numerical simulations are not able to fully characterise the DM distribution on the entire sub-galactic scale range, they have shown tension between the ΛCDM model predictions and the observations in the last decades. Besides, assuming that very small DM clumps exist they may provide interesting characteristic signatures yielding a substantial impact for current or next-generation direct or indirect detection experiments. Therefore the DM fine-grained structure in the Universe is, more than ever, worth being investigated. In this work, I have explored many aspects of DM structuring on small scales throughout these four interdependent chapters. The main goal was to provide a new or consolidated analytical insight on DM distribution and its intrinsic nature: from the subhalo population in the MW and other astrophysical objects to the impact for (indirect) detection experiments, through its relation to particle models.

In Chapter 2, I reviewed the thermodynamics of WIMPs in the early Universe and their chemical and kinetic decouplings. Then, I introduced a simplified particle model which can be explored with a C++ code that I developed from scratch. It allows relating particle physics properties to the minimal cosmological mass of halos. I performed an illustrative analysis of two scenarios (constrained by the DM abundance) including a scalar and a pseudoscalar mediator respectively. I showed the pertinent behaviours of the different cross-sections involved, especially with the velocity and I extracted the main scaling relations between the coupling constant, the particle masses and the minimal mass of subhalos. I particularly evaluated the self-interaction cross-section and compared it to the expected values to solve the small scale cusp-core issue. In the low mass scalar mediator scenario, self-interactions can become sufficiently important to enter the SIDM regime. Eventually, I discussed the possible consequences for detection experiments. This analysis shows how probing the signature of small structures can tell us more about DM particle nature.

In Chapter 3, I reviewed the framework underlying the formation of halos in the CDM paradigm, from quantum fluctuations to growth, collapse and virialisation. Afterwards, I summarised some notions of excursion set theory and the associated merger trees. Using one such algorithm I evaluated the first order subhalo mass function in a given host halo for the entire mass range (up to 30 orders of magnitude) using a physically motivated constrained fit. This fit gives a power low scaling, $m^{-\alpha}$ at small mass, with $\alpha \sim 1.95$ and produces a realistic behaviour at large mass. Thus, I gave a new calibration method of the SL17 model that no longer depends on cos-

mological simulations. I compared my results to similar studies in the literature and found reasonable agreements. Furthermore, my fit was then used to study the effect of Sommerfeld enhancement in various size objects, from dwarfs to clusters.

In Chapter 4 I introduced the details of the SL17 model and I showed how one can derive the current distribution of subhalos in a galaxy like the MW from the cosmological distribution with the addition of tidal effects. More importantly, I introduced a new analytical study of stellar encounters and their impact on the total population of subhalos. I improved the usual calculation done in the literature to account for the impact of one star on a single subhalo. Subsequently, I derived the effect of the entire stellar disc. In order to be as precise as possible, I performed a full probabilistic treatment of the energy gain of the particle inside the structure. I showed the approximate impact on the subhalo profile. Note that, this analysis, centred on the central limit theorem happens to exhibit several subtleties which had to be taken into consideration. Eventually, using the recipe of SL17, I showed the consequences for the total subhalo population, the subsequent mass function and the subhalo number density. The results point towards important effects on the lighter subhalos in the central regions of the Galaxy (< 10 kpc). Stellar encounters can even enhance the disruption of fragile subhalos and deplete their local number density. If subhalos are resilient, stars still strongly prune them. This may have different effects for detection experiments depending on the local distribution of DM and lead to interesting signatures (such as the heating of the Galactic disc).

In Chapter 5, using the SL17 model, I evaluated the probability to detect subhalos as point-like sources of gamma rays with Fermi-LAT-like and CTA-like experiments. With an analytical model for the baryonic diffuse emission correlated to SL17, I have analysed if we could realistically hope to observe one subhalo before detecting the diffuse DM emission (due to to the smooth distribution and to the unresolved sources) in the MW. This study was motivated both by the presence of 1525 non-associated point-sources in the fourth Fermi-LAT catalogue and the future launch of the more precise experiment CTA. I have shown that, with both instruments, the diffuse emission is more likely to be detected first, even though some optimistic configurations may predict $\mathcal{O}(10)$ visible structures in the years to come. I derived the regions of the sky where one should search for the emission of point-like subhalos in order to optimise the probabilities (around $20°$ to $60°$ from the GC) and thus set a guide for the experimental collaborations. The results being model-dependent a detection or a non-detection detection with more collected data will help, in any case, to obtain information on the nature of DM and/or on its distribution in the Galaxy or to further constrain the models.

Since the emergence of the missing mass problem, all the observational and experimental efforts invested in DM search have been pending an unambiguous detection. The current research around DM gets more and more exciting with the new experiments and data releases coming up. One can cite for instance (amongst many) CTA, Gaia, SKA, all the observatory of the 21-cm signal, the space-based laser interferometers, the next generation direct detectors etc. The fine-grained structuring may be particularly interesting to learn more about DM nature in the future. Small scales already point towards tensions or inconsistencies emerging in the current cosmological paradigm. The detection of a single light substructure would give critical information on DM intrinsic constitution. In this context, it becomes crucial to accurately model the full DM distribution. Analytical models, such as the one I have contributed to in this work, are very powerful tools to describe the entire

population of subhalos in the Galaxy and other objects. Working at the crossroad between particle physics, cosmology, astrophysics and gravitational dynamics, in a consistent global picture, further brings the various connections between different aspects of the models and enhances the different constraints and detection prospects.

This entire document can be divided in several articles:

- (FACCHINETTI et al. 2020): Facchinetti G., Lavalle J. Stref M., *Statistics for dark matter subhalo searches in gamma rays from a kinematically constrained population model. I: Fermi-LAT-like telescopes*, submitted to physical review D. Based on Chapter 5
- Facchinetti G., Lavalle J. Stref M., *Statistics for dark matter subhalo searches in gamma rays from a kinematically constrained population model. II: CTA-like telescopes*. Based on Chapter 5.
- Facchinetti G, Stref M. Lavalle J., *Effect of stars on the Galactic dark matter subhalo population*. Chapter 4
- Facchinetti G, Lavalle J., *Subhalo population in a simplified dark matter model*. Based on Chapter 2 and the end of Chapter 3
- Lacroix T., Facchinetti G., Pérez-Romero J., Stref M., Lavalle J., Maurin D., Sánchez-Conde M. A., *Classification of targets for gamma-ray dark matter searches with velocity-dependent annihilation and substructure boost I: detailed prediction*. I contributed to this collective work by providing the subhalo mass function for the SL17 that allows its application to various size objects. This point is discussed in Chapter 3. Besides, I participated in the discussions for the interpretation of the results.

Most of the articles listed above have been or are on the verge to be submitted – except for the full study of the simplified model which is an ongoing task. This thesis paves the way toward further improvements around the SL17 model and new studies, related to this work, are foreseen. In particular, I would like to make the model able to properly describe the halo distribution at higher redshifts, with the aim to use it in different contexts (*e.g.* for the study of the 21 cm line). In addition, I should also resume working on the DM phenomenology in the CP-odd sector of the NMSSM that takes place in a larger collaboration around a project of supergravity. Eventually, on a larger time scale, I also want to search for new possible collaborations. Firstly, with experts of simulations or Newtonian dynamics, to work around the stellar encounters and more generally on the impact of tidal effects. Secondly with CMB experts to further develop around the simplified model. I would like to plug in DM interactions beyond the effective-coupling way and track more systematically velocity-dependent signatures. To conclude, I look forward to many new projects on DM related topics.

Appendices

A

Mathematical and numerical tools

This appendix is devoted to detail the different mathematical and numerical tools used in this work. We start by defining several special functions. Then we introduce notions of probabilities that are largely used in different analysis and in particular we focus on the central limit theorem. Afterwards, we describe the maximisation algorithm used in our likelihood analysis and the Fourier transform. Eventually, we give the structure of our codes.

A.1 Common special functions

A.1.1 Error function and its complementary

The error function and the complementary error function are defined as

$$\mathrm{erf} : \begin{cases} \mathbb{R} \to &]-1,1[\\ x \mapsto & \dfrac{2}{\sqrt{\pi}} \displaystyle\int_0^x e^{-t^2} \mathrm{d}t \end{cases} \quad \text{and} \quad \mathrm{erfc} : \begin{cases} \mathbb{R} \to &]0,2[\\ x \mapsto & 1 - \mathrm{erf}(x) \end{cases} \tag{A.1}$$

This function are of particular interest when studying Gaussian probability distribution functions as the erf function gives the cumulative distribution function and erfc the complementary cumulative distribution function – see App. A.2.

A.1.2 Gamma function

The Gamma function is defined, for all $z \in \mathbb{C}_+ \equiv \{z \in \mathbb{C} \,|\, \Re(z) > 0\}$ by the

$$\Gamma : z \mapsto \int_0^{+\infty} t^{z-1} e^{-t} \mathrm{d}t \,. \tag{A.2}$$

Note that the notation $\mathbb{C}_+$ is not universal and is just a short notation introduced here. This definition can be extended to the entire complex plane except for the non-positive integers, denoted E in the following, by analytic continuation. One of the most interesting properties of the Gamma function is that

$$\Gamma(z+1) = z\Gamma(z) \quad \forall z \in E \tag{A.3}$$

This result can be obtained by integration by part for $z \in \mathbb{C}_+$, and by unicity of the analytic continuation it also holds for $z \in E$. A direct consequence of this property is

that if $n \in \mathbb{N}^\star$, the Gamma function evaluated in n is $\Gamma(n) = (n-1)!$. Moreover this recursion formula is also useful when used with the special value $\Gamma(1/2) = \sqrt{\pi}$.

It is possible to introduce *incomplete* versions of this function. Namely, the upper-incomplete gamma function and the lower-incomplete gamma function defined, for $s \in \mathbb{R}_+$ and $z \in \mathbb{C}_+$ by

$$\Gamma : (z,s) \mapsto \int_s^{+\infty} t^{z-1}e^{-t}\mathrm{d}t \quad \text{and} \quad \gamma : (z,s) \mapsto \int_0^{s} t^{z-1}e^{-t}\mathrm{d}t\,. \tag{A.4}$$

These two quantities straightforwardly satisfy $\Gamma(z,s) + \gamma(z,s) = \Gamma(z)$ for all $(z,s) \in (\mathbb{C}_+, \mathbb{R}_+)$. However one of the most interesting properties for this work is

$$\frac{\Gamma(n,s)}{\Gamma(n)} = e^{-s}\sum_{k=0}^{n-1}\frac{s^k}{k!} \quad \forall n \in \mathbb{N}^* \tag{A.5}$$

as it relates the cumulative distribution function for a Poisson distribution to the Gamma functions – see App. A.2. The ratio $\Gamma(n,s)/\Gamma(n)$ is often referred as the regularised incomplete gamma function evaluated in (n,s).

A.1.3 Euler-Beta function

The Euler beta function is given by

$$\mathrm{B} : \left\{ \begin{array}{ccc} \mathbb{C}_+ \times \mathbb{C}_+ & \to & \mathbb{C} \\ (x,y) & \mapsto & \displaystyle\int_0^1 t^{x-1}(1-t)^{y-1}\mathrm{d}t\,. \end{array} \right. \tag{A.6}$$

We can notice that by a simple change of variable in the integral, $\mathrm{B}(x,y) = \mathrm{B}(y,x)$ for all $(x,y) \in \mathbb{C}_+ \times \mathbb{C}_+$. Moreover, a key property of the Beta function is that it can be written using Gamma function as

$$\mathrm{B}(x,y) = \frac{\Gamma(x)\Gamma(y)}{\Gamma(x+y)} \quad \forall (x,y) \in \mathbb{C}_+ \times \mathbb{C}_+\,. \tag{A.7}$$

Eventually, it is also possible to introduce an *incomplete* beta function as

$$\mathrm{B} : \left\{ \begin{array}{ccc} [0,1] \times \mathbb{C}_+ \times \mathbb{C}_+ & \to & \mathbb{C} \\ (s,x,y) & \mapsto & \displaystyle\int_0^s t^{x-1}(1-t)^{y-1}\mathrm{d}t\,. \end{array} \right. \tag{A.8}$$

A.1.4 Riemann zeta function

The Riemann-zeta function is defined on $\mathbb{C}_1 \equiv \{z \in \mathbb{C} \,|\, \Re(z) > 1\}$ as

$$\zeta : \left\{ \begin{array}{ccc} \mathbb{C}_1 & \to & \mathbb{C} \\ s & \mapsto & \displaystyle\sum_{n=1}^{\infty}\frac{1}{n^s}\,. \end{array} \right. \tag{A.9}$$

Interestingly, the Riemann zeta function is related to the Gamma function by

$$\zeta(s) = \frac{1}{\Gamma(s)}\int_0^{\infty}\frac{t^{s-1}}{e^t-1}\mathrm{d}t \quad \forall s \in \mathbb{C}_1 \tag{A.10}$$

This equality can also be used as the main definition of the zeta function. Similarly as the Gamma function, the zeta function has an analytical continuation on the entire complex plane except in $s = 1$ where it has a simple pole. Several particular values of this function are

$$\zeta(-1) = -\frac{1}{12}, \quad \zeta(0) = -\frac{1}{2}, \quad \zeta(2) = \frac{\pi^2}{6}, \quad \zeta(4) = \frac{\pi^4}{90}. \tag{A.11}$$

While the first two are of particular mathematical interest and can have surprising meaningful consequences in physics (e.g. for the Casimir effect and in string theory) only the last two are relevant in our analysis.

A.1.5 Modified Bessel function of the second kind

The modified Bessel function of the second kind (or hyperbolic Bessel function of the second kind), is defined as the solution the decaying solution of the ordinary differential equation of unknown y,

$$x^2 \frac{\mathrm{d}^2 y}{\mathrm{d}x^2} + x \frac{\mathrm{d}y}{\mathrm{d}x} - \left(x^2 + \alpha^2\right) y = 0 \tag{A.12}$$

with $\alpha \in \mathbb{R}$ a parameter. When $\alpha > -1/2$ the solution can be expressed as an integral

$$K_\alpha(x) = \frac{\sqrt{\pi}}{\Gamma\left(\alpha + \frac{1}{2}\right)} \left(\frac{x}{2}\right)^\alpha \int_1^\infty e^{-tx} (t^2 - 1)^{\alpha - \frac{1}{2}} \mathrm{d}t \quad \forall x > 0\,. \tag{A.13}$$

Moreover it is possible to prove that

$$K_{\alpha+1}(x) - K_{\alpha-1}(x) = \frac{2\alpha}{x} K_\alpha(x) \quad \forall x > 0\,. \tag{A.14}$$

A last interesting properties of these function concerns their limit at infinity. More precisely an equivalent is given, for every values of $\alpha \in \mathbb{R}$ as

$$K_\alpha(x) \underset{x \to \infty}{\sim} \sqrt{\frac{\pi}{2x}} e^{-x}\,. \tag{A.15}$$

A.2 A few words on probabilities

A.2.1 Formal mathematical definition

Because a large part of the work presented in this document relies on the use of probabilities, we introduce here a few formal notions about probabilities. This brief summary is based on the dedicated chapters on probabilities in Appel (2007) and the reader is invited to refer to this book for complements that are omitted here.

Probability space. In a very formal way, probabilities are defined through a probability space (Ω, Σ, P) made of Ω a set called the sample space, Σ a σ-algebra on Ω and P a measure that satisfy $P(\Omega) = 1$. In other words, a probability space is nothing more than a measured space of measure unity. In practice we work with $\Omega = \mathbb{R}$ and therefore the σ-algebra we consider are $\Sigma = \mathcal{B}(\mathbb{R})$, the corresponding Borel sets.

Random variable. In general, let (Ω, Σ) and (Ω', Σ') be two measurable spaces. A function $X : \Omega \to \Omega'$ is measurable if $X^{-1}(A) \in \Sigma$ for all $A \in \sigma'$, we say that $X \in m\Sigma$.

A random variable is a real-valued measurable function in a probability space. The space $X(\Omega)$ is called the sample image or definition domain of X.

Probability law. Let (Ω, Σ, P) be a probability space and let X be a random variable. The probability law for the random variable X is given by

$$P_X : \left\{ \begin{array}{ccc} \mathcal{B}(\mathbb{R}) & \to & [0,1] \\ B & \mapsto & P(X^{-1}(B)) \, . \end{array} \right. \tag{A.16}$$

More conveniently it is common to introduce the notation $\{X \in B\} \equiv X^{-1}(B)$. Indeed since this quantity is the probability to have X in B it is more intuitive written under that form. Moreover we can also associate to X another function that is called the cumulative density function (CDF)

$$F_X : \left\{ \begin{array}{ccc} \mathbb{R} & \to & [0,1] \\ x & \mapsto & P\{X \leq x\} = P_X\left(]-\infty, x]\right) \, . \end{array} \right. \tag{A.17}$$

It is also common to work with the complementary cumulative density function (CCDF) given by $\overline{F}_X : x \mapsto 1 - F_X(x)$. When F_X is a continuous function the random variable X is said to be continuous too. Moreover, X is absolutely continuous if there exist a positive and measurable function $p_X : \mathbb{R} \to \mathbb{R}^+$ such that one can write

$$F_X(x) = \int_{-\infty}^{x} p_X(t) \mathrm{d}t \, . \tag{A.18}$$

The function p_X is then called the probability density function (PDF) of X. On the contrary, we say that a random variable is discrete if there exists $D \in \mathcal{B}(\mathbb{R})$ countable, such that $P\{X \notin D\} = 0$.

Random vectors. Let $X_1, ...X_n$ be n random variables, then $\mathbf{X} = (X_0, .., X_n)$ is called a random vector. The joint cumulative distribution function for $\mathbf{X}$ is given by

$$F_{\mathbf{X}} : \left\{ \begin{array}{ccc} \mathbb{R}^n & \to & [0,1] \\ \mathbf{x} & \mapsto & P\left\{ \bigcap_{i=1}^{n} \{X_i \leq x_i\} \right\} \, . \end{array} \right. \tag{A.19}$$

If $X_0, ..., X_n$ are discrete random variables, then we can write $X_i(\Omega) = \{x_i^j \,|\, j \in \mathbb{N}\}$ so that everything is determined by the knowledge of $p_{i_1,..i_n} \equiv P\{\{X_0 = x_0^{i_1}\} \cap ... \cap \{X_n = x_n^{i_n}\}\}$. However when they are continuous random variable, things get more involved and therefore we will focus on that configuration in the following. We introduce a joint PDF under the form

$$p_{\mathbf{X}}(\mathbf{x}) = \frac{\partial}{\partial z_0} \frac{\partial}{\partial z_1} \cdots \frac{\partial}{\partial z_n} F_{\mathbf{X}}(\mathbf{z}) \Big|_{\mathbf{z}=\mathbf{x}} \, . \tag{A.20}$$

For two random vectors $\mathbf{X}, \mathbf{Y}$ we can define similarly the joint PDF denoted $p_{(\mathbf{X},\mathbf{Y})}$. The marginal PDF for $\mathbf{X}$ is the function given by the integral

$$p_{\mathbf{X}}(\mathbf{x}) = \int p_{(\mathbf{X},\mathbf{Y})}(\mathbf{x}, \mathbf{y}) \mathrm{d}\mathbf{y} \tag{A.21}$$

and the conditional PDF $p_{(\mathbf{X}|\mathbf{Y})}$ is defined as

$$p_{(\mathbf{X}|\{\mathbf{Y}=\mathbf{y}\})} : \mathbf{x} \mapsto \frac{p_{(\mathbf{X},\mathbf{Y})}(\mathbf{x}, \mathbf{y})}{p_{\mathbf{Y}}(\mathbf{y})} \, . \tag{A.22}$$

This definition is well motivated by Bayes' theorem. For all $\mathbf{y}$ such that $p_{\mathbf{Y}}(\mathbf{y}) = 0$ then $p_{(\mathbf{X},\mathbf{Y})}(\mathbf{x},\mathbf{y}) = 0$ for almost all $\mathbf{x}$ and in that case $p_{(\mathbf{X}|\{\mathbf{Y}=\mathbf{y}\})}(\mathbf{x}) = 0$ for almost all $\mathbf{x}$ too. Conditional PDF are useful because it is usual in physics to only know, a priori, the probability densities $p_{(\mathbf{X}|\{\mathbf{Y}=\mathbf{y}\})}$ and $p_{\mathbf{Y}}$. From the definition we can recover the joint PDF $p_{(\mathbf{X},\mathbf{Y})}$ and the marginal PDF $p_{\mathbf{X}}$ easily. This is something largely used in this work. In practice, however, we adopt simpler notation and we denote

$$"p_{(\mathbf{X}|\{\mathbf{Y}=\mathbf{y}\})}(\mathbf{x}) \equiv p_{\mathbf{X}}(\mathbf{x}\,|\,\{\mathbf{Y}=\mathbf{y}\}) = p_{\mathbf{x}}(\mathbf{x}\,|\,\mathbf{y})" \tag{A.23}$$

when the random vector $\mathbf{Y}$ is implicit and can be guessed from context. Moreover note that here the distinction between the random vector $\mathbf{X}$ (upper case) and its values $\mathbf{x}$ (lower case) is omitted and everything is written with the same letter in order to gain space and because in physical context there is usually no need for the distinction as long as we remain careful.

A.2.2 Central limit theorem

The central limit theorem is a powerful mathematical tool which gives the probability distribution of a sum of random variables. In this work, we rely on this theorem, especially in Chapter 2 where we are confronted with its limitations. More insights on the issue is given here. Firstly, let us assume that we have a succession N of random variables x_i that are independent and identically distributed (i.i.d.). We want to know the PDF p_X of the random variable

$$X = \sum_{i=1}^{N} x_i \,. \tag{A.24}$$

The PDF for every x_i is denoted p_x. In order to do so, one convenient method relies on the characteristic function

$$\phi_x(\omega) \equiv \overline{e^{i\omega x}} = \int p_x(x) e^{i\omega x} \mathrm{d}x \quad \text{and} \quad \phi_X(\omega) \equiv \overline{e^{i\omega X}} = \int p_X(X) e^{i\omega X} \mathrm{d}X \tag{A.25}$$

which is the Fourier transform of the PDF. Indeed, because the Fourier transform of a convolution is the product of the Fourier transforms, it can be shown that

$$\phi_X(\omega) = \phi_x^N(\omega) \quad \forall\omega \tag{A.26}$$

Consequently, by the inverse Fourier transform it yields

$$p_X(X) = \frac{1}{2\pi} \int \phi_x^N(\omega) e^{-i\omega X} \mathrm{d}\omega \,. \tag{A.27}$$

Nevertheless, this expression is not necessarily easy to work with as it implies two Fourier transforms and the evaluation of a function to a power N where N can be arbitrary here. The central limit consists in looking at what happens when $N \to \infty$ as it makes things simpler. In the following it is convenient to work with the reduced variable

$$y \equiv \frac{x - \overline{x}}{\sigma_x} \tag{A.28}$$

where $\overline{x}$ is the average value of x and σ_x its standard deviation. Here the existence of $\sigma_x \neq 0$ is implicitly assumed. The PDF for y is denoted p_y and is directly related to p_x

via $p_y(y) = p_x(\sigma_x y + \overline{x})\sigma_x$. By a direct evaluation the average and standard deviation of X are $N\overline{x}$ and $\sqrt{N}\sigma_x$. We can further introduce two last random variables

$$Y \equiv \sum_{i=1}^{N} y_i = \frac{X - N\overline{x}}{\sqrt{N}\sigma_x} \quad \text{and} \quad Z \equiv \frac{1}{\sqrt{N}} Y \tag{A.29}$$

Because the PDF satisfy $p_Y(Y)\mathrm{d}Y = p_Z(Z)\mathrm{d}Z$ and because the property Eq. (A.26) holds for Y it yields

$$\phi_Z(\omega) = \phi_Y\left(\frac{\omega}{\sqrt{N}}\right) = \phi_y^N\left(\frac{\omega}{\sqrt{N}}\right). \tag{A.30}$$

It is now time to use the main property of the characteristic function (the reason why it is called that way) which is

$$\phi_y(\omega) = \sum_{k=0}^{n} \frac{(i\omega)^k}{k!} m_k + \mathcal{O}\left(\omega^{n+1}\right) \quad \text{with} \quad m_k \equiv \int y^k p_y(y)\mathrm{d}y\,. \tag{A.31}$$

where by definition of y the moments are $m_0 = 1$, $m_1 = 0$ and $m_2 = 1$. Plugging this expression in Eq. (A.30) and taking the logarithm gives

$$\begin{aligned} \ln\phi_Z(\omega) &= N \ln\left[1 + \frac{1}{N}\sum_{k=2}^{n} i^k \frac{m_k}{k! N^{k/2-1}}\omega^k + \mathcal{O}\left(\frac{1}{N^{(n+1)/2}}\right)\right] \\ \ln\phi_Z(\omega) &= -\frac{\omega^2}{2}\left[1 + \frac{i m_3}{3}\frac{\omega}{N^{1/2}} - \left(3 - \frac{m_4}{12}\right)\frac{\omega^2}{N} + \mathcal{O}\left(\frac{1}{N}\right)^{5/2}\right]. \end{aligned} \tag{A.32}$$

In the infinite N limit it yields

$$\lim_{N\to\infty} \phi_Z(\omega) = e^{-\frac{\omega^2}{2}} \tag{A.33}$$

which implies that $Z \sim \mathcal{N}(0,1)$ where $\mathcal{N}(0,1)$ is the normal distribution of mean 0 and variance 1. Therefore by the different relations involved $Y \sim \mathcal{N}(0, \sqrt{N})$ and $X \sim \mathcal{N}(N\overline{x}, \sqrt{N}\sigma_x)$. However as in physics nothing is ever infinite, it is necessary to be careful when the large N limit is applied to simplify a problem. When the distribution has large high-order moments the value of N must be sufficiently large. In practice here a very rough order of magnitude is given by

$$N \gg m_k^{\frac{2}{k-2}} \quad \forall k \geq 3\,. \tag{A.34}$$

The important point is that the threshold value for N, which allows to safely approximate the PDF of the sum X as a Gaussian, depends on the PDF of the i.i.d. A highly non symmetrical distribution for instance gives a large m_3, m_5, ... that may impose to use a larger N in comparison to an initially symmetric distribution.

A.3 Dimensional reduction and maximisation algorithm

In this paragraph we are interested in the maximisation of a function $L(\boldsymbol{\theta}, \boldsymbol{\zeta}, \boldsymbol{\xi})$. The different arguments are three set of parameters such that $\boldsymbol{\xi}$ is fixed. Moreover we assume that we can write the solution of the equation

$$\frac{\partial L}{\partial \boldsymbol{\zeta}} = 0 \quad \text{as} \quad \boldsymbol{\zeta} = \mathbf{z}(\theta)\,. \tag{A.35}$$

Therefore we first want to reduce the maximisation problem to the hypersurface $\mathbf{z}(\theta)$ and then numerically find a solution. To do so we will define the restriction λ on the hypersurface and compute all its derivative that will then be plugged in a Newton-Ralphson algorithm.

A.3.1 First and second derivatives on the hypersurface

We introduce $\lambda(\boldsymbol{\theta},\boldsymbol{\xi}) = L\left(\boldsymbol{\theta},\mathbf{z}(\boldsymbol{\theta}),\boldsymbol{\xi}\right)$. The first derivative of λ can be easily found via a direct differentiation,

$$\frac{\partial\lambda}{\partial\theta_i} = \left.\frac{\partial L}{\partial\theta_i}\right|_{\boldsymbol{\zeta}=\mathbf{z}(\boldsymbol{\theta})} + \sum_q \frac{\partial z_q}{\partial\theta_i}\left.\frac{\partial L}{\partial\zeta_q}\right|_{\boldsymbol{\zeta}=\mathbf{x}(\boldsymbol{\theta})} = \left.\frac{\partial L}{\partial\theta_i}\right|_{\boldsymbol{\zeta}=\mathbf{z}(\boldsymbol{\theta})} \tag{A.36}$$

since, indeed, the second term is equal to 0 by definition of $\mathbf{z}$. Let us now evaluate the second derivative as

$$\frac{\partial^2\lambda}{\partial\theta_j\partial\theta_i} = \left.\frac{\partial^2 L}{\partial\theta_j\partial\theta_i}\right|_{\boldsymbol{\zeta}=\mathbf{z}(\boldsymbol{\theta})} + \sum_q \frac{\partial z_q}{\partial\theta_j}\left.\frac{\partial^2 L}{\partial\zeta_q\partial\theta_i}\right|_{\boldsymbol{\zeta}=\mathbf{z}(\boldsymbol{\theta})} \tag{A.37}$$

Although this expression could be use directly, we want to express it in a more convenient form, making explicit the symmetry under the exchange $\theta_i \leftrightarrow \theta_j$. Thus let us simplify the expression by first noticing that in

$$\frac{\partial}{\partial\theta_i}\left(\left.\frac{\partial L}{\partial\zeta_q}\right|_{\boldsymbol{\zeta}=\mathbf{z}(\boldsymbol{\theta})}\right) = \left.\frac{\partial^2 L}{\partial\zeta_q\partial\theta_i}\right|_{\boldsymbol{\zeta}=\mathbf{z}(\boldsymbol{\theta})} + \sum_p \frac{\partial z_p}{\partial\theta_i}\left.\frac{\partial^2 L}{\partial\zeta_p\partial\zeta_q}\right|_{\boldsymbol{\zeta}=\mathbf{z}(\boldsymbol{\theta})}, \tag{A.38}$$

by definition the left-hand side of this equation is equal to 0. Therefore we can relate the two terms in the right hand side according to

$$\left.\frac{\partial^2 L}{\partial\zeta_q\partial\theta_i}\right|_{\boldsymbol{\zeta}=\mathbf{z}(\boldsymbol{\theta})} = -\sum_p \frac{\partial z_p}{\partial\theta_i}\left.\frac{\partial^2 L}{\partial\zeta_p\partial\zeta_q}\right|_{\boldsymbol{\zeta}=\hat{\mathbf{e}}(\boldsymbol{\theta})}. \tag{A.39}$$

Replacing Eq. (A.39) in Eq. (A.37) yields

$$\frac{\partial^2\lambda}{\partial\theta_j\partial\theta_i} = \left.\frac{\partial^2 L}{\partial\theta_j\partial\theta_i}\right|_{\boldsymbol{\zeta}=\mathbf{z}(\boldsymbol{\theta})} - \sum_{q,p} \frac{\partial z_q}{\partial\theta_j}\frac{\partial z_p}{\partial\theta_i}\left.\frac{\partial^2 L}{\partial\zeta_p\partial\zeta_q}\right|_{\boldsymbol{\zeta}=\mathbf{z}(\boldsymbol{\theta})}. \tag{A.40}$$

In addition of being explicitly symmetric, this expression can happen to be more convenient to use in lengthy computations.

A.3.2 The Newton-Ralphson algorithm

Now that we have determined the expression of the first and second derivative of λ we can use the Newton-Ralphson algorithm to find its maximum. First we introduce the derivative vector $\mathcal{D}(\boldsymbol{\theta},\boldsymbol{\xi}) = \nabla_{\boldsymbol{\theta}}\lambda(\boldsymbol{\theta},\boldsymbol{\xi})$ such that, by definition of the best fit $\hat{\boldsymbol{\theta}}$ it satisfies $\mathcal{D}(\hat{\boldsymbol{\theta}},\boldsymbol{\xi}) = 0$. Let us now Taylor-expand the expression of $\mathcal{D}$ around the best fit point as

$$\mathcal{D}(\boldsymbol{\theta},\boldsymbol{\xi}) = \left[(\boldsymbol{\theta}-\hat{\boldsymbol{\theta}}).\nabla_{\boldsymbol{\theta}}\right]\mathcal{D}(\boldsymbol{\theta},\boldsymbol{\xi}) + \mathcal{O}\left(|\boldsymbol{\theta}-\hat{\boldsymbol{\theta}}|^2\right) \tag{A.41}$$

The left hand side can be written in terms of its components as

$$\begin{gathered}\left[(\boldsymbol{\theta}-\hat{\boldsymbol{\theta}}).\nabla_{\boldsymbol{\theta}}\right]\mathcal{D}(\boldsymbol{\theta},\boldsymbol{\xi}) = \sum_j(\theta_j-\hat{\theta}_j)\frac{\partial^2\lambda}{\partial\theta_j\partial\theta_i} = \sum_j(\theta_j-\hat{\theta}_j)\mathcal{H}_{ji}(\boldsymbol{\theta},\boldsymbol{\xi}) \\ \text{with} \quad \mathcal{H}_{ji}(\boldsymbol{\theta},\boldsymbol{\xi}) \equiv \frac{\partial^2\lambda}{\partial\theta_j\partial\theta_i}\end{gathered} \tag{A.42}$$

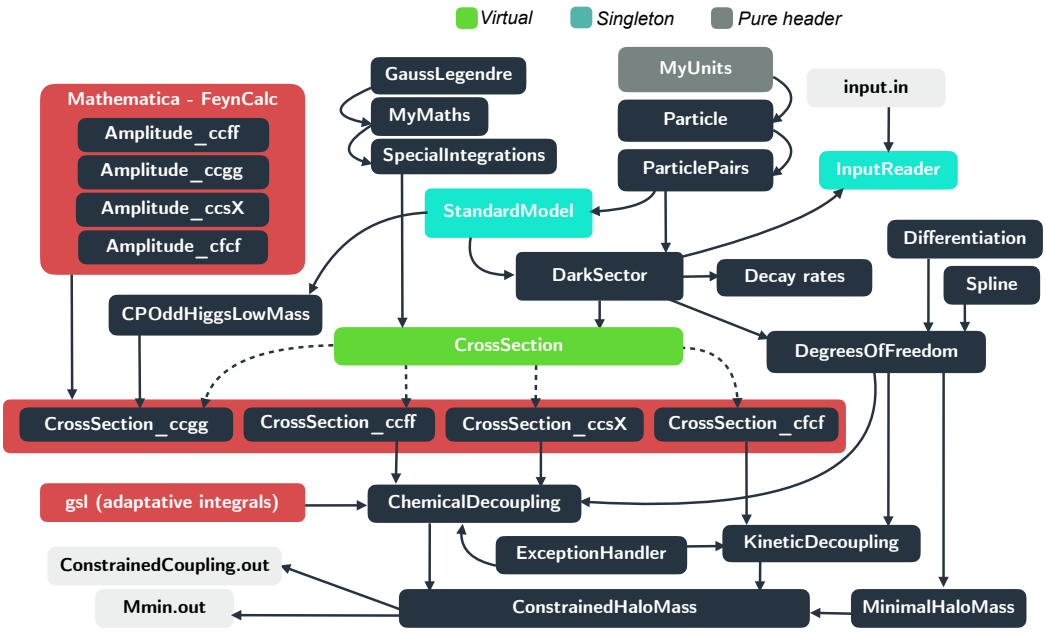

Figure A.1 – Class structure of the C++ code. The upper panel is related to Chapter 2 and DM evolution in the Early Universe in a particle physics model. In red are highlighted the parts that depend on outer libraries and tools such as FeynCalc (SHTABOVENKO et al. 2020) and the GNU Scientific Library (GSL). The plain arrows represent the "inclusion" of the header files while the dashed arrows symbolises a mother-daughter relationship. Singletons are in blue/green and pure header files are in dark grey.

the Hessian matrix. Therefore we can rewrite the previous equation in matrix notation

$$\mathcal{D}(\boldsymbol{\theta}, \boldsymbol{\xi}) = [\mathcal{H}(\boldsymbol{\theta}, \boldsymbol{\xi})] (\boldsymbol{\theta} - \hat{\boldsymbol{\theta}}) + \mathcal{O}\left(|\boldsymbol{\theta} - \hat{\boldsymbol{\theta}}|^2\right) . \tag{A.43}$$

Note that here we make use of the symmetry of the Hessian matrix. By inverting $\mathcal{H}$ it then yields the approximation

$$\hat{\boldsymbol{\theta}} = \boldsymbol{\theta} - \left[\mathcal{H}^{-1}(\boldsymbol{\theta}, \boldsymbol{\xi})\right] \mathcal{D}(\boldsymbol{\theta}, \boldsymbol{\xi}) + \mathcal{O}\left(\left|\left[\mathcal{H}^{-1}(\boldsymbol{\theta}, \boldsymbol{\xi})\right] (\boldsymbol{\theta} - \hat{\boldsymbol{\theta}})\right|^2\right) \tag{A.44}$$

The idea behind the Newton-Ralphson algorithm is, as in its 1D version, to start from a value $\hat{\boldsymbol{\theta}}_0$ and try to approximate $\hat{\boldsymbol{\theta}}$ by the sequence

$$\hat{\boldsymbol{\theta}}_{n+1} \equiv \hat{\boldsymbol{\theta}}_n - \left[\mathcal{H}^{-1}(\hat{\boldsymbol{\theta}}_n, \boldsymbol{\xi})\right] \mathcal{D}(\hat{\boldsymbol{\theta}}_n, \boldsymbol{\xi}) \tag{A.45}$$

such that

$$\hat{\boldsymbol{\theta}} = \lim_{n \to \infty} \hat{\boldsymbol{\theta}}_n . \tag{A.46}$$

A.4 Fourier transform

Let f be a function from $\mathbb{R}^n$ to $\mathbb{R}^m$ where $n, m > 0$. We assume that $f \in L_1(\mathbb{R}^n, \mathbb{R}^m)$. Then it is possible to define the Fourier transform of f as

$$\hat{f} : \mathbf{k} \mapsto \int f(\mathbf{x}) e^{-i\mathbf{x}.\mathbf{k}} \mathrm{d}^n\mathbf{x} \tag{A.47}$$

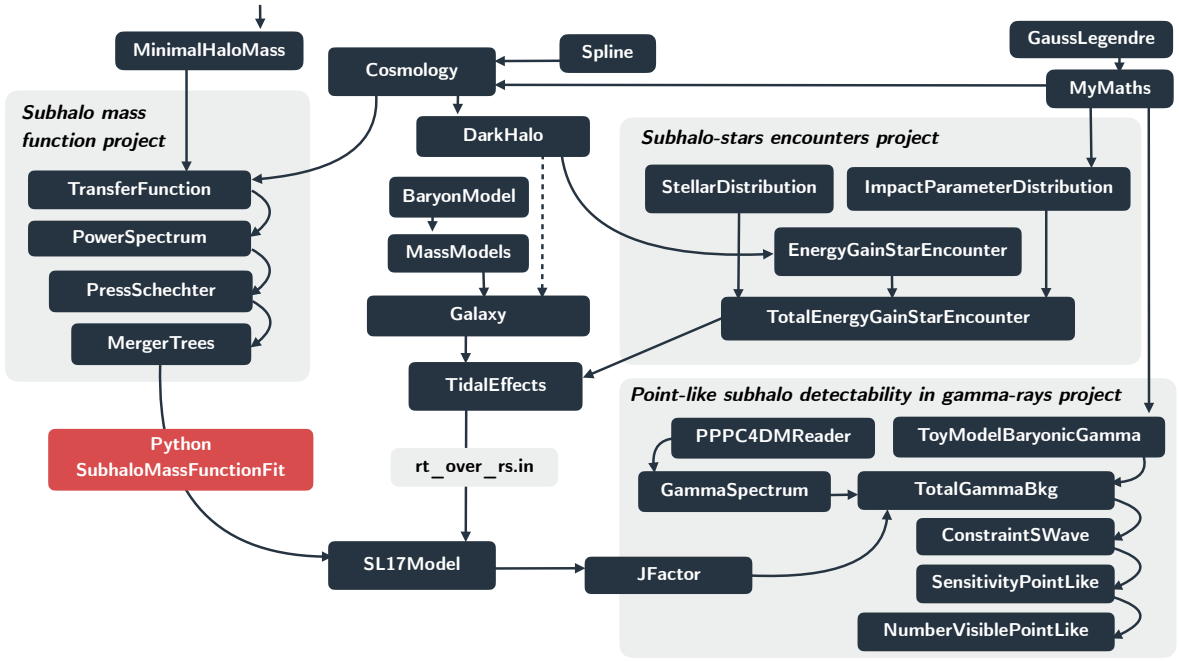

Figure A.2 – Class structure of the C++ code for the three projects presented in Chapter 3, Chapter 4 and Chapter 5. Colour coding it the same than that of Fig. A.1. Here python tools are used to fit functions and analyse large amount of data coming from Merger Trees Monte-Carlos.

If $\hat{f}$ is Lebesgue integrable too then is it also possible to inverse this transformation. Indeed one can show that the function defined by

$$\hat{\hat{f}} : \mathbf{x} \mapsto \frac{1}{(2\pi)^n} \int \hat{f}\,(\mathbf{k})\, e^{i\mathbf{x}.\mathbf{k}} \mathrm{d}^n\mathbf{k} \tag{A.48}$$

is such that $\hat{\hat{f}} = f(\mathbf{x})$ for almost all $\mathbf{x}$. When the function f is L_2 instead of L_1 similar properties hold and the notion of almost everywhere is no longer necessary if the function is sufficiently smooth. In order to prove results in L_2 it is useful to introduce first Schwartz's space $\mathcal{S}$ that is dense in L_2 and define the Fourier transform in that space. Because L_2 is compact and the Fourier transform is linear, properties in $\mathcal{S}$ can be continued in L_2. Moreover, for distributions, this space is even more useful. Indeed one can introduce the tempered distributions as the function in the dual $\mathcal{S}'$. If $\mathcal{D}$ is the space of test functions then one can show that $\mathcal{S}' \subset \mathcal{D}'$ and therefore tempered distribution are a subclass of the usual distributions. The Fourier transform of a tempered distribution T can be defined by its action on a test function $\varphi \in \mathcal{S}$ as

$$\left\langle \hat{T}, \varphi \right\rangle = \langle T, \hat{\varphi} \rangle \ . \tag{A.49}$$

This definition coincides with the Fourier transform introduced above for functions. Therefore, if we take the example of the Dirac distribution,

$$\left\langle \hat{\delta}, \varphi \right\rangle = \langle \delta, \hat{\varphi} \rangle = \hat{\varphi}(0) = \int \varphi(\mathbf{x}) \mathrm{d}^n\mathbf{x} = \langle T_1, \varphi \rangle \tag{A.50}$$

so that the Fourier transform of the Dirac distribution is the constant function $T_1 : x \mapsto 1$ and the inverse is also true. In physics, for conventions, we are careful to make

```
## Number of points/models to evaluate ##
Npoints :: 2

## Dark sector particles ##
# DS particle of the form DSi :: (type, num of dof)
DSCONT :: NDM :: 2
DSCONT :: DSPart :: (scalar, 1)
DSCONT :: DSPart :: (pseudoscalar, 1)
DSCONT :: DSPart :: (vector, 3)

## Dark matter particle type ##
# By default it is "Majorana" but can also be set to "Dirac"
TYPEDM :: 0 :: Majorana
TYPEDM :: 1 :: Majorana

# Masses dark sector [GeV] ##
# -> set m_0 = 100, m_1 = 200, m_s = 5, m_ps = 50, m_V = 500
MDMDS :: 0 :: 100 200, 5, 50, 500
# -> set m_0 = 100, m_1 = 300, m_s = 4, m_ps = 40, m_V = 400
MDMDS :: 1 :: 100 300, 4, 40, 400

# Interactions Dark sector - SM elementary particles (DS-SMSM)
# By default couplings are set to 0
# ...   :: #model :: #mediator particle number :: couplings
IntDSSM :: 0 :: 0 :: l_e=0.1, l_tau=0.2
IntDSSM :: 0 :: 1 :: l_e=0.1, l_mu=0.2
IntDSSM :: 0 :: 2 :: a_e=0.1, b_e=0.2
IntDSSM :: 1 :: 0 :: l_e=0.1, l_tau=0.2
IntDSSM :: 1 :: 1 :: l_e=0.1, l_mu=0.2
IntDSSM :: 1 :: 2 :: a_e=0.1, b_e=0.2

## Interactions Dark matter - Dark sector ##
IntDSDM :: 0 :: 0 :: l_0_0=0.1, l_0_1=0.1, l_1_1 = 0.2
IntDSDM :: 1 :: 0 :: l_0_0=0.1, l_0_1=0.1, l_1_1 = 0.2

## Interaction Dark sector - Dark sector ##
IntDSDS :: 0 :: csss_0_0_0=0.1, dspp_0_1_1=0.1
IntDSDS :: 1 :: csss_0_0_0=0.1, dspp_0_1_1=0.1
```

Figure A.3 – Example of configuration file

the distinction between the "real space" where the original distribution is defined and the "Fourier space" where the Fourier transform is defined. If x represents a position in real space, for instance, one has the following identities

$$\delta^{(n)}(\mathbf{x}) = \frac{1}{(2\pi)^n}\int e^{\pm i\mathbf{x}.\mathbf{k}}\mathrm{d}^n\mathbf{k} \quad \text{and} \quad \delta^{(n)}(\mathbf{k}) = \int e^{\pm i\mathbf{x}.\mathbf{k}}\mathrm{d}^n\mathbf{x} \tag{A.51}$$

with the factors of (2π) in that order. The first one is defined as the inverse transform of the distribution T_1 that is itself the transform of δ while the second one is the direct transform of T_1. In practice the convention does not matter as long as we track down all the factors 2π until the end of the computation, however, this is the most common convention - especially used in Quantum Field Theory.

A.5 Code structure and numerical tools

For this work, we have developed an entire C++ code from scratch in order to perform the different analysis. This code is structured in an oriented-object programming manner according to Fig. A.1 and Fig. A.2. When there is no need to instantiate several objects from a class and that this class can be used in multiple parts of the code we construct it as a singleton. The *Pure header* files are not really classes and cannot be used to create objects, they often correspond to structures repositories of generic functions. The CrossSection class is special as it is virtual (defines all the tools to compute cross-sections but is not related to any specific processes) and also can not be used to instantiate an object. The classes Spline, PPC4DMReader, TransferFunction, DarkHalo, BaryonModel, MassModels, and Galaxy were given by the authors of SL17 and only slightly modified. The connection between the two parts in the two figures is given by the class MinimalMassHalo.

An example of the input file is given in Fig. A.3. There is a set of models defined that is read by the code and converted into a vector of DarkSectorModel objects. We define Npoints, the total number of models treated (used to initialised the table and be sure that we are not forgetting any model). Then we define the particle content, the number of DM particles NDM, the number of mediators and their type. Afterwards for each model, the DM particles can either be set as Majorana or Dirac fermions. The MDMDS lines set the mass of the particle in the order they have been defined. The rest of the file initialises the coupling constants to a value different from 0.

Let us also detail the numerical recipes. We have already shown the numerical maximisation procedure through the Newton-Ralphson algorithm. Numerical integrations are usually performed through our own implementation of the Gauss Legendre method. When it is necessary to integrate highly non-smooth function (such as tree-level cross-sections around a pole with a small propagator width) we use the adaptative methods given in the GNU Scientific Library and in particular the adaptative Gauss Kronrod method. We also compared their performances with Simpson's methods. The interpolations are done through our own Spline functions and numerical derivatives are evaluated with our implementation of the different scheme according to the situation. In order to solve ordinary differential equations, we rely mostly on the implicit Euler scheme whenever possible as it is generally fast to execute and has good stability and convergence. We also investigated other higher-order schemes, implicit or explicit, such as Adam-Moulton or Runge-Kutta.

B

Complements for chemical and kinetic decoupling computations

This appendix is devoted to giving more details on different computations that are not done in Chapter 2. Firstly, we develop the expression of the equilibrium thermodynamic quantities in the Early Universe (pressure, density and entropy). Then we detail the evaluation of the thermally averaged cross-sections and decay rates for DM annihilation and production. In particular, we focus on the numerical implementation that we created to compute tree-level cross-sections in a systematic way and how to overcome the technical difficulties given by scenarios where DM is made of Majorana fermions.

B.1 The equilibrium quantities

B.1.1 Number density, energy density and pressure

In this section we develop the value of the expression for ρ, P and n at equilibrium. In order to solve everything at once we evaluate the quantity

$$A(\alpha,\gamma) = \frac{g}{2\pi^2}\int_0^\infty \frac{q^{2(1+\alpha)}E^\gamma(q)}{e^{\beta E(q)}-\varepsilon}\mathrm{d}q \tag{B.1}$$

and we recover the different values of the different quantities at equilibrium taking $(\alpha=0,\gamma=1)$ for ρ^{eq}, $(\alpha=0,\gamma=0)$ for n^{eq} and $(\alpha=1,\gamma=-1)$ for $3P^{\mathrm{eq}}$. First we make the change of variable $\beta E(q)\to u$ and $\beta m\to x$ so that

$$A(\alpha,\gamma) = \frac{g}{2\pi^2}\frac{1}{\beta^{3+2\alpha+\gamma}}\int_x^\infty \frac{(u^2-x^2)^{1/2+\alpha}u^{\gamma+1}}{e^u+\varepsilon}\mathrm{d}u \tag{B.2}$$

Then, the usual trick is to write the exponential as

$$\frac{1}{e^u-\varepsilon} = \frac{e^{-u}}{1-\varepsilon e^{-u}} = e^{-u}\sum_{n=0}^\infty \varepsilon^n e^{-un} = \sum_{n=1}^\infty \varepsilon^{n+1}e^{-un} \tag{B.3}$$

so that the factor A can be written under the form

$$A(\alpha,\gamma) = \frac{g}{2\pi^2}\frac{1}{\beta^{3+2\alpha+\gamma}}\sum_{n=1}^\infty \varepsilon^{n+1}\int_x^\infty u^{\gamma+1}(u^2-x^2)^{1/2+\alpha}e^{-un}\mathrm{d}u \tag{B.4}$$

Now let us perform another change of variable $u/x \to z$ (if $x > 0$) so that

$$A = \frac{g}{2\pi^2}\left(\frac{x}{\beta}\right)^{3+2\alpha+\gamma}\sum_{n=1}^{\infty}\varepsilon^{n+1}\int_1^{\infty} z^{\gamma+1}(z^2-1)^{1/2+\alpha}e^{-z(xn)}\mathrm{d}z\,. \tag{B.5}$$

Now, in order to make progress in the computation, let us move on to the evaluation of the different quantities separately

$$\begin{aligned} n^{\mathrm{eq}} &= A(0,0) = \frac{g}{2\pi^2}\frac{x^3}{\beta^3}\sum_{n=1}^{\infty}\varepsilon^{n+1}\int_1^{\infty} z(z^2-1)^{1/2}e^{-z(xn)}\mathrm{d}z \\ \rho^{\mathrm{eq}} &= A(0,1) = \frac{g}{2\pi^2}\frac{x^4}{\beta^4}\sum_{n=1}^{\infty}\varepsilon^{n+1}\int_1^{\infty} z^2(z^2-1)^{1/2}e^{-z(xn)}\mathrm{d}z \\ P^{\mathrm{eq}} &= \frac{1}{3}A(1,-1) = \frac{g}{6\pi^2}\frac{x^4}{\beta^4}\sum_{n=1}^{\infty}\varepsilon^{n+1}\int_1^{\infty} (z^2-1)^{3/2}e^{-z(xn)}\mathrm{d}z \end{aligned} \tag{B.6}$$

By an integration by part for the number density,

$$n^{\mathrm{eq}} = \frac{g}{6\pi^2}\frac{x^3}{\beta^3}\sum_{n=1}^{\infty}\varepsilon^{n+1}(xn)\int_1^{\infty} (z^2-1)^{3/2}e^{-z(xn)}\mathrm{d}z \tag{B.7}$$

and by separation of integrals for the energy density

$$\rho^{\mathrm{eq}} = \frac{g}{2\pi^2}\frac{x^4}{\beta^4}\sum_{n=1}^{\infty}\varepsilon^{n+1}\left\{\int_1^{\infty} (z^2-1)^{3/2}e^{-z(xn)}\mathrm{d}z + \int_1^{\infty} (z^2-1)^{1/2}e^{-z(xn)}\mathrm{d}z\right\} \tag{B.8}$$

everything now depends on two integrals. Using the Bessel functions they can be expressed as

$$\begin{aligned} \int_1^{\infty} (z^2-1)^{3/2}e^{-z(xn)}\mathrm{d}z &= K_2(xn)\frac{1}{\sqrt{\pi}}\Gamma\left(\frac{5}{2}\right)\left(\frac{2}{xn}\right)^2 = \frac{3}{(xn)^2}K_2(xn) \\ \int_1^{\infty} (z^2-1)^{1/2}e^{-z(xn)}\mathrm{d}z &= K_1(xn)\frac{1}{\sqrt{\pi}}\Gamma\left(\frac{3}{2}\right)\frac{2}{xn} = \frac{1}{xn}K_1(xn) \end{aligned} \tag{B.9}$$

In the end, combining everything yields

$$\begin{aligned} n^{\mathrm{eq}} &= \frac{g}{2\pi^2}\frac{1}{\beta^3}\sum_{n=1}^{\infty}\varepsilon^{n+1}\frac{x^2}{n}K_2(xn) \\ \rho^{\mathrm{eq}} &= \frac{g}{2\pi^2}\frac{1}{\beta^4}\sum_{n=1}^{\infty}\varepsilon^{n+1}\left\{\frac{3x^2}{n^2}K_2(xn) + \frac{x^3}{n}K_1(xn)\right\} \\ P^{\mathrm{eq}} &= \frac{g}{2\pi^2}\frac{1}{\beta^4}\sum_{n=1}^{\infty}\varepsilon^{n+1}\frac{x^2}{n^2}K_2(xn) \end{aligned} \tag{B.10}$$

Using the relation

$$K_2(xn) = \frac{2}{xn}K_1(xn) + K_0(xn) \tag{B.11}$$

it is also possible to rewrite these expression using only the first two order of the modified Bessel functions of the second kind,

$$\begin{aligned} n^{\mathrm{eq}} &= \frac{g}{2\pi^2}\frac{1}{\beta^3}\sum_{n=1}^{\infty}\varepsilon^{n+1}\left\{\frac{2x}{n^2}K_1(xn) + \frac{x^2}{n}K_0(xn)\right\} \\ \rho^{\mathrm{eq}} &= \frac{g}{2\pi^2}\frac{1}{\beta^4}\sum_{n=1}^{\infty}\varepsilon^{n+1}\left\{\left(\frac{6x}{n^3} + \frac{x^3}{n}\right)K_1(xn) + \frac{3x^2}{n^2}K_0(xn)\right\} \\ P^{\mathrm{eq}} &= \frac{g}{2\pi^2}\frac{1}{\beta^4}\sum_{n=1}^{\infty}\varepsilon^{n+1}\left\{\frac{2x}{n^3}K_1(xn) + \frac{x^2}{n^2}K_0(xn)\right\} \end{aligned} \tag{B.12}$$

B.1.2 The massless case

In the massless scenario the expressions are analytic. Indeed we can write

$$A(\alpha,\gamma) = \frac{g}{2\pi^2}\frac{1}{\beta^{3+2\alpha+\gamma}}\sum_{n=1}^{\infty}\varepsilon^{n+1}\int_0^\infty u^{2+2\alpha+\gamma}e^{-un}\mathrm{d}u \tag{B.13}$$

now we perform the change of variable $un \to \omega$ in the integral and we also introduce the variable $s = 3+2\alpha+\gamma$. It yields

$$A(\alpha,\gamma) = \frac{g}{2\pi^2\beta^s}\sum_{n=1}^{\infty}\frac{\varepsilon^{n+1}}{n^s}\int_0^\infty \omega^{s-1}e^{-\omega}\mathrm{d}\omega = \frac{g}{2\pi^2\beta^s}\Gamma(s)\sum_{n=1}^{\infty}\frac{\varepsilon^{n+1}}{n^s} \tag{B.14}$$

For bosons $\epsilon = +1$ and one recovers the expression of the Riemann-zeta function. For Fermions $\epsilon = -1$ and things are less trivial. However, it is still possible to use the Riemann-zeta function. For that let us write

$$\begin{aligned}\sum_{n=1}^{\infty}\frac{(-1)^{n+1}}{n^s} &= \sum_{p=0}^{\infty}\frac{1}{(2p+1)^s} - \sum_{p=1}^{\infty}\frac{1}{(2p)^s}\\ &= \sum_{p=0}^{\infty}\frac{1}{(2p+1)^s} - \frac{1}{2^s}\zeta(s)\end{aligned} \tag{B.15}$$

Moreover from the same decomposition it is possible to write

$$\zeta(s) = \sum_{p=0}^{\infty}\frac{1}{(2p+1)^s} + \frac{1}{2^s}\zeta(s) \tag{B.16}$$

Therefore the sum over odd terms is given as

$$\sum_{p=0}^{\infty}\frac{1}{(2p+1)^s} = \frac{2^s-1}{2^s}\zeta(s) \tag{B.17}$$

ans plugging this result in the previous expression yields

$$\sum_{n=1}^{\infty}\frac{(-1)^{n+1}}{n^s} = \frac{2^s-1}{2^s}\zeta(s) - \frac{1}{2^s}\zeta(s) = \frac{2^{s-1}-1}{2^{s-1}}\zeta(s)\,. \tag{B.18}$$

At the end of the day we can summarize

$$A(\alpha,\gamma) = \begin{cases}\dfrac{g}{2\pi^2\beta^s}\Gamma(s)\zeta(s) & \text{for bosons}\\ \dfrac{g}{2\pi^2\beta^s}\dfrac{2^{s-1}-1}{2^{s-1}}\Gamma(s)\zeta(s) & \text{for fermions}\,.\end{cases} \tag{B.19}$$

It implies for the physical quantities

$$n^{\mathrm{eq}} = \begin{cases}\dfrac{g}{2\pi^2\beta^3}\Gamma(3)\zeta(3) = \dfrac{g}{\pi^2\beta^3}\zeta(3) & \text{for bosons}\\ \dfrac{g}{2\pi^2\beta^3}\dfrac{3}{4}\Gamma(3)\zeta(3) = \dfrac{3g}{4\pi^2\beta^3}\zeta(3) & \text{for fermions}\end{cases} \tag{B.20}$$

$$\rho^{\mathrm{eq}} = \begin{cases}\dfrac{g}{2\pi^2\beta^4}\Gamma(4)\zeta(4) = \dfrac{g\pi^2}{30\beta^4} & \text{for bosons}\\ \dfrac{g}{2\pi^2\beta^4}\dfrac{7}{8}\Gamma(4)\zeta(4) = \dfrac{7}{8}\dfrac{g\pi^2}{30\beta^4} & \text{for fermions}\end{cases} \tag{B.21}$$

and since A only depends on the combination $s = 3+2\alpha+\gamma$ that is the same for $(\alpha=0,\gamma=1)$ and $(\alpha=1,\gamma=-1)$, the pressure satisfies $P^{\mathrm{eq}} = \rho^{\mathrm{eq}}/3$.

B.1.3 The massive case

In the massive case $x \to \infty$ and therefore, only the leading terms are important in the expansion of Bessel functions. More precisely, because the modified Bessel function of the second kind are decreasing fast we can approximate for the number density

$$n^{\rm eq} = \frac{g}{2\pi^2}\frac{x^2}{\beta^3}K_2(x) \sim g\left(\frac{mT}{2\pi}\right)^{3/2} e^{-m/T} \tag{B.22}$$

Similarly the expansion of $\rho^{\rm eq}$ can be written

$$\rho^{\rm eq} = \frac{g}{2\pi^2}\frac{1}{\beta^4}x^3K_1(x) \tag{B.23}$$

Because the behaviour is the same $K_2 \sim K_1 \sim K_0$ at infinity,

$$\rho^{\rm eq} \sim \frac{x}{\beta}n^{\rm eq} = mn^{\rm eq} \tag{B.24}$$

Eventually the pressure satisfies

$$P^{\rm eq} = \frac{g}{2\pi^2}\frac{1}{\beta^4}x^2K_0(x) \sim \frac{1}{\beta}n^{\rm eq} = n^{\rm eq}T \tag{B.25}$$

B.1.4 The entropy density

The total entropy contained in a volume V satisfies, when local thermodynamic equilibrium is maintained, the second law of thermodynamics. In this section only we will omit the label eq to denote that we work with equilibrium quantity.

$$T\mathrm{d}S = \mathrm{d}(\rho V) + P\mathrm{d}V = \mathrm{d}\left[(\rho+P)V\right] - V\mathrm{d}P\,. \tag{B.26}$$

Now consider S and $U = \rho V$ as functions of T and V. It is possible to write

$$\begin{aligned}\mathrm{d}S &= \left(\frac{\partial S}{\partial T}\right)_V \mathrm{d}T + \left(\frac{\partial S}{\partial V}\right)_T \mathrm{d}V\\ \mathrm{d}U &= \left(\frac{\partial U}{\partial T}\right)_V \mathrm{d}T + \left(\frac{\partial U}{\partial V}\right)_T \mathrm{d}V\end{aligned} \tag{B.27}$$

And in the meantime the law of thermodynamics we wrote above gives

$$\mathrm{d}S = \frac{1}{T}\mathrm{d}U + \frac{P}{T}\mathrm{d}V = \frac{1}{T}\left[\left(\frac{\partial U}{\partial T}\right)_V \mathrm{d}T + \left\{\left(\frac{\partial U}{\partial V}\right)_T + P\right\}\mathrm{d}V\right] \tag{B.28}$$

which yields

$$\left(\frac{\partial S}{\partial T}\right)_V = \frac{1}{T}\left(\frac{\partial U}{\partial T}\right)_V \quad \text{and} \quad \left(\frac{\partial S}{\partial V}\right)_T = \frac{1}{T}\left[\left(\frac{\partial U}{\partial V}\right)_T + P\right] \tag{B.29}$$

In order to have integrability

$$\frac{\partial^2 S}{\partial V\partial T} = \frac{\partial^2 S}{\partial T\partial V} \quad \Rightarrow \quad \frac{1}{T}\frac{\partial^2 U}{\partial T\partial V} = -\frac{P}{T^2} + \frac{1}{T}\left(\frac{\partial P}{\partial T}\right)_V - \frac{1}{T^2}\left(\frac{\partial U}{\partial V}\right)_T + \frac{1}{T}\frac{\partial^2 U}{\partial V\partial T} \tag{B.30}$$

and therefore it yields the equality

$$T\left(\frac{\partial P}{\partial T}\right)_V = P + \rho \tag{B.31}$$

and because P does not vary with the volume this equation can also be written

$$\mathrm{d}P = \frac{P+\rho}{T}\mathrm{d}T\,. \tag{B.32}$$

Remark that this equation can be consistently obtained directly by computing the derivative of P at equilibrium with respect to the temperature from the definition of pressure,

$$\frac{\mathrm{d}P}{\mathrm{d}T} = \frac{g}{6\pi^2}\int \frac{\partial f(q,t)}{\partial T}\frac{q^4}{E(q)}\mathrm{d}q \tag{B.33}$$

And because the dependence of f with T is such that $f(q,t) = g(E(q)/T)$ it yields that

$$\frac{\partial f(q,t)}{\partial T} = -\frac{E(q)}{T^2}\frac{\mathrm{d}g(x)}{\mathrm{d}x}\Big|_{x=E(q)/T} \quad \text{and} \quad \frac{\partial f(q,t)}{\partial q} = \frac{p}{E(q)T}\frac{\mathrm{d}g(x)}{\mathrm{d}x}\Big|_{x=E(q)/T} \tag{B.34}$$

so that the different derivatives on the PDF are related by

$$\frac{\partial f(q,t)}{\partial T} = -\frac{E^2(q)}{qT}\frac{\partial f(q,t)}{\partial q}\,. \tag{B.35}$$

Therefore the derivative of the pressure with the temperature is

$$\begin{aligned}\frac{\mathrm{d}P}{\mathrm{d}T} &= -\frac{g}{6\pi^2 T}\int \frac{\partial f(q,t)}{\partial q}q^3 E(q)\mathrm{d}q \\ &= \frac{g}{6\pi^2 T}\int f(q,t)\left[3p^2E(q) + \frac{p^4}{E(q)}\right]\mathrm{d}q = \frac{\rho+P}{T}\,.\end{aligned} \tag{B.36}$$

Replacing this condition in the first equation gives

$$\mathrm{d}S = \frac{1}{T}\left\{\mathrm{d}\left[(\rho+P)V\right] - V\frac{\rho+P}{T}\mathrm{d}T\right\} = \mathrm{d}\left[\frac{(\rho+P)V}{T}\right] \tag{B.37}$$

and integrating this differential yields

$$S = \frac{(\rho+P)V}{T} + \mathrm{cst} \tag{B.38}$$

where the constant can be taken to 0. In the end the entropy density (or sometime called comoving entropy) $s \equiv S/V$ satisfies

$$s = \frac{\rho+P}{T} \tag{B.39}$$

B.2 Collision term for chemical decoupling

In this section we detail the different steps of computation that have been omitted in the main text in order to keep the discussion as simple as possible. First we show how we can generically simplify the collision term for the annihilation and creation of WIMPs. In a second part we show how to evaluate the effective quantities of the co-annihilation regime.

B.2.1 General simplification of the collision term

Let us consider in the following that the only interactions that change the total number of WIMPs and have an impact on n_χ are the annihilations/creations into/by SM particles and or mediators and the possible decay or inverse decay of mediators into WIMPs. We focus more on the associated zeroth-moment collision operator of these interactions.

Contribution of the $2 \leftrightarrow n$ interactions. Let us first consider a $2 \leftrightarrow n$ annihilation and creation process $\chi_i + \chi_j \to Z$. The thermally averaged cross-section is given by

$$\left\langle \sigma_{ij\to Z} v^{ij}_{\text{Møl}} \right\rangle = \frac{1}{n_i n_j} \frac{1}{\mathcal{S}_Z} \int \frac{\mathcal{F}_{\{ij\},Z}}{4E_i(q_i)E_j(q_j)} W_{\{ij\};\mathcal{Z}} \mathrm{d}\Pi_{\{ij\},\mathcal{Z}} \mathrm{d}\mathcal{P}_{\{ij\}} \tag{B.40}$$

which we can slightly simplify into

$$\left\langle \sigma_{ij\to Z} v^{ij}_{\text{Møl}} \right\rangle = \frac{g_i g_j}{n_i n_j} \int \frac{\mathrm{d}\sigma_{ij\to Z}}{\mathrm{d}\Pi_{\{ij\},\mathcal{Z}}} v^{ij}_{\text{Møl}} \mathcal{F}_{\{ij\},Z} \mathrm{d}\Pi_{\{ij\},\mathcal{Z}} \mathrm{d}\mathcal{P}_{\{ij\}} \,. \tag{B.41}$$

The next step is now to simplify the phase space factor $\mathcal{F}_{\{ij\},Z}$ using the fact that the WIMPs are assumed to be non relativistic at the time of chemical decoupling. The conservation of energy imposed by the Dirac delta function in the expression of the differential cross section yields

$$E_{\mathcal{Z}} \equiv \sum_{\kappa' \in \mathcal{Z}} E_{\kappa'}(q_{\kappa'}) \sim m_i + m_j \gg T \tag{B.42}$$

such that

$$\prod_{\kappa\in\mathcal{Z}} (1 + \varepsilon_{\kappa'} f_{\kappa'}) = \frac{e^{\alpha_Z + \beta E_{\mathcal{Z}}}}{\prod_{\kappa\in\mathcal{Z}} (e^{\beta E_\kappa(q_\kappa)} - \varepsilon_\kappa)} \simeq e^{\alpha_Z} \,. \tag{B.43}$$

We write n_i^{eq} the equilibrium number density at zero chemical potential. Because WIMPs are assumed to be non relativistic, their PSDF takes the simple form of a Boltzmann distribution

$$f_i(q_i) = e^{-\beta E_i(q_i) - \alpha_i} = \frac{n_i}{n_i^{\text{eq}}} e^{-\beta E_i(q_i)} \,, \tag{B.44}$$

therefore, it yields

$$n_i = \int e^{-\alpha_i - \beta E_i} \frac{1}{2E_i(q)} \frac{\mathrm{d}^3\mathbf{q}}{(2\pi)^3} = e^{-\alpha_i} n_i^{\text{eq}} \,. \tag{B.45}$$

Combining Eq. (B.43) and Eq. (B.44) allows to write the phase space factor as

$$\mathcal{F}_{\{ij\};\mathcal{Z}} = f_i f_j \prod_{\kappa\in\mathcal{Z}} (1 + \varepsilon_{\kappa'} f_{\kappa'}) \simeq \frac{n_i n_j}{n_i^{\text{eq}} n_j^{\text{eq}}} e^{-\beta(E_i + E_j)} e^{\alpha_Z} = \frac{n_i n_j}{n_i^{\text{eq}} n_j^{\text{eq}}} \mathcal{F}^{\text{eq}}_{\{ij\},Z} e^{\alpha_Z} \,. \tag{B.46}$$

Consequently we can simply write down

$$\left\langle \sigma_{ij\to Z} v^{ij}_{\text{Møl}} \right\rangle = \left\langle \sigma_{\chi_i\chi_j\to Z} v^{ij}_{\text{Møl}} \right\rangle^{\text{eq}} e^{\alpha_Z} \,. \tag{B.47}$$

where here, in particular, we define

$$\left\langle \sigma_{ij\to Z} v^{ij}_{\text{Møl}} \right\rangle^{\text{eq}} \equiv \frac{g_i g_j}{n_i^{\text{eq}} n_j^{\text{eq}}} \int \sigma_{ij\to Z} v^{ij}_{\text{Møl}} e^{-\beta(E_i(q_i) + E_j(q_j))} \frac{\mathrm{d}^3\mathbf{q}_i}{(2\pi)^3} \frac{\mathrm{d}^3\mathbf{q}_j}{(2\pi)^3} \,. \tag{B.48}$$

We will show later on how this latter expression can be further simplified and be convenient for numerical evaluations. In the end the zeroth order collision operator for annihilation becomes

$$\hat{\mathcal{C}}_{ij\to Z} = n_i n_j \left\langle \sigma_{ij\to Z} v^{ij}_{\text{Møl}} \right\rangle \left[\frac{n_i^{\text{eq}}}{n_i} \frac{n_j^{\text{eq}}}{n_j} e^{-\alpha_Z} - 1 \right] = \left\langle \sigma_{ij\to Z} v^{ij}_{\text{Møl}} \right\rangle^{\text{eq}} \left[n_i^{\text{eq}} n_j^{\text{eq}} - e^{\alpha_Z} n_i n_j \right] . \quad \text{(B.49)}$$

Contribution of the $1 \leftrightarrow 2$ interactions. Secondly, let us look now at the decay interaction $y \leftrightarrow \chi_i + \chi_j$. The general derivation has shown that for the decays and inverse decay it is possible to write everything in terms of the thermally averaged decay rate

$$\langle \Gamma_{y\to ij} \rangle = \frac{1}{n_y} \frac{1}{S_{\{ij\}}} \int \frac{\mathcal{F}_{\{y\},\{ij\}}}{2E_y(q_y)} W_{\{y\};\{ij\}} \, \mathrm{d}\Pi_{\{y\},\{ij\}} \mathrm{d}\mathcal{P}_{\{y\}} = \frac{m_y}{E_y(q_y)} \mathrm{d}\Gamma_{y\to\mathcal{Z}} \quad \text{(B.50)}$$

which can also be slightly simplified under the form

$$\langle \Gamma_{y\to ij} \rangle = \frac{1}{n_y} \int \frac{m_y}{E_y(q_y)} \frac{\mathrm{d}\Gamma_{y\to ij}}{\mathrm{d}\Pi_{\{y\},\{ij\}}} \mathcal{F}_{\{y\},\{ij\}} \, \mathrm{d}\Pi_{\{y\},\{ij\}} \mathrm{d}\mathcal{P}_{\{y\}} \quad \text{(B.51)}$$

Here because of the Dirac delta distribution in the expression of $\mathrm{d}\Gamma_{y\to ij}$ we necessarily have $E_y = E_i + E_j \gg T$. Moreover because WIMPs are non relativistic $f_i(q_i) \ll 1$ and $f_j(q_j) \ll 1$ such that

$$f_y(q_y)(1 + \varepsilon_i f_i(q_i))(1 + \varepsilon_j f_j(q_j)) \simeq e^{-\alpha_y} e^{-\beta E_y(q_y)} . \quad \text{(B.52)}$$

The thermally averaged decay rate takes a simple form

$$\langle \Gamma_{y\to ij} \rangle = \frac{n_y^{\text{eq}} e^{-\alpha_y}}{n_y} \langle \Gamma_{y\to ij} \rangle^{\text{eq}} \quad \text{(B.53)}$$

where, in particular, we define

$$\begin{aligned} \langle \Gamma_{y\to ij} \rangle^{\text{eq}} &\equiv \frac{g_y}{n_y^{\text{eq}}} \Gamma_{y\to ij} \int \frac{m_y}{E_y(q_y)} e^{-\beta E_y(q_y)} \frac{\mathrm{d}^3\mathbf{q}_y}{(2\pi)^3} \\ &= \frac{g_y}{n_y^{\text{eq}}} \frac{T m_y^2}{2\pi^2} \Gamma_{ij\to Y} = \frac{K_1(m_y/T)}{K_2(m_y/T)} \Gamma_{ij\to Y} . \end{aligned} \quad \text{(B.54)}$$

This expression is analytical and which will be shown in the next section. For the moment let us write down the contribution to the zeroth-moment of the collision operator as

$$\hat{\mathcal{C}}_{y\to ij} = (1 + \delta_{\chi_i\chi_j}) \langle \Gamma_{y\to ij} \rangle^{\text{eq}} \frac{n_y^{\text{eq}}}{n_i^{\text{eq}} n_j^{\text{eq}}} \left[n_i^{\text{eq}} n_j^{\text{eq}} e^{-\alpha_y} - n_i n_j \right] \quad \text{(B.55)}$$

where $\delta_{\chi_i\chi_j}$ is one if $\chi_i = \chi_j$ and zero otherwise.

The total number density of WIMPs is

$$n_\chi \equiv \sum_i n_i . \quad \text{(B.56)}$$

Thus, by summing the equations of evolution for every n_i and taking into account all possible interactions which change the total number of WIMPs yields

$$\begin{aligned}\frac{\mathrm{d}n_\chi}{\mathrm{d}t}+3Hn_\chi=&\sum_{ij}\left\langle\sigma_{ij\to}v^{ij}_{\text{Møl}}\right\rangle^{\text{eq}}\left[n_i^{\text{eq}}n_j^{\text{eq}}-e^{\alpha_Z}n_in_j\right]\\&+\sum_{ij}\langle\Gamma_{y\to ij}\rangle^{\text{eq}}\frac{n_y^{\text{eq}}}{n_i^{\text{eq}}n_j^{\text{eq}}}\left[n_i^{\text{eq}}n_j^{\text{eq}}e^{-\alpha_y}-n_in_j\right].\end{aligned}\tag{B.57}$$

with the notations

$$\left\langle\sigma_{ij\to}v^{ij}_{\text{Møl}}\right\rangle^{\text{eq}}=\sum_Z\left\langle\sigma_{ij\to Z}v^{ij}_{\text{Møl}}\right\rangle^{\text{eq}}\quad\text{and}\quad\langle\Gamma_{\to ij}\rangle^{\text{eq}}=\sum_y\langle\Gamma_{y\to ij}\rangle^{\text{eq}}\,.\tag{B.58}$$

B.2.2 The effective quantities for co-annihilation

In order to simplify further this expression, we assume that the pseudo chemical potential of all the WIMPs species are the same and we denote $\alpha_i\simeq\alpha_\chi$ for all i. Moreover, we also assume that the chemical potential of the incoming and outgoing particles that are not WIMPs is also zero – see the full discussion in the main text. A direct consequence is that $n_i/n_i^{\text{eq}}\simeq n_\chi/n_\chi^{\text{eq}}$. Subsequently, when used in the previous equation, it gives

$$\frac{\mathrm{d}n_\chi}{\mathrm{d}t}+3Hn_\chi=\left(\langle\sigma v_{\text{Møl}}\rangle^{\text{eq}}_{\text{eff}}+\langle\Gamma\rangle^{\text{eq}}_{\text{eff}}\right)\left[(n_\chi^{\text{eq}})^2-n_\chi^2\right]\tag{B.59}$$

with the definitions

$$\begin{aligned}\langle\sigma v_{\text{Møl}}\rangle^{\text{eq}}_{\text{eff}}&\equiv\sum_{ij}\left\langle\sigma_{ij\to}v^{ij}_{\text{Møl}}\right\rangle^{\text{eq}}\frac{n_i^{\text{eq}}n_j^{\text{eq}}}{(n_\chi^{\text{eq}})^2}\\\langle\Gamma\rangle^{\text{eq}}_{\text{eff}}&\equiv\sum_{i,j}(1+\delta_{\chi_i\chi_j})\,\langle\Gamma_{\to ij}\rangle^{\text{eq}}\frac{n_y^{\text{eq}}}{(n_\chi^{\text{eq}})^2}\,,\end{aligned}\tag{B.60}$$

as introduced in Eq. (2.118). The first thing worth mentioning it the value of n_χ^{eq} that can be deduced from the equilibrium number density of massive, non relativistic, particles given in Eq. (B.22),

$$n_\chi^{\text{eq}}=\frac{T}{2\pi^2}\sum_i g_im_i^2K_2\left(\frac{m_i}{T}\right).\tag{B.61}$$

In a second time we write, according to EDSJO et al. (1997),

$$\langle\sigma v_{\text{Møl}}\rangle^{\text{eq}}_{\text{eff}}=\frac{1}{(n_\chi^{\text{eq}})^2}\frac{g_0^2T}{8\pi^4}\int_{4m_0^2}^\infty\left\{\sigma_{\text{eff}}(s)\equiv\sum_{ij}\frac{g_ig_j}{g_0^2}\frac{\overline{p}_{ij}^2(s)}{\overline{p}_{00}^2(s)}\sigma_{ij\to}(s)\right\}\overline{p}_{00}^2(s)\sqrt{s}K_1\left(\frac{\sqrt{s}}{T}\right)\mathrm{d}s\tag{B.62}$$

where s is the Mandelstam variable and $\overline{p}_{ij}$ is the centre of mass frame incoming momentum given by

$$\overline{p}_{ij}^2(s)=\frac{1}{4s}\left[s-(m_i+m_j)^2\right]\left[s-(m_i-m_j)^2\right]\tag{B.63}$$

Note that we do not have negative values of $\overline{p}_{ij}^2$ as, by definition, the cross-sections satisfy $\sigma_{ij\to}(s<(m_i+m_j)^2)=0$. The value of $\overline{p}_{00}^2(s)$ can further be simplified as $\overline{p}_{00}^2(s)=(s-4m_0^2)/4$. Putting together Eq. (B.61) and Eq. (B.62) gives

$$\langle\sigma v_{\text{Møl}}\rangle^{\text{eq}}_{\text{eff}}=\frac{g_0^2}{8T}\frac{1}{\left[\sum_i g_im_i^2K_2(m_i/T)\right]^2}\int_{4m_0^2}^\infty\sigma_{\text{eff}}(s)(s-4m_0^2)\sqrt{s}K_1\left(\frac{\sqrt{s}}{T}\right)\mathrm{d}s\,.\tag{B.64}$$

For the decay rate the computation is slightly easier and gives

$$\langle\Gamma\rangle_{\rm eff}^{\rm eq} = \frac{16\pi^5}{T}\frac{1}{\left[\sum_i g_i m_i^2 K_2(m_i/T)\right]^2}\sum_{ij}(1+\delta_{\chi_i\chi_j})\sum_y g_y m_y^2 K_1\left(\frac{m_y}{T}\right)\Gamma_{y\to ij}\,. \tag{B.65}$$

B.3 The tree-level $2 \leftrightarrow 2$ cross-sections

Here we detail the formalism behind the numerical tool we have developed to evaluate the tree-level $2 \leftrightarrow 2$ cross-sections. After a general introduction we mention, in a second part, a necessary trick to account for Majorana fermion specific configurations in FeynCalc (SHTABOVENKO et al. 2016), the software we use to evaluate the squared amplitudes.

B.3.1 General evaluation for numerical implementation

Let us consider a process $i+j \to k+\ell$ mediated by different particles. We introduce $\mathcal{V}$ the set of particles that contributes to the interaction in the $v = s,t,u$ channels – where s,t,u are the Mandelstam variables here. For instance, mediators contributing to the t-channel are all in the set $\mathcal{T}$. Then the total amplitude can be written as

$$\mathcal{M}_{ij\to k\ell} = \sum_{v\in\{s,t,u\}}\left[\sum_{a\in\mathcal{V}}\mathcal{P}_v^a S_v^a\right] \tag{B.66}$$

where we introduced the propagators as

$$\mathcal{P}_v^a = \frac{1}{v - m_a^2 + i m_a \Gamma_a}\,. \tag{B.67}$$

The associated cross-section and transfer cross-sections are then given by

$$\begin{aligned}\sigma_{ij\to k\ell} &= \frac{1}{64\pi s}\frac{1}{\overline{p}_{ij}^2}\frac{1}{\mathcal{S}_{k\ell}}\frac{1}{g_i g_j}\int\left\{\mathcal{M}^2 \equiv \sum_{\rm spins}|\mathcal{M}_{ij\to k\ell}|^2\right\}{\rm d}t \\ \sigma^T_{ij\to k\ell} &= \frac{1}{128\pi s}\frac{1}{\overline{p}_{ij}^4}\frac{1}{\mathcal{S}_{k\ell}}\frac{1}{g_i g_j}\int\left\{\mathcal{M}^2 \equiv \sum_{\rm spins}|\mathcal{M}_{ij\to k\ell}|^2\right\}(-t){\rm d}t\end{aligned} \tag{B.68}$$

where the integral goes from $t_{\rm min}(s)$ to $t_{\rm max}(s)$ and $\overline{p}_{ij}(s)$ is the incoming 3-momentum norm in the centre of mass. We also denoted by $\mathcal{S}_{k\ell}$ a symmetry factor that is 2 if the outgoing particles are the same or 1 otherwise and g_i, g_j the number of degrees of freedom of particles i and j. Moreover, we introduced the factor $\mathcal{M}^2$ that we aim to compute in this section. With the decomposition of the amplitude its squared sum over spins can be written

$$\mathcal{M}^2 = \sum_{v,w}\left[\sum_{a\in\mathcal{V}}\sum_{b\in\mathcal{W}}\left((\mathcal{P}_v^a)^*\,\mathcal{P}_w^b\sum_{\rm spins}\left[(S_v^a)^\dagger\,S_w^b\right]\right)\right] \tag{B.69}$$

The * represents the complex conjugation. Thanks to the spinor sum rules and polarisation sum rules, we can always simplify the spin sum and write it as a polynomial function of the variables s and t under the simple form

$$\sum_{\rm spins}\left[(S_v^a)^\dagger\,S_w^b\right] = \sum_{n=0}^{\infty} q_{vw,n}^{ab}(s)t^n \equiv Q_{vw}^{ab}\,. \tag{B.70}$$

Note that an important property of Q_{vw}^{ab}, which will be useful later, is the symmetry $Q_{vw}^{ab} = \left(Q_{wv}^{ba}\right)^*$. Thus the $\mathcal{M}^2$ term can be written as

$$\mathcal{M}^2(s,t) = \sum_{v,w}\left[\sum_{a\in\mathcal{V}}\sum_{b\in\mathcal{W}}\left(\left(\mathcal{P}_v^a\right)^*\mathcal{P}_w^b Q_{vw}^{ab}\right)\right] \tag{B.71}$$

which represent a given value of v. We now develop the sums on v, w as

$$\begin{aligned}\mathcal{M}^2 = &\sum_{\substack{a\in\mathcal{S}\\b\in\mathcal{S}}}\left(\mathcal{P}_s^a\right)^*\mathcal{P}_s^b Q_{ss}^{ab} + \sum_{\substack{a\in\mathcal{T}\\b\in\mathcal{T}}}\left(\mathcal{P}_t^a\right)^*\mathcal{P}_t^b Q_{tt}^{ab} + \sum_{\substack{a\in\mathcal{U}\\b\in\mathcal{U}}}\left(\mathcal{P}_s^a\right)^*\mathcal{P}_s^b Q_{uu}^{ab}\\
&+\sum_{\substack{a\in\mathcal{S}\\b\in\mathcal{T}}}\left(\mathcal{P}_s^a\right)^*\mathcal{P}_t^b Q_{st}^{ab} + \sum_{\substack{a\in\mathcal{T}\\b\in\mathcal{S}}}\left(\mathcal{P}_s^a\right)^*\mathcal{P}_t^b Q_{ts}^{ab} + \sum_{\substack{a\in\mathcal{S}\\b\in\mathcal{U}}}\left(\mathcal{P}_s^a\right)^*\mathcal{P}_u^b Q_{su}^{ab}\\
&+\sum_{\substack{a\in\mathcal{U}\\b\in\mathcal{S}}}\left(\mathcal{P}_u^a\right)^*\mathcal{P}_s^b Q_{us}^{ab} + \sum_{\substack{a\in\mathcal{T}\\b\in\mathcal{U}}}\left(\mathcal{P}_t^a\right)^*\mathcal{P}_u^b Q_{tu}^{ab} + \sum_{\substack{a\in\mathcal{U}\\b\in\mathcal{T}}}\left(\mathcal{P}_u^a\right)^*\mathcal{P}_t^b Q_{st}^{ab}\end{aligned} \tag{B.72}$$

Henceforth we isolate the squared terms from the interference terms. Therefore we write, for the first three sums in the first line of the equation above

$$\sum_{\substack{a\in\mathcal{V}\\b\in\mathcal{V}}}\left(\mathcal{P}_v^a\right)^*\mathcal{P}_v^b Q_{vv}^{ab} = \sum_{a\in\mathcal{V}}|\mathcal{P}_v^a|^2 Q_{vv}^{aa} + 2\sum_{\substack{a\in\mathcal{V}\\b\in\mathcal{V}\\a<b}}\Re\left[\left(\mathcal{P}_v^a\right)^*\mathcal{P}_v^b Q_{vv}^{ab}\right] \quad \forall v = s,t,u \tag{B.73}$$

Where the notation $a < b$ means that if we have summed on (a, b) we do not also sum on (b, a) (since this term is implicitly taken into account by the factor of 2 and the real part function). Moreover the terms in the second and third lines of Eq. (B.72) all correspond to interference terms therefore it yields

$$\sum_{\substack{a\in\mathcal{V}\\b\in\mathcal{W}}}\left(\mathcal{P}_v^a\right)^*\mathcal{P}_w^b Q_{vw}^{ab} + \sum_{\substack{a\in\mathcal{W}\\b\in\mathcal{V}}}\left(\mathcal{P}_w^a\right)^*\mathcal{P}_v^b Q_{wv}^{ab} = 2\sum_{\substack{a\in\mathcal{V}\\b\in\mathcal{W}}}\Re\left[\left(\mathcal{P}_v^a\right)^*\mathcal{P}_w^b Q_{vw}^{ab}\right] \quad \forall v \neq w \tag{B.74}$$

In other words we write the squared matrix element as

$$\begin{aligned}\mathcal{M}^2 = &\sum_{a\in\mathcal{S}}|\mathcal{P}_s^a|^2 Q_{ss}^{aa} + \sum_{a\in\mathcal{T}}|\mathcal{P}_t^a|^2 Q_{tt}^{aa} + \sum_{a\in\mathcal{U}}|\mathcal{P}_u^a|^2 Q_{uu}^{aa}\\
&+2\sum_{\substack{a\in\mathcal{S}\\b\in\mathcal{T}}}\Re\left[\left(\mathcal{P}_s^a\right)^*\mathcal{P}_t^b Q_{st}^{ab}\right] + 2\sum_{\substack{a\in\mathcal{S}\\b\in\mathcal{U}}}\Re\left[\left(\mathcal{P}_s^a\right)^*\mathcal{P}_u^b Q_{su}^{ab}\right] + 2\sum_{\substack{a\in\mathcal{T}\\b\in\mathcal{U}}}\Re\left[\left(\mathcal{P}_t^a\right)^*\mathcal{P}_u^b Q_{tu}^{ab}\right]\\
&+2\sum_{\substack{a\in\mathcal{S}\\b\in\mathcal{S}\\a<b}}\Re\left[\left(\mathcal{P}_s^a\right)^*\mathcal{P}_s^b Q_{ss}^{ab}\right] + 2\sum_{\substack{a\in\mathcal{T}\\b\in\mathcal{T}\\a<b}}\Re\left[\left(\mathcal{P}_t^a\right)^*\mathcal{P}_t^b Q_{tt}^{ab}\right] + 2\sum_{\substack{a\in\mathcal{U}\\b\in\mathcal{U}\\a<b}}\Re\left[\left(\mathcal{P}_u^a\right)^*\mathcal{P}_u^b Q_{uu}^{ab}\right]\end{aligned} \tag{B.75}$$

Therefore the first thing to do in our algorithm is to consider all possible mediators in every possible channel. Then we dress a table of the different couples and evaluate the polynomials Q which is done using FeynCalc (SHTABOVENKO et al. 2016). Let us see an example with generic mediators ϕ_1, ϕ_2, ϕ_3 and for an interaction where ϕ_1, ϕ_2, ϕ_3 contribute to the s-channel, ϕ_1, ϕ_3 to the t-channel and ϕ_2, ϕ_3 to the u-channel. Then

we dress the following tables

$$\begin{aligned}
\mathcal{SS}^2 \text{ table}: &\quad \{(\phi_1,\phi_1),(\phi_2,\phi_2),(\phi_3,\phi_3)\}\\
\mathcal{TT}^2 \text{ table}: &\quad \{(\phi_1,\phi_1),(\phi_3,\phi_3)\}\\
\mathcal{UU}^2 \text{ table}: &\quad \{(\phi_2,\phi_2),(\phi_3,\phi_3)\}\\
\mathcal{SS}^< \text{ table}: &\quad \{(\phi_1,\phi_2),(\phi_1,\phi_3),(\phi_2,\phi_3)\}\\
\mathcal{TT}^< \text{ table}: &\quad \{(\phi_1,\phi_3)\}\\
\mathcal{UU}^< \text{ table}: &\quad \{(\phi_2,\phi_3)\}\\
\mathcal{ST} \text{ table}: &\quad \{(\phi_1,\phi_1),(\phi_1,\phi_3),(\phi_2,\phi_1),(\phi_2,\phi_3),(\phi_3,\phi_1),(\phi_3,\phi_3)\}\\
\mathcal{SU} \text{ table}: &\quad \{(\phi_1,\phi_2),(\phi_1,\phi_3),(\phi_2,\phi_2),(\phi_2,\phi_3),(\phi_3,\phi_2),(\phi_3,\phi_3)\}\\
\mathcal{TU} \text{ table}: &\quad \{(\phi_1,\phi_2),(\phi_1,\phi_3),(\phi_3,\phi_1),(\phi_3,\phi_3)\}
\end{aligned} \tag{B.76}$$

Note that for the $\mathcal{TU}$ table for instance we need to have both (ϕ_1,ϕ_3) and (ϕ_3,ϕ_1) as in the first case ϕ_1 contributes to the t-channel and ϕ_3 to the u-channel while in the second case it is the opposite. We need to evaluate all the polynomials Q for these 28 couples. Fortunately, we are never facing such a complex system because if ϕ_1 and ϕ_2 for instance are from the same species we can generically compute polynomials for general couples $(\phi_{1/2},\phi_{1/2})$ which reduces the problem. The next step is to evaluate the integral over the Mandelstam variable t. First, for simplicity, we introduce the squared effective complex mass $\mu = m(m-i\Gamma) \in \mathbb{C}$ so that the propagators becomes

$$\mathcal{P}_v^a = \frac{1}{v-\mu_a} \tag{B.77}$$

Because of the linearity of the expression $\mathcal{M}^2$ we generically have to evaluate integrals of the form

$$\mathcal{I}_{vw}^{ab}(n) = \int_{t_{\min}}^{t_{\max}} (\mathcal{P}_v^a)^* \, \mathcal{P}_w^b t^n \mathrm{d}t \tag{B.78}$$

and as a matter of fact they can all be written under the form

$$\mathcal{J}_{p,q}^n(\alpha,\beta) = \int_{t_{\min}}^{t_{\max}} \frac{t^n}{(t-\alpha^*)^p (t-\beta)^q} \mathrm{d}t \tag{B.79}$$

where $(\alpha,\beta) \in \mathbb{C}$. Indeed, even that is straightforward for combination of s and t-channel propagators it is not obvious for u-channels. This comes from the property $s+t+u = m_i^2+m_j^2+m_k^2+m_\ell^2 \equiv M^2$ which gives

$$\mathcal{P}_u^a = \frac{1}{u-\mu_a} = \frac{-1}{t-\rho_a} \tag{B.80}$$

with the definition $\rho_a = M^2 - s - \mu_a$. Therefore we can rewrite

$$\begin{aligned}
&\mathcal{I}_{ss}^{ab}(n) = \frac{1}{(s-\mu_a^*)(s-\mu_b)} \mathcal{J}_{0,0}^n(0,0)\,, \quad \mathcal{I}_{tt}^{ab}(n) = \mathcal{J}_{1,1}^n(\mu_a,\mu_b)\,, \quad \mathcal{I}_{uu}^{ab}(n) = \mathcal{J}_{1,1}^n(\rho_a,\rho_b)\\
&\mathcal{I}_{st}^{ab}(n) = \frac{1}{s-\mu_a^*} \mathcal{J}_{0,1}^n(0,\mu_b)\,, \quad \mathcal{I}_{su}^{ab} = \frac{-1}{s-\mu_a^*} \mathcal{J}_{0,1}^n(0,\rho_b) \quad \mathcal{I}_{st}^{ab}(n) = -\mathcal{J}_{1,1}^n(\mu_a,\rho_b)
\end{aligned} \tag{B.81}$$

So let us know give an expression for $\mathcal{J}_n^{\alpha,\beta}$. The first step is to perform a partial fraction decomposition of the integrand. Indeed we can always write

$$\frac{1}{(t-\alpha^*)^p (t-\beta)^q} = \sum_{l=1}^{p} \frac{A_l}{(t-\alpha^*)^l} + \sum_{l=1}^{q} \frac{B_l}{(t-\beta)^l} \tag{B.82}$$

and it is thus convenient to introduce

$$j_l^n(\alpha) = \int_{t_{\min}}^{t_{\max}} \frac{t^n}{(t-\alpha)^l} \mathrm{d}t \tag{B.83}$$

such that the total integral $\mathcal{J}$ can be written

$$\mathcal{J}_{p,q}^n(\alpha,\beta) = \sum_{l=1}^{p} A_l j_l^n(\alpha^*) + \sum_{l=1}^{q} B_l j_l^n(\beta)\,. \tag{B.84}$$

In particular, for $p=1$ and $q=1$ we have $A_1 = 1/(\alpha^*-\beta)$ and $B_1 = -1/(\alpha^*-\beta)$. In order to simplify the small j integral we can start by introducing the change of variable $y = (t-\alpha)/\alpha$ so that

$$j_l^n(\alpha) = \alpha^{n-l+1}\int_{y_{\min}}^{y_{\max}} (y+1)^n y^{-l}\mathrm{d}y = \alpha^{n-l+1}\sum_{r=0}^{n}\binom{n}{r}\int_{y_{\min}}^{y_{\max}} y^{r-l}\mathrm{d}y \tag{B.85}$$

Then being careful in treating the element $r = l-1$ in the sum, to introduce a logarithm dependence, it yields

$$j_l^n(\alpha) = \alpha^{n-l+1}\left\{\sum_{\substack{r=0\\ r\neq l-1}}^{n}\binom{n}{r}\frac{y_{\max}^{r-l+1}-y_{\min}^{r-l+1}}{r-l+1} - \binom{n}{l-1}\ln\left(\frac{y_{\max}}{y_{\min}}\right)\right\} \tag{B.86}$$

A convenient parameter to introduce is $u = (t_{\min}-t_{\max})/(t_{\max}-\alpha) = y_{\max}/y_{\min}-1$. Indeed in the non relativistic limit, that we investigate further below, $t_{\max}-t_{\min}\sim 0$ and therefore $|u|<1$ which allows for further developments in series. Written in terms of u the integral j becomes

$$j_l^n(\alpha) = \alpha^{n-l+1}\left\{\sum_{\substack{r=0\\ r\neq l-1}}^{n}\binom{n}{r}\frac{y_{\max}^{r-l+1}}{r-l+1}\left[1-(1+u)^{r-l+1}\right] - \binom{n}{l-1}\ln(1+u)\right\}. \tag{B.87}$$

Combining everything allows to evaluate the total integral over the squares matrix element systematically, whatever the tree-level $2\to 2$ interaction we consider.

B.3.2 Mandelstam variables and kinematics

In order to pursue the computation we review here some properties of the Mandelstam variables for a generic $i+j\to k+\ell$ interaction with particles of respective mass m_i, m_j, m_k, m_ℓ. Using the lorentz factor associated to the relative velocity $\gamma_{\rm rel} = (1-v_{\rm rel}^2)^{1/2}$ on can write s under three different ways

$$\begin{aligned} s &= (m_i+m_j)^2 + 2m_i m_j(\gamma_{\rm rel}-1)\\ s &= m_i^2+m_j^2+2\left(\sqrt{m_i^2+\bar{p}_{ij}^2}\sqrt{m_j^2+\bar{p}_{ij}^2}+\bar{p}_{ij}^2\right)\\ s &= m_k^2+m_\ell^2+2\left(\sqrt{m_k^2+\bar{p}_{k\ell}^2}\sqrt{m_\ell^2+\bar{p}_{k\ell}^2}+\bar{p}_{k\ell}^2\right). \end{aligned} \tag{B.88}$$

Massaging the second and third expressions yields

$$\begin{aligned} \bar{p}_{ij}^2 &= \frac{1}{4s}\left(s-(m_i-m_j)^2\right)\left(s-(m_i+m_j)^2\right)\\ \bar{p}_{k\ell}^2 &= \frac{1}{4s}\left(s-(m_k-m_\ell)^2\right)\left(s-(m_k+m_\ell)^2\right) \end{aligned} \tag{B.89}$$

Combining this expression with the value of s in terms of $\gamma_{\rm rel}$ we can express $\bar{p}_{ij}$ as well in terms of the Lorentz boost factor and the masses as

$$\bar{p}_{ij} = m_i m_j \sqrt{\frac{\gamma_{\rm rel}^2 - 1}{(m_i + m_j)^2 + 2 m_i m_j (\gamma_{\rm rel} - 1)}} \,. \tag{B.90}$$

Eventually, now that we have expressed s we wan look at t. First, we define the scattering angle in the center of mass frame $\bar{\theta}$ through the implicit relation $\cos\bar{\theta} = \bar{\mathbf{p}}_1 \bar{\mathbf{p}}_3 / \bar{p}^2$. Then t is given by

$$\begin{aligned} t &= m_i^2 + m_k^2 - 2\left(\sqrt{m_i^2 + \bar{p}_{ij}^2}\sqrt{m_k^2 + \bar{p}_{k\ell}^2} - \bar{p}_{ij}\bar{p}_{k\ell}\cos\bar{\theta}\right) \\ &= m_j^2 + m_\ell^2 - 2\left(\sqrt{m_j^2 + \bar{p}_{ij}^2}\sqrt{m_\ell^2 + \bar{p}_{k\ell}^2} - \bar{p}_{ij}\bar{p}_{k\ell}\cos\bar{\theta}\right) \,. \end{aligned} \tag{B.91}$$

In particular in the next section we rely on $t_{\rm max} - t_{\rm min}$ that is given always

$$t_{\rm max} - t_{\rm min} = 4\bar{p}_{ij}\bar{p}_{k\ell} \tag{B.92}$$

and therefore tends to 0 at small relative velocity when $\gamma_{\rm rel} \to 1$.

B.3.3 The small velocity expansion

Relative velocity and a classical view of temperature

Let us here address a bit more in details the definition of the temperature. So far it has been introduced through the thermodynamic equalities, in the Maxwell-Juttner distribution. Here we present a simple computation that links the temperature to its statistical representation as a measure of the average kinetic energy of particles. Consider two particles labelled 1 with momentum q_1 and 2 with momentum q_2 in the LIF then we can define the Lorentz invariant concept of relative velocity as

$$v_{\rm rel} \equiv \frac{1}{(\eta_{\mu\nu} q_1^\mu q_2^\nu)} \sqrt{(\eta q_1^\mu q_2^\nu)^2 - m_1^2 m_2^2} \tag{B.93}$$

Note that this definition is slightly different than the Møller velocity. It is, more particularly,

$$v_{\text{Møl}} \equiv \frac{(q_1.q_2)}{E(q_1)E(q_2)} v_{\rm rel} \tag{B.94}$$

and they become the same in the non-relativistic case, when the mass of the involved particles is much higher than the momenta. Now let us focus at the average value of the relative velocity squared between two particles of a same species of mass m. With n the number density of particles, it can be defined as

$$\left\langle v_{\rm rel}^2 \right\rangle \equiv \frac{g_a^2}{n_a^2} \int f_a(q_1^i) f_a(q_2^i) v_{\rm rel}^2 \frac{{\rm d}^3\mathbf{q}_1}{(2\pi)^3} \frac{{\rm d}^3\mathbf{q}_2}{(2\pi)^3} \tag{B.95}$$

where for shorthand notations the space-time dependence of the functions in y^μ is omitted. For an isotropic PSDF it is possible to integrate over the angle between the two momenta $\mathbf{q}_1$ and $\mathbf{q}_2$ so that it yields

$$\left\langle v_{\rm rel}^2 \right\rangle = \frac{g_a^2}{n_a^2} \int f_a(q_1) f_a(q_2) \frac{q_1^2 + q_2^2}{m_a^2 + q_1^2 + q_2^2} \frac{{\rm d}^3\mathbf{q}_1}{(2\pi)^3} \frac{{\rm d}^3\mathbf{q}_2}{(2\pi)^3} \,. \tag{B.96}$$

In the non-relativistic limit the mass dominates, $m^2 \gg q_1^2 + q_2^2$, and the average relative velocity squared takes the form of a kinetic energy per units of mass. Indeed, it can be written

$$\left\langle v_{\rm rel}^2 \right\rangle_{\rm NR} = 2\left\langle \frac{q^2}{m_a^2} \right\rangle = \frac{2g_a}{n_a}\int f_a(q)\frac{q^2}{m_a^2}\frac{{\rm d}^3\mathbf{q}}{(2\pi)^3} \tag{B.97}$$

In the case of the Fermi-Dirac and Bose-Einstein distributions, in the non-relativistic case, $f(q) = f^{\rm eq}(q)$ reduces to a Maxwell-Boltzmann distribution so that

$$\left\langle v_{\rm rel}^2 \right\rangle_{\rm NR} = \frac{6T}{m_a} \tag{B.98}$$

which relates the velocity dispersion of the gas to its temperature. Let us emphasize however that this definition is only valid for non-relativistic species.

General development

In order to properly evaluate some cross-sections, it is necessary to evaluate the small u series expansion of Eq. (B.87). Indeed, we just have mentionned above that, for a small relative velocity, u goes to 0. Therefore, annihilation cross-sections of non-relativistic DM are in this regime. Moreover, let us look at scattering cross-sections for a process involving non relativistic DM and a DM fermion $\chi\psi \to \chi\psi$ in the t-channel with propagator of effective mass $\mu_a \simeq m_a^2$. The value of u is always given by $-4\overline{p}_{ij}(s)\overline{p}_{ab}(s)$

$$|u| = \frac{4m_\chi^2}{|\mu_a|}\frac{\omega^2 - m_\psi^2}{m_\chi^2 + m_\psi^2 + 2\omega m_\chi} \tag{B.99}$$

where ω is here the SM fermion energy in the rest frame of the DM particle. Therefore in order to evaluate the scattering rate for kinetic decoupling, we need to integrate over the full distribution of SM fermions we have to evaluate configurations where $\omega \simeq m_\psi^2$. This amounts to say that we need to integrate on slow DM fermions so that the relative velocity with DM is small. Therefore $|u|$ can go close to 0 as well.

For $|u| < 1$, the expression of Eq. (B.87) can be developed in a power series by using

$$1 - (1+u)^{r-l+1} = -\sum_{q=0}^{\infty}\binom{r-l+1}{q+1}u^{q+1} \tag{B.100}$$

where the binomial coefficient corresponds to the generalised version. That is, for every $z \in \mathbb{C}$ – in practice here we only need $z \in \mathbb{Z}$ – and $n \geq 0$ it is

$$\binom{z}{n} \equiv \frac{z(z-1)(z-2)\dots(z-n+1)}{n!} \tag{B.101}$$

From this definition one can straightforwardly see that

$$\binom{r-l+1}{q+1} = \frac{r-l+1}{q+1}\binom{r-l}{q} \tag{B.102}$$

holds. Moreover one can also use the power series of the logarithm given by

$$\ln(1+u) = \sum_{q=0}^{\infty}\frac{(-1)^q}{q+1}u^{q+1}\,. \tag{B.103}$$

From the definition of the binomial coefficient one can further check that it is possible to given a similar expression between the series of the logarithm $\ln(1+u)$ and $1-(1+u)^{r-l+1}$ simply since

$$\binom{-1}{q} = (-1)^q \,. \tag{B.104}$$

In the end one just showed that

$$\begin{aligned} 1-(1+u)^{r-l+1} &= -(r-l+1)\sum_{q=0}^{\infty}\binom{r-l}{q}\frac{u^{q+1}}{q+1} \\ \ln(1+u) &= \sum_{q=0}^{\infty}\binom{-1}{q}\frac{u^{q+1}}{q+1}\,. \end{aligned} \tag{B.105}$$

Plugging this results in Eq. (B.87) gives

$$j_\ell^n(\alpha) = -\alpha^{n-l+1}\sum_{q=0}^{\infty}\frac{u^{q+1}}{q+1}\sum_{r=0}^{n}\binom{n}{r}\binom{r-l}{q}y_{\max}^{r-l+1}\,. \tag{B.106}$$

Therefore for small u one numerically uses this expansion for a few orders in q until convergence. It is also now possible to obtain the leading order of the small velocity expansion for any cross-section. First one can rewrite the previous expression as

$$j_l^n(\alpha) = -\sum_{q=0}^{\infty}\frac{(-4\bar{p}_{ij}\bar{p}_{k\ell})^{q+1}}{q+1}\sum_{r=0}^{n}\binom{n}{r}\binom{r-l}{q}\alpha^{n-r}(t_{\max}(s)-\alpha)^{r-l+q}\,. \tag{B.107}$$

Then, using the expression of the 3-momentum norm in the centre of mass with the relative velocity we obtain that, at zeroth order,

$$v_{\rm rel}\frac{1}{64\pi s\bar{p}_{ij}^2}j_l^n(\alpha) \underset{v_{\rm rel}\to 0}{\sim} \frac{1}{32\pi}\lambda_{ij}^{kl}\frac{\hat{t}_{\max}^n}{(\hat{t}_{\max}-\alpha)^l} \tag{B.108}$$

where $\hat{t}_{\max} = t_{\max}((m_i+m_j)^2)$ and

$$\lambda_{ij}^{k\ell} \equiv \frac{\sqrt{((m_k-m_\ell)^2-(m_i+m_j)^2)\,((m_k+m_\ell)^2-(m_i+m_j)^2)}}{m_i m_j (m_i+m_j)^2}\,. \tag{B.109}$$

All in all, one can then compute the total s-wave term of any cross-section simply by replacing all the terms j_l^n by the previous expression. In particular, for an annihilation cross section with $m_i = m_j$ and $m_k = m_\ell$ one can further simplify $\lambda_{ii}^{kk} = (1-m_k^2/m_i^2)^{1/2}/m_i^2$ and $\hat{t}_{\max} = m_i^2 - m_k^2$ which makes the evaluation straightforward in simple examples.

Example: transfer scattering cross-section

Because for an elastic scattering the momentum are such that $\bar{p}_{ij} = \bar{p}_{k\ell}$ and $t_{\max} = 0$, we can simplify even further the expression of j_ℓ^n in that case. It yields

$$j_\ell^n(\alpha) = (-1)^\ell\sum_{q=0}^{\infty}\frac{(2\bar{p}_{ij})^{2(q+1)}}{q+1}\alpha^{n-\ell-q}\mathcal{G}(n,q,\ell) \tag{B.110}$$

where we introduced the term

$$\mathcal{G}_q^{nl} = \sum_{r=0}^{n} \binom{n}{r} \binom{r-l}{q} (-1)^r \,. \tag{B.111}$$

The transfer cross-section, with mediator of mass $m_{\rm m}$, width $\Gamma_{\rm m} \neq 0$ and reduced complex mass squared associated $\mu_{\rm m} = m_{\rm m}(m_{\rm m} - i\Gamma_{\rm m})$, is

$$\bar{\sigma}_{\rm T} = \frac{1}{128\pi m_{\rm m}\Gamma_{\rm m}} \frac{-1}{g_i g_j} \sum_n \frac{q_n(s)}{s} \sum_{q=0}^{\infty} \frac{4^{(q+1)}}{q+1} \bar{p}_{ij}^{2(q-1)} \Im\left\{\mu_{\rm m}^{n-q}\right\} \mathcal{G}_q^{n+1,1} \tag{B.112}$$

We can notice that when $\bar{p}_{ij} \to 0$ (which corresponds to $v_{\rm rel} \to 0$) this expression is a priori divergent, which is a problem. However by noticing that

$$\mathcal{G}_{q=0}^{n+1,l} = \sum_{r=0}^{n+1} \binom{n+1}{r} (-1)^r = 0 \tag{B.113}$$

it yields that the sum over q begins at $q = 1$ effectively and that there are no divergence at all. By a redefinition of $q \to q - 1$ the result for the transfer cross section is then

$$\bar{\sigma}_{\rm T} = \frac{1}{8\pi m_p^2} \frac{1}{g_i g_j} \sum_n q_n(s) \frac{m_{\rm m}^{2(n-1)}}{s} \sum_{q=0}^{\infty} \frac{-1}{q+2} \left(\frac{2\bar{p}_{ij}}{m_{\rm m}}\right)^{2q} \Im\left\{\left(1 - i\frac{\Gamma_{\rm m}}{m_{\rm m}}\right)^{n-q-1}\right\} \frac{m_p}{\Gamma_p} \mathcal{G}_{q+1}^{n+1,1} \,. \tag{B.114}$$

In the case $\Gamma_{\rm m} = 0$ the final expression is similar,

$$\bar{\sigma}_{\rm T} = \frac{1}{8\pi m_{\rm m}^2} \frac{1}{g_i g_j} \sum_n q_n(s) \frac{m_{\rm m}^{2(n-1)}}{s} \sum_{q=0}^{\infty} \frac{-1}{q+2} \left(\frac{2\bar{p}_{ij}}{m_{\rm m}}\right)^{2q} \mathcal{G}_{q+1}^{n+1,2} \,. \tag{B.115}$$

In order to make a correct development we can use the following relations

$$\begin{aligned} \mathcal{G}_1^{n+1,l} &= -\delta_{n,0} \\ \mathcal{G}_2^{n+1,l} &= l\delta_{n,0} + \delta_{n,1} \\ \mathcal{G}_3^{n+1,l} &= -l(l+1)\delta_{n,0}/2 - l\delta_{n,1} - \delta_{n,2} \end{aligned} \tag{B.116}$$

which indicate that the leading term in the velocity expansion for a given value of n is given by $q = n$ and that it is of order $v_{\rm rel}^{2n}$. Therefore we can parametrize in a very simple way

$$\bar{\sigma}_{\rm T} = \frac{1}{8\pi m_p^2} \frac{1}{g_i g_j} \sum_n q_n \left((m_i + m_j)^2\right) b_n v_{\rm rel}^{2n} + \mathcal{O}\left(v_{\rm rel}^{2(n+1)}\right) \tag{B.117}$$

and in both cases, $\Gamma_p = 0$ the factors b_n can be expressed under the form

$$b_n = \frac{1}{m_{\rm m}^2 + \Gamma_{\rm m}^2} \frac{(-4)^n}{n+2} \frac{(m_i m_j)^{2n}}{(m_i + m_j)^{2(n+1)}} \,. \tag{B.118}$$

B.3.4 Self-interaction of Majorana fermions

The Feynman rules given in DENNER et al. (1992) or HABER et al. (1985) are globally similar for Dirac and Majorana particles – up to a change in the normalisation of the coupling constant. However, when considering the self-interaction, the associated amplitude for Majorana particles has a u-channel diagram which has no counterpart

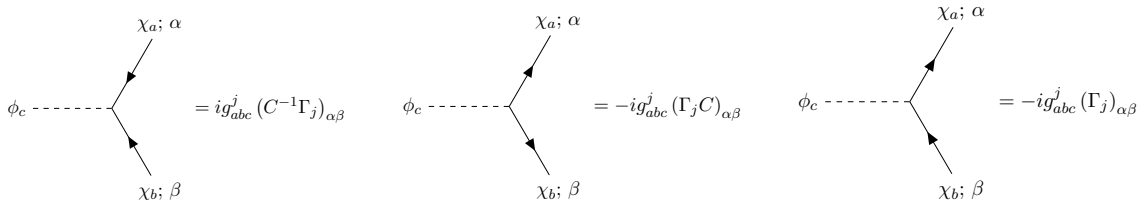

Figure B.1 – Our convention for the three different Majorana vertices

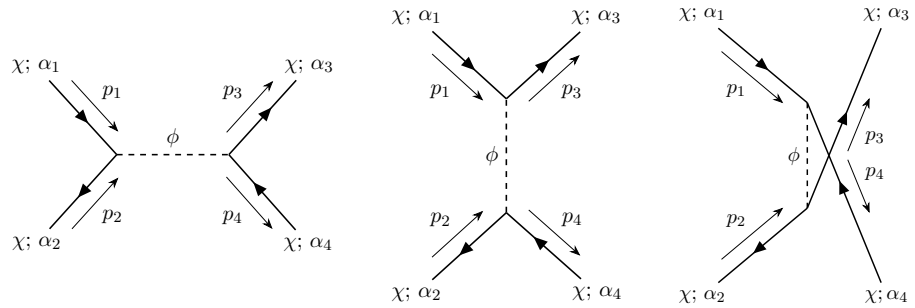

Figure B.2 – Feynman diagrams for the self-interaction with Majorana particles

in the Dirac scenario. In version 9.2, FeynCalc does not temper well with Majorana fermions. In practice, the u-channel in itself is not problematic and could be evaluated with the usual Dirac rules on its own, but its interference with the s and t-channels produce spinor configurations that are not understood. The new version 9.3, released in 2020, solves the issue but since we started working on version 9.2 we describe here the solution we adopted in the first place (the same that authors of version 9.3 have implemented). The idea relies on taking the transpose of certain fermion chains. Consider the generic Lagrangian

$$\mathcal{L} = -\frac{1}{2} g^j_{abc} \chi_a \Gamma_j \chi_b \phi_c \tag{B.119}$$

such that $\Gamma_j = 1, i\gamma^5, \gamma^\mu\gamma^5, \gamma^\mu$ spans all the possible operators. In Fig. B.1 are shown our convention for the corresponding vertices. In the following, we simply focus on a single mediator ϕ_c and the self-interaction amplitude. The different S terms introduced in Eq. (B.66) are, for the three available channels,

$$\begin{aligned} S_s &= -(g^j_c)^2 \left[\overline{v}(p_2)\Gamma_j u(p_1)\right]\left[\overline{u}(p_3)\Gamma_j v(p_4)\right] \\ S_t &= +(g^j_c)^2 \left[\overline{u}(p_3)\Gamma_j u(p_1)\right]\left[\overline{v}(p_2)\Gamma_j v(p_4)\right] \\ S_u &= +(g^j_c)^2 \left[\overline{v}(p_1)\Gamma_j v(p_4)\right]\left[\overline{v}(p_2)\Gamma_j v(p_3)\right] . \end{aligned} \tag{B.120}$$

Note that following Denner et al. (1992), the term S_s fixes the fermion chain ordering 2134. The sign in front of S_t comes from a (-1) due to the negative permutation $2134 \to 3124$. Similarly, the sign in front of S_u also comes from the negative permutation $2134 \to 1423$. The total amplitude is given by $\mathcal{M} = \mathcal{M}_s + \mathcal{M}_t + \mathcal{M}_u$. In order to evaluate the matrix element squared it is necessary to evaluate $\overline{S_s} S_u$ and $\overline{S_t} S_u$. However, when evaluating the fermion spin sum FeynCalc v9.2 can only treat the following terms

$$\sum_s u_s(p)\overline{u}_s(p) = \not{p} + m \quad \text{and} \quad \sum_s v_s(p)\overline{v}_s(p) = \not{p} - m \tag{B.121}$$

therefore it is straightforward to show that this can not work. Indeed the spinor content is not the same in S_s and S_u, thus the need to transform the expressions.

The idea is to rely on the the following property that relates the spinors thanks to the charge conjugation matrix

$$u_s(p) = C\overline{v}_s^T(p) \quad \text{and} \quad v_s(p) = C\overline{u}_s^T(p)\,, \tag{B.122}$$

and with $C^\dagger = C^{-1}$ and $C^T = -C$. Moreover one can also show, thanks to the properties of the gamma matrices, the following general identity

$$C^{-1}\Gamma_j C = \eta_j \Gamma_j^T \tag{B.123}$$

where $\eta_j = 1$ if $\Gamma_j = 1, \gamma^5, \gamma^\mu\gamma^5$ and it is -1 otherwise. Let us look now at the expression of S_u and in particular at the two different fermion chains. By a transpose operation the two chains are

$$\begin{aligned}\overline{v}(p_2)\Gamma_j v(p_3) &= \left[\overline{v}(p_2)\Gamma_j v(p_3)\right]^T = v^T(p_3)\Gamma_j^T\overline{v}^T(p_2)\\ &= -\overline{u}(p_3)C\Gamma_j^T C^{-1}u(p_2) = -\eta_j\overline{u}(p_3)\Gamma_j u(p_2)\end{aligned} \tag{B.124}$$

and $\overline{v}(p_1)\Gamma_j v(p_4) = -\eta_j\overline{u}(p_4)\Gamma_j u(p_1)$. In the end the term S_u can be given in four different ways listed here

$$S_u = +(g_c^j)^2 \times \left\{\begin{array}{l} +\left[\overline{v}(p_1)\Gamma_j v(p_4)\right]\left[\overline{v}(p_2)\Gamma_j v(p_3)\right]\\ -\eta_j\left[\overline{u}(p_4)\Gamma_j u(p_1)\right]\left[\overline{v}(p_2)\Gamma_j v(p_3)\right]\\ -\eta_j\left[\overline{v}(p_1)\Gamma_j v(p_4)\right]\left[\overline{u}(p_3)\Gamma_j u(p_2)\right]\\ +\left[\overline{u}(p_4)\Gamma_j u(p_1)\right]\left[\overline{u}(p_3)\Gamma_j u(p_2)\right]\end{array}\right. \tag{B.125}$$

where we used the fact that $\eta_j^2 = 1$ in the last equality. In order to evaluate $\overline{S_s}S_u$ we now also transpose the fermion chains in S_s to obtain

$$S_s = -(g_c^j)^2 \times \left\{\begin{array}{l} +\left[\overline{v}(p_2)\Gamma_j u(p_1)\right]\left[\overline{u}(p_3)\Gamma_j v(p_4)\right]\\ -\eta_j\left[\overline{v}(p_1)\Gamma_j u(p_2)\right]\left[\overline{u}(p_3)\Gamma_j v(p_4)\right]\\ -\eta_j\left[\overline{v}(p_2)\Gamma_j u(p_1)\right]\left[\overline{u}(p_4)\Gamma_j v(p_3)\right]\\ +\left[\overline{v}(p_1)\Gamma_j u(p_2)\right]\left[\overline{u}(p_4)\Gamma_j v(p_3)\right]\end{array}\right. . \tag{B.126}$$

Now, we only need to choose one expression of S_s and one expression of S_u such that they share the same spinor content. For instance, we can choose the third expression of S_s and the second of S_u or the second expression of S_s and the third of S_u that are the only two combinations that work. Therefore it is now possible to use the usual spin sum rules without any ambiguity for the term $\overline{S_s}S_u$. Similarly, for the term S_t we can also transform the fermion chains as

$$S_t = +(g_c^j)^2 \times \left\{\begin{array}{l} +\left[\overline{u}(p_3)\Gamma_j u(p_1)\right]\left[\overline{v}(p_2)\Gamma_j v(p_4)\right]\\ -\eta_j\left[\overline{v}(p_1)\Gamma_j v(p_3)\right]\left[\overline{v}(p_2)\Gamma_j v(p_4)\right]\\ -\eta_j\left[\overline{u}(p_3)\Gamma_j u(p_1)\right]\left[\overline{u}(p_4)\Gamma_j u(p_2)\right]\\ +\left[\overline{v}(p_1)\Gamma_j v(p_3)\right]\left[\overline{u}(p_4)\Gamma_j u(p_2)\right]\end{array}\right. . \tag{B.127}$$

In that case, the second (resp. third) expression of S_t matches with the first (resp. fourth) of S_u. Two combinations are thus possible to implement fermion chains that FeynCalc v9.2 can treat.

B.4 Triangle diagram production of photons and gluons

We focus here on the production from a pseudo-scalar from a Dirac fermion triangle loop. The scalar case has been widely studied in the literature for the Higgs particle decay into two photons (Bergström et al. 1985; Djouadi 2008; Marciano et al. 2012). The amplitude of the triangle plot represented in Fig. B.3, amputated from the polarisation vectors, is proportional to

$$T^{\mu\nu} = -\int \frac{\mathrm{d}^4k}{(2\pi)^4}\mathrm{Tr}\left\{i\gamma^\mu\frac{i(\not{k}+\not{p}_1+m)}{(k+p_1)^2-m^2}\gamma^5\frac{i(\not{k}-\not{p}_2+m)}{(k-p_2)^2-m^2}i\gamma^\nu\frac{i(\not{k}+m)}{k^2-m^2}\right\} \tag{B.128}$$

Using the properties of the gamma matrices

$$\mathrm{Tr}\left\{\gamma^\mu(\not{k}+\not{p}_1+m)\gamma^5(\not{k}-\not{p}_2+m)\gamma^\nu(\not{k}+m)\right\} = 4im\varepsilon^{\mu\nu\rho\sigma}(p_1)_\rho(p_2)_\sigma\,, \tag{B.129}$$

and it yields a much simpler formulation,

$$T^{\mu\nu} = 4m\varepsilon^{\mu\nu\rho\sigma}(p_1)_\rho(p_2)_\sigma\int\frac{\mathrm{d}^4k}{(2\pi)^4}\frac{1}{(k+p_1)^2-m^2}\frac{1}{(k-p_2)^2-m^2}\frac{1}{k^2-m^2}\,. \tag{B.130}$$

that we can compute using the Feynman parametrisation for integration. First let us denote the three factors appearing un the denominator

$$\begin{aligned} D_1 &= k^2-m^2 \\ D_2 &= (k+p_1)^2-m^2 \\ D_3 &= (k-p_2)^2-m^2 \end{aligned} \tag{B.131}$$

and the integral as

$$C_0 \equiv \int\frac{\mathrm{d}^dk}{(2\pi)^d}\frac{1}{D_1D_2D_3}\,. \tag{B.132}$$

The Feynman parametrisation consists in writing

$$\frac{1}{D_1D_2D_3} = 2\int_0^1\mathrm{d}y\int_0^y\mathrm{d}z\,\frac{1}{\left[D_1+(D_2-D_1)y+(D_3-D_2)z\right]^3}\,. \tag{B.133}$$

Massaging the denominator $\mathcal{D}(y,z) = D_1+(D_2-D_1)y+(D_3-D_2)z$ it is possible to factorise the dependence in k as

$$\begin{aligned} \mathcal{D}(y,z) &= k^2-m^2+y\left[(k+p_1)^2-k^2\right]+z\left[(k-p_2)^2-(k+p_1)^2\right] \\ &= k^2-m^2+2ykp_1-2zk(p_1+p_2) \\ &= [k+yp_1-z(p_1+p_2)]^2-2z^2p_1p_2+2yzp_1p_2-m^2 \end{aligned} \tag{B.134}$$

where we used the fact that $p_1^2 = p_2^2 = 0$. With a change of variables $k \to k-yp_1+z(p1+p2)$ and by introducing the Mandelstam variable $s = (p_1+p_2)^2 = 2p_1p_2$ it yields $\mathcal{D} \to \mathcal{D}'(y,z) = k^2-sz(z-y)-m^2$, thus giving

$$C_0 = 2\int_0^1\mathrm{d}y\int_0^y\mathrm{d}z\int\frac{\mathrm{d}^4k}{(2\pi)^4}\frac{1}{\left[k^2-sz(z-y)-m^2\right]^3}\,. \tag{B.135}$$

By a Wick rotation it yields

$$C_0 = -i\frac{1}{8\pi^2\Gamma(3)}\int_0^1\mathrm{d}y\int_0^y\mathrm{d}z\,\frac{1}{sz(z-y)+m^2} \tag{B.136}$$

Using the complex square root and the complex logarithm and with the definition of a *reduced* mass squared $x = 4m^2/s$ (compared to the energy in the centre of mass),

$$\begin{aligned}\int_0^y \mathrm{d}z\, \frac{1}{sz(z-y)+m^2} &= \frac{x^2}{2m^2}\int_{-y}^{+y} \mathrm{d}v\, \frac{1}{v^2-y^2+x} \\ &= \frac{x}{2m^2\sqrt{y^2-x}}\int_{-y/\sqrt{y^2-x^2}}^{y/\sqrt{y^2-x^2}} \mathrm{d}w\, \frac{1}{w^2-1} \\ &= \frac{x}{4m^2\sqrt{y^2-x}}\ln\left(\frac{\sqrt{y^2-x}-y}{\sqrt{y^2-x}+y}\right).\end{aligned} \tag{B.137}$$

The second integration gives

$$\begin{aligned}\int_0^1 \mathrm{d}y\int_0^y \mathrm{d}z\, \frac{1}{sz(z-y)+m^2} &= \frac{x}{4m^2}\int_0^1 \mathrm{d}y\, \frac{1}{\sqrt{y^2-x}}\ln\left(\frac{\sqrt{y^2-x}-y}{\sqrt{y^2-x}+y}\right) \\ &= -\frac{x}{8m^2}\left[\ln^2\left(\frac{\sqrt{y^2-x}-y}{\sqrt{y^2-x}+y}\right)\right]_0^1 \\ &= -\frac{x}{8m^2}\ln^2\left(\frac{\sqrt{1-x}-1}{\sqrt{1-x}+1}\right).\end{aligned} \tag{B.138}$$

The common notation is to introduce the function f_φ defined by

$$f_\varphi(x) = \frac{x}{4}\ln^2\left(\frac{\sqrt{1-x}-1}{\sqrt{1-x}+1}\right). \tag{B.139}$$

It yields the value of the coefficient C_0

$$C_0 = \frac{i}{32\pi^2 m^2} f_\varphi\left(\frac{4m^2}{s}\right), \tag{B.140}$$

such that the amplitude writes

$$T^{\mu\nu} = 4m\varepsilon^{\mu\nu\rho\sigma}(p_1)_\rho(p_2)_\sigma C_0 = \frac{i}{16\pi^2 m} f_\varphi\left(\frac{4m^2}{s}\right) 2\varepsilon^{\mu\nu\rho\sigma}(p_1)_\rho(p_2)_\sigma\,. \tag{B.141}$$

Now, if we want to write a complete amplitude for the disintegration of a pseudo-scalar φ_k into two photons or two gluons though the fermion ψ_j we need to add the charges at each vertex and the sum over colour indices in each quark propagator so that

$$\begin{aligned}i\mathcal{M}^{\mu\nu}_{\gamma\gamma} &= i\mathcal{B}^j_k \frac{N_j(Q_j e)^2}{16\pi^2 m} f_\varphi\left(\frac{4m^2}{s}\right) 2\varepsilon^{\mu\nu\rho\sigma}(p_1)_\rho(p_2)_\sigma \epsilon^*_\mu(p_1)\epsilon^*_\nu(p_2) \\ i\mathcal{M}^{\mu\nu}_{gg} &= i\mathcal{B}^j_k \frac{g_s^2\delta^{\mathrm{q}}_j}{16\pi^2 m} f_\varphi\left(\frac{4m^2}{s}\right) \mathrm{Tr}\{T^a T^b\} 2\varepsilon^{\mu\nu\rho\sigma}(p_1)_\rho(p_2)_\sigma \epsilon^*_\mu(p_1)\epsilon^*_\nu(p_2)\end{aligned} \tag{B.142}$$

where $N_j = 3$, the number of colours, if ψ_j is a quark and $N_\psi = 1$ if it is a lepton. Moreover here we introduce δ^{q}_j that is 1 if ψ_j is a quark and 0 otherwise as well as $T^a \equiv \lambda^a/2$, the Gell-Mann matrices divided by the factor 2. They are normalised according such that

$$\mathrm{Tr}\{T^a T^b\} = 2\delta^{ab}\,. \tag{B.143}$$

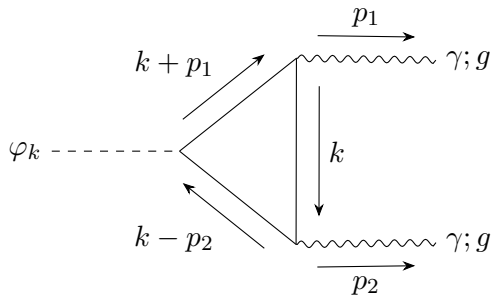

Figure B.3 – Triangle diagram

In addition, we introduce the fine structure constant and its strong counterpart, $\alpha_{\rm em} = e^2/(4\pi)$ and $\alpha_s = g_s^2/(4\pi)$ respectively, so that the previous expressions summarises to

$$\begin{aligned} i\mathcal{M}^{\mu\nu}_{\gamma\gamma} &= i\mathcal{B}^j_k \frac{\alpha_{\rm em}}{4\pi}\frac{N_j Q_j^2}{m} f_\varphi\left(\frac{4m^2}{s}\right) 2\varepsilon^{\mu\nu\rho\sigma}(p_1)_\rho (p_2)_\sigma \epsilon^*_\mu(p_1)\epsilon^*_\nu(p_2) \\ i\mathcal{M}^{\mu\nu}_{gg} &= i\mathcal{B}^j_k \frac{\alpha_s}{4\pi}\frac{\delta^{\rm q}_j}{2m} f_\varphi\left(\frac{4m^2}{s}\right) 2\varepsilon^{\mu\nu\rho\sigma}(p_1)_\rho (p_2)_\sigma \epsilon^*_\mu(p_1)\epsilon^*_\nu(p_2)\,. \end{aligned} \tag{B.144}$$

Let us now introduce the dual of the field strength $\tilde{F}^{\mu\nu} = \varepsilon^{\mu\nu\rho\sigma}F_{\rho\sigma}/2$ and $\tilde{G}^{a,\mu\nu} = \varepsilon^{\mu\nu\rho\sigma}G^a_{\rho\sigma}/2$, where $F_{\mu\nu} = (\partial_\mu A_\nu - \partial_\nu A_\mu)$ and $G^a_{\mu\nu} = (\partial_\mu A^a_\nu - \partial_n u A^a_\mu + g f^{abc} A^b_\mu A^c_\mu)$. We can compute, in Fourier space (with $\partial_\mu \to i p_\mu$),

$$\begin{aligned} F_{\mu\nu}\tilde{F}^{\mu\nu} &\to 2\varepsilon^{\mu\nu\rho\sigma}(p_1)_\rho(p_2)_\sigma A_{1,\mu}A_{2,\nu} \\ G^a_{\mu\nu}\tilde{G}^{a,\mu\nu} &\to 2\varepsilon^{\mu\nu\rho\sigma}(p_1)_\rho(p_2)_\sigma A^a_{1,\mu}A^a_{2,\nu} + \mathcal{O}(A^3)\,. \end{aligned} \tag{B.145}$$

Therefore the interaction between pseudo-scalars and two photons or gluons at one loop-level can be described with the two effective terms in the Lagrangian

$$\mathcal{L} \ni -\frac{\alpha_{\rm em}}{4\pi} C_\gamma \varphi_k F_{\mu\nu}\tilde{F}^{\mu\nu} - \frac{\alpha_s}{4\pi} C_g \varphi_k \mathrm{Tr}\{G_{\mu\nu}\tilde{G}^{\mu\nu}\} \tag{B.146}$$

with $G_{\mu\nu} \equiv G^a_{\mu\nu}T^a$ (sum over a implicit here) and with the definition of the coupling coefficients being

$$C_\gamma = -\mathcal{B}^j_k \frac{N_j Q_j^2}{m} f_\varphi\left(\frac{4m^2}{s}\right) \quad \text{and} \quad C_g = -\mathcal{B}^j_k \frac{1}{m} f_\varphi\left(\frac{4m^2}{s}\right). \tag{B.147}$$

In the case studied in Domingo (2017) one would have to set the couplings of the pseudo-scalar to the fermions as $\mathcal{B}^j_k = P_{11}/(\sqrt{2}v)m(\tan\beta)^{\pm 1}$ and we find the exact same results for the effective couplings, namely,

$$C_\gamma = -\frac{P_{11}}{2\sqrt{2}v} N_c Q^2 (\tan\beta)^{\pm 1}\mathcal{F}\left(\frac{m^2}{s}\right) \quad \text{and} \quad C_g = -\frac{P_{11}}{2\sqrt{2}v}(\tan\beta)^{\pm 1}\mathcal{F}\left(\frac{m^2}{s}\right). \tag{B.148}$$

with $\mathcal{F}(x) = 2f_\varphi(4x)$. Note that there is also a second diagrams to consider, inverting p_1 and p_2 as well as μ and ν in the expressions above. This additional diagram is equal to the one we computed here and it is taken into account from the new effective terms in the Lagrangian due to the factor of 2 appearing in the Feynman rules (for two identical outgoing states).

C

Complements on structure formation

In this appendix we give some formulas and performed computations used in Chapter 2. The first order perturbed Einstein equations are derived in a first section. The following section is devoted to the comoving curvature perturbation and finally, the last section addresses the initial conditions for the spherical collapse model.s

C.1 Perturbed Einstein equations

In order to evaluate the perturbed Einstein equations we first need to give the expression of the christoffel symbols and of the order 1 Einstein tensor. Firstly, the Christoffel symbols are

$$\begin{aligned}
\Gamma^0_{00} &= \mathcal{H} + \psi' \\
\Gamma^0_{0i} &= \partial_i \psi \\
\Gamma^i_{00} &= \delta^{ij}\partial_j \psi \\
\Gamma^0_{ij} &= \mathcal{H}\delta_{ij} - \left[\phi' + 2\mathcal{H}(\phi+\psi)\right]\delta_{ij} \\
\Gamma^i_{j0} &= \mathcal{H}\delta^i_j - \phi'\delta^i_j \\
\Gamma^i_{jk} &= -\left[\delta^i_k\partial_j\phi + \delta^i_j\partial_k\phi\right] + \delta_{jk}\delta^{il}\partial_l\phi = -2\delta^i_{(j}\partial_{k)}\phi + \delta_{jk}\delta^{il}\partial_l\phi
\end{aligned} \tag{C.1}$$

so that the Einstein tensor at first order becomes

$$\begin{aligned}
\delta G_{00} &= 2\nabla^2\phi - 6\mathcal{H}\phi' \\
\delta G_{0i} &= 2\partial_i(\phi' + \mathcal{H}\psi) \\
\delta G_{ij} &= \left[\nabla^2(\psi-\phi) + 2\phi'' + 2(2\mathcal{H}' + \mathcal{H}^2)(\phi+\psi) + 2\mathcal{H}\psi' + 4\mathcal{H}\phi'\right]\delta_{ij} + \partial_i\partial_j(\phi-\psi)\,.
\end{aligned} \tag{C.2}$$

Before going further one recall the Friedmann equations for the background, written in terms of $\mathcal{H}$ (and not H as in the main text). They are

$$\mathcal{H}^2 = \frac{8\pi G_{\rm N}}{3}\bar{\rho}a^2 \quad \text{and} \quad \mathcal{H}' + \mathcal{H}^2 = \frac{4\pi G_{\rm N}}{3}\bar{\rho}a^2(1-3w)\,. \tag{C.3}$$

Then using the first order of the stress energy tensor, the equation $\delta G_{\mu\nu} = 8\pi G_{\rm N} T_{\mu\nu}$ can be decomposed in four parts listed below.

- **The spatial traceless part:**

$$\delta\left[G_{ij}-\frac{1}{3}G_{mn}g^{mn}g_{ij}\right]=8\pi G_{\rm N}\delta\left[T_{ij}-\frac{1}{3}T_{mn}g^{mn}g_{ij}\right] \tag{C.4}$$

Keeping only the 1st order terms of this expression yields

$$\delta G_{ij}-\frac{1}{3}\delta G_{mn}\overline{g}^{mn}\overline{g}_{ij}=8\pi G_{\rm N}\left[\delta T_{ij}-\frac{1}{3}\delta T_{mn}\overline{g}^{mn}\overline{g}_{ij}\right]. \tag{C.5}$$

In order to use this equation it is necessary to write the first order perturbation of the strees energy tensor with indices down. This can be done quite easily, because at first order $\delta T_{\mu\nu}=\overline{g}_{\mu\rho}\delta T^{\rho}{}_{\nu}+\delta g_{\mu\rho}\overline{T}^{\rho}{}_{\nu}$ and therefore $\delta T_{ij}=-a^2\delta_{im}\delta T^{m}{}_{j}+2\phi a^2\delta_{ij}$. Remembering that indices of the stress-energy tensor are lowered and raised in Minkowsky's flat metric it yields

$$\left(\partial_i\partial_j-\frac{1}{3}\delta_{ij}\nabla^2\right)(\phi-\psi)=8\pi G_{\rm N}a^2\Pi_{ij}\,. \tag{C.6}$$

Writing now this equation in Fourier space and using the identity of Eq. (3.19) it simplifies to

$$\phi-\psi=12\pi G_{\rm N}a^2(\overline{\rho}+\overline{P})\sigma\,. \tag{C.7}$$

In most applications $\sigma=0$, which then implies that $\phi=\psi$. However for the moment let us write the most general equations possible and keep σ.

- **The 00-th component:**

$$\delta G_{00}=8\pi G_{\rm N}\delta T_{00}\,. \tag{C.8}$$

Developing the different term yields

$$\begin{aligned}2\nabla^2\phi-6\mathcal{H}\phi' &= 8\pi G_{\rm N}\left(\overline{g}_{0\mu}\delta T^{\mu}{}_{0}+\delta g_{0\mu}\overline{T}^{\mu}{}_{0}\right)\\ &= 8\pi G_{\rm N}\left(\overline{g}_{00}\delta T^{00}+\delta g_{00}\overline{T}^{0}{}_{0}\right)\\ &= 8\pi G_{\rm N}a^2\left(\delta\rho+2\psi\overline{\rho}\right)\end{aligned} \tag{C.9}$$

then using Friedmann equation (i.e. the zeroth order part of this equation) leaves

$$\nabla^2\phi=4\pi G_{\rm N}a^2\overline{\rho}\delta+3\mathcal{H}(\phi'+\mathcal{H}\psi)\,. \tag{C.10}$$

By using Friedmann equation we can further simplify this expression as

$$\nabla^2\phi=\frac{3}{2}\mathcal{H}^2\delta+3\mathcal{H}(\phi'+\mathcal{H}\psi)\,. \tag{C.11}$$

This equation is Poisson's equation in terms of δ.

- **The 0i component:**

$$\delta G_{0i}=8\pi G_{\rm N}\delta T_{0\rm i}\,. \tag{C.12}$$

It gives the differential equation

$$\partial_i\left[\phi'+\mathcal{H}\psi+4\pi G_{\rm N}a^2(\overline{\rho}+\overline{P})v\right]=0 \tag{C.13}$$

that we can integrate, assuming that perturbation vanish at infinity. Therefore

$$\phi' + \mathcal{H}\psi + 4\pi G_{\rm N} a^2(\overline{\rho} + \overline{P})v = 0 \tag{C.14}$$

and with this equation it is possible to relate the comoving density contrast Δ to the density contrast using only the potentials. Indeed by replacing the value of v in the expression, it yields

$$\Delta = \delta + \frac{2\phi'}{\mathcal{H}} + 2\psi\,. \tag{C.15}$$

Introducing this result in Eq. (C.10) one obtains Poisson's equation written in terms of the co-moving gauge density contrast Δ according to

$$\nabla^2\phi = 4\pi G_{\rm N} a^2\overline{\rho}\left[\delta - 3\mathcal{H}(1+w)v\right] = 4\pi G_{\rm N} a^2\overline{\rho}\Delta\,. \tag{C.16}$$

- **The spatial trace:**

$$\delta\left[g^{i\mu}G_{\mu j}\right] = 8\pi G_{\rm N}\delta T^{i}{}_{j}\,. \tag{C.17}$$

Since $\delta\left[g^{i\mu}G_{\mu j}\right] = \delta g^{i\mu}\overline{G}_{\mu j} + \overline{g}^{i\mu}\delta G_{\mu j}$, it yields

$$-a^{-2}\left[2\phi\delta^{im}\overline{G}_{mj} + \delta^{im}\delta G_{mi}\right] = -24\pi G_{\rm N}\delta P \tag{C.18}$$

and using the expression of the zeroth-order spatial component of Einstein's tensor $\overline{G}_{ij} = -(2\mathcal{H}' + \mathcal{H}^2)\delta_{ij}$ it is possible to develop the first part inside the brackets

$$\begin{aligned} 2\phi\delta^{im}\overline{G}_{mi} + \delta^{im}\delta G_{mi} &= 3\left[\nabla^2(\psi-\phi) + 2\phi'' + 2(2\mathcal{H}' + \mathcal{H}^2)\psi + 2\mathcal{H}\psi' + 4\mathcal{H}\phi'\right] + \nabla^2(\phi-\psi) \\ &= 6\left[\phi'' + (2\mathcal{H}' + \mathcal{H}^2)\psi + \mathcal{H}(\psi' + 2\phi')\right] - 2\nabla^2(\phi-\psi)\,. \end{aligned} \tag{C.19}$$

Eventually, combining this equation with the expression of $\phi - \psi$ gives the last formula we will derive with Einstein's equation. It relates the potentials to δP and σ in the following way

$$\phi'' + (2\mathcal{H}' + \mathcal{H}^2)\psi + \mathcal{H}(\psi' + 2\phi') = 4\pi G_{\rm N} a^2(\overline{\rho} + \overline{P})\left[\frac{\delta P}{\overline{\rho} + \overline{P}} + \nabla^2\sigma\right]. \tag{C.20}$$

C.2 The comoving curvature perturbation

Using the 0i$^{\rm th}$ component of Einstein's equation the comoving curvature perturbation in the Newtonian gauge transforms into

$$\mathcal{R} = -\phi - \mathcal{H}\frac{\phi' + \mathcal{H}\psi}{4\pi G_{\rm N} a^2\left(\overline{\rho} + \overline{P}\right)}\,. \tag{C.21}$$

Differentiating now this expression and using the continuity equation for the background yields the expression of the co-moving curvature variation rate

$$\mathcal{R}' = -\phi' - \mathcal{H}'\frac{\phi' + \mathcal{H}\psi}{4\pi G_{\rm N} a^2(\overline{\rho} + \overline{P})} - \mathcal{H}\frac{\phi'' + \mathcal{H}'\psi + \mathcal{H}\psi'}{4\pi G_{\rm N} a^2(\overline{\rho} + \overline{P})} - \mathcal{H}^2\frac{\phi' + \mathcal{H}\psi}{4\pi G_{\rm N} a^2(\overline{\rho} + \overline{P})}\left(1 + 3\frac{\overline{P}'}{\overline{\rho}'}\right). \tag{C.22}$$

Henceforth, with the Friedmann equations for the background $\mathcal{H}^2-\mathcal{H}' = 4\pi G_{\rm N}a^2(\overline{\rho}+\overline{P})$, and furthermore using the fact that $3\mathcal{H}(\phi'+\mathcal{H}\psi) = \nabla^2\phi - 4\pi G_{\rm N}a^2\delta\rho$, rearranging terms and using the definition of the non adiabatic pressure fluctuation yields

$$\begin{aligned}-4\pi G_{\rm N}a^2(\overline{\rho}+\overline{P})\mathcal{R}' &= \mathcal{H}(\mathcal{H}\phi' + \mathcal{H}'\psi) + \mathcal{H}\left(\phi'' + \mathcal{H}'\psi + \mathcal{H}\psi'\right) \\ &\quad + \mathcal{H}^2\left(\phi' + \mathcal{H}\psi\right)\left(1 + 3\frac{\overline{P}'}{\overline{\rho}'}\right) \\ &= \mathcal{H}\left[\phi'' + \mathcal{H}(2\phi' + \psi') + (\mathcal{H}^2 + 2\mathcal{H}')\psi\right] \\ &\quad + \mathcal{H}\frac{\overline{P}'}{\overline{\rho}'}\nabla^2\phi - 4\pi G_{\rm N}a^2\mathcal{H}\delta\rho\frac{\overline{P}'}{\overline{\rho}'} \\ &= 4\pi G_{\rm N}a^2\mathcal{H}\left[\delta P_{\rm nad} + \left(c_s^2 - \frac{\overline{P}'}{\overline{\rho}'}\right)\delta\rho + (\overline{\rho}+\overline{P})\nabla^2\sigma\right] + \mathcal{H}\frac{\overline{P}'}{\overline{\rho}'}\nabla^2\phi\,.\end{aligned} \tag{C.23}$$

For isentropic initial conditions with an adiabatic evolution and a zero anisotropic stress-energy tensor this equation reduces to

$$\mathcal{R}' = -3\frac{k^2}{\mathcal{H}}\frac{\overline{\rho}}{\overline{\rho}+\overline{P}}(\mathcal{R} - \mathcal{H}v) \quad \text{and gives the scaling} \quad \frac{{\rm d}\ln\mathcal{R}}{{\rm d}\ln a} \sim \left(\frac{k}{\mathcal{H}}\right)^2 . \tag{C.24}$$

C.3 Initial conditions for the spherical collapse

Here we follow the treatment done in (Mo et al. 2010 – chapter 5.1). We assume that we are in a matter dominated Universe. The initial radius at time t_i is related to the constant mass of the structure and to the initial overdensity δ_i and background density $\overline{\rho}_i$ as

$$M = \frac{4}{3}\pi(1+\delta_i)\overline{\rho}_i R_i^3 \tag{C.25}$$

Using Fridemann equation we get

$$R_i^3 = \frac{2G_{\rm N}M}{\Omega_i(1+\delta_i)H_i^2}\,. \tag{C.26}$$

Moreover we can also show from the conservation of the mass that

$$\frac{{\rm d}R_i}{{\rm d}t_i} = H_i R_i\left[1 - \frac{1}{3H_i t_i}\frac{\delta_i}{1+\delta_i}\frac{{\rm d}\ln\delta_i}{{\rm d}\ln t_i}\right]\,. \tag{C.27}$$

Plugging this result in the equation for the energy $\mathcal{E} = G_{\rm N}M/R_i - ({\rm d}R_i/{\rm d}t_i)^2/2$ yields

$$\frac{G_{\rm N}M}{R_i} - \frac{(H_i R_i)^2}{2}\left[1 - \frac{1}{3H_i t_i}\frac{\delta_i}{1+\delta_i}\frac{{\rm d}\ln\delta_i}{{\rm d}\ln t_i}\right]^2 = \mathcal{E} \tag{C.28}$$

The combination of Eq. (C.26) and Eq. (C.28) gives

$$\frac{\mathcal{E}R_i}{G_{\rm N}M} = 1 - \frac{1}{\Omega_i(1+\delta_i)}\left[1 - \frac{1}{3H_i t_i}\frac{\delta_i}{1+\delta_i}\frac{{\rm d}\ln\delta_i}{{\rm d}\ln t_i}\right]^2 \tag{C.29}$$

In a matter dominated Universe at t_i, one has $\delta_i \propto t_i^{2/3} \ll 1$, $\Omega_i \sim 1$ and $H_i t_i \sim 2/3$. Therefore it yields

$$\frac{\mathcal{E}R_i}{G_{\rm N}M} \sim 1 - \left[1 - \frac{\delta_i}{3}\right]^2 \sim \frac{2}{9}\delta_i \tag{C.30}$$

which proves that $(\mathcal{E}R_i)/(G_{\rm N}M) \ll 1$.

D

Complements on baryonic tides

D.1 Jean's equation and velocity dispersion

Let us consider a self-gravitating system. The PSDF $f(\mathbf{x},\mathbf{v})$ of such a system follows the collisionless Boltzmann equation

$$\frac{\partial f}{\partial t} + [\mathbf{v}.\nabla_{\mathbf{x}}]f - \nabla\Phi.\nabla_{\mathbf{v}}f = 0\,. \tag{D.1}$$

Finding solutions to this equation is however not trivial and here because we are mainly interested in the velocity dispersion we can evaluate the velocity moments. In particular the combination of the zeroth and first order moments yields

$$\frac{\partial \rho\left\langle v_j\right\rangle}{\partial t} + \left\langle v_j\right\rangle \frac{\partial\left\langle v_i\right\rangle}{\partial x_j} = -\frac{\partial\Phi}{\partial x_i} - \frac{1}{\rho}\frac{\partial(\rho\sigma_{ij}^2)}{\partial x_j} \tag{D.2}$$

with $\sigma_{ij}^2 = \left\langle v_i v_j\right\rangle - \left\langle v_i\right\rangle\left\langle v_j\right\rangle$ the velocity variance tensor such that this equation resemble the Euler equation with $p_{ij} = \rho\sigma_{ij}^2$ an effective pressure term in the Euler equation. This equation is called the Jeans equation. In a spherical system, using spherical coordinates we can rewrite

$$\frac{1}{\rho}\frac{\partial(\rho\left\langle v_r^2\right\rangle)}{\partial r} + 2\,\frac{\beta(r)}{r}\left\langle v_r^2\right\rangle = -\frac{\mathrm{d}\Phi}{\mathrm{d}r} \quad \text{where} \quad \beta(r) \equiv 1 - \frac{\left\langle v_\theta^2\right\rangle + \left\langle v_\phi^2\right\rangle}{2\left\langle v_r^2\right\rangle} \tag{D.3}$$

is the anisotropy parameter. Here, for particles in subhalos, isotropy is assumed, therefore we have $\beta(r) = 0$ and $\sigma_{\rm sub}^2 = \left\langle v_r^2\right\rangle$ thus, for a finite size structure of tidal radius $r_{\rm t}$,

$$\sigma_{\rm sub}^2(r) = \frac{G}{\rho(r)}\int_r^{r_{\rm t}} \frac{\rho(r')\,m(r')}{r'^2}\,\mathrm{d}r'\,. \tag{D.4}$$

The same approach is used to compute the velocity distribution of subhalos in the dark halo of the Galaxy. One major difference is that baryons now contribute to the potential Φ and the mass of the system is

$$m_{\rm tot}(R) = m_{\rm DM}(R) + \int_{|\mathbf{r}'|<R} \rho_b(\mathbf{r}')\,\mathrm{d}^3\mathbf{r}'\,. \tag{D.5}$$

where $\rho_{\rm b}$ is the baryonic mass density, which is axisymmetric rather than spherical. The DM velocity variance can then be approximated the same formula, but changing the mass in the integrand,

$$\sigma^2(R) = \frac{G}{\rho}\int_R^{R_{\rm max}} \frac{\rho(R')\, m_{\rm tot}(R')}{R'^2}\,{\rm d}R' \,. \tag{D.6}$$

The boundaries of the MW are fixed at $R_{\rm max} = 500\,{\rm kpc}$.

D.2 Distribution of impact parameters

Let us define a galactic frame with origin the centre of the galaxy $(G, \hat{\mathbf{e}}_x, \hat{\mathbf{e}}_y, \hat{\mathbf{e}}_z)$ where the z-axis is perpendicular to the galactic plane (in the following, when referring to the galactic plane we mean the middle of the stellar disc) and $\hat{\mathbf{e}}_x$ and $\hat{\mathbf{e}}_y$ are arbitrary orthonormal vectors. We assume that all along the disc crossing the subhalo keeps a rectilinear trajectory that intercepts the galactic plane at position $\mathbf{R}$, at time $t = 0$, in the galactic frame, with a velocity $\mathbf{v}_c$. Let us now consider a star tagged by the letter i that has a position $\mathbf{R}_i$ at $t = 0$ in the same frame. We assume that on the time the subhalo crosses the disc it keeps a linear trajectory with a velocity $\mathbf{v}_i$ such that $\mathbf{v}_i.\mathbf{R}_i \sim 0$. For simplicity we also introduce $\mathbf{S}_i = \mathbf{R}_i - \mathbf{R}$. Then, at an arbitrary time, t the distance between the star and the subhalo is given by

$$d_i(t) = |\mathbf{S}_i - \mathbf{v}_{{\rm r},i}t| \tag{D.7}$$

where we introduce the relative velocity between the star and the subhalo $\mathbf{v}_{{\rm r},i} = \mathbf{v}_c - \mathbf{v}_i$. The impact parameter for this specific star is defined as $b_i \equiv \min\{d_i(t)\}$, it yields

$$b_i = \frac{|\mathbf{S}_i \times \mathbf{v}_{{\rm r},i}|}{|\mathbf{v}_{{\rm r},i}|}\,. \tag{D.8}$$

Now we want to know what is the probability for this star to be at position $\mathbf{R}_i$ and have a mass m_i. We call the associated probability distribution quantity $p_{(m_\star,\mathbf{R}_\star)}(m_i, \mathbf{R}_i) = p_{m_\star}(m_i\,|\,\mathbf{R}_i)p_{\mathbf{R}_\star}(\mathbf{R}_i)$. In our model we make the usual approximation that $p_{m_\star}(m_i\,|\,\mathbf{R}_i) = p_{m_\star}(m_i)$ so that it does not depend on the position. Moreover the probability distribution of positions is given by the mass density as

$$p_{\mathbf{R}_i}(\mathbf{R}_i) = \rho_\star(\mathbf{R}_i)\left[\int {\rm d}^3\mathbf{R}\,\rho_\star(\mathbf{R})\right]^{-1} = \frac{\rho_\star(\mathbf{R}_i)}{m_\star^{\rm tot}} \tag{D.9}$$

where $m_\star^{\rm tot}$ is the total mass of stars and $\rho_\star(\mathbf{R}_i)$ their mass density at position $\mathbf{R}_i$. All stars being independent the joint PDF for their mass and position is

$$p_{(m_\star,\mathbf{R}_\star)}\left(\{m_i\}_i, \{\mathbf{R}_i\}_i\right) = \prod_{i=1}^{N_\star}\left[p_{m_\star}(m_i)p_{\mathbf{R}_\star}(\mathbf{R}_i)\right] \tag{D.10}$$

with $N_\star = m_\star^{\rm tot}/\overline{m_\star}$ the total number of stars. With all these ingredients it is possible to evaluate the number density of stars that are crossed with impact parameter b and mass $M_\star$, knowing the trajectory of the subhalo, as

$$\frac{{\rm d}^2\mathcal{N}}{{\rm d}b{\rm d}m_\star} = \int \prod_{i=1}^{N_\star} {\rm d}m_i{\rm d}^3\mathbf{R}_i\, p_{m_\star}(m_i)p_{\mathbf{R}_\star}(\mathbf{R}_i)\left[\sum_{i=1}^{N_\star}\delta_{\rm D}(b_i - b)\delta_{\rm D}(m_i - m_\star)\right]\,. \tag{D.11}$$

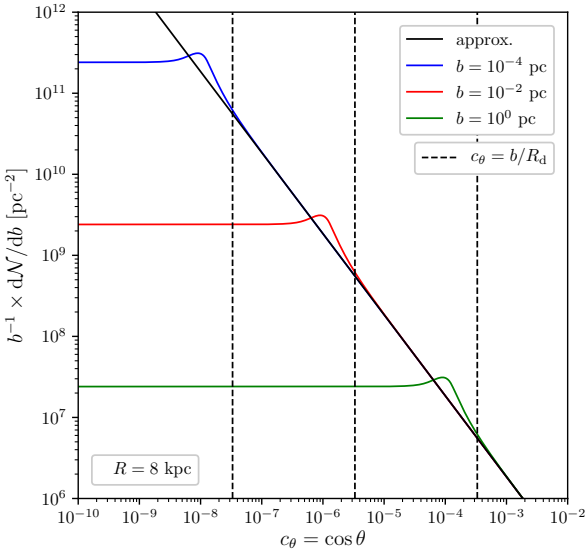

Figure D.1 – Number density of stars encountered with an impact parameter b divided by b (to ease the comparison between the approximation and the full expression) vs the cosine of the angle between the subhalo trajectory and the normal to the galactic plane θ. The lowest $\cos\theta$ is the closer the subhalo passes to the stellar disc. The approximate computation is given by the black solid line and is independent of b while the full expression gives the coloured solid line for different values of b. There is a change in behaviour around $\cos\theta \sim b/R_\mathrm{d}$ where $R_\mathrm{d} \sim 3$ kpc is the approximate typical length scale of the stellar disc.

Massaging this expression, it is straightforward to prove that the mass probability distribution can be factored out and it leaves us with the number of density of stars with a given impact parameter that can be written under the compact form

$$\frac{\mathrm{d}\mathcal{N}}{\mathrm{d}b} = \frac{1}{\overline{m_\star}} \int \mathrm{d}^3\mathbf{R}_\star \, \rho_\star(\mathbf{R}_\star) \delta_\mathrm{D}(b_\star - b) \,. \tag{D.12}$$

Form the expression of the impact parameter it is convenient to make the change of variables in this integral $\mathbf{R}_\star \to \mathbf{S}_\star = \mathbf{R}_\star - \mathbf{R}$ and define the Dirac distribution on the squared value of the impact parameter. Eventually, in order to simplify the computation we will assume that all stars lay within an infinitely thin axi-symmetric disc of surface density $\Sigma_\star$ and the integration over the entire 3D space reduces to the integration on the galactic plane. We therefore write

$$\frac{\mathrm{d}\mathcal{N}}{\mathrm{d}b} = \frac{2b}{\overline{m_\star}} \int \mathrm{d}^2\mathbf{S}_\star \, \Sigma_\star \left[R_\star(\mathbf{S}_\star)\right] \delta_\mathrm{D}(b_\star^2 - b^2) \,. \tag{D.13}$$

Now in order to continue the computation we can choose, without loss of generality, the convenient orientation of the basis $(\hat{\mathbf{e}}_x, \hat{\mathbf{e}}_y)$ such that $\mathbf{R} = (R, 0, 0)$. Moreover we parametrise the relative velocity direction with two angles θ and φ as $\mathbf{v}_{\mathrm{r},i}/|\mathbf{v}_{\mathrm{r},i}| = (\sin\theta\cos\varphi, \sin\theta\sin\varphi, \cos\theta)$ and $\mathbf{S}_\star = (S\cos\phi, S\sin\phi, 0)$ such that $\mathrm{d}^2\mathbf{S}_\star = s\mathrm{d}s\mathrm{d}\phi$. Then the expression of the impact parameter becomes

$$b_\star^2 = s^2 \left[1 - \sin^2\theta \cos^2(\phi - \varphi)\right] \,. \tag{D.14}$$

The integration over the Dirac delta distribution in Eq. (D.12) after the change of variable can be done analytically by solving the delta for the angle ϕ. It gives four

distinct solutions in $[\varphi-\pi,\varphi+\pi]$ when $Sc_\theta < b < S$, that can be written under the form,

$$\phi_j = \varphi + \eta_j \arccos\left[\frac{\chi_j}{\sin\theta}\sqrt{1-\frac{b^2}{s^2}}\right] . \tag{D.15}$$

where we have introduced $\chi_j = (+1,+1,-1,-1)$ and $\eta_j = (+1,-1,+1,-1)$. The arccos function image being in the range $[0,\pi]$ only, the χ_j factor parametrises the two solutions in the interval $[\varphi,\varphi+\pi]$ while the η_j gives the two symmetric solutions in the interval $[\varphi-\pi,\varphi]$. Henceforth in order to perform the integration over the Dirac distribution it is also necessary to provide the absolute value for the derivative of $b_\star^2$ with the variable ϕ evaluated in the four solution points. Using the properties of these solutions, this takes a simple form

$$\left|\frac{\mathrm{d}b_\star^2}{\mathrm{d}\phi}\right|_{\phi=\phi_j} = 2s^2\sin^2\theta|\cos(\phi_j-\varphi)||\sin(\phi_j-\varphi)| = 2\sqrt{s^2-b^2}\sqrt{b^2-s^2\cos^2\theta} \tag{D.16}$$

Then the only thing we need to do last is relate the value of $R_\star$ to s in the four solution points. We denote R_j these four quantities and introduce a new variable $y = s^2/b^2$. Using the simple relation $\mathbf{R}_\star = \mathbf{S}_\star + \mathbf{R}$ – that is the definition of $\mathbf{S}_\star$ – it is straightforward to show that $R_j^2 = R^2 + b^2y + 2h_j(y,c_\theta,\varphi)$ with the shorter notation $c_\theta = \cos\theta$ and the functions h_j being

$$h_j(y,c_\theta,\varphi) \equiv \frac{\chi_j Rb}{\sqrt{1-c_\theta^2}}\left[\cos\varphi\sqrt{y-1} - \frac{\eta_j}{\chi_j}\sin\varphi\sqrt{1-yc_\theta^2}\right] \tag{D.17}$$

In the end, the number density of stars with impact parameter b can be written as

$$\frac{\mathrm{d}\mathcal{N}}{\mathrm{d}b} = \frac{b}{2}\int_1^{\frac{1}{c_\theta^2}} \frac{\mathrm{d}y}{\sqrt{1-yc_\theta^2}\sqrt{y-1}} \sum_{j=1}^{4}\frac{\Sigma_\star(R_j)}{\overline{m_\star}} \tag{D.18}$$

and the computation is complete. Eventually we would like to relate the angles φ and θ to physical quantities (i.e. the angle marking the direction of the stars and the subhalo). In practice this is difficult in a general case. We will therefore consider that stars are motionless during all subhalo crossing so that $\mathbf{v}_{\mathrm{r},i} = \mathbf{v}_c$.

Eventually let us mention that formally the functions h_j can be rewritten in a more convenient way as

$$h_j = \chi_j Rb\sqrt{y}\cos\left(\varphi + \frac{\eta_j}{\chi_j}\arctan\left[\sqrt{\frac{1-yc_\theta^2}{y-1}}\right]\right) \tag{D.19}$$

Under this form it becomes easier to see that the functions h_j and the associated radii R_j are bounded

$$|h_j| \leq Rb\sqrt{y} \quad \text{and} \quad |R-b\sqrt{y}| < R_j < R+b\sqrt{y} \tag{D.20}$$

In particular, since $y < 1/c_\theta^2$ this previous inequality implies that $|R_j - R| < b/c_\theta$. If we consider that the variations of $\Sigma_\star$ on R are of typical length R_d it yields that $\Sigma_\star(R_j) = \Sigma_\star(R)$ as long as $c_\theta \gg b/R_\mathrm{d}$. Therefore one can simply rewrite the density of encountered stars as

$$\frac{\mathrm{d}\mathcal{N}}{\mathrm{d}b} = 2b\frac{\Sigma_\star(R)}{\overline{m_\star}}\int_1^{\frac{1}{c_\theta^2}}\frac{\mathrm{d}y}{\sqrt{1-yc_\theta^2}\sqrt{y-1}} = \frac{\Sigma_\star(R)}{\overline{m_\star}}\frac{2\pi b\mathrm{d}b}{c_\theta} . \tag{D.21}$$

D.3 Energy and velocity distributions in stellar encounters

In this appendix, we detail the PDF of several functions of interest and we prove several properties claimed in the main text. We start by introducing the PDF of final velocity in a given shell and give an analytical derivation. With the results, we prove the relation between the median and the average kinetic energy kick of Eq. (4.109) on general grounds. In a third part, we illustrate this formal derivation with the example of the initial velocity following a Maxwell-Boltzmann distribution. Eventually, we conclude by studying the impact of stellar encounters on the density profile using a simple criterion in order to justify the use of the median as the typical kinetic energy kick felts by all particles in a given shell during one crossing of the disc.

D.3.1 Probability distribution for the final velocity

We suppose that we know the PDF, $p_{\mathbf{v}}(\mathbf{v}\,|\,r)$,for the initial velocity $\mathbf{v}$ of particles at position r in a subhalo and the probability for particles in that shell to receive a velocity kick $\Delta\mathbf{v}$ then the probability distribution of final velocity v_f at position r can be written under the form

$$p_{v_f}(v_f\,|\,r) = \int \mathrm{d}^3\mathbf{v}\, p_{\mathbf{v}}(\mathbf{v}\,|\,r) \int \mathrm{d}^d\Delta\mathbf{v}\, p_{\Delta\mathbf{v}}(\Delta\mathbf{v}\,|\,r)\delta_{\mathrm{D}}\left[v_f - |\mathbf{v}+\Delta\mathbf{v}|\right] . \tag{D.22}$$

We leave room here for the possibility of $\Delta\mathbf{v}$ being a 3D or 2D random vector with the dimension parameter d. Let us assume an isotropic initial velocity distribution so that $p_{\mathbf{v}}(\mathbf{v}\,|\,r) = p_{\mathbf{v}}(v\,|\,r)$ with $v = |\mathbf{v}|$. Then it is possible to integrate first on the angular distribution of $\mathbf{v}$ in order to remove unnecessary degrees of freedom and get rid of the Dirac delta term. It yields

$$p_{v_f}(v_f\,|\,r) = \int \mathrm{d}^3\mathbf{v}\, p_{\mathbf{v}}(v\,|\,r) p_{v_f}(v_f\,|\,v,r) \tag{D.23}$$

with the definition of the PDF of v_f knowing v and r being

$$p_{v_f}(v_f\,|\,v,r) = \frac{v_f}{v}\int \mathrm{d}^d\Delta\mathbf{v}\, \frac{p_{\Delta\mathbf{v}}(\Delta\mathbf{v}\,|\,r)}{\Delta v}\Theta\left[\Delta v - |v+v_f|\right]\Theta\left[(v+v_f)-\Delta v\right] \tag{D.24}$$

and where we introduced the velocity kick norm $\Delta v = |\Delta\mathbf{v}|$. For an isotropic distribution of $\Delta\mathbf{v}$ such that $p_{\Delta\mathbf{v}}(\Delta\mathbf{v}\,|\,r) = p_{\Delta\mathbf{v}}(\Delta v\,|\,r)$ it further simplifies to

$$p_{v_f}(v_f\,|\,v,r) = \frac{v_f}{v}\frac{\pi^{d/2}}{\Gamma(d/2)}\int_{|v-v_f|}^{|v+v_f|} \mathrm{d}\Delta v\,(\Delta v)^{d-2} p_{\Delta\mathbf{v}}(\Delta v\,|\,r) . \tag{D.25}$$

Let us now assume that $\Delta\mathbf{v}$ follows a Gaussian distribution according to the result of the central limit theorem. Then the distribution on $\Delta\mathbf{v}$ takes a simple form

$$p_{\Delta\mathbf{v}}(\Delta v\,|\,r) = \frac{\pi^{-d/2}}{u^d} e^{-\frac{(\Delta v)^2}{u^2}} \quad \text{with} \quad u = u(r) = \sqrt{\frac{2\mathcal{N}\overline{(\delta\mathbf{v})^2}}{d}} \tag{D.26}$$

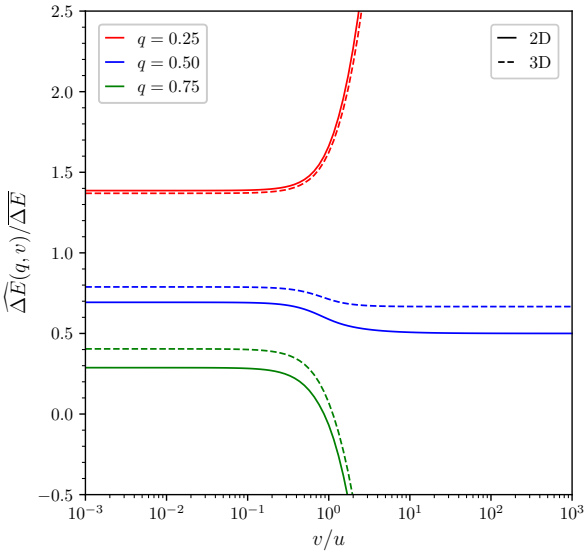

Figure D.2 – The inverse CCDF of kinetic energy knowing the velocity at three values $q = 0.25$, $q = 0.5$ and $q = 0.75$ with respect to the initial velocity v

which yields, with the change of variable $\Delta v \to u\sqrt{t}$ in the second line, and the introduction of the incomplete Gamma function in the third line,

$$p_{v_f}(v_f \,|\, v, r) = \frac{v_f}{v}\frac{1}{\Gamma(d/2)}\int_{|v-v_f|}^{|v+v_f|} \mathrm{d}\Delta v\, \frac{(\Delta v)^{d-2}}{u^d} e^{-\frac{(\Delta v)^2}{u^2}} \tag{D.27}$$

$$= \frac{v_f}{uv}\frac{1}{2\Gamma(d/2)}\int_{\left(\frac{v-v_f}{u}\right)^2}^{\left(\frac{v+v_f}{u}\right)^2} \mathrm{d}t\, t^{\frac{d-3}{2}} e^{-t} \tag{D.28}$$

$$= \frac{v_f}{uv}\frac{1}{2\Gamma(d/2)}\left[\Gamma\left(\frac{d-1}{2}, \left(\frac{v-v_f}{u}\right)^2\right) - \Gamma\left(\frac{d-1}{2}, \left(\frac{v+v_f}{u}\right)^2\right)\right] . \tag{D.29}$$

In the end, here we have found a generic expression for the PDF of v_f for any initial velocity distribution. Another interesting quantity is the associated CDF of v_f that is defined as

$$\begin{aligned} F_{v_f}(< v_f \,|\, r) &\equiv \int_0^{v_f} p_{v_f}(v'_f \,|\, r)\, \mathrm{d}v'_f \\ &= \int \mathrm{d}^3 v\, p_{\mathbf{v}}(v \,|\, r) \left\{ F_{v_f}(< v_f \,|\, v, r) \equiv \int_0^{v_f} p_{v_f}(v'_f \,|\, v, r) \mathrm{d}v'_f \right\} . \end{aligned} \tag{D.30}$$

The CDF knowing v and r can therefore be computed with the expression of the PDF derived above. We will see the utility of this expression in the following paragraphs and especially when discussing the density profile modifications due to the encounter. However let us first inspect the properties of the median energy kick in light of the previous derivation.

D.3.2 Properties of the median energy kick

In the main text, we have introduced the median value of the energy kick received by particles in a subhalo during the encounter with stars when it crosses the stellar disc. Moreover, we have based our computation of the tidal radius on the fact that

the typical energy received in a shell is defined as the median value that can be approximated by the average value modulated by a coefficient between 0.5 and 0.7 (in the case of a 2D random walk in the velocity space). We prove this property here and show that it is independent of the initial velocity distribution. Similarly to the CDF for v_f it is possible to introduce a related CDF for the kinetic energy kick ΔE as follows

$$F_{\Delta E}(<\Delta E\,|\,r) = \int \mathrm{d}^3 v\, p_{\mathbf{v}}(v\,|\,r) F_{v_f}(<\sqrt{v^2+2\Delta E}\,|\,v,r)\,. \tag{D.31}$$

Henceforth we can define a median value for ΔE knowing v and r as $\mathrm{Med}(\Delta E\,|\,v,r)$. In Fig. D.2 we show that value of $\widehat{\Delta E}(q,v)$ that is given by the implicit equation

$$F_{v_f}\left(<\sqrt{v^2+2\widehat{\Delta E}(q,v)}\,|\,v,r\right) = 1-q, \tag{D.32}$$

for three different values of q. In particular, the median $\mathrm{Med}(\Delta E\,|\,v,r) = \widehat{\Delta E}(0.5,v)$ is bounded by the asymptotes in $v=0$ and $v\to\infty$. Series expansions in these two regime then show that the value of the boundaries are such that

$$\frac{d-1}{d} < \frac{\mathrm{Med}(\Delta E\,|\,v,r)}{\overline{\Delta E}} < x \quad \text{with } x \text{ solution of} \quad \frac{\Gamma(d/2,xd/2)}{\Gamma(d/2)} = \frac{1}{2}\,. \tag{D.33}$$

In practice for $d=2$, it yields $x=\ln(2)$ and for $d=3$ it yields $x=0.789$. Eventually, even though the total median value $\mathrm{Med}(\Delta E)$ cannot be easily computed from $\mathrm{Med}(\Delta E\,|\,v,r)$, the properties of the boundaries have to be conserved. Therefore we have shown that whatever the initial velocity distribution of velocity the median kinetic energy kick is always equivalent to the average up to an $\mathcal{O}(1)$ pre-factor.

D.3.3 The example of a Maxwellian initial velocity

In order to illustrate the theoretical development above and to connect with the main text we consider now that the PDF of the initial velocity is a Maxwell-Boltzmann distribution Eq. (4.106) such that

$$p_{\mathbf{v}}(v\,|\,r) = \frac{1}{(2\pi\sigma^2_{\mathrm{sub}}(r))^{3/2}} e^{-\frac{v^2}{2\sigma^2_{\mathrm{sub}}(r)}}\,. \tag{D.34}$$

In order to compute the median of ΔE we can start by computing the exact PDF and CDF. The PDF for ΔE is given by

$$\begin{aligned}
p_{\Delta E}(\Delta E\,|\,r) &= \int \mathrm{d}^3\mathbf{v}\, p_{\mathbf{v}}(v\,|\,r) \int \mathrm{d}^d\Delta\mathbf{v}\, p_{\Delta\mathbf{v}}(\Delta v\,|\,r)\delta_{\mathrm{D}}\left[\Delta E - \frac{(\Delta v)^2}{2} + \mathbf{v}.\Delta\mathbf{v}\right] && \text{(D.35)}\\
&= \int \mathrm{d}^d\Delta\mathbf{v}\, p_{\Delta v}(\Delta v\,|\,r)\frac{2\pi}{\Delta v}\int_{\frac{|2\Delta E-(\Delta v)^2|}{2\Delta v}} \mathrm{d}v\, p_{\mathbf{v}}(v\,|\,r) && \text{(D.36)}\\
&= \int \mathrm{d}^d\Delta\mathbf{v}\, p_{\Delta v}(\Delta v\,|\,r)\frac{1}{\sqrt{2\pi\sigma^2_{\mathrm{sub}}(\Delta v)^2}}\exp\left(\frac{\left(\Delta E-\frac{(\Delta v)^2}{2}\right)^2}{2\sigma^2_{\mathrm{sub}}|\Delta\mathbf{v}|^2}\right) && \text{(D.37)}
\end{aligned}$$

Note that here we integrate over v before integrating over Δv for simplicity. According to the dimensionality of the random walk it yields

$$p_{\Delta E}\left(\Delta E\,|\,r\right) = \begin{cases} \dfrac{\exp\left(\frac{\Delta E}{2\sigma^2_{\mathrm{sub}}}-\frac{|\Delta E|}{2\sigma^2_{\mathrm{sub}}}\frac{\sqrt{1+s^2}}{s}\right)}{4\sigma^2_{\mathrm{sub}}s\sqrt{1+s^2}} & \text{if } d=2 \\ \dfrac{|\Delta E|e^{\frac{\Delta E}{2\sigma^2_{\mathrm{sub}}}}}{4\pi\sigma^4_{\mathrm{sub}}s^2\sqrt{1+s^2}}K_1\left[\frac{|\Delta E|}{2\sigma^2_{\mathrm{sub}}}\frac{\sqrt{1+s^2}}{s}\right] & \text{if } d=3 \end{cases} \tag{D.38}$$

where $s^2 \equiv u^2/(8\sigma_{\rm sub}^2) = \mathcal{N}\overline{\delta v^2}/(4d\sigma^2) = \overline{\Delta E}/(2d\sigma_{\rm sub}^2)$ and K_1 is the modified Bessel function of the second kind of order 1. Now we focus on the $d = 2$ case and write down the CDF as

$$F(<\Delta E\,|\,r) = \begin{cases} 1 - \dfrac{1+\xi}{2\xi} e^{-\frac{\Delta E}{2\sigma^2}(\xi-1)} & \text{if} \quad \Delta E \geq 0 \\ \dfrac{\xi-1}{2\xi} e^{\frac{\Delta E}{2\sigma^2}(1+\xi)} & \text{else.} \end{cases} \tag{D.39}$$

with $\xi = \sqrt{1+s^2}/s$. The complementary CDF, i.e. CCDF, introduced in the main text is denoted $\overline{F}(>\Delta E) \equiv 1 - F(<\Delta E)$. Eventually the energy $\Delta E(q)$ is defined implicitly through the CCDF as the solution of $\overline{F}(>\Delta E(q)) = q$. Therefore according to the value of q the energy $\Delta E(q)$ can be written

$$\frac{\Delta E(q)}{2\sigma^2} = \begin{cases} \dfrac{1}{1-\xi} \ln\left(\dfrac{2q\xi}{1+\xi}\right) & \text{if} \quad q < \frac{1+\xi}{2\xi} \\ \dfrac{1}{1+\xi} \ln\left(\dfrac{2(1-q)\xi}{\xi-1}\right) & \text{else}\,. \end{cases} \tag{D.40}$$

As the average kinetic energy kick is such that $\overline{\Delta E}/(2\sigma_{\rm sub}^2) = 2s^2 = 2(\xi^2-1)$, when $q \leq 0.5$, it yields

$$\frac{\mathrm{Med}(\Delta E)}{\overline{\Delta E}} = \frac{\xi+1}{2} \ln\left(\frac{1+\xi}{2q\xi}\right) \geq \frac{\xi(1-2q)+1}{2} \geq \frac{1}{2} \tag{D.41}$$

with $\mathrm{Med}(\Delta E) = \Delta E(0.5)$ and where we used the inequality $\ln(1/x) \geq 1-x$. Eventually, when $q \neq 0.5$ the ratio diverges as $\xi \to \infty$ (corresponding to $s \to 0$). When $q = 0.5$ the ratio is a decreasing function of ξ and

$$\frac{\mathrm{Med}(\Delta E)}{\overline{\Delta E}} \leq \lim_{\xi\to 1} \frac{\mathrm{Med}(\Delta E)}{\overline{\Delta E}} = \ln(2)\,. \tag{D.42}$$

which proves in this specific case the result of Eq. (D.33).

D.4 Probability distributions of the total energy kick (stars + disc shocking)

As mentioned in the main text we define a total energy kick as $\Delta E_{\rm tot} = \Delta E + \Delta E_{\rm d}$ where $\Delta E_{\rm d}$ is the energy kick due to the disc shocking and ΔE is the energy kick due to the encounters with stars. In the following we assume that ΔE is distributed along as in Eq. (D.38) in the $d = 2$ case and $\Delta E_{\rm d}$ is distributed along a Gaussian according to

$$p_{\Delta E_{\rm d}}(\Delta E_{\rm d}) = \frac{1}{\sqrt{2\pi\sigma_{\rm sub}^2 (\Delta \mathbf{v}_{\rm d})^2 A_2(\eta)}} e^{-\frac{\left(\Delta E_{\rm d} - A_1(\eta)\frac{(\Delta \mathbf{v}_{\rm d})^2}{2}\right)^2}{2\sigma_{\rm sub}^2 (\Delta \mathbf{v}_{\rm d})^2 A_2(\eta)}} \tag{D.43}$$

where $\Delta \mathbf{v}_{\rm d}$ is given in Eq. (4.34) and the adiabatic correction A_1 is introdueced in Eq. (4.36). We also introduced a new adiabatic corrective factor $A_2(\eta)$ for the disperion – according to GNEDIN et al. (1999). In the following we also use a parameter $s_{\rm d} \equiv (\Delta \mathbf{v}_{\rm d})^2/(4\sigma_{\rm sub}^2)$. Then it is possible to deduce a PDF for $\Delta E_{\rm tot}$. In order to do so we introduce two variables

$$\nu_\pm \equiv \frac{1}{2}\left(\frac{\sqrt{1+s^2}}{s} \pm 1\right)\sqrt{2A_2 s_{\rm d}^2} \tag{D.44}$$

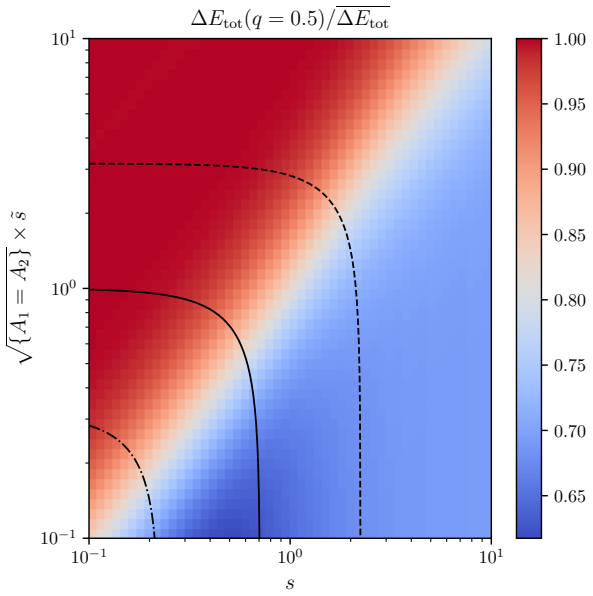

Figure D.3 – Evolution of $\Delta E_{\rm tot}(q=0.5)/\overline{\Delta E_{\rm tot}}$ with the parameters s and $s_{\rm d}$ under the assumption that $A_2 = A_2$ for simplicity. The black curves represent contours of constant $\overline{\Delta E_{\rm tot}}$: $\overline{\Delta E_{\rm tot}} = 0.2\sigma^2$ (dash-dotted), $\overline{\Delta E_{\rm tot}} = 2\sigma^2$ (solid), $\overline{\Delta E_{\rm tot}} = 20\sigma^2$ (dashed).

and we define a pseudo centred reduced variable corresponding to $\Delta E_{\rm tot}$ of the form

$$\varepsilon \equiv \frac{1}{\sqrt{2A_2 s_{\rm d}^2}} \left(\frac{\Delta E_{\rm tot}}{2\sigma_{\rm sub}^2} - s_{\rm d}^2 A_1 \right) \tag{D.45}$$

in order to simplify the expressions. The main goal of this analysis is to quantify the asymmetry of the PDF around the average value in order to evaluate whether considering an average value for $\Delta E_{\rm tot}$ is relevant and if not what should be the better choice. Therefore using an affine shift to define this new variable we do not lose in generality in that sense. With these two definitions we can evaluate a PDF for ε under the form

$$p_\varepsilon(\varepsilon \,|\, \nu_-, \nu_+) = \frac{\nu_+\nu_-}{\nu_+ + \nu_-} e^{-2\varepsilon\nu_- + \nu_-^2} \operatorname{erfc}(\nu_- - \varepsilon) + \frac{\nu_+\nu_-}{\nu_+ + \nu_-} e^{2\varepsilon\nu_+ + \nu_+^2} \operatorname{erfc}(\nu_+ + \varepsilon)\,. \tag{D.46}$$

In addition, the average value of ε can be rewritten $\overline{\varepsilon} = (\nu_+ - \nu_-)/(2\nu_+\nu_-)$ and from this PDF we can also derive a CCDF for ε. It yields the following expression

$$\begin{aligned} \overline{F}_\varepsilon(\varepsilon \,|\, \nu_-, \nu_+) = &- \frac{\nu_+\nu_-}{\nu_+ + \nu_-} \frac{e^{2\varepsilon\nu_+ + \nu_+^2}}{2\nu_+} \operatorname{erfc}(\nu_+ + \varepsilon) \\ &+ \frac{\nu_+\nu_-}{\nu_+ + \nu_-} \frac{e^{-2\varepsilon\nu_- + \nu_-^2}}{2\nu_-} \operatorname{erfc}(\nu_- - \varepsilon) + \frac{1}{2} \operatorname{erfc}(\varepsilon)\,. \end{aligned} \tag{D.47}$$

The main advantage of this parametrisation is to be only depends on two parameters ν_+ and ν_- and therefore to be easy to compute numerically. Moreover it can be used to show that the value of the CCDF at the average yields

$$\frac{1}{e} \sim 0.368 < \overline{F}_\varepsilon(\overline{\varepsilon} \,|\, \nu_+, \nu_-) < \frac{1}{2} \tag{D.48}$$

therefore considering the average value is a good way to evaluate that the maximal energy gain for a fraction of at least 37% of the particle. This is understandable as

we had, $\mathrm{Med}(\Delta E_{\mathrm{tot}}) \leq \overline{\Delta E}$ in the case without disc shocking and because the disc shocking that has a symmetric distribution only tends to re-symmetrise the PDF for ΔE_{tot}. Therefore, this justifies entirely the fact that we can evaluate the total energy as roughly being the sum of the means. In Fig. D.3 is represented the evolution of $\mathrm{Med}(\Delta E)/\overline{\Delta E_{\mathrm{tot}}}$ with the parameters s and s_{d} under the assumption $A_1(\eta) = A_2(\eta)$ for simplicity. When $s_{\mathrm{d}} \gg s$ the distribution is symmetrised again with respect to the average and the ratio is close to 1. When $s \gg s_{\mathrm{d}}$ the symmetry is maximally broken and that yields a ratio of ~ 0.7 as discussed in the scenario with the only star encounters effect.

E

Complements on the detectability of subhalos

E.1 Internal properties of the visible point-like subhalos

In this section, we show the internal properties of the most visible point-like subhalos. As an example we consider a sensitivity evaluated in a Fermi-LAT like configuration with 20 yr of observation and for $\theta_{\rm r} = 0.1^\circ$ or 1°. Moreover, we also use the 3σ upper limit for the annihilation cross-section for 10 yr of observation (which implies that the diffuse DM emission has already been detected first). In Fig. E.3 we first show the position along the line of sight of the visible subhalos for different pointing directions. They are mostly gathered around the HC at $s \sim 10$ kpc for pointing direction not too far from the GC. In Fig. E.1 and Fig. E.2 we show the concentration and tidal mass of the visible subhalos in the direction $(l, b) = (0^\circ, 20^\circ)$ in the left panel. Moreover, we also represent the evolution of the median concentration with $m_{\rm t}$ at three different distances (indeed while the median concentration directly depends on the cosmological mass, its dependence on the tidal mass depends on the tidal effects and the position). We observe that a band in the parameter space reaches the median concentration. These are the regions that contribute the most to the total number of visible point-like subhalos. On the right panel, we show, in terms of the distances which regions of the parameter spaces are not integrated over because the subhalo is either not point-like, destroyed or too faint.

E.2 Cross-section limits for CTA

This section is devoted to showing the limits that can be set with CTA in the four regions defined in Sect. 5.2. They are displayed according to each regions in Fig. E.4, Fig. E.5, Fig. E.6 and Fig. E.7. We can observe that the constraint from subhalos (solid curves) is better for extended objects in comparison to the 2.17σ upper limit of $\langle \sigma v \rangle$ set by the assumed non-observation of the DM diffuse emission in the GC (dashed). However, we recall that, as said in the main text, here we assume an exposure of 100 hr sr^{-1} which is extremely high for a field of view of ~ 0.024 sr. Therefore we can safely say that the stronger constraint may never come from the non-detection of subhalos. For extended objects the limits are roughly similar in every region however,

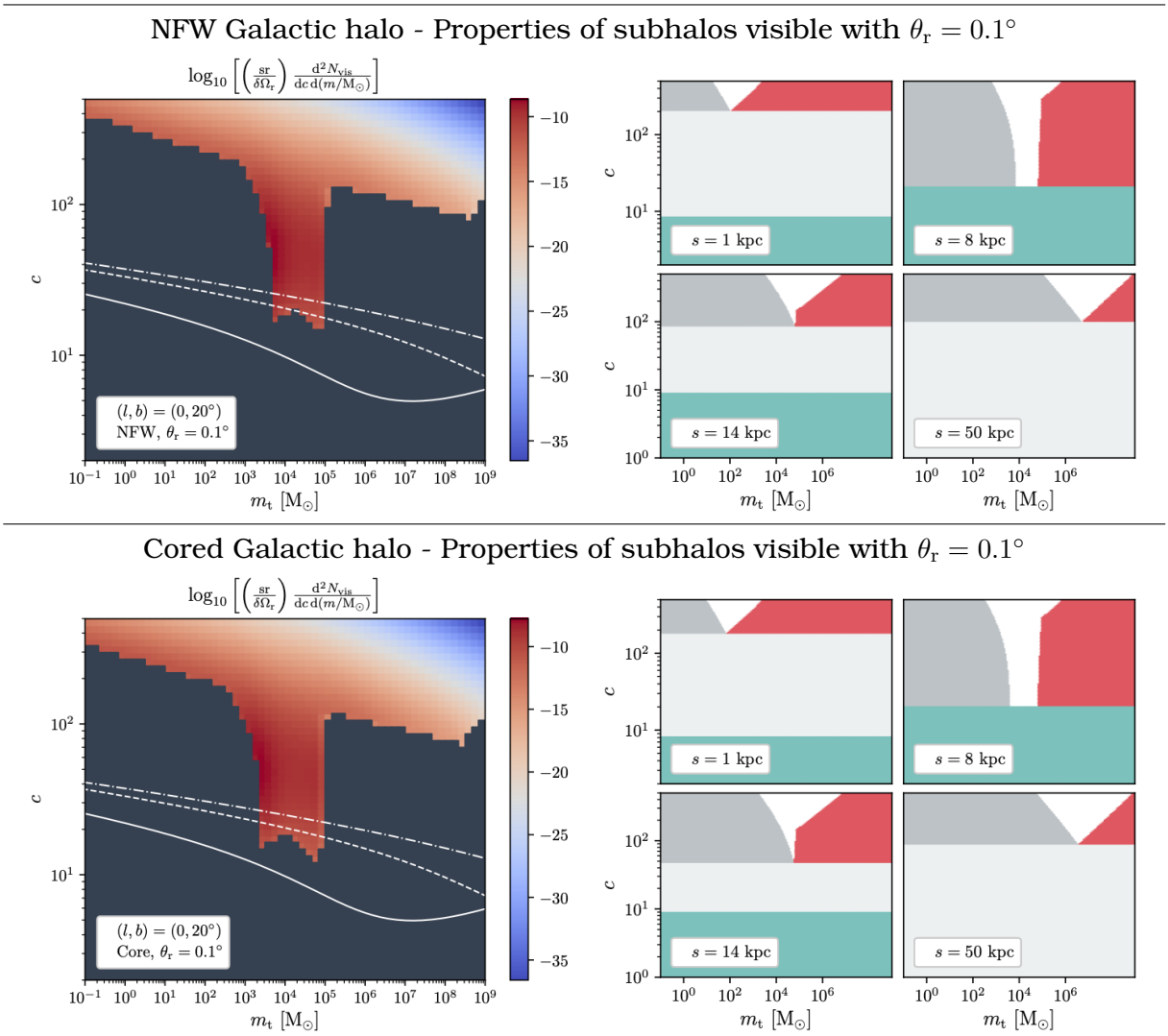

Figure E.1 – Left panels: Concentrations and physical masses of the most visible subhalos in the direction of Galactic coordinates $(l, b) = (0°, 20°)$. The solid (dashed, dotted-dashed) white curve indicates the median concentration of a subhalo of virial mass m_{200} that would be pruned off down to the tidal mass m_t in abscissa at a Galactocentric distance of 1 kpc (10 and 100 kpc, respectively) if tidal disruption were unplugged (though not tidal stripping). This shows that subhalos with a given m_t originate from heavier and heavier objects as they are found closer and closer to the GC (*i.e.* tidal stripping is more and more efficient), should tidal stripping not be destructive —see in comparison the minimal concentration needed to survive tidal effects in the associated right panels. **Right panels**: Exclusion areas for the computation of the probability and for different distances to the observer: subhalos that are not seen as points (red), subhalos that are below the critical/minimal allowed concentration and then tidally disrupted (turquoise—$\epsilon_t = 0.01$), subhalos that are too faint (dark gray on the left), subhalos that are either too faint or not point sources (light gray). Visible: those lying in the white area. **Top panels**: NFW Galactic halo. **Bottom panels**: Cored Galactic halo.

for point-like structures the constraint gets worse and worse with the distance of the region to the GC, consequently Region 1 is optimal.

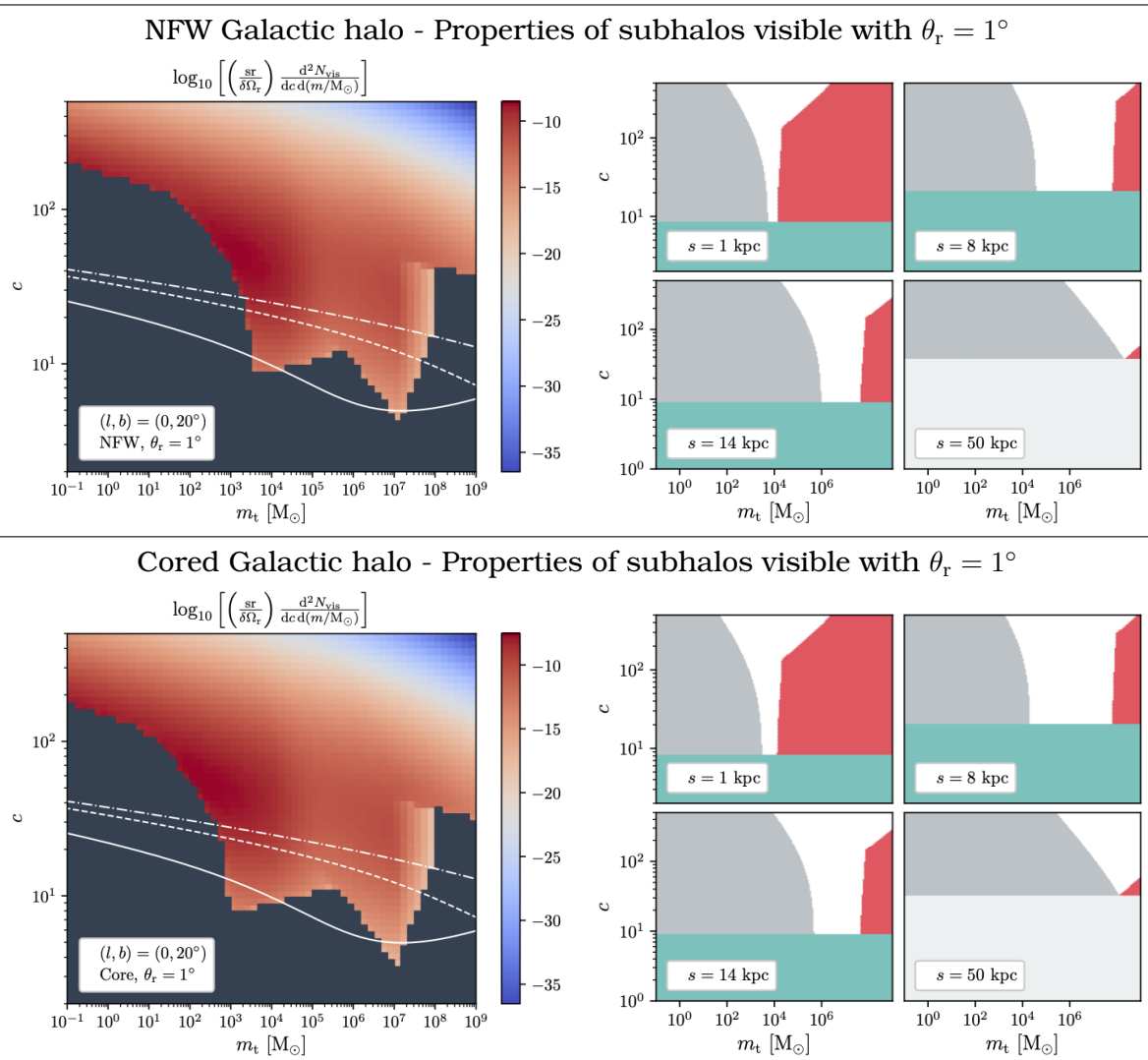

Figure E.2 – Same as Fig. E.1 but with $\theta_r = 1°$.

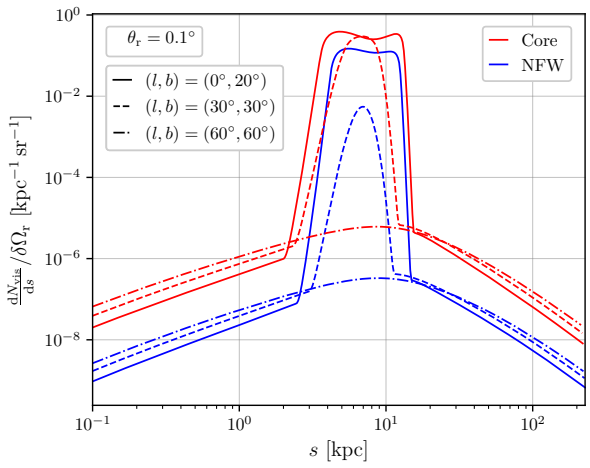

Figure E.3 – Distribution of number of visible subhalo with the distance to the observer s and for different pointing directions. Here the sensitivity is evaluated for a Fermi-LAT instrument, 20 yr of observation and $\theta_r = 0.1°$ while the annihilation cross-section into $b\bar{b}$ is set as the upper 3σ limit for 10 yr of observation (the smooth halo should have already been detected).

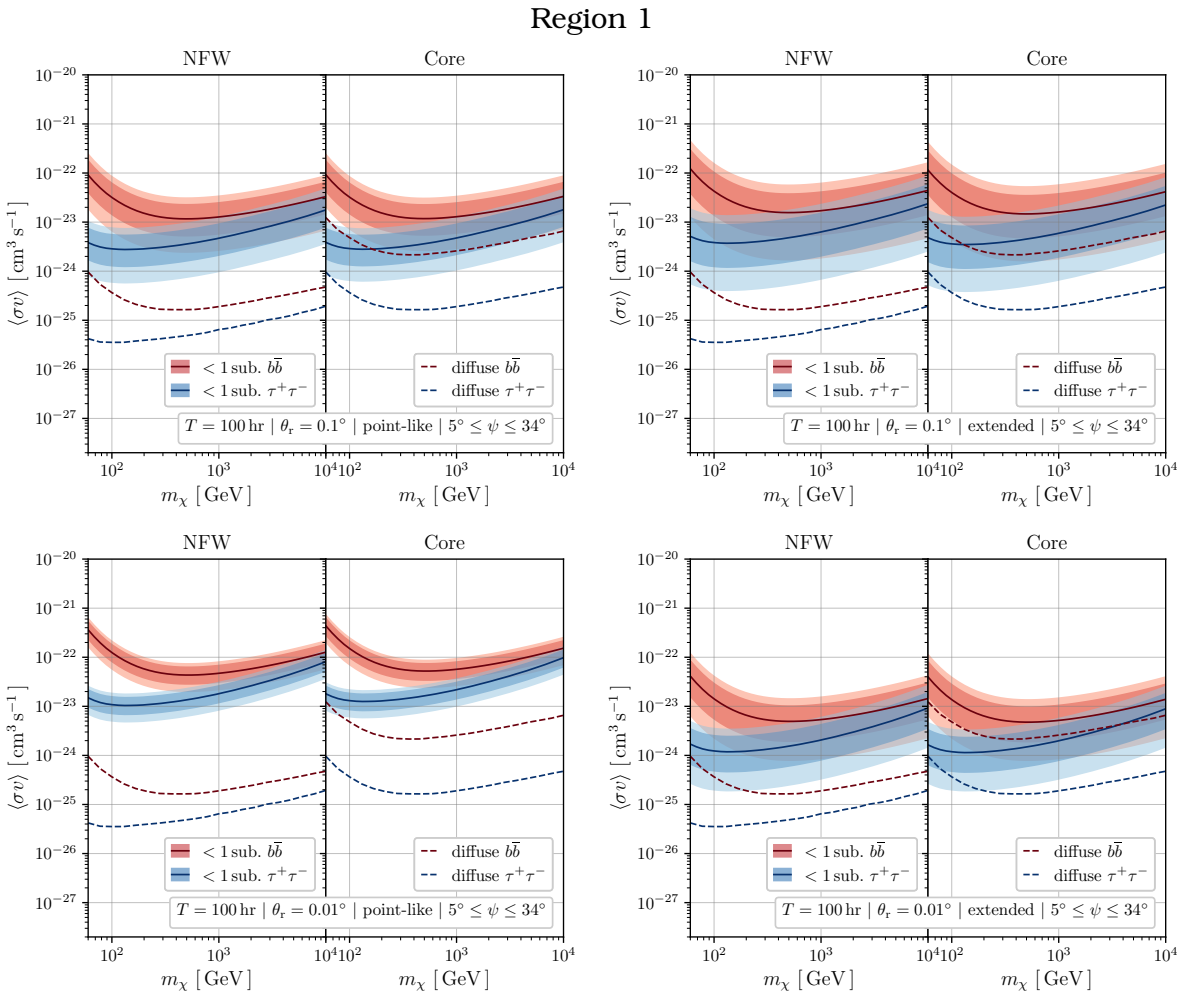

Figure E.4 – Annihilation cross-section necessary to detect at least one subhalo (solid lines) with the shaded areas corresponding to the confidence levels at 68% and 95%. These curves can also be interpreted as the maximal value of the cross-section possible if no subhalos are discovered. The limit is set for an homogeneous observation of the sky over 100 hr in the region 1: $5° \leq \psi \leq 34°$ (where detection is favored as seen in a previous plot). The comparison is made with the diffuse constraint already derived above also for an observation of 100 hr. The left panel is the limit for point-like sources and the right panel for extended objects where $\theta_e = 10 \times \theta_r$ (the extension is 10 times the angular resolution).

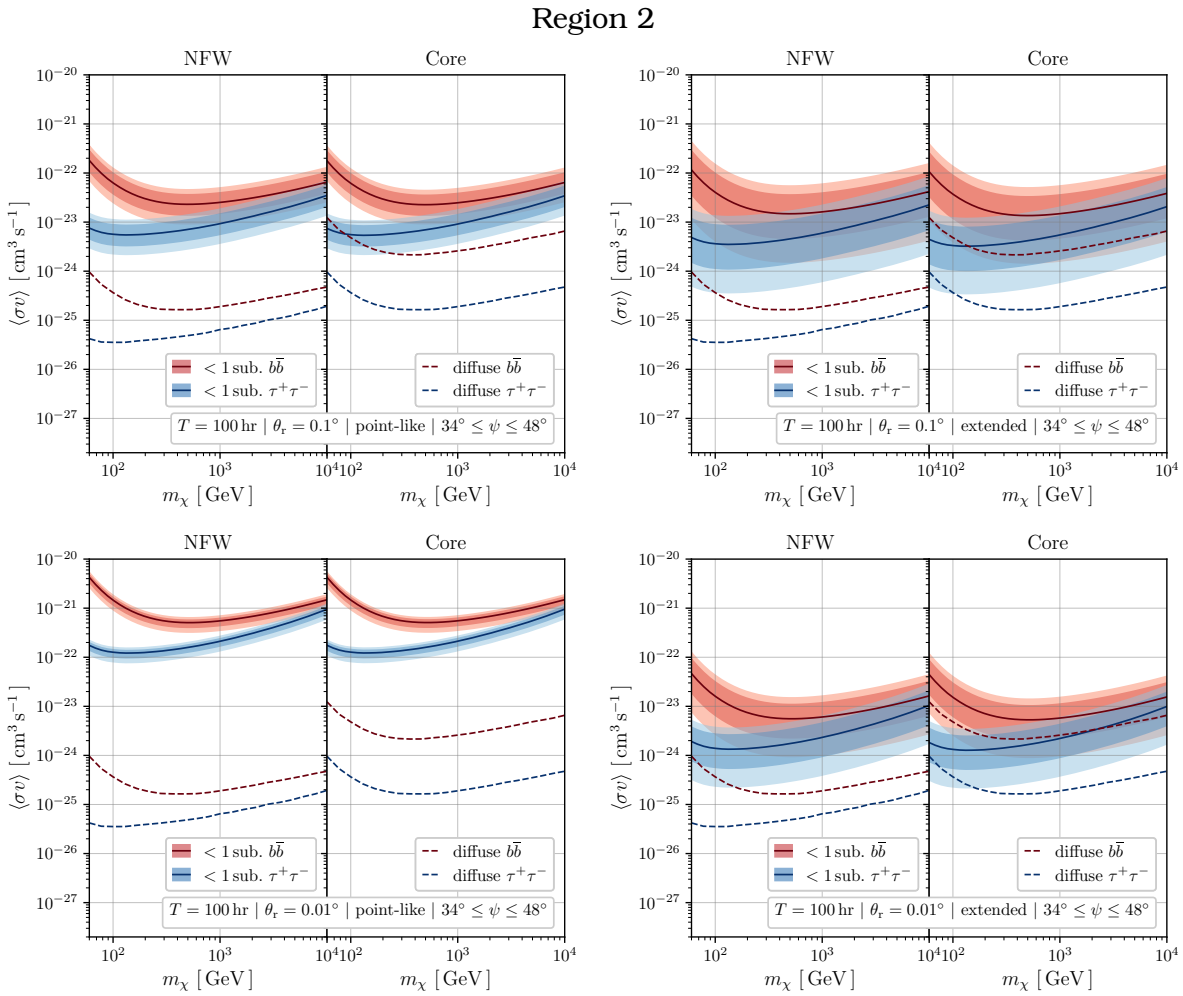

Figure E.5 – Annihilation cross-section necessary to detect at least one subhalo (solid lines) with the shaded areas corresponding to the confidence levels at 68% and 95%. These curves can also be interpreted as the maximal value of the cross-section possible if no subhalos are discovered. The limit is set for an homogeneous observation of the sky over 100 hr in the region 2: $34° \leq \psi < 48°$ (where detection is favored as seen in a previous plot). The comparison is made with the diffuse constraint already derived above also for an observation of 100 hr. The left panel is the limit for point-like sources and the right panel for extended objects where $\theta_e = 10 \times \theta_r$ (the extension is 10 times the angular resolution).

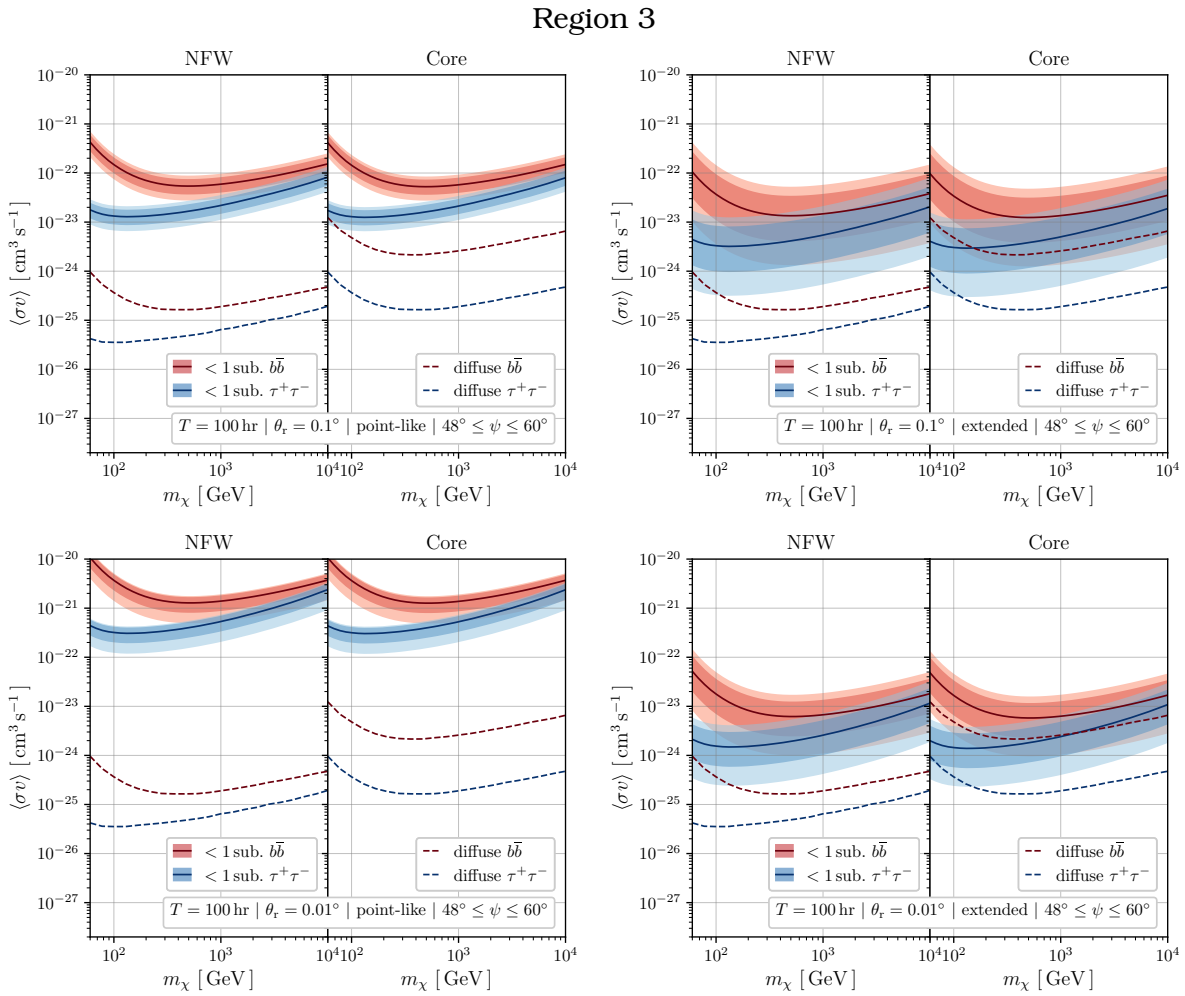

Figure E.6 – Annihilation cross-section necessary to detect at least one subhalo (solid lines) with the shaded areas corresponding to the confidence levels at 68% and 95%. These curves can also be interpreted as the maximal value of the cross-section possible if no subhalos are discovered. The limit is set for an homogeneous observation of the sky over 100 hr in the region 3: $48° \leq \psi \leq 60°$ (where detection is favored as seen in a previous plot). The comparison is made with the diffuse constraint already derived above also for an observation of 100 hr. The left panel is the limit for point-like sources and the right panel for extended objects where $\theta_e = 10 \times \theta_r$ (the extension is 10 times the angular resolution).

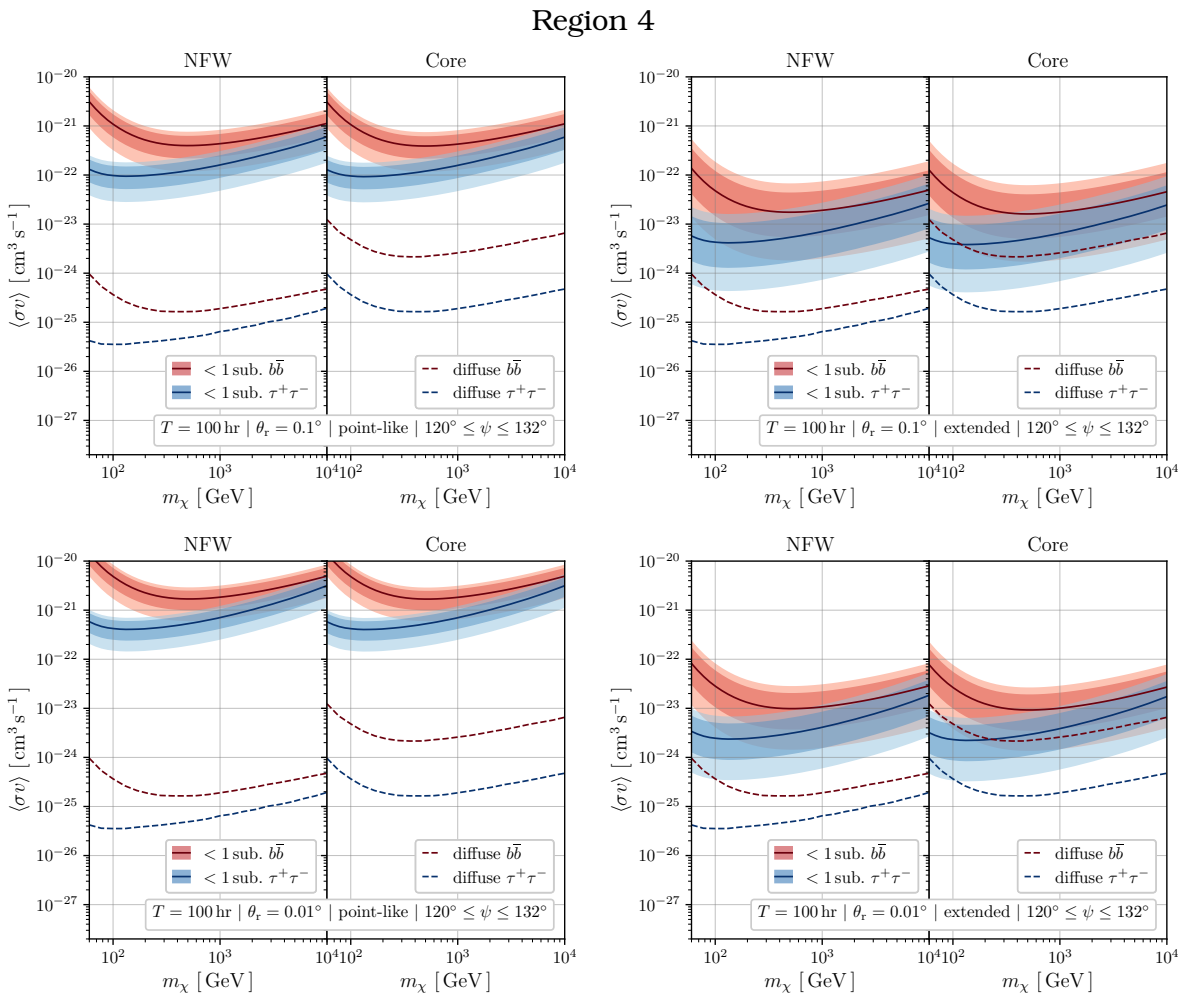

Figure E.7 – Annihilation cross-section necessary to detect at least one subhalo (solid lines) with the shaded areas corresponding to the confidence levels at 68% and 95%. These curves can also be interpreted as the maximal value of the cross-section possible if no subhalos are discovered. The limit is set for an homogeneous observation of the sky over 100 hr in the region 4: $120° < \psi < 132°$ (where detection is favored as seen in a previous plot). The comparison is made with the diffuse constraint already derived above also for an observation of 100 hr. The left panel is the limit for point-like sources and the right panel for extended objects where $\theta_e = 10 \times \theta_r$ (the extension is 10 times the angular resolution).

F

Résumé détaillé en français

F.1 Problème de masse manquante et petites échelles

Le problème de la masse manquante est l'un des mystères les plus intrigants de la physique moderne; il semblerait que la majorité de la matière présente dans l'Univers nous soit inconnue. Cette conclusion résulte de plusieurs observations à plusieures échelles. Au niveau des galaxies spirales nous observons, depuis les années 1970, des vitesses de rotation des étoiles et du gaz anormalement importantes dans les régions externes. De fait, ces vitesses sont supérieures à ce que prédit de théorie de la gravitation appliquée à la distribution de masse visible (Rubin et al. 1970). Un phénomène similaire existe dans les amas de galaxies et avait déjà intrigué les chercheurs dès les années 1930 (Zwicky 1933). Deux solutions sont envisageables pour réconcilier théorie et observation. La première est de chercher à savoir si la relativité générale est bien la bonne théorie de la gravité où si, dans certaines limites, elle doit être modifiée. Nous pouvons citer la théorie MOdified Newtonian Dynamics (MOND) s'inscrivant dans ce cadre (Milgrom 1983). La seconde option est de considérer la possible présence de matière non visible englobant les galaxies et les amas. Elle donne alors un terme supplémentaire dans les distributions de masse qui, une fois introduit dans les équations, permet de retrouver le résultat des observations. Cette nouvelle matière est appelée la matière noire ou matière obscure. Dans ce travail nous postulons son existence. Enfin, notons qu'il n'est pas exclu que les deux options cohabitent avec l'existence d'une matière noire associée à une théorie de la gravité modifiée.

La cosmologie, et plus particulièrement l'observation du fond diffus cosmologique (Alpher et al. 1948a,b ; Gamow 1948a), donne un argument fort en faveur de la matière noire. Elle met en évidence le pouvoir de prédiction du modèle ΛCDM fondé sur l'existence d'une constante cosmologique et de la matière noire dite froide (avec une vitesse faible comparée à la vitesse de la lumière et ce depuis les premières époques de l'Univers). La formation des structures comme les galaxies, les amas ou les superamas est aussi difficile à expliquer sans sa présence et son agragation en halos dans lesquels les baryons se concentrent pour former étoiles et galaxies. Les simulations cosmologiques basées sur le modèle ΛCDM reproduisent notamment des univers ayant une ressemblance inouïe avec le notre (Springel et al. 2005). En revanche en ce concentrant sur l'échelle des galaxies et en dessous, les simulations et les observations montrent des divergences, cela donne lieu au problème des petites échelles (Bullock et al. 2017). Certaines de ces différences s'estompent à mesure que les si-

mulations deviennent plus précises et les observations s'accumulent. Il reste tout de même intéressant de pouvoir étudier analytiquement la distribution des sous-halos dans les halos galactiques afin de se confronter aux simulations et aux observations.

La question est aussi de savoir de quoi est faite intrinsèquement la matière noire. Etant donné le succès du modèle standard de la physique des particules nous pouvons nous attendre à ce quelle soit elle même composée de particules élémentaires (FENG 2010). Plusieurs scénarios sont alors possibles; les neutrinos stériles (BOYARSKY et al. 2009b), les axions (PECCEI et al. 1977) ou encore les WIMPs (particules massives interagissant faiblement en anglais) pouvant provenir des modèles de supersymmétrie (MARTIN 1998) ou de dimensions supérieures (KALUZA 1921 ; KLEIN 1926) par exemple. Une autre option serait une matière noire faite d'objet macroscopiques et compacts, comme des étoiles très peu lumineuse (scénario déjà exclus par les observations) ou des trous noirs primordiaux (formé dans les tous premiers instants de l'Univers) (ZEL'DOVICH et al. 1967 ; S. HAWKING 1971). Enfin il n'est ici pas impossible non plus que plusieurs scénarios soient mêlés.

Devant l'enjeu du problème, de nombreuses collaborations ont traqué la matière noire afin de la détecter autrement que par ses interactions gravitationnelles. Trois techniques sont alors à l'oeuvre. La première consiste a rechercher la matière noire comme produit des interactions réalisées à l'intérieur des collectionneurs de particules comme le LHC. La seconde repose sur la présence de matière noire dans notre environnement proche et attend d'observer l'interaction d'une ou plusieurs de ces particules avec des noyaux d'atomes. Enfin la troisième option se concentre sur la recherche de phénomène astrophysiques qui ne pourraient être causés que par la présence de matière noire. En particulier des excès de particules (photons, neutrinos) reçu depuis des sources identifiées et pour lesquelles il est possible de différencier la contribution de la matière noire des sources classiques.

Ce travail est centré autour d'un modèle cohérent et analytique de distribution des sous-halos dans la Voie-Lactée le modèle SL17. Le but est ici de l'améliorer, de lui donner de nouvelles bases théorique et de l'utiliser pour faire des prédictions de détection indirecte. L'ensemble du document est présenté de façon chronologique par rapport à l'évolution de la matière noire dans l'Univers. Premièrement je m'intéresse à son comportement dans l'Univers primordial et à l'effet que cela a produit sur sa distribution actuelle, notamment à travers la masse minimale des halos. Ensuite, à l'aide du modèle de l'excursion set et des arbres de fusion, je prédis la distribution en masse non évoluée des sous-halos présents dans les halos. Dans un quatrième chapitre je me concentre, par la suite, sur la Voie-Lactée. Je rappelle comment le modèle SL17 permet de passer d'une distribution de masse non évoluée à sa version évoluée en incluant les effets dynamiques. J'étudie alors un effet non pris en compte originellement due à l'interaction des sous-halos avec les étoiles individuelles dans le disque Galactique. Enfin j'utilise SL17 pour évaluer la possibilité de détecter des sous-halos de matière noire comme point-source de rayons gamma dans des expériences type Fermi-LAT and CTA.

F.2 Masse minimale des halos dans un modèle simplifié

Dans un scénario WIMP, la matière noire est produite grâce à ses nombreuses interactions avec les particules du modèle standard dans les premiers instants de l'Univers. Au tout début, matière noire et particules du modèle standard sont dans un état d'équilibre thermodynamique et forment le plasma primordial. Cependant, les

WIMPs étant des particules massives, elles deviennent rapidement non relativistes et leur densité décroit exponentiellement. En effet, elles sont alors plus difficile à produire à mesure que la densité d'énergie du plasma, fait de particule majoritairement moins massive, décroit avec l'expansion de l'Univers. Cependant, le taux d'annihilation des particules de matière noire chute également car elles sont plus rares dans le plasma. De fait, après un certain temps, l'expansion gèle tous les processus de création et d'annihilation de matière noire et son abondance se trouve fixée. Ce processus s'appelle le découplage chimique (Lee et al. 1977). En revanche les WIMPs peuvent encore diffuser sur le plasma et conservent un équilibre thermique avec ce dernier en échangeant de l'énergie. L'expansion fait cependant chuter le taux de diffusion de la même manière, de sorte qu'après une certaine période de temps, la matière noire se trouve priver de toute interaction avec le plasma. On appelle ce processus le découplage cinétique (Hofmann et al. 2001). Les WIMPs commencent alors une période de propagation dite libre dans l'Univers ayant une influence directe sur la masse minimale que les halos de matière noire peuvent former par la suite (Green et al. 2005 ; Bertschinger 2006 ; Bringmann 2009). Dans le modèle SL17 la masse minimale des halos est un paramètre libre. Ici nous cherchons à savoir quelle valeur est attendue pour différents modèles de physique des particules. De plus, nous souhaitons aussi classifier les différents processus microscopiques et en extraire les propriétés pertinentes. Pour cela nous utilisons un modèle simplifié avec des interactions matière noire - modèle standard produites à l'aide de particule médiatrices scalaire, pseudo-scalaire et (axial)-vecteur à l'ordre de l'arbre. Ces modèles sont en effets de plus en plus utilisés aujourd'hui (Abdallah et al. 2015 ; Kahlhoefer et al. 2016 ; Arina 2018) afin d'obtenir des résultats génériques qui peuvent se rapporter à des modèles UV-complets. Nous montrons cela avec l'exemple du secteur CP-impair dans le NMSSM (Domingo 2017).

Tout d'abord nous rappelons les lois mathématiques régissant le modèle ΛCDM. En second lieu, nous introduisons la notion d'espace des phases en relativité générale et la fonction de distribution associée. Nous montrons comment son comportement est régi par l'équation de Boltzmann relativiste ; ce qui nous permet de dériver, par la suite, différentes propriétés thermodynamiques pour les particules présentes dans l'Univers primordial. En troisième lieu nous développons plus en détail les équations régissant le découplage chimique et le découplage cinétique en montrant quelques exemples simples. Enfin nous abordons l'étude de notre modèle simplifié. Nous commençons par introduire le Lagrangien ainsi que tous les processus à l'arbre pertinents. Nous développons aussi les différentes contraintes théoriques sur le modèle. Nous imposons notamment que les couplages soient suffisamment faibles pour éviter les effets non perturbatifs (comme les corrections à une ou plusieurs boucles, ou l'effet de Sommerfeld) et nous vérifions que le découplage chimique se passe suffisamment tôt avant le découplage cinétique pour éviter toute contamination — les équations que nous utilisons ne prenant pas en compte les cas où les deux se produisent simultanément. La méthode d'analyse est alors la suivante. A l'aide d'un code que nous avons entièrement conçu nous commençons par contraindre les couplages des particules en imposant que l'abondance prédite par le découplage cinétique soit l'abondance observée aujourd'hui (en supposant que les WIMPs forment toute la matière noire). Puis, une fois les bons couplages déterminés, nous calculons la température du plasma primordial au moment du découplage cinétique. Cette dernière est finalement directement reliée à la masse minimale des halos. En guise d'illustration nous montrons aussi le nombre de sous-halos alors prédit dans la Voie-Lactée. En particulier nous pouvons dériver des lois d'échelles et montrer que la masse minimale

se comporte comme $M_{\rm min} \sim m_\chi^{-3}$ et le nombre de sous-halos comme $N_{\rm sub} \sim m_\chi^3$ où m_χ est la masse des WIMPs. Nous attachons une importance particulière à dériver le comportement en vitesse des différentes section-efficaces entrant dans les calculs. Ainsi nous montrons qu'un médiateur pseudo-scalaire induit un découplage chimique plus tardif (à couplage équivalent) qu'un médiateur scalaire, du à des suppression en vitesse des interactions pour ce dernier. A l'inverse le découplage cinétique se produit plus tôt pour le pseudo-scalaire que pour le scalaire. Notons que les dépendances en vitesse sont importantes à characteriser car elle ont un impact sur les possibilités de detection aujourd'hui. Enfin, nous nous intéressons aussi à la section efficace d'auto-interaction de la matière noire qui, si suffisante, pourrait être une solution au problème coeur-pic (un des problèmes aux petites échelles de ΛCDM).

F.3 Fonction de masse cosmologique

Afin de comprendre la distribution des halos dans le modèle SL17 il est nécessaire d'en étudier la formation. Elle prend source dans les fluctuations quantiques de l'inflaton, champ responsable de l'inflation, s'étant transmises à la distribution de densité de matière. L'ensemble des fluctuations ayant survécu aux premières époques de l'Univers commencent à croire plusieurs centaines de milliers d'années après le Big Bang, sous l'effet de la gravité, lorsque la matière noire devient la composante dominante. Les régions les plus fortement sur-denses s'effondrent ensuite, se virilisent et forment les halos (MO et al. 2010). Alors que les premières étapes peuvent être décrites à l'aide de la théorie des perturbations linéaires en relativité générale, l'effondrement gravitationnel étant un phénomène non linéaire, il ne peut-être analytiquement évalué que dans des configurations simples.

La distribution cosmologique en masse des halos (sans considérer d'aspects dynamiques) peut tout de même être calculée analytiquement grâce à la théorie dite de l'excursion set (BOND et al. 1991). Cette dernière fournie aussi une trame pour simuler la formation hiérarchique des halos à l'aide des arbres de fusion. Nous utilisons dans ce travail l'algorithme C00 pour étudier la distribution des sous-halos de rang un dans un halo hôte. En effet, les halos sont faits de sous-halos, eux-même faits de sous-halos qui sont des sous-sous-halos dits de rang deux pour l'hôte etc. Dans sa version originelle le modèle SL17 utilise une fonction de masse des halos de rang un en loi de puissance, $\mathrm{d}N_{\rm sub}/\mathrm{d}m \propto m^{-\alpha}$ avec $\alpha \in [1.9, 2.0]$ et une normalisation fixée par des simulations cosmologiques. L'objectif est d'être ici plus précis et de s'affranchir de l'étape de normalisation sur les simulations. Plusieurs études se sont déjà penchées sur le sujet (GIOCOLI et al. 2008b ; Y. LI et al. 2009 ; JIANG et al. 2014). Cependant elles ne se sont intéressées principalement qu'aux sous-halos de grandes masses. En effet, les arbres de fusion sont trop gourmands en temps pour pouvoir simuler des sous-halos plus léger que $\sim 10^{-5}M$ où M est la masse de l'hôte. Une extrapolation d'ajustement sur des fonctions biens choisies est alors nécessaire. La nouveauté est qu'ici nous contraignons cet ajustement en supposant que toute la masse du halo hôte est contenu dans des sous-halos de rang un. Ceci étant thoriquement motivé dans un modèle de formation hierarchique et quasi auto-similaire. Ceci nous permet de retrouver à petite masse le comportement en loi de puissance avec $\alpha \in [1.9, 2.0]$, la littérature, où l'ajustement n'est pas contraint, donne généralement un exposant plus faible, *e.g.* $\alpha \sim 1.8$. De plus si l'on compare le nombre total de sous-halos obtenu avec cette nouvelle fonction de masse, il est comparable à celui de la calibration originale. Enfin nous avons aussi comparé le modèle SL17 augmenté de cette nou-

velle fonction de masse à un modèle semblable de distribution de sous-halos dans la littérature (Hiroshima et al. 2018). Nous trouvons des résultats cohérents mais légèrement différents. Cela n'est pas surprenant dans la mesure où cet autre modèls qui s'appuie sur des simulations cosmologiques, incorpore des recettes de physique plus complètes pour caractériser la dynamique des halos. Ce résultat est donc une motivation pour une amélioration accrue du modèle SL17, qui pourra se faire en partie autour des arbres de fusion à la manière de Cole et al. (2002), Zentner et al. (2003), Benson (2012) et Hiroshima et al. (2018). La différence avec ces dernières études étant notre souhait de s'affranchir au maximum des résultats de simulations numériques afin d'en être le plus indépendant possible.

En dernier lieu, nous abordons dans ce chapitre les très petites échelles et montrons comment le découplage cinétique de la matière noire influence la masse minimale des halos qu'elle peut former. Cela permet de faire le lien formel avec le chapitre précédent.

F.4 Effet des baryons sur les sous-halos de la Voie-Lactée

Au sein du modèle SL17, les halos sont décrits de manière statistique. L'idée principale est de considérer une distribution cosmologique, notamment à l'aide de la fonction de masse discutée précédemment, et de la contraindre en incorporant des effets dynamiques. L'impact principal est une réduction de la taille des sous-halos et leur destruction lorsqu'ils deviennent trop petit. Notons que le critère de destruction est sujet à discussion et de récentes études tendent à montrer que les sous-halos pourraient survivre même avec une taille infiniment réduite (Bosch et al. 2018b ; Errani et al. 2020b). Dans sa version originelle, deux effets dynamiques principaux sont inclus. Le premier est l'effet de marrée lisse qui arrache les particules externes des sous-halos par l'attraction gravitationelle du halo hôte. Le second et l'effet de choc par le potentiel du disque de baryons (Gnedin et al. 1999). A chaque passage d'un sous-halo par le disque les particules reçoivent un gain positif d'énergie cinétique qui permet à celles qui sont dans les régions externes de s'échapper. Dans ce travail nous étudions plus précisément une troisième forme d'effets dus aux interactions individuelles avec les étoiles. Lorsqu'un sous-halo croise une étoile, les particules qui le composent, reçoivent, de même, un gain en énergie cinétique qui peut alors aussi exclure certaines d'entre elles. Cet effet a déjà été considéré dans la littérature (V. Berezinsky et al. 2005 ; Angus et al. 2007 ; Green et al. 2007 ; Delos 2019a) mais jamais appliqués avec précision sur une population complète de sous-halos.

Nous regardons d'abord l'effet d'une seule étoile sur un sous-halo et nous améliorons le calcul usuellement utilisé, produit dans GF83, en remarquant que des simplifications peuvent être faite de part l'aspect ponctuel d'une étoile devant la taille d'un sous-halo. Ensuite, nous nous intéressons à l'impact de plusieurs étoiles. Nous dérivons une description probabiliste du gain en énergie cinétique total reçu ΔE par les particulesd'un sous halos donné. Nos calculs reposent sur le théorème central limite dont les hypothèses ne s'avèrent pas entièrement vérifiées si un soin particulier n'est pas apporté aux propriétés des rencontres entre étoiles et sous-halos. N'ayant pas d'autres alternatives pour un calcul analytique nous adaptons donc notre technique au mieux afin d'avoir la meilleure description possible de ΔE. Nous obtenons alors des résultats très satisfaisants malgré ces ajustements. Nous nous intéressons aussi à l'impact de ce gain en énergie sur la distribution finale de matière noire dans le sous-halo juste après le choc ; ce qui n'avait pas été considéré dans SL17. Cepen-

dant, cela ne peut être appliqué sur une population globale de halos et seule l'effet de la réduction en taille des sous-halos est retenu par la suite — comme dans SL17. Enfin nous nous intéressons à l'effet des étoiles sur l'ensemble de la population de sous-halos. Nous observons qu'il est principalement important pour les sous-halos ayant une masse $m < 10^{-3}$ $M_\odot$. En particulier, il décale la fonction de masse initiale vers les petites valeurs et dans un scénario ou les sous-halos sont facilement destructibles, il réduit leur population de plusieurs ordres de grandeur dans les régions les plus centrales de la Galaxies — où le nombre de croisement du disque est important et les étoiles plus nombreuses. Le nombre total de sous-halos fragiles se retrouve alors réduit d'un ordre de grandeur comparé aux prédictions originelles de SL17 à 8 kpc du centre Galactique. Dans une configuration de sous-halos dit résistants les effets sur le nombre total sont réduits et ne sont visibles qu'en deçà de 4 kpc du centre. La modification de la fonction de masse pourrait, dans tous les cas, avoir des conséquences sur les prédictions des recherches locales de matière noire.

F.5 Détectabilité de sous-halos ponctuels

Dans les sections précédentes nous avons travaillé sur la distribution de sous-halos, dans la Voie-Lactée en particulier. Ici nous utilisons ce travail pour étudier la possibilité de détecter des sous-halos de matière noire comme points-sources de rayons gammas dans la Galaxie. En effet, la collaboration Fermi-LAT à relevé dans un catalogue récent, 1525 points sources non résolus de rayons gamma qu'ils n'ont pas pu associer à des objets astrophysiques connus (FERMI-LAT COLLABORATION 2019). La plupart doivent être des object extragalactiques dont l'identification n'est pas encore certaine. Cependant, il est interessant de se demander si certains d'entres-eux peuvent être des sous-halos de matière noire, en supposant que cette dernière s'annihile et produit des rayons gamma. Plusieurs études se sont penchées sur la question et les conclusions semblent s'orientées vers un nombre d'au maximum $\mathcal{O}(10)$ sous-halos visibles (PIERI et al. 2011 ; BERTONI et al. 2015 ; HÜTTEN et al. 2016 ; CALORE et al. 2017, 2019a ; CORONADO-BLAZQUEZ et al. 2019). En revanche toutes les techniques employées jusqu'à présent reposent, soit sur une analyse directe des données du Fermi-LAT, soit sur des Monte-Carlo sans fond réaliste, soit sur des simulations cosmologiques et des reproductions de Voie-Lactée. Dans ce dernier cas, une galaxies type Voie-Lactée prise dans une simulation n'est pas vraiment identique à la Voie-Lactée elle-même et elle ne permet pas de résoudre toute la population de sous-halos (jusqu'aux plus petits d'entre eux). De fait, il est interessant de regarder si dans un modèle analytique contraint nous obtenons aussi une probabilité non nulle de détecter un ou plusieurs sous-halos. Si oui, nous attendons nous à les détecter avant de détecter la matière noire dite diffuse émise par le halo hôte et les sous-halos non résolus ? Pour répondre à ces questions nous ajoutons à SL17 un modèle de fond diffus gamma émis par des sources astrophysiques identifiées et dépendant de la distribution de baryons utilisée pour contraindre la population de sous-halos. Nous l'appelons le fond diffus baryonique. De fait nous prenons en compte la corrélation implicite qu'il existe entre fond de rayons gamma et distribution de sous-halos. L'idée ici n'est donc pas de dériver des limites exactes en se basant sur une analyse des données des instruments, la philosophie de l'étude est d'obtenir des nombres suffisamment précis pour être prédictifs, à l'aide d'un modèle avec lequel il est facile de jouer et de dériver des résultats analytiques. De plus, nous nous intéressons à la fois à des instruments type Fermi-LAT dont les données sont accessibles mais aussi

à des instruments type CTA qui n'estluimême pas encore opérationnel et pour lequel, seules des prédictions peuvent être faites. Ces instruments fictifs reprennent dans les grandes lignes les principales caractéristiques des vrais sans pour autant en être des descriptions parfaites.

La première étape est de définir l'émission de photons gamma produits par la matière noire ; par les sous-halos dits ponctuels, par rapport à la résolution d'un instrument, mais aussi par la composante diffuse. Cette quantité est caractérisée par une grandeur appelée le J-facteur. Ensuite nous évaluons, avec SL17, la probabilité qu'un sous-halos donnée ait un J-facteur plus grand qu'un seuil donné dans une direction donnée. Nous faisons cela pour un halo hôte ayant différents profils de densités dits NFW ou coeur. L'étape suivante est alors d'évaluer le seuil en J-facteur pour qu'un sous-halo soit détectable au dessus du fond de gammas après un certain temps d'observation. De même nous évaluons aussi la section efficace d'annihilation nécessaire pour que le fond diffus de matière noire soit détecté au dessus du fond diffus baryonique. Pour cela nous employons deux techniques, une première simple, basée sur une analyse On-Off et une seconde plus complexe utilisant la notion de vraisemblance (T.-P. Li et al. 1983). Nous nous assurons que la seconde approche donne des contraintes sur les sections efficaces d'annihilation de la matière noire comparable avec les résultats d'analyse de données ou de Monte-Carlo présents dans la littérature (Fermi-LAT Collaboration 2012a ; Silverwood et al. 2015). Une fois ceci fait nous pouvons alors extrapoler les limites à des temps d'observation aussi grands que nous le souhaitons. L'avantage de la première approche, en contrepartie, est de fournir le comportement simple des différents seuils en fonction du temps d'observation et des différents paramètre de l'instrument. Nous dérivons notamment l'existence d'un seuil critique en J-facteur tel que, si l'on ne détecte jamais le fond diffuse de matière noire (situation dans laquelle nous sommes actuellement), un sous-halos avec un J-facteur plus faible ne pourra jamais être détecté non plus.

Enfin, nous évaluons la probabilité d'avoir des sous-halos ponctuels dépassant le seul de détectabilité dans différentes configurations. Dans les scénarios les plus optimistes ou les sous-halos sont résistants à la destruction nous pouvons espérer une dizaine d'objets maximum pour Fermi-LAT après 10 ans de prises de données. Dans le cas de CTA, son faible champ de vue, sa meilleur précision et son temps d'observation réduit rendent les résultats moins optimistes et la détection de points-sources ne semble pas possible avant la détection de la composante diffuse. Nous avons pu observer que dans tous les cas, même si la direction d'observation la plus propice pour une détection varie avec la résolution de l'instrument, elle se trouve globalement à une angle entre $20°$ et $60°$ du centre Galactique. Les sous-halos les plus détectable sont alors de masse relativement élevée $> 10^3$ $M_\odot$ et proche du centre. Ceci s'explique car les sous-halos très massifs à cette position sont fortement épluchés par les effets dynamiques, et s'ils sont résistants, ils survivent en étant ponctuels et suffisamment proche pour produire un J-facteur fort. Enfin pour CTA nous avons aussi examiné la possibilité de détecter des sous-halos non ponctuels mais les résultats, sont sensiblement similaires à ceux des sources ponctuelles, ce qui induit une détection, avant la composante diffuse de matière noire, peu probable.

Bibliography

[1] U. Le Verrier. “Comptes rendus hebdomadaires des séances de l’Académie des sciences. Lettre de M. Le Verrier à M. Faye sur la théorie de Mercure et sur le mouvement du périhélie de cette planète.” *Académie des sciences. Centre national de la recherche scientifique* 49 (1859), pp. 379–383 [pp. 2, 19].

[2] H. Poincaré. “La Voie lactée et la théorie des gaz”. *Bulletin de la Société astronomique de France* 20 (1906), pp. 153–165 [p. 3].

[3] F. Jüttner. “Das Maxwellsche Gesetz der Geschwindigkeitsverteilung in der Relativtheorie”. *Annalen der Physik* 339.5 (1911), pp. 856–882. ISSN: 1521-3889. DOI: https://doi.org/10.1002/andp.19113390503 [p. 56].

[4] H. C. Plummer. “On the Problem of Distribution in Globular Star Clusters: (Plate 8.)” *Monthly Notices of the Royal Astronomical Society* 71.5 (Mar. 10, 1911), pp. 460–470. ISSN: 0035-8711, 1365-2966. DOI: 10.1093/mnras/71.5.460 [pp. 137, 140].

[5] V. Slipher. “The detection of nebular rotation”. *Lowell Observatory Bulletin* 2.62 (June 8, 1914), p. 66 [p. 6].

[6] F. G. Pease. “The Rotation and Radial Velocity of the Central Part of the Andromeda Nebula”. *Proceedings of the National Academy of Sciences* 4.1 (Jan. 1, 1918), pp. 21–24. ISSN: 0027-8424, 1091-6490. DOI: 10.1073/pnas.4.1.21 [p. 6].

[7] F. W. Dyson, A. S. Eddington, and C. Davidson. “IX. A determination of the deflection of light by the sun’s gravitational field, from observations made at the total eclipse of May 29, 1919”. *Philosophical Transactions of the Royal Society of London. Series A, Containing Papers of a Mathematical or Physical Character* 220.571 (Jan. 1920), pp. 291–333. ISSN: 0264-3952, 2053-9258. DOI: 10.1098/rsta.1920.0009 [p. 19].

[8] T. Kaluza. “Zum unit{\"a}tsproblem der physik”. *Sitzungsber. Preuss. Akad. Wiss. Berlin.(Math. Phys.)* 1921.966972 (1921), pp. 45–46 [pp. 26, 296].

[9] O. Klein. “Quantentheorie und f{\"u}nfdimensionale Relativit{\"a}tstheorie”. *Zeitschrift f{\"u}r Physik* 37.12 (Dec. 1926), pp. 895–906. ISSN: 1434-6001, 1434-601X. DOI: 10.1007/BF01397481 [pp. 26, 296].

[10] J. H. Oort. “The force exerted by the stellar system in the direction perpendicular to the galactic plane and some related problems”. *Bulletin of the Astronomical Institutes of the Netherlands* 6 (Sept. 1932), p. 249 [p. 3].

[11] F. Zwicky. “Die Rotverschiebung von extragalaktischen Nebeln”. *Helv. Phys. Acta* 6 (1933), pp. 110–127. DOI: 10.1007/s10714-008-0707-4 [pp. 3, 38, 295].

[12] F. Zwicky. “On the Masses of Nebulae and of Clusters of Nebulae”. *The Astrophysical Journal* 86 (1937), p. 217 [pp. 3, 4, 38].

[13] S. S. Wilks. “The Large-Sample Distribution of the Likelihood Ratio for Testing Composite Hypotheses”. *The Annals of Mathematical Statistics* 9.1 (Mar. 1938), pp. 60–62. ISSN: 0003-4851. DOI: 10.1214/aoms/1177732360 [p. 210].

[14] H. W. Babcock. “The rotation of the Andromeda Nebula”. *Lick Observatory Bulletins* 19 (1939), pp. 41–51. ISSN: 0075-9317. DOI: 10.5479/ADS/bib/1939LicOB.19.41B [p. 6].

[15] S. Chandrasekhar. “Stochastic Problems in Physics and Astronomy”. *Reviews of Modern Physics* 15.1 (Jan. 1, 1943), pp. 1–89. ISSN: 0034-6861. DOI: 10.1103/RevModPhys.15.1 [p. 116].

[16] R. A. Alpher and R. Herman. “Evolution of the Universe”. *Nature* 162.4124 (Nov. 1948), pp. 774–775. ISSN: 0028-0836, 1476-4687. DOI: 10.1038/162774b0 [pp. 9, 295].

[17] R. A. Alpher and R. C. Herman. "On the Relative Abundance of the Elements". *Physical Review* 74.12 (Dec. 15, 1948), pp. 1737–1742. ISSN: 0031-899X. DOI: 10.1103/PhysRev.74.1737 [pp. 9, 295].

[18] G. Gamow. "The Evolution of the Universe". *Nature* 162.4122 (Oct. 1948), pp. 680–682. ISSN: 0028-0836, 1476-4687. DOI: 10.1038/162680a0 [pp. 9, 295].

[19] G. Gamow. "The Origin of Elements and the Separation of Galaxies". *Physical Review* 74.4 (Aug. 15, 1948), pp. 505–506. ISSN: 0031-899X. DOI: 10.1103/PhysRev.74.505.2 [p. 9].

[20] H. Primakoff. "Photo-Production of Neutral Mesons in Nuclear Electric Fields and the Mean Life of the Neutral Meson". *Physical Review* 81.5 (Mar. 1, 1951), pp. 899–899. ISSN: 0031-899X. DOI: 10.1103/PhysRev.81.899 [p. 31].

[21] L. Spitzer Jr. "Distribution of Galactic Clusters." *The Astrophysical Journal* 127 (Jan. 1958), p. 17. ISSN: 0004-637X, 1538-4357. DOI: 10.1086/146435 [pp. 136, 150].

[22] A. Salam and J. C. Ward. "Weak and electromagnetic interactions". *Il Nuovo Cimento* 11.4 (Feb. 1959), pp. 568–577. ISSN: 0029-6341, 1827-6121. DOI: 10.1007/BF02726525 [p. 21].

[23] S. L. Glashow. "Partial-symmetries of weak interactions". *Nuclear Physics* 22.4 (Feb. 1961), pp. 579–588. ISSN: 00295582. DOI: 10.1016/0029-5582(61)90469-2 [p. 21].

[24] J. Goldstone, A. Salam, and S. Weinberg. "Broken Symmetries". *Physical Review* 127.3 (Aug. 1962) [p. 21].

[25] F. Englert and R. Brout. "Broken Symmetry and the Mass of Gauge Vector Mesons". *Physical Review Letters* 13.9 (Aug. 31, 1964), pp. 321–323. ISSN: 0031-9007. DOI: 10.1103/PhysRevLett.13.321 [p. 21].

[26] P. W. Higgs. "Broken Symmetries and the Masses of Gauge Bosons". *Physical Review Letters* 13.16 (Oct. 19, 1964), pp. 508–509. ISSN: 0031-9007. DOI: 10.1103/PhysRevLett.13.508 [p. 21].

[27] R. H. Dicke et al. "Cosmic Black-Body Radiation." *The Astrophysical Journal* 142 (July 1965), p. 414. ISSN: 0004-637X, 1538-4357. DOI: 10.1086/148306 [p. 9].

[28] A. A. Penzias and R. W. Wilson. "A Measurement of Excess Antenna Temperature at 4080 Mc/s." *The Astrophysical Journal* 142 (July 1965), p. 419. ISSN: 0004-637X, 1538-4357. DOI: 10.1086/148307 [p. 9].

[29] K. Bichteler. "On the Cauchy problem of the relativistic Boltzmann equation". *Communications in Mathematical Physics* 4.5 (Oct. 1, 1967), pp. 352–364. ISSN: 1432-0916. DOI: 10.1007/BF01653649 [p. 50].

[30] R. K. Sachs and A. M. Wolfe. "Perturbations of a Cosmological Model and Angular Variations of the Microwave Background". *The Astrophysical Journal* 147 (Jan. 1967), p. 73. ISSN: 0004-637X, 1538-4357. DOI: 10.1086/148982 [p. 10].

[31] S. Weinberg. "A Model of Leptons". *Physical Review Letters* 19.21 (Nov. 20, 1967), pp. 1264–1266. ISSN: 0031-9007. DOI: 10.1103/PhysRevLett.19.1264 [p. 21].

[32] Y. B. Zel'dovich and I. D. Novikov. "The Hypothesis of Cores Retarded during Expansion and the Hot Cosmological Model". *Soviet Astronomy* 10 (Feb. 1967), p. 602 [pp. 27, 296].

[33] J. Silk. "Cosmic Black-Body Radiation and Galaxy Formation". *The Astrophysical Journal* 151 (Feb. 1968), p. 459. DOI: 10.1086/149449 [pp. 11, 112, 132].

[34] C. Marle. "Sur l'établissement des équations de l'hydrodynamique des fluides relativistes dissipatifs. I.-L'equation de Boltzmann relativiste". *Annales de l'IHP Physique théorique* 10.1 (1969), pp. 67–126 [p. 50].

[35] Y. B. Zeldovich and R. A. Sunyaev. "The interaction of matter and radiation in a hot-model universe". *Astrophysics and Space Science* 4.3 (July 1969), pp. 301–316. ISSN: 0004-640X, 1572-946X. DOI: 10.1007/BF00661821 [p. 10].

[36] K. C. Freeman. "On the Disks of Spiral and S0 Galaxies". *Astrophysical Journal* 160 (1970), p. 811 [p. 6].

[37] V. C. Rubin and W. K. Ford Jr. "Rotation of the Andromeda nebula from a spectroscopic survey of emission regions". *The Astrophysical Journal* 159 (1970), p. 379 [pp. 6, 38, 295].

[38] C. S. Shen. "Pulsars and Very High-Energy Cosmic-Ray Electrons". *The Astrophysical Journal* 162 (Dec. 1970), p. L181. ISSN: 0004-637X, 1538-4357. DOI: 10.1086/180650 [p. 35].

[39] R. A. Sunyaev and Y. B. Zeldovich. “Small-scale fluctuations of relic radiation”. *Astrophysics and Space Science* 7.1 (Apr. 1970), pp. 3–19 [p. 10].

[40] Y. B. Zel’dovich. “Gravitational instability: An approximate theory for large density perturbations.” *Astronomy and Astrophysics* 5 (Mar. 1970), pp. 84–89 [p. 118].

[41] J.-L. Gervais and B. Sakita. “Field theory interpretation of supergauges in dual models”. *Nuclear Physics B* 34.2 (1971), pp. 632–639 [p. 25].

[42] S. Hawking. “Gravitationally Collapsed Objects of Very Low Mass”. *Monthly Notices of the Royal Astronomical Society* 152.1 (Apr. 1, 1971), pp. 75–78. issn: 0035-8711. doi: 10.1093/mnras/152.1.75 [pp. 27, 296].

[43] A. Neveu and J. Schwarz. “Factorizable dual model of pions”. *Nuclear Physics B* 31.1 (Aug. 1971), pp. 86–112 [p. 25].

[44] P. Ramond. “Dual Theory for Free Fermions”. *Physical Review D* 3.10 (May 15, 1971), pp. 2415–2418. issn: 0556-2821. doi: 10.1103/PhysRevD.3.2415 [p. 25].

[45] J. M. Stewart. *Non-Equilibrium Relativistic Kinetic Theory*. Lecture Notes in Physics. Berlin Heidelberg: Springer-Verlag, 1971. isbn: 978-3-540-05652-2. doi: 10.1007/BFb0025374 [p. 50].

[46] J. P. Ostriker, L. Spitzer Jr., and R. A. Chevalier. “On the Evolution of Globular Clusters”. *The Astrophysical Journal* 176 (Sept. 1972), p. L51. doi: 10.1086/181018 [p. 146].

[47] D. H. Rogstad and G. S. Shostak. “Gross Properties of Five Scd Galaxies as Determined from 21-CENTIMETER Observations”. *The Astrophysical Journal* 176 (Sept. 1972), p. 315. issn: 0004-637X, 1538-4357. doi: 10.1086/151636 [p. 6].

[48] S. Weinberg. *Gravitation and cosmology: principles and applications of the general theory of relativity*. 1972 [pp. 45, 104].

[49] R. N. Whitehurst and M. S. Roberts. “High-Velocity Neutral Hydrogen in the Central Region of the Andromeda Galaxy”. *The Astrophysical Journal* 175 (July 1972), p. 347. issn: 0004-637X, 1538-4357. doi: 10.1086/151562 [p. 6].

[50] M. S. Roberts and A. H. Rots. “Comparison of Rotation Curves of Different Galaxy Types”. *Astronomy and Astrophysics* 26 (1973), pp. 483–485 [p. 6].

[51] B. J. Carr and S. W. Hawking. “Black Holes in the Early Universe”. *Monthly Notices of the Royal Astronomical Society* 168.2 (Aug. 1, 1974), pp. 399–415. issn: 0035-8711, 1365-2966. doi: 10.1093/mnras/168.2.399 [pp. 27, 38].

[52] J. Einasto, A. Kaasik, and E. Saar. “Dynamic evidence on massive coronas of galaxies”. *Nature* 250.5464 (July 1974), pp. 309–310. issn: 0028-0836, 1476-4687. doi: 10.1038/250309a0 [pp. 6, 32].

[53] S. W. Hawking. “Black hole explosions?” *Nature* 248.5443 (Mar. 1974), pp. 30–31. issn: 0028-0836, 1476-4687. doi: 10.1038/248030a0 [p. 28].

[54] J. P. Ostriker, P. J. E. Peebles, and A. Yahil. “The size and mass of galaxies, and the mass of the universe”. *The Astrophysical Journal* 193 (Oct. 1974), pp. L1–L4. doi: 10.1086/181617 [p. 6].

[55] W. H. Press and P. Schechter. “Formation of Galaxies and Clusters of Galaxies by Self-Similar Gravitational Condensation”. *The Astrophysical Journal* 187 (Feb. 1974), p. 425. issn: 0004-637X, 1538-4357. doi: 10.1086/152650 [pp. 96, 109, 114].

[56] J. Wess and B. Zumino. “Supergauge transformations in four dimensions”. *Nuclear Physics B* 70.1 (Feb. 1974), pp. 39–50. issn: 05503213. doi: 10.1016/0550-3213(74)90355-1 [p. 25].

[57] A. Belavin et al. “Pseudoparticle solutions of the Yang-Mills equations”. *Physics Letters B* 59.1 (Oct. 1975), pp. 85–87. issn: 03702693. doi: 10.1016/0370-2693(75)90163-X [p. 23].

[58] G. F. Chapline. “Cosmological effects of primordial black holes”. *Nature* 253.5489 (Jan. 1975), pp. 251–252. issn: 0028-0836, 1476-4687. doi: 10.1038/253251a0 [p. 38].

[59] P. Nath and R. Arnowitt. “Generalized super-gauge symmetry as a new framework for unified gauge theories”. *Physics Letters B* 56.2 (Apr. 14, 1975), pp. 177–180 [p. 25].

[60] M. S. Roberts and R. N. Whitehurst. “The rotation curve and geometry of M 31 at large galactocentric distances.” *The Astrophysical Journal* 201 (Oct. 1975), p. 327. issn: 0004-637X, 1538-4357. doi: 10.1086/153889 [p. 6].

[61] I. B. Zeldovich and I. D. Novikov. *Structure and evolution of the universe.* Publication Title: Moscow. Jan. 1, 1975 [p. 42].

[62] E. Gildener. "Gauge-symmetry hierarchies". *Physical Review D* 14.6 (Sept. 15, 1976). DOI: https://doi.org/10.1103/PhysRevD.14.1667 [p. 25].

[63] B. W. Lee and S. Weinberg. "Cosmological lower bound on heavy-neutrino masses". *Physical Review Letters* 39 (July 1977), pp. 165–168. DOI: 10.1103/PhysRevLett.39.165 [pp. 25, 37, 42, 69, 297].

[64] R. D. Peccei and H. R. Quinn. "CP Conservation in the Presence of Pseudoparticles". *Physical Review Letters* 38.25 (June 20, 1977), pp. 1440–1443. ISSN: 0031-9007. DOI: 10.1103/PhysRevLett.38.1440 [pp. 24, 296].

[65] M. Vysotskii, A. Dolgov, and Y. B. Zeldovich. "Cosmological limits on the masses of neutral leptons". *Soviet Journal of Experimental and Theoretical Physics Letters* 26 (Aug. 5, 1977), pp. 188–190 [p. 37].

[66] S. Weinberg. "A New Light Boson?" *Physical Review Letters* 40.4 (Jan. 23, 1978), pp. 223–226. ISSN: 0031-9007. DOI: 10.1103/PhysRevLett.40.223 [p. 24].

[67] F. Wilczek. "Problem of Strong P and T Invariance in the Presence of Instantons". *Physical Review Letters* 40.5 (Jan. 30, 1978), pp. 279–282. ISSN: 0031-9007. DOI: 10.1103/PhysRevLett.40.279 [p. 24].

[68] A. Bosma and P. C. van der Kruit. "The local mass-to-light ratio in spiral galaxies." *stronomy and Astrophysics* 79.3 (1979), pp. 281–286 [p. 6].

[69] J. E. Kim. "Weak-Interaction Singlet and Strong CP Invariance". *Physical Review Letters* 43.2 (July 9, 1979), pp. 103–107. ISSN: 0031-9007. DOI: 10.1103/PhysRevLett.43.103 [p. 24].

[70] G. Steigman. "Cosmology Confronts Particle Physics". *Annual Review of Nuclear and Particle Science* 29.1 (Dec. 1979), pp. 313–338. ISSN: 0163-8998, 1545-4134. DOI: 10.1146/annurev.ns.29.120179.001525 [p. 37].

[71] S. Tremaine and J. E. Gunn. "Dynamical Role of Light Neutral Leptons in Cosmology". *Physical Review Letters* 42.6 (Feb. 5, 1979). Publisher: American Physical Society, pp. 407–410. DOI: 10.1103/PhysRevLett.42.407 [p. 22].

[72] R. N. Mohapatra and G. Senjanović. "Neutrino Mass and Spontaneous Parity Nonconservation". *Physical Review Letters* 44.14 (Apr. 7, 1980), pp. 912–915. ISSN: 0031-9007. DOI: 10.1103/PhysRevLett.44.912 [p. 23].

[73] V. C. Rubin, N. Thonnard, and W. K. Ford Jr. "Rotational properties of 21 SC galaxies with a large range of luminosities and radii, from NGC 4605 /R = 4kpc/ to UGC 2885 /R = 122 kpc/". *The Astrophysical Journal* 238 (June 1980), p. 471. ISSN: 0004-637X, 1538-4357. DOI: 10.1086/158003 [p. 6].

[74] M. Shifman, A. Vainshtein, and V. Zakharov. "Can confinement ensure natural CP invariance of strong interactions?" *Nuclear Physics B* 166.3 (Apr. 1980), pp. 493–506. ISSN: 05503213. DOI: 10.1016/0550-3213(80)90209-6 [p. 24].

[75] A. R. Zhitnitsky. "On Possible Suppression of the Axion Hadron Interactions". *Sov. J. Nucl. Phys.* 31.260 (1980) [p. 24].

[76] R. J. Adler. "The Geometry of Random Fields". *The Geometry of Random Fields, Chichester: Wiley, 1981* (1981) [p. 110].

[77] M. Dine, W. Fischler, and M. Srednicki. "A simple solution to the strong CP problem with a harmless axion". *Physics Letters B* 104.3 (Aug. 1981), pp. 199–202. ISSN: 03702693. DOI: 10.1016/0370-2693(81)90590-6 [p. 24].

[78] P. J. E. Peebles. "Large-scale background temperature and mass fluctuations due to scale-invariant primeval perturbations". *The Astrophysical Journal* 263 (Dec. 1982), p. L1. ISSN: 0004-637X, 1538-4357. DOI: 10.1086/183911 [p. 10].

[79] P. J. E. Peebles. "Primeval adiabatic perturbations - Effect of massive neutrinos". *The Astrophysical Journal* 258 (July 1982), p. 415. ISSN: 0004-637X, 1538-4357. DOI: 10.1086/160094 [p. 10].

[80] O. E. Gerhard and S. Michael Fall. "Tidal interactions of disc galaxies". *Monthly Notices of the Royal Astronomical Society* 203.4 (Aug. 1983), pp. 1253–1268. ISSN: 0035-8711, 1365-2966. DOI: 10.1093/mnras/203.4.1253 [pp. 136, 150].

[81] T.-P. Li and Y.-Q. Ma. "Analysis methods for results in gamma-ray astronomy". *The Astrophysical Journal* 272 (Sept. 1983), p. 317. ISSN: 0004-637X, 1538-4357. DOI: 10.1086/161295 [pp. 203, 301].

[82] M. Milgrom. "A Modification of the Newtonian dynamics as a possible alternative to the hidden mass hypothesis". *The Astrophysical Journal* 270 (1983), pp. 365–370. DOI: 10.1086/161130 [pp. 19, 38, 295].

[83] J. Bekenstein and M. Milgrom. "Does the missing mass problem signal the breakdown of Newtonian gravity?" *The Astrophysical Journal* 286 (Nov. 1984), p. 7. ISSN: 0004-637X, 1538-4357. DOI: 10.1086/162570 [p. 20].

[84] P. Binétruy, G. Girardi, and P. Salati. "Constraints on a system of two neutral fermions from cosmology". *Nuclear Physics B* 237.2 (May 1984), pp. 285–306. ISSN: 05503213. DOI: 10.1016/0550-3213(84)90161-5 [pp. 37, 42, 68].

[85] R. M. Wald. *General Relativity*. University of Chicago Press, 1984. ISBN: 978-0-226-87033-5. DOI: 10.7208/chicago/9780226870373.001.0001 [p. 43].

[86] L. Bergström and G. Hulth. "Induced Higgs couplings to neutral bosons in e+e- collisions". *Nuclear Physics B* 259.1 (Sept. 1985), pp. 137–155. ISSN: 05503213. DOI: 10.1016/0550-3213(85)90302-5 [p. 269].

[87] J. Bernstein, L. S. Brown, and G. Feinberg. "Cosmological heavy-neutrino problem". *Physical Review D* 32.12 (Dec. 15, 1985), pp. 3261–3267. ISSN: 0556-2821. DOI: 10.1103/PhysRevD.32.3261 [p. 37].

[88] M. W. Goodman and E. Witten. "Detectability of certain dark-matter candidates". *Physical Review D* 31.12 (June 15, 1985), pp. 3059–3063. ISSN: 0556-2821. DOI: 10.1103/PhysRevD.31.3059 [p. 30].

[89] H. E. Haber and G. L. Kane. "The search for supersymmetry: Probing physics beyond the standard model". *Physics Reports* 117.2 (1985), pp. 75–263. ISSN: 0370-1573. DOI: https://doi.org/10.1016/0370-1573(85)90051-1 [p. 266].

[90] S. Nussinov. "Technocosmology — could a technibaryon excess provide a "natural" missing mass candidate?" *Physics Letters B* 165.1 (Dec. 1985), pp. 55–58. ISSN: 03702693. DOI: 10.1016/0370-2693(85)90689-6 [p. 27].

[91] P. Salati. "The distortions of the microwave background radiation, heavy neutral decaying leptons and decaying gravitinos". *Physics Letters B* 163.1 (Nov. 21, 1985), pp. 236–242 [p. 37].

[92] A. K. Drukier, K. Freese, and D. N. Spergel. "Detecting cold dark-matter candidates". *Physical Review D* 33.12 (June 15, 1986), pp. 3495–3508. ISSN: 0556-2821. DOI: 10.1103/PhysRevD.33.3495 [p. 31].

[93] C. L. Sarazin. "X-ray emission from clusters of galaxies". *Reviews of Modern Physics* 58.1 (Jan. 1, 1986), pp. 1–115. ISSN: 0034-6861. DOI: 10.1103/RevModPhys.58.1 [p. 4].

[94] G. Soucail et al. "A blue ring-like structure in the center of the A 370 cluster of galaxies." *Astronomy & Astrophysics* 172 (1987), pp. L14–L16 [p. 4].

[95] J. Bernstein. *Kinetic theory in the expanding universe*. Cambridge University Press, 1988 [pp. 56, 58, 65].

[96] M. Srednicki, R. Watkins, and K. A. Olive. "Calculations of relic densities in the early universe". *Nuclear Physics B* 310.3 (Dec. 1988), pp. 693–713. ISSN: 05503213. DOI: 10.1016/0550-3213(88)90099-5 [p. 42].

[97] M. J. Geller and J. P. Huchra. "Mapping the Universe". *Science* 246.4932 (Nov. 17, 1989), pp. 897–903. ISSN: 0036-8075, 1095-9203. DOI: 10.1126/science.246.4932.897 [p. 12].

[98] S. F. Shandarin and Y. B. Zeldovich. "The large-scale structure of the universe: Turbulence, intermittency, structures in a self-gravitating medium". *Reviews of Modern Physics* 61.2 (Apr. 1, 1989), pp. 185–220. ISSN: 0034-6861. DOI: 10.1103/RevModPhys.61.185 [p. 118].

[99] K. Griest and M. Kamionkowski. "Unitarity limits on the mass and radius of dark-matter particles". *Physical Review Letters* 64 (Feb. 1990), pp. 615–618. DOI: 10.1103/PhysRevLett.64.615 [p. 72].

[100] G. D. Starkman et al. "Opening the window on strongly interacting dark matter". *Physical Review D* 41.12 (June 15, 1990), pp. 3594–3603. ISSN: 0556-2821. DOI: 10.1103/PhysRevD.41.3594 [p. 27].

[101] M. S. Turner and F. Wilczek. "Positron line radiation as a signature of particle dark matter in the halo". *Physical Review D* 42.4 (Aug. 15, 1990), pp. 1001–1007. ISSN: 0556-2821. DOI: 10.1103/PhysRevD.42.1001 [p. 35].

[102] J. R. Bond et al. "Excursion set mass functions for hierarchical Gaussian fluctuations". *The Astrophysical Journal* 379 (Oct. 1991), p. 440. ISSN: 0004-637X, 1538-4357. DOI: 10.1086/170520 [pp. 96, 109, 114, 298].

[103] S. Cole. "Modeling galaxy formation in evolving dark matter halos". *The Astrophysical Journal* 367 (Jan. 1991), p. 45. ISSN: 0004-637X, 1538-4357. DOI: 10.1086/169600 [p. 120].

[104] P. Gondolo and G. Gelmini. "Cosmic abundances of stable particles: Improved analysis". *Nuclear Physics B* 360.1 (1991), pp. 145–179 [pp. 42, 71].

[105] K. Griest and D. Seckel. "Three exceptions in the calculation of relic abundances". *Physical Review* D43 (1991), pp. 3191–3203. DOI: 10.1103/PhysRevD.43.3191 [pp. 42, 68].

[106] E. D. Carlson, M. E. Machacek, and L. J. Hall. "Self-interacting dark matter". *The Astrophysical Journal* 398 (Oct. 1992), p. 43. ISSN: 0004-637X, 1538-4357. DOI: 10.1086/171833 [p. 18].

[107] S. M. Carroll, W. H. Press, and E. L. Turner. "The Cosmological Constant". *Annual Review of Astronomy and Astrophysics* 30.1 (Sept. 1992), pp. 499–542. ISSN: 0066-4146, 1545-4282. DOI: 10.1146/annurev.aa.30.090192.002435 [p. 104].

[108] A. Denner et al. "Feynman rules for fermion-number-violating interactions". *Nuclear Physics B* 387.2 (Nov. 1992), pp. 467–481. ISSN: 05503213. DOI: 10.1016/0550-3213(92)90169-C [pp. 266, 267].

[109] D. B. Kaplan. "Single explanation for both baryon and dark matter densities". *Physical Review Letters* 68.6 (Feb. 10, 1992), pp. 741–743. ISSN: 0031-9007. DOI: 10.1103/PhysRevLett.68.741 [p. 27].

[110] J. Wess and J. Bagger. *Supersymmetry and supergravity*. Princeton university press, 1992 [p. 25].

[111] C. Lacey and S. Cole. "Merger rates in hierarchical models of galaxy formation". *Monthly Notices of the Royal Astronomical Society* 262.3 (June 1, 1993), pp. 627–649. ISSN: 0035-8711, 1365-2966. DOI: 10.1093/mnras/262.3.627 [pp. 96, 119, 120].

[112] B. Moore. "An upper limit to the mass of black holes in the halo of the galaxy". *The Astrophysical Journal* 413 (Aug. 1993), p. L93. ISSN: 0004-637X, 1538-4357. DOI: 10.1086/186967 [p. 158].

[113] J. Silk and A. Stebbins. "Clumpy cold dark matter". *The Astrophysical Journal* 411 (July 1993), p. 439. ISSN: 0004-637X, 1538-4357. DOI: 10.1086/172846 [p. 90].

[114] S. Dodelson and L. M. Widrow. "Sterile Neutrinos as Dark Matter". *Physical Review Letters* 72.1 (Jan. 3, 1994), pp. 17–20. ISSN: 0031-9007. DOI: 10.1103/PhysRevLett.72.17. arXiv: hep-ph/9303287 [pp. 23, 63].

[115] C. Lacey and S. Cole. "Merger rates in hierarchical models of galaxy formation – II. Comparison with N-body simulations". *Monthly Notices of the Royal Astronomical Society* 271.3 (Dec. 1994), pp. 676–692. ISSN: 0035-8711, 1365-2966. DOI: 10.1093/mnras/271.3.676 [p. 119].

[116] F. Aharonian, A. Atoyan, and H. Voelk. "High energy electrons and positrons in cosmic rays as an indicator of the existence of a nearby cosmic tevatron". *Astronomy and Astrophysics* 294 (Feb. 1995), pp. L41–L44 [p. 35].

[117] A. Burkert. "The Structure of Dark Matter Haloes in Dwarf Galaxies" (Apr. 12, 1995). DOI: 10.1086/309560. arXiv: astro-ph/9504041 [p. 15].

[118] C.-P. Ma and E. Bertschinger. "Cosmological Perturbation Theory in the Synchronous and Conformal Newtonian Gauges". *The Astrophysical Journal* 455 (Dec. 1995), p. 7. ISSN: 0004-637X, 1538-4357. DOI: 10.1086/176550 [p. 109].

[119] M. E. Peskin and D. V. Schroeder. *Quantum field theory*. 1995 [p. 54].

[120] S. Weinberg. *The quantum theory of fields*. Cambridge university press. 1995 [p. 54].

[121] C. L. Bennett et al. "4-Year COBE DMR Cosmic Microwave Background Observations: Maps and Basic Results". *The Astrophysical Journal* 464.1 (June 10, 1996), pp. L1–L4. ISSN: 0004637X. DOI: 10.1086/310075. arXiv: astro-ph/9601067 [p. 9].

[122] G. Jungman, M. Kamionkowski, and K. Griest. "Supersymmetric dark matter". *Physics Reports* 267.5 (Mar. 1996), pp. 195–373. ISSN: 03701573. DOI: 10.1016/0370-1573(95)00058-5 [pp. 26, 30, 35].

[123] J. Lewin and P. Smith. "Review of mathematics, numerical factors, and corrections for dark matter experiments based on elastic nuclear recoil". *Astroparticle Physics* 6.1 (Dec. 1996), pp. 87–112. ISSN: 09276505. DOI: 10.1016/S0927-6505(96)00047-3 [p. 30].

[124] J. F. Navarro, C. S. Frenk, and S. D. M. White. "The Structure of Cold Dark Matter Halos". *The Astrophysical Journal* 462 (May 1996), p. 563. ISSN: 0004-637X, 1538-4357. DOI: 10.1086/177173 [p. 137].

[125] S. Sarkar. "Big Bang nucleosynthesis and physics beyond the Standard Model". *Reports on Progress in Physics* 59.12 (Dec. 1, 1996), pp. 1493–1609. ISSN: 0034-4885, 1361-6633. DOI: 10.1088/0034-4885/59/12/001. arXiv: hep-ph/9602260 [p. 13].

[126] K. S. Babu, C. Kolda, and J. March-Russell. "Implications of Generalized Z-Z' Mixing" (Oct. 22, 1997). DOI: 10.1103/PhysRevD.57.6788. arXiv: hep-ph/9710441 [p. 77].

[127] J. Edsjo and P. Gondolo. "Neutralino Relic Density including Coannihilations". *Physical Review D* 56.4 (Aug. 15, 1997), pp. 1879–1894. ISSN: 0556-2821, 1089-4918. DOI: 10.1103/PhysRevD.56.1879. arXiv: hep-ph/9704361 [pp. 64, 68, 69, 258].

[128] K. Jedamzik. "Primordial Black Hole Formation during the QCD Epoch". *arXiv:astro-ph/9605152* (Apr. 22, 1997). DOI: 10.1103/PhysRevD.55.5871. arXiv: astro-ph/9605152 [p. 28].

[129] N. Arkani–Hamed, S. Dimopoulos, and G. Dvali. "The hierarchy problem and new dimensions at a millimeter". *Physics Letters B* 429.3 (June 1998), pp. 263–272. ISSN: 03702693. DOI: 10.1016/S0370-2693(98)00466-3 [p. 26].

[130] L. Bergstrom, P. Ullio, and J. Buckley. "Observability of Gamma Rays from Dark Matter Neutralino Annihilations in the Milky Way Halo". *Astroparticle Physics* 9.2 (Aug. 1998), pp. 137–162. ISSN: 09276505. DOI: 10.1016/S0927-6505(98)00015-2. arXiv: astro-ph/9712318 [p. 184].

[131] G. L. Bryan and M. L. Norman. "Statistical Properties of X-ray Clusters: Analytic and Numerical Comparisons". *The Astrophysical Journal* 495.1 (Mar. 1998), pp. 80–99. ISSN: 0004-637X, 1538-4357. DOI: 10.1086/305262. arXiv: astro-ph/9710107 [p. 139].

[132] D. J. H. Chung, E. W. Kolb, and A. Riotto. "Superheavy dark matter". *Physical Review D* 59.2 (Nov. 25, 1998), p. 023501. ISSN: 0556-2821, 1089-4918. DOI: 10.1103/PhysRevD.59.023501. arXiv: hep-ph/9802238 [p. 27].

[133] D. J. Eisenstein and W. Hu. "Baryonic Features in the Matter Transfer Function". *The Astrophysical Journal* 496.2 (Apr. 1998), pp. 605–614. ISSN: 0004-637X, 1538-4357. DOI: 10.1086/305424. arXiv: astro-ph/9709112 [pp. 10, 112, 113].

[134] E. W. Kolb, D. J. H. Chung, and A. Riotto. "WIMPZILLAS!" (Oct. 14, 1998). arXiv: hep-ph/9810361 [p. 27].

[135] S. P. Martin. "A SUPERSYMMETRY PRIMER". G. L. Kane. *Advanced Series on Directions in High Energy Physics*. Vol. 18. WORLD SCIENTIFIC, July 1998, pp. 1–98. DOI: 10.1142/9789812839657_0001 [pp. 25, 296].

[136] I. V. Moskalenko and A. W. Strong. "Production and propagation of cosmic-ray positrons and electrons". *The Astrophysical Journal* 493.2 (Feb. 1998), pp. 694–707. ISSN: 0004-637X, 1538-4357. DOI: 10.1086/305152. arXiv: astro-ph/9710124 [p. 35].

[137] A. G. Riess et al. "Observational Evidence from Supernovae for an Accelerating Universe and a Cosmological Constant". *The Astronomical Journal* 116.3 (Sept. 1998), pp. 1009–1038. ISSN: 00046256. DOI: 10.1086/300499 [pp. 14, 19].

[138] G. Tormen, A. Diaferio, and D. Syer. "Survival of Substructure within Dark Matter Haloes". *Monthly Notices of the Royal Astronomical Society* 299.3 (Sept. 1998), pp. 728–742. ISSN: 0035-8711, 1365-2966. DOI: 10.1046/j.1365-8711.1998.01775.x. arXiv: astro-ph/9712222 [p. 143].

[139] N. Arkani-Hamed, S. Dimopoulos, and G. Dvali. "Phenomenology, astrophysics, and cosmology of theories with submillimeter dimensions and TeV scale quantum gravity". *Physical Review D* 59.8 (Mar. 23, 1999), p. 086004. ISSN: 0556-2821, 1089-4918. DOI: 10.1103/PhysRevD.59.086004 [p. 26].

[140] L. Bergström et al. “Clumpy neutralino dark matter”. *Physical Review D* 59 (Feb. 1999), p. 043506. DOI: 10.1103/PhysRevD.59.043506 [p. 90].

[141] B. J. Carr and M. Sakellariadou. “Dynamical constraints on Dark Matter in compact objects”. *The Astrophysical Journal* 516 (May 1999), pp. 195–220 [p. 136].

[142] M. Colless. “First results from the 2dF galaxy redshift survey”. *Philosophical Transactions of the Royal Society of London. Series A: Mathematical, Physical and Engineering Sciences* 357.1750 (Jan. 15, 1999), pp. 105–116. ISSN: 1364-503X, 1471-2962. DOI: 10.1098/rsta.1999.0317. arXiv: astro-ph/9804079 [p. 12].

[143] O. Y. Gnedin and J. P. Ostriker. “On the self-consistent response of stellar systems to gravitational shocks”. *The Astrophysical Journal* 513 (Mar. 1999), pp. 626–637 [pp. 146, 284, 299].

[144] K. Jedamzik and J. C. Niemeyer. “Primordial Black Hole Formation during First-Order Phase Transitions”. *Physical Review D* 59.12 (May 18, 1999), p. 124014. ISSN: 0556-2821, 1089-4918. DOI: 10.1103/PhysRevD.59.124014. arXiv: astro-ph/9901293 [p. 28].

[145] S. Perlmutter et al. “Measurements of \Omega and \Lambda from 42 High-Redshift Supernovae”. *The Astrophysical Journal* 517.2 (June 1999), pp. 565–586. ISSN: 0004-637X, 1538-4357. DOI: 10.1086/307221 [p. 19].

[146] L. Randall and R. Sundrum. “Large Mass Hierarchy from a Small Extra Dimension”. *Physical Review Letters* 83.17 (Oct. 25, 1999), pp. 3370–3373. ISSN: 0031-9007, 1079-7114. DOI: 10.1103/PhysRevLett.83.3370 [p. 26].

[147] X. Shi and G. M. Fuller. “A New Dark Matter Candidate: Non-thermal Sterile Neutrinos”. *Physical Review Letters* 82.14 (Apr. 5, 1999), pp. 2832–2835. ISSN: 0031-9007, 1079-7114. DOI: 10.1103/PhysRevLett.82.2832. arXiv: astro-ph/9810076 [pp. 23, 63].

[148] R. S. Somerville and T. S. Kolatt. “How to plant a merger tree”. *Monthly Notices of the Royal Astronomical Society* 305.1 (May 1, 1999), pp. 1–14. ISSN: 0035-8711, 1365-2966. DOI: 10.1046/j.1365-8711.1999.02154.x [p. 120].

[149] W. Buchmuller and S. Fredenhagen. “Quantum mechanics of baryogenesis”. *Physics Letters B* 483 (June 2000), pp. 217–224. DOI: 10.1016/S0370-2693(00)00573-6 [p. 54].

[150] J. S. Bullock, A. V. Kravtsov, and D. H. Weinberg. “Reionization and the abundance of galactic satellites”. *The Astrophysical Journal* 539.2 (Aug. 20, 2000), pp. 517–521. ISSN: 0004-637X, 1538-4357. DOI: 10.1086/309279. arXiv: astro-ph/0002214 [p. 16].

[151] E. Corbelli and P. Salucci. “The extended rotation curve and the dark matter halo of M33”. *Monthly Notices of the Royal Astronomical Society* 311.2 (Jan. 15, 2000), pp. 441–447. ISSN: 0035-8711, 1365-2966. DOI: 10.1046/j.1365-8711.2000.03075.x [p. 5].

[152] Y. P. Jing. “The density profile of equilibrium and non-equilibrium dark matter halos”. *The Astrophysical Journal* 535.1 (May 20, 2000), pp. 30–36. ISSN: 0004-637X, 1538-4357. DOI: 10.1086/308809. arXiv: astro-ph/9901340 [p. 144].

[153] K. A. Olive, G. Steigman, and T. P. Walker. “Primordial Nucleosynthesis: Theory and Observations”. *Physics Reports* 333-334 (Aug. 2000), pp. 389–407. ISSN: 03701573. DOI: 10.1016/S0370-1573(00)00031-4. arXiv: astro-ph/9905320 [p. 13].

[154] D. N. Spergel and P. J. Steinhardt. “Observational Evidence for Self-Interacting Cold Dark Matter”. *Physical Review Letters* 84.17 (Apr. 24, 2000), pp. 3760–3763. ISSN: 0031-9007, 1079-7114. DOI: 10.1103/PhysRevLett.84.3760 [p. 18].

[155] T. Appelquist, H.-C. Cheng, and B. A. Dobrescu. “Bounds on universal extra dimensions”. *Physical Review D* 64.3 (June 21, 2001), p. 035002. ISSN: 0556-2821, 1089-4918. DOI: 10.1103/PhysRevD.64.035002 [p. 26].

[156] R. Bernabei et al. “Search for solar axions by Primakoff effect in NaI crystals”. *Physics Letters B* 515.1 (Aug. 2001), pp. 6–12. ISSN: 03702693. DOI: 10.1016/S0370-2693(01)00840-1 [p. 31].

[157] C. Boehm, P. Fayet, and R. Schaeffer. “Constraining Dark Matter candidates from structure formation”. *Physics Letters B* 518.1 (Oct. 2001), pp. 8–14. ISSN: 03702693. DOI: 10.1016/S0370-2693(01)01060-7. arXiv: astro-ph/0012504 [pp. 37, 132].

[158] J. S. Bullock et al. “A universal angular momentum profile for galactic halos”. *The Astrophysical Journal* 555.1 (July 2001), pp. 240–257. ISSN: 0004-637X, 1538-4357. DOI: 10.1086/321477. arXiv: astro-ph/0011001 [p. 144].

[159] J. S. Bullock et al. “Profiles of dark haloes: evolution, scatter, and environment”. *Monthly Notices of the Royal Astronomical Society* 321.3 (Mar. 1, 2001), pp. 559–575. ISSN: 0035-8711, 1365-2966. DOI: 10.1046/j.1365-8711.2001.04068.x. arXiv: astro-ph/9908159 [p. 140].

[160] S. Hofmann, D. J. Schwarz, and H. Stoecker. “Damping scales of neutralino cold dark matter”. *Physical Review D* 64.8 (Sept. 25, 2001), p. 083507. ISSN: 0556-2821, 1089-4918. DOI: 10.1103/PhysRevD.64.083507. arXiv: astro-ph/0104173 [pp. 132, 297].

[161] R. K. Sheth, H. J. Mo, and G. Tormen. “Ellipsoidal collapse and an improved model for the number and spatial distribution of dark matter haloes”. *Monthly Notices of the Royal Astronomical Society* 323.1 (May 1, 2001), pp. 1–12. ISSN: 0035-8711, 1365-2966. DOI: 10.1046/j.1365-8711.2001.04006.x [p. 118].

[162] J. E. Taylor and A. Babul. “The Dynamics of Sinking Satellites Around Disk Galaxies: A Poor Man’s Alternative to High-Resolution Numerical Simulations”. *The Astrophysical Journal* 559.2 (Oct. 2001), pp. 716–735. ISSN: 0004-637X, 1538-4357. DOI: 10.1086/322276. arXiv: astro-ph/0012305 [p. 136].

[163] S. M. K. Alam, J. S. Bullock, and D. H. Weinberg. “Dark Matter Properties and Halo Central Densities”. *The Astrophysical Journal* 572.1 (June 10, 2002), pp. 34–40. ISSN: 0004-637X, 1538-4357. DOI: 10.1086/340190 [p. 16].

[164] E. A. Baltz et al. “The cosmic ray positron excess and neutralino dark matter”. *Physical Review D* 65.6 (Feb. 28, 2002), p. 063511. ISSN: 0556-2821, 1089-4918. DOI: 10.1103/PhysRevD.65.063511. arXiv: astro-ph/0109318 [p. 35].

[165] A. Benoit et al. “Improved exclusion limits from the edelweiss wimp search”. *Phys. Lett.* B545 (2002), pp. 43–49. DOI: 10.1016/S0370-2693(02)02238-4 [p. 38].

[166] C. Boehm et al. “Interacting Dark Matter disguised as Warm Dark Matter”. *Physical Review D* 66.8 (Oct. 14, 2002), p. 083505. ISSN: 0556-2821, 1089-4918. DOI: 10.1103/PhysRevD.66.083505. arXiv: astro-ph/0112522 [pp. 11, 37].

[167] S. Cole et al. “Hierarchical galaxy formation: Hierarchical galaxy formation”. *Monthly Notices of the Royal Astronomical Society* 319.1 (Apr. 4, 2002), pp. 168–204. ISSN: 00358711, 13652966. DOI: 10.1046/j.1365-8711.2000.03879.x [pp. 120, 133, 299].

[168] G. D’Ambrosio et al. “Minimal Flavour Violation: an effective field theory approach”. *Nuclear Physics B* 645.1 (Nov. 2002), pp. 155–187. ISSN: 05503213. DOI: 10.1016/S0550-3213(02)00836-2. arXiv: hep-ph/0207036 [p. 77].

[169] J. Kouba. “Relativistic Time Transformations in GPS”. *GPS Solutions* 5.4 (Apr. 2002), pp. 1–9. ISSN: 1080-5370, 1521-1886. DOI: 10.1007/PL00012907 [p. 19].

[170] J. McDonald. “Thermally Generated Gauge Singlet Scalars as Self-Interacting Dark Matter”. *Physical Review Letters* 88.9 (Feb. 15, 2002), p. 091304. ISSN: 0031-9007, 1079-7114. DOI: 10.1103/PhysRevLett.88.091304. arXiv: hep-ph/0106249 [p. 63].

[171] P. Rosati, S. Borgani, and C. Norman. “The Evolution of X-Ray Clusters of Galaxies”. *Annual Review of Astronomy and Astrophysics* 40.1 (Sept. 2002), pp. 539–577. ISSN: 0066-4146, 1545-4282. DOI: 10.1146/annurev.astro.40.120401.150547 [p. 4].

[172] R. S. Somerville. “Can Photoionization Squelching Resolve the Sub-structure Crisis?” *The Astrophysical Journal* 572.1 (June 10, 2002), pp. L23–L26. ISSN: 0004637X, 15384357. DOI: 10.1086/341444. arXiv: astro-ph/0107507 [p. 16].

[173] R. H. Wechsler et al. “Concentrations of Dark Halos from their Assembly Histories”. *The Astrophysical Journal* 568.1 (Mar. 20, 2002), pp. 52–70. ISSN: 0004-637X, 1538-4357. DOI: 10.1086/338765. arXiv: astro-ph/0108151 [p. 144].

[174] S. Weinberg. “Cosmological Fluctuations of Small Wavelength”. *The Astrophysical Journal* 581.2 (Dec. 20, 2002), pp. 810–816. ISSN: 0004-637X, 1538-4357. DOI: 10.1086/344441 [p. 103].

[175] V. Berezinsky, V. Dokuchaev, and Y. Eroshenko. “Small-scale clumps in the galactic halo and dark matter annihilation”. *Physical Review D* 68.10 (Nov. 20, 2003), p. 103003. ISSN: 0556-2821, 1089-4918. DOI: 10.1103/PhysRevD.68.103003. arXiv: astro-ph/0301551 [p. 42].

[176] G. Chabrier. “The Galactic disk mass function: Reconciliation of the Hubble Space telescope and nearby determinations”. *The Astrophysical Journal* 586 (Apr. 2003), pp. L133–L136 [p. 159].

[177] S. Dodelson. *Modern cosmology*. San Diego, Calif: Academic Press, 2003. 440 pp. ISBN: 978-0-12-219141-1 [pp. 10, 109].

[178] S. Fukuda et al. "The Super-Kamiokande detector". *Nuclear Instruments and Methods in Physics Research Section A: Accelerators, Spectrometers, Detectors and Associated Equipment* 501.2 (Apr. 2003), pp. 418–462. ISSN: 01689002. DOI: 10.1016/S0168-9002(03)00425-X [p. 36].

[179] E. Hawkins et al. "The 2dF Galaxy Redshift Survey: Correlation functions, peculiar velocities and the matter density of the universe". *Monthly Notices of the Royal Astronomical Society* 346 (2003), p. 78. DOI: 10.1046/j.1365-2966.2003.07063.x [p. 38].

[180] E. Hayashi et al. "The Structural Evolution of Substructure". *The Astrophysical Journal* 584.2 (Feb. 20, 2003), pp. 541–558. ISSN: 0004-637X, 1538-4357. DOI: 10.1086/345788. arXiv: astro-ph/0203004 [pp. 143, 176].

[181] J. D. Jackson. "Electrodynamics, Classical". *digital Encyclopedia of Applied Physics*. Ed. by Wiley-VCH Verlag GmbH & Co. KGaA. Weinheim, Germany: Wiley-VCH Verlag GmbH & Co. KGaA, Apr. 15, 2003, eap109. ISBN: 978-3-527-60043-4. DOI: 10.1002/3527600434.eap109 [p. 116].

[182] R. H. Sanders. "Clusters of galaxies with modified Newtonian dynamics (MOND)". *Monthly Notices of the Royal Astronomical Society* 342.3 (July 2003), pp. 901–908. ISSN: 00358711, 13652966. DOI: 10.1046/j.1365-8711.2003.06596.x. arXiv: astro-ph/0212293 [p. 20].

[183] G. Servant and T. M. P. Tait. "Is the Lightest Kaluza-Klein Particle a Viable Dark Matter Candidate?" *Nuclear Physics B* 650.1 (Feb. 2003), pp. 391–419. ISSN: 05503213. DOI: 10.1016/S0550-3213(02)01012-X. arXiv: hep-ph/0206071 [p. 26].

[184] D. N. Spergel et al. "First year Wilkinson Microwave Anisotropy Probe (WMAP) observations: Determination of cosmological parameters". *The Astrophysical Journal Supplement Series* 148 (2003), pp. 175–194. DOI: 10.1086/377226 [pp. 9, 38].

[185] A. R. Zentner and J. S. Bullock. "Halo Substructure and the Power Spectrum". *The Astrophysical Journal* 598.1 (Nov. 20, 2003), pp. 49–72. ISSN: 0004-637X, 1538-4357. DOI: 10.1086/378797 [p. 299].

[186] A. W. Adams and J. S. Bloom. "Direct Detection of Dark Matter with Space-based Laser Interferometers" (May 19, 2004). arXiv: astro-ph/0405266 [p. 91].

[187] K. Agashe and G. Servant. "Warped Unification, Proton Stability and Dark Matter". *Physical Review Letters* 93.23 (Dec. 3, 2004), p. 231805. ISSN: 0031-9007, 1079-7114. DOI: 10.1103/PhysRevLett.93.231805. arXiv: hep-ph/0403143 [p. 26].

[188] D. Clowe, A. Gonzalez, and M. Markevitch. "Weak lensing mass reconstruction of the interacting cluster 1E0657-558: Direct evidence for the existence of dark matter". *The Astrophysical Journal* 604.2 (Apr. 2004), pp. 596–603. ISSN: 0004-637X, 1538-4357. DOI: 10.1086/381970. arXiv: astro-ph/0312273 [p. 20].

[189] S. Colafrancesco. "SZ effect from Dark Matter annihilation". *Astronomy & Astrophysics* 422.2 (Aug. 2004), pp. L23–L27. ISSN: 0004-6361, 1432-0746. DOI: 10.1051/0004-6361:20040175. arXiv: astro-ph/0405456 [p. 32].

[190] J. Diemand, B. Moore, and J. Stadel. "Velocity and spatial biases in cold dark matter subhalo distributions". *Monthly Notices of the Royal Astronomical Society* 352.2 (Aug. 2004), pp. 535–546. ISSN: 00358711, 13652966. DOI: 10.1111/j.1365-2966.2004.07940.x [p. 143].

[191] J. Hisano, S. Matsumoto, and M. M. Nojiri. "Explosive Dark Matter Annihilation". *Physical Review Letters* 92.3 (Jan. 22, 2004), p. 031303. ISSN: 0031-9007, 1079-7114. DOI: 10.1103/PhysRevLett.92.031303 [p. 33].

[192] M. Markevitch et al. "Direct constraints on the dark matter self-interaction cross-section from the merging galaxy cluster 1E0657-56". *The Astrophysical Journal* 606.2 (May 10, 2004), pp. 819–824. ISSN: 0004-637X, 1538-4357. DOI: 10.1086/383178. arXiv: astro-ph/0309303 [p. 18].

[193] P. D. Serpico and G. G. Raffelt. "MeV-mass dark matter and primordial nucleosynthesis" (May 27, 2004). DOI: 10.1103/PhysRevD.70.043526. arXiv: astro-ph/0403417 [p. 37].

[194] T. Asaka, S. Blanchet, and M. Shaposhnikov. "The νMSM, Dark Matter and Neutrino Masses". *Physics Letters B* 631.4 (Dec. 2005), pp. 151–156. ISSN: 03702693. DOI: 10.1016/j.physletb.2005.09.070. arXiv: hep-ph/0503065 [p. 23].

[195] J. D. Bekenstein. "Relativistic gravitation theory for the MOND paradigm" (Aug. 23, 2005). DOI: 10.1103/PhysRevD.71.069901. arXiv: astro-ph/0403694 [p. 20].

[196] V. Berezinsky, V. Dokuchaev, and Y. Eroshenko. "Destruction of small-scale dark matter clumps in the hierarchical structures and galaxies" (Nov. 16, 2005). DOI: 10.1103/PhysRevD.73.063504. arXiv: astro-ph/0511494 [pp. 136, 299].

[197] C. Boehm and R. Schaeffer. "Constraints on Dark Matter interactions from structure formation: damping lengths". *Astronomy & Astrophysics* 438.2 (Aug. 2005), pp. 419–442. ISSN: 0004-6361, 1432-0746. DOI: 10.1051/0004-6361:20042238 [pp. 11, 37, 42, 132].

[198] F. C. van den Bosch, G. Tormen, and C. Giocoli. "The Mass Function and Average Mass Loss Rate of Dark Matter Subhaloes" (Mar. 1, 2005). DOI: 10.1111/j.1365-2966.2005.08964.x/abs/. arXiv: astro-ph/0409201 [pp. 133, 136, 142].

[199] A. M. Green, S. Hofmann, and D. J. Schwarz. "The first WIMPy halos". *Journal of Cosmology and Astroparticle Physics* 2005.8 (Aug. 17, 2005), pp. 003–003. ISSN: 1475-7516. DOI: 10.1088/1475-7516/2005/08/003 [pp. 42, 97, 99, 101, 128, 132, 297].

[200] A. Loeb and M. Zaldarriaga. "The Small-scale power spectrum of cold dark matter". *Phys. Rev.* D71 (2005), p. 103520. DOI: 10.1103/PhysRevD.71.103520 [p. 132].

[201] G. Mangano et al. "Relic neutrino decoupling including flavour oscillations". *Nuclear Physics B* 729.1 (Nov. 2005), pp. 221–234. ISSN: 05503213. DOI: 10.1016/j.nuclphysb.2005.09.041. arXiv: hep-ph/0506164 [p. 61].

[202] M. Markevitch. "Chandra observation of the most interesting cluster in the Universe" (Nov. 11, 2005). arXiv: astro-ph/0511345 [p. 18].

[203] S. S. McGaugh. "The Baryonic Tully-Fisher Relation of Galaxies with Extended Rotation Curves and the Stellar Mass of Rotating Galaxies" (Aug. 3, 2005). DOI: 10.1086/432968. arXiv: astro-ph/0506750 [p. 16].

[204] J. Penarrubia and A. J. Benson. "Effects of dynamical evolution on the distribution of substructures". *Monthly Notices of the Royal Astronomical Society* 364.3 (Dec. 11, 2005), pp. 977–989. ISSN: 0035-8711, 1365-2966. DOI: 10.1111/j.1365-2966.2005.09633.x. arXiv: astro-ph/0412370 [pp. 136, 142].

[205] R. H. Sanders. "A tensor-vector-scalar framework for modified dynamics and cosmic dark matter" (July 1, 2005). DOI: 10.1111/j.1365-2966.2005.09375.x. arXiv: astro-ph/0502222 [p. 20].

[206] V. Springel et al. "Simulating the joint evolution of quasars, galaxies and their large-scale distribution" (Apr. 6, 2005). DOI: 10.1038/nature03597. arXiv: astro-ph/0504097 [pp. 11, 295].

[207] A. R. Zentner et al. "The Physics of Galaxy Clustering I: A Model for Subhalo Populations". *The Astrophysical Journal* 624.2 (May 10, 2005), pp. 505–525. ISSN: 0004-637X, 1538-4357. DOI: 10.1086/428898. arXiv: astro-ph/0411586 [pp. 133, 136].

[208] H. Zhao et al. "Earth-mass dark halos are torn into dark mini-streams by stars" (Feb. 2, 2005). arXiv: astro-ph/0502049 [p. 176].

[209] S. Ando and E. Komatsu. "Anisotropy of the cosmic gamma-ray background from dark matter annihilation" (Jan. 14, 2006). DOI: 10.1103/PhysRevD.73.023521. arXiv: astro-ph/0512217 [p. 34].

[210] G. W. Angus, B. Famaey, and H. Zhao. "Can MOND take a bullet? Analytical comparisons of three versions of MOND beyond spherical symmetry". *Monthly Notices of the Royal Astronomical Society* 371.1 (Aug. 1, 2006), pp. 138–146. ISSN: 00358711, 13652966. DOI: 10.1111/j.1365-2966.2006.10668.x. arXiv: astro-ph/0606216 [p. 20].

[211] T. Asaka, K. Ishiwata, and T. Moroi. "Right-Handed Sneutrino as Cold Dark Matter". *Physical Review D* 73.5 (Mar. 10, 2006), p. 051301. ISSN: 1550-7998, 1550-2368. DOI: 10.1103/PhysRevD.73.051301. arXiv: hep-ph/0512118 [pp. 26, 63].

[212] E. Bertschinger. "The Effects of Cold Dark Matter Decoupling and Pair Annihilation on Cosmological Perturbations". *Physical Review* D74 (2006), p. 063509. DOI: 10.1103/PhysRevD.74.063509 [pp. 42, 73, 130, 297].

[213] M. Cacciato et al. "Combining weak and strong lensing in cluster potential reconstruction". *Astronomy & Astrophysics* 458.2 (Nov. 2006), pp. 349–356. ISSN: 0004-6361, 1432-0746. DOI: 10.1051/0004-6361:20054582 [p. 4].

[214] M. Cirelli, N. Fornengo, and A. Strumia. "Minimal Dark Matter". *Nuclear Physics B* 753.1 (Oct. 2006), pp. 178–194. ISSN: 05503213. DOI: 10.1016/j.nuclphysb.2006.07.012. arXiv: hep-ph/0512090 [pp. 27, 33].

[215] J. M. Cline. "Baryogenesis". *arXiv:hep-ph/0609145* (Nov. 22, 2006). arXiv: hep-ph/0609145 [p. 9].

[216] D. Clowe et al. "A direct empirical proof of the existence of dark matter". *Astrophys. J.* 648 (2006), pp. L109–L113. DOI: 10.1086/508162 [pp. 18, 20, 38].

[217] J. Diemand, M. Kuhlen, and P. Madau. "Early supersymmetric cold dark matter substructure". *The Astrophysical Journal* 649.1 (Sept. 20, 2006), pp. 1–13. ISSN: 0004-637X, 1538-4357. DOI: 10.1086/506377. arXiv: astro-ph/0603250 [pp. 124, 144].

[218] S. R. Furlanetto, S. Peng Oh, and F. H. Briggs. "Cosmology at low frequencies: The 21cm transition and the high-redshift Universe". *Physics Reports* 433.4 (Oct. 2006), pp. 181–301. ISSN: 03701573. DOI: 10.1016/j.physrep.2006.08.002 [p. 37].

[219] IceCube Collaboration. "First Year Performance of The IceCube Neutrino Telescope". *Astroparticle Physics* 26.3 (Oct. 2006), pp. 155–173. ISSN: 09276505. DOI: 10.1016/j.astropartphys.2006.06.007. arXiv: astro-ph/0604450 [p. 36].

[220] U. F. Katz. "KM3NeT: Towards a km3 Mediterranean Neutrino Telescope". *Nuclear Instruments and Methods in Physics Research Section A: Accelerators, Spectrometers, Detectors and Associated Equipment* 567.2 (Nov. 2006), pp. 457–461. ISSN: 01689002. DOI: 10.1016/j.nima.2006.05.235. arXiv: astro-ph/0606068 [p. 36].

[221] N. Kollerstrom. "An Hiatus in History: The British Claim for Neptune's Co-prediction 1845-1846: Part 2" (2006) [p. 2].

[222] N. Kollerstrom. "An Hiatus in History: The British Claim for Neptune's Co-prediction, 1845-1846: Part 1" (2006) [p. 2].

[223] J. Lesgourgues and S. Pastor. "Massive neutrinos and cosmology". *Physics Reports* 429.6 (July 2006), pp. 307–379. ISSN: 03701573. DOI: 10.1016/j.physrep.2006.04.001. arXiv: astro-ph/0603494 [p. 22].

[224] E. Ma. "Verifiable Radiative Seesaw Mechanism of Neutrino Mass and Dark Matter". *Physical Review D* 73.7 (Apr. 14, 2006), p. 077301. ISSN: 1550-7998, 1550-2368. DOI: 10.1103/PhysRevD.73.077301. arXiv: hep-ph/0601225 [p. 27].

[225] C. Skordis et al. "Large Scale Structure in Bekenstein's theory of relativistic Modified Newtonian Dynamics". *Physical Review Letters* 96.1 (Jan. 3, 2006), p. 011301. ISSN: 0031-9007, 1079-7114. DOI: 10.1103/PhysRevLett.96.011301. arXiv: astro-ph/0505519 [p. 20].

[226] V. Springel, C. S. Frenk, and S. D. M. White. "The large-scale structure of the Universe". *Nature* 440.7088 (Apr. 2006), pp. 1137–1144. ISSN: 0028-0836, 1476-4687. DOI: 10.1038/nature04805. arXiv: astro-ph/0604561 [p. 12].

[227] T. Verechtchaguina, I. M. Sokolov, and L. Schimansky-Geier. "First Passage Time Densities in Non-Markovian Models with Subthreshold Oscillations". *Europhysics Letters (EPL)* 73.5 (Mar. 2006), pp. 691–697. ISSN: 0295-5075, 1286-4854. DOI: 10.1209/epl/i2005-10449-7. arXiv: cond-mat/0506811 [p. 115].

[228] S. Ando et al. "Dark matter annihilation or unresolved astrophysical sources? Anisotropy probe of the origin of cosmic gamma-ray background". *Physical Review D* 75.6 (Mar. 27, 2007), p. 063519. ISSN: 1550-7998, 1550-2368. DOI: 10.1103/PhysRevD.75.063519. arXiv: astro-ph/0612467 [p. 34].

[229] G. W. Angus and H. Zhao. "Analysis of galactic tides and stars on CDM microhalos". *Monthly Notices of the Royal Astronomical Society* 375.4 (Feb. 5, 2007), pp. 1146–1156. ISSN: 00358711, 13652966. DOI: 10.1111/j.1365-2966.2007.11400.x. arXiv: astro-ph/0608580 [pp. 136, 170, 171, 299].

[230] W. Appel. *Mathematics for physics and physicists*. Princeton university press, 2007 [p. 241].

[231] C. Arina and N. Fornengo. "Sneutrino cold dark matter, a new analysis: relic abundance and detection rates". *Journal of High Energy Physics* 2007.11 (Nov. 13, 2007), pp. 029–029. ISSN: 1029-8479. DOI: 10.1088/1126-6708/2007/11/029. arXiv: 0709.4477 [p. 26].

[232] T. Bringmann and S. Hofmann. "Thermal decoupling of WIMPs from first principles". *JCAP* 0704 (2007), p. 016. DOI: 10.1088/1475-7516/2007/04/016, 10.1088/1475-7516/2016/03/E02 [pp. 42, 74].

[233] J. Diemand, M. Kuhlen, and P. Madau. "Dark matter substructure and gamma-ray annihilation in the Milky Way halo". *The Astrophysical Journal* 657.1 (Mar. 2007), pp. 262–270. ISSN: 0004-637X, 1538-4357. DOI: 10.1086/510736. arXiv: astro-ph/0611370 [pp. 124, 144].

[234] T. Goerdt et al. "The survival and disruption of CDM micro-haloes: implications for direct and indirect detection experiments". *Monthly Notices of the Royal Astronomical Society* 375.1 (Feb. 11, 2007), pp. 191–198. ISSN: 0035-8711, 1365-2966. DOI: 10.1111/j.1365-2966.2006.11281.x. arXiv: astro-ph/0608495 [pp. 158, 170].

[235] A. M. Green and S. P. Goodwin. "On mini-halo encounters with stars". *Monthly Notices of the Royal Astronomical Society* 375.3 (Mar. 1, 2007), pp. 1111–1120. ISSN: 0035-8711, 1365-2966. DOI: 10.1111/j.1365-2966.2007.11397.x. arXiv: astro-ph/0604142 [pp. 136, 158, 171, 299].

[236] L. L. Honorez et al. "The Inert Doublet Model: an Archetype for Dark Matter". *Journal of Cosmology and Astroparticle Physics* 2007.2 (Feb. 23, 2007), pp. 028–028. ISSN: 1475-7516. DOI: 10.1088/1475-7516/2007/02/028. arXiv: hep-ph/0612275 [p. 27].

[237] D. Hooper and S. Profumo. "Dark matter and collider phenomenology of universal extra dimensions". *Physics Reports* 453.2 (Dec. 2007), pp. 29–115. ISSN: 03701573. DOI: 10.1016/j.physrep.2007.09.003 [p. 26].

[238] J. Lavalle et al. "Clumpiness of dark matter and the positron annihilation signal". *Astronomy and Astrophysics* 462 (Feb. 2007), pp. 827–840. DOI: 10.1051/0004-6361:20065312 [p. 35].

[239] A. V. Maccio' et al. "Concentration, Spin and Shape of Dark Matter Haloes: Scatter and the Dependence on Mass and Environment". *Monthly Notices of the Royal Astronomical Society* 378.1 (June 11, 2007), pp. 55–71. ISSN: 0035-8711, 1365-2966. DOI: 10.1111/j.1365-2966.2007.11720.x. arXiv: astro-ph/0608157 [p. 144].

[240] H. Parkinson, S. Cole, and J. Helly. "Generating dark matter halo merger trees: Merger trees". *Monthly Notices of the Royal Astronomical Society* 383.2 (Dec. 10, 2007), pp. 557–564. ISSN: 00358711. DOI: 10.1111/j.1365-2966.2007.12517.x [p. 120].

[241] J. Polchinski. *String theory. Vol. 1: An introduction to the bosonic string*. Cambridge University Press, 2007 [p. 21].

[242] J. Polchinski. *String theory. Vol. 2: Superstring theory and beyond*. Cambridge University Press, 2007 [p. 21].

[243] P. Tisserand et al. "Limits on the Macho Content of the Galactic Halo from the EROS-2 Survey of the Magellanic Clouds". *Astronomy & Astrophysics* 469.2 (July 2007), pp. 387–404. ISSN: 0004-6361, 1432-0746. DOI: 10.1051/0004-6361:20066017. arXiv: astro-ph/0607207 [p. 27].

[244] A. R. Zentner. "THE EXCURSION SET THEORY OF HALO MASS FUNCTIONS, HALO CLUSTERING, AND HALO GROWTH". *International Journal of Modern Physics D* 16.5 (May 2007), pp. 763–815. ISSN: 0218-2718, 1793-6594. DOI: 10.1142/S0218271807010511 [pp. 109, 119].

[245] T. G. Zlosnik, P. G. Ferreira, and G. D. Starkman. "Modifying gravity with the Aether: an alternative to Dark Matter". *Physical Review D* 75.4 (Feb. 16, 2007), p. 044017. ISSN: 1550-7998, 1550-2368. DOI: 10.1103/PhysRevD.75.044017. arXiv: astro-ph/0607411 [p. 20].

[246] J. Binney and S. Tremaine. *Galactic dynamics*. Vol. 20. Princeton university press, 2008 [pp. 126, 145].

[247] M. Cirelli, R. Franceschini, and A. Strumia. "Minimal Dark Matter predictions for galactic positrons, anti-protons, photons". *Nuclear Physics B* 800.1 (Sept. 2008), pp. 204–220. ISSN: 05503213. DOI: 10.1016/j.nuclphysb.2008.03.013. arXiv: 0802.3378 [p. 35].

[248] CMS Collaboration. "The CMS experiment at the CERN LHC". *Journal of Instrumentation* 3.8 (Aug. 14, 2008), S08004–S08004. ISSN: 1748-0221. DOI: 10.1088/1748-0221/3/08/S08004 [p. 29].

[249] S. Davidson, E. Nardi, and Y. Nir. "Leptogenesis". *Physics Reports* 466.4 (Sept. 2008), pp. 105–177. ISSN: 03701573. DOI: 10.1016/j.physrep.2008.06.002. arXiv: 0802.2962 [p. 9].

[250] J. Diemand et al. "Clumps and streams in the local dark matter distribution". *Nature* 454.7205 (Aug. 2008), pp. 735–738. ISSN: 0028-0836, 1476-4687. DOI: 10.1038/nature07153. arXiv: 0805.1244 [pp. 124, 143, 144, 147].

[251] A. Djouadi. "The anatomy of electroweak symmetry breaking". *Physics Reports* 457.1 (Feb. 2008), pp. 1–216. ISSN: 03701573. DOI: 10.1016/j.physrep.2007.10.004 [p. 269].

[252] C. Giocoli, L. Pieri, and G. Tormen. "Analytical Approach to Subhaloes Population in Dark Matter Haloes". *Monthly Notices of the Royal Astronomical Society* 387.2 (June 2008), pp. 689–697. ISSN: 0035-8711, 1365-2966. DOI: 10.1111/j.1365-2966.2008.13283.x. arXiv: 0712.1476 [p. 133].

[253] C. Giocoli, G. Tormen, and F. C. van den Bosch. "The population of dark matter subhaloes: mass functions and average mass-loss rates". *Monthly Notices of the Royal Astronomical Society* 386.4 (June 2008), pp. 2135–2144. ISSN: 0035-8711, 1365-2966. DOI: 10.1111/j.1365-2966.2008.13182.x [pp. 96, 121, 122, 124, 125, 298].

[254] J. Lavalle et al. "Full calculation of clumpiness boost factors for antimatter cosmic rays in the light of Lambda-CDM N-body simulation results". *Astronomy & Astrophysics* 479.2 (Feb. 2008), pp. 427–452. ISSN: 0004-6361, 1432-0746. DOI: 10.1051/0004-6361:20078723. arXiv: 0709.3634 [pp. 35, 90].

[255] A. V. Maccio', A. A. Dutton, and F. C. v. d. Bosch. "Concentration, Spin and Shape of Dark Matter Haloes as a Function of the Cosmological Model: WMAP1, WMAP3 and WMAP5 results". *Monthly Notices of the Royal Astronomical Society* 391.4 (Dec. 21, 2008), pp. 1940–1954. ISSN: 00358711, 13652966. DOI: 10.1111/j.1365-2966.2008.14029.x. arXiv: 0805.1926 [pp. 140, 144, 145].

[256] R. K. de Naray, S. S. McGaugh, and W. J. G. de Blok. "Mass Models for Low Surface Brightness Galaxies with High Resolution Optical Velocity Fields". *The Astrophysical Journal* 676.2 (Apr. 2008), pp. 920–943. ISSN: 0004-637X, 1538-4357. DOI: 10.1086/527543. arXiv: 0712.0860 [p. 16].

[257] T. Okamoto, L. Gao, and T. Theuns. "Massloss of galaxies due to a UV-background". *Monthly Notices of the Royal Astronomical Society* 390.3 (Nov. 1, 2008), pp. 920–928. ISSN: 00358711, 13652966. DOI: 10.1111/j.1365-2966.2008.13830.x. arXiv: 0806.0378 [p. 16].

[258] C. Skordis. "Generalizing TeVeS Cosmology" (Jan. 13, 2008). DOI: 10.1103/PhysRevD.77.123502. arXiv: 0801.1985 [p. 20].

[259] V. Springel et al. "The Aquarius Project: the subhalos of galactic halos". *Monthly Notices of the Royal Astronomical Society* 391.4 (Dec. 21, 2008), pp. 1685–1711. ISSN: 00358711, 13652966. DOI: 10.1111/j.1365-2966.2008.14066.x. arXiv: 0809.0898 [pp. 11, 39, 124, 137, 141, 143, 144].

[260] J. Zhang, O. Fakhouri, and C.-P. Ma. "How to grow a healthy merger tree: Growing healthy merger trees". *Monthly Notices of the Royal Astronomical Society* 389.4 (Oct. 1, 2008), pp. 1521–1538. ISSN: 00358711. DOI: 10.1111/j.1365-2966.2008.13671.x [p. 120].

[261] O. Adriani et al. "Observation of an anomalous positron abundance in the cosmic radiation". *Nature* 458.7238 (Apr. 2009), pp. 607–609. ISSN: 0028-0836, 1476-4687. DOI: 10.1038/nature07942. arXiv: 0810.4995 [p. 35].

[262] S. Ando. "Gamma-ray background anisotropy from galactic dark matter substructure". *Physical Review D* 80.2 (July 23, 2009), p. 023520. ISSN: 1550-7998, 1550-2368. DOI: 10.1103/PhysRevD.80.023520. arXiv: 0903.4685 [p. 34].

[263] N. Arkani-Hamed et al. "A Theory of Dark Matter". *Physical Review D* 79.1 (Jan. 27, 2009), p. 015014. ISSN: 1550-7998, 1550-2368. DOI: 10.1103/PhysRevD.79.015014. arXiv: 0810.0713 [pp. 33, 81, 183].

[264] W. B. Atwood et al. "The Large Area Telescope on the Fermi Gamma-ray Space Telescope Mission". *Astrophys. J.* 697 (2009), pp. 1071–1102. DOI: 10.1088/0004-637X/697/2/1071 [p. 38].

[265] G. Bertone et al. "Gamma-ray and radio tests of the $e^{\pm}$ excess from DM annihilations". *Journal of Cosmology and Astroparticle Physics* 2009.3 (Mar. 5, 2009), pp. 009–009. ISSN: 1475-7516. DOI: 10.1088/1475-7516/2009/03/009 [p. 35].

[266] A. Boyarsky, O. Ruchayskiy, and D. Iakubovskyi. "A lower bound on the mass of Dark Matter particles". *Journal of Cosmology and Astroparticle Physics* 2009.3 (Mar. 3, 2009), pp. 005–005. ISSN: 1475-7516. DOI: 10.1088/1475-7516/2009/03/005. arXiv: 0808.3902 [p. 22].

[267] A. Boyarsky, O. Ruchayskiy, and M. Shaposhnikov. "The Role of Sterile Neutrinos in Cosmology and Astrophysics". *Annual Review of Nuclear and Particle Science* 59.1 (Nov. 2009), pp. 191–214. ISSN: 0163-8998, 1545-4134. DOI: 10.1146/annurev.nucl.010909.083654 [pp. 23, 296].

[268] T. Bringmann. "Particle Models and the Small-Scale Structure of Dark Matter". *New J. Phys.* 11 (2009), p. 105027. DOI: 10.1088/1367-2630/11/10/105027 [pp. 42, 297].

[269] F. Debbasch and W. van Leeuwen. "General relativistic Boltzmann equation, I: Covariant treatment". *Physica A: Statistical Mechanics and its Applications* 388.7 (Apr. 2009), pp. 1079–1104. ISSN: 03784371. DOI: 10.1016/j.physa.2008.12.023 [p. 52].

[270] F. Debbasch and W. van Leeuwen. "General relativistic Boltzmann equation, II: Manifestly covariant treatment". *Physica A: Statistical Mechanics and its Applications* 388.9 (May 2009), pp. 1818–1834. ISSN: 03784371. DOI: 10.1016/j.physa.2009.01.009 [p. 52].

[271] T. Delahaye et al. "Galactic secondary positron flux at the Earth". *Astronomy & Astrophysics* 501.3 (July 2009), pp. 821–833. ISSN: 0004-6361, 1432-0746. DOI: 10.1051/0004-6361/200811130. arXiv: 0809.5268 [p. 35].

[272] D. J. Fixsen. "The Temperature of the Cosmic Microwave Background". *The Astrophysical Journal* 707 (Dec. 2009), pp. 916–920. DOI: 10.1088/0004-637X/707/2/916 [pp. 9, 72].

[273] P. J. Fox and E. Poppitz. "Leptophilic dark matter". *Physical Review D* 79.8 (Apr. 24, 2009), p. 083528. ISSN: 1550-7998, 1550-2368. DOI: 10.1103/PhysRevD.79.083528 [p. 35].

[274] D. Hooper, P. Blasi, and P. D. Serpico. "Pulsars as the sources of high energy cosmic ray positrons". *Journal of Cosmology and Astroparticle Physics* 2009.1 (Jan. 12, 2009), pp. 025–025. ISSN: 1475-7516. DOI: 10.1088/1475-7516/2009/01/025 [p. 35].

[275] W. Hu. "Wandering in the Background: A CMB Explorer". PhD thesis. July 16, 2009. arXiv: astro-ph/9508126 [p. 10].

[276] A. Ibarra et al. "Cosmic rays from leptophilic dark matter decay via kinetic mixing". *Journal of Cosmology and Astroparticle Physics* 2009.8 (Aug. 14, 2009), pp. 017–017. ISSN: 1475-7516. DOI: 10.1088/1475-7516/2009/08/017 [p. 35].

[277] R. Iengo. "Sommerfeld enhancement: general results from field theory diagrams". *Journal of High Energy Physics* 2009.5 (May 6, 2009), pp. 024–024. ISSN: 1029-8479. DOI: 10.1088/1126-6708/2009/05/024. arXiv: 0902.0688 [pp. 33, 81, 183].

[278] D. E. Kaplan, M. A. Luty, and K. M. Zurek. "Asymmetric Dark Matter". *Physical Review D* 79.11 (June 23, 2009), p. 115016. ISSN: 1550-7998, 1550-2368. DOI: 10.1103/PhysRevD.79.115016. arXiv: 0901.4117 [p. 27].

[279] D. E. Kaplan et al. "Atomic Dark Matter" (Sept. 3, 2009). DOI: 10.1088/1475-7516/2010/05/021. arXiv: 0909.0753 [p. 27].

[280] Y. Li and H. Mo. "Mass distribution and accretion of sub-halos" (Aug. 3, 2009). arXiv: 0908.0301 [pp. 96, 121, 122, 298].

[281] S. Profumo. "Dissecting cosmic-ray electron-positron data with Occam's Razor: the role of known Pulsars" (Apr. 28, 2009). DOI: 10.2478/s11534-011-0099-z. arXiv: 0812.4457 [p. 35].

[282] T. R. Slatyer, N. Padmanabhan, and D. P. Finkbeiner. "CMB Constraints on WIMP Annihilation: Energy Absorption During the Recombination Epoch". *Physical Review D* 80.4 (Aug. 24, 2009), p. 043526. ISSN: 1550-7998, 1550-2368. DOI: 10.1103/PhysRevD.80.043526. arXiv: 0906.1197 [p. 37].

[283] A. A. Abdo et al. "FERMI LARGE AREA telESCOPE FIRST SOURCE CATALOG". *The Astrophysical Journal Supplement Series* 188.2 (May 2010). Publisher: American Astronomical Society, pp. 405–436. ISSN: 0067-0049. DOI: 10.1088/0067-0049/188/2/405 [p. 180].

[284] S. Ando and A. Kusenko. "Interactions of keV sterile neutrinos with matter". *Physical Review D* 81.11 (June 18, 2010), p. 113006. ISSN: 1550-7998, 1550-2368. DOI: 10.1103/PhysRevD.81.113006. arXiv: 1001.5273 [p. 29].

[285] S. J. Asztalos et al. "SQUID-Based Microwave Cavity Search for Dark-Matter Axions". *Physical Review Letters* 104.4 (Jan. 28, 2010), p. 041301. ISSN: 0031-9007, 1079-7114. DOI: 10.1103/PhysRevLett.104.041301 [p. 31].

[286] V. Berezinsky et al. "Superdense cosmological dark matter clumps" (Apr. 29, 2010). DOI: 10.1103/PhysRevD.81.103529. arXiv: 1002.3444 [p. 91].

[287] W. J. G. de Blok. "The Core-Cusp Problem". *Advances in Astronomy* 2010 (2010), pp. 1–14. ISSN: 1687-7969, 1687-7977. DOI: 10.1155/2010/789293. arXiv: 0910.3538 [p. 16].

[288] J. D. Bowman and A. E. E. Rogers. "A lower limit of dz > 0.06 for the duration of the reionization epoch". *Nature* 468.7325 (Dec. 2010), pp. 796–798. ISSN: 0028-0836, 1476-4687. DOI: 10.1038/nature09601. arXiv: 1209.1117 [p. 37].

[289] M. R. Buckley and D. Hooper. "Dark Matter Subhalos In the Fermi First Source Catalog". *Physical Review* D82 (2010), p. 063501. DOI: 10.1103/PhysRevD.82.063501 [pp. 34, 186].

[290] S. Cassel. "Sommerfeld factor for arbitrary partial wave processes". *Journal of Physics G: Nuclear and Particle Physics* 37.10 (Oct. 1, 2010), p. 105009. ISSN: 0954-3899, 1361-6471. DOI: 10.1088/0954-3899/37/10/105009. arXiv: 0903.5307 [pp. 33, 81, 183].

[291] R. Catena and P. Ullio. "A novel determination of the local dark matter density". *Journal of Cosmology and Astroparticle Physics* 2010.8 (Aug. 3, 2010), pp. 004–004. ISSN: 1475-7516. DOI: 10.1088/1475-7516/2010/08/004. arXiv: 0907.0018 [p. 3].

[292] M. Cirelli, P. Panci, and P. D. Serpico. "Diffuse gamma ray constraints on annihilating or decaying Dark Matter after Fermi" (July 29, 2010). DOI: 10.1016/j.nuclphysb.2010.07.010. arXiv: 0912.0663 [pp. 34, 180].

[293] T. Delahaye et al. "Galactic electrons and positrons at the Earth:new estimate of the primary and secondary fluxes". *Astronomy & Astrophysics* 524 (Dec. 2010), A51. ISSN: 0004-6361, 1432-0746. DOI: 10.1051/0004-6361/201014225. arXiv: 1002.1910 [p. 35].

[294] A. Derevianko et al. "Axio-electric effect". *Physical Review D* 82.6 (Sept. 8, 2010), p. 065006. ISSN: 1550-7998, 1550-2368. DOI: 10.1103/PhysRevD.82.065006. arXiv: 1007.1833 [p. 31].

[295] U. Ellwanger, C. Hugonie, and A. M. Teixeira. "The Next-to-Minimal Supersymmetric Standard Model". *Physics Reports* 496.1 (Nov. 2010), pp. 1–77. ISSN: 03701573. DOI: 10.1016/j.physrep.2010.07.001 [pp. 26, 92].

[296] J. L. Feng. "Dark Matter Candidates from Particle Physics and Methods of Detection". *Annual Review of Astronomy and Astrophysics* 48.1 (Aug. 2010), pp. 495–545. ISSN: 0066-4146, 1545-4282. DOI: 10.1146/annurev-astro-082708-101659. arXiv: 1003.0904 [pp. 22, 296].

[297] J. L. Feng, M. Kaplinghat, and H.-B. Yu. "Sommerfeld enhancements for thermal relic dark matter". *Physical Review D* 82.8 (Oct. 26, 2010), p. 083525. ISSN: 1550-7998, 1550-2368. DOI: 10.1103/PhysRevD.82.083525 [pp. 81, 183].

[298] Fermi-LAT Collaboration. "Constraints on Cosmological Dark Matter Annihilation from the Fermi-LAT Isotropic Diffuse Gamma-Ray Measurement". *Journal of Cosmology and Astroparticle Physics* 2010.4 (Apr. 15, 2010), pp. 014–014. ISSN: 1475-7516. DOI: 10.1088/1475-7516/2010/04/014. arXiv: 1002.4415 [p. 180].

[299] A. M. Green. "Dependence of direct detection signals on the WIMP velocity distribution". *Journal of Cosmology and Astroparticle Physics* 2010.10 (Oct. 28, 2010), pp. 034–034. ISSN: 1475-7516. DOI: 10.1088/1475-7516/2010/10/034. arXiv: 1009.0916 [p. 30].

[300] L. J. Hall et al. "Freeze-In Production of FIMP Dark Matter". *Journal of High Energy Physics* 2010.3 (Mar. 2010), p. 80. ISSN: 1029-8479. DOI: 10.1007/JHEP03(2010)080. arXiv: 0911.1120 [p. 63].

[301] J. Lavalle, C. Boehm, and J. Barthes. "On the Sunyaev-Zel'dovich effect from dark matter annihilation or decay in galaxy clusters". *Journal of Cosmology and Astroparticle Physics* 2010.2 (Feb. 3, 2010), pp. 005–005. ISSN: 1475-7516. DOI: 10.1088/1475-7516/2010/02/005. arXiv: 0907.5589 [p. 32].

[302] M. Maggiore and A. Riotto. "THE HALO MASS FUNCTION FROM EXCURSION SET THEORY. I. GAUSSIAN FLUCTUATIONS WITH NON-MARKOVIAN DEPENDENCE ON THE SMOOTHING SCALE". *The Astrophysical Journal* 711.2 (Mar. 10, 2010), pp. 907–927. ISSN: 0004-637X, 1538-4357. DOI: 10.1088/0004-637X/711/2/907 [p. 115].

[303] R. Massey, T. Kitching, and J. Richard. "The dark matter of gravitational lensing". *Reports on Progress in Physics* 73.8 (Aug. 1, 2010), p. 086901. ISSN: 0034-4885, 1361-6633. DOI: 10.1088/0034-4885/73/8/086901. arXiv: 1001.1739 [p. 4].

[304] M. Milgrom. "Bimetric MOND gravity" (Jan. 25, 2010). DOI: 10.1103/PhysRevD.80.123536. arXiv: 0912.0790 [p. 20].

[305] H. Mo, F. C. van den Bosch, and S. White. *Galaxy formation and evolution*. Cambridge University Press, 2010 [pp. 11, 96, 97, 99, 105, 118, 126–128, 276, 298].

[306] A. R. Parsons et al. "The Precision Array for Probing the Epoch of Reionization: 8 Station Results". *The Astronomical Journal* 139.4 (Apr. 1, 2010), pp. 1468–1480. ISSN: 0004-6256, 1538-3881. DOI: 10.1088/0004-6256/139/4/1468. arXiv: 0904.2334 [p. 37].

[307] J. Peñarrubia et al. "The impact of dark matter cusps and cores on the satellite galaxy population around spiral galaxies: Impact of cusps and cores on the satellite population". *Monthly Notices of the Royal Astronomical Society* (May 2010), no–no. ISSN: 00358711, 13652966. DOI: 10.1111/j.1365-2966.2010.16762.x [p. 136].

[308] S. Profumo and P. Ullio. "Multi-wavelength Searches for Particle Dark Matter" (Jan. 22, 2010). arXiv: 1001.4086 [p. 32].

[309] A. Schneider, L. M. Krauss, and B. Moore. "Impact of Dark Matter Microhalos on Signatures for Direct and Indirect Detection". *Physical Review D* 82.6 (Sept. 21, 2010), p. 063525. ISSN: 1550-7998, 1550-2368. DOI: 10.1103/PhysRevD.82.063525. arXiv: 1004.5432 [pp. 136, 176].

[310] M. Wadepuhl and V. Springel. "Satellite galaxies in hydrodynamical simulations of Milky Way sized galaxies". *Monthly Notices of the Royal Astronomical Society* (Oct. 2010), no–no. ISSN: 00358711. DOI: 10.1111/j.1365-2966.2010.17576.x. arXiv: 1004.3217 [p. 16].

[311] C. E. Aalseth et al. "Results from a Search for Light-Mass Dark Matter with a P-type Point Contact Germanium Detector". *Physical Review Letters* 106 (2011), p. 131301. DOI: 10.1103/PhysRevLett.106.131301 [p. 38].

[312] ANTARES Collaboration. "ANTARES: the first undersea neutrino telescope". *Nuclear Instruments and Methods in Physics Research Section A: Accelerators, Spectrometers, Detectors and Associated Equipment* 656.1 (Nov. 2011), pp. 11–38. ISSN: 01689002. DOI: 10.1016/j.nima.2011.06.103. arXiv: 1104.1607 [p. 36].

[313] M. Boylan-Kolchin, J. S. Bullock, and M. Kaplinghat. "Too big to fail? The puzzling darkness of massive Milky Way subhaloes". *Monthly Notices of the Royal Astronomical Society* 415 (July 2011), pp. L40–L44. DOI: 10.1111/j.1745-3933.2011.01074.x [p. 16].

[314] M. Cirelli et al. "PPPC 4 DM ID: a poor particle physicist cookbook for dark matter indirect detection". *Journal of Cosmology and Astroparticle Physics* 2011.3 (Mar. 31, 2011), pp. 051–051. ISSN: 1475-7516. DOI: 10.1088/1475-7516/2011/03/051 [p. 183].

[315] G. Cowan et al. "Asymptotic formulae for likelihood-based tests of new physics". *The European Physical Journal C* 71.2 (Feb. 2011), p. 1554. ISSN: 1434-6044, 1434-6052. DOI: 10.1140/epjc/s10052-011-1554-0. arXiv: 1007.1727 [p. 210].

[316] J. Diemand and B. Moore. "The Structure and Evolution of Cold Dark Matter Halos". *Advanced Science Letters* 4.2 (Feb. 1, 2011), pp. 297–310. ISSN: 19366612, 19367317. DOI: 10.1166/asl.2011.1211 [p. 11].

[317] J. Ehlers. "General-Relativistc Kinetic Theory Of Gases". *Relativistic Fluid Dynamics*. Ed. by C. Cattaneo. C.I.M.E. Summer Schools. Berlin, Heidelberg: Springer, 2011, pp. 301–388. ISBN: 978-3-642-11099-3. DOI: 10.1007/978-3-642-11099-3_4 [p. 50].

[318] P. J. Fox et al. "LEP Shines Light on Dark Matter". *Physical Review D* 84.1 (July 22, 2011), p. 014028. ISSN: 1550-7998, 1550-2368. DOI: 10.1103/PhysRevD.84.014028. arXiv: 1103.0240 [p. 29].

[319] J. Goodman et al. "Constraints on Light Majorana Dark Matter from Colliders". *Physics Letters B* 695.1 (Jan. 2011), pp. 185–188. ISSN: 03702693. DOI: 10.1016/j.physletb.2010.11.009. arXiv: 1005.1286 [p. 29].

[320] IceCube Collaboration. "Search for Dark Matter from the Galactic Halo with the IceCube Neutrino Observatory". *Physical Review D* 84.2 (July 29, 2011), p. 022004. ISSN: 1550-7998, 1550-2368. DOI: 10.1103/PhysRevD.84.022004. arXiv: 1101.3349 [p. 36].

[321] J. Lavalle. "Impact of the spectral hardening of TeV cosmic rays on the prediction of the secondary positron flux". *Monthly Notices of the Royal Astronomical Society* 414.2 (June 21, 2011), pp. 985–991. ISSN: 00358711. DOI: 10.1111/j.1365-2966.2011.18294.x. arXiv: 1011.3063 [p. 35].

[322] G. Paciga et al. "The GMRT-EoR Experiment: A new upper limit on the neutral hydrogen power spectrum at z~8.6". *Monthly Notices of the Royal Astronomical Society* 413.2 (May 11, 2011), pp. 1174–1183. ISSN: 00358711. DOI: 10.1111/j.1365-2966.2011.18208.x. arXiv: 1006.1351 [p. 37].

[323] L. Pieri et al. "Implications of High-Resolution Simulations on Indirect Dark Matter Searches". *Physical Review D* 83.2 (Jan. 21, 2011), p. 023518. ISSN: 1550-7998, 1550-2368. DOI: 10.1103/PhysRevD.83.023518. arXiv: 0908.0195 [pp. 34, 35, 180, 300].

[324] SUPER-KAMIOKANDE COLLABORATION. "An Indirect Search for WIMPs in the Sun using 3109.6 days of upward-going muons in Super-Kamiokande". *The Astrophysical Journal* 742.2 (Dec. 1, 2011), p. 78. ISSN: 0004-637X, 1538-4357. DOI: 10.1088/0004-637X/742/2/78. arXiv: 1108.3384 [p. 36].

[325] M. ACKERMANN et al. "Anisotropies in the diffuse gamma-ray background measured by the Fermi LAT" (Feb. 13, 2012). DOI: 10.1103/PhysRevD.85.083007. arXiv: 1202.2856 [p. 34].

[326] M. ACKERMANN et al. "*FERMI* -LAT OBSERVATIONS OF THE DIFFUSE \gamma -RAY EMISSION: IMPLICATIONS FOR COSMIC RAYS AND THE INTERSTELLAR MEDIUM". *The Astrophysical Journal* 750.1 (May 1, 2012), p. 3. ISSN: 0004-637X, 1538-4357. DOI: 10.1088/0004-637X/750/1/3 [pp. 198, 199].

[327] S. ANDO and D. NAGAI. "Fermi-LAT constraints on dark matter annihilation cross section from observations of the Fornax cluster" (June 6, 2012). DOI: 10.1088/1475-7516/2012/07/017. arXiv: 1201.0753 [p. 34].

[328] G. ANGLOHER et al. "Results from 730 kg days of the CRESST-II Dark Matter Search". *The European Physical Journal C* 72.4 (Apr. 2012), p. 1971. ISSN: 1434-6044, 1434-6052. DOI: 10.1140/epjc/s10052-012-1971-8. arXiv: 1109.0702 [p. 30].

[329] A. V. BELIKOV, D. HOOPER, and M. R. BUCKLEY. "Searching For Dark Matter Subhalos In the Fermi-LAT Second Source Catalog". *Physical Review D* 86.4 (Aug. 2, 2012), p. 043504. ISSN: 1550-7998, 1550-2368. DOI: 10.1103/PhysRevD.86.043504. arXiv: 1111.2613 [p. 180].

[330] A. J. BENSON. "Galacticus: A semi-analytic model of galaxy formation". *New Astronomy* 17.2 (Feb. 2012), pp. 175–197. ISSN: 13841076. DOI: 10.1016/j.newast.2011.07.004 [pp. 96, 133, 142, 299].

[331] S. BLANCHET and J. LAVALLE. "Diffuse gamma-ray constraints on dark matter revisited. I: the impact of subhalos". *Journal of Cosmology and Astroparticle Physics* 2012.11 (Nov. 13, 2012), pp. 021–021. ISSN: 1475-7516. DOI: 10.1088/1475-7516/2012/11/021. arXiv: 1207.2476 [p. 180].

[332] J. BOVY and S. TREMAINE. "On the local dark matter density". *The Astrophysical Journal* 756.1 (Sept. 1, 2012), p. 89. ISSN: 0004-637X, 1538-4357. DOI: 10.1088/0004-637X/756/1/89. arXiv: 1205.4033 [p. 3].

[333] T. BRINGMANN and C. WENIGER. "Gamma Ray Signals from Dark Matter: Concepts, Status and Prospects". *Physics of the Dark Universe* 1.1 (Nov. 2012), pp. 194–217. ISSN: 22126864. DOI: 10.1016/j.dark.2012.10.005. arXiv: 1208.5481 [p. 180].

[334] J. O. BURNS et al. "Probing the First Stars and Black Holes in the Early Universe with the Dark Ages Radio Explorer (DARE)". *Advances in Space Research* 49.3 (Feb. 2012), pp. 433–450. ISSN: 02731177. DOI: 10.1016/j.asr.2011.10.014. arXiv: 1106.5194 [p. 37].

[335] R. CATENA and P. ULLIO. "The local dark matter phase-space density and impact on WIMP direct detection". *Journal of Cosmology and Astroparticle Physics* 2012.5 (May 3, 2012), pp. 005–005. ISSN: 1475-7516. DOI: 10.1088/1475-7516/2012/05/005. arXiv: 1111.3556 [p. 30].

[336] A. CHARBONNIER, C. COMBET, and D. MAURIN. "CLUMPY: a code for gamma-ray signals from dark matter structures". *Computer Physics Communications* 183.3 (Mar. 2012), pp. 656–668. ISSN: 00104655. DOI: 10.1016/j.cpc.2011.10.017. arXiv: 1201.4728 [pp. 180, 186].

[337] M. CIRELLI et al. "Gamma ray constraints on Decaying Dark Matter" (Sept. 8, 2012). DOI: 10.1103/PhysRevD.86.083506. arXiv: 1205.5283 [p. 34].

[338] B. FAMAEY and S. MCGAUGH. "Modified Newtonian Dynamics (MOND): Observational Phenomenology and Relativistic Extensions". *Living Reviews in Relativity* 15.1 (Dec. 2012), p. 10. ISSN: 2367-3613, 1433-8351. DOI: 10.12942/lrr-2012-10. arXiv: 1112.3960 [pp. 19, 38].

[339] FERMI-LAT COLLABORATION. "Constraints on the Galactic Halo Dark Matter from Fermi-LAT Diffuse Measurements". *The Astrophysical Journal* 761.2 (Dec. 20, 2012), p. 91. ISSN: 0004-637X, 1538-4357. DOI: 10.1088/0004-637X/761/2/91. arXiv: 1205.6474 [pp. 34, 180, 212, 213, 301].

[340] FERMI-LAT COLLABORATION. "Measurement of separate cosmic-ray electron and positron spectra with the Fermi Large Area Telescope" (Mar. 27, 2012). DOI: 10.1103/PhysRevLett.108.011103. arXiv: 1109.0521 [p. 35].

[341] P. Gondolo, J. Hisano, and K. Kadota. "The effect of quark interactions on dark matter kinetic decoupling and the mass of the smallest dark halos". *Physical Review D* 86.8 (Oct. 10, 2012), p. 083523. ISSN: 1550-7998, 1550-2368. DOI: 10.1103/PhysRevD.86.083523. arXiv: 1205.1914 [pp. 130, 132].

[342] L. J. Greenhill and G. Bernardi. "HI Epoch of Reionization Arrays" (Jan. 9, 2012). arXiv: 1201.1700 [p. 37].

[343] IceCube Collaboration. "The Design and Performance of IceCube DeepCore". *Astroparticle Physics* 35.10 (May 2012), pp. 615–624. ISSN: 09276505. DOI: 10.1016/j.astropartphys.2012.01.004. arXiv: 1109.6096 [p. 36].

[344] C. Knobel. "An Introduction into the Theory of Cosmological Structure Formation" (Aug. 2012) [pp. 97, 98, 104, 109].

[345] J. Lavalle and P. Salati. "Dark Matter Indirect Signatures" (Nov. 2, 2012). DOI: 10.1016/j.crhy.2012.05.001. arXiv: 1205.1004 [pp. 32, 35].

[346] A. V. Maccio' et al. "Cores in warm dark matter haloes: a Catch 22 problem". *Monthly Notices of the Royal Astronomical Society* 424.2 (Aug. 1, 2012), pp. 1105–1112. ISSN: 00358711. DOI: 10.1111/j.1365-2966.2012.21284.x. arXiv: 1202.1282 [p. 17].

[347] W. J. Marciano, C. Zhang, and S. Willenbrock. "Higgs decay to two photons". *Physical Review D* 85.1 (Jan. 4, 2012), p. 013002. ISSN: 1550-7998, 1550-2368. DOI: 10.1103/PhysRevD.85.013002 [p. 269].

[348] P. L. Nolan et al. "FERMI LARGE AREA telESCOPE SECOND SOURCE CATALOG". *The Astrophysical Journal Supplement Series* 199.2 (Mar. 2012). Publisher: American Astronomical Society, p. 31. ISSN: 0067-0049. DOI: 10.1088/0067-0049/199/2/31 [p. 180].

[349] A. Pontzen and F. Governato. "How supernova feedback turns dark matter cusps into cores: Supernova feedback and dark matter cores". *Monthly Notices of the Royal Astronomical Society* 421.4 (Apr. 21, 2012), pp. 3464–3471. ISSN: 00358711. DOI: 10.1111/j.1365-2966.2012.20571.x [p. 17].

[350] P. D. Serpico. "Astrophysical models for the origin of the positron "excess"" (June 6, 2012). DOI: 10.1016/j.astropartphys.2011.08.007. arXiv: 1108.4827 [p. 35].

[351] G. Steigman, B. Dasgupta, and J. F. Beacom. "Precise Relic WIMP Abundance and its Impact on Searches for Dark Matter Annihilation". *Phys. Rev.* D86 (2012), p. 023506. DOI: 10.1103/PhysRevD.86.023506 [pp. 37, 72].

[352] C. E. Aalseth et al. "CoGeNT: A Search for Low-Mass Dark Matter using p-type Point Contact Germanium Detectors". *Physical Review D* 88.1 (July 8, 2013), p. 012002. ISSN: 1550-7998, 1550-2368. DOI: 10.1103/PhysRevD.88.012002. arXiv: 1208.5737 [p. 30].

[353] AMS Collaboration. "First result from the alpha magnetic spectrometer on the international space station: Precision measurement of the positron fraction in primary cosmic rays of 0.5–350 GeV". *Physical Review Letters* 110.14 (Apr. 3, 2013), p. 141102. DOI: 10.1103/PhysRevLett.110.141102 [p. 35].

[354] S. Ando and E. Komatsu. "Constraints on the annihilation cross section of dark matter particles from anisotropies in the diffuse gamma-ray background measured with Fermi-LAT" (Jan. 24, 2013). DOI: 10.1103/PhysRevD.87.123539. arXiv: 1301.5901 [p. 34].

[355] E. Armengaud et al. "Axion searches with the EDELWEISS-II experiment". *Journal of Cosmology and Astroparticle Physics* 2013.11 (Nov. 29, 2013), pp. 067–067. ISSN: 1475-7516. DOI: 10.1088/1475-7516/2013/11/067. arXiv: 1307.1488 [p. 31].

[356] ATLAS Collaboration. "Search for dark matter candidates and large extra dimensions in events with a jet and missing transverse momentum with the ATLAS detector". *Journal of High Energy Physics* 2013.4 (Apr. 2013), p. 75. ISSN: 1029-8479. DOI: 10.1007/JHEP04(2013)075. arXiv: 1210.4491 [p. 29].

[357] W. Atwood et al. "Pass 8: Toward the Full Realization of the Fermi-LAT Scientific Potential" (Mar. 14, 2013). arXiv: 1303.3514 [p. 200].

[358] K. Bernlöhr et al. "Monte Carlo design studies for the Cherenkov Telescope Array". *Astroparticle Physics* 43 (Mar. 2013), pp. 171–188. ISSN: 09276505. DOI: 10.1016/j.astropartphys.2012.10.002. arXiv: 1210.3503 [pp. 201, 202].

[359] M. Cirelli. "Indirect Searches for Dark Matter: a status review" (Mar. 4, 2013). DOI: 10.1007/s12043-012-0419-x. arXiv: 1202.1454 [p. 32].

[360] M. Cirelli, E. D. Nobile, and P. Panci. "Tools for model-independent bounds in direct dark matter searches". *Journal of Cosmology and Astroparticle Physics* 2013.10 (Oct. 10, 2013), pp. 019–019. ISSN: 1475-7516. DOI: 10.1088/1475-7516/2013/10/019 [p. 91].

[361] R. Essig et al. "Constraining Light Dark Matter with Diffuse X-Ray and Gamma-Ray Observations". *Journal of High Energy Physics* 2013.11 (Nov. 2013), p. 193. ISSN: 1029-8479. DOI: 10.1007/JHEP11(2013)193. arXiv: 1309.4091 [p. 180].

[362] S. Ettori et al. "Mass Profiles of Galaxy Clusters from X-ray Analysis". *Space Science Reviews* 177.1 (Aug. 2013), pp. 119–154. ISSN: 0038-6308, 1572-9672. DOI: 10.1007/s11214-013-9976-7 [p. 4].

[363] K. Freese, M. Lisanti, and C. Savage. "Annual Modulation of Dark Matter: A Review". *Reviews of Modern Physics* 85.4 (Nov. 1, 2013), pp. 1561–1581. ISSN: 0034-6861, 1539-0756. DOI: 10.1103/RevModPhys.85.1561. arXiv: 1209.3339 [p. 31].

[364] T. Frossard et al. "Systematic approach to thermal leptogenesis". *Phys. Rev. D* 87 (Apr. 2013), p. 085009. DOI: 10.1103/PhysRevD.87.085009 [p. 54].

[365] M. P. van Haarlem et al. "LOFAR: The LOw-Frequency ARray". *Astronomy & Astrophysics* 556 (Aug. 2013), A2. ISSN: 0004-6361, 1432-0746. DOI: 10.1051/0004-6361/201220873. arXiv: 1305.3550 [p. 37].

[366] H. Hoekstra et al. "Masses of Galaxy Clusters from Gravitational Lensing". *Space Science Reviews* 177.1 (Aug. 2013), pp. 75–118. ISSN: 0038-6308, 1572-9672. DOI: 10.1007/s11214-013-9978-5 [p. 4].

[367] IceCube Collaboration. "Search for dark matter annihilations in the Sun with the 79-string IceCube detector". *Physical Review Letters* 110.13 (Mar. 28, 2013), p. 131302. ISSN: 0031-9007, 1079-7114. DOI: 10.1103/PhysRevLett.110.131302. arXiv: 1212.4097 [p. 36].

[368] IceCube Collaboration. "Search for neutrinos from annihilating dark matter in the direction of the galactic center with the 40-String IceCube neutrino observatory" (Apr. 10, 2013). arXiv: 1210.3557 [p. 36].

[369] J. Lesgourgues et al. *Neutrino cosmology*. Cambridge University Press, 2013. ISBN: 978-1-139-61958-5 [p. 100].

[370] G. Mellema et al. "Reionization and the Cosmic Dawn with the Square Kilometre Array". *Experimental Astronomy* 36.1 (Aug. 2013), pp. 235–318. ISSN: 0922-6435, 1572-9508. DOI: 10.1007/s10686-013-9334-5. arXiv: 1210.0197 [p. 37].

[371] P. Peter and J.-P. Uzan. *Primordial cosmology*. Oxford University Press, 2013 [pp. 10, 109].

[372] K. Petraki and R. R. Volkas. "Review of asymmetric dark matter" (Aug. 1, 2013). DOI: 10.1142/S0217751X13300287. arXiv: 1305.4939 [p. 27].

[373] C. Rott. "Review of Indirect WIMP Search Experiments". *Nuclear Physics B - Proceedings Supplements* 235-236 (Feb. 2013), pp. 413–420. ISSN: 09205632. DOI: 10.1016/j.nuclphysbps.2013.04.040. arXiv: 1210.4161 [p. 36].

[374] S. J. Tingay et al. "The Murchison Widefield Array: the Square Kilometre Array Precursor at low radio frequencies". *Publications of the Astronomical Society of Australia* 30 (2013), e007. ISSN: 1323-3580, 1448-6083. DOI: 10.1017/pasa.2012.007. arXiv: 1206.6945 [p. 37].

[375] M. G. Aartsen et al. "Observation of High-Energy Astrophysical Neutrinos in Three Years of IceCube Data". *Physical Review Letters* 113.10 (Sept. 2, 2014), p. 101101. ISSN: 0031-9007, 1079-7114. DOI: 10.1103/PhysRevLett.113.101101 [p. 36].

[376] R. Agnese et al. "Search for Low-Mass Weakly Interacting Massive Particles with SuperCDMS". *Phys. Rev. Lett.* 112.24 (2014), p. 241302. DOI: 10.1103/PhysRevLett.112.241302 [p. 38].

[377] M. Arik et al. "CAST solar axion search with 3^He buffer gas: Closing the hot dark matter gap". *Physical Review Letters* 112.9 (Mar. 4, 2014), p. 091302. ISSN: 0031-9007, 1079-7114. DOI: 10.1103/PhysRevLett.112.091302. arXiv: 1307.1985 [p. 31].

[378] E. Armengaud et al. "Conceptual Design of the International Axion Observatory (IAXO)". *Journal of Instrumentation* 9.5 (May 12, 2014), T05002–T05002. ISSN: 1748-0221. DOI: 10.1088/1748-0221/9/05/T05002. arXiv: 1401.3233 [p. 31].

[379] V. S. Berezinsky, V. I. Dokuchaev, and Y. N. Eroshenko. "Small-scale clumps of dark matter". *Physics-Uspekhi* 57.1 (Jan. 31, 2014), pp. 1–36. ISSN: 1063-7869, 1468-4780. DOI: 10.3367/UFNe.0184.201401a.0003. arXiv: 1405.2204 [p. 136].

[380] J. Billard, L. Strigari, and E. Figueroa-Feliciano. "Implication of neutrino backgrounds on the reach of next generation dark matter direct detection experiments". *Physical Review D* 89.2 (Jan. 27, 2014), p. 023524. ISSN: 1550-7998, 1550-2368. DOI: 10.1103/PhysRevD.89.023524. arXiv: 1307.5458 [p. 31].

[381] D. Budker et al. "Proposal for a Cosmic Axion Spin Precession Experiment (CASPEr)". *Physical Review X* 4.2 (May 19, 2014), p. 021030. ISSN: 2160-3308. DOI: 10.1103/PhysRevX.4.021030 [p. 31].

[382] Y. Choquet-Bruhat. *Introduction to general relativity, black holes, and cosmology*. OUP Oxford, 2014 [p. 50].

[383] A. A. Dutton and A. V. Macciò. "Cold dark matter haloes in the Planck era: evolution of structural parameters for Einasto and NFW profiles". *Monthly Notices of the Royal Astronomical Society* 441.4 (July 11, 2014), pp. 3359–3374. ISSN: 1365-2966, 0035-8711. DOI: 10.1093/mnras/stu742. arXiv: 1402.7073 [p. 145].

[384] R. Foot. "Mirror dark matter: Cosmology, galaxy structure and direct detection". *International Journal of Modern Physics A* 29.11 (May 10, 2014), p. 1430013. ISSN: 0217-751X, 1793-656X. DOI: 10.1142/S0217751X14300130. arXiv: 1401.3965 [p. 27].

[385] Y. Hochberg et al. "The SIMP Miracle" (Oct. 28, 2014). DOI: 10.1103/PhysRevLett.113.171301. arXiv: 1402.5143 [p. 27].

[386] F. Jiang and F. C. van den Bosch. "Generating merger trees for dark matter haloes: a comparison of methods". *Monthly Notices of the Royal Astronomical Society* 440.1 (May 1, 2014), pp. 193–207. ISSN: 1365-2966, 0035-8711. DOI: 10.1093/mnras/stu280 [pp. 96, 120–122, 124, 125, 298].

[387] A. D. Ludlow et al. "The mass–concentration–redshift relation of cold dark matter haloes". *Monthly Notices of the Royal Astronomical Society* 441.1 (June 11, 2014), pp. 378–388. ISSN: 1365-2966, 0035-8711. DOI: 10.1093/mnras/stu483 [pp. 140, 141].

[388] P. Madau, S. Shen, and F. Governato. "DARK MATTER HEATING AND EARLY CORE FORMATION IN DWARF GALAXIES". *The Astrophysical Journal* 789.1 (June 17, 2014), p. L17. ISSN: 2041-8205, 2041-8213. DOI: 10.1088/2041-8205/789/1/L17 [p. 17].

[389] M. Musso and R. K. Sheth. "The excursion set approach in non-Gaussian random fields". *Monthly Notices of the Royal Astronomical Society* 439.3 (Mar. 15, 2014), pp. 3051–3063. ISSN: 0035-8711, 1365-2966. DOI: 10.1093/mnras/stu165 [p. 115].

[390] M. S. Pawlowski et al. "Co-orbiting satellite galaxy structures are still in conflict with the distribution of primordial dwarf galaxies". *Monthly Notices of the Royal Astronomical Society* 442.3 (Aug. 11, 2014), pp. 2362–2380. ISSN: 1365-2966, 0035-8711. DOI: 10.1093/mnras/stu1005. arXiv: 1406.1799 [p. 16].

[391] T. Piffl et al. "Constraining the Galaxy's dark halo with RAVE stars". *Monthly Notices of the Royal Astronomical Society* 445.3 (Dec. 11, 2014), pp. 3133–3151. ISSN: 1365-2966, 0035-8711. DOI: 10.1093/mnras/stu1948. arXiv: 1406.4130 [p. 3].

[392] J. I. Read. "The Local Dark Matter Density". *Journal of Physics G: Nuclear and Particle Physics* 41.6 (June 1, 2014), p. 063101. ISSN: 0954-3899, 1361-6471. DOI: 10.1088/0954-3899/41/6/063101. arXiv: 1404.1938 [p. 3].

[393] M. A. Sánchez-Conde and F. Prada. "The flattening of the concentration–mass relation towards low halo masses and its implications for the annihilation signal boost". *Monthly Notices of the Royal Astronomical Society* 442.3 (Aug. 11, 2014), pp. 2271–2277. ISSN: 1365-2966, 0035-8711. DOI: 10.1093/mnras/stu1014 [pp. 141, 144, 145, 170, 171].

[394] K. Schutz and T. R. Slatyer. "Self-Scattering for Dark Matter with an Excited State" (Sept. 30, 2014). DOI: 10.1088/1475-7516/2015/01/021. arXiv: 1409.2867 [p. 18].

[395] M. D. Schwartz. *Quantum field theory and the standard model*. Cambridge University Press., 2014 [p. 54].

[396] The Planck Collaboration. "Planck 2013 results. XVI. Cosmological parameters". *Astronomy & Astrophysics* 571 (Nov. 2014), A16. ISSN: 0004-6361, 1432-0746. DOI: 10.1051/0004-6361/201321591. arXiv: 1303.5076 [p. 141].

[397] M. Vogelsberger et al. "Properties of galaxies reproduced by a hydrodynamic simulation". *Nature* 509.7499 (May 2014), pp. 177–182. ISSN: 0028-0836, 1476-4687. DOI: 10.1038/nature13316. arXiv: 1405.1418 [p. 11].

[398] Q. Yuan et al. "Implications of the AMS-02 positron fraction in cosmic rays" (May 14, 2014). DOI: 10.1016/j.astropartphys.2014.05.005. arXiv: 1304.1482 [p. 35].

[399] J. Zavala and N. Afshordi. "Clustering in the phase space of dark matter haloes – II. Stable clustering and dark matter annihilation". *Monthly Notices of the Royal Astronomical Society* 441.2 (June 21, 2014), pp. 1329–1339. ISSN: 1365-2966, 0035-8711. DOI: 10.1093/mnras/stu506 [p. 142].

[400] K. M. Zurek. "Asymmetric Dark Matter: Theories, Signatures, and Constraints". *Physics Reports* 537.3 (Apr. 2014), pp. 91–121. ISSN: 03701573. DOI: 10.1016/j.physrep.2013.12.001. arXiv: 1308.0338 [p. 27].

[401] J. Abdallah et al. "Simplified Models for Dark Matter Searches at the LHC". *Phys. Dark Univ.* 9-10 (2015), pp. 8–23. DOI: 10.1016/j.dark.2015.08.001 [pp. 26, 29, 42, 91, 297].

[402] F. Acero et al. "*FERMI* LARGE AREA TELESCOPE THIRD SOURCE CATALOG". *The Astrophysical Journal Supplement Series* 218.2 (June 12, 2015), p. 23. ISSN: 1538-4365. DOI: 10.1088/0067-0049/218/2/23 [p. 180].

[403] Y. Ali-Haïmoud, J. Chluba, and M. Kamionkowski. "Constraints on dark matter interactions with standard model particles from CMB spectral distortions" (July 29, 2015). DOI: 10.1103/PhysRevLett.115.071304. arXiv: 1506.04745 [p. 37].

[404] R. Bartels and S. Ando. "Boosting the annihilation boost: Tidal effects on dark matter subhalos and consistent luminosity modeling". *Physical Review D* 92.12 (Dec. 9, 2015), p. 123508. ISSN: 1550-7998, 1550-2368. DOI: 10.1103/PhysRevD.92.123508. arXiv: 1507.08656 [p. 142].

[405] B. Bertoni, D. Hooper, and T. Linden. "Examining The Fermi-LAT Third Source Catalog In Search Of Dark Matter Subhalos". *Journal of Cosmology and Astroparticle Physics* 2015.12 (Dec. 17, 2015), pp. 035–035. ISSN: 1475-7516. DOI: 10.1088/1475-7516/2015/12/035. arXiv: 1504.02087 [pp. 34, 180, 300].

[406] M. Cautun et al. "Planes of satellite galaxies: when exceptions are the rule". *Monthly Notices of the Royal Astronomical Society* 452.4 (Oct. 1, 2015), pp. 3838–3852. ISSN: 0035-8711, 1365-2966. DOI: 10.1093/mnras/stv1557. arXiv: 1506.04151 [p. 16].

[407] T. K. Chan et al. "The Impact of Baryonic Physics on the Structure of Dark Matter Halos: the View from the FIRE Cosmological Simulations" (Sept. 23, 2015). DOI: 10.1093/mnras/stv2165. arXiv: 1507.02282 [p. 17].

[408] M. Cirelli et al. "Gamma ray tests of Minimal Dark Matter". *Journal of Cosmology and Astroparticle Physics* 2015.10 (Oct. 12, 2015), pp. 026–026. ISSN: 1475-7516. DOI: 10.1088/1475-7516/2015/10/026. arXiv: 1507.05519 [pp. 27, 180].

[409] DES Collaboration. "Eight Ultra-faint Galaxy Candidates Discovered in Year Two of the Dark Energy Survey". *The Astrophysical Journal* 813.2 (Nov. 4, 2015), p. 109. ISSN: 1538-4357. DOI: 10.1088/0004-637X/813/2/109. arXiv: 1508.03622 [p. 16].

[410] B. Diemer and A. V. Kravtsov. "A universal model for halo concentrations". *The Astrophysical Journal* 799.1 (Jan. 20, 2015), p. 108. ISSN: 1538-4357. DOI: 10.1088/0004-637X/799/1/108. arXiv: 1407.4730 [p. 140].

[411] O. D. Elbert et al. "Core formation in dwarf haloes with self-interacting dark matter: no fine-tuning necessary". *Monthly Notices of the Royal Astronomical Society* 453.1 (Oct. 11, 2015), pp. 29–37. ISSN: 0035-8711, 1365-2966. DOI: 10.1093/mnras/stv1470 [p. 18].

[412] A. Esmaili, S. K. Kang, and P. D. Serpico. "IceCube events and decaying dark matter: hints and constraints" (Jan. 8, 2015). DOI: 10.1088/1475-7516/2014/12/054. arXiv: 1410.5979 [p. 36].

[413] Fermi-LAT Collaboration. "Fermi Large Area Telescope Third Source Catalog" (June 9, 2015). arXiv: 1501.02003 [p. 196].

[414] Fermi-LAT Collaboration. "Searching for Dark Matter Annihilation from Milky Way Dwarf Spheroidal Galaxies with Six Years of Fermi-LAT Data". *Physical Review Letters* 115.23 (Nov. 30, 2015), p. 231301. ISSN: 0031-9007, 1079-7114. DOI: 10.1103/PhysRevLett.115.231301. arXiv: 1503.02641 [pp. 34, 212].

[415] M. Fornasa and M. A. Sanchez-Conde. "The nature of the Diffuse Gamma-Ray Background". *Physics Reports* 598 (Oct. 2015), pp. 1–58. ISSN: 03701573. DOI: 10.1016/j.physrep.2015.09.002. arXiv: 1502.02866 [p. 180].

[416] A. B. Fry et al. "All about baryons: revisiting SIDM predictions at small halo masses". *Monthly Notices of the Royal Astronomical Society* 452.2 (Sept. 11, 2015), pp. 1468–1479. ISSN: 0035-8711, 1365-2966. DOI: 10.1093/mnras/stv1330 [p. 18].

[417] F. Iocco, M. Pato, and G. Bertone. "Evidence for dark matter in the inner Milky Way" (Feb. 12, 2015). DOI: 10.1038/nphys3237. arXiv: 1502.03821 [p. 6].

[418] M. Jauzac et al. "*Hubble Frontier Fields* : a high-precision strong-lensing analysis of the massive galaxy cluster Abell 2744 using ∼180 multiple images". *Monthly Notices of the Royal Astronomical Society* 452.2 (Sept. 11, 2015), pp. 1437–1446. ISSN: 0035-8711, 1365-2966. DOI: 10.1093/mnras/stv1402 [p. 4].

[419] D. Kraljic and S. Sarkar. "How rare is the Bullet Cluster (in a ΛCDM universe)?" *Journal of Cosmology and Astroparticle Physics* 2015.4 (Apr. 28, 2015), pp. 050–050. ISSN: 1475-7516. DOI: 10.1088/1475-7516/2015/04/050. arXiv: 1412.7719 [p. 20].

[420] J. Lavalle and S. Magni. "Making sense of the local Galactic escape speed estimates in direct dark matter searches". *Physical Review D* 91.2 (Jan. 20, 2015), p. 023510. ISSN: 1550-7998, 1550-2368. DOI: 10.1103/PhysRevD.91.023510. arXiv: 1411.1325 [p. 30].

[421] V. Lefranc et al. "Prospects for Annihilating Dark Matter in the inner Galactic halo by the Cherenkov Telescope Array". *Physical Review D* 91.12 (June 25, 2015), p. 122003. ISSN: 1550-7998, 1550-2368. DOI: 10.1103/PhysRevD.91.122003. arXiv: 1502.05064 [pp. 34, 180, 201].

[422] K. Mimasu and V. Sanz. "ALPs at Colliders" (June 10, 2015). arXiv: 1409.4792 [p. 29].

[423] K. Murase et al. "Testing the Dark Matter Scenario for PeV Neutrinos Observed in IceCube". *Physical Review Letters* 115.7 (Aug. 11, 2015), p. 071301. ISSN: 0031-9007, 1079-7114. DOI: 10.1103/PhysRevLett.115.071301 [p. 36].

[424] S.-H. Oh et al. "HIGH-RESOLUTION MASS MODELS OF DWARF GALAXIES FROM LITTLE THINGS". *The Astronomical Journal* 149.6 (May 12, 2015), p. 180. ISSN: 1538-3881. DOI: 10.1088/0004-6256/149/6/180 [pp. 15, 16, 137].

[425] K. A. Oman et al. "The unexpected diversity of dwarf galaxy rotation curves". *Monthly Notices of the Royal Astronomical Society* 452.4 (Oct. 1, 2015), pp. 3650–3665. ISSN: 0035-8711, 1365-2966. DOI: 10.1093/mnras/stv1504 [p. 16].

[426] J. Oñorbe et al. "Forged in fire: cusps, cores and baryons in low-mass dwarf galaxies". *Monthly Notices of the Royal Astronomical Society* 454.2 (Dec. 1, 2015), pp. 2092–2106. ISSN: 0035-8711, 1365-2966. DOI: 10.1093/mnras/stv2072 [p. 17].

[427] M. Rigault et al. "Confirmation of a Star Formation Bias in Type Ia Supernova Distances and its Effect on Measurement of the Hubble Constant". *The Astrophysical Journal* 802.1 (Mar. 17, 2015), p. 20. ISSN: 1538-4357. DOI: 10.1088/0004-637X/802/1/20. arXiv: 1412.6501 [p. 14].

[428] H. Silverwood et al. "A realistic assessment of the CTA sensitivity to dark matter annihilation". *Journal of Cosmology and Astroparticle Physics* 2015.3 (Mar. 30, 2015), pp. 055–055. ISSN: 1475-7516. DOI: 10.1088/1475-7516/2015/03/055. arXiv: 1408.4131 [pp. 34, 180, 200, 201, 209, 301].

[429] T. R. Slatyer. "Indirect Dark Matter Signatures in the Cosmic Dark Ages I. Generalizing the Bound on s-wave Dark Matter Annihilation from Planck" (Aug. 3, 2015). DOI: 10.1103/PhysRevD.93.023527. arXiv: 1506.03811 [p. 37].

[430] D. H. Weinberg et al. "Cold dark matter: controversies on small scales". *Proceedings of the National Academy of Sciences* 112.40 (Oct. 6, 2015), pp. 12249–12255. ISSN: 0027-8424, 1091-6490. DOI: 10.1073/pnas.1308716112. arXiv: 1306.0913 [p. 15].

[431] R. Bartels, S. Krishnamurthy, and C. Weniger. "Strong support for the millisecond pulsar origin of the Galactic center GeV excess" (Mar. 9, 2016). DOI: 10.1103/PhysRevLett.116.051102. arXiv: 1506.05104 [p. 33].

[432] N. Bernal et al. "Production Regimes for Self-Interacting Dark Matter". *Journal of Cosmology and Astroparticle Physics* 2016.3 (Mar. 8, 2016), pp. 018–018. ISSN: 1475-7516. DOI: 10.1088/1475-7516/2016/03/018. arXiv: 1510.08063 [p. 27].

[433] G. Bertone and D. Hooper. "A History of Dark Matter". *Submitted to: Rev. Mod. Phys.* (2016) [p. 2].

[434] T. Binder et al. "Matter Power Spectrum in Hidden Neutrino Interacting Dark Matter Models: A Closer Look at the Collision Term". *JCAP* 1611 (2016), p. 043. DOI: 10.1088/1475-7516/2016/11/043 [p. 73].

[435] B. Carr, F. Kuhnel, and M. Sandstad. "Primordial Black Holes as Dark Matter". *Phys. Rev.* D94.8 (2016), p. 083504. DOI: 10.1103/PhysRevD.94.083504 [pp. 38, 224].

[436] S.-M. Choi and H. M. Lee. "Resonant SIMP dark matter". *Physics Letters B* 758 (July 2016), pp. 47–53. ISSN: 03702693. DOI: 10.1016/j.physletb.2016.04.055 [p. 27].

[437] X. Chu, C. Garcia-Cely, and T. Hambye. "Can the relic density of self-interacting dark matter be due to annihilations into Standard Model particles?" (Nov. 15, 2016). arXiv: 1609.00399 [p. 27].

[438] T. Daylan et al. "The Characterization of the Gamma-Ray Signal from the Central Milky Way: A Compelling Case for Annihilating Dark Matter". *Physics of the Dark Universe* 12 (June 2016), pp. 1–23. ISSN: 22126864. DOI: 10.1016/j.dark.2015.12.005. arXiv: 1402.6703 [p. 33].

[439] E. Di Valentino, A. Melchiorri, and J. Silk. "Reconciling Planck with the local value of H_0 in extended parameter space". *Physics Letters B* 761 (Oct. 2016), pp. 242–246. ISSN: 03702693. DOI: 10.1016/j.physletb.2016.08.043. arXiv: 1606.00634 [p. 14].

[440] J. M. Gaskins. "A review of indirect searches for particle dark matter" (Mar. 31, 2016). DOI: 10.1080/00107514.2016.1175160. arXiv: 1604.00014 [pp. 32, 196].

[441] M. Hütten et al. "Dark matter substructure modelling and sensitivity of the Cherenkov Telescope Array to Galactic dark halos". *Journal of Cosmology and Astroparticle Physics* 2016.9 (Sept. 30, 2016), pp. 047–047. ISSN: 1475-7516. DOI: 10.1088/1475-7516/2016/09/047 [pp. 34, 180, 195, 197, 201, 202, 211, 300].

[442] F. Jiang and F. C. van den Bosch. "Statistics of dark matter substructure – I. Model and universal fitting functions". *Monthly Notices of the Royal Astronomical Society* 458.3 (May 21, 2016), pp. 2848–2869. ISSN: 0035-8711, 1365-2966. DOI: 10.1093/mnras/stw439 [pp. 96, 133, 136].

[443] F. Kahlhoefer et al. "Implications of unitarity and gauge invariance for simplified dark matter models". *Journal of High Energy Physics* 2016.2 (Feb. 2016), p. 16. ISSN: 1029-8479. DOI: 10.1007/JHEP02(2016)016. arXiv: 1510.02110 [pp. 77, 297].

[444] Y. Kahn, B. R. Safdi, and J. Thaler. "Broadband and Resonant Approaches to Axion Dark Matter Detection". *Physical Review Letters* 117.14 (Sept. 30, 2016), p. 141801. ISSN: 0031-9007, 1079-7114. DOI: 10.1103/PhysRevLett.117.141801. arXiv: 1602.01086 [p. 31].

[445] M. Kaplinghat, S. Tulin, and H.-B. Yu. "Dark Matter Halos as Particle Colliders: A Unified Solution to Small-Scale Structure Puzzles from Dwarfs to Clusters". *Physical Review Letters* 116.4 (Jan. 28, 2016), p. 041302. ISSN: 0031-9007, 1079-7114. DOI: 10.1103/PhysRevLett.116.041302. arXiv: 1508.03339 [pp. 81, 87, 88].

[446] S. Kumar and R. C. Nunes. "Probing the interaction between dark matter and dark energy in the presence of massive neutrinos". *Physical Review D* 94.12 (Dec. 12, 2016), p. 123511. ISSN: 2470-0010, 2470-0029. DOI: 10.1103/PhysRevD.94.123511. arXiv: 1608.02454 [p. 14].

[447] J. Lesgourgues, G. Marques-Tavares, and M. Schmaltz. "Evidence for dark matter interactions in cosmological precision data?" *Journal of Cosmology and Astroparticle Physics* 2016.2 (Feb. 16, 2016), pp. 037–037. ISSN: 1475-7516. DOI: 10.1088/1475-7516/2016/02/037. arXiv: 1507.04351 [p. 15].

[448] LIGO and Virgo Collaborations. "Observation of Gravitational Waves from a Binary Black Hole Merger". *Physical Review Letters* 116.6 (Feb. 11, 2016), p. 061102. ISSN: 0031-9007, 1079-7114. DOI: 10.1103/PhysRevLett.116.061102 [p. 19].

[449] H. Liu, T. R. Slatyer, and J. Zavala. "The Darkest Hour Before Dawn: Contributions to Cosmic Reionization from Dark Matter Annihilation and Decay". *Physical Review D* 94.6 (Sept. 8, 2016), p. 063507. ISSN: 2470-0010, 2470-0029. DOI: 10.1103/PhysRevD.94.063507. arXiv: 1604.02457 [p. 37].

[450] L. Lopez-Honorez et al. "The 21 cm signal and the interplay between dark matter annihilations and astrophysical processes". *Journal of Cosmology and Astroparticle Physics* 2016.8 (Aug. 2, 2016), pp. 004–004. ISSN: 1475-7516. DOI: 10.1088/1475-7516/2016/08/004. arXiv: 1603.06795 [pp. 37, 133].

[451] D. J. E. Marsh. "Axion cosmology". *Physics Reports* 643 (July 2016), pp. 1–79. ISSN: 03701573. DOI: 10.1016/j.physrep.2016.06.005 [p. 23].

[452] S. S. McGaugh, F. Lelli, and J. M. Schombert. "Radial Acceleration Relation in Rotationally Supported Galaxies". *Physical Review Letters* 117.20 (Nov. 9, 2016), p. 201101. ISSN: 0031-9007, 1079-7114. DOI: 10.1103/PhysRevLett.117.201101 [p. 15].

[453] N. Mirabal et al. "3FGL Demographics Outside the Galactic Plane using Supervised Machine Learning: Pulsar and Dark Matter Subhalo Interpretations". *The Astrophysical Journal* 825.1 (June 30, 2016), p. 69. ISSN: 1538-4357. DOI: 10.3847/0004-637X/825/1/69. arXiv: 1605.00711 [p. 180].

[454] R. Murgia, S. Gariazzo, and N. Fornengo. "Constraints on the Coupling between Dark Energy and Dark Matter from CMB data". *Journal of Cosmology and Astroparticle Physics* 2016.4 (Apr. 7, 2016), pp. 014–014. ISSN: 1475-7516. DOI: 10.1088/1475-7516/2016/04/014. arXiv: 1602.01765 [p. 15].

[455] C. Okoli and N. Afshordi. "Concentration, ellipsoidal collapse, and the densest dark matter haloes". *Monthly Notices of the Royal Astronomical Society* 456.3 (Mar. 1, 2016), pp. 3068–3078. ISSN: 0035-8711, 1365-2966. DOI: 10.1093/mnras/stv2905 [pp. 107, 140, 141].

[456] J. I. Read, O. Agertz, and M. L. M. Collins. "Dark matter cores all the way down". *Monthly Notices of the Royal Astronomical Society* 459.3 (July 1, 2016), pp. 2573–2590. ISSN: 0035-8711, 1365-2966. DOI: 10.1093/mnras/stw713 [p. 17].

[457] P. F. de Salas and S. Pastor. "Relic neutrino decoupling with flavour oscillations revisited". *JCAP* 1607.7 (2016), p. 051. DOI: 10.1088/1475-7516/2016/07/051 [p. 61].

[458] T. Sawala et al. "The chosen few: the low mass halos that host faint galaxies". *Monthly Notices of the Royal Astronomical Society* 456.1 (Feb. 11, 2016), pp. 85–97. ISSN: 0035-8711, 1365-2966. DOI: 10.1093/mnras/stv2597. arXiv: 1406.6362 [p. 16].

[459] D. Schoonenberg et al. "Dark matter subhalos and unidentified sources in the Fermi 3FGL source catalog". *Journal of Cosmology and Astroparticle Physics* 2016.5 (May 11, 2016), pp. 028–028. ISSN: 1475-7516. DOI: 10.1088/1475-7516/2016/05/028. arXiv: 1601.06781 [p. 180].

[460] V. Shtabovenko, R. Mertig, and F. Orellana. "New Developments in FeynCalc 9.0". *Computer Physics Communications* 207 (Oct. 2016), pp. 432–444. ISSN: 00104655. DOI: 10.1016/j.cpc.2016.06.008. arXiv: 1601.01167 [pp. 259, 260].

[461] T. R. Slatyer and C.-L. Wu. "General Constraints on Dark Matter Decay from the Cosmic Microwave Background" (Nov. 9, 2016). DOI: 10.1103/PhysRevD.95.023010. arXiv: 1610.06933 [p. 37].

[462] The Gaia Collaboration. "The Gaia mission". *aap* 595 (Nov. 2016), A1. DOI: 10.1051/0004-6361/201629272 [p. 38].

[463] R. J. Wilkinson et al. "Ruling out the light WIMP explanation of the galactic 511 keV line". *Physical Review D* 94.10 (Nov. 28, 2016), p. 103525. ISSN: 2470-0010, 2470-0029. DOI: 10.1103/PhysRevD.94.103525. arXiv: 1602.01114 [p. 37].

[464] Q. Zhu et al. "Baryonic impact on the dark matter distribution in Milky Way-size galaxies and their satellites". *Monthly Notices of the Royal Astronomical Society* 458.2 (May 11, 2016), pp. 1559–1580. ISSN: 0035-8711, 1365-2966. DOI: 10.1093/mnras/stw374. arXiv: 1506.05537 [pp. 124, 144].

[465] R. Adhikari et al. "A White Paper on keV Sterile Neutrino Dark Matter". *Journal of Cosmology and Astroparticle Physics* 2017.1 (Jan. 13, 2017), pp. 025–025. ISSN: 1475-7516. DOI: 10.1088/1475-7516/2017/01/025. arXiv: 1602.04816 [p. 23].

[466] D. S. Akerib et al. "Results from a search for dark matter in the complete LUX exposure". *Physical Review Letters* 118.2 (Jan. 11, 2017), p. 021303. ISSN: 0031-9007, 1079-7114. DOI: 10.1103/PhysRevLett.118.021303. arXiv: 1608.07648 [p. 30].

[467] E. Armengaud et al. "Constraining the mass of light bosonic dark matter using SDSS Lyman-α forest". *Monthly Notices of the Royal Astronomical Society* 471.4 (Nov. 2017), pp. 4606–4614. ISSN: 0035-8711, 1365-2966. DOI: 10.1093/mnras/stx1870. arXiv: 1703.09126 [p. 24].

[468] N. Bernal et al. "The Dawn of FIMP Dark Matter: A Review of Models and Constraints". *International Journal of Modern Physics A* 32.27 (Sept. 30, 2017), p. 1730023. ISSN: 0217-751X, 1793-656X. DOI: 10.1142/S0217751X1730023X. arXiv: 1706.07442 [p. 63].

[469] T. Binder et al. "Early kinetic decoupling of dark matter: when the standard way of calculating the thermal relic density fails". *Phys. Rev.* D96.11 (2017), p. 115010. DOI: 10.1103/PhysRevD.96.115010 [p. 62].

[470] L. Blanchet and L. Heisenberg. "Dipolar Dark Matter as an Effective Field Theory". *Phys. Rev.* D96.8 (2017), p. 083512. DOI: 10.1103/PhysRevD.96.083512 [p. 20].

[471] K. K. Boddy et al. “Sommerfeld-Enhanced J-Factors For Dwarf Spheroidal Galaxies”. *Physical Review D* 95.12 (June 16, 2017), p. 123008. ISSN: 2470-0010, 2470-0029. DOI: 10.1103/PhysRevD.95.123008. arXiv: 1702.00408 [p. 183].

[472] F. C. van den Bosch. “Dissecting the Evolution of Dark Matter Subhaloes in the Bolshoi Simulation”. *Monthly Notices of the Royal Astronomical Society* 468.1 (June 2017), pp. 885–909. ISSN: 0035-8711, 1365-2966. DOI: 10.1093/mnras/stx520. arXiv: 1611.02657 [p. 143].

[473] M. Boudaud et al. “The pinching method for Galactic cosmic ray positrons: implications in the light of precision measurements”. *Astronomy & Astrophysics* 605 (Sept. 2017), A17. ISSN: 0004-6361, 1432-0746. DOI: 10.1051/0004-6361/201630321. arXiv: 1612.03924 [p. 35].

[474] M. Boudaud, J. Lavalle, and P. Salati. “Novel cosmic-ray electron and positron constraints on MeV dark matter particles”. *Physical Review Letters* 119.2 (July 13, 2017), p. 021103. ISSN: 0031-9007, 1079-7114. DOI: 10.1103/PhysRevLett.119.021103. arXiv: 1612.07698 [p. 35].

[475] J. S. Bullock and M. Boylan-Kolchin. “Small-Scale Challenges to the \Lambda CDM Paradigm”. *Ann. Rev. Astron. Astrophys.* 55 (2017), pp. 343–387. DOI: 10.1146/annurev-astro-091916-055313 [pp. 15, 295].

[476] F. Calore et al. “Realistic estimation for the detectability of dark matter sub-halos with Fermi-LAT”. *Physical Review D* 96.6 (Sept. 15, 2017), p. 063009. ISSN: 2470-0010, 2470-0029. DOI: 10.1103/PhysRevD.96.063009. arXiv: 1611.03503 [pp. 34, 180, 211, 213, 300].

[477] A. Cuoco, M. Krämer, and M. Korsmeier. “Novel dark matter constraints from antiprotons in the light of AMS-02”. *Physical Review Letters* 118.19 (May 9, 2017), p. 191102. ISSN: 0031-9007, 1079-7114. DOI: 10.1103/PhysRevLett.118.191102. arXiv: 1610.03071 [p. 35].

[478] F. Domingo. “Decays of a NMSSM CP-odd Higgs in the low-mass region”. *Journal of High Energy Physics* 2017.3 (Mar. 2017). ISSN: 1029-8479. DOI: 10.1007/JHEP03(2017)052 [pp. 42, 92, 271, 297].

[479] Fermi-LAT Collaboration. “The Fermi Galactic Center GeV Excess and Implications for Dark Matter” (June 26, 2017). DOI: 10.3847/1538-4357/aa6cab. arXiv: 1704.03910 [p. 33].

[480] D. Hooper and S. J. Witte. “Gamma Rays From Dark Matter Subhalos Revisited: Refining the Predictions and Constraints”. *JCAP* 1704.4 (2017), p. 018. DOI: 10.1088/1475-7516/2017/04/018 [p. 180].

[481] L. Hui et al. “Ultralight scalars as cosmological dark matter” (Feb. 24, 2017). DOI: 10.1103/PhysRevD.95.043541. arXiv: 1610.08297 [p. 19].

[482] V. Iršič et al. “First constraints on fuzzy dark matter from Lyman-α forest data and hydrodynamical simulations”. *Physical Review Letters* 119.3 (July 20, 2017), p. 031302. ISSN: 0031-9007, 1079-7114. DOI: 10.1103/PhysRevLett.119.031302. arXiv: 1703.04683 [p. 24].

[483] F. Kahlhoefer. “Review of LHC Dark Matter Searches” (Mar. 6, 2017). DOI: 10.1142/S0217751X1730006X. arXiv: 1702.02430 [p. 29].

[484] S. Kraml et al. “Simplified dark matter models with a spin-2 mediator at the LHC”. *The European Physical Journal C* 77.5 (May 2017), p. 326. ISSN: 1434-6044, 1434-6052. DOI: 10.1140/epjc/s10052-017-4871-0 [pp. 29, 42].

[485] F. Lelli et al. “One Law To Rule Them All: The Radial Acceleration Relation of Galaxies”. *The Astrophysical Journal* 836.2 (Feb. 16, 2017), p. 152. ISSN: 1538-4357. DOI: 10.3847/1538-4357/836/2/152. arXiv: 1610.08981 [p. 16].

[486] MADMAX Working Group. “Dielectric Haloscopes: A New Way to Detect Axion Dark Matter”. *Physical Review Letters* 118.9 (Mar. 3, 2017), p. 091801. ISSN: 0031-9007, 1079-7114. DOI: 10.1103/PhysRevLett.118.091801. arXiv: 1611.05865 [p. 31].

[487] D. J. E. Marsh. “Axions and ALPs: a very short introduction” (Dec. 8, 2017). arXiv: 1712.03018 [p. 23].

[488] P. J. McMillan. “The mass distribution and gravitational potential of the Milky Way”. *MNRAS* 465 (Feb. 2017), pp. 76–94. DOI: 10.1093/mnras/stw2759 [pp. 3, 5, 6, 142, 144, 146, 148, 159, 180, 181, 197].

[489] J. F. Navarro et al. “The origin of the mass discrepancy-acceleration relation in ΛCDM”. *Monthly Notices of the Royal Astronomical Society* 471.2 (Oct. 2017), pp. 1841–1848. ISSN: 0035-8711, 1365-2966. DOI: 10.1093/mnras/stx1705. arXiv: 1612.06329 [p. 17].

[490] P. J. E. Peebles. "How the Nonbaryonic Dark Matter Theory Grew" (Jan. 20, 2017). arXiv: 1701.05837 [p. 2].

[491] J. Renk et al. "Galileon Gravity in Light of ISW, CMB, BAO and H_0 data". *Journal of Cosmology and Astroparticle Physics* 2017.10 (Oct. 17, 2017), pp. 020–020. ISSN: 1475-7516. DOI: 10.1088/1475-7516/2017/10/020. arXiv: 1707.02263 [p. 14].

[492] A. J. Ross et al. "The clustering of galaxies in the completed SDSS-III Baryon Oscillation Spectroscopic Survey: Observational systematics and baryon acoustic oscillations in the correlation function". *Monthly Notices of the Royal Astronomical Society* 464.1 (Jan. 1, 2017), pp. 1168–1191. ISSN: 0035-8711, 1365-2966. DOI: 10.1093/mnras/stw2372. arXiv: 1607.03145 [p. 12].

[493] T. R. Slatyer. "TASI Lectures on Indirect Detection of Dark Matter" (Oct. 14, 2017). arXiv: 1710.05137 [p. 32].

[494] M. Stref and J. Lavalle. "Modeling dark matter subhalos in a constrained galaxy: Global mass and boosted annihilation profiles". *Phys. Rev.* D95.6 (2017), p. 063003. DOI: 10.1103/PhysRevD.95.063003 [pp. 34, 96, 136, 142].

[495] C. E. Aalseth et al. "DarkSide-20k: A 20 Tonne Two-Phase LAr TPC for Direct Dark Matter Detection at LNGS". *The European Physical Journal Plus* 133.3 (Mar. 2018), p. 131. ISSN: 2190-5444. DOI: 10.1140/epjp/i2018-11973-4. arXiv: 1707.08145 [p. 30].

[496] R. Agnese et al. "First Dark Matter Constraints from a SuperCDMS Single-Charge Sensitive Detector". *Physical Review Letters* 121.5 (Aug. 3, 2018), p. 051301. ISSN: 0031-9007, 1079-7114. DOI: 10.1103/PhysRevLett.121.051301 [p. 29].

[497] E. Aprile et al. "Dark Matter Search Results from a One Tonne x Year Exposure of XENON1T". *Physical Review Letters* 121.11 (Sept. 12, 2018), p. 111302. ISSN: 0031-9007, 1079-7114. DOI: 10.1103/PhysRevLett.121.111302. arXiv: 1805.12562 [pp. 30, 38].

[498] C. Arina. "Impact of cosmological and astrophysical constraints on dark matter simplified models". *Frontiers in Astronomy and Space Sciences* 5 (Sept. 11, 2018), p. 30. ISSN: 2296-987X. DOI: 10.3389/fspas.2018.00030. arXiv: 1805.04290 [pp. 26, 42, 297].

[499] Q. Arnaud et al. "Optimizing EDELWEISS detectors for low-mass WIMP searches". *Phys. Rev.* D97.2 (2018), p. 022003. DOI: 10.1103/PhysRevD.97.022003 [pp. 29, 38].

[500] N. Bar et al. "Galactic Rotation Curves vs. Ultra-Light Dark Matter: Implications of the Soliton – Host Halo Relation". *arXiv:1805.00122 [astro-ph, physics:hep-ph]* (Nov. 6, 2018). DOI: 10.1103/PhysRevD.98.083027. arXiv: 1805.00122 [p. 24].

[501] R. Bartels et al. "The Fermi-LAT GeV Excess Traces Stellar Mass in the Galactic Bulge". *Nature Astronomy* 2.10 (Oct. 2018), pp. 819–828. ISSN: 2397-3366. DOI: 10.1038/s41550-018-0531-z. arXiv: 1711.04778 [p. 33].

[502] G. Bélanger et al. "micrOMEGAs5.0 : freeze-in". *Computer Physics Communications* 231 (Oct. 2018), pp. 173–186. ISSN: 00104655. DOI: 10.1016/j.cpc.2018.04.027. arXiv: 1801.03509 [p. 67].

[503] R. Bernabei et al. "First model independent results from DAMA/LIBRA-phase2". *Nuclear Physics and Atomic Energy* 19.4 (Dec. 25, 2018), pp. 307–325. ISSN: 1818331X, 20740565. DOI: 10.15407/jnpae2018.04.307. arXiv: 1805.10486 [pp. 29, 31].

[504] T. Binder, L. Covi, and K. Mukaida. "Dark matter Sommerfeld-enhanced annihilation and bound-state decay at finite temperature". *Physical Review D* 98.11 (Dec. 17, 2018), p. 115023. ISSN: 2470-0010, 2470-0029. DOI: 10.1103/PhysRevD.98.115023 [p. 83].

[505] F. C. van den Bosch and G. Ogiya. "Dark matter substructure in numerical simulations: a tale of discreteness noise, runaway instabilities, and artificial disruption". *Monthly Notices of the Royal Astronomical Society* 475.3 (Apr. 11, 2018), pp. 4066–4087. ISSN: 0035-8711, 1365-2966. DOI: 10.1093/mnras/sty084 [p. 143].

[506] F. C. van den Bosch et al. "Disruption of Dark Matter Substructure: Fact or Fiction?" *Monthly Notices of the Royal Astronomical Society* 474.3 (Mar. 1, 2018), pp. 3043–3066. ISSN: 0035-8711, 1365-2966. DOI: 10.1093/mnras/stx2956. arXiv: 1711.05276 [pp. 136, 143, 299].

[507] M. Boudaud et al. "Robust cosmic-ray constraints on p-wave annihilating MeV dark matter" (Oct. 3, 2018). arXiv: 1810.01680 [p. 35].

[508] M. Boudaud et al. "What do Galactic electrons and positrons tell us about dark matter?" *Proceedings of 35th International Cosmic Ray Conference — PoS(ICRC2017)*. 35th International Cosmic Ray Conference. Vol. 301. SISSA Medialab, Aug. 3, 2018, p. 915. DOI: 10.22323/1.301.0915 [p. 35].

[509] J. D. Bowman et al. “An absorption profile centred at 78 megahertz in the sky-averaged spectrum”. *Nature* 555.7694 (Mar. 1, 2018), pp. 67–70. ISSN: 0028-0836, 1476-4687. DOI: 10.1038/nature25792 [p. 27].

[510] A. Boyarsky et al. “Sterile Neutrino Dark Matter” (Oct. 26, 2018). DOI: 10.1016/j.ppnp.2018.07.004. arXiv: 1807.07938 [p. 23].

[511] P. Bruel et al. “Fermi-LAT improved Pass~8 event selection” (Oct. 26, 2018). arXiv: 1810.11394 [p. 200].

[512] L. J. Chang, M. Lisanti, and S. Mishra-Sharma. “A Search for Dark Matter Annihilation in the Milky Way Halo”. *Physical Review D* 98.12 (Dec. 11, 2018), p. 123004. ISSN: 2470-0010, 2470-0029. DOI: 10.1103/PhysRevD.98.123004. arXiv: 1804.04132 [pp. 34, 180].

[513] S. Clesse and J. García-Bellido. “Seven Hints for Primordial Black Hole Dark Matter” (May 29, 2018). arXiv: 1711.10458 [p. 28].

[514] R. J. Cooke, M. Pettini, and C. C. Steidel. “One Percent Determination of the Primordial Deuterium Abundance”. *The Astrophysical Journal* 855.2 (Mar. 12, 2018), p. 102. ISSN: 1538-4357. DOI: 10.3847/1538-4357/aaab53 [p. 14].

[515] B. Diemer. “COLOSSUS: A python toolkit for cosmology, large-scale structure, and dark matter halos”. *The Astrophysical Journal Supplement Series* 239.2 (Dec. 18, 2018), p. 35. ISSN: 1538-4365. DOI: 10.3847/1538-4365/aaee8c. arXiv: 1712.04512 [p. 140].

[516] X. Du et al. “Tidal disruption of fuzzy dark matter subhalo cores”. *arXiv:1801.04864 [astro-ph, physics:gr-qc, physics:hep-ph]* (Mar. 7, 2018). DOI: 10.1103/PhysRevD.97.063507. arXiv: 1801.04864 [p. 24].

[517] M. Fairbairn et al. “Despicable Dark Relics: generated by gravity with unconstrained masses” (Aug. 24, 2018). arXiv: 1808.08236 [p. 27].

[518] Gaia Collaboration. “Gaia Data Release 2. Summary of the contents and survey properties”. *Astronomy & Astrophysics* 616 (Aug. 2018), A1. ISSN: 0004-6361, 1432-0746. DOI: 10.1051/0004-6361/201833051. arXiv: 1804.09365 [pp. 3, 38].

[519] C. Giganti, S. Lavignac, and M. Zito. “Neutrino oscillations: the rise of the PMNS paradigm”. *Progress in Particle and Nuclear Physics* 98 (Jan. 2018), pp. 1–54. ISSN: 01466410. DOI: 10.1016/j.ppnp.2017.10.001. arXiv: 1710.00715 [p. 22].

[520] V. Gluscevic and K. K. Boddy. “Constraints on scattering of keV–TeV dark matter with protons in the early Universe”. *Physical Review Letters* 121.8 (Aug. 20, 2018), p. 081301. ISSN: 0031-9007, 1079-7114. DOI: 10.1103/PhysRevLett.121.081301. arXiv: 1712.07133 [p. 91].

[521] N. Hiroshima, S. Ando, and T. Ishiyama. “Modeling evolution of dark matter substructure and annihilation boost”. *Physical Review D* 97.12 (June 8, 2018), p. 123002. ISSN: 2470-0010, 2470-0029. DOI: 10.1103/PhysRevD.97.123002. arXiv: 1803.07691 [pp. 96, 133, 142, 147, 149, 299].

[522] I. G. Irastorza and J. Redondo. “New experimental approaches in the search for axion-like particles”. *Progress in Particle and Nuclear Physics* 102 (Sept. 2018), pp. 89–159. ISSN: 01466410. DOI: 10.1016/j.ppnp.2018.05.003. arXiv: 1801.08127 [pp. 29, 31].

[523] M. Korsmeier, F. Donato, and N. Fornengo. “Prospects to verify a possible dark matter hint in cosmic antiprotons with antideuterons and antihelium”. *Physical Review D* 97.10 (May 18, 2018). Publisher: American Physical Society, p. 103011. DOI: 10.1103/PhysRevD.97.103011 [p. 35].

[524] T. Lacroix, M. Stref, and J. Lavalle. “Anatomy of Eddington-like inversion methods in the context of dark matter searches”. *Journal of Cosmology and Astroparticle Physics* 2018.9 (Sept. 26, 2018), pp. 040–040. ISSN: 1475-7516. DOI: 10.1088/1475-7516/2018/09/040 [pp. 30, 169].

[525] R. K. Leane et al. “GeV-Scale Thermal WIMPs: Not Even Slightly Dead”. *Physical Review D* 98.2 (July 18, 2018), p. 023016. ISSN: 2470-0010, 2470-0029. DOI: 10.1103/PhysRevD.98.023016. arXiv: 1805.10305 [p. 25].

[526] H. Liu and T. R. Slatyer. “Too Hot, Too Cold or Just Right? Implications of a 21-cm Signal for Dark Matter Annihilation and Decay”. *Physical Review D* 98.2 (July 2, 2018), p. 023501. ISSN: 2470-0010, 2470-0029. DOI: 10.1103/PhysRevD.98.023501. arXiv: 1803.09739 [p. 37].

[527] O. Macias et al. “Galactic Bulge Preferred Over Dark Matter for the Galactic Center Gamma-Ray Excess”. *Nature Astronomy* 2.5 (May 2018), pp. 387–392. ISSN: 2397-3366. DOI: 10.1038/s41550-018-0414-3. arXiv: 1611.06644 [p. 33].

[528] T. Markkanen, A. Rajantie, and T. Tenkanen. “Spectator Dark Matter” (Nov. 6, 2018). arXiv: 1811.02586 [p. 27].

[529] T. Nakama et al. “Constraints on small-scale primordial power by annihilation signals from extragalactic dark matter minihalos”. *Physical Review D* 97.2 (Jan. 30, 2018). ISSN: 2470-0010, 2470-0029. DOI: 10.1103/PhysRevD.97.023539 [p. 112].

[530] M. Stref. “Dark Matter on the Galactic Scale : from Particle Physics and Cosmology to Local Properties”. PhD thesis. Universit{\'e} de Montpellier, Sept. 2018 [p. 39].

[531] G. Torrealba et al. “Discovery of two neighboring satellites in the Carina constellation with MagLiteS”. *Monthly Notices of the Royal Astronomical Society* 475.4 (Apr. 21, 2018), pp. 5085–5097. ISSN: 0035-8711, 1365-2966. DOI: 10.1093/mnras/sty170. arXiv: 1801.07279 [p. 16].

[532] S. Tulin and H.-B. Yu. “Dark Matter Self-interactions and Small Scale Structure”. *Physics Reports* 730 (Feb. 2018), pp. 1–57. ISSN: 03701573. DOI: 10.1016/j.physrep.2017.11.004. arXiv: 1705.02358 [p. 18].

[533] S. Ando, T. Ishiyama, and N. Hiroshima. “Halo substructure boosts to the signatures of dark matter annihilation” (Mar. 27, 2019). arXiv: 1903.11427 [pp. 34, 180].

[534] M. Antonello et al. “The SABRE project and the SABRE PoP”. *The European Physical Journal C* 79.4 (Apr. 2019), p. 363. ISSN: 1434-6044, 1434-6052. DOI: 10.1140/epjc/s10052-019-6860-y. arXiv: 1806.09340 [p. 31].

[535] ATLAS Collaboration. “Constraints on mediator-based dark matter and scalar dark energy models using $\sqrt{s} = 13$ TeV pp collision data collected by the ATLAS detector”. *Journal of High Energy Physics* 2019.5 (May 2019), p. 142. ISSN: 1029-8479. DOI: 10.1007/JHEP05(2019)142. arXiv: 1903.01400 [pp. 26, 29, 42].

[536] Baikal-GVD Collaboration. “The Baikal-GVD neutrino telescope: First results of multi-messenger studies” (Aug. 15, 2019). arXiv: 1908.05450 [p. 36].

[537] C. Boehm et al. “How high is the neutrino floor?” *Journal of Cosmology and Astroparticle Physics* 2019.1 (Jan. 21, 2019), pp. 043–043. ISSN: 1475-7516. DOI: 10.1088/1475-7516/2019/01/043. arXiv: 1809.06385 [p. 31].

[538] M. Boudaud and M. Cirelli. “Voyager 1 $e^\pm$ Further Constrain Primordial Black Holes as Dark Matter”. *Physical Review Letters* 122.4 (Jan. 30, 2019), p. 041104. ISSN: 0031-9007, 1079-7114. DOI: 10.1103/PhysRevLett.122.041104. arXiv: 1807.03075 [p. 35].

[539] J. Buch, J. S. C. Leung, and J. Fan. “Using Gaia DR2 to Constrain Local Dark Matter Density and Thin Dark Disk”. *Journal of Cosmology and Astroparticle Physics* 2019.4 (Apr. 15, 2019), pp. 026–026. ISSN: 1475-7516. DOI: 10.1088/1475-7516/2019/04/026. arXiv: 1808.05603 [p. 3].

[540] F. Calore, M. Hütten, and M. Stref. “Gamma-ray sensitivity to dark matter subhalo modelling at high latitudes” (Oct. 30, 2019). arXiv: 1910.13722 [pp. 34, 180, 196, 300].

[541] F. Calore, T. Regimbau, and P. D. Serpico. “Probing the Fermi-LAT GeV excess with gravitational waves”. *Physical Review Letters* 122.8 (Mar. 1, 2019), p. 081103. ISSN: 0031-9007, 1079-7114. DOI: 10.1103/PhysRevLett.122.081103. arXiv: 1812.05094 [p. 34].

[542] I. Cholis, T. Linden, and D. Hooper. “A robust excess in the cosmic-ray antiproton spectrum: Implications for annihilating dark matter”. *Physical Review D* 99.10 (May 31, 2019). Publisher: American Physical Society, p. 103026. DOI: 10.1103/PhysRevD.99.103026 [p. 35].

[543] J. Coronado-Blazquez et al. “Unidentified Gamma-ray Sources as Targets for Indirect Dark Matter Detection with the Fermi-Large Area Telescope” (June 27, 2019). arXiv: 1906.11896 [pp. 180, 300].

[544] J. Coronado-Blázquez et al. “Spectral and spatial analysis of the dark matter subhalo candidates among Fermi Large Area Telescope unidentified sources”. *Journal of Cosmology and Astroparticle Physics* 2019.11 (Nov. 28, 2019), pp. 045–045. ISSN: 1475-7516. DOI: 10.1088/1475-7516/2019/11/045. arXiv: 1910.14429 [p. 180].

[545] CTA Consortium. “Science with the Cherenkov Telescope Array” (Mar. 2019). DOI: 10.1142/10986. arXiv: 1709.07997 [pp. 33, 201].

[546] A. Cuoco et al. “Scrutinizing the evidence for dark matter in cosmic-ray antiprotons”. *Physical Review D* 99.10 (May 23, 2019). Publisher: American Physical Society, p. 103014. DOI: 10.1103/PhysRevD.99.103014 [p. 35].

[547] M. S. Delos. “Evolution of dark matter microhalos through stellar encounters”. *Physical Review D* 100.8 (Oct. 18, 2019), p. 083529. ISSN: 2470-0010, 2470-0029. DOI: 10.1103/PhysRevD.100.083529. arXiv: 1907.13133 [pp. 136, 158, 170, 176, 299].

[548] M. S. Delos. “Tidal evolution of dark matter annihilation rates in subhalos”. *Physical Review D* 100.6 (Sept. 3, 2019), p. 063505. ISSN: 2470-0010, 2470-0029. DOI: 10.1103/PhysRevD.100.063505. arXiv: 1906.10690 [p. 136].

[549] B. Diemer and M. Joyce. “An accurate physical model for halo concentrations”. *The Astrophysical Journal* 871.2 (Jan. 30, 2019), p. 168. ISSN: 1538-4357. DOI: 10.3847/1538-4357/aafad6. arXiv: 1809.07326 [pp. 140, 141].

[550] EHT Collaboration. “First M87 Event Horizon Telescope Results. I. The Shadow of the Supermassive Black Hole” (June 26, 2019). DOI: 10.3847/2041-8213/ab0ec7. arXiv: 1906.11238 [p. 19].

[551] Fermi-LAT Collaboration. “Fermi Large Area Telescope Fourth Source Catalog” (Feb. 26, 2019). arXiv: 1902.10045 [pp. 180, 196, 200, 211, 300].

[552] R. Garani, Y. Genolini, and T. Hambye. “New Analysis of Neutron Star Constraints on Asymmetric Dark Matter”. *Journal of Cosmology and Astroparticle Physics* 2019.5 (May 21, 2019), pp. 035–035. ISSN: 1475-7516. DOI: 10.1088/1475-7516/2019/05/035. arXiv: 1812.08773 [p. 27].

[553] D. Glawion et al. “Unidentified Fermi Objects in the view of H.E.S.S. – Possible Dark Matter Clumps” (Sept. 3, 2019). arXiv: 1909.01072 [p. 180].

[554] A. Ibarra, B. J. Kavanagh, and A. Rappelt. “Impact of substructure on local dark matter searches” (Aug. 2, 2019). arXiv: 1908.00747 [pp. 30, 90].

[555] F. Kahlhoefer et al. “Diversity in density profiles of self-interacting dark matter satellite halos” (Apr. 23, 2019). DOI: 10.1088/1475-7516/2019/12/010. arXiv: 1904.10539 [p. 18].

[556] T. Kelley et al. “Phat ELVIS: The inevitable effect of the Milky Way’s disk on its dark matter subhaloes”. *Monthly Notices of the Royal Astronomical Society* 487.3 (Aug. 11, 2019), pp. 4409–4423. ISSN: 0035-8711, 1365-2966. DOI: 10.1093/mnras/stz1553. arXiv: 1811.12413 [p. 180].

[557] Y. J. Ko et al. “Comparison between DAMA/LIBRA and COSINE-100 in the light of Quenching Factors”. *Journal of Cosmology and Astroparticle Physics* 2019.11 (Nov. 11, 2019), pp. 008–008. ISSN: 1475-7516. DOI: 10.1088/1475-7516/2019/11/008. arXiv: 1907.04963 [p. 31].

[558] R. K. Leane and T. R. Slatyer. “Dark Matter Strikes Back at the Galactic Center” (Apr. 17, 2019). DOI: 10.1103/PhysRevLett.123.241101. arXiv: 1904.08430 [p. 33].

[559] LIGO and Virgo Collaborations. “GWTC-1: A Gravitational-Wave Transient Catalog of Compact Binary Mergers Observed by LIGO and Virgo during the First and Second Observing Runs”. *Physical Review X* 9.3 (Sept. 4, 2019), p. 031040. ISSN: 2160-3308. DOI: 10.1103/PhysRevX.9.031040. arXiv: 1811.12907 [p. 28].

[560] H. Liu et al. “Reviving Millicharged Dark Matter for 21-cm Cosmology”. *Physical Review D* 100.12 (Dec. 16, 2019), p. 123011. ISSN: 2470-0010, 2470-0029. DOI: 10.1103/PhysRevD.100.123011. arXiv: 1908.06986 [p. 27].

[561] D. J. E. Marsh and J. C. Niemeyer. “Strong Constraints on Fuzzy Dark Matter from Ultrafaint Dwarf Galaxy Eridanus II”. *arXiv:1810.08543 [astro-ph, physics:hep-ph]* (July 30, 2019). DOI: 10.1103/PhysRevLett.123.051103. arXiv: 1810.08543 [p. 24].

[562] G. Moultaka, M. Rausch de Traubenberg, and D. Tant. “Low energy supergravity revisited (I)”. *International Journal of Modern Physics A* 34.1 (Jan. 10, 2019), p. 1950004. ISSN: 0217-751X, 1793-656X. DOI: 10.1142/S0217751X19500040 [p. 93].

[563] G. Ogiya et al. “DASH: a library of dynamical subhalo evolution”. *Monthly Notices of the Royal Astronomical Society* 485.1 (May 1, 2019), pp. 189–202. ISSN: 0035-8711, 1365-2966. DOI: 10.1093/mnras/stz375 [p. 136].

[564] J. L. Ouellet et al. “First Results from ABRACADABRA-10 cm: A Search for Sub-μeV Axion Dark Matter”. *Physical Review Letters* 122.12 (Mar. 29, 2019), p. 121802. ISSN: 0031-9007, 1079-7114. DOI: 10.1103/PhysRevLett.122.121802. arXiv: 1810.12257 [p. 31].

[565] V. Poulin et al. “Early Dark Energy Can Resolve The Hubble Tension”. *Physical Review Letters* 122.22 (June 4, 2019), p. 221301. ISSN: 0031-9007, 1079-7114. DOI: 10.1103/PhysRevLett.122.221301. arXiv: 1811.04083 [p. 14].

[566] V. H. Robles et al. “The Milky Way’s halo and subhaloes in self-interacting dark matter”. *Monthly Notices of the Royal Astronomical Society* 490.2 (Dec. 1, 2019), pp. 2117–2123. ISSN: 0035-8711, 1365-2966. DOI: 10.1093/mnras/stz2345 [p. 18].

[567] M. Schumann. “Direct Detection of WIMP Dark Matter: Concepts and Status”. *Journal of Physics G: Nuclear and Particle Physics* 46.10 (Oct. 1, 2019), p. 103003. ISSN: 0954-3899, 1361-6471. DOI: 10.1088/1361-6471/ab2ea5. arXiv: 1903.03026 [pp. 29, 30].

[568] L. Verde, T. Treu, and A. G. Riess. “Tensions between the Early and the Late Universe”. *Nature Astronomy* 3.10 (Oct. 2019), pp. 891–895. ISSN: 2397-3366. DOI: 10.1038/s41550-019-0902-0. arXiv: 1907.10625 [p. 14].

[569] M. Vogelsberger et al. “Cosmological Simulations of Galaxy Formation”. *arXiv:1909.07976 [astro-ph]* (Dec. 19, 2019). arXiv: 1909.07976 [pp. 17, 96].

[570] Y.-M. Zhong et al. “A New Mask for An Old Suspect: Testing the Sensitivity of the Galactic Center Excess to the Point Source Mask” (Nov. 27, 2019). DOI: 10.1103/PhysRevLett.124.231103. arXiv: 1911.12369 [p. 33].

[571] K. N. Abazajian et al. “Strong constraints on thermal relic dark matter from Fermi-LAT observations of the Galactic Center” (Aug. 20, 2020). DOI: 10.1103/PhysRevD.102.043012. arXiv: 2003.10416 [p. 34].

[572] G. F. Abellan et al. “Hints for decaying dark matter from S_8 measurements” (Aug. 21, 2020). arXiv: 2008.09615 [p. 15].

[573] R. Ahumada et al. “The Sixteenth Data Release of the Sloan Digital Sky Surveys: First Release from the APOGEE-2 Southern Survey and Full Release of eBOSS Spectra” (May 11, 2020). DOI: 10.3847/1538-4365/ab929e. arXiv: 1912.02905 [p. 12].

[574] E. Aprile et al. “Observation of Excess Electronic Recoil Events in XENON1T” (June 17, 2020). arXiv: 2006.09721 [pp. 32, 38].

[575] A. Banihashemi, N. Khosravi, and A. H. Shirazi. “Ups and Downs in Dark Energy: phase transition in dark sector as a proposal to lessen cosmological tensions”. *Physical Review D* 101.12 (June 19, 2020), p. 123521. ISSN: 2470-0010, 2470-0029. DOI: 10.1103/PhysRevD.101.123521. arXiv: 1808.02472 [p. 14].

[576] C. Boehm et al. “Light new physics in XENON1T”. *Physical Review D* 102.11 (Dec. 7, 2020), p. 115013. ISSN: 2470-0010, 2470-0029. DOI: 10.1103/PhysRevD.102.115013. arXiv: 2006.11250 [p. 31].

[577] S. Bohr et al. “ETHOS – An effective parametrization and classification for structure formation: the non-linear regime at $z\gtrsim5$”. *Monthly Notices of the Royal Astronomical Society* 498.3 (Sept. 22, 2020), pp. 3403–3419. ISSN: 0035-8711, 1365-2966. DOI: 10.1093/mnras/staa2579. arXiv: 2006.01842 [p. 15].

[578] M. Boudaud et al. “AMS-02 antiprotons’ consistency with a secondary astrophysical origin”. *Physical Review Research* 2.2 (Apr. 9, 2020), p. 023022. ISSN: 2643-1564. DOI: 10.1103/PhysRevResearch.2.023022. arXiv: 1906.07119 [p. 35].

[579] B. Carr, S. Clesse, and J. García-Bellido. “Primordial black holes from the QCD epoch: Linking dark matter, baryogenesis and anthropic selection” (Dec. 15, 2020). arXiv: 1904.02129 [p. 28].

[580] B. Carr et al. “Constraints on Primordial Black Holes” (Feb. 27, 2020). arXiv: 2002.12778 [p. 28].

[581] CTA Consortium. “Pre-construction estimates of the Cherenkov Telescope Array sensitivity to a dark matter signal from the Galactic centre” (July 31, 2020). arXiv: 2007.16129 [pp. 32, 34, 215].

[582] V. De Luca et al. “Primordial Black Holes Confront LIGO/Virgo data: Current situation”. *Journal of Cosmology and Astroparticle Physics* 2020.6 (June 22, 2020), pp. 044–044. ISSN: 1475-7516. DOI: 10.1088/1475-7516/2020/06/044. arXiv: 2005.05641 [p. 28].

[583] L. Di Luzio et al. “Solar axions cannot explain the XENON1T excess”. *Physical Review Letters* 125.13 (Sept. 24, 2020), p. 131804. ISSN: 0031-9007, 1079-7114. DOI: 10.1103/PhysRevLett.125.131804. arXiv: 2006.12487 [p. 32].

[584] R. Errani and J. F. Navarro. "The asymptotic tidal remnants of cold dark matter subhalos". *arXiv:2011.07077 [astro-ph]* (Nov. 13, 2020). arXiv: 2011.07077 [pp. 143, 176].

[585] R. Errani and J. Peñarrubia. "Can tides disrupt cold dark matter subhaloes?" *Monthly Notices of the Royal Astronomical Society* 491.4 (Feb. 1, 2020), pp. 4591–4601. ISSN: 0035-8711, 1365-2966. DOI: 10.1093/mnras/stz3349. arXiv: 1906.01642 [pp. 143, 176, 299].

[586] G. Facchinetti, J. Lavalle, and M. Stref. "Statistics for dark matter subhalo searches in gamma rays from a kinematically constrained population model. I: Fermi-LAT-like telescopes" (July 23, 2020). arXiv: 2007.10392 [pp. 181, 235].

[587] A. Hall, A. D. Gow, and C. T. Byrnes. "Bayesian analysis of LIGO-Virgo mergers: Primordial vs. astrophysical black hole populations". *Physical Review D* 102.12 (Dec. 11, 2020), p. 123524. ISSN: 2470-0010, 2470-0029. DOI: 10.1103/PhysRevD.102.123524. arXiv: 2008.13704 [p. 28].

[588] T. Hambye and L. Vanderheyden. "Minimal self-interacting dark matter models with light mediator". *Journal of Cosmology and Astroparticle Physics* 2020.5 (May 4, 2020), pp. 001–001. ISSN: 1475-7516. DOI: 10.1088/1475-7516/2020/05/001. arXiv: 1912.11708 [p. 27].

[589] C. Heymans et al. "KiDS-1000 Cosmology: Multi-probe weak gravitational lensing and spectroscopic galaxy clustering constraints" (Dec. 8, 2020). arXiv: 2007.15632 [p. 14].

[590] T. Ishiyama and S. Ando. "The Abundance and Structure of Subhaloes near the Free Streaming Scale and Their Impact on Indirect Dark Matter Searches". *Monthly Notices of the Royal Astronomical Society* 492.3 (Mar. 1, 2020), pp. 3662–3671. ISSN: 0035-8711, 1365-2966. DOI: 10.1093/mnras/staa069. arXiv: 1907.03642 [p. 142].

[591] K. Jedamzik. "Evidence for primordial black hole dark matter from LIGO/Virgo merger rates" (July 13, 2020). arXiv: 2007.03565 [p. 28].

[592] K. Jedamzik. "Primordial Black Hole Dark Matter and the LIGO/Virgo observations". *Journal of Cosmology and Astroparticle Physics* 2020.9 (Sept. 14, 2020), pp. 022–022. ISSN: 1475-7516. DOI: 10.1088/1475-7516/2020/09/022. arXiv: 2006.11172 [p. 28].

[593] P. Mijakowski and The Super-Kamiokande Collaboration. "Dark Matter Searches at Super-Kamiokande". *Journal of Physics: Conference Series* 1342 (Jan. 2020), p. 012075. ISSN: 1742-6588, 1742-6596. DOI: 10.1088/1742-6596/1342/1/012075 [p. 36].

[594] H. Nishikawa, K. K. Boddy, and M. Kaplinghat. "Accelerated core collapse in tidally stripped self-interacting dark matter halos" (Mar. 9, 2020). DOI: 10.1103/PhysRevD.101.063009. arXiv: 1901.00499 [p. 18].

[595] Particle Data Group et al. "Review of Particle Physics". *Progress of Theoretical and Experimental Physics* 2020.8 (Aug. 14, 2020), p. 083C01. ISSN: 2050-3911. DOI: 10.1093/ptep/ptaa104 [p. 21].

[596] C. Pérez de los Heros. "Status, Challenges and Directions in Indirect Dark Matter Searches". *Symmetry* 12.10 (Oct. 2020). Number: 10 Publisher: Multidisciplinary Digital Publishing Institute, p. 1648. DOI: 10.3390/sym12101648 [p. 32].

[597] M. Petac. "Equilibrium axisymmetric halo model for the Milky Way and its implications for direct and indirect DM searches" (Aug. 25, 2020). arXiv: 2008.11172 [pp. 5, 6].

[598] H. Ramani, T. Trickle, and K. M. Zurek. "Observability of Dark Matter Substructure with Pulsar Timing Correlations". *Journal of Cosmology and Astroparticle Physics* 2020.12 (Dec. 17, 2020), pp. 033–033. ISSN: 1475-7516. DOI: 10.1088/1475-7516/2020/12/033. arXiv: 2005.03030 [p. 91].

[599] O. Sameie et al. "Self-Interacting Dark Matter Subhalos in the Milky Way's Tides" (Apr. 6, 2020). DOI: 10.1103/PhysRevLett.124.141102. arXiv: 1904.07872 [p. 18].

[600] A. Schneider, S. Giri, and J. Mirocha. "A halo model approach for the 21-cm power spectrum at cosmic dawn" (Nov. 24, 2020). arXiv: 2011.12308 [p. 37].

[601] V. Shtabovenko, R. Mertig, and F. Orellana. "FeynCalc 9.3: New features and improvements". *Computer Physics Communications* 256 (Nov. 2020), p. 107478. ISSN: 00104655. DOI: 10.1016/j.cpc.2020.107478 [p. 246].

[602] C. Skordis and T. Zlosnik. "A new relativistic theory for Modified Newtonian Dynamics" (Dec. 17, 2020). arXiv: 2007.00082 [pp. 20, 38].

[603] The Planck Collaboration. "*Planck* 2018 results: X. Constraints on inflation". *Astronomy & Astrophysics* 641 (Sept. 2020), A10. ISSN: 0004-6361, 1432-0746. DOI: 10.1051/0004-6361/201833887 [p. 48].

[604] The Planck Collaboration et al. "*Planck* 2018 results: I. Overview and the cosmological legacy of *Planck*". *Astronomy & Astrophysics* 641 (Sept. 2020), A1. ISSN: 0004-6361, 1432-0746. DOI: 10.1051/0004-6361/201833880 [pp. 8, 9].

[605] M. Aker et al. "First direct neutrino-mass measurement with sub-eV sensitivity". *arXiv:2105.08533 [hep-ex, physics:nucl-ex]* (May 18, 2021). arXiv: 2105.08533 [p. 22].

[606] T. Binder et al. "DRAKE: Dark matter Relic Abundance beyond Kinetic Equilibrium" (Mar. 2, 2021). arXiv: 2103.01944 [p. 83].

[607] G. Franciolini et al. "Evidence for primordial black holes in LIGO/Virgo gravitational-wave data". *arXiv:2105.03349 [astro-ph, physics:gr-qc, physics:hep-ph]* (May 7, 2021). arXiv: 2105.03349 [p. 28].

[608] L. Hui. "Wave Dark Matter" (Jan. 27, 2021). arXiv: 2101.11735 [p. 19].

[609] A. Paranjape and R. K. Sheth. "The radial acceleration relation in a ΛCDM universe" (Feb. 25, 2021). arXiv: 2102.13116 [p. 17].

[610] D. Baumann. "Comsomogy, Part III Mathematical Tripos". *a* [pp. 97, 102].

[611] D. Baumann. "Physics of the Cosmic Microwave Background". *b* [pp. 10, 97–99].

[612] T. Lacroix et al. "Classification of targets for gamma-ray dark matter searches with velocity-dependent annihilation and substructure boost I: detailed predictions". *in prep.* [pp. 225, 229, 231].

Abstract

The problem of the missing mass of the Universe is one of the most puzzling conundrums of modern physics. Assuming that it stems from the existence of yet unknown dark matter (DM) particles, one can probe the cosmos in the hope of detecting unambiguous signatures thereof. The properties of cold DM (CDM) particle candidates lead to the prediction that gravitational structures form on scales much smaller than typical galaxies, below the resolution scope of current cosmological simulations. This clustering translates into a large population of subhalos in galaxies, hence in the Milky Way. Only analytical models can encompass and describe their full distribution. My work is centred upon building a theoretically consistent and dynamically constrained subhalo population model. This relies mostly on three ingredients: the minimal subhalo mass, the cosmological mass function, and dynamical effects. I start from a simplified model of thermally produced dark matter (with scalar, pseudo-scalar, vector and axial-vector interactions with standard model particles). I classify models in terms of small-scale cut-off on the matter power spectrum, which is directly related to the minimal halo mass, making explicit the role of velocity dependence in the interaction processes. Secondly, I improve on the determination of the cosmological subhalo mass function by deriving it from the excursion set theory and a merger tree, while it was previously calibrated on simulations. Thirdly, I incorporate new dynamical effects by analytically studying the impact of stellar encounters susceptible of occurring in galactic discs. Besides, I illustrate an application of this model for indirect detection experiments looking for traces of DM annihilation in the Milky Way. In light of the 1525 unassociated point sources discovered by the Fermi-LAT collaboration, I give prospects for the detection of point-like subhalos as gamma-ray sources with Fermi-LAT-like and CTA-like instruments. I also shortly discuss the impact of additional effects, like the Sommerfeld effect.

Résumé

Le problème de masse manquante de l'univers est l'une des plus grandes énigmes de la cosmologie et de la physique fondamentale moderne. En supposant qu'elle soit résolue par l'existence de particules exotiques de matière noire, nous pouvons sonder le cosmos à la recherche des signatures spécifiques que ces dernières seraient susceptibles de laisser. Les candidats de type "particule" pour la matière noire froide ont des propriétés donnant lieu à la formation de structures gravitationnelles à des échelles bien plus petites que celles des halos galactiques typiques, hors de portée des simulations cosmologiques actuelles. Cette structuration, prédite théoriquement et dérivant des propriétés d'interactions des particules supposées de matière noire froide, se traduit en principe par l'existence d'un grand nombre de sous-halos composés exclusivement de matière noire dans des galaxies telles que la Voie Lactée. Seuls des modèles analytiques permettent alors de décrire leur distribution dans ses détails. Mon travail est centré sur le développement d'un tel modèle. Ce modèle est construit en respectant un principe d'auto-cohérence théorique auquel s'ajoutent des contraintes dynamiques, et repose principalement sur trois ingrédients : la masse minimale des sous-halos, leur fonction de masse cosmologique, et l'adjonction d'effets dynamiques dépendant de l'environnement. Le premier de ces éléments est déterminé dans le cadre d'un scénario simplifié de matière noire produite thermiquement dans l'univers primordial (particules exotiques dotées d'interactions scalaires, pseudo-scalaires, vectorielles et axiales aux particules du modèle standard). Je détermine l'impact des différents paramètres de ce scénario sur l'échelle de coupure prédite dans le spectre de puissance de la matière, qui se trouve corrélée à la masse minimale des sous-halos. En particulier, je rends explicite le rôle de la dépendance en vitesse des taux d'interactions. En second lieu, j'améliore la détermination de la fonction de masse des sous-halos en la calculant à partir d'une théorie statistique de formation des structures et d'un arbre de fusion. Cela permet de s'affranchir d'une étape de calibration sur des simulations cosmologiques qui représentait une forte limitation du modèle avant ce travail. De plus, j'ajoute de nouveaux effets dynamiques en déterminant, de façon analytique, les effets de marée gravitationnelle induits par les rencontres individuelles successives des sous-halos avec les étoiles du disque galactique. Pour terminer, j'illustre une application de ce modèle de population de sous-halos en ré-évaluant les prédictions de signaux de matière noire pour des expériences de détection indirecte. Je donne notamment des perspectives plus réalistes pour la détection de sous-halos ponctuels comme sources de rayons gamma avec des instruments de types Fermi-LAT et CTA, et pour l'association potentielle de certaines des 1525 sources non-associées figurant actuellement dans le catalogue de Fermi-LAT avec des sous-structures de matière noire. Je discute enfin très brièvement l'impact d'autres effets plus subtils associés à des interactions entre particules à longue portée, comme l'effet Sommerfeld.